Study of the anisotropic electronic, and atomic structures of novel layered materials using polarised x-ray absorption spectroscopy.

Sinéad Rowe

A thesis submitted in accordance of the requirements for the degree of Doctor of Philosophy at the University of Kent

School of Physical Sciences
University of Kent
25th March 2020

Abstract

Charge ordering in materials is often paired with interesting electronic properties, such as charge/spin density waves (C/SDW) or Mott-insulator transitions. It also leads to many interesting ground states, such as spin-Peierls, antiferromagnetism, and superconductivity. This has lead to an increased interest in the physics field to study materials that exhibit these properties.
The materials presented in this thesis are interesting due to their charge ordering properties. Such as the predicted CDW in $M_2Mo_6Se_6$ (M=Rb,Tl), this has been investigated with diffraction but due to suspected breaking in the long range order it has not been experimentally observed. Or the elusive nature of the Mott insulator transition in Ca_2RuO_4, where it is not clear whether the driving force of the transition is orbital selective or not.
The work presented in this thesis will focus on x-ray absorption experiments. One of the main properties of synchrotron radiation is that the x-rays are produced linearly polarised in the plane of the orbit of the electron. By taking advantage of this, more information can be obtained from an x-ray absorption spectroscopy (XAS) experiment than by the standard application used to measure powder samples.
In this work single crystals have been measured, allowing for more direct comparisons to be made with other techniques, such as diffraction. By measuring the x-ray absorption at different angles between the polarisation of the beam and a specific crystallographic axis, it is possible to directly measure anisotropic changes in the structure of a sample. This is very useful when investigating transitions which are paired with an angular change, such as a Jahn-Teller distortion.
This technique takes advantage of the adaptability of XAS beamlines, where the only requirements are a linearly polarised beam and the ability to rotate the sample. When using a bending magnet beamline with a highly focused beam it is possible to measure small crystals ($\sim 500\mu m$ x $500\mu m$). This is an advantage as some single crystals are difficult to grow to a large size.
This work will present the measurements and analysis of three different materials using Polarised XAS (P-XAS), $Sr_2MnCu_{1.5-\delta}S_2O_2$, $M_2Mo_6Se_6$ (M=Rb, Tl), Ca_2RuO_4. The advantages and difficulties of this technique and analysis method will be discussed, along with the information gained about these materials using this technique.
A general weighting factor is introduced which increases the usefulness of P-XAS measurements, allowing for more freedom in the fitting process. The $Sr_2MnCu_{1.5-\delta}S_2O_2$ chapter shows that P-XAS provides a greater sensitivity than powder XAS. The analysis of the $M_2Mo_6Se_6$ data provides evidence of a structural transition that may be due to the presence of a CDW. The Ca_2RuO_4 chapter shows how P-XAS can be used to directly observe the nature of a Jahn-Teller distortion.

Acknowledgements

I would like to thank my supervisor Dr Silvia Ramos for all of the support during my PhD, especially her patience during my write up. She has been there for me every step of the way and without her encouragement I don't believe I would have made it this far.
I would also like to thank Dr Giannantonio Cibin for all the help he has given us during the experimental time of my PhD. He has been an integral part of our experimental group, and has also provided much needed help and advice for the analysis portion of my work.
Thank you to Laura Swansbury, for being my friend and confidant during our PhD time (as well as during our undergrad years). She has always been there to lend an ear, and to watch films and tv with as we try to distract ourselves from the stress of work.
Thank you to Philip Whittlesea who was very helpful whenever I had any coding questions. Also thank you for helping me make one of the plots I have used in this thesis.
I would like to thank my Mom for always supporting me, and always encouraging me to not give up when things got hard. My Dad, who always encouraged me throughout this process. My uncle Johnny, who has supported me so much during my PhD.
I would like to thank my friend George Whittaker for reminding me of my quote, and who's endless questions on my work has helped me with viva practice.
I would like to thank the team at B18, Diamond Light Source, U.K., where two of my experiments occurred. They were all very helpful during our experimental time.
I would like to thank the team at XMaS, European Synchrotron Research Facility, France, where one of my experiments took place. Everyone was very helpful during our experimental time. I would especially like to thank Laurence Bouchenoire for helping me with understanding the beamline set up.

Authors declaration

I declare that the work presented in this thesis is, unless otherwise stated, the result of my own research, which was undertaken in the School of Physical Sciences at the University of Kent. The work was carried out in accordance with the regulations of the University of Kent. No part of this thesis has been presented to any other University for examination either in the United Kingdom or overseas.

Sinéad Rowe

25th March 2020

“Hey presto, here are the results...
論文を書きはたいへんです
저는 이것은 명제 를 좋아지않입니다”

Sinéad Rowe (審艶露, 신앤 로) Aged 10 (十歳でした)

Contents

1 Introduction. 1

1.1 Charge ordering: properties and materials. 1

1.1.1 Examples of physical effects due to charge ordering, relevant to this work. 2

1.1.2 Materials investigated for this thesis. 3

1.2 Historical background of synchrotron radiation and x-ray absorption spectroscopy. 6

1.2.1 Conventional x-ray absorption spectroscopy experiments. 9

1.2.2 Polarised x-ray absorption spectroscopy techniques. 12

1.3 Complementary techniques for single crystal work 13

1.4 Chapter summary and thesis goals 14

2 Experimental methods. 15

2.1 Synchrotron radiation 15

2.2 X-ray absorption spectroscopy experiments 19

2.3 Linearly polarised x-ray absorption spectroscopy experiments 22

2.4 Scanning electron microscope experiments 24

2.5 Single crystal x-ray diffraction 27

2.6 Chapter summary 27

3 XAS: Theoretical concepts and data analysis 28

3.1 Theoretical concepts 28

3.1.1 General x-ray absorption spectroscopy theory 28

3.1.2 Dipole approximation and simplification of x-ray absorption spectroscopy due to symmetry 31

3.1.3 EXAFS equation: single scattering 33

3.1.4 EXAFS equation for single crystal measurements, weighting factor 36

3.1.5 Multiple scattering in EXAFS 41

3.2 Data analysis 42

3.2.1 Isolating XANES and $\chi(k)$ 42

3.2.2 Self-absorption correction 44

3.2.3 Fitting $\chi(k)$ 52

3.2.4 Evaluating the model 53

3.3 Chapter summary 54

4 Investigating the mobility of Cu ions in $Sr_2MnCu_{1.5-x}S_2O_2$ using both powder XAS and single crystal P-XAS. 55

4.1 Introduction 55

4.2 SEM images 58

4.3 $Sr_2MnCu_{1.5-x}S_2O_2$(x = 0.0, 0.2, 0.3) powder XAS 62

4.3.1 Experimental set-up 62

4.3.2 Powder XAS results . . . 63
4.4 $Sr_2MnCu_{1.5}S_2O_2$ single crystal P-XAS . . . 94
4.4.1 Experimental set-up . . . 94
4.4.2 Single crystal XAS results . . . 95
4.5 Discussion . . . 124
4.6 Conclusion . . . 127

5 Investigating structural changes due to a CDW in $M_2Mo_6Se_6$ (M=Rb, Tl) using single crystal P-XAS. 129
5.1 Introduction . . . 129
5.2 SEM images . . . 131
5.3 $M_2Mo_6Se_6$ (M=Rb, Tl) single crystal P-XAS . . . 135
5.3.1 Experimental set up . . . 135
5.3.2 $Rb_2Mo_6Se_6$ results . . . 138
5.3.3 $Tl_2Mo_6Se_6$ results . . . 157
5.4 Discussion . . . 175
5.5 Conclusion . . . 179

6 Investigating Jahn-Teller distortions in Ca_2RuO_4 using single crystal P-XAS. 180
6.1 Introduction . . . 180
6.2 SEM images . . . 182
6.3 Ca_2RuO_4 single crystal P-XAS . . . 185
6.3.1 Experimental set-up . . . 185
6.3.2 Ca_2RuO_4 results . . . 187
6.4 Discussion . . . 209
6.5 Conclusion . . . 211

7 Conclusion. 213

8 Future work. 218

Bibliography 221

A Theoretical methods calculations and codes used. 235
A.1 General XAS theory. . . . 235
A.2 Dipole approximation calculations. . . . 238
A.3 Self-absorption correction. . . . 245
A.4 Building XAS code. . . . 251
A.5 Self-absorption correction code. . . . 253

B $M_2Mo_6Se_6$ plots. 272
B.1 $Rb_2Mo_6Se_6$ . . . 272
B.1.1 XANES . . . 272
B.1.2 EXAFS . . . 272
B.1.3 Fits of EXAFS . . . 273
B.2 $Tl_2Mo_6Se_6$ . . . 274
B.2.1 XANES . . . 274
B.2.2 EXAFS . . . 275
B.2.3 Fits of EXAFS . . . 277

List of Figures

1.1 Examples of typical charger order patterns, in a 2 dimensional scenario. 1
1.2 Structure of $Sr_2MnCu_{1.5}S_2O_2$. 4
1.3 Structure of $M_2Mo_6Se_6$. 5
1.4 Structure of Ca_2RuO_4. 6
1.5 Photograph of the General Electric synchrotron accelerator. 7
1.6 Schematic of the trajectory of an electron in a circle, and the resulting radiation cones. 8
1.7 Normalised intensities of the horizontal and veritcal components of the x-ray polarisation produced from a bending magnet. 9
1.8 Simple schematic of the absorption edge nomenclature. 10
1.9 Example of K-edge XAS, (Mn K-edge of $Sr_2MnCu_{1.2}S_2O_2$ at 260K)the different regions have been labelled, and the transitions that contribute to these regions have been stated. 11

2.1 Simple schematic of the essential components of a synchrotron. 16
2.2 Simple schematic of the set up of the beamline B18 at Diamond Light Source, Oxfordshire, UK. 17
2.3 Experimental and control hutches, respectively, at the beamline B18 at Diamond Light Source. 17
2.4 Schematic of emission device and spectral brightness. 18
2.5 An internal view of a bending magnet beamline. 18
2.6 Quadrupole and sextupole magnets, used at the European Synchrotron Radiation Facility. 19
2.7 Schematic of a transmission detection XAS experiment. 21
2.8 Schematic of a fluorescence detection XAS experiment. 21
2.9 Simple schematic of the sample set up of a P-XAS experiment. 23
2.10 View of an anisotropic structure ($Sr_2MnCu_{1.5}S_2O_2$) with the x-ray polarisation parallel and perpendicular to the c-axis. 23
2.11 Schematic of a scanning electron microscope. 24
2.12 Interaction volume of the specimen during an SEM experiment. 25
2.13 EDX spectrum of the mineral crust of the vent shrimp Rimicaris exoculata. 26

3.1 A simple schematic of the process occurring during an x-ray absorption event. 29
3.2 A simple schematic of the scattering process occurring during an XAS experiment. 30
3.3 XAS absorption of the Cu K-edge of the $Sr_2MnCu_{1.5}S_2O_2$ powder sample. 30
3.4 Orientation of the incoming x-rays. 31
3.5 Orientation of the scattering paths and the incoming x-rays. 37
3.6 Comparing the paths produced by using the weighting factor and the polarisation function in FEFF. 39

3.7 Absorption of the Se K-edge, of $Rb_2Mo_6Se_6$, data at 90° and 4K. The background function, pre and post edges are shown. 43
3.8 EXAFS, (a), and FT-EXAFS, (b), of the Cu K-edge, of $Sr_2MnCu_{1.5}S_2O_2$, data at 15° and 300K, without spline. 44
3.9 EXAFS, (a), and FT-EXAFS, (b), of the Cu K-edge, of $Sr_2MnCu_{1.5}S_2O_2$, data at 15° and 300K, with spline. 44
3.10 Geometry used in calculating self-absorption correction in XAS. 45
3.11 XANES of the Cu K-edge $Sr_2MnCu_{1.5}S_2O_2$, at 15° (a) and 75° (b), before and after the correction. 50
3.12 EXAFS of the Cu K-edge $Sr_2MnCu_{1.5}S_2O_2$, at 15° (a) and 75° (b), before and after the correction. 51

4.1 Model of the magnetic ordering in $Sr_2MnCu_{1.5}S_2O_2$. 56
4.2 Structure of $Sr_2MnCu_{1.5}S_2O_2$, in the orthorhombic, (a), and tetragonal, (b), phase. 58
4.3 SEM image of a chip from the single crystal $Sr_2MnCu_{1.5}S_2O_2$. 59
4.4 Spectra measured from the homogenous region of $Sr_2MnCu_{1.5}S_2O_2$. . . 60
4.5 Spectra measured from the impurities observed in $Sr_2MnCu_{1.5}S_2O_2$. . . 61
4.6 Spectra measured from the carbon sticky pad used to hold the sample. 62
4.7 XANES of the Cu K-edge for each sample, measured at 10K and 260K. There is no visible energy shift between the samples. 64
4.8 XANES, (a), and first derivative, (b), of the Cu K-edge of $Sr_2MnCu_{1.5}S_2O_2$, for different temperatures. 65
4.9 XANES, (a), and first derivative, (b), of the Cu K-edge of $Sr_2MnCu_{1.3}S_2O_2$, for different temperatures. 66
4.10 XANES, (a), and first derivative, (b), of the Cu K-edge of $Sr_2MnCu_{1.2}S_2O_2$, for different temperatures. 67
4.11 XANES of the Mn K-edge of all three samples. 68
4.12 EXAFS, (a), and FT-EXAFS, (b), of the Cu K-edge of the $Sr_2MnCu_{1.5}S_2O_2$ sample, at different temperatures. 70
4.13 EXAFS, (a), and FT-EXAFS, (b), of the Cu K-edge of the $Sr_2MnCu_{1.3}S_2O_2$ sample, at different temperatures. 71
4.14 EXAFS, (a), and FT-EXAFS, (b), of the Cu K-edge of the $Sr_2MnCu_{1.2}S_2O_2$ sample, at different temperatures. 72
4.15 EXAFS, (a), and FT-EXAFS, (b), of the Cu K-edge of all three samples, at the highest and lowest temperature measured. 73
4.16 EXAFS, (a), and FT-EXAFS, (b), of the Mn K-edge of all three samples. 75
4.17 The Debye-Waller values for each path used in the fit of the tetragonal structure to the Cu K-edge measurement of $Sr_2MnCu_{1.5}S_2O_2$ sample. . 81
4.18 The Debye-Waller values for each path used in the fit of the tetragonal structure to the Cu K-edge measurement of the $Sr_2MnCu_{1.3}S_2O_2$ sample. 82
4.19 The Debye-Waller values for each path used in the fit of the tetragonal structure to the Cu K-edge measurement of the $Sr_2MnCu_{1.2}S_2O_2$ sample. 82
4.20 The Debye-Waller values for both Cu-Cu scattering paths used in the fit of the tetragonal structure to the Cu K-edge measurement of the $Sr_2MnCu_{1.5-x}S_2O_2$ samples. 83
4.21 Fit of the Cu K-edge of the $Sr_2MnCu_{1.5}S_2O_2$ sample, and the individual paths, in R space, at 10K (a) and 260K (b). 84
4.22 Fit of the Cu K-edge of the $Sr_2MnCu_{1.3}S_2O_2$ sample, and the individual paths, in R space, at 10K (a) and 260K (b). 85

4.23 Fit of the Cu K-edge of the $Sr_2MnCu_{1.2}S_2O_2$ sample, and the individual paths, in R space, at 10K (a) and 260K (b). 85
4.24 Fit of the Cu K-edge of the $Sr_2MnCu_{1.5}S_2O_2$ sample, in q space(a) and R space (b). 86
4.25 Fit of the Cu K-edge of the $Sr_2MnCu_{1.3}S_2O_2$ sample, in q space (a) and R space (b). 87
4.26 Fit of the Cu K-edge of the $Sr_2MnCu_{1.2}S_2O_2$ sample, in q space (a) and R space (b). 88
4.27 Fit of the Mn K-edge of the $Sr_2MnCu_{1.5}S_2O_2$ sample, in q space(a) and R space (b). 91
4.28 Fit of the Mn K-edge of the $Sr_2MnCu_{1.3}S_2O_2$ sample, in q space (a) and R space (b). 92
4.29 Fit of the Mn K-edge of the $Sr_2MnCu_{1.2}S_2O_2$ sample, in q space (a) and R space (b). 93
4.30 Sample holder used in the experiment at B18 to measure a single crystal of $Sr_2MnCu_{1.5}S_2O_2$. 95
4.31 Simulated and measured XANES, (a), and EXAFS, (b), of the Cu K-edge of $Sr_2MnCu_{1.5}S_2O_2$, at 300K. 96
4.32 Simulated and measured XANES, (a), and EXAFS, (b), of the Cu K-edge of $Sr_2MnCu_{1.5}S_2O_2$, at 112K. 97
4.33 Simulated and measured XANES, (a), and EXAFS, (b), of the Mn K-edge of $Sr_2MnCu_{1.5}S_2O_2$, at 300K. 98
4.34 Simulated and measured XANES, (a), and EXAFS, (b), of the Mn K-edge of $Sr_2MnCu_{1.5}S_2O_2$, at 112K. 98
4.35 XANES of the Cu K-edge $Sr_2MnCu_{1.5}S_2O_2$, for 300K (a) and 112K (b). A range of angles are included, 0° to 90° in steps of 15°. 101
4.36 Comparison of the XANES of the Cu K-edge $Sr_2MnCu_{1.5}S_2O_2$, for the two extreme angles at both temperatures. 102
4.37 XANES of the Mn K-edge $Sr_2MnCu_{1.5}S_2O_2$, for 300K (a) and 112K (b). A range of angles are included, 15° to 75° in steps of 15°. 104
4.38 Comparison of the XANES of the Mn K-edge $Sr_2MnCu_{1.5}S_2O_2$, for the two extreme angles at both temperatures. 105
4.39 EXAFS, (a), and FT-EXAFS, (b), of the Cu K-edge $Sr_2MnCu_{1.5}S_2O_2$, at 300K. A range of angles are included, 0° to 90° in steps of 15°. . . . 108
4.40 EXAFS, (a), and FT-EXAFS, (b), of the Cu K-edge $Sr_2MnCu_{1.5}S_2O_2$, at 112K. A range of angles are included, 0° to 90° in steps of 15°. . . . 109
4.41 Comparison of the EXAFS (a) and FT-EXAFS (b) of the Cu K-edge $Sr_2MnCu_{1.5}S_2O_2$, for the two extreme angles at both temperatures. . . 110
4.42 EXAFS, (a), and FT-EXAFS, (b), of the Mn K-edge $Sr_2MnCu_{1.5}S_2O_2$, at 300K. A range of angles are included, 15° to 75° in steps of 15°. . . . 113
4.43 EXAFS, (a), and FT-EXAFS, (b), of the Mn K-edge $Sr_2MnCu_{1.5}S_2O_2$, at 112K. A range of angles were measured, 15° to 75° in steps of 15°. . 114
4.44 Comparison of the EXAFS (a) and FT-EXAFS (b) of the Mn K-edge $Sr_2MnCu_{1.5}S_2O_2$, for the two extreme angles at both temperatures. . . 115
4.45 The single scattering paths used in the fit of the Cu K-edge $Sr_2MnCu_{1.5}S_2O_2$ data. 117
4.46 Fit of the Cu K-edge at 300K, in q space(a) and R space (b). 120
4.47 Fit of the Cu K-edge at 112K, in q space (a) and R space (b). 121
4.48 Comparison of the fit to the two extreme angles, in q space (a) and R space (b), measured at 300K. 122

4.49 Comparison of the fit to the two extreme angles, in q space (a) and R space (b), measured at 112K. 123
4.50 Comparison of the R space of the Cu K-edge of $Sr_2MnCu_{1.5-\delta}S_2O_2$, for the different samples with respect to temperature. 125
4.51 The change in the x, y, and z components of the scattering paths that contribute to the first three peaks. 127

5.1 Top down view, (a), and side view, (b), of the $M_2Mo_6Se_6$ structure, where M = Rb, Tl. 130
5.2 Resistivity of $M_2Mo_6Se_6$ normalised to 300K, for $Tl_2Mo_6Se_6$, $In_2Mo_6Se_6$, and $Rb_2Mo_6Se_6$. 131
5.3 SEM image of the single crystal $Rb_2Mo_6Se_6$, measured with secondary electron (a) and backscattering electron (b) detection. 132
5.4 SEM image of the single crystal $Tl_2Mo_6Se_6$, measured with secondary electron (a) and backscattering electron (b) detection. 133
5.5 Spectra of $Tl_2Mo_6Se_6$, the crystal is homogeneous, and only the expected elements are present. 134
5.6 Spectra of $Tl_2Mo_6Se_6$, the crystal is homogeneous, and only the expected elements are present. 135
5.7 $Tl_2Mo_6Se_6$ sample, glued onto the Al puck with Ag paint. The puck is attached to the sample holder used at the beamline. 137
5.8 $Rb_2Mo_6Se_6$ sample, glued onto the Cu puck with Ag paint. The puck is attached to the sample holder used when taking SEM measurements. . 137
5.9 XANES, (a), and first derivative, (b), of the Se K-edge of $Rb_2Mo_6Se_6$, at 4K and different angles, with respect to the c-axis. 140
5.10 XANES, (a), and first derivative, (b), of the Se K-edge of $Rb_2Mo_6Se_6$, at 150K and different angles, with respect to the c-axis. 141
5.11 XANES of the Se K-edge of $Rb_2Mo_6Se_6$, at 10° (a) and 90° (b), at different temperatures. 142
5.12 EXAFS, (a), and FT-EXAFS, (b), of the Se K-edge, at 4K, of $Rb_2Mo_6Se_6$, at different angles. 145
5.13 EXAFS, (a), and FT-EXAFS, (b), of the Se K-edge, at 150K, of $Rb_2Mo_6Se_6$, at different angles. 146
5.14 EXAFS, (a), and FT-EXAFS, (b), of the Se K-edge, at 90°, of $Rb_2Mo_6Se_6$, at different temperatures. 147
5.15 EXAFS, (a), and FT-EXAFS, (b), of the Se K-edge, at 10°, of $Rb_2Mo_6Se_6$, at different temperatures. 148
5.16 The single scattering paths used in the fit of the Se K-edge $Rb_2Mo_6Se_6$ data. 150
5.17 Fit of the Se K-edge at 4K, in q space (a) and R space (b). 153
5.18 Fit of the Se K-edge at 150K, in q space (a) and R space (b). 154
5.19 Fit of the Se K-edge at $\theta_p = 90^o$, in q space (a) and R space (b). 155
5.20 Fit of the Se K-edge at $\theta_p = 10^o$, in q space (a) and R space (b). 156
5.21 XANES, (a), and first derivative, (b), of the Se K-edge of $Tl_2Mo_6Se_6$, at 4K and different angles, with respect to the c-axis. 158
5.22 XANES, (a), and first derivative, (b), of the Se K-edge of $Tl_2Mo_6Se_6$, at 150K and different angles, with respect to the c-axis. 159
5.23 XANES of the Se K-edge of $Tl_2Mo_6Se_6$, at 0° (a) and 90° (b), at different temperatures. 160

5.24 EXAFS, (a), and FT-EXAFS, (b), of the Se K-edge, at 4K, of $Tl_2Mo_6Se_6$, at different angles. 163
5.25 EXAFS, (a), and FT-EXAFS, (b), of the Se K-edge, at 150K, of $Tl_2Mo_6Se_6$, at different angles. 164
5.26 EXAFS, (a), and FT-EXAFS, (b), of the Se K-edge, at 0°, of $Tl_2Mo_6Se_6$, at different temperatures. 165
5.27 EXAFS, (a), and FT-EXAFS, (b), of the Se K-edge, at 90°, of $Tl_2Mo_6Se_6$, at different temperatures. 166
5.28 The single scattering paths used in the fit of the Se K-edge $Tl_2Mo_6Se_6$ data. 168
5.29 Fit of the Se K-edge at 4K, in q space (a) and R space (b). 171
5.30 Fit of the Se K-edge at 150K, in q space (a) and R space (b). 172
5.31 Fit of the Se K-edge at $\theta_p = 0^o$, in q space (a) and R space (b). 173
5.32 Fit of the Se K-edge at $\theta_p = 90^o$, in q space (a) and R space (b). 174
5.33 Two simple diagrams of the most likely distortion observed in the fit of $Rb_2Mo_6Se_6$ at 4K. 177

6.1 Simple schematic of the possible Jahn-Teller distortions for a metal ligand octahedra. 180
6.2 Structure of Ca_2RuO_4, at room temperature (a), and at 400K (b). . . . 182
6.3 SEM image of the single crystal Ca_2RuO_4, measured with secondary electron (a) and backscattering electron (b) detection. 183
6.4 Spectra of Ca_2RuO_4, the crystal is homogeneous, and only the expected elements are present. 184
6.5 Spectra of the carbon paint used to glue the sample to the sample holder. 185
6.6 Sr_2RhO_4 sample, top, Ca_2RuO_4, middle and bottom, glued onto an Al sample holder with C paint. 186
6.7 Simulated and measured XANES, (a), and EXAFS, (b), of the Ru K-edge of Ca_2RuO_4, at 300K. 188
6.8 Simulated and measured XANES, (a), and EXAFS, (b), of the Ru K-edge of Ca_2RuO_4, at 400K. 189
6.9 XANES of the Ru K-edge of Ca_2RuO_4, at 300K and different angles, with respect to the *c*-axis. 191
6.10 XANES, (a), and first derivative, (b), of the Ru K-edge of Ca_2RuO_4, at 400K and different angles, with respect to the *c*-axis. 192
6.11 XANES of the Ru K-edge of Ca_2RuO_4 for the two extreme angles measured, comparing the temperatures 300K and 400K. 193
6.12 XANES of the Ru K-edge of Ca_2RuO_4, at 300K, and at different angles, with respect to the *c*-axis. Where the sample has been rotated in the *ab*-plane. 195
6.13 The single scattering paths that contribute to the first peak of the FT-EXAFS of Ca_2RuO_4 197
6.14 Tilted cuboid formed by the first four Ru-Ca single scattering paths, obtained from the models, (a) at room temperature and (b) at 400K. . 198
6.15 EXAFS, (a), and FT-EXAFS, (b), of the Ru K-edge of Ca_2RuO_4, at 300K and different angles, with respect to the *c*-axis. 199
6.16 EXAFS, (a), and FT-EXAFS, (b), of the Ru K-edge of Ca_2RuO_4, at 400K and different angles, with respect to the *c*-axis. 200
6.17 EXAFS, (a), and FT-EXAFS, (b), of the Ru K-edge of Ca_2RuO_4, comparing the temperatures 300K and 400K, at the two extreme angles. . . 201

6.18 The single scattering paths used in the fit of the Ru K-edge Ca_2RuO_4 data, up to 3.491Å. 203
6.19 The single scattering paths used in the fit of the Ca_2RuO_4 data, around the Ru atoms in a unit cell, from 3.855Å to 4.216Å. 204
6.20 Fit of the Ru K-edge at 300K, in q space (a) and R space (b). 207
6.21 Fit of the Ru K-edge at 400K, in q space (a) and R space (b). 208
6.22 A simple diagram of the effect of a Jahn-Teller compression on d orbitals. 209
6.23 The change in the x, y, and z components of the scattering paths that contribute to the first peak. 211

7.1 A simple diagram of the most likely distortion observed in the fit of $Rb_2Mo_6Se_6$ at 4K (a), side view of distortion (b). 214
7.2 Comparison of the Ru-O octahedra in Ca_2RuO_4 at room temperature (a), and 400K (b). 215

A.1 Geometry used in calculating self-absorption correction in EXAFS. . . 245

B.1 XANES of the Se K-edge of $Rb_2Mo_6Se_6$, at 75K (a) and 100K (b), at different angles. 272
B.2 EXAFS, (a), and Fourier transformed EXAFS, (b), of the Se K-edge, at 75K, of $Rb_2Mo_6Se_6$, at different angles. 273
B.3 EXAFS, (a), and Fourier transformed EXAFS, (b), of the Se K-edge, at 100K, of $Rb_2Mo_6Se_6$, at different angles. 273
B.4 Fit of the Se K-edge of $Rb_2Mo_6Se_6$ at 75K, in q space(a) and R space (b). 274
B.5 Fit of the Se K-edge of $Rb_2Mo_6Se_6$ at 100K, in q space(a) and R space (b). 274
B.6 XANES of the Se K-edge of $Tl_2Mo_6Se_6$, at 8K, at different angles. . . . 275
B.7 XANES of the Se K-edge of $Tl_2Mo_6Se_6$, at 75K (a) and 100K (b), at different angles. 275
B.8 EXAFS, (a), and Fourier transformed EXAFS, (b), of the Se K-edge, at 8K, of $Tl_2Mo_6Se_6$, at different angles. 276
B.9 EXAFS, (a), and Fourier transformed EXAFS, (b), of the Se K-edge, at 75K, of $Tl_2Mo_6Se_6$, at different angles. 276
B.10 EXAFS, (a), and Fourier transformed EXAFS, (b), of the Se K-edge, at 100K, of $Tl_2Mo_6Se_6$, at different angles. 276
B.11 Fit of the Se K-edge of $Tl_2Mo_6Se_6$ at 8K, in q space(a) and R space (b). 277
B.12 Fit of the Se K-edge of $Tl_2Mo_6Se_6$ at 75K, in q space(a) and R space (b). 278
B.13 Fit of the Se K-edge of $Tl_2Mo_6Se_6$ at 100K, in q space(a) and R space (b). 278

List of Tables

4.1 Path lengths, with respect to Cu, obtained from both models of $Sr_2MnCu_{1.5}S_2O_2$. 69
4.2 Path lengths, with respect to Mn, obtained from both models of $Sr_2MnCu_{1.5}S_2O_2$. 74
4.3 Fit parameters for the Cu K-edge EXAFS of $Sr_2MnCu_{1.5}S_2O_2$. 78
4.4 Fit parameters for the Cu K-edge EXAFS of $Sr_2MnCu_{1.3}S_2O_2$. 79
4.5 Fit parameters for the Cu K-edge EXAFS of $Sr_2MnCu_{1.2}S_2O_2$. 80
4.6 Fit parameters for the Mn K-edge EXAFS of $Sr_2MnCu_{1.5-x}S_2O_2$ (x=0.0,0.2,0.3), alongside the value obtained from the tetragonal structural model. . . . 90
4.7 E_0's (eV) of the Cu K-edge, of $Sr_2MnCu_{1.5}S_2O_2$, for all θ_b's and temperatures. 99
4.8 E_0's (eV) of the Mn K-edge, of $Sr_2MnCu_{1.5}S_2O_2$, for all θ_b's and temperatures measured. 99
4.9 Structural information, of the Cu single scattering paths, obtained from the tetragonal model of $Sr_2MnCu_{1.5}S_2O_2$. 106
4.10 Structural information, of the Mn single scattering paths, obtained from the tetragonal model of $Sr_2MnCu_{1.5}S_2O_2$. 111
4.11 Fit parameters for the Cu K-edge EXAFS of the 300K and 112K single crystal data. 118

5.1 E_0's (eV) of the Se K-edge, of $Rb_2Mo_6Se_6$, for all θ_p's and temperatures measured. 138
5.2 Structural information, of the single scattering paths, obtained from the room temperature model of $Rb_2Mo_6Se_6$. 143
5.3 Fit parameters for the Se K-edge EXAFS of the $Rb_2Mo_6Se_6$ single crystal. 151
5.4 E_0's (eV) of the Se K-edge, of $Tl_2Mo_6Se_6$, for all θ_p's and temperatures measured. 157
5.5 Structural information, of the single scattering paths, obtained from the room temperature model of $Tl_2Mo_6Se_6$. 161
5.6 Fit parameters for the Se K-edge EXAFS of the $Tl_2Mo_6Se_6$ single crystal. 169

6.1 E_0's (eV) of the Ru K-edge for all θ_b's and both temperatures measured. 187
6.2 E_0's (eV) of the Ru K-edge for all θ_b's and ϕ_b's measured. 194
6.3 Structural information, of the single scattering paths, obtained from the room temperature model of Ca_2RuO_4 196
6.4 Fit parameters for the Ru K-edge EXAFS of the 300K and 400K single crystal data. 205

Chapter 1

Introduction.

1.1 Charge ordering: properties and materials.

Understanding the properties of charge ordered materials is very important to the advancement of physics, for both theoretical and practical uses. Charge ordering is a first- or second-order phase transition which mostly occurs in strongly correlated materials. The materials that exhibit charge ordering are not limited to inorganic materials and can also be observed in organic conductors, such as the Bechgaard-Tabre salt family [1]. Charge ordering is due to strong interactions between electrons within the material, charges localised on different sites will lead to a disproportionation and the emergence of an ordered super-lattice. These super-lattices can form different patterns, for example a checker-board like pattern or vertical stripes (see Figure 1.1) [2, 3].

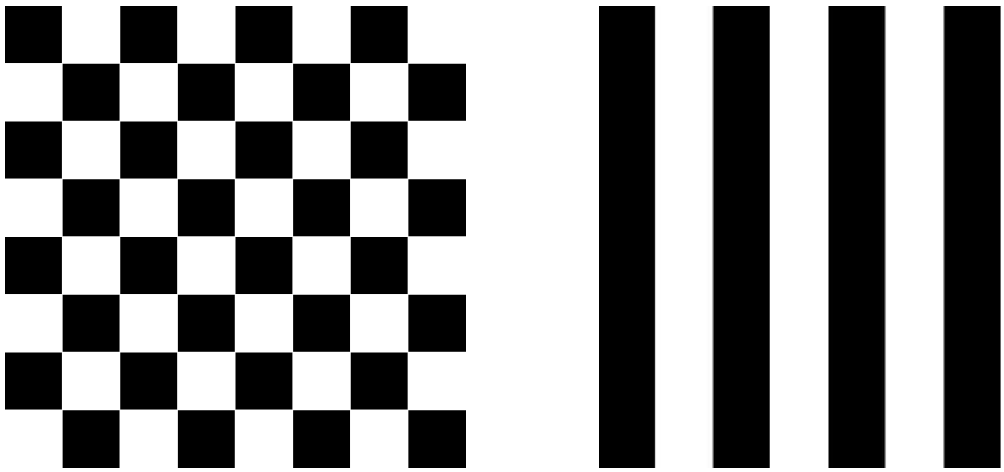

Figure 1.1: Examples of typical charger order patterns, in a 2 dimensional scenario.

Structural charge ordering is not restricted to two-dimensional materials, but occurs mostly in materials with anisotropic electronic or atomic structures, where the structure is not the same across different axes. A charge order transition is always accompanied by symmetry breaking and can lead to ferroelectricity, superconductivity, and/or magnetoresistance.
Due to charge ordering, certain physical effects can occur within a material, such as the material becoming a Mott-insulator, the formation of a charge density wave (CDW), or a spin density wave (SDW), as well as superconductivity, and colossal magnetoresistance.

1.1.1 Examples of physical effects due to charge ordering, relevant to this work.

A physical effect, *e.g.* an electronic structural change, that can occur in a material due to charge ordering is a Mott-insulator transition. A Mott-insulator is a material that should allow for electronic conduction, however it behaves as an insulator. In this case the materials electron configuration should allow the conduction of electricity under conventional band theories. However due to the effects of electron-electron interaction the material becomes insulating instead. The band gap that emerges in these materials is between like character bands, such as the 3d electrons, whereas in a charge transfer insulator the band gap is between anion and cation states [4]. The first hint of this type of behaviour was discovered in 1937 in the work of Jan de Boer and Evert Verway [5], where they compiled a list of materials that were predicted to be conductors based on conventional theory, but instead were found to be insulators. Working from the information presented in this paper Nevill Mott and Rudolf Peierls suggested that this anomaly could be explained by including electron-electron interactions [6]. Mott continued to work on explaining this behaviour, and in 1949 he proposed a model for NiO as an insulator, where an energy gap forms which prevents conduction and can be seen as the competition between the Coulomb potential between the 3d electrons and the transfer integral of the 3d electrons and the neighbouring atoms [7].
In general, Mott insulators occur when the Coulomb repulsion is large enough compared to the transfer integral that an energy gap is created. The point in which a material will go from a metal to a Mott insulator as the Coulomb repulsion increases can be calculated with dynamical mean field theory [8, 9, 10, 11].
To fully describe a Mott insulator, both antiferromagnetic ordering and 'mottness' need to be accounted for. Mottness accounts for the properties of a Mott insulator that cannot be explained by antiferromagnetic ordering. These properties include vanishing of the single particle Green function along a connected surface in momentum space in the first Brillouin zone [12], a pseudogap away from half filling (n=1) [13], two sign changes of the Hall coefficient as electron doping goes from n=0 to n=2 [14], the presence of a charge 2e boson at low energies [15], and spectral weight transfer on the Mott scale [16].
Mott insulating materials can have many uses in physics, as the material is an insulator that can become a conductor under certain conditions, such as composition, pressure, strain, voltage, or magnetic field. Thanks to this behaviour these materials can be used to build smaller field-effect transistors, switches, and memory devices [17, 18, 19].
Another example of a physical effect due to charge ordering is the emergence of charge density waves (CDW). CDWs can occur in metallic crystals that are quasi-one-dimensional (Q1D), or quasi-two-dimensional (Q2D). When the crystal is Q1D the crystal will form in a thin ribbon, while it will form a flat sheet when it is Q2D. The first evidence of a CDW in a linear chain compound, $NbSe_3$, was discovered in 1976 by Monceau *et al.* [20]. Examples of Q2D materials that form CDWs are organic conductors such as TTF-TCNQ (first investigated in the 1970s [21]). While TTF-TCNQ was theorised to become superconducting, a metal-insulator transition was observed instead. Further work into these measurements eventually lead to this being the first observation of a Peierls transition, which is an indication of a CDW. Peierls theorem states a one-dimensional equal spaced system, where the ions each have one electron, is unstable [22]. To improve the stability, the ions in the chain will move closer to one neighbour and further from the other, this is referred to as a Peierls transition. CDWs have also been observed in layered dichalcogenides [23, 24], and layered cuprates

[25, 26, 27].
The electrons within a CDW form a standing wave pattern and can sometimes carry an electric current. A CDW allows for the electrons to carry a current due to the combined affects of impurities in the material and electrostatic interactions (from net electric charges in any of the CDW kinks). The current will often flow in a jerky fashion due to its electrostatic properties. This jerky flow separates the properties of a CDW from the properties of a superconductor, where the flow of electrons is smooth. The electric current in $NbSe_3$ was observed by Fleming *et al.* [28] and Monceau *et al.* [29], where it was confirmed the current in a CDW flows in a jerky fashion above the threshold field. In the quantum model, a CDW can be viewed as a sticky quantum fluid, or deformable quantum solid with dislocations. This was a concept discussed by Anderson [30]. A CDW can lead to other interesting properties in a material, such as the formation of a superlattice [31, 32, 3]
As the properties that develop due to charge ordering are often directional dependent, such as a CDW, or paired with anisotropy in the electronic structure, like in a Mott-insulator, they are perfect candidates to measure with a technique with directional resolution.

1.1.2 Materials investigated for this thesis.

In this thesis three materials will be studied and discussed. The first is an oxychalcogenide, $Sr_2MnCu_{1.5-\delta}S_2O_2$, which has displayed mobile Cu ions in previous studies [33]. The second is a molybdenum selenide, $M_2Mo_6Se_6$ (M=Rb, Tl), which is predicted to exhibit CDWs. While there has been no direct observation of this in the diffraction data, they are strongly suggested by bulk transport measurements. The third is calcium ruthenate, Ca_2RuO_4, this material undergoes a Mott-insulator transition, of which the driving force is unknown.
The material discussed in Chapter 4, $Sr_2MnCu_{1.5-\delta}S_2O_2$ (see Figure 1.2), comes from an interesting family of materials, the oxychalcogenides. The mixed anion nature of this family leads to a layered structure. As a layered structure is highly anisotropic, this family are good candidates to measure with a direction sensitive technique, such as polarised x-ray absorption spectroscopy (P-XAS). $Sr_2MnCu_{1.5-\delta}S_2O_2$ has interesting magnetic properties, where the Mn ions are found with a mean oxidation state of +2.5 [33], and their magnetic moments ferromagnetically order in zigzag stripes that are aligned antiferromagnetically [34]. The Cu ions in the Cu-S layer have been found to be extremely delocalised, suggesting that they are mobile [33].

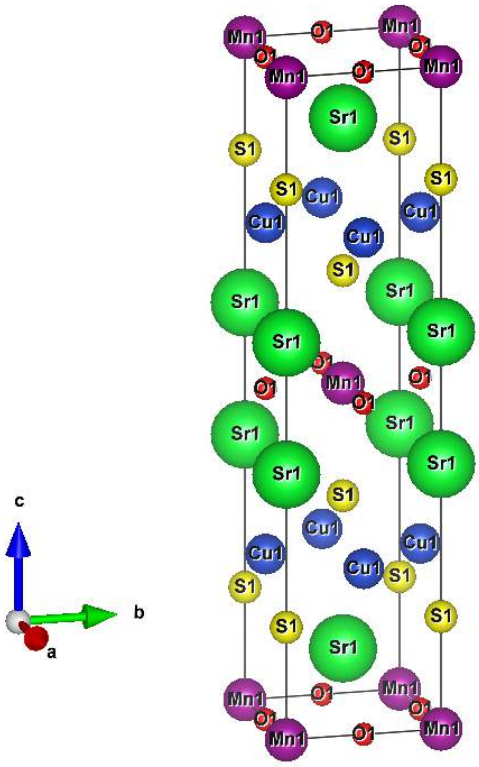

Figure 1.2: Structure of $Sr_2MnCu_{1.5}S_2O_2$, in the tetragonal phase [33].

$Sr_2MnCu_{1.5-\delta}S_2O_2$ has a well understood structure and physical properties, and was considered ideal to confirm whether P-XAS is a viable experimental technique which can separate the absorption along different directions in an anisotropic structure.
While this family of oxychalcogenides have interesting properties, such as unusual magnetism [35, 36], and thermoelectric properties [37, 38], the quality of the single crystals currently available made it difficult to continue with this family for the technique developed in this thesis. This was due to the samples including Mn rich impurities with unknown structures. Therefore our direction of research was shifted to different materials that exhibit charge ordering, where the electronic and atomic properties are coupled, and are also anisotropic.
In the case of the materials investigated in Chapters 5 and 6, (shown in Figures 1.3 and 1.4, respectively), they show strong evidence of charge ordering, where $M_2Mo_6Se_6$ appears to have CDWs, and Ca_2RuO_4 undergoes a Mott insulator transition with an ambiguous driving force. However direct observation or confirmation of their nature has been elusive by other probes. This suggests that the long-range order is somehow broken, making these materials ideal candidates to measure using the technique described in this thesis.
The material discussed in Chapter 5, $M_2Mo_6Se_6$ (M=Tl, Rb) (see Figure 1.3), is interesting due to the different properties with respect to the guest ion. $M_2Mo_6Se_6$ forms a hexagonal unit cell with $(Mo_3Se_3)_\infty$ chains along the *c*-axis, and guest ions between these chains [39]. They form needle like single crystals, with the *c*-axis forming the length, where the analogues containing an alkali metal form more fibrous crystals than the analogues containing IIIA metals [40]. Due to their structure, these materials can be thought of as quasi-one-dimensional, making them very useful for testing out predictions of low dimensional physics.

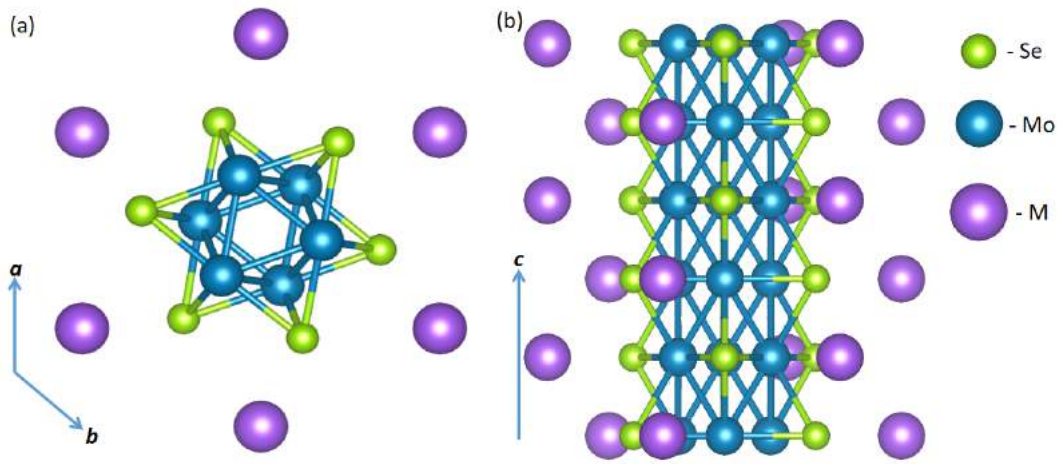

Figure 1.3: Top down view, (a), and side view, (b), of the $M_2Mo_6Se_6$ structure, where M = Rb, Tl [41, 42].

The main question in these materials is how their properties depend on the guest ion. For the analogues with an alkali metal ion there is a sharp upturn in the resistivity with respect to decreasing temperature, suggesting a metal-insulator transition [40]. While for the analogues with a IIIA metal ion their resistivity drops with temperature and eventually drops completely, leading to a transition from a metallic state to a superconducting state [40]. To explain this difference, the presence of a CDW has been suspected. However no direct observations of a CDW in either type of material has been achieved. This leads to the conclusion that the possible CDW is causing either fluctuating or short-range ordered lattice distortions. If this is the case then a short-range probe would be the best technique to use to confirm or deny the presence of a CDW. An ideal technique to use for this investigation is P-XAS, as this technique is both a local probe and dependent on the direction measured along the sample.
The material discussed in Chapter 6, Ca_2RuO_4 (see Figure 1.4), undergoes a Mott insulator transition, but its precise nature is under debate [43, 44, 45]. It is unclear how the orbital degree of freedom plays a role in the driving force of this transition. Two scenarios have been proposed i) the transition is orbital selective and only effects the xy-band, or ii) it is not orbital selective and is simply assisted by crystal field splitting. This has lead to increased interest in the spin-orbit interaction occurring in the Ru $4d$ shell, and how this determines the properties of the material.

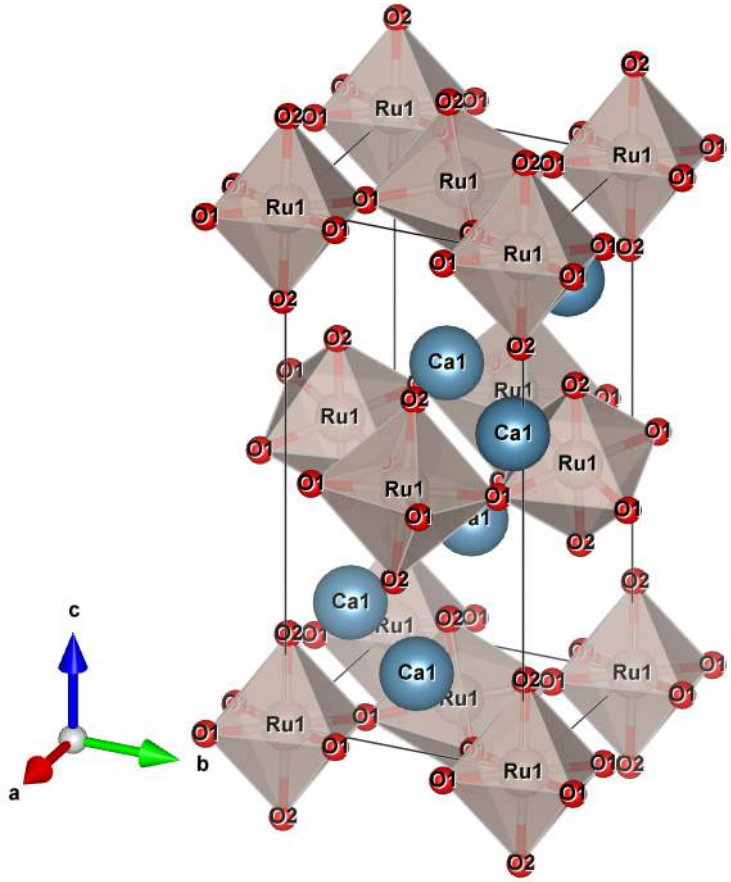

Figure 1.4: Structure of Ca_2RuO_4, at room temperature [46].

To determine whether the Mott transition is orbital selective or not, a probe that can distinguish between directions along the crystal is needed. P-XAS is an ideal probe to use in this case as it measures the local environment around the excited atom. Due to hybridisation of the Ru 4*d* and O 2*p* orbitals, the Ru 4*d* orbitals may be investigated with K-edge absorption, which is simpler to model.
When the effects due to charge ordering do not display long-range ordering, or if its long-range order is fluctuating, it can make it impossible to observe using the more common techniques for this field *i.e.* diffraction. In this case a local probe will prove more useful. However, when the charge ordering is paired with a subtle angular change, Jahn-Teller distortions [47], or a directional specific distortion, CDWs [31], powder measurements may average out the affect. In these cases single crystal measurements can be more useful. As P-XAS measures the absorption along a specific direction along the crystallographic axis, it is sensitive to angular changes and properties that are directional. This makes it an ideal technique to use for investigating charge ordered materials, as its increased sensitivity can observe things other techniques might average over.

1.2 Historical background of synchrotron radiation and x-ray absorption spectroscopy.

The synchrotron principle, of a circular particle accelerator, was first published by Vladimir Veksler in 1944 [48]. However the first electron synchrotron was built by Edwin McMillan in 1945 [49] independently, as Veksler only published his work in the

Soviet Union. The idea behind a synchrotron was to accelerate charged particles in a circular manner, this concept allowed for large facilities to be designed as the bending, focusing, and acceleration can be separated into different components. Synchrotron radiation was first observed in 1946 (however it was not announced until 1947 [50]). The first observation of this type of radiation was performed in a General Electric synchrotron accelerator (see Figure 1.5) built by Frank Elder, Anatole Gurewitsch, Robert Langmuir, and Herb Pollock, hence the name synchrotron radiation.

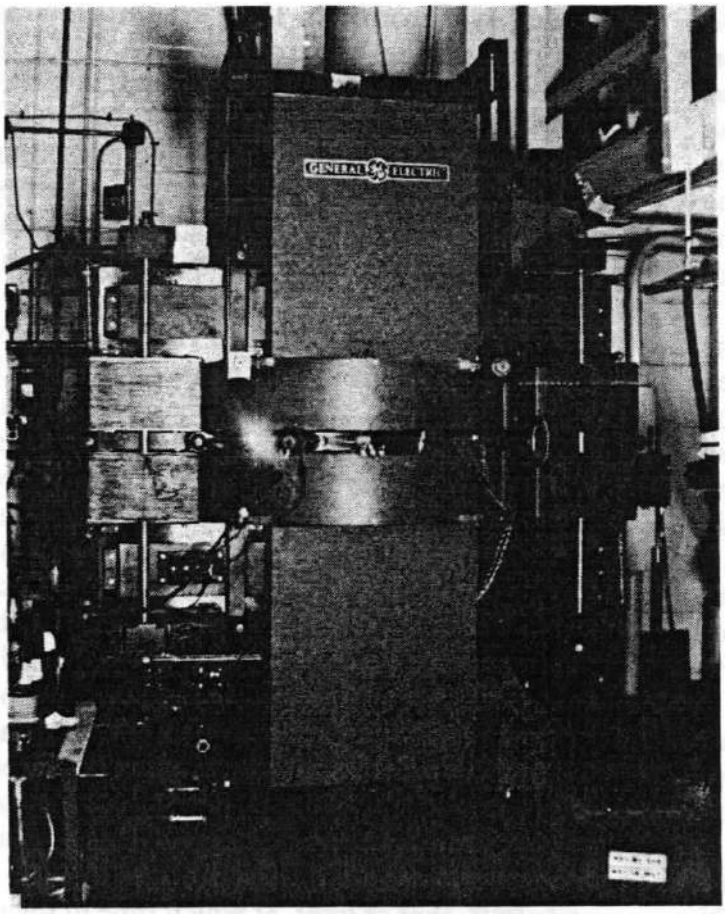

Figure 1.5: Photograph of the General Electric synchrotron accelerator. A 70 MeV synchrotron with optical radiation from the electron beam visible through the glass wall of the vacuum "doughnut" tangent to the beam orbit [51].

Synchrotron radiation is produced when a charged particle (usually an electron) is accelerated radially, therefore the acceleration is perpendicular to the particle velocity, $\vec{a} \perp \vec{v}$. When the electron is travelling at relativistic velocities, a change in its trajectory causes the production of synchrotron radiation. This radiation ranges in wavelength depending on the curvature of the electron beam trajectory, which can be controlled by the strength of the magnets.
Properties of synchrotron radiation include a broad range of energies (from microwaves to hard x-rays), high flux (for in-situ experiments or studying weakly scattering crystals), high brilliance (highly collimated therefore a small size source is possible), high stability (stable in submicron range), polarisation (both linear and circular), and pulse time structure (experiments can be performed at very small time scales). This type of radiation has a large range of uses, from biological investigation, to testing predictions from theoretical physics in condensed matter. The broad applicability is largely due to

its tunability, as it is a continuous radiation source. With beamlines having the capability of fine tuning the energy of the radiation, experiments can be easily performed at specific energies, or range of energies. The use of synchrotron radiation has also greatly reduced the experimental time needed to obtain usable measurements, as there is such a high flux of x-rays.
Synchrotron radiation is produced in a narrow cone with an angular width of $1/\gamma$, where γ is the energy of the electron (ε_e) in terms of its rest mass energy $\gamma = \varepsilon_e/mc^2$ (see Figure 1.6). The radiation produced has both horizontal and vertical polarisation components, and depending on the observation angle this polarisation can be selected (see Figure 1.7). The selectivity of the type of polarisation of the synchrotron radiation is a very useful property, where linear polarisation can be selected by only allowing the x-rays in the orbital plane to reach the material. This is controlled by changing the size of the slits to only accept the centre of the beam, in the case of linearly polarised x-rays. Circularly polarised x-rays can be used by selecting the x-rays at a small angle to the orbital plane.

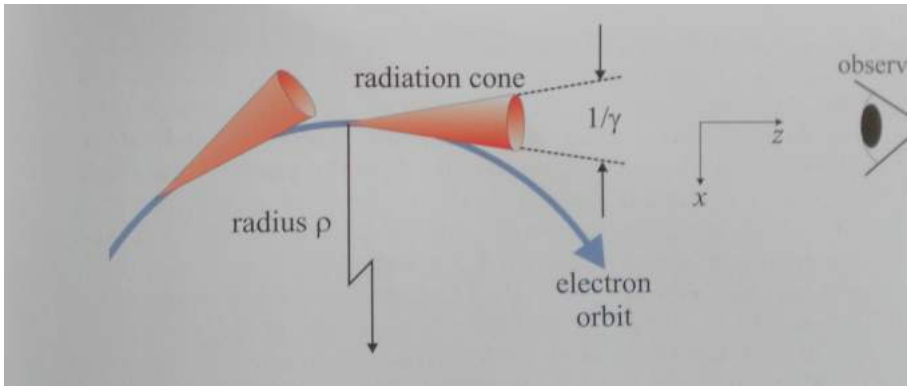

Figure 1.6: Schematic of the trajectory of an electron in a circle, of radius ρ, and the resulting radiation cones, opening angle $1/\gamma$ ($\gamma = \varepsilon_e/mc^2$) [52].

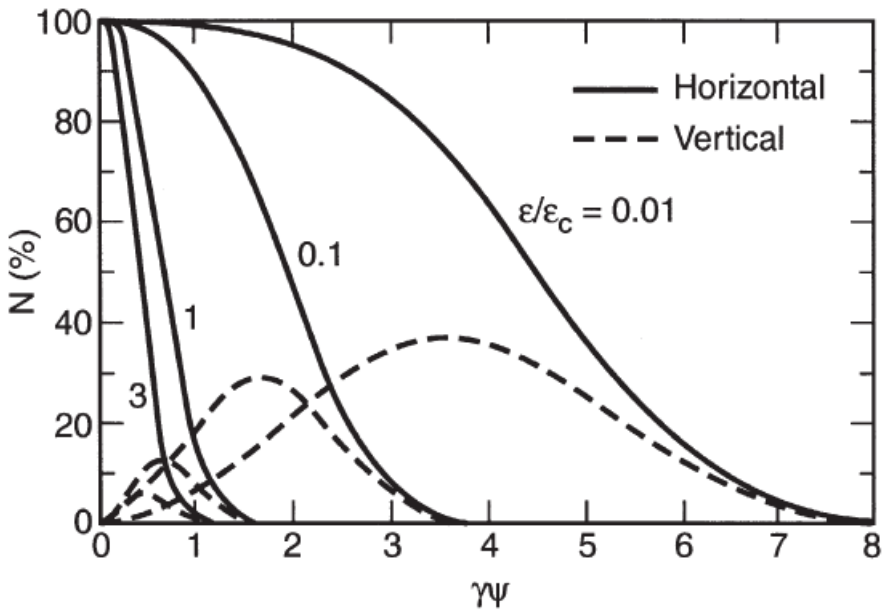

Figure 1.7: Normalised intensities of the horizontal and vertical components of the x-ray polarisation produced from a bending magnet, as functions of the vertical observation angle, ψ, photon energies, ϵ, and the critical photon energy ϵ_c [53].

In a synchrotron facility there are beamlines situated along the synchrotron ring. The beamlines are where experiments are carried out, and they are each designed for specific types of experiment. Beamlines are classified by x-ray source into two groups, which are discussed in more detail in Chapter 2, these are insertion devices and bending magnets (insertion devices can be further classified into two sub groups, undulators and wigglers). The difference between these two beamlines is how the x-rays are produced, in an insertion device the electron beam is 'wiggled' by a series of magnets that have opposite poles, while in a bending magnet the electron beam is accelerated in a bend. Both of these methods change the trajectory of the electron beam, which results in the production of x-rays. The x-rays are then directed into the experiment section of the beamline. The research that can be carried out at a beamline is determined by the optics, detectors, and the sample environments available.

1.2.1 Conventional x-ray absorption spectroscopy experiments.

The type of experiments discussed in this thesis are x-ray absorption spectroscopy (XAS) measurements. In a XAS experiment, a beam of x-rays is fired toward the sample at a range of energies to measure the absorption of a certain element within the sample. This takes advantage of the fact that every element has its own absorption energies depending on what core electron is being excited (see Figure 1.8). The energy of each edge is dependent on the elements electronic configuration, therefore this technique is element specific. XAS is also dependent on selection rules, this determines the nature of the absorption event, e.g. dipole or quadrupole. For a K-edge measurement the transition that determines the absorption is $1s$ to p. This is a dipolar transition, due to the nature of the s and p orbitals. Dipole transitions occur when the difference between the orbitals angular momentum quantum number ℓ is 1, where s ($\ell = 0$), p ($\ell = 2$), and d ($\ell = 3$). Other dipole transitions are the L-II and L-III edges, which are governed by a $2p$ to d transition. The L-I edge results in a quadrupole transition, as the absorption

process is from a $2s$ to a d orbital.

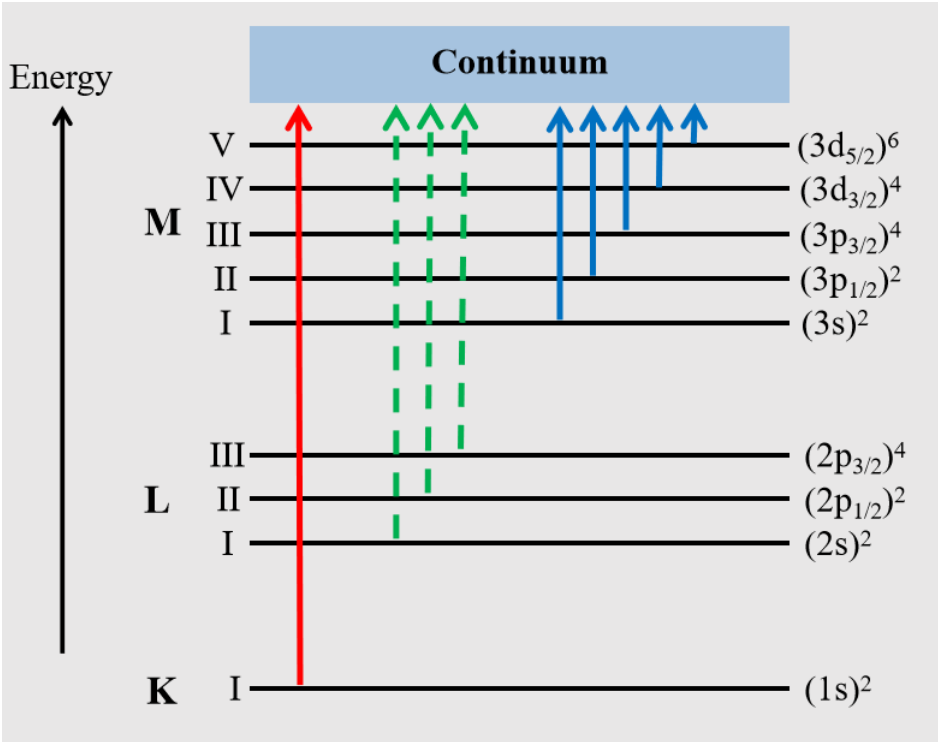

Figure 1.8: Simple schematic of the absorption edge nomenclature. The electronic shells are labelled as $(n\ell_i)^{2j+1}$, where n, ℓ and j are the principle, orbital angular momentum, and total angular momentum quantum numbers, respectively.

When the x-rays are at an energy high enough to be absorbed by the element of interest, a photoelectron will be released and will scatter against the local environment. The measured photons (or photoelectrons if measuring electron yield) will carry information of the local environment based off of this scattering process. This is due to interference between the photoelectrons and the scattered waves. An example of K-edge XAS measurement can be seen in Figure 1.9, where the different regions are labelled. In the x-ray absorption near edge structure (XANES) region, the process that produces the rising edge is a $1s$ electron being excited into the nearest unoccupied p state. Within the XANES region there may also be a pre-edge feature, this is produced by a $1s$ electron being excited into an unoccupied d state, this can only occur in a material where the symmetry allows for a quadrupole transition. The position and intensity of the first peak after the rising edge can be analysed to obtain information about the electronic state of the measured element within the material, such as its oxidation state. In the extended x-ray absorption fine structure (EXAFS) region, the process occurring is a $1s$ electron being excited into the continuum and released as a photoelectron. The constructive and destructive interference due to the photoelectron scattering within the local structure will cause the oscillations seen. The oscillations can be analysed to interpret information on the local atomic structure of the excited element in the material.

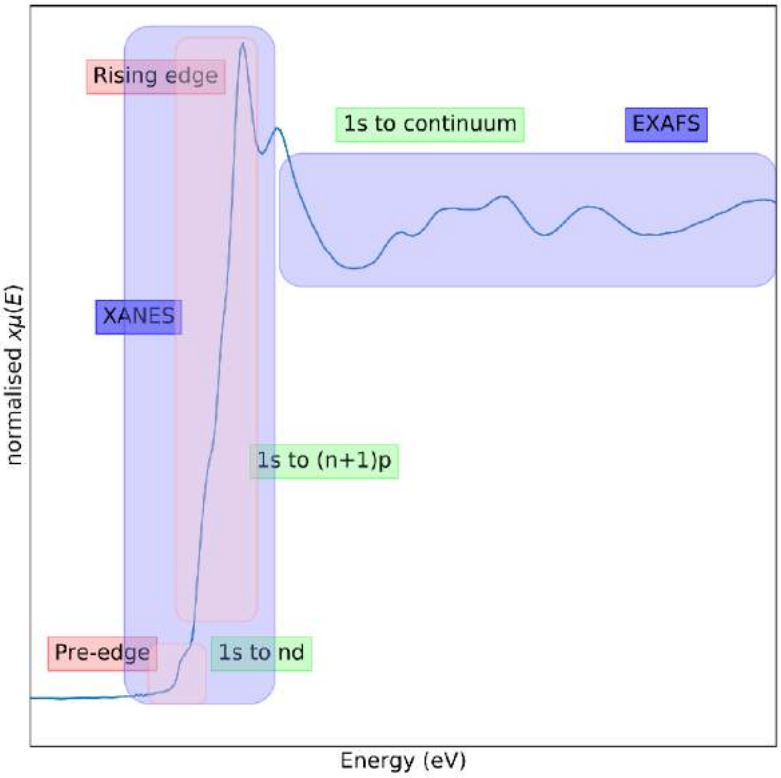

Figure 1.9: Example of K-edge XAS, (Mn K-edge of $Sr_2MnCu_{1.2}S_2O_2$ at 260K)the different regions have been labelled, and the transitions that contribute to these regions have been stated.

When XAS was first developed as a technique to measure properties of materials, single crystals were rotated in a beam of polarised x-rays [54]. It was later discovered that the same averaged local environment measurements could be obtained from measuring a static powder of a material. This lead to the more common XAS experiments being performed on powdered materials rather than single crystals. The benefits of working with powdered materials is that it opens up the sample range that can be measured using this technique. Single crystals can be difficult to grow to the size needed for an experiment, especially if the sample needs to be purely one phase. Whereas when working with a powder the crystals will be ground down so multiple small single phase crystals can be used.

The main hurdle in the development of EXAFS as a technique for measuring materials was obtaining a theory that could be used to interpret EXAFS signals accurately. Initially it was debated whether or not the EXAFS signal was due to long-range or short-range interactions within a material. However it was discovered in 1974 by Edward A Stern [55] that both interactions play an integral part in producing an EXAFS signal and are therefore required for a complete EXAFS theory. In a disordered material there is no periodicity in the long-range interactions, however the EXAFS signal can still be modelled if the disorder in the material is acknowledged by the theory [56, 57, 58].

This discovery is the basis of the modelling software, FEFF [59], used in the analysis of EXAFS signals for the work presented in this thesis[1]. Where a signal calculated from information of a base structural model is compared to the experimental signal

[1]The analysis in this thesis was performed used Demeter software [60] which utilises FEFF6. Other modelling software is available, such as EXCURV [61] and GNXAS [62].

and the similarities and differences can be used to obtain an idea of the local atomic structure of the material measured. Before this theory was developed and implemented into fitting software, the EXAFS signal measured would be compared to the signal of a sample with a well known structure and the similarities and differences could be used to gain a picture of the most likely local atomic structure of the material measured. This could be quite difficult when working with complex structures, as there would be many difference between the measured and the known signal.

1.2.2 Polarised x-ray absorption spectroscopy techniques.

The polarisation of synchrotron radiation has been used in XAS experiments since the beginning [54], but the application of XAS to powdered materials has taken the forefront for absorption measurements. However the earlier use of P-XAS experiments differ from the use discussed in this thesis. The technique discussed in this thesis uses linearly polarised x-rays to measure the absorption along different directions of a single crystal. This can distinguish the electronic and atomic structure along different directions in the local environment, therefore it can be used to investigate properties that affect specific directions within the material. One of the other ways P-XAS has been utilised is on oriented powders [63, 64], where the material is magnetic and the powder is ordered along the c-axis via the application of a magnetic field. A disadvantage of this technique is that the material is required to be magnetic, otherwise the powder cannot be accurately oriented along the desired axis. Another method for measuring P-XAS on powdered samples it to apply a thin film of the sample onto a surface, e.g. glass [65]. The limitation of this method is that the sample may not be completely oriented which will affect the angular dependence of the signal, as the local environment of each exited site may not have the same orientation along the crystallographic axis of interest.

The idea that spectra obtained from a single crystal would differ depending on the nature of the x-rays used for the measurement (polarised or unpolarised) was first discussed by Kronig in 1932 [66]. In 1990 Adrian Brouder investigated EXAFS theory with angular dependence in mind [67], using the fact that the EXAFS signal would theoretically change based on the angle of incidence when measuring a single crystal, or oriented sample. Therefore the structure of an anisotropic material can be measured with more definition when using linearly polarised x-rays, and different orientations of the sample. The method for the analysis of angular dependent EXAFS is further developed in this thesis.

The requirements for a P-XAS experiment are relatively simple, there are three main requirements: a sample that can be oriented (whether it is a powder or a single crystal), a linearly polarised x-ray source (either from a synchrotron, or a beam that has traversed through a polarising plate), and a sample environment that can provide different orientations for the sample (a rotating table or a diffractometer can work). When using single crystals, as is the case in this thesis, the measurements are made in fluorescence mode. Therefore a fluorescence detector is necessary, such as a Silicon Drift Detector (SDD), or a multiple element Ge detector. If using a lab based x-ray source with a polarising plate, to produce good quality absorption spectra there is a limitation due to the flux of the x-rays, therefore much higher acquisition times would be required. Hence a synchrotron is preferred for these measurements.

One advantage of adapting XAS experiments to work with single crystals is that it opens up direct comparison to many other techniques. Many techniques in condensed matter physics already rely upon working with single crystals, as this allows for more

accurate information on the properties of a bulk material than when measuring a powdered sample. The key gain is that additional information can also be obtained from measuring a single crystal as it is three-dimensional space being probed, and measurements along directions of interest can be distinguished.

1.3 Complementary techniques for single crystal work

A useful measurement technique to use in conjunction with P-XAS is the scanning electron microscope (SEM). As the P-XAS experiments, discussed in this thesis, require a single crystal it is important to confirm the material is a homogeneous single crystal (as in single phase). This can be checked with SEM measurements, as the images of the crystal measured with this technique are sensitive to changes in the composition of the material. It is also possible to measure the spectra of the material, depending on the SEM used, as the characteristic x-rays that are produced from the electron beam interacting with material can be measured and analysed. The use of an SEM within the context of this thesis is discussed further in Chapter 2.
X-ray diffraction is another technique that can be combined with XAS. As diffraction is a long-range order measurement technique, there are properties of materials that may be hard to observe. If a material has a property that has no long-range order, diffraction measurements may average this out. If the property has a periodic nature but still has long-range order, it is possible to observe in diffraction measurements but may be more difficult. Therefore XAS is a good partner measurement, as it is a local probe and can be used to observe properties with short-range order. Diffraction experiments can be performed using synchrotron radiation but they can also be performed on lab based x-ray equipment [68, 69, 70].
Other complementary techniques include neutron diffraction, conductivity and resistivity transport measurements, and angle resolved photoemission spectroscopy (ARPES). Each of these techniques can be (and often are) conducted on single crystals, and comparing these measurements with P-XAS carries the advantage that the results can be directly compared. Neutron diffraction experiments often benefit from being carried out on single crystals, where the crystals are typically larger than those used in x-ray measurements [71]. In neutron diffraction experiments, the neutron beam will interact with the nucleus of an atom, allowing the atomic and magnetic properties of a material to be measured [72, 69, 73]. While in XAS experiments, the x-ray beam will interact with the electron cloud surrounding an atom, allowing the local atomic and electronic properties to be measured. As neutrons have a high penetration depth, neutron diffraction is suitable for measuring bulk samples. The penetration depth of x-rays is smaller, making them ideal complementary techniques. Transport measurements can be performed to study conductivity or resistivity of a material. When using a single crystal the direct path of the electronic transport along the material can be tracked [74, 75, 76]. ARPES is a complementary technique for P-XAS as the Fermi-surface along different planes in a crystal can be measured [77, 78, 79, 80], and this will be complementary to XANES measurements. Another reason they are complementary is that ARPES measures the density of the occupied states in a material, whereas XAS measures the density of the unoccupied states. However ARPES is limited in the fact that it is only a surface probe, meaning that some properties measured could be due to surface effects rather than a property of the bulk material. This is not a limitation for P-XAS, making them ideal complementary techniques.

1.4 Chapter summary and thesis goals

This chapter has discussed the type of properties that can occur in charge ordered materials. The materials investigated in this thesis have been introduced and their relevance to the technique developed for this research has been stated. The history of synchrotron radiation has been introduced and its use in x-ray absorption spectroscopy has been discussed. The two techniques used in this research, conventional XAS and P-XAS, have been introduced, where both their history and relevance to this work is discussed. Complementary techniques for both XAS and P-XAS were introduced in this chapter, and the different information they provide is briefly discussed.
Chapters 2 and 3 introduce and explain the experimental and theoretical components of P-XAS experiments. The experimental set up is very similar to conventional XAS experiments, where the main differences involve the sample set up. The analysis of P-XAS is a lot more involved than conventional XAS, the method developed for this thesis is introduced and explained.
The goal of Chapter 4 is to discuss the viability of the P-XAS technique developed for this thesis. The results from both conventional powder XAS and single crystal P-XAS, on the same material $Sr_2MnCu_{1.5}S_2O_2$, are investigated. The Cu ions in this material are potentially mobile [33], this is investigated using both techniques. The results for both are compared to determine if the XAS signal can be separated its angular dependence, and the analysis method is tested to confirm that sensible fits can be produced.
In Chapter 5, single crystal P-XAS of $M_2Mo_6Se_6$ (M=Rb,Tl) is measured and analysed to investigate potential CDWs that have been predicted in these materials [40, 81]. The material has different electronic properties depending on the guest ion, by using this technique the affect this has on the local structure can be investigated. While in Chapter 6 the same technique is used to investigate the nature of the Jahn-Teller distortion in Ca_2RuO_4. This material undergoes and Mott-insulator transition [44], and the nature of the Jahn-Teller distortion may provide insight into the driving force of this transition.

Chapter 2

Experimental methods.

In this chapter the basics of x-ray spectroscopy experimentation will be discussed. This thesis focuses on single crystal polarised x-ray absorption spectroscopy (P-XAS) experiments, performed with linearly polarised x-rays at a synchrotron [82]. The production of x-rays in a synchrotron will be discussed in this chapter. The adaptation of the experimental set up when taking angular dependent measurements will also be discussed below.

2.1 Synchrotron radiation

A synchrotron produces x-ray radiation by accelerating a beam of electrons around a ring and then directing the beam along the beamlines situated around the ring, Figure 2.1. A synchrotron is not actually a circle, rather it is composed of straight sections and bends which form a ring. The main components of a synchrotron are the electron gun, linear accelerator (LINAC), booster ring, the radio-frequency (RF) cavity, and the storage ring. The electron gun inserts electrons into the system, where they reach the LINAC. The LINAC will accelerate the electrons to high energies, from hundreds of MeV to several GeV. The electron beam will then travel to the booster ring, this will make sure that all of the electrons are at the correct energy to enter the storage ring. Another function of the booster ring is that the electrons will be 'injected' in discrete pulses into the storage ring forming electron bunches. Once the electrons, typically one or two hundred bunches, are in the storage ring they will travel around the ring. This is where the RF cavity becomes important. As the electrons travel in the storage ring they will reach points where they will produce radiation, such as the curved parts of the ring, or the insertion devices found in the straight sections. As the electrons produce radiation they will lose energy, the RF cavity will boost the energy of the electron bunches so that they are all at a constant energy. The sections of the ring that produce radiation are where the beamlines are situated.

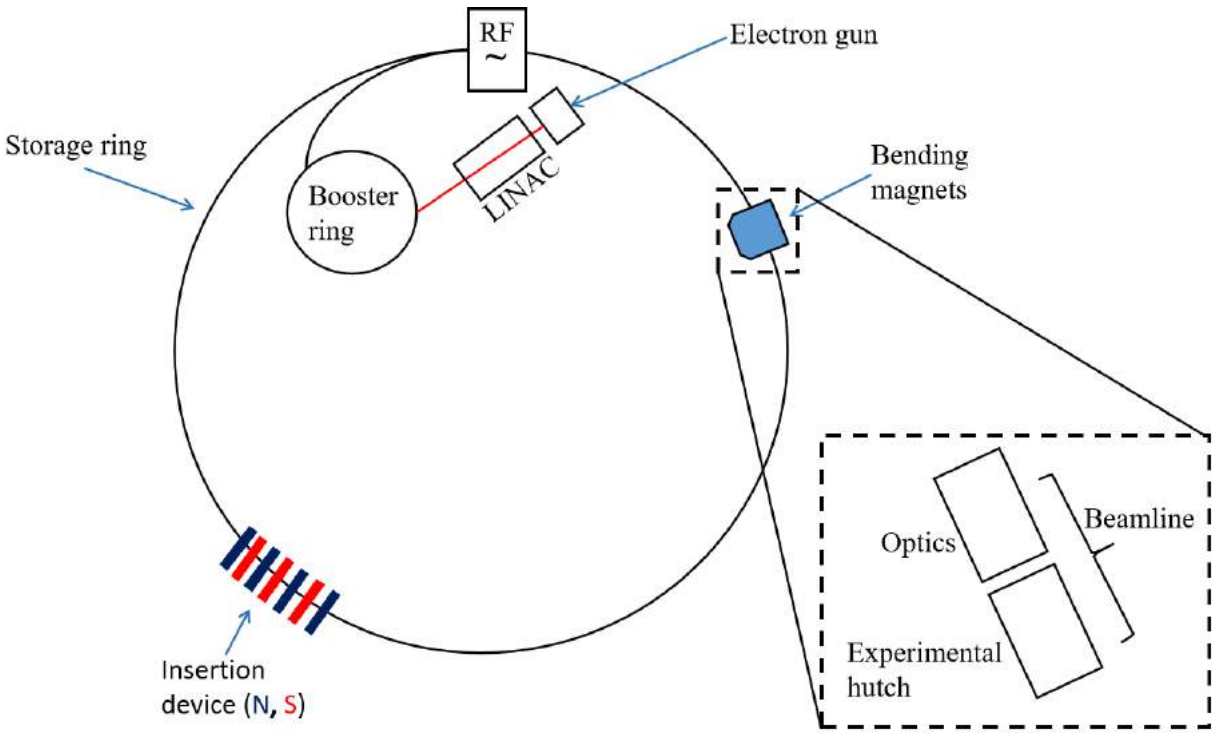

Figure 2.1: Simple schematic of the essential components of a synchrotron.

A beamline comprises of three separate environments, the optics hutch, the experimental section and the control room (see Figures 2.2 and 2.3)[1]. The optics hutch houses the components that define the x-ray beam that will be used in the experiment. These normally include crystal monochromators, mirrors, and slits, in the case of a beamline designed for hard x-rays. A beamline designed for soft x-rays requires ultra high vacuum conditions, to avoid photon absorption by the air. Due to the vacuum conditions the only optical elements used in these beamlines are mirrors and diffraction gratings [83].
The experimental hutch is where the sample environment is housed, the detectors used for the experiment, as well as additional slits and mirrors. The sample environments will differ depending on the type of experiment and what is available at each beamline. The control room is where the data measured can be observed and extracted. In some cases, parts of the experimental hutch can be automated, and they are controlled from the control room.

[1]The components, in each environment, discussed in this thesis will be specific to those found in an XAS beamline.

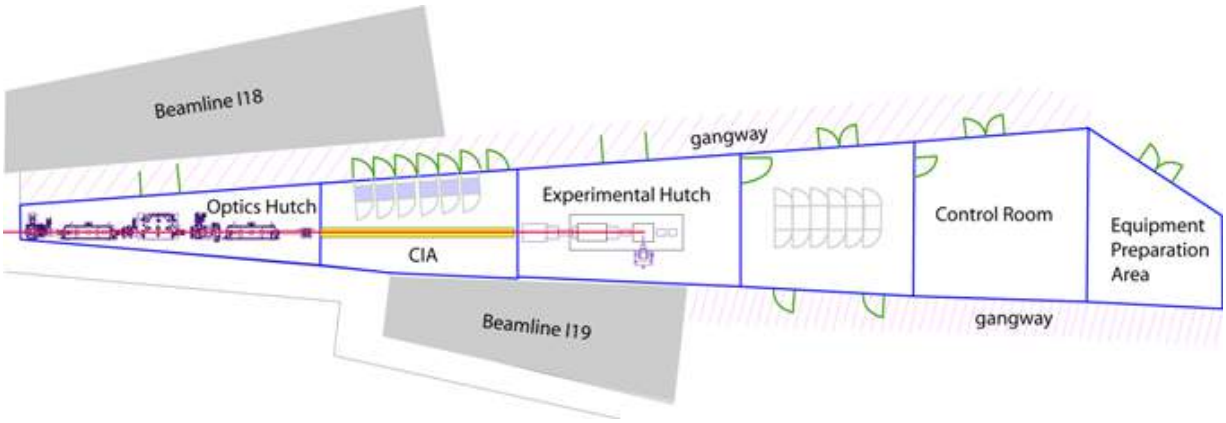

Figure 2.2: Simple schematic of the set up of the beamline B18 at Diamond Light Source, Oxfordshire, UK [84].

Figure 2.3: Experimental and control hutches, respectively, at the beamline B18 at Diamond Light Source.

There are three main types of x-ray sources, which differ in their method of x-ray production, Figure 2.4 shows the different emission devices and their spectral profile. When an electron is travelling along a straight path its motion is uniform and linear, therefore it will not radiate. However when the electron reaches a bend its velocity will change therefore it will have a short period of acceleration which will result in the release of x-rays, if it is travelling at relativistic velocities [52]. In the straight sections of the synchrotron there are insertion devices [82], where the electron beam passes through a wiggler or an undulator. Undulators and wigglers consist of a series of magnetic poles with alternating polarisation, when the electron beam travels through it they oscillate in their path and this oscillation produces x-rays. In a wiggler a cone of light is emitted at each bend, where the cones superimpose onto each other. This results in a beam of incoherent synchrotron light when viewed in the horizontal plane of the wiggler. The magnetic poles in an undulator are less powerful, this produces gentler oscillations of the electron beam. The means the cones of radiation produced will overlap and constructively interfere with each other resulting in a coherent beam. The specific wavelengths of the synchrotron radiation produced from an undulator can be tuned by changing the gap between the magnets. The other type are bending magnets. They are responsible for the bending of the electron beam in the synchrotron and are made out of just two poles with the correct strength required for the ring. The synchrotron radiation produced from the bending magnet is a white beam with a range of energies.

The experiments discussed in this thesis all took place at bending magnet beamlines (B18, Diamond Light Source, Oxforshire, U.K., and XMaS, European Synchrotron Radiation Facility, Grenoble, France.).

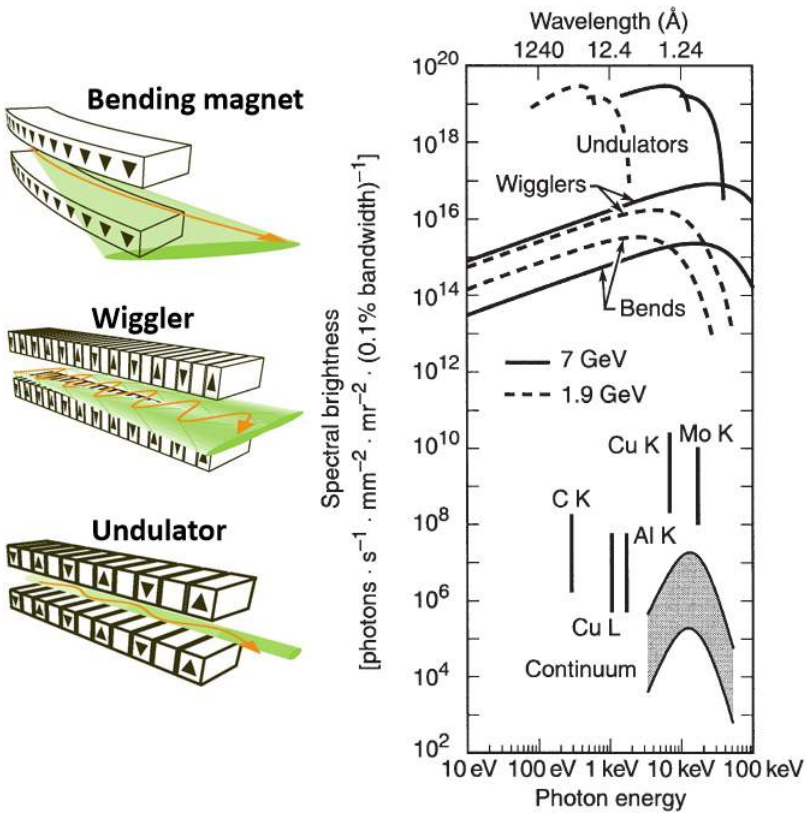

Figure 2.4: Schematic of emission devices found in a synchrotron [85] and the spectral brightness of different synchrotron radiation sources and conventional x-ray sources [53].

In the storage ring of the synchrotron there are magnets for bending the beam between the straight sections (dipole magnets) and the magnets for focusing the beam (the quadrupole and sextupole magnets), Figures 2.5 and 2.6.

Figure 2.5: An internal view of a synchrotron [86] (Diamond Light Source), where the red components are the quadrupole magnets, the yellow components are the sextupole magnets, and the green components are the dipole magnets.

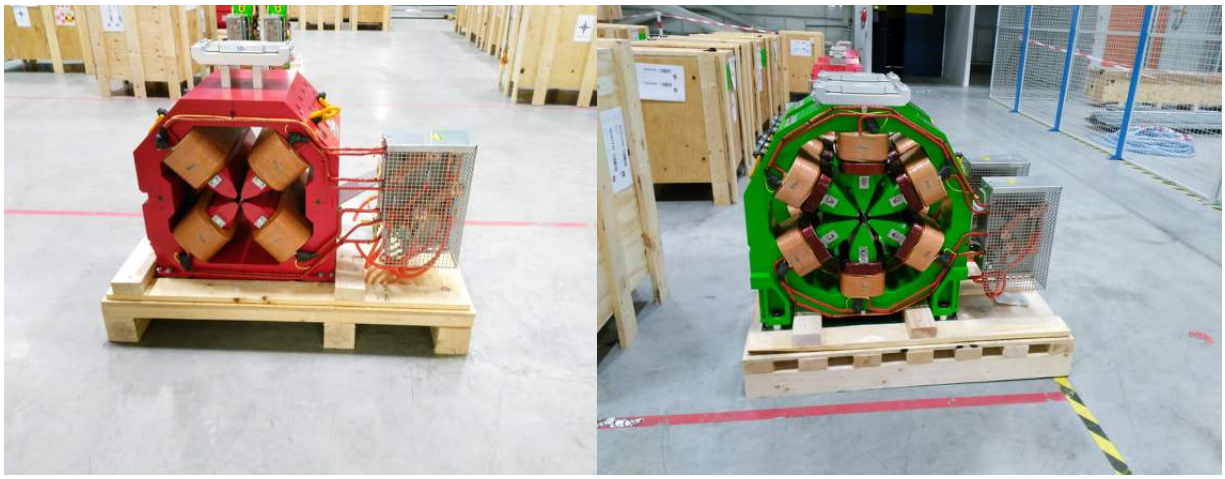

Figure 2.6: Quadrupole and sextupole magnets, used at the European Synchrotron Radiation Facility.

Beamlines are specialised depending on the type of experiment that can be carried out. Therefore the beamline used for an experiment will depend on many different factors, such as the type of sample (radioactive or non-radioactive), or the type of measurement (e.g. Angle resolved photo-emission spectroscopy (ARPES), Resonant inelastic x-ray scattering (RIXS), or XAS). For a P-XAS experiment a beamline with a tunable energy range and focused beam is required, although it does not need to be designed specifically for P-XAS. An advantage to using synchrotron radiation for a P-XAS experiment is that the x-rays produced are linearly polarised in the direction of the electrons orbital by default. This means that there is no need to do anything additional to the beam, which would normally result in a loss of intensity. The only additional requirement for a beamline used in P-XAS experiments is a sample environment that allows the orientation of the sample to be changed. This could be either a rotating table or a diffractometer, as the sample needs to be rotated with respect to a specific crystallographic axis.

2.2 X-ray absorption spectroscopy experiments

X-ray absorption spectroscopy is a spectroscopy technique that can be used to probe the local electronic and atomic structure of specific elements within a material. As x-rays pass through, the absorption coefficient, $\mu(E)$, of an element will decrease with energy as the x-ray becomes more penetrating. When an x-ray with high enough energy encounters an element, it can be absorbed by one of the core electrons. When the energy of the x-ray is high enough to release an electron from a bound state into an unoccupied state, there will be a sharp rise in the absorption coefficient measured. This is known as the absorption edge, depending on the element it can have many absorption edges which are determined by the quantum number of the core-electron excited and the electronic configuration of the excited element. The absorption edges occur at specific energies depending on the nature of the excited element. As the energy of the x-rays increase, the core electrons absorbing the x-rays will be excited into the continuum and will be released as a photoelectron. The photoelectron will be scattered by the neighbours of the excited element, this will produce interference between the outgoing and scattered wave. Another process that occurs is when a higher energy core electron will relax to fill the core hole produced from the ejection of the photoelectron.

This relaxation process will result in the release of a photon, which will scatter in the local environment which will result in interference between the outgoing and scattered wave. Whether the interference is constructive or destructive will cause oscillations in the absorption coefficient, and these oscillations can be interpreted quantitatively to provide structural information, see Chapter 3.
In the work reported in this thesis there were two types of detection methods used for the XAS experiments, transmission and fluorescence. Transmission measures the effect on the transmitted beam due to the absorption process. Whereas fluorescence measures the x-rays emitted from the relaxation process, when an electron with a higher energy fills the core-hole formed by the absorption of an x-ray.
The type of detection used depends on the type of sample being measured. For a transmission experiment the key is to have enough photons penetrate the sample and then reach the detector. To do this it is advantageous if the sample is between 1 and 2 absorption lengths thick. This results in a large enough amount of the element of interest within the sample to interact with the beam, with enough transmitted x-rays reaching the detector. The sample can be thinner and still result in enough absorption for a transmission experiment, but it should not be larger than 2 absorption lengths thick. To minimise noise the sample must also be uniform and homogeneous. For a fluorescence experiment, the element of interest must either be dilute in a thick sample, or dense in a thin sample. This means that more concentrated samples such as single crystals can be measured with this technique. For both types of detection there needs to be something in place to reduce any loss of photons, allowing as many as possible to reach the detector, this can be done by running the experiment under vacuum conditions if possible. Running under vacuum conditions stops any scattering that may occur from the air, while the photons are travelling between the sample and the detector. In an absorption experiment there will always be transmitted x-rays and fluorescence x-rays produced by the sample, therefore only the set up of the experiment can determine which will be measured fully.
Transmission is the most straightforward detection mode, during which the intensity of the initial beam of x-rays and the intensity of the transmitted photons are measured. Rearranging Beer-Lambert's law [87], an expression for the absorption coefficient can be produced, Equation (2.1).

$$\mu(E)t = \ln(\frac{I_0}{I_t}) \tag{2.1}$$

where I_0 is the intensity of the incoming x-rays, I_t is the intensity of the transmitted photoelectrons, and t is the thickness of the sample.
The set up for transmission detection is also simple, Figure 2.7, where along the beam path are the incoming photons detector, the sample, and the transmitted photons detector, in that order. The ratio between the intensity of the initial beam and intensity of transmitted photons will include information of the local environment of the excited element, this is discussed in Chapter 3.

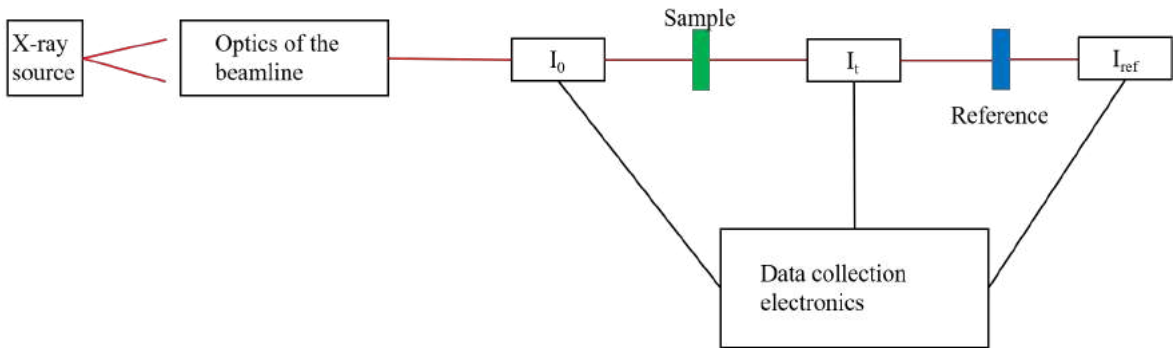

Figure 2.7: Schematic of a transmission detection XAS experiment.

In a fluorescence XAS experiment the initial intensity of the incoming x-rays and the intensity of the fluorescence of the sample is measured. Using Equation (2.2), the absorption coefficient can be calculated.

$$\mu(E) \approx \frac{I_f}{I_0} \tag{2.2}$$

where I_0 is the intensity of the incoming x-rays, and I_f is the intensity of the fluorescence x-rays.
However it is not as simple as transmission to deal with, as self-absorption needs to be taken into account. Self-absorption occurs when the lifetime of the emitted photon is small and does not allow it to escape the sample. How the self-absorption is dealt with for fluorescence data is discussed in Chapter 3. The set up for fluorescence detection is different than that for transmission. In order to reduce the noise produced from diffraction peaks, which have a $\cos\theta$ term in the cross-section, the fluorescence detector is set up at a 90° angle to the initial beam, Figure 2.8. The sample is typically set to a 45° angle to the initial beam to obtain the balance of a large fluorescence yield and a small self-absorption. The affect of the self-absorption is smaller when the sample surface is at a shallow angle to the detector, as the detector will view more of the fluorescing surface. However if that angle is too shallow the beam will not directly impact much of the surface, reducing the amount of absorption occurring.

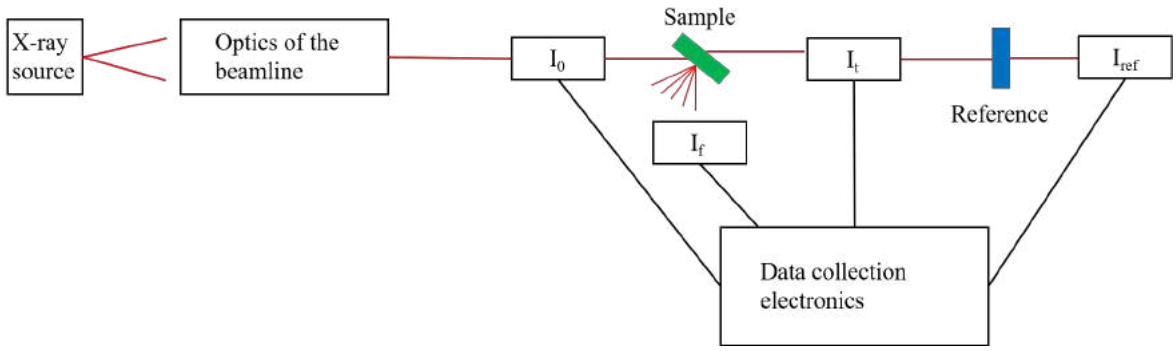

Figure 2.8: Schematic of a fluorescence detection XAS experiment.

2.3 Linearly polarised x-ray absorption spectroscopy experiments

While the fundamental set up of a P-XAS experiment is the same as that for a normal fluorescence XAS experiment there are differences in the sample environment. Taking advantage of the fact that synchrotron radiation is linearly polarised, due to the nature of how it is produced, a P-XAS experiment can be performed at any XAS beamline. X-rays produced from an electron travelling at relativistic velocities in a curve are linearly polarised when viewed in the direction of the electrons trajectory. To make sure that the incoming beam is linearly polarised, slits need to be added to cut off any unwanted x-rays (those with circular polarisation).
When a linearly polarised x-ray causes an absorption (and consequent scattering) event, the initial wavefunction will include an angular dependence (for the mathematics see Chapter 3). This angular dependence is important when measuring an oriented sample, as the angle between the polarisation and the oriented crystal axis will affect the signal measured. In K-edge measurements the absorption event is dipolar, as it is a $1s$ to p transition. As the interaction is dipolar this will restrict certain photoelectron scattering events from contributing to the XAS signal (e.g. paths that are perpendicular to the polarisation of the initial beam) [88]. The experiments discussed in this thesis all consist of K-edge measurements.
The sample set up for a P-XAS experiment is different as the sample will need to be moved to different angles with respect to the incoming beam. This can be done by using a rotating table where the sample is oriented so that the c-axis is parallel to the polarisation of the incoming beam at $\theta = 0^o$, and perpendicular when $\theta = 90^o$ (see Figure 2.9). Another way to set up this type of experiment is to use a diffractometer and orient the sample with respect to the beam and rotate the sample along the correct axis. It is also possible to measure the same data with a static sample and a rotating beam, however this requires a beamline with the capability to rotate the polarisation of the beam. It is also possible to change the orientation of the sample by hand after each measurement, but it will be quite difficult to maintain accurate orientations.
The set up of a P-XAS experiment depends on two things, what is available at the beamline and the orientation of the crystallographic axes of the sample. The view of the incoming x-ray will change depending on the angle between the c-axis of the sample and the initial beam, Figure 2.10. When a sample is anisotropic the incoming beam will interact with a different environment for each angle with respect to the sample, producing XAS with different information on the local environment. How the EXAFS equation takes into account the orientation of the sample with respect to the polarisation of the beam is discussed in detail in Chapter 3.

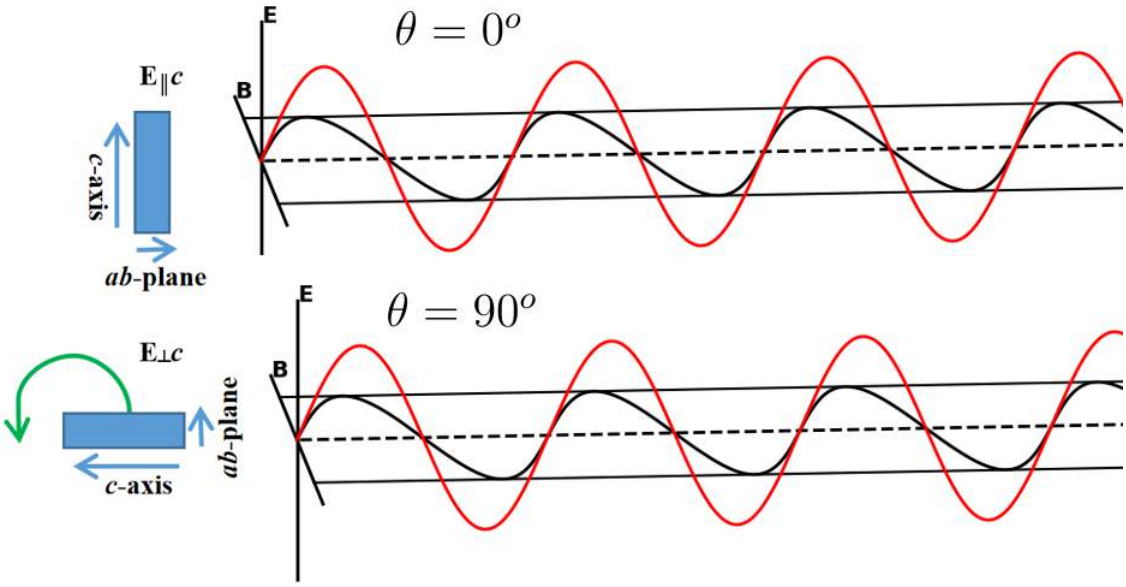

Figure 2.9: Simple schematic of the set up of a P-XAS experiment. The sample will be rotated with respect to a static linearly polarised beam. Where the direction of the magnetic field is black, and the electric field is red.

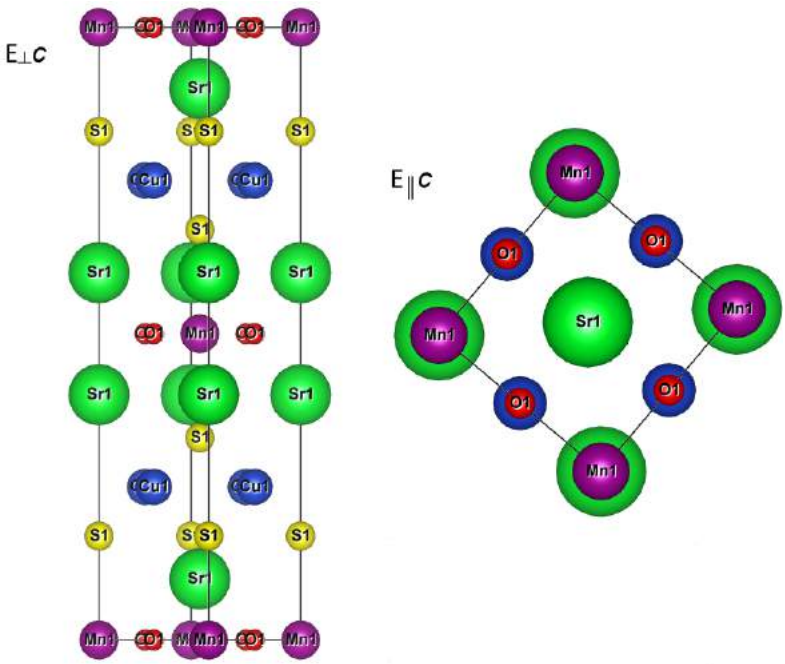

Figure 2.10: View of an anisotropic structure ($Sr_2MnCu_{1.5}S_2O_2$) with the x-ray polarisation parallel and perpendicular to the c-axis. Where the x-ray polarisation is going into the page.

The P-XAS experiments performed for this thesis measure the XAS at different angles with respect to the beam and the c-axis. The sample is set up to measure XAS spectra at $E \parallel c$ and intermediate steps until $E \perp c$, or as close to this as feasible, is reached. The steps in angle are dependent on the amount of time available and the amount of spectra needed to be measured during the experiment. If it is not possible to measure $E \parallel c$ or $E \perp c$ then only the intermediate angles are measured. Based on the analysis method developed for this thesis, a fit can be produced for the data at any

angle, this is discussed further in Chapter 3.
A weighting factor has been calculated for the analysis of the data in this thesis (see Chapter 3 for further details). By implementing this weighting factor, several angles can be fit simultaneously. This improves the quality of the fit as more guess parameters are available, due to more data being read into a single fit. As the samples discussed in this thesis have anisotropic properties, being able to study them with respect to a crystallographic axis is highly advantageous. By comparing the fit at each angle, a more thorough idea of the local electronic and atomic structure of the excited element can be obtained.

2.4 Scanning electron microscope experiments

A scanning electron microscope (SEM) uses a focused beam of electrons to scan a material to produce an image of the surface. This process produces various signals which can be used to determine the topography and composition of the material. The electrons in the initial beam interact with the surface of the sample and reflect into the detectors. The basic set-up for a SEM can be seen in Figure 2.11, with each component labelled.

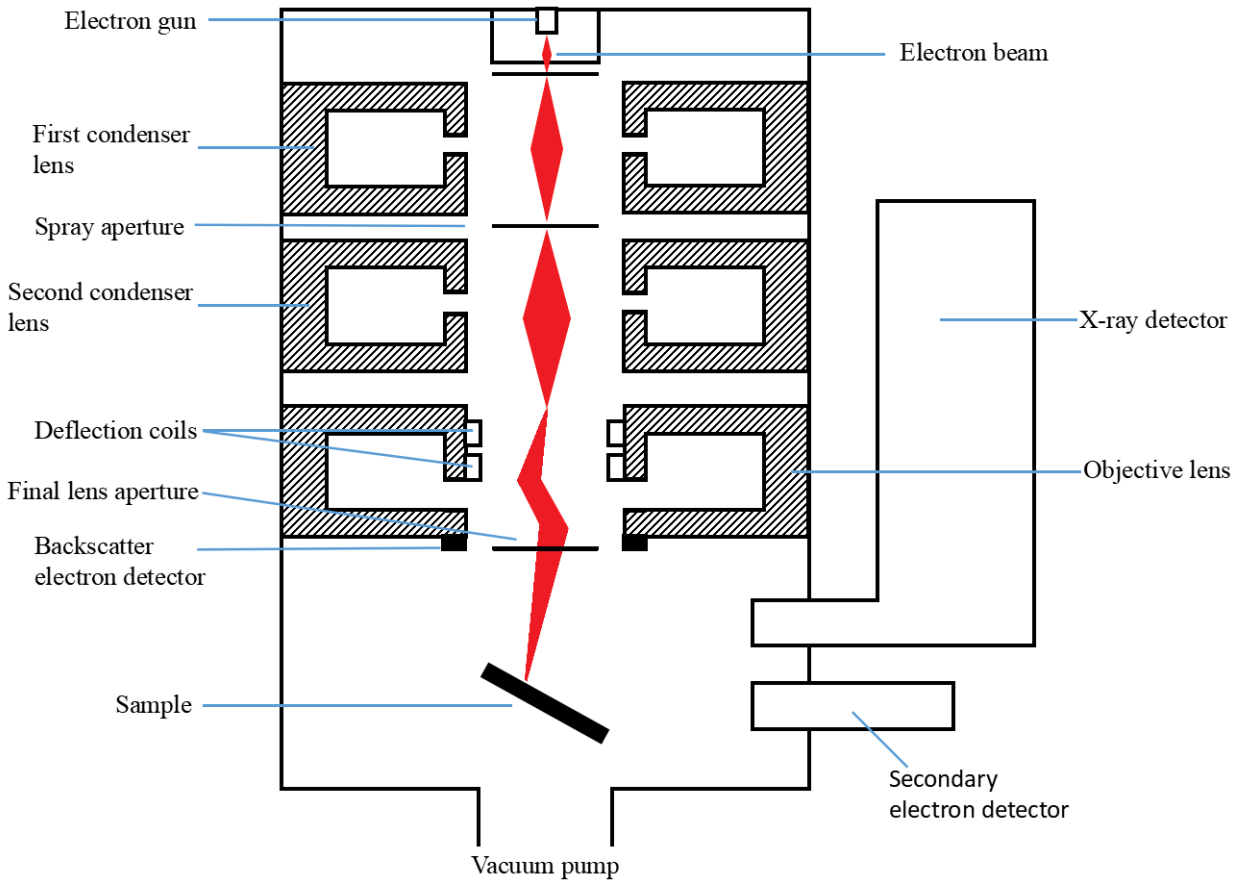

Figure 2.11: Schematic of a scanning electron microscope.

In SEM measurements there are three modes of detection: secondary electrons, backscattered electrons, and characteristic x-rays. The secondary and backscattered electron detection is used to produce surface map images of the sample. Secondary electrons are released from the very surface of the sample, while backscattered electrons are released from slightly deeper within the sample (see Figure 2.12). Measuring both

is useful for determining if a feature seen with one mode of detection is consistent with the other mode of detection. A simple schematic of the interaction process of an SEM measurement can be seen in Figure 2.12. The secondary electrons are released via inelastic scattering between the electron beam and the sample, while the backscattered electrons are produced by high energy electrons in the beam being reflected by the sample. Images are produced by comparing the intensity of the electron beam and the intensity of secondary or backscattered electrons, depending on the detection mode. This produces a contrast image of the surface of the material, therefore the topography of the surface can be examined. The magnification of the image is controlled by the focus of the electron beam. If the beam is larger (unfocused) the image produced will be of a larger area of the surface, while if the beam is smaller (focused) then the image produced will be of a smaller area, effectively magnifying the image.

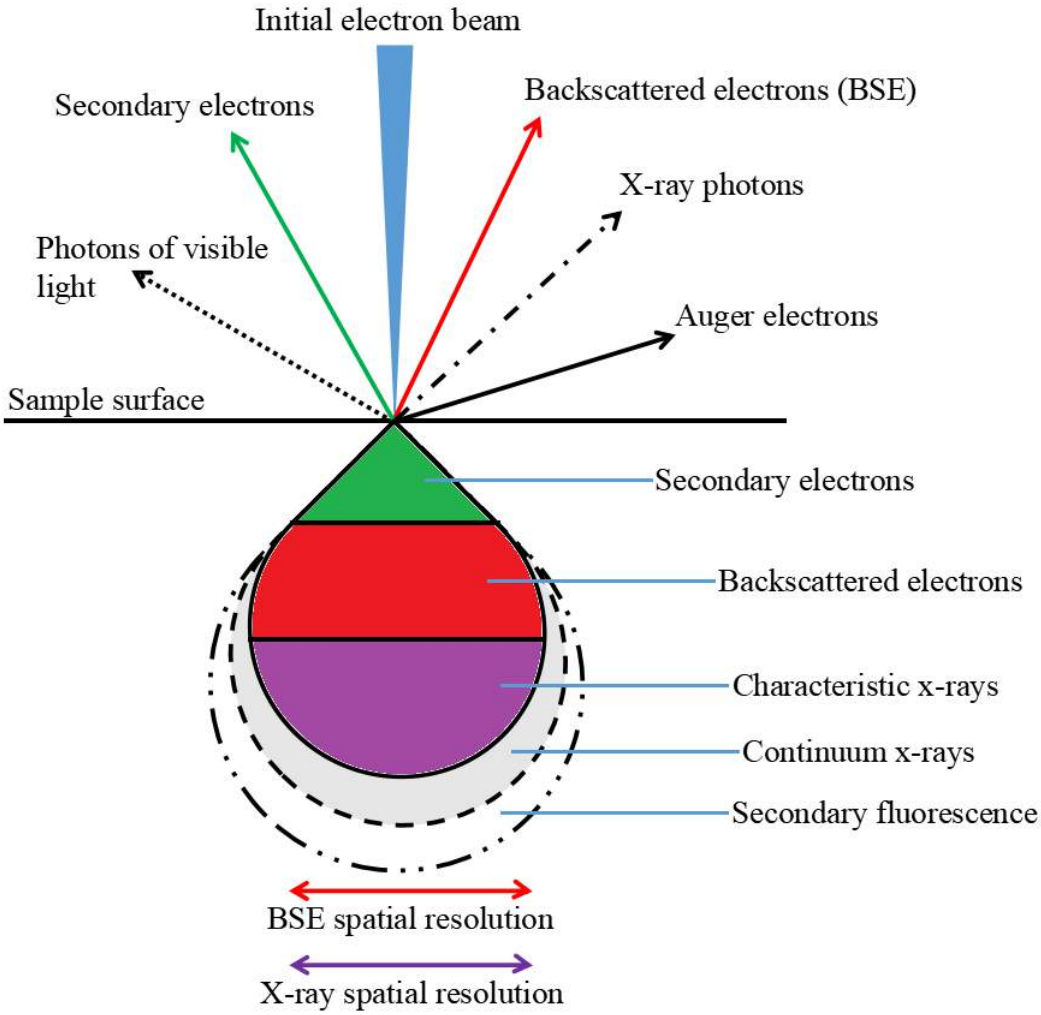

Figure 2.12: Interaction volume of the specimen during an SEM experiment.

The characteristic x-rays measured from the electron interactions with the sample can be used to determine the stoichiometry of the material. The elemental composition of the sample can be worked out using energy-dispersive x-ray spectroscopy (EDX). This technique requires an interaction with the sample that will result in the release of x-rays, by excitation from a beam of charged particles such as electrons, protons , or a beam of x-rays. This technique takes advantage of the unique electronic structure of the elements within the sample, which result in a unique set of peaks on an emission

spectrum, which enables compositional analysis in terms of atomic composition. An example of an emission spectrum with the peaks labelled by their elemental marker, and transition responsible, can be seen in Figure 2.13.

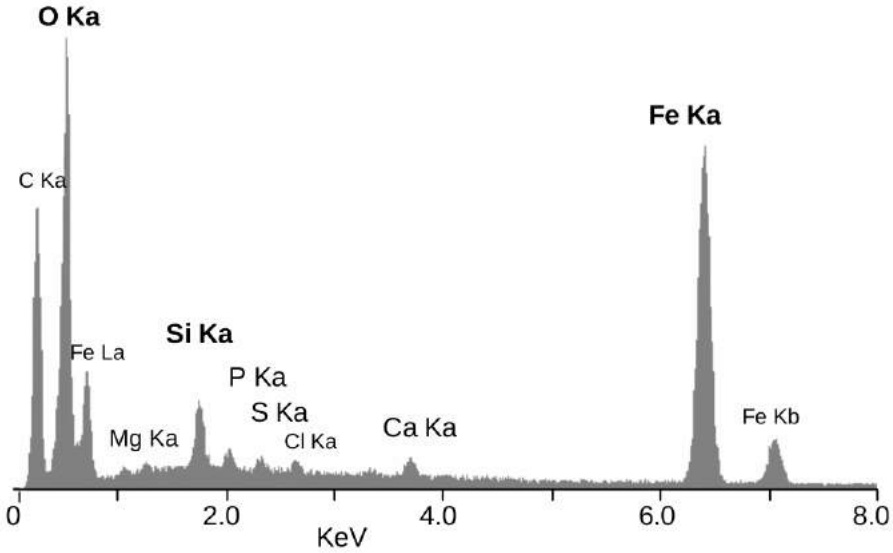

Figure 2.13: EDX spectrum of the mineral crust of the vent shrimp Rimicaris exoculata [89].

The characteristic x-rays can be used to determine the elemental composition of the sample, but obtaining a stoichiometry from this should be backed up by another technique as the accuracy of this technique is limited. A rough estimate of the stoichiometry was found by focusing the electron beam on various parts of the homogeneous regions of the samples and measuring spectra at each point. The SEM was first calibrated by measuring a sample of pure Cobalt. The weight percentages of the each element were extracted from the spectra and compared with each other by using the INCA software [90]. Measurements that included peaks from other elements, such as from the sample holder or glue, were discarded and an average was calculated of the weight percentage of each element in the sample. A ratio of these weights were used to estimate the stoichiometry of the samples used in each P-XAS experiment. As the samples measured were single crystals, the intensity of the emitted x-rays was less than expected due to self-absorption of the crystal. This is another reason the stoichiometries found using these measurements cannot be reported as accurate, as the data was not processed to account for this.
There are other techniques that can be used to measure the stoichiometry of a sample, such as Auger electron spectroscopy (AES) [91] where the excess energy is transferred to a third electron (an Auger electron), rather than an x-ray, which can be measured and analysed. X-ray photoelectron spectroscopy (XPS) [92] is similar to both EDX and AES, in that the photoelectron resulting from the excitation of the Auger electron is measured and analysed. Both AES and XPS are surface probes, therefore a pure sample is needed for it to be assumed that the stoichiometry measured is correct for the bulk material. Wavelength-dispersive x-ray spectroscopy (WDS) [93] is a common technique used alongside EDX, where it is the diffraction of the x-rays from the sample that is measured. Unlike in EDX which measures a spectrum of energies and wavelengths simultaneously, WDS only counts x-rays of a single wavelength at a time. This improves the reliability of the measurement as the raw data is separated into spectral components, which may remove the artefacts of EDX such as false peaks, noise from

the amplifiers, and microphonics. However none of these techniques were used for this thesis.

2.5 Single crystal x-ray diffraction

Another method used to check the quality of the samples was single crystal x-ray diffraction (SC-XRD). The results were used only to confirm space group and location of the c-axis, and no further analysis was carried out. Therefore the SC-XRD data will not be reported in this thesis.
When a beam of x-rays scatters off electrons within a material interference patterns will be formed. The scattered x-rays will either destructively or constructively interfere, the condition that needs to be met for constructive interference is determined by Bragg's law:

$$2d \sin\theta = n\lambda \tag{2.3}$$

where d is the spacing between diffracting planes, θ is the angle between the sample and the beam, n is an integer, and λ is the wavelength of the beam. At the points of constructive interference a large intensity of reflected x-rays will be measured, which appear as bright spots and produce a diffraction pattern.
The quality of the crystal can be determined by the diffraction pattern measured. If a sample is a pure phase single crystal then the bright spots observed in a diffraction pattern should be sharp and correspond to one crystal structure.

2.6 Chapter summary

This chapter has introduced the set up and components of a synchrotron. The experimental set up of XAS experiments, and the requirements of a single crystal P-XAS experiment have been discussed. Where the set up of P-XAS is very similar to fluorescence mode XAS experiments, however a degree of rotational freedom is useful for measuring at different orientations with respect to the beam and the c-axis. The change in the sample orientation can be implemented by moving the sample holder by hand after each measurement, by using a rotating table, or using a diffractometer. The quality of the single crystals, used in the P-XAS experiments discussed in this thesis, was important and needed to be confirmed. To do this SEM measurements and SC-XRD measurements were performed to confirm the samples were homogeneous and single phase. Both of these techniques were introduced in this chapter, and how they were used for the work in this thesis was discussed.

Chapter 3

XAS: Theoretical concepts and data analysis

In this chapter the basic concepts of x-ray absorption spectroscopy (XAS) theory, and analysis will be discussed. This thesis focuses on single crystal polarised x-ray absorption spectroscopy (P-XAS) experiments, performed with linearly polarised x-rays. The principles behind this technique will be discussed below.
P-XAS has been a known technique since the development of XAS experiments. The use of this technique for XANES experiments can be seen in [94, 95, 96], and its use in oriented powders has been carried out by many groups [63, 65, 97]. Another use of P-XAS is to investigate quadrupole effects, which has been carried out by many groups [98, 99]. This thesis focuses on using XAS and linearly polarised x-rays to study single crystals. This technique has been used in the past [67, 100, 101]. However the analysis techniques of the data vary between groups. Here we will describe how we have extracted structural information from this type of data.

3.1 Theoretical concepts

3.1.1 General x-ray absorption spectroscopy theory

Considering the interaction of an x-ray with a bound electron in an atomic core state, $|i>$, the cross-section of a transition in which this core electron is released into an unbound state, $|f>$, is given by Fermi's golden rule [102]. A full derivation for Equation (3.1) can be seen in Appendix A.

$$\sigma(\omega) = 4\pi^2 \alpha_{fs} \omega\hbar |<f|\vec{r}\cdot\vec{\epsilon}|i>|^2 \delta(E_f - E_i - \hbar\omega)\rho(E_f) \tag{3.1}$$

where $\alpha_{fs} = e^2/(\hbar c)$ is the fine structure constant, $\rho(E_f)$ is the density of unoccupied states at energy E_f, $\vec{\epsilon}$ is a unit vector along the linear polarisation direction of the x-ray, $\vec{r}$ is the vector between the atoms involved in the scattering process, ω is the frequency of the incoming x-ray, and $\delta(E)$ is a Dirac delta function that reduces all other energies points to zero. The energy of the incoming photon is $E_\gamma = \omega\hbar$.
A simple schematic of the process occurring during an x-ray absorption event can be seen in Figure 3.1. The incoming photon needs to have an energy equal to or greater than the binding energy of the core electron to release it. As the binding energies differ for each element and edge, x-ray absorption spectroscopy is an element specific tool.

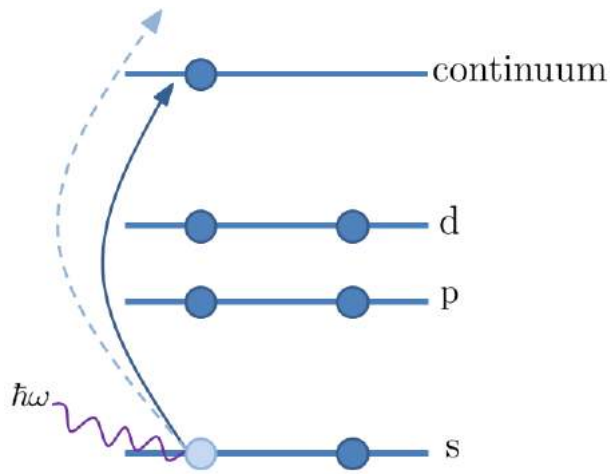

Figure 3.1: A simple schematic of the process occurring during an x-ray absorption event.

When measuring the absorption as a function of energy, a jump in the absorption cross-section will occur at energies above the binding energy. For an isolated atom the absorption cross-section will vary smoothly with energy, and after the absorption edge it will decrease with no oscillations. If the absorbing atom is surrounded by neighbours, like in a solid, then the released photoelectron will scatter from the potential due to those atoms (see Figure 3.2). The scattered wave will constructively or destructively interfere with the outgoing wave, causing the oscillations seen after the absorption edge. These oscillations are referred to as extended x-ray absorption fine structure (EXAFS) and will contain information on the local atomic structure around the absorbing atoms. Figure 3.3 shows the XAS of the Cu K-edge for a $Sr_2MnCu_{1.5}S_2O_2$ powder sample, the oscillations seen past $\sim 9020eV$ contribute to the EXAFS signal, while the x-ray absorption near edge structure (XANES) signal is seen in the $\sim 8990 - 9020eV$ range.

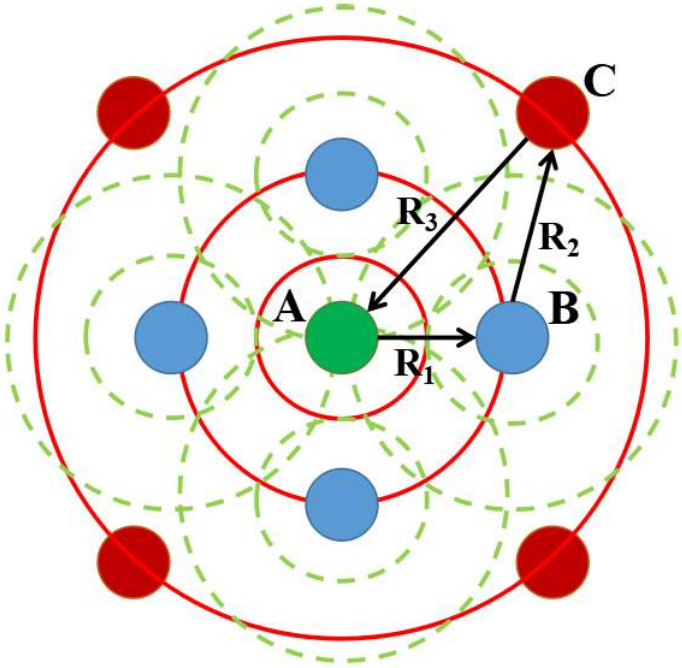

Figure 3.2: A simple schematic of the scattering process occurring during an XAS experiment. Where A is the excited atom, B is its nearest neighbour, and C is the next nearest neighbour. With R_1, R_2, and R_3 as the distance between them.

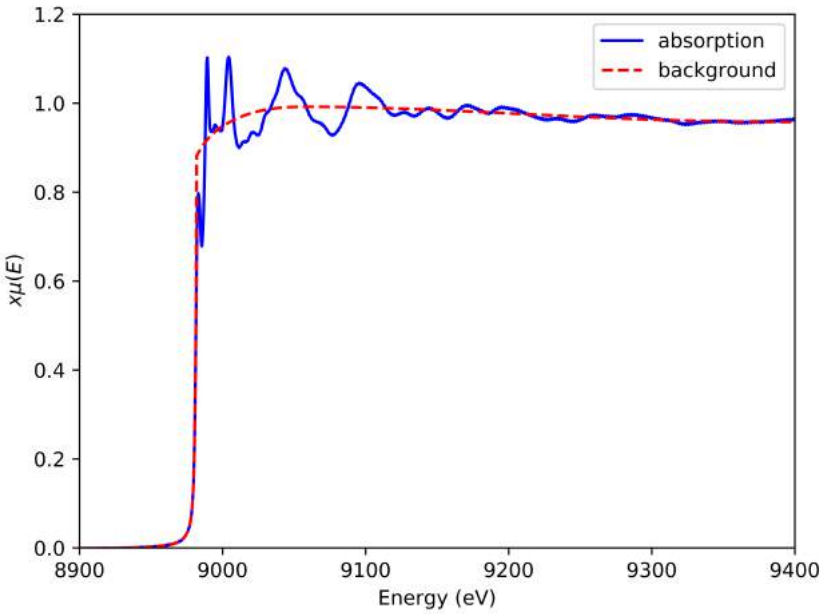

Figure 3.3: XAS absorption of the Cu K-edge of the $Sr_2MnCu_{1.5}S_2O_2$ powder sample. The background indicated simulates the absorption of an isolated atom. This data was measured at B18 in Diamond Light Source, in Oxfordshire, UK, by Prof. Simon Clarke's group in April 2013.

3.1.2 Dipole approximation and simplification of x-ray absorption spectroscopy due to symmetry

The theoretical representation of the absorption, in a K-edge measurement, can be simplified by taking into account the symmetry of the sample being measured. This simplification is sufficient for the XAS reported in this thesis, as they are all K-edge measurements which, due to selection rules, is a dipole transition.
By using commutation relations [82], the dipole approximation of the absorption probability can be written as:

$$\mu \propto \hat{\epsilon} \cdot M \cdot \hat{\epsilon} \tag{3.2}$$

where the second rank tensor M represents the scattering process between two points in 3D space, and has components:

$$M_{jk} \propto \sum_f < \psi_i | r_j | \psi_f >< \psi_f | r_k | \psi_i > \tag{3.3}$$

and $\hat{\epsilon}$ is the x-ray polarisation vector expressed in spherical coordinates θ, and ϕ:

$$\hat{\epsilon} = (\sin\theta\cos\phi, \sin\theta\sin\phi, \cos\theta) \tag{3.4}$$

The orientation of the incoming x-ray can be seen in Figure 3.4, with the angles from Equation (3.4) labelled.

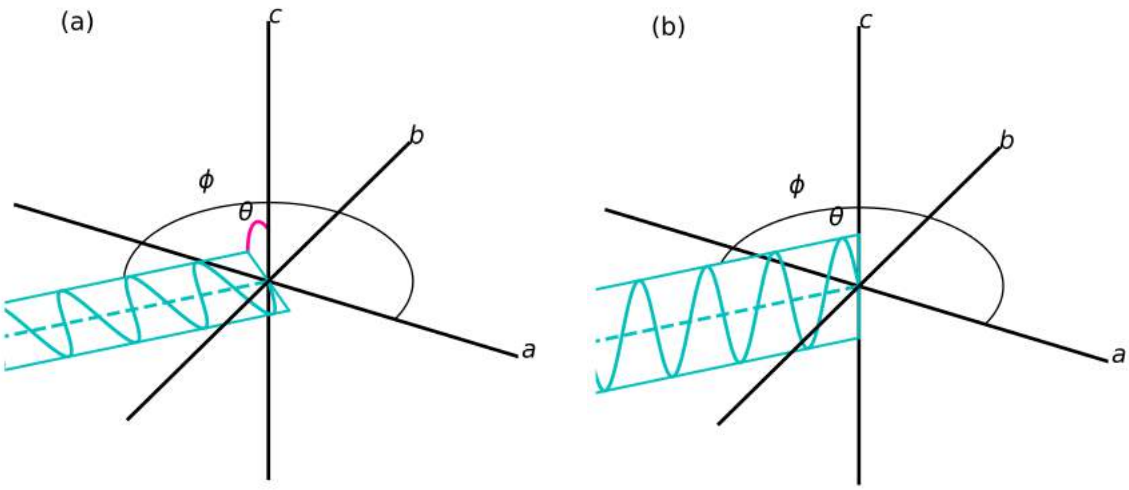

Figure 3.4: Relative orientation of the incoming x-rays. Where the polarisation of the x-ray is parallel to the ab plane in (a), and parallel to the c axis in (b). θ and ϕ are between the polarisation of the incoming x-ray and the crystallographic axes.

Combining Equations (3.2) to (3.4), a general equation for the absorption, in the dipole approximation, can be found[1]:

$$\mu \propto (\sin\theta\cos\phi, \sin\theta\sin\phi, \cos\theta) \cdot \begin{pmatrix} M_{aa} & M_{ab} & M_{ac} \\ M_{ba} & M_{bb} & M_{bc} \\ M_{ca} & M_{cb} & M_{cc} \end{pmatrix} \cdot \begin{pmatrix} \sin\theta\cos\phi \\ \sin\theta\sin\phi \\ \cos\theta \end{pmatrix}$$

$$= \sin^2\theta\cos^2\phi M_{aa} + \sin^2\theta\sin^2\phi M_{bb} + \cos^2\theta M_{cc} + \sin^2\theta\sin\phi\cos\phi M_{ba} + \sin^2\theta\cos\phi\sin\phi M_{ab} + \sin\theta\cos\theta\cos\phi M_{ca} + \sin\theta\cos\theta\cos\phi M_{ac} + \sin\theta\cos\theta\sin\phi M_{cb} + \sin\theta\cos\theta\sin\phi M_{bc}$$

[1]The full derivation can be seen in Appendix A.

We can say that $M_{jk} = M_{kj}$ without losing any generality, because the double sum of Equation (3.3) is symmetric [82], therefore the above equation can be simplified further to:

$$\begin{aligned} \mu \propto \sin^2\theta\cos^2\phi M_{aa} + \sin^2\theta\sin^2\phi M_{bb} + \cos^2\theta M_{cc} \\ +2(\sin^2\theta\sin\phi\cos\phi M_{ba} + \sin\theta\cos\theta\cos\phi M_{ca} + \sin\theta\cos\theta\sin\phi M_{cb}) \end{aligned} \tag{3.5}$$

Taking into account the symmetry of the crystal, this equation can be simplified significantly for certain symmetries. The samples used in this thesis were layered non-cubic crystals, this means that the signal measured will be affected by changes in angle with respect to the z-axis. To account for a change in angle with respect to the z-axis, M_{jk} is rotated. The matrix for a rotation by an angle $\alpha = 2\pi/N$ about the z-axis is [82]:

$$R(\alpha) = \begin{pmatrix} \cos(\alpha) & -\sin(\alpha) & 0 \\ \sin(\alpha) & \cos(\alpha) & 0 \\ 0 & 0 & 1 \end{pmatrix}$$

A second rank tensor is rotated by applying the rotation matrix and its inverse:

$$M = R \cdot M \cdot R^{-1} \tag{3.6}$$

$$= \begin{pmatrix} \cos(\alpha) & -\sin(\alpha) & 0 \\ \sin(\alpha) & \cos(\alpha) & 0 \\ 0 & 0 & 1 \end{pmatrix} \cdot \begin{pmatrix} M_{aa} & M_{ab} & M_{ac} \\ M_{ba} & M_{bb} & M_{bc} \\ M_{ca} & M_{cb} & M_{cc} \end{pmatrix} \cdot \begin{pmatrix} \cos(\alpha) & \sin(\alpha) & 0 \\ -\sin(\alpha) & \cos(\alpha) & 0 \\ 0 & 0 & 1 \end{pmatrix}$$

This leads to 9 equations, one for each element of the tensor.

$$M_{aa} = \cos^2\alpha M_{aa} + \sin^2\alpha M_{bb} - 2\cos\alpha\sin\alpha M_{ba} \tag{3.7}$$
$$M_{ab} = \cos^2\alpha M_{ab} - \sin^2\alpha M_{ba} + \cos\alpha\sin\alpha(M_{aa} - M_{bb}) \tag{3.8}$$
$$M_{ac} = \cos\alpha M_{ac} - \sin\alpha M_{bc} \tag{3.9}$$
$$M_{ba} = \cos^2\alpha M_{ba} - \sin^2\alpha M_{ab} + \cos\alpha\sin\alpha(M_{aa} - M_{bb}) \tag{3.10}$$
$$M_{bb} = \sin^2\alpha M_{aa} + \cos^2\alpha M_{bb} + 2\cos\alpha\sin\alpha M_{ba} \tag{3.11}$$
$$M_{bc} = \sin\alpha M_{ac} + \cos\alpha M_{bc} \tag{3.12}$$
$$M_{ca} = \cos\alpha M_{ca} - \sin\alpha M_{cb} \tag{3.13}$$
$$M_{cb} = \sin\alpha M_{ca} + \cos\alpha M_{cb} \tag{3.14}$$
$$M_{cc} = M_{cc} \tag{3.15}$$

For a crystal with $N > 2$ rotational axes the rotated tensor simplifies greatly to [82]:

$$M_{N>2} = \begin{pmatrix} M_{aa} & M_{ab} & M_{ac} \\ -M_{ab} & M_{aa} & M_{bc} \\ -M_{ac} & -M_{bc} & M_{cc} \end{pmatrix} \tag{3.16}$$

This means that the dipole absorption for crystals with this symmetry can be written as:

$$\mu \propto \sin^2\theta M_{aa} + \cos^2\theta M_{cc} \tag{3.17}$$

For a crystal symmetry with $N = 2$ rotational axes, the rotated tensor does not simplify as much:

$$M_{N=2} = \begin{pmatrix} M_{aa} & M_{ab} & 0 \\ M_{ba} & M_{bb} & 0 \\ 0 & 0 & M_{cc} \end{pmatrix} \tag{3.18}$$

Therefore the dipole absorption for crystals with this symmetry can be written as:

$$\mu \propto \sin^2\theta\cos^2\phi M_{aa} + \sin^2\theta\sin^2\phi M_{bb} + \cos^2\theta M_{cc} + 2\sin^2\theta\sin\phi\cos\phi M_{ab} \tag{3.19}$$

The full derivations for the simplification of the dipole absorption based on crystal symmetry can be seen in Appendix A.
The crystals investigated in this thesis have hexagonal, tetragonal and orthorhombic symmetry, $N = 6, 4,$ and 2 rotational axes, respectively.
By using this relationship it is possible to calculate a theoretical XAS signal for angles that are hard to measure experimentally. As for symmetries with $N > 2$ rotational axes, the absorption simplifies to Equation (3.17), the absorption can be written to get:

$$\mu(E) \propto \cos^2\theta(\mu_\perp - \mu_\parallel) + \mu_\parallel \tag{3.20}$$

where $M_{aa} = \mu_\parallel$ and $M_{cc} = \mu_\perp$, if $\mu_\perp$ is taken as the XAS along the c-axis. Taking advantage of this dependence, the absorption at each energy point, for each angle measured, can be fit to a straight line and this line can be extrapolated to find the absorption at any angle with respect to the c-axis. Equation (3.20) can be recognised as a line of best fit, $y = mx + c$ where $y = \mu(E)$, $m = (\mu_\perp - \mu_\parallel)$, $x = \cos^2\theta$, and $c = \mu_\parallel$. This means that the absorption for structures with an $N > 2$-fold rotational axis along the z-direction should have a linear dependence to $\cos^2\theta$. Another approach to this simplification has been published by Brouder [67], where the angular dependence of the XAS spectra is calculated in terms of spherical tensors. The results of both approaches are equivalent therefore this thesis will only include the above approach.
A code was written in Python [103] for this thesis, which uses Equation (3.20) to produce a value for the absorption at each energy point, for any angle. This code can be seen in Appendix A. Comparisons of the experimental data and the XAS simulated by the code can be seen in Chapters 4 and 6. This is used for experimental set ups where the two extreme angles $\theta = 90^o, 0^o$ cannot be measured, but it is still interesting to look at the structure in terms of two orthogonal components.
Another use for this code is to confirm the crystal does have the symmetry it has been reported to have. If the crystal has a lower symmetry than reported, where its rotational axes are ≤ 2 rather than > 2, then the simulated data will not match the experimental data. This will indicate that the crystal does not have the symmetry expected and can be used as an additional quality check before performing analysis. This can also indicate if the orthorhombic symmetries of $Sr_2MnCu_{1.5}S_2O_2$ and Ca_2RuO_4 have a small enough orthorhombic distortion to be assumed tetragonal, for the purpose of simulating XAS data.

3.1.3 EXAFS equation: single scattering

The x-ray absorption coefficient above the absorption edge can be written as:

$$\mu(k) = \mu_0(k)(1 + \chi(k)) \tag{3.21}$$

where $k = \sqrt{2m(E_{p.e.} - E_f)}/\hbar$, $\mu_0(k)$ is the absorption coefficient of the excited atom if it was isolated, $\chi(k)$ is the EXAFS signal, and $k = 0$ at the energy corresponding to the absorption edge (close to the continuum state). For K-edge measurements, considering only single scattering paths, the EXAFS equation is given by [55, 104, 105, 106, 107, 108]:

$$\chi(k) = \sum_j \chi_j(k) = -\sum_j 3(\vec{\epsilon}\cdot\vec{r_j})^2 \frac{N_j S_0^2 F_j(\pi, k, r_j)}{kr_j^2} e^{-2k^2\sigma_j^2} e^{-2r_j/\lambda(k)} \sin(2kr_j + \delta_j(k, r_j)) \tag{3.22}$$

where $\vec{\epsilon}$ is the x-ray polarisation vector, $\vec{r_j}$ is the vector between the absorbing and scattering atom, N_j is the degeneracy of the scattering path, S_0^2 is the amplitude reduction factor, $F_j(\pi, k, r_j)$ is the scattering amplitude of the scatterer j, $k = \sqrt{2m(E - E_0)}/\hbar$ is the wavenumber with respect to the Fermi level, σ_j^2 is a Debye-Waller factor that takes into account the thermal and static disorder in the position of the atoms, $\lambda(k)$ is the mean-free-path of the photoelectron, and $\delta_j(k, r_j)$ is the phase shift in the wavefunction due to the species of the absorbing and scattering atom.
To discuss this equation it is more efficient to separate the components into those which affect the amplitude of the EXAFS, and those which affect the phase of the EXAFS *i.e.*

$$\chi(k) = \sum_j \chi_j(k) = Re[\sum_j A_j(k, r_j) e^{i\Phi_j(k,r_j)}] \tag{3.23}$$

$$A_j(k, r_j) = 3(\vec{\epsilon} \cdot \vec{r_j})^2 \frac{N_j S_0^2 F_j(\pi, k, r_j)}{k r_j^2} e^{-2k^2\sigma_j^2} e^{-2r_j/\lambda(k)}$$

$$\Phi_j(k, r_j) = 2kr_j + \delta_j(k, r_j)$$

where the sum is over all single scattering centres j.
When discussing Equation (3.23), $\chi_j(k)$ will be the focus, with the understanding that a sum over all sites is needed at the end. As the origin of the EXAFS is the interference, at the position of the absorber (r=0), between the outgoing and backscattered wave, the phase Φ_j is the phase difference between the two waves. The 'optical path' phase, $2kr_j$, in the sine term of Equation (3.22), is the phase of the photoelectron (p.e) after travelling to the centre of the scatterer and back to the central absorber, a distance of $2r_j$. Other phase shifts, δ_j, are due to the scattering of the p.e. at r_j; *i.e.* $\delta_j(k, r_j) = 2\delta_c(k) + \delta_{b,j}(k, r_j)$ where c, and b stand for the central and backscattering atoms, respectively. The phase of the scatterer needs to take into account both the distance and k, this is due to the curved wave nature of the p.e. [106]. This is not the case for the phase of the absorber, as the incoming x-rays are linear. These are the terms that make up the phase component of the EXAFS. However Equation (3.23) would suggest that the phase has a cosine dependence, rather than the sine dependence seen in Equation (3.22). This cannot be explained qualitatively but is due to an additional $\pi/2$ phase shift in the asymptotic form ($kr_j \gg 1$) of the outgoing spherical Hankel function at the scatterer, $h_l^+(kr_j)$, with $l = 1$ [104, 102].
The backscattering amplitude, $F_j(\pi, k, r_j)$, is a main contributor to the amplitude of the EXAFS [106]. This is the amplitude of the scattering from the potential of the scatterer at r_j in an angle π, *i.e.* back towards the absorber. The k dependence of F_j is complicated [109] but its variation with atomic number Z means it can distinguish between different types of back-scatterers in an unknown structure.
One thing that needs to be taken into account for EXAFS measurements is the coherence of the final state. Effects that will destroy the final state coherence will also destroy the interference process which will result in a loss in the EXAFS amplitude. These include the deviations from the average interatomic distances due to lattice vibrations, this affects the term $e^{-2k^2\sigma^2}$ in Equation (3.22), also static disorder. Another effect is due to the lifetimes of the core-hole (c.h.) and p.e. being finite, this is reflected in the term $e^{-2r_j/\lambda(k)}$ in Equation (3.22).
Finite lifetime effects are phenomenologically described in terms of a mean free path, $\lambda(k)$. The mean free path is compared to the travelling distance over which coherence is preserved, $2r_j$. The c.h. decays with a lifetime $\tau_{c.h.}$, the p.e. decays with an independent lifetime, $\tau_{p.e.}$ as it scatters inelastically into a different state. This means the total lifetime is $1/\tau = 1/\tau_{c.h.} + 1/\tau_{p.e.}$. While $\tau_{c.h.}$ does not depend on the energy of

the p.e., $\tau_{p.e.}$ depends on k reflecting the energy dependence of the spectrum of excitation of the surrounding atoms in which the p.e. travels to. A consequence of the finite lifetime is energy broadening ($\Delta E \sim \hbar/\tau$), which results in a loss of amplitude. FEFF takes this into account by introducing a complex p.e. wavenumber, $p = p' + ip''$, *i.e.* $p = \sqrt{2m(E - V_{int}(E) + i\Lambda/2)}$, where $V_{int}(E)$ is the complex, energy dependent interstitial potential and $\Lambda/2$ is the half line width of the c.h. [110, 107]. The mean free path, $1/\lambda(k) = 1/\lambda_{c.h.}(k) + 1/\lambda_{p.e.}(k)$ is obtained from the the imaginary part of the complex wavenumber, $\lambda(p) = 1/p'' = 1/\mathrm{Im}(p)$. To obtain $\lambda(k)$ from $\lambda(p)$ a correction for the different energy references used in the definitions of p and k needs to be performed [110, 107]. This explains the origin of the mean free path in Equation (3.22), as with a complex wavenumber the 'optical path' phase shift becomes $e^{-i2kr_j} = e^{2\mathrm{Re}(k)r_j}e^{-2\mathrm{Im}(k)r_j}$. Using the definition $\mathrm{Im}(p) = 1/\lambda(p)$ and applying the correction you can obtain the amplitude correction term for the mean free path, $e^{-2r_j/\lambda(k)}$. The typical value for the mean free path at intermediate p.e. energies is ~ 10Å [110, 111]. This means that $\chi_j(k)$ is reduced by $\sim 90\%$ at distances $r_j \sim 10$Å. Therefore the spacial length scale limits the technique to probing only the local structure of the absorber.
Another effect that needs to be taken into account when estimating the loss in the EXAFS signal is the Debye-Waller like term, $e^{-2k^2\sigma^2}$. This takes into account the loss of coherence due to lattice vibrations, and small static disorder, in the harmonic approximation causing deviations from the average interatomic distance, therefore changing the 'optical path' phase. As the lifetime of the p.e. ($\sim 10^{-15}s$) is shorter than the characteristic time for lattice vibrations ($\sim 10^{-13}s$), the EXAFS signal will show a 'snapshot' of the local structure. However XAS measurements typically consist of $\sim 10^8$ absorption events for each energy step which means that the scattering distances for each event will differ slightly, from one absorbing atom to the next (or the original absorber at a later time), this leads to a loss of coherence. To take this into account when dealing with the EXAFS a 'weighted optical phase' term is considered, where the weight is given by a Gaussian distribution of distances about r_j (root mean squared (rms) $\sigma_j = \sqrt{< (r_i - r_j)^2 >_i}$)

$$\int_{-\infty}^{+\infty} \frac{1}{\sqrt{2\pi\sigma_j^2}} e^{-(r_i - r_j)^2/2\sigma_j^2} e^{i2kr_i} dr_i \tag{3.24}$$

where $r_i = r_j + \Delta r$, therefore:

$$\frac{1}{\sqrt{2\pi\sigma_j^2}} \int_{-\infty}^{+\infty} e^{-(\Delta r)^2/2\sigma_j^2} e^{i2kr_j + \Delta r} d(\Delta r)$$

$$= e^{i2kr_j} \frac{2}{2\pi\sigma_j^2} \int_0^{+\infty} e^{-(\Delta r)^2/2\sigma_j^2} \cos(2k\Delta r) d(\Delta r) \tag{3.25}$$

$$= e^{i2kr_j} e^{-2k^2\sigma_j^2} \tag{3.26}$$

where only the real, even in Δr, part of $e^{i2k\Delta r}$ contributes to the first integral in Equation (3.25). The correction to the 'optical phase' due to disorder is given by the amplitude correction $e^{-2k^2\sigma_j^2}$. With this notation, σ_j^2 represents the mean squared deviation in the distribution of distances about the average 'shell' distance r_j. The Debye-Waller like term in Equation (3.22) is responsible for the disappearance of the EXAFS oscillations at high k. This is due to the fact that when k increases the p.e. wavelength will decrease therefore the negative effect that disorder has on the interference is greatly increased.

Another term in Equation (3.22) that takes into account the loss of EXAFS oscillations is the amplitude reduction factor S_0^2 [112]. This factor is a many-body correction which accounts for the changes in the passive electrons wavefunctions due to the presence of the core-hole. The overlap of the initial and final state of these passive electrons, $| < \psi^f|\psi^i > |$, where $\psi^{i,f}$ are the many body wavefunctions, is reduced which leads to a reduction in the strength of the transition given by the matrix element in Equation (3.1). By definition $S_0^2 \equiv | < \psi^f|\psi^i > |^2$ [112], however when fitting the data this variable accounts for more possible variations in the EXAFS signal. When there is more than one atom of the same type, at the same distance from the absorber ('shell') in the local structure, the degeneracy of the scattering paths needs to be taken into account. This is accounted for by the N_j term in Equation (3.22), which is the number of identical atoms in each 'j^{th}-shell'. When modelling EXAFS data, S_0^2 and N_j are dependent on each other, therefore understanding the changes in S_0^2 will provide insight of the changes in N_j

The last two terms in Equation (3.22) are the $1/kr_j^2$ term and the polarisation dependence $3(\vec{\epsilon} \cdot \vec{r_j})^2$. The backscattered wave is proportional to the the amplitude of the outgoing wave at the scatterer as well as the backscattering amplitude, F_j, *i.e.* $\sim F_j \frac{e^{ikr_j}}{r_j} \frac{e^{ik|r-r_j|}}{|r-r_j|}$, where the outgoing wave originates at $r = 0$ and the backscattered wave originates at $r = r_j$. For EXAFS the quantity of interest is the value of the backscattered wave at the origin, which in complex form is $\sim F_j \frac{e^{i2kr_j}}{r_j^2}$, this is how the $1/r^2$ factor is introduced. The $1/k$ factor can be introduced, as the wavefunction of the scattered photoelectron is described as a spherical wave, *i.e.* $\psi(k, r) = e^{ikr}/kr$. As the EXAFS signal is proportional to the amplitude of the scattered photoelectron at the absorbing atom.

The polarisation term results from the angular dependence of the dipole operator $\vec{\epsilon} \cdot \vec{r}$ in Equation (3.1) as well as the angular dependence of the initial state. For K-edge measurements the initial state is isotropic ($l = 0$). The dipole operator has a $\cos\theta$ dependence [113], so the final state should also have a $\cos\theta$ dependence to allow a none zero matrix element in Equation (3.1), due to dipole selection rules. This means that the scattering contribution to the final state is proportional to the amplitude of the outgoing wave at the backscatterer, $\sim \cos\theta_j$, where $\theta_j = \cos^{-1}(\vec{r_j} \cdot \vec{\epsilon})$, this results in the angular dependence in Equation (3.22), the square originates from the squared matrix element in Equation (3.1). For randomly oriented powders the EXAFS equation, Equation (3.22), must be averaged over all possible directions of the incoming x-ray with respect to the scattering paths. This averaging is calculated by:

$$\frac{1}{4\pi} \int_0^{2\pi} \int_0^{\pi} 3\cos^2\theta_j \sin\theta_j d\theta_j d\phi_j = 1 \tag{3.27}$$

This thesis will be dealing with measurements of single crystals with linearly polarised x-rays, therefore the orientation of the crystal should not be averaged over. How the polarisation factor is dealt with for this thesis is discussed in Section 3.1.4.

3.1.4 EXAFS equation for single crystal measurements, weighting factor

As described in the previous section, the angular dependence of the EXAFS comes in through this term:

$$\chi(k) \propto < (\hat{\epsilon} \cdot \hat{r})^2 >_{\theta,\phi} \tag{3.28}$$

where $\hat{\epsilon}$ is the electric field of the x-ray, and is represented by $\hat{\epsilon} = (\sin\theta\cos\phi, \sin\theta\sin\phi, \cos\theta)$ (θ and ϕ are the angles between the sample and the beam), $\hat{r}$ is the vector between the central atom and its neighbour, and is represented by $\hat{r} = (\sin\theta_i\cos\phi_i, \sin\theta_i\sin\phi_i, \cos\theta_i)$ (θ_i and ϕ_i are the angles between the central atom and its ith neighbour), as shown in Figure 3.5.

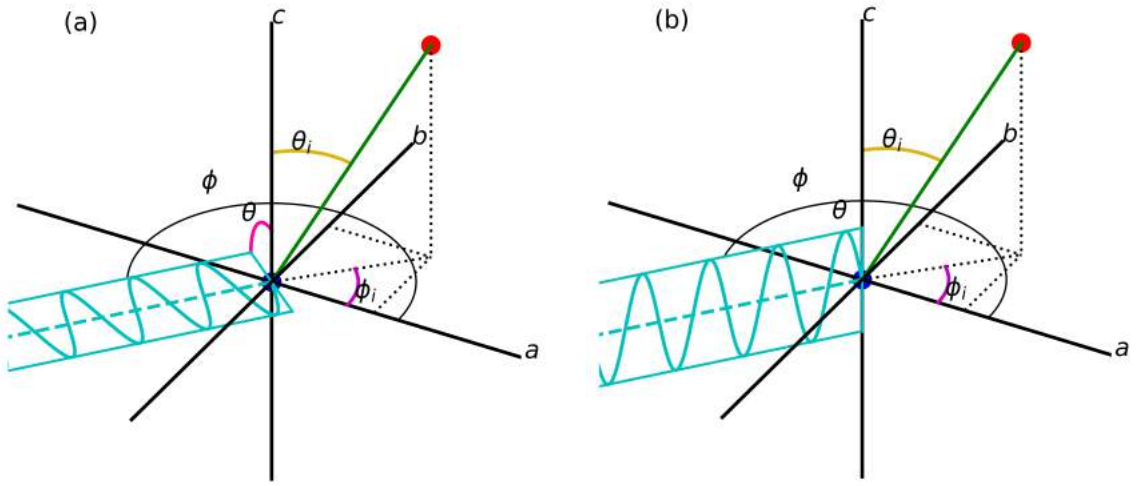

Figure 3.5: Relative orientation of the scattering paths and the incoming x-rays. Where the polarisation of the x-ray is parallel to the ab-plane in (a), and parallel to the c-axis in (b). θ_i and ϕ_i are between the scattering path and the crystallographic axes. θ and ϕ are between the polarisation of the incoming x-ray and the crystallographic axes.

When averaging in spherical coordinates for a randomly oriented sample, we calculate the integral $\frac{1}{4\pi}\int_0^{2\pi}\int_0^{\pi}\cos^2\theta\sin\theta d\theta d\phi$. This leads the polarisation component of randomly oriented EXAFS to become:

$$\chi_{ran}(k) \propto \frac{1}{3} \tag{3.29}$$

For our experiments we worked with single crystals so the samples were not randomly oriented and the angular dependence of the measured signal should not be averaged over.

When fitting the data we have used ARTEMIS [60], where ARTEMIS utilises FEFF6. As FEFF [59] by default calculates scattering paths for a randomly oriented sample, we need to determine a weighting factor which will take into account the angular dependence of our data, for each scattering path. It is possible to calculate scattering paths for a given angle between the sample and the polarisation in FEFF, however this restricts the fit to the angles of the model. Using a weighting factor has an advantage over using the polarisation function in ARTEMIS, as the angles for each path can be added in as guess parameters.

To calculate a weighting factor, we must first calculate the polarisation dependence of the EXAFS signal for a single crystal. For our experiment we measured EXAFS at different angles to the c-axis, so θ changes for each data set. We were not rotating about the ab-plane, so ϕ is constant for all data sets. The crystals exact orientation with respect to the beam can be measured during the experiment, however due to time constraints the value of ϕ was not measured and will be determined when fitting the data. The angular dependence can be seen in one term of the EXAFS equation $|<f|\vec{r}\cdot\vec{\epsilon}|i>|^2$ (from Equations (3.1) and (3.22)). Where the path between two atoms, $\vec{r} = r\cdot(\sin\theta_i\cos\phi_i, \sin\theta_i\sin\phi_i, \cos\theta_i)$, and the polarisation of the x-ray $\vec{\epsilon} =$

$\epsilon \cdot (\sin\theta\cos\phi, \sin\theta\sin\phi, \cos\theta)$. Taking only the angular dependent components of this equation we can calculate a weighting factor:

$$\chi_p(k) \propto ((\sin\theta_i\cos\phi_i, \sin\theta_i\sin\phi_i, \cos\theta_i) \cdot (\sin\theta\cos\phi, \sin\theta\sin\phi, \cos\theta))^2 \tag{3.30}$$

$$\chi_p(k) \propto \sin^2\theta_i \sin^2\theta \cos^2(\phi - \phi_i) + \frac{\sin(2\theta_i)\sin(2\theta)\cos(\phi - \phi_i)}{2} + \cos^2\theta_i \cos^2\theta \tag{3.31}$$

We know that when the polarisation is along the c-axis, $\theta = 0$, the angular dependence of Equation (3.22) is $\cos^2\theta_i$ [82]. To confirm the reliability of Equation (3.31), we must show that for $\theta = 0$ the angular dependence becomes $\cos^2\theta_i$.

$$\chi_p(k) \propto \sin^2\theta_i \sin^2(0) \cos^2(\phi - \phi_i) + \frac{\sin(2\theta_i)\sin(2\cdot 0)\cos(\phi - \phi_i)}{2} + \cos^2\theta_i \cos^2(0)$$

$$\chi_p(k) \propto \sin^2\theta_i \cdot 0 \cos^2(\phi - \phi_i) + \frac{\sin(2\theta_i)\cdot 0\cos(\phi - \phi_i)}{2} + \cos^2\theta_i \cdot 1$$

$$\chi_p(k) \propto 0 + 0 + \cos^2\theta_i$$

$$\chi_p(k) \propto \cos^2\theta_i \tag{3.32}$$

As the only component that differs between $\chi_{ran}(k)$ and $\chi_p(k)$ is the angular dependence, we can rewrite $\chi_p(k)$ in terms of $\chi_{ran}(k)$. Where the $\chi(k)$ term represents the other components of the EXAFS equation.

$$\chi_{ran}(k) \sim \frac{1}{3}\chi(k) \tag{3.33}$$

and:

$$\chi_p(k) \sim (\sin^2\theta_i \sin^2\theta \cos^2(\phi - \phi_i) + \frac{\sin(2\theta_i)\sin(2\theta)\cos(\phi - \phi_i)}{2} + \cos^2\theta_i \cos^2\theta)\chi(k) \tag{3.34}$$

combining these equations we can find $\chi_p(k)$ in terms of $\chi_{ran}(k)$:

$$\chi_p(k) \sim 3(\sin^2\theta_i \sin^2\theta \cos^2(\phi - \phi_i) + \frac{\sin(2\theta_i)\sin(2\theta)\cos(\phi - \phi_i)}{2} + \cos^2\theta_i \cos^2\theta)\chi_{ran}(k) \tag{3.35}$$

From Equation (3.35), it can be seen that including this weighting factor to the FEFF calculation for a randomly oriented signal a polarisation dependence can be implemented to the calculated EXAFS signal.
A comparison of the single scattering paths, for the Cu K-edge of $Sr_2MnCu_{1.5}S_2O_2$ [33], built using the ARTEMIS function and those built using the weighting factor can be seen in Figure 3.6. Using the ARTEMIS function can be a good comparison for the fits of the parallel (ab-plane) and perpendicular (c-axis) data sets, however it can get more difficult to account for the polarisation in ARTEMIS for other angles.

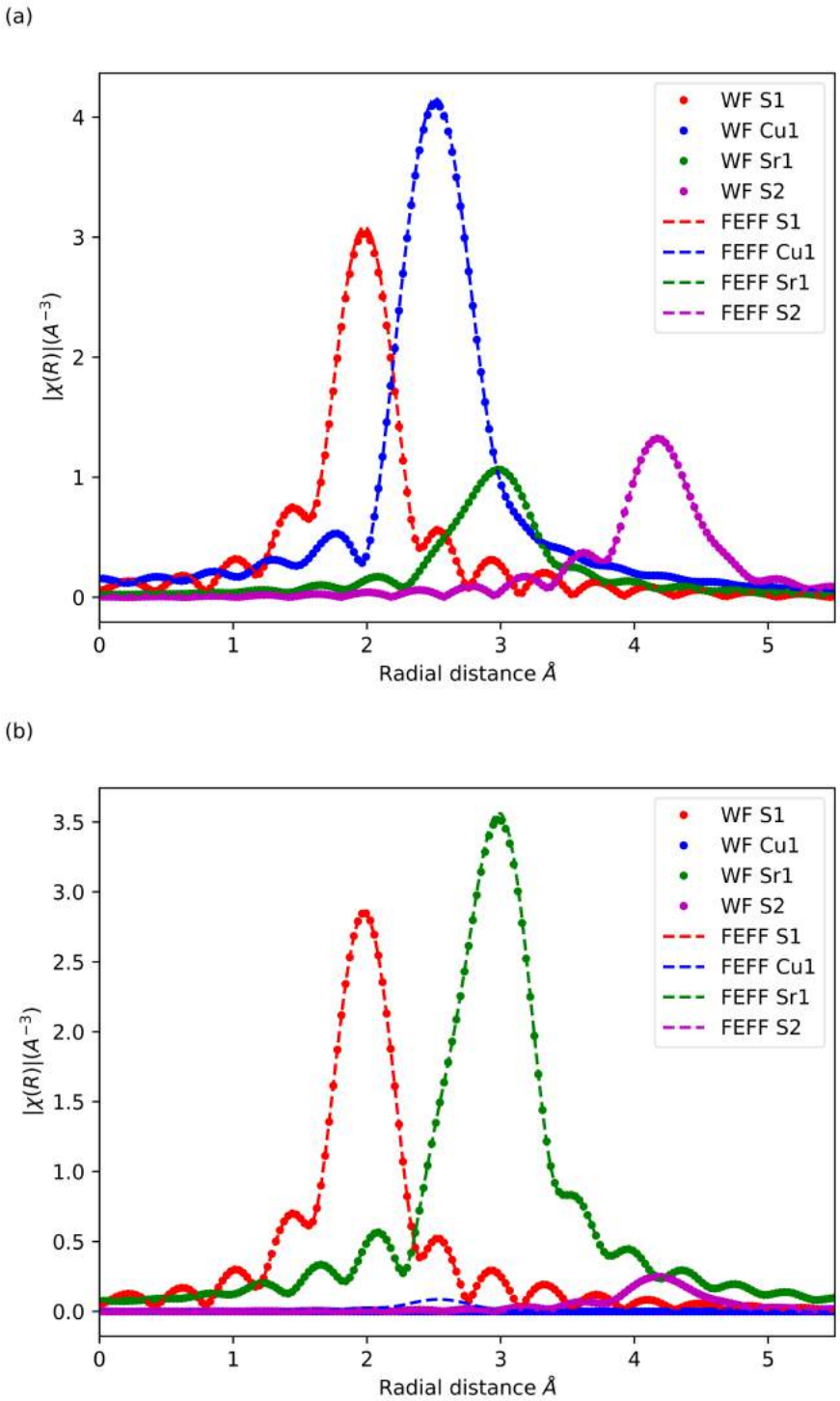

Figure 3.6: The single scattering paths used in the fit of the Cu K-edge of $Sr_2MnCu_2S_2O_2$, with $\theta = 0^o$ (a), and $\theta = 90^o$ (b), at room temperature. Comparing the paths produced by using the weighting factor (WF) and the polarisation function in FEFF. This plot shows that the paths produced by both methods are very similar, leading to the conclusion that the WF can be used when fitting the data.

The angles used in the weighting factor can be set as a guess parameters so the angle of each scattering path can be evaluated. When using the polarised FEFF calculation produced by ARTEMIS the angles are set to the structure input and this fixes the relative angular positions, so angle changes will not be possible to distinguish. Another advantage of using the weighting factor is that only the position of the po-

larisation with respect to the c-axis is needed. The complete orientation of the crystal with respect to the incoming beam is not needed as it can be set as a parameter for the fit, this simplifies the experiment allowing more time for EXAFS measurements. The position of the polarisation with respect to the ab-plane, ϕ, can be set after fitting the first peak or it can be left as a guess parameter in the full fit. Using the simplification of the XAS in section 3.1.2, all path parameters can be found more accurately by using all of the data sets in one fit. Having more data sets to use for each fit frees up more guess parameters which can lead to better fits.
As the weighting factor deals with the angles of the scattering path, the fitting procedure is more intricate than for powder data. Each scattering path, of the same type and length, will separated based on its angles, meaning the degeneracy of each path (N) input into the fit will be set to 1. The angles for each scattering path must be calculated before the fits, however they can be changed to guess parameters if the observed transition is coupled with angular changes. To calculate the angles for the paths, both θ_i and ϕ_i, the positions of the atoms in the model can be translated into Cartesian coordinates. In the work presented in this thesis the angles have been calculated with respect to specific axes, for θ_i the angle is calculated with respect to the z-axis, and for ϕ_i the angle is calculated with respect to the x-axis. In the case of the materials investigated in this thesis the z-axis is equivalent to the c-axis, and the x-axis is equivalent to the a-axis.
To calculate these angles the coordinates of the path need to be extracted from the model, this can be done using a 3D visualisation program, such as Vesta [114]. Once the coordinates have been extracted they will need to be converted into Cartesian space, this can be done by applying the following matrix to the x, y, z values obtained from the model:

$$M^{-1} = \begin{pmatrix} a & b\cos\gamma & c\cos\gamma \\ 0 & b\sin\gamma & \frac{c(\cos\alpha - \cos\beta\cos\gamma)}{\sin\gamma} \\ 0 & 0 & \frac{V}{ab\sin\gamma} \end{pmatrix} \tag{3.36}$$

where $V = abc(1-\cos^2\alpha - \cos^2\beta - \cos^2\gamma + 2\cos\alpha\cos\beta\cos\gamma)^{\frac{1}{2}}$, and a, b, and c are the lattice axes and α, β, and γ are the lattice angles. This is know as the orthogonalisation matrix.
The conversions for the coordinates can be found as Equation (3.37) for the tetragonal and orthorhombic materials, and Equation (3.38) for the hexagonal material, reported in this thesis.

$$\begin{aligned} X &= a \cdot x \\ Y &= b \cdot y \\ Z &= c \cdot z \end{aligned} \tag{3.37}$$

$$\begin{aligned} X &= a \cdot x + b \cdot y \cdot \cos\gamma \\ Y &= b \cdot z \cdot \sin\gamma \\ Z &= c \cdot z \end{aligned} \tag{3.38}$$

Once the coordinates have been converted to Cartesian space, the angles they make with the x and z axes can be calculated.

$$\theta_i = \arccos\left(\frac{z}{\sqrt{x^2+y^2+z^2}}\right) \tag{3.39}$$

$$\phi_i = \arctan\left(\frac{y}{x}\right) \tag{3.40}$$

The local environment of the excited element also needs to be taken into account. As there are often more than one of the excited element, in a unit cell of the crystal, there can be more than one local environment. This is not an issue when measuring powder data as all paths are averaged over. In the case of P-XAS the angle that each scattering path makes needs to be taken into account therefore each environment within the unit cell needs to be included in the fit. This can produce many paths for a single peak, however in the unit cell there are often degenerate environments which can be accounted for by multiplying the amplitude of the path by the overall frequency the specific path occurs in the unit cell. As each environment, for the same single scattering path, will only differ by the angles they make with the c- and a-axis the paths can still be fit simultaneously as the weighting factor accounts for the angle, this reduces the number of guess parameters needed for the fit.

3.1.5 Multiple scattering in EXAFS

When modelling the measured EXAFS signal using only single scattering events may not be sufficient if the weight of multiple scattering events in the signal is substantial. However, in Section 3.1.3 only single scattering events were considered.
The mathematics required to include multiple scattering events is more complex than that used for single scattering [104, 105, 115]. The strategy followed in this thesis to account for multiple scattering contributions (when needed), is to use the multiple scattering paths as calculated by FEFF, via the implementation of the Rehr-Albers scattering-matrix algorithm [105]. Using ϕ and θ as determined by the single scattering fits to the measured EXAFS, a FEFF calculation including the polarisation can be built.The polarisation dependence of the paths was included in FEFF6 (and onwards) [116].
The concept of a path length is introduced in FEFF, where the path length is the sum of the distances of each 'leg' in the scattering process, r_{tot}. The interatomic distance r_j, for single scattering, is replaced by an effective half-path length $r_{eff} = r_{tot}/2$, for each path j, when adapting to include multiple scattering. The curved-wave single scattering amplitude is also replaced, for an N-leg path, by a product of (N-1) curved-wave effective scattering matrices, $F^j_{eff} \sim F^{(N-1)}...F^2F^1$, with F^i being the scattering matrix at site i, where the amplitude depends on not only the photoelectron energy, but also the scattering angle $\beta_i = \cos^{-1}(\overrightarrow{r_i} \cdot \overrightarrow{r_{i+1}})$, the angle between the incoming and outgoing legs at site i, as well as the distance to site $(i-1), |r_i - r_{i-1}|$ due to curved wave effects [105]. The 'optical path' phase term is also replaced by a product, $e^{ik(\rho_i+\rho_2...\rho_N)}$ where $\rho_i = |r_i - r_{i-1}|$. An effective scattering phase, $\Phi_eff(k)$, is used as the F^i scattering matrices are complex, therefore $\Phi_eff(k)$ depends on the distances and angles of the path.
The EXAFS equation for multiple scattering can now be written as:

$$\chi(k) = \sum_j \frac{N_j S_0^2}{kr_{eff}^2} |F^j_{eff}(k)| e^{-2k^2\sigma_j^2} e^{-2r_{eff}/\lambda(k)} \sin(2kr_{eff} + \Phi_eff(k) + 2\delta_c(k)) \quad (3.41)$$

where δ_c is the phase shift of the central atom, S_0^2 is the amplitude reduction factor, and N_j is the degeneracy of path j. The mean square deviation for Equation (3.41) is $\sigma =< (r_i - r_{eff})^2 >_i$, where r_i is the instantaneous half path length. The $1/r^2_{eff}$ term is introduced manually to make Equation (3.41) resemble the single scattering equation, Equation (3.22). The polarisation dependence is not included in this equation, but it is

properly accounted for in the FEFF calculations, and the method in which it is dealt with can be seen in [117, 116].
A weighting factor to take into account multiple scattering paths will be much more complex than the one calculated for single scattering paths, as the only the first leg of the path will depend on the polarisation. Therefore in this thesis the multiple scattering paths will be calculated using FEFF.

3.2 Data analysis

3.2.1 Isolating XANES and $\chi(\mathbf{k})$

Before any quantitative analysis can be carried out on the XAS data collected at an experiment, the data must be processed to extract EXAFS and normalise the XANES. Changes in the sample thickness, absorber concentration, detector and amplifier settings, or other changes that may occur in an experiment, will affect the absorption jump measured. By normalising the data, the XANES can be directly compared, and is essential for comparing to theoretical XANES. When measuring XAS at an experiment it is best to obtain as much information as possible, therefore more than one scan at each angle and temperature will be measured. This guarantees the accuracy of the extracted data, and produces more reliable data, as there are more statistics. Another way to gain more statistics would be to count each energy step longer.
As there will be more than one data set for each point of interest the data must be merged. In this case, the spectra for each angle, at each temperature, were merged after normalisation. To normalise the data, the first step is to make the absorption jump equal to 1, this is achieved by setting a pre-, and post-edge range to the data and setting the edge-step energy. To determine the edge-step energy, E_0^+, the position of the absorption edge, E_0, is necessary. E_0 can be determined by the position of the first peak in the first derivative of the XAS, or by the mid point of the rising edge observed in the XAS. This may change with angle or temperature, see Chapters 4 to 6 for examples of absorption edges. The value for E_0^+ is necessary for the normalisation, as the data is normalised to an edge-step energy *i.e.* $N = \frac{\frac{I_f}{I_0}(E)}{\frac{I_f}{I_0}(E_0^+)}$. The edge-step energy is evaluated by extrapolating the pre- and post-edge lines to E_0, and subtracting the value where the pre-edge crosses E_0^+ from the value where the post-edge crosses E_0. The pre- and post-edge ranges can be changed in ATHENA [60]. The ranges selected should make the lines follow the pre- or post-edge data. Another parameter involved in the normalisation of the data is the normalisation order, which can be set to 1, 2, or 3. This sets the nature of the post-edge polynomial, *i.e.* a normalisation order of 1 would produce a straight line, allowing for it to follow the post-edge data more closely. Figure 3.7 shows an example of the ranges chosen for the Se K-edge of $Rb_2Mo_6Se_6$, measured at 90° and 4K.

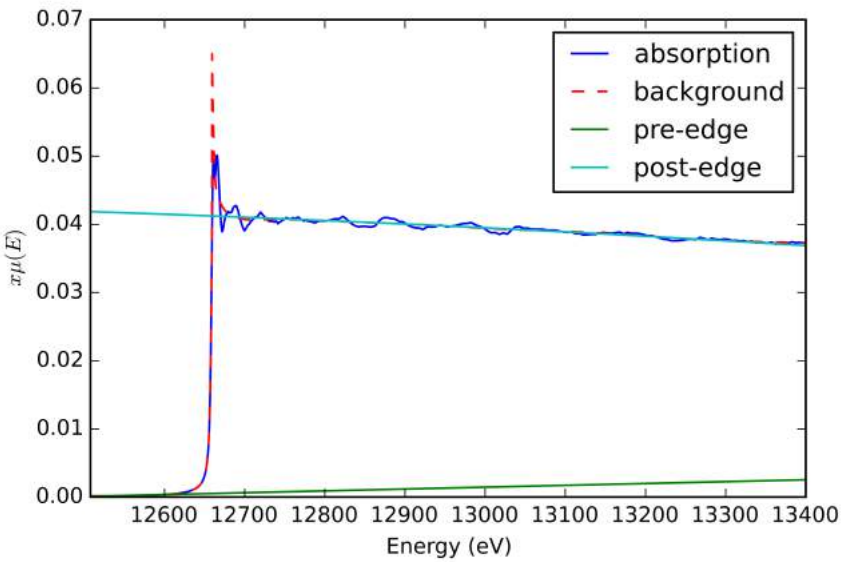

Figure 3.7: Absorption of the Se K-edge, of $Rb_2Mo_6Se_6$, data at 90° and 4K. The background function, pre and post edges are shown.

The next stage is the background subtraction. In an XAS measurement the transition of interest will not be the only process that will occur and be detected. Other absorptions can occur and affect the signal measured, there can also be statistical noise included in the signal. To account for this a background function is produced by ATHENA, where the value of E_0 selected determines the start of the background function. It is possible to require the background function to be oscillatory, when an oscillatory nature is introduced from the beamline optics, or sample set up. However it is not possible to add an oscillatory nature to the background function in ATHENA. There may be other affects to the signal that are not accounted for completely by the initial background function produced by ATHENA. To compensate for this, the other affects can be approximately removed from the data. This is achieved by adding a background parameter (Rbkg) into the background function. This is produced by selecting a range in the Fourier transformed EXAFS (FT-EXAFS) before the first true EXAFS peak and including the Fourier transform of this range to the background function. This suppresses oscillations seen in the EXAFS that are not contributing to the EXAFS of the measured element. The range can be selected by looking at the FT-EXAFS and observing the position of the first peaks, for example if there is a peak before 1Å it will not be real EXAFS. As the diameter of a hydrogen atom is ≈ 1.06Å, it can be sensibly assumed that there will be no nearest neighbours closer than this distance.
Another method to reduce the oscillations that are not from the atomic structure, is to add a spline clamp to the data. This is achieved by adding the structure outside of the spline range to the background function, therefore these oscillations will be set to zero and the EXAFS will be smoothed. Figure 3.8 shows the EXAFS and FT-EXAFS of the Cu K-edge measurement of $Sr_2MnCu_{2-x}S_2O_2$, at $\theta = 15^o$ and 300K, this plot shows that the usable range is $0 - 12\text{Å}^{-1}$. Adding a spline range of $0 - 12\text{Å}^{-1}$ will reduce the oscillations outside of this range, which removes any unnecessary high frequency oscillations from the Fourier transform.
The FT-EXAFS signal provides insight into the local structure of the absorber, and is used to determine distances between the absorber and scatterer, also the nature of the scatterer can be determined. The positions, intensity, and broadness of the peaks

can be analysed to obtain information on the local environment of the excited element in the material. The data is further processed as only a certain range of the EXAFS will be Fourier transformed. The range selected in the Fourier transform is determined qualitatively, observing the EXAFS signal a good range can be selected, see Figures 3.8 and 3.9. The EXAFS is also weighted by k, this will accentuate the part of the signal of interest, a k-weight of 2 will accentuate the middle of the EXAFS spectrum. Examples of Fourier transformed EXAFS data with and without a spline clamp are shown in Figures 3.8b and 3.9b, respectively.

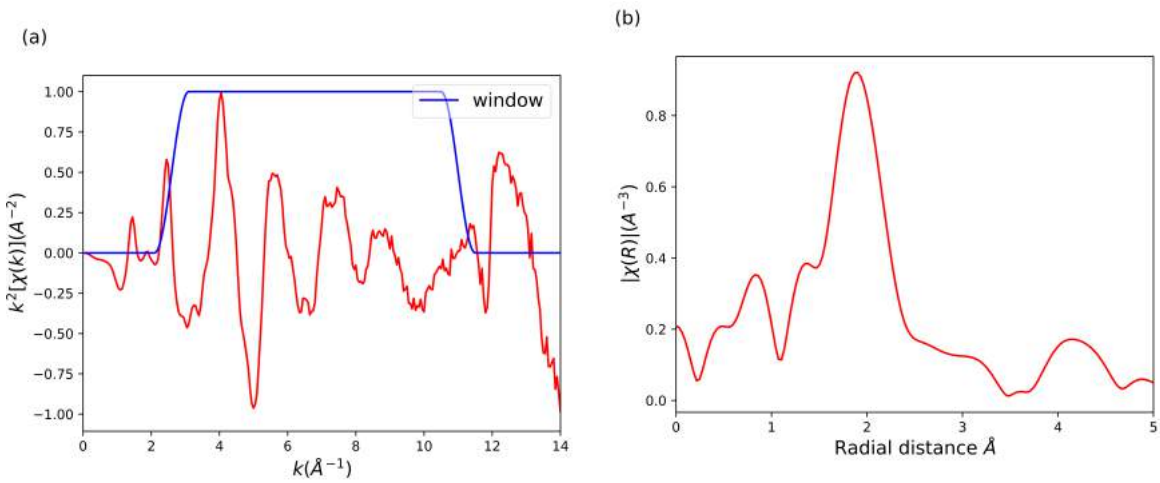

Figure 3.8: EXAFS, (a), and FT-EXAFS, (b), of the Cu K-edge, of $Sr_2MnCu_{1.5}S_2O_2$, data at 15° and 300K, before a spline clamp has been included.

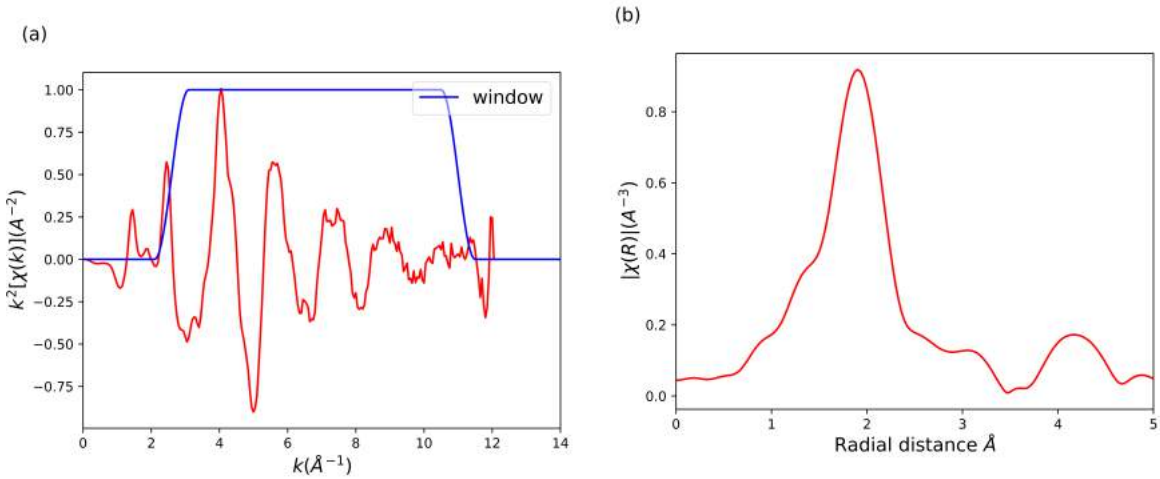

Figure 3.9: EXAFS, (a), and FT-EXAFS, (b), of the Cu K-edge, of $Sr_2MnCu_{1.5}S_2O_2$, data at 15° and 300K. With the $0 - 12Å^{-1}$ spline clamp in k.

The process of fitting the data to a theoretical structure is discussed in Section 3.2.3. The software used to process the data presented in this thesis is Demeter [60]. Other software is also available for data processing (e.g. PySpline [118] and SIXpack [119].

3.2.2 Self-absorption correction

When measuring absorption of a single crystal the detection must be in fluorescence mode, in most cases. This is due to the sample being too thick, therefore the x-rays

cannot travel entirely through the sample. When measuring XAS in fluorescence mode, self-absorption must be taken into account, as the fluorescent photons produced from the x-ray absorption can be re-absorbed by the sample before reaching the surface. As a result, the measured fluorescence intensity will be lower than the expected intensity. This can be accounted for mathematically and many procedures have been implemented [120, 121, 122, 123]. The software discussed in Section 3.2.1, used for data processing, has a built in function to deal with the self-absorption. However, in order to have control over the approximations and method, the author has written her own code (see Appendix A). The method followed is described below. Figure 3.10 shows the relevant geometry for fluorescence XAS experiments.

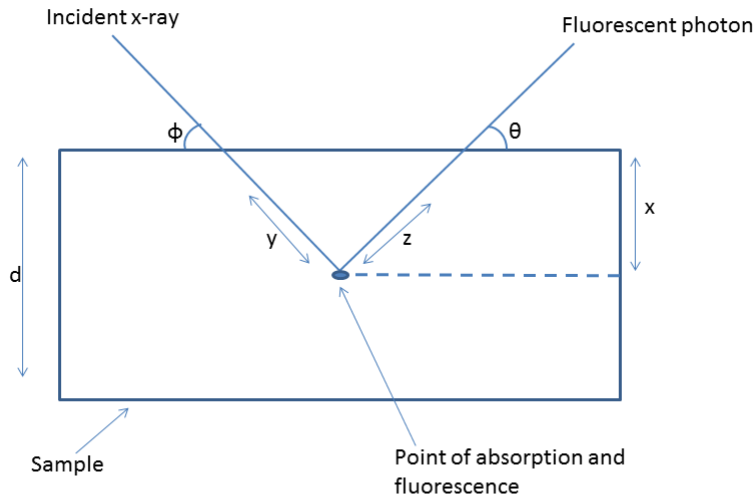

Figure 3.10: Geometry used in calculating self-absorption correction in XAS.

In a fluorescence experiment the intensity of the fluorescence photons is calculated by:

$$I_f = I_0 e^{-\mu(E)y} \cdot e^{-\mu(E_f)z} \epsilon_a(E)\mu_a(E) \tag{3.42}$$

where I_0 is the intensity of the incoming beam, $\mu_a(E)$ is the absorption due to the core excitation of the absorbing atom, $\mu(E)$ is the total absorption due to all of the elements in the sample, $\mu(E_f)$ is the absorption due to all of the elements in the sample at the fluorescence energy of the excited atom, $\epsilon_a(E)$ is the fluorescence efficiency per unit solid angle, and y and z are the distance the x-ray and fluorescence photon have travelled in the sample, respectively.
Equation (3.42) is only true for a specific y and z value, so to make it more general it can be integrated over x (as y and z can be written in terms of x), which leads to Equation (3.43)[2].

$$I_f = \int_0^d I_0 e^{\frac{-\mu(E)x}{\sin\phi}} \cdot e^{\frac{-\mu(E_f)x}{\sin\phi}} \frac{\epsilon_a(E)\mu_a(E)}{\sin\phi} dx$$

$$I_f = \frac{I_0 \epsilon_a \mu_a}{\mu_T + g\mu_f} \left(1 - e^{-d(\frac{\mu_T}{\sin\phi} + \frac{\mu_f}{\sin\theta})}\right) \tag{3.43}$$

[2]The full derivation can be seen in Appendix A

where g is the ratio of the incoming and outgoing angle $\sin(\phi)/\sin(\theta)$, and variables from Equation (3.42) are written in a simpler form *i.e.* $\mu_T = \mu(E)$, $\mu_f = \mu(E_f)$, $\mu_a = \mu_a(E)$, and $\epsilon_a = \epsilon_a(E)$. This equation describes the fluorescence in the direction of θ (from Figure 3.10). To be complete this equation needs to be integrated over the solid angle of the detector. In the case where $\theta + \phi = 90^o$ the maximum error in g is $\sim$7% even for $\Delta\theta \approx 5^o$ at $\theta = 10^o$ so the solid angle can be neglected and this equation can be used for the fluorescence intensity.
When correcting the self-absorption in the XANES region, the self-absorption corrected signal is $\mu_a(E)/\mu_a(E_0^+)$ where E_0^+ is an energy above the absorption edge (usually the edge-step energy used in the normalisation). However, what is actually measured in an XAS experiment is the initial intensity of x-ray beam and the fluorescence intensity produced by the sample. Around the XANES region certain approximations can be made to simplify Equation (3.43) and obtain an equation for the self-absorption corrected signal. In most XAS experiments $0^o \geq \theta + \phi \leq 90^o$, it is also assumed that the sample is infinitely thick so $\mu_T \gg d^{-1}$, therefore:

$$\left[\frac{\mu_T}{\sin\phi} + \frac{\mu_f}{\sin\theta}\right] \gg d^{-1} \tag{3.44}$$

This means we can neglect the exponential term as it will go to $e^{-\infty}$. This leaves the equation as:

$$\frac{I_f}{I_0} = \epsilon_a \frac{\mu_a}{\mu_T + g\mu_f} \tag{3.45}$$

The total absorption, μ_T above the edge includes contributions from both the element of interest and the other atoms in the sample, so it can be rewritten as:

$$\mu_T = \mu_a + \mu_b \tag{3.46}$$

where μ_b is the absorption due to the other atoms in the sample.
When correcting for the self-absorption the normalised data is used. The data in this thesis has been normalised using ATHENA [60]. The normalised XANES signal can be calculated by:

$$N = \frac{\frac{I_f}{I_0}(E)}{\frac{I_f}{I_0}(E_0^+)} = \left[\frac{\epsilon_a(E)\mu_a(E)}{\epsilon_a(E_0^+)\mu_a(E_0^+)}\right]\left[\frac{\mu_f g + \mu_b(E_0^+) + \mu_a(E_0^+)}{\mu_f g + \mu_b(E) + \mu_a(e)}\right] \tag{3.47}$$

Dividing the numerator and denominator by $\mu_a(E_0^+)$ an expression for the self-absorption corrected signal can be produced.

$$N = \frac{(\epsilon_a(E)\mu_a(E))/\mu_a(E_0^+)}{(\epsilon_a(E_0^+)\mu_a(E_0^+))/\mu_a(E_0^+)}\left[\frac{(\mu_f/\mu_a(E_0^+))g + \mu_b(E_0^+)/\mu_a(E_0^+) + \mu_a(E_0^+)/\mu_a(E_0^+)}{(\mu_f/\mu_a(E_0^+))g + \mu_b(E)/\mu_a(E_0^+) + \mu_a(E)/\mu_a(E_0^+)}\right] \tag{3.48}$$

This can be simplified by letting $\beta = \frac{\mu_f}{\mu_a(E_0^+)}$, $\gamma = \frac{\mu_b(E)}{\mu_a(E_0^+)}$, and $\gamma' = \frac{\mu_b(E_0^+)}{\mu_a(E_0^+)}$. As the fluorescence efficiency is roughly equal at E and E_0^+, $\frac{\epsilon_a(E)}{\epsilon_a(E_0^+)} \approx 1$. Therefore the equation becomes:

$$N = \frac{\mu_a(E)}{\mu_a(E_0^+)}\left[\frac{\beta g + \gamma' + 1}{\beta g + \gamma + \mu_a(E)/\mu_a(E_0^+)}\right]$$

As the self-absorption corrected signal in the XANES region is $\mu_a(E)/\mu_a(E_0^+)$, this equation needs to be rearranged to find the expression for this. The energy range is small so we can estimate $\mu_b(E) \approx \mu_b(E_0^+)$.

$$\frac{\mu_a(E)}{\mu_a(E_0^+)} = \frac{N(\beta g + \gamma)}{\beta g + \gamma + 1 - N} \tag{3.49}$$

This equation is utilised in the code, written by the author, to correct for the self absorption in the XANES region.
The approach to the self-absorption correction is slightly different when dealing with the EXAFS region. In an EXAFS experiment the signal is extracted from the measurement by:

$$\chi(k) = \frac{\mu_a - \bar{\mu}_a}{\bar{\mu}_a} \tag{3.50}$$

where $\bar{\mu}_a$ is the absorption due to the core excitation of the absorbing atom in isolation. This can be approximated by the absorption at an energy above the absorption edge, the typical energy to use is the edge-step in the normalisation. As discussed for the XANES region, it is the ratio of photon intensities that is measured during a fluorescence experiment, rather than the pure EXAFS signal.
Using equation 3.43 we can derive an equation for the experimental EXAFS:

$$\chi_{exp}(k) + 1 = \frac{\mu_a(\bar{\mu}_T + g\mu_f)}{\bar{\mu}_a(\mu_T + g\mu_f)} \frac{\left(1 - e^{-d(\frac{\mu_t}{\sin\phi} + \frac{\mu_f}{\sin\theta})}\right)}{\left(1 - e^{-d(\frac{\bar{\mu}_t}{\sin\phi} + \frac{\mu_f}{\sin\theta})}\right)}$$

This can be rewritten with a few substitutions, let $\alpha = \bar{\mu}_T + g\mu_f$ and $\mu_T = \bar{\mu}_T + \chi(k)\bar{\mu}_a$. Then dividing both sides by $1+\chi(k)$, and substituting $\mu_a = \bar{\mu}_a(1+\chi(k))$. This gives an expression of the experimental EXAFS in terms of the self-absorption corrected signal and the other components in the measured signal.

$$\chi_{exp}(k) = \frac{\alpha(1+\chi(k))}{(\alpha + \chi(k)\bar{\mu}_a)} \frac{\left(1 - e^{-\frac{d}{\sin\phi}(\alpha + \chi(k)\bar{\mu}_a)}\right)}{\left(1 - e^{-\frac{d}{\sin\phi}(\alpha)}\right)} - 1 \tag{3.51}$$

The relationship between $\chi(k)$ and $\chi_{exp}(k)$ is exact. In order to calculate the self-absorption corrected EXAFS we need to have $\chi(k)$ in terms of $\chi_{exp}(k)$. To invert Equation (3.51) we can make a simple approximation. Assuming that $\frac{\chi(k)\bar{\mu}_a d}{\sin\phi} \ll 1$ [123], we can then do a Taylor expansion of the exponential in the numerator:

$$1 - e^{\frac{-d}{\sin\phi}(\alpha + \chi(k)\bar{\mu}_a)} = 1 - e^{\frac{-d\alpha}{\sin\phi}} e^{\frac{-d}{\sin\phi}(\chi(k)\bar{\mu}_a)}$$

$$\text{Taylor expand } e^{\frac{-d}{\sin\phi}(\chi(k)\bar{\mu}_a)}:$$

$$1 - \frac{\chi(k)\bar{\mu}_a d}{\sin\phi} + ...$$

$$\therefore 1 - e^{\frac{-d}{\sin\phi}(\alpha + \chi(k)\bar{\mu}_a)} = (1 - e^{\frac{-d\alpha}{\sin\phi}}) \left(1 - \frac{\chi(k)\bar{\mu}_a d}{\sin\phi}\right)$$

This approximation gets worse with large $\chi(k)$ and $\bar{\mu}_a$. It also has a maximum for both ϕ and d, because of the $e^{\frac{-d\alpha}{\sin\phi}}$ term. Various combinations of the above parameters can contribute to produce errors above 1%, so the approximation should be monitored

when making the corrections outlined below.
With the above approximation, and making the following substitutions:

$$\beta = \frac{\bar{\mu}_a d\alpha}{\sin\phi} e^{\frac{-d\alpha}{\sin\phi}}, \text{ and } \gamma = 1 - e^{\frac{-d\alpha}{\sin\phi}}$$

We can derive an equation with $\chi(k)$ in terms of $\chi_{exp}(k)$:

$$\chi(k) = \frac{-[\gamma(\alpha - \bar{\mu}_a(\chi_{exp}(k)+1)) + \beta] \pm \sqrt{[\gamma(\alpha - \bar{\mu}_a(\chi_{exp}(k)+1)) + \beta]^2 + 4\beta\gamma\alpha\chi_{exp}(k)}}{2\beta} \tag{3.52}$$

Taking the thin and thick limits you find that the sign of the square root is positive. In the thin limit this equation reduces to $\chi(k) = \chi_{exp}(k)$ as expected.
For the thick limit, we can introduce a limit where $d \to \infty$, this means that β will go to zero and γ will go to 1, reducing the equation to:

$$\chi_{exp}(k) + 1 = \frac{\alpha\chi(k) + \alpha}{\alpha + \chi(k)\bar{\mu}_a} \frac{1+0}{1}$$

Therefore in the thick limit, $\chi(k)$ can be calculated by equation 3.53:

$$\chi(k) = \frac{\chi_{exp}(k)}{1 - \frac{\bar{\mu}_a}{\alpha} - \frac{\bar{\mu}_a \chi_{exp}(k)}{\alpha}} \tag{3.53}$$

A code using these formulas has been written for this thesis, this can be seen in Appendix A, the code works for both XANES and EXAFS data and produces a correction both with the thickness taken into account and above thickness limit. The code was written in Python [103], and uses Equation (3.49) for the correction in the XANES region, and Equations (3.52) and (3.53) for the correction in the EXAFS region. The code reads in the experimental data, either a '.nor' or '.chi' file, depending on whether it is reading in XANES or EXAFS data, respectively. Components of Equations (3.49), (3.52) and (3.53) are either input by the user or calculated by the code. To calculate the absorption for each element in the material for the energy range being measured, the following equation is used:

$$\mu = \rho \sum g_i (\frac{\mu}{\rho})_i \tag{3.54}$$

where ρ is the density of the material, g_i is the mass fraction of the element i in the material, and $(\frac{\mu}{\rho})_i$ is the mass attenuation of the element i in the material. The tables of mass attenuation values for all elements can be found in [124]. As the code is only dealing with the energy range of the measurements, only the mass attenuation values in this range are needed. This range will often fall in between two points on the table of μ/ρ values, to work out $(\frac{\mu}{\rho})_i$ in this range a linear interpolation is used. Then the energy range from the experimental XAS measurements can be input into this equation and the mass attenuation values can be calculated. The mass attenuation for the excited element will include a jump in the values, for this energy range, due to the absorption edge, to take this into account the attenuations before and after the jump must be calculated separately. The mass fraction of each element in the sample can be calculated by the following equation (using $Rb_2Mo_6Se_6$ as an example):

$$g_{Se} = \frac{6m_{Se}}{(2m_{Rb} + 6m_{Mo} + 6m_{Se})} \tag{3.55}$$

where m_i is the atomic mass of the element i.
The thickness and density of the sample, and the orientation of the surface of the sample with respect to the beam, need to be input to the code by the user. The absorption

at the fluorescence energy of the excited element can be calculated by Equation (3.54). TPlots of the self-absorption corrected data, for the $Sr_2MnCu_{1.5}S_2O_2$ single crystal, using this code can be seen in Figures 3.11 and 3.12, for XANES and EXAFS respectively. Due to the geometry of the experimental set up, discussed in Chapter 2, the correction will be smaller for larger angles from the beam. This is because the detector will be seeing more of the fluorescing surface.

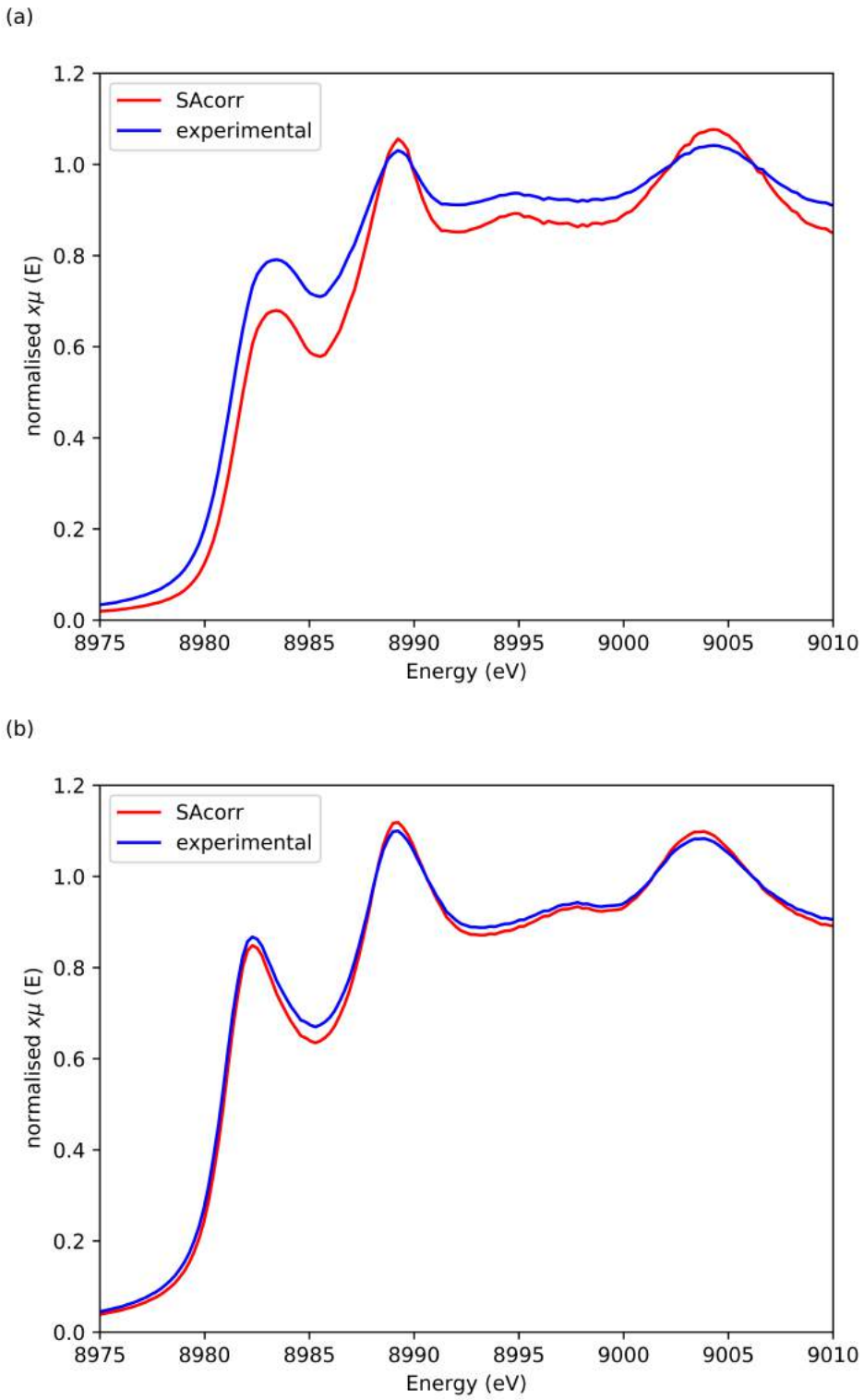

Figure 3.11: XANES of the Cu K-edge $Sr_2MnCu_{1.5}S_2O_2$, at 15° (a) and 75° (b), before and after the correction.

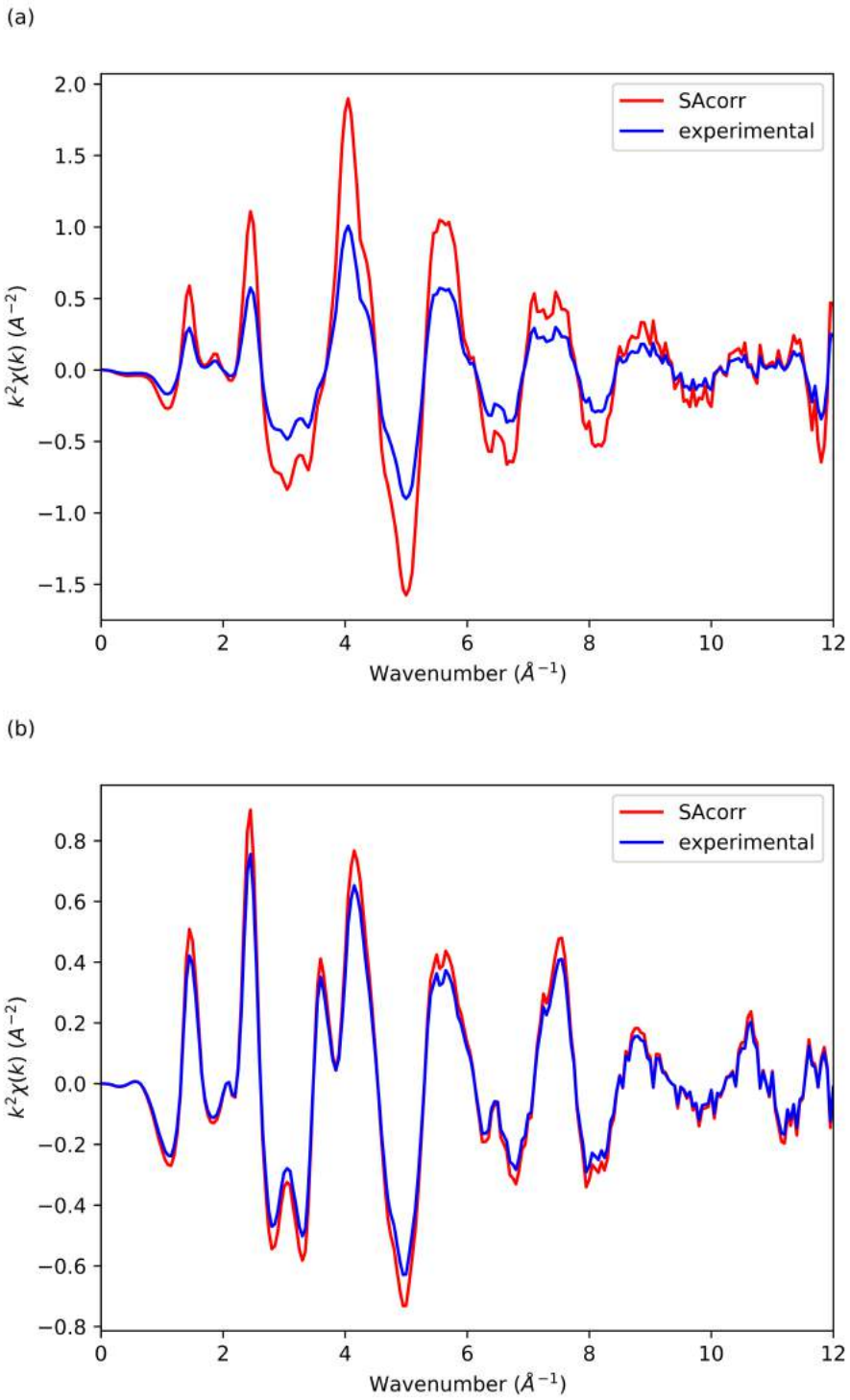

Figure 3.12: EXAFS of the Cu K-edge $Sr_2MnCu_{1.5}S_2O_2$, at 15° (a) and 75° (b), before and after the correction.

3.2.3 Fitting $\chi(\mathbf{k})$

Once the data has been fully processed and the EXAFS signal has been extracted, a quantitative analysis can be carried out. This analysis is achieved by fitting a theoretical EXAFS signal to the measured signal and comparing them. The theoretical EXAFS signal is calculated using a model structure as a basis (from diffraction measurements of the material, or a known structure that is a parent of the material). In this thesis ARTEMIS [60] is used to produce the fits of the data. ARTEMIS uses FEFF6 to produce theoretical EXAFS based on structural information. The structural model is read into FEFF and scattering paths are calculated and their importance weighted. From this a model EXAFS signal is built using the EXAFS equation [125].

$$\chi(k) = \sum_j \frac{N_j S_0^2}{kr_j^2} |F_j(k)| e^{-2k^2\sigma_j^2} e^{-2r_j/\lambda(k)} \sin(2kr_j + \delta_j(k))$$

Using the EXAFS equation, certain parameters can be calculated for a given path by FEFF. They are the scattering amplitude $F_j(k)$, the mean-free-path of the photoelectron $\lambda(k)$, and the phase shift in the wavefunction $\delta_j(k)$. The other parameters are refined by fitting the theoretical to the measured EXAFS; N_j, S_0^2, σ_j^2, and r_j. A global alignment is performed to the energy origin of the theoretical signal ($k = 0$) to the measured signal, this produces a global fitting parameter, ΔE_0.
ARTEMIS fits on a path by path basis, the complete EXAFS signal is a sum over all of the scattering paths. Selected paths are fit to the measured EXAFS signal, and the refined parameters in the EXAFS equation will be varied until a good fit is produced. ARTEMIS provides a list of the variables and their values. The parameters that are free to vary can be set to specific values or to a mathematical expression in terms of other parameters, or they can be left to vary freely. The fits discussed in this thesis are performed on the real space data with a k-weight of 2. ARETMIS also fits for all k-weights, simultaneously. The real space data is obtained by performing a Fourier transform on the EXAFS signal:

$$\chi(R) = \frac{1}{\sqrt{2\pi}} \int_{k_{min}}^{k_{max}} k^w \chi(k) e^{-2ikR} dk \tag{3.56}$$

where k_{min} and k_{max} are determined by the Fourier transform window, and k^w is the k-weighting used. Fitting in real space is preferable as there is more control over the range of data included in the fit, and the paths can be fit on a peak by peak basis. However, in ARTEMIS, it is possible to perform fits in k-space and the Fourier transformed real space (q-space) data.
The change in the parameters will give an insight into what is happening in the local structure when external factors have been varied, such as temperature, pressure or magnetic field changes. For the data discussed in this thesis the local structures have been investigated with varying temperature. How these models are implemented in order to track these changes is discussed in Section 3.2.4
ARTEMIS by default calculates the EXAFS using the powder average equation, Equation (3.22) [107]. As discussed in Section 3.1.3 it does have the capabilities to introduce polarisation into the calculation. However, for the work presented in this thesis, this was only used for including multiple scattering paths to the fits. By using the weighting factor calculated for single scattering paths, discussed in Section 3.1.4, the powder averaged EXAFS can be adapted to include the polarisation dependence. The weighting factor is introduced into the amplitude parameter, where $3(\sin\theta_i \sin\theta \cos\phi - \phi_i + \cos\theta_i \cos\theta)^2 S_0^2$ is input into the fit (in place of S_0). This is important as the intensity

of the scattering paths depend on the orientation of the crystal with respect to the direction of the polarisation of the incoming x-rays. The addition of the weighting factor allows the angles between the scattering paths to be varied, meaning there are less restrictions to the fit.

3.2.4 Evaluating the model

The first stage of evaluating a fit is to check that the parameters that are allowed to vary make physical sense. The values guessed for the amplitude reduction factor, S_0^2, and Debye-Waller factor, σ_j^2, should not be negative as there will always be losses in the EXAFS due to the existence of a core-hole and atomic vibrations, a negative S_0^2 would invert the data. A negative value for σ_j^2 can be acceptable, when the fit is trying to account for a peak without all contributing paths it will compensate with a negative σ_j^2. When σ_j^2 is too large this can indicate a problem in the fit, meaning the structural model or the paths included in the fit should be re-evaluated. The values guessed for the energy shift between the theoretical signal and measured signal, ΔE_0, and the change in the length of the scattering path, ΔR, need to be evaluated more qualitatively. As the measured data is normalised and the energy is calibrated with respect to a reference, the energy shift between the theoretical and measured signal should not be large, e.g. $-10eV < \Delta E_0 < 10eV$. If the value of ΔR for a path is very large, ~ 0.5Å it can be concluded that either this path is not contributing to the experimentally measured EXAFS or the model used in the fit needs to be re-evaluated. The next stage of evaluating the goodness of a fit is considering two numbers calculated by FEFF. These numbers are the χ^2 statistic and the R-factor [125, 126]. As FEFF performs the fitting with the Levenberg-Marquardt [127] method of non-linear least-squares minimisation, the most likely values for the guess parameters are those that minimise χ^2:

$$\chi^2 = \frac{N_I}{N_G} \sum_{i=1}^{N} \left| \frac{\tilde{\chi}_{data}(R_i) - \tilde{\chi}_{model}(R_i)}{\varepsilon_i} \right|^2 \tag{3.57}$$

where $N_I \simeq (2\Delta k \Delta R)/\pi$ and is the number of independent parameters the fit can use, Δk and ΔR are the ranges included in the fit, N_G is the number of guess parameters used in the fit, $\tilde{\chi}(R)$ represents both the real and imaginary parts of the Fourier transform of $\chi(k)$, and ε is the estimated uncertainty of the data, this is evaluated by the average of the FT-EXAFS between 15Å to 25Å where the signal should only include intrinsic noise [128]. The sum of χ^2 is performed over the range of data points included in the fit. When fitting multiple data sets, χ^2 is extended to include a sum over data sets as well as the sum of data points used in the fit to each data set.
Estimates for the uncertainties in the guessed parameters, and the correlations between parameters are made at the 'best-fit' condition, according to the standard statistical treatment of experimental data [126]. As the estimated uncertainty (ε) for the experimental data is not always reliable, a reduced χ^2 (χ_ν^2) can be calculated.

$$\chi_\nu^2 = \frac{\chi^2}{\nu} \tag{3.58}$$

where ν is the number of guess parameters unused in the fit ($N_I - N_G$). The reduced χ^2 takes into account the amount of information used in the fit and the total amount of information available. Both χ^2 and χ_ν^2 are reported by ARTEMIS for each fit. For a good fit the value of χ_ν^2 should be $\sim 1 \pm \sqrt{2/\nu}$. In this thesis the values found for this are much higher. There are two explanations for this, either the model is bad or

the value of ε has been underestimated. This is a typical problem when fitting EXAFS data in ARTEMIS, as statistical errors rarely dominate systematic errors therefore it can be difficult to estimate ε accurately. To confirm that a large χ^2_ν is not due to a bad model the R-factor needs to be taken into consideration. The R-factor is the measure of agreement between the experimental data and the model, this is calculated by:

$$R = \frac{\sum_{i=1}^{N} |\tilde{\chi}_{data}(R_i) - \tilde{\chi}_{model}(R_i)|^2}{\sum_{i=1}^{N} |\tilde{\chi}_{data}(R_i)|^2} \tag{3.59}$$

If the fit is good then the R-factor should be small, $R \ll 1$, this is the case for the fits reported in this thesis. This rules out that the models used in the fits are bad, and leads to the conclusion that ε has been underestimated.

3.3 Chapter summary

This chapter has introduced the mathematics involved in x-ray absorption spectroscopy, where the basic mathematical components of an absorption event have been discussed. As the experiments discussed in this thesis were all K-edge measurements, the dipole approximation of an absorption event can be used. This leads to a simplified nature of an absorption process based on the symmetry of the material and the orientation of the sample with respect to the beam. The EXAFS equation in terms of dipole events has been introduced, and a weighting factor accounting for the polarisation dependence has been calculated. How this is implemented in the fits of the data presented in this thesis was explained in this chapter. The process for dealing with XAS data measured at an experiment and how the XANES and EXAFS are isolated from the raw data was discussed. As the single crystal P-XAS measurements were taken in fluorescence mode the data needed to be further processed to account for self-absorption events. The mathematical principles behind this were introduced and a code written by the author was described. The fitting process used in the analysis of the data presented in this thesis was explained, and the process of evaluating the fit was discussed in this chapter.

Chapter 4

Investigating the mobility of Cu ions in $Sr_2MnCu_{1.5-x}S_2O_2$ using both powder XAS and single crystal P-XAS.

4.1 Introduction

There is an interest in materials with mobile ions at room temperature, as they can be good candidates for battery research. The mobility of ions within a solid is driven by an electric potential or thermal energy. For an ion to move within a solid the energy supplied must be equal to or greater than the activation energy for ionic hoping. Often these materials also posses vacancy defects, where there is an empty site where an ion should be, allowing the nearest same type ion to move to this position with less energy loss. Materials capable of losing and gaining charged particles without degrading, or with reduced degradation, is at the forefront of battery research.
Oxychalcogenides with a layered structure and composition $A_2MO_2X_2Ch_2$, where A=Sr, Ba, M=1st row transition metal ion, X=Cu, and Ch=S, Se, were first discovered by Zhu *et al.* [129]. Oxychalcogenides can display semiconducting properties [129, 33], when the valence band is not doped and the metal ion in the compound is a mid to late transition metal. Unusual magnetic properties are exhibited by the class $Sr_2MCu_{2-\delta}S_2O_2$ (M= Mn, Co, Ni), where the Mn analogue has an unusual magnetic ordering, where the moments are arranged in ferromagnetic zigzag stripes (see Figure 4.1). The Co analogue has an unusual high-spin Co^{2+} [130]. The Ni analogue might have a high-spin to low-spin transition while cooling [34], but there is no magnetic signature of this, which may be due to a Ni-Cu alloy impurity [131].

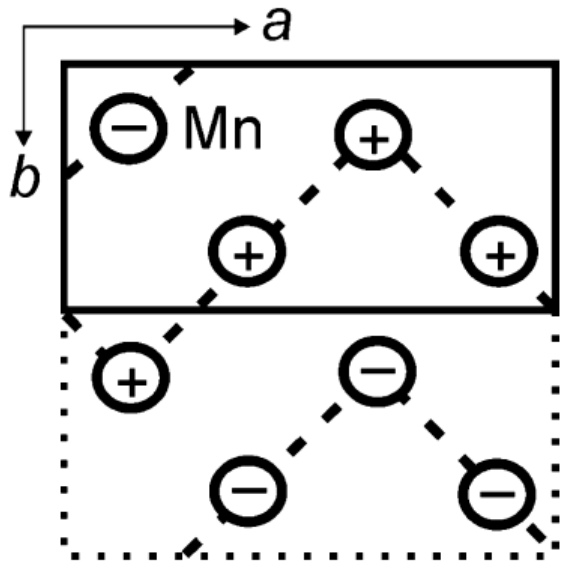

Figure 4.1: A model of the magnetic ordering in $Sr_2MnCu_{1.5}S_2O_2$. In which the magnetic moments, localised on the Mn ions and directed perpendicularly to the MnO_2 planes, are arranged in ferromagnetic zigzag stripes that are aligned antiferromagnetically along the *b*-axis. The unit cell produced from the Cu/vacancy ordering is shown by the solid line. A single MnO_2 plane within the magnetic unit cell is shown by the dotted line [34].

The material investigated in this thesis is $Sr_2MnCu_{1.5-x}S_2O_2$ (x=0.0,0.2,0.3), which has a distinct layered structure, see Figure 4.2, and interesting magnetic properties in the Mn ions, see Figure 4.1. The material is reported to be tetragonal, I4/mmm, at higher temperatures (>240K) and undergoes a structural transition at ∼240K to an orthorhombic structure, Ibam [132]. To the knowledge of the author, $Sr_2MnCu_{2m-\delta}S_{m+1}O_2$, (m=1-3; $\delta \approx 0.5$) is one of the few examples of material where there is a thick, copper sulfide, antifluorite-type layer separated by thin perovskite-type oxide layers, with chalcogenide atoms separating both layers.
The magnetic moments in $Sr_2MnCu_{1.5}S_2O_2$ are perpendicular to the MnO_2 planes, which also occurs in compounds with thicker copper sulfide layers, such as $Sr_2MnCu_{3.5}S_2O_2$ and $Sr_2MnCu_{5.5}S_2O_2$ as discussed by Gál *et al.* [33] and Clarke *et al.* [34]. $Sr_2MnCu_{3.5}S_2O_2$ and $Sr_2MnCu_{5.5}S_2O_2$ have ferromagnetic MnO_2 planes, where the moments between the planes align antiferromagnetically forming an A-type antiferromagnet, below 100K [33]. This magnetic structure occurs in a zero applied magnetic field, but the materials behave as metamagnets and enter a fully ferromagnetic phase with an applied magnetic field below 5T [33]. The moments within each MnO_2 plane in $Sr_2MnCu_{1.5}S_2O_2$ align slightly differently, they form a CE-type magnetic structure (see Figure 4.1), arranged in zigzag ferromagnetic stripes that are aligned antiferromagnetically to each other along the *b*-axis. This is similar to the magnetic structure found in the half-doped $Mn^{3+/4+}$ $La_{0.5}Sr_{1.5}MnO_4$. The structure in $La_{0.5}Sr_{1.5}MnO_4$ can be explained by the charge ordering of Mn^{4+} and Mn^{3+} ions and the orientation of the Jahn-Teller distortion of the Mn^{3+} ions (*i.e.* orbital ordering as octahedra) [133]. However in $Sr_2MnCu_{1.5}S_2O_2$ the Mn ions are found to have a mean oxidation state of +2.5 [33], and there is extreme anisotropy of the Mn site which prevents orbital ordering of the type seen in $La_{0.5}Sr_{1.5}MnO_4$. This means that the magnetic structure observed in $Sr_2MnCu_{1.5}S_2O_2$ cannot be explained in the same way, and it is currently unclear how this emerges.
An important aspect about the structure of this material is the occupancy of the Cu

sites. While it was initially reported with a stoichiometry of $Sr_2MnCu_2S_2O_2$, a more accurate stoichiometry of $Sr_2MnCu_{1.5}S_2O_2$ was obtained from the diffraction data [33]. In addition there is evidence of long range ordering of the Cu/vacancy below 240K [132]. The ordering of the Cu ions and vacancies leads to the formation a superstructure at low temperatures, that is a $2\sqrt{2a} \times \sqrt{2a} \times c$ 4-fold basal expansion of the tetragonal structure [134]. The superstructure could explain the CE-type magnetic ordering in the Mn sites, as both occur in this material. This copper deficiency also leads to the oxidisation of the transition metal, for Mn there is an average oxidation state of 2.5+, which has been shown in the work by Gál *et al.* [33].
Research into practical applications of this material have been carried by Rutt *et al.* [135] and Indris *et al.* [136]. As the Cu ions in $Sr_2MnCu_{2m-\delta}S_{m+1}O_2$, $(m = 1 - 3; \delta \approx 0.5)$ appear to be mobile, this makes it a good candidate for battery applications and research has been carried out on its potential as a component in a rechargeable battery, by both groups. In both studies the Cu ions were replaced with Li ions. It was found that there is a complete replacement of the Cu^+ ions in the sulfide layer by the Li^+ ions. This process is quasi-reversible in moist air [135], the Li ions are extracted as lithium hydroxide and the copper reinserts into the structure. Indris *et al.* [136] shows that the lithium insertion/copper extrusion process may be carried out reversibly in an electromagnetic cell and, by using nuclear magnetic resonance (NMR) spectroscopy, that the Li ions in the sulfide layer are mobile. This study showed that due to the rigidity of the structure there was more cyclability using this material, rather than using bulk Cu_2S. Although there was less reversibility in the higher capacity materials (m=2, 3), meaning a compromise would have to be taken between capacity and stability. This research [135, 136] opens up the possibility of improved Li ion batteries with more stability using this family of materials.
Other research into this material has been carried out by Blandy *et al.* [137] where the Cu ions have been substituted with Ag ions. However due to the octahedron becoming too distorted when replacing the Cu ions with Ag ions, a stable sample of $Sr_2MnAg_{1.5}S_2O_2$ could not be formed. The selenide analogue of this material was successfully substituted with Ag ions. The magnetic structure in both the Cu and Ag analogues is the same, an A-type antiferromagnet in low magnetic field. There is no superstructure formation in either $Sr_2MnCu_2Se_2O_2$ or $Sr_2MnAg_2Se_2O_2$, which is seen in $Sr_2MnCu_{1.5}S_2O_2$. The replacement of the Cu ions with Ag ions resulted in an elongation in the *c*-axis. While there is no change in the magnetic structure, the Néel temperature for three-dimensional ordering, increases. The Se and S analogues, of $Sr_2MnCu_{2-x}Ch_2O_2$, have different magnetic properties [132, 34]. In the Se analogue there is a similar Cu deficiency but the magnetic ordering seen in the S analogue does not occur, neither does the superstructure below 240K.
$Sr_2MnCu_{1.5}S_2O_2$, was the first material measured using P-XAS at the B18 beamline (at Diamond Light Source, Oxfordshire, UK), as part of this thesis. It was a particularly good candidate for testing the viability of this technique as powder data had already been measured at the same beamline. The anisotropy of the structure makes it a good test compound to measure using P-XAS, and check the resolution of the measurements as a function of orientation. Due to the material having a layered unit cell, Figure 4.2, there should be a clear distinction between measurements along the *c*-axis and in the *ab*-plane. The powder data suggested that the Cu ions were mobile and P-XAS is a suitable technique to investigate this in more detail. For example, using P-XAS it could be possible to determine if the ions are mobile within the plane or if they are not restricted to a specific direction in the material.

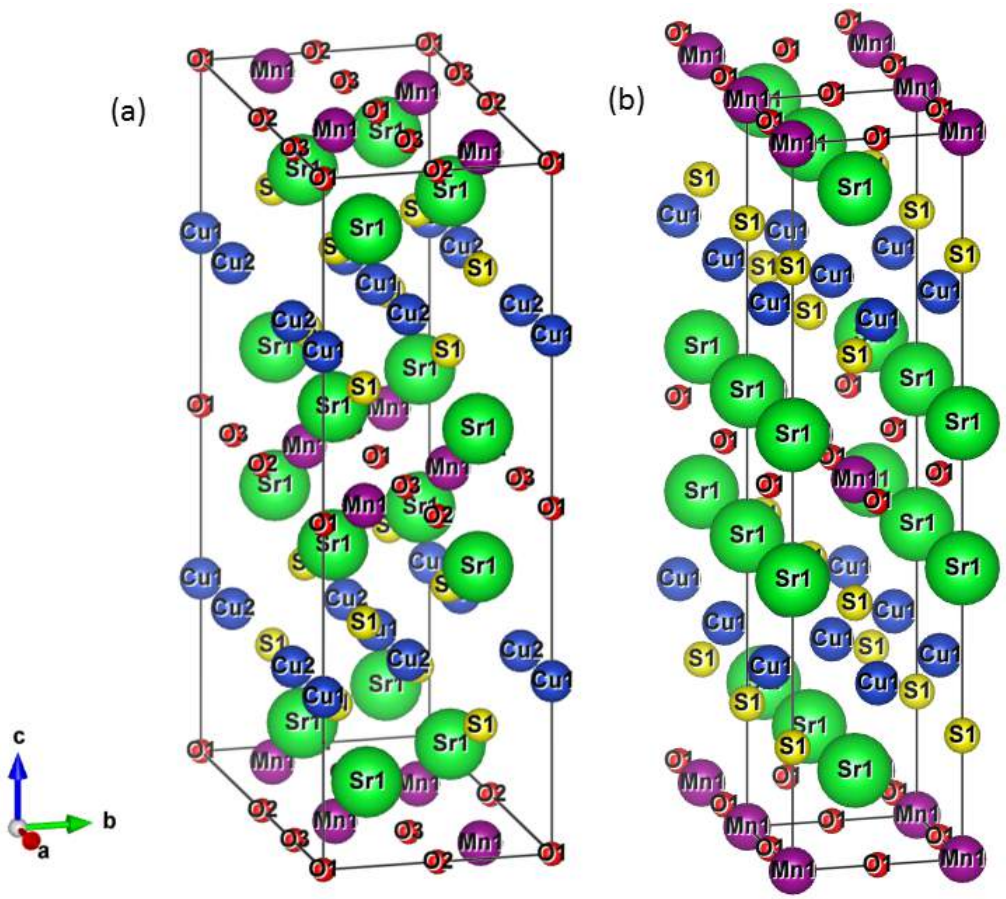

Figure 4.2: Structure of $Sr_2MnCu_{1.5}S_2O_2$, in the orthorhombic phase [34] (a), and the tetragonal phase [33] (b). The tetragonal phase displays two unit cells for a more direct comparison to the orthorhombic phase.

4.2 SEM images

SEM images were taken of the $Sr_2MnCu_{1.5}S_2O_2$ sample used in the P-XAS experiment. The procedure for the SEM measurements and the detection methods are discussed in Chapter 2. Measurements were made using both secondary and backscattering electron detection. The goal of these measurements was to determine if the sample was homogeneous in composition. This could be shown by mapping the surface of the sample, and by measuring spectra at different parts of the surface.
A chip of the crystal that was used in the P-XAS experiment was measured, this was to be sure that the SEM data matched the XAS data. The surface mapping can be seen in Figure 4.3, for both secondary and backscattering electron detection. The SEM images of the sample clearly show that the crystal is not homogeneous, as a homogeneous sample would be the same shade of grey across the whole surface.

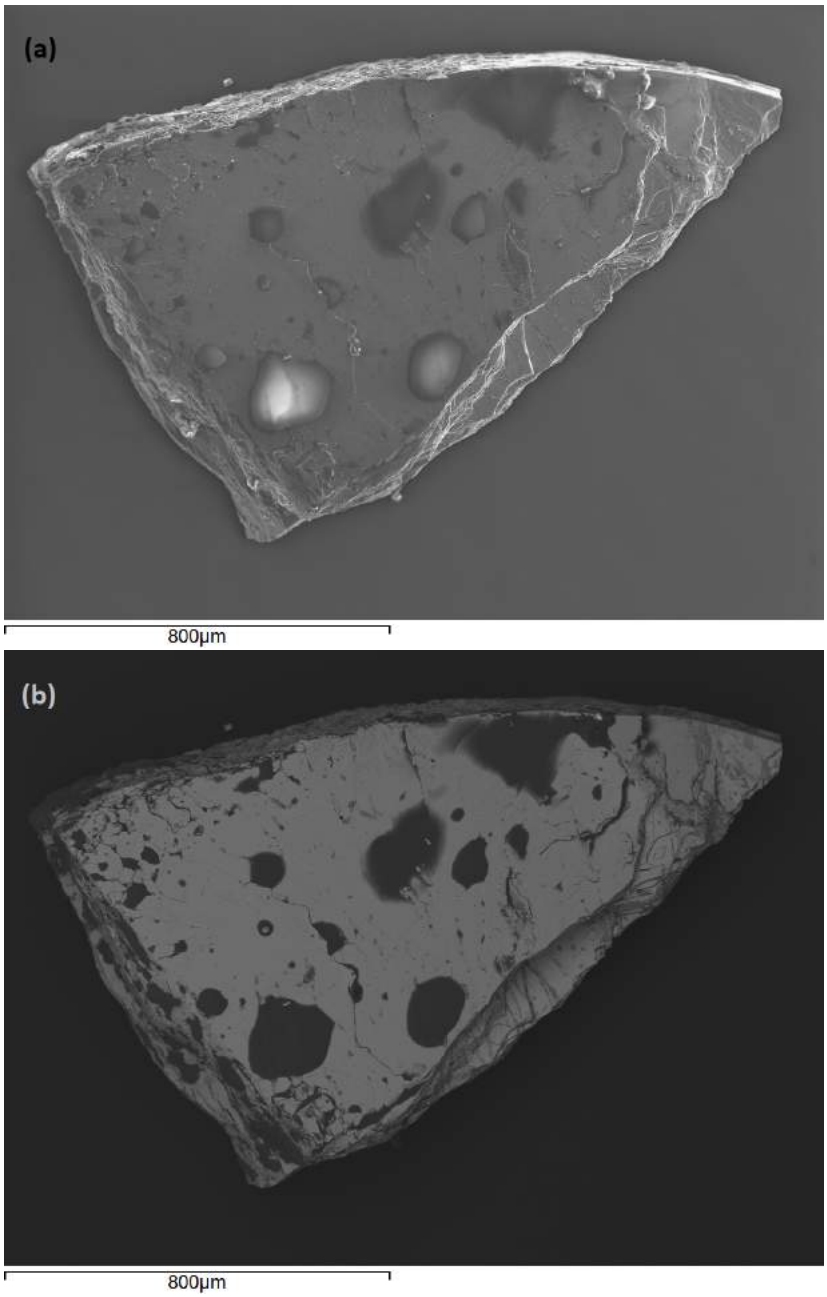

Figure 4.3: SEM image of a chip from the single crystal $Sr_2MnCu_{1.5}S_2O_2$, measured with secondary electron (a) and backscattering electron (b) detection. The lighter grey areas are the more homogeneous parts of the sample, the darker grey areas correspond to the impurities.

It is possible to use the characteristic x-ray spectra obtained from the SEM measurements to determine the stoichiometry of the sample. However, this was a secondary application of the SEM measurements taken for this thesis, and other experimental techniques would need to be used to obtain an accurate stoichiometry (as discussed in Chapter 2).
Spectra of the characteristic x-rays produced from the interaction between the sample and the electron beam at different points of the surface were measured to determine the composition of the features on the surface map. By comparing the spectra from the lighter grey to the darker grey areas (see Figures 4.4 and 4.5) the composition of the impurities can be inferred. The spectra show that the lighter grey areas have the expected composition for the sample, while the darker grey areas display a strong Mn signal. The spectra measured at different parts in the homogeneous region show that the expected composition is reproducible in these areas. While the spectra of the Mn rich impurities show that the composition is not constant. This may be due to there being less of the impurity in certain regions, leading to signal from the expected composition being stronger.

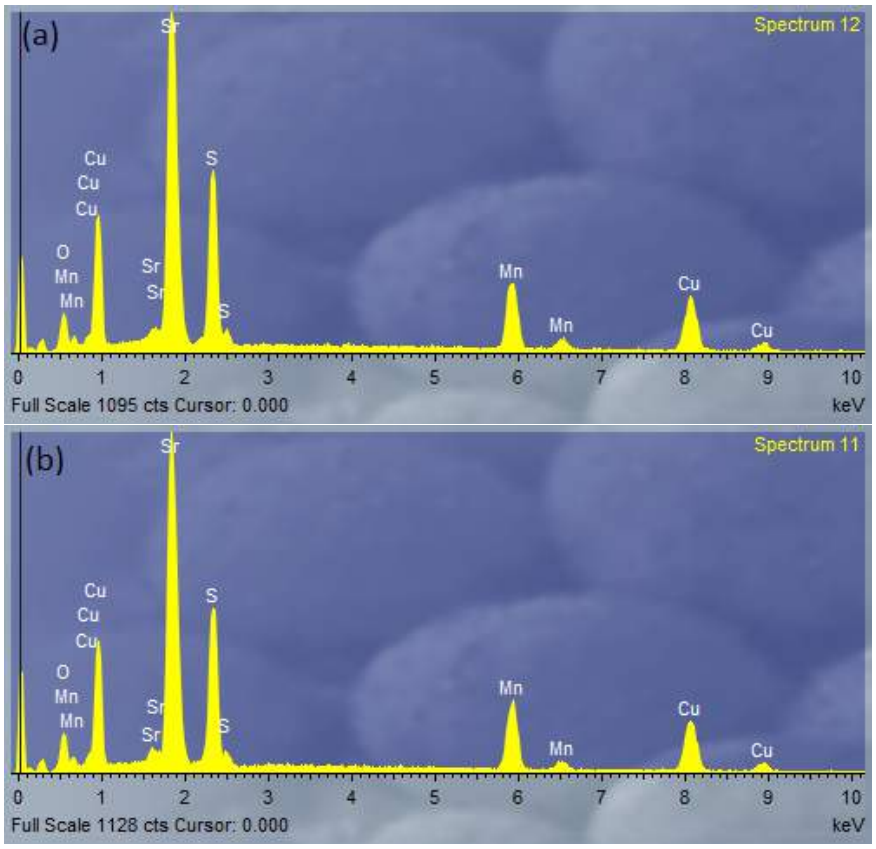

Figure 4.4: Both of the spectra were measured from points in the lighter grey areas of the sample, (a) was measured from a point on the left of the sample and (b) was measured from a point in the middle of the sample. The elements in the spectra are consistent with the elements expected to be seen in this material.

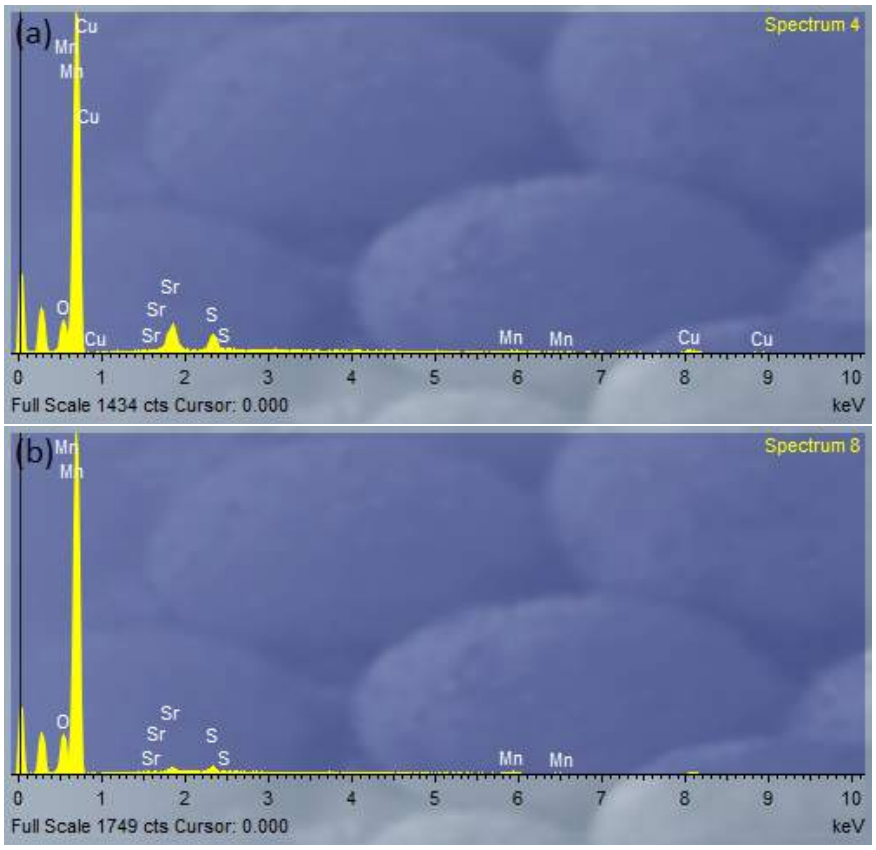

Figure 4.5: Both of the spectra were measured from points in the darker grey areas of the sample, (a) was measured from a point on the bottom middle of the sample and (b) was measured from a point on the right of the sample. The elements in the spectra show that these areas are impurities within the sample. The spectra also show that these impurities are mostly comprised of manganese compounds.

As the impurities seen in the sample do not have a constant composition it is not possible to calculate an accurate stoichiometry. The stoichiometry of the homogeneous regions of the sample can be estimated, however as the sample includes oxygen, and due to it being such a light element, it is hard to accurately calculate how much is present. There is also oxygen in the carbon sticky pad used to hold the sample (see Figure 4.6). This adds to the background spectra that has been removed from the spectra of the sample and can also introduce uncertainty into the amount of oxygen within the sample. Consequently only an estimate of the stoichiometry can be made, for which we have made the assumption that the weight percentage of the oxygen is 2. Within these constraints, the most likely stoichiometry of this sample is $Sr_2MnCu_{1.5}S_2O_2$, as reported by Gál *et al.* [33].

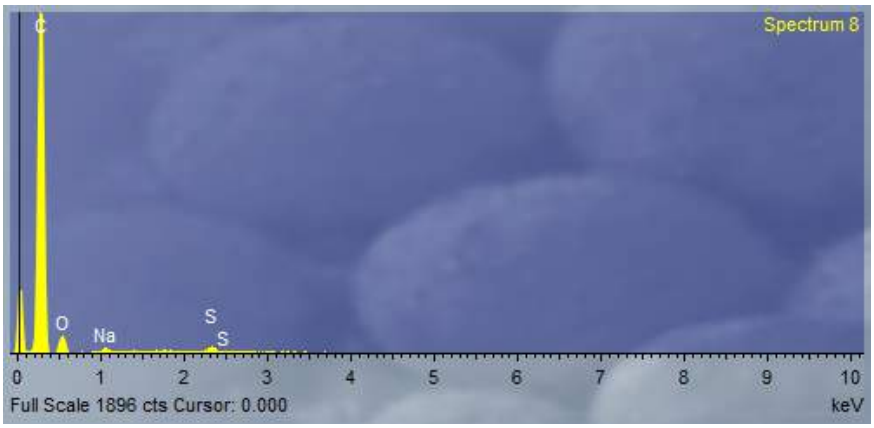

Figure 4.6: Spectra measured from the carbon sticky pad used to hold the sample. The elements in the spectra are also seen in the spectra of the sample suggesting that this is a background and can be removed from the other spectra.

4.3 $Sr_2MnCu_{1.5-x}S_2O_2(x = 0.0, 0.2, 0.3)$ powder XAS

4.3.1 Experimental set-up

The goal of this experiment was to track the reported transition of $Sr_2MnCu_{1.5-x}S_2O_2$, (x=0.0,0.2,0.3), from tetragonal, above 240K, to orthorhombic, below 240K. Also to see how the different magnetic structures observed for each sample [138] are related to the crystal structure and the oxidation state. The long-range magnetic ordering is destroyed when x=0.2, and a new magnetic structure is formed when x=0.3 [138]. The samples were provided by Prof. Simon Clarke's group in Oxford University. The samples were synthesised following the procedure described by Adamson *et al.* [132]. For this experiment the Cu and Mn K-edges were measured at a range of temperatures, at the B18 beamline in Diamond Light Source, in Oxfordshire, UK.[1]
As powder samples of $Sr_2MnCu_{1.5-x}S_2O_2$ were being measured pellets needed to be formed of each sample. The pellets were formed by measuring out enough sample to produce an absorption jump of 1, and mixed with a matrix, cellulose, so that there was enough powder to be pressed into 13mm pellets. The amount of sample needed in each pellet was calculated using Hephaestus [60]. This was found, for 13mm pellets, to be ∼10mg of sample and ∼80mg of cellulose, for both the Cu K-edge and Mn K-edge. Cellulose was chosen as the matrix as it has no absorption edge in the energy range we were measuring, it is not very absorbing over all, and it is stable in the temperature range used in the experiment. The pellets were loaded onto the sample holder and placed into a liquid helium pulse tube cryostat. This cryostat, available at B18 and manufactured by Oxford Instruments, has a temperature range of 300K to 1.5K, and can hold up to 3 samples at a time. This cryostat was used as the temperatures measured for this experiment were lower than 77K (the temperature of liquid nitrogen). To measure the samples the beamline was set up with the Si 111 monochromator crystals. The Pt branch and harmonic rejection mirrors were used, and an energy calibration was performed using a Cu foil. The XAS measurements were taken in transmission, and XAS spectra were measured for temperatures from 260K to 10K. Both Cu K-edge and Mn K-edge XAS were measured. For the Cu K-edge, each spectra was measured twice under the same conditions, with an energy step of $\sim 0.4eV$ before the absorption

[1]Note that I was not personally involved in the collection of this powder data. My contribution was to the data analysis, that was carried out by me in full.

edge at $1s$ per point, $\sim 0.4eV$ in the XANES region at $0.5s$ per point, and $\sim 0.5eV$ in the EXAFS region at $0.2s$ per point. For the Mn K-edge, each spectra was measured once, with an energy step of $\sim 3eV$ before the absorption edge at $1s$ per point, $\sim 0.2eV$ in the XANES region at $0.5s$ per point, $\sim 2eV$ in the EXAFS region at $1s$ per point, and $\sim 5eV$ for the tail end of the EXAFS region at $\sim 2s$ per point. A more complete set of measurements was made for the Cu K-edge, while the Mn K-edge was only measured for the two extreme temperatures. This experiment occurred before SEM measurements were taken of the sample, therefore the potential Mn rich impurities in these samples were not known before taking these measurements.

4.3.2 Powder XAS results

In this experiment all three samples of $Sr_2MnCu_{1.5-x}S_2O_2$ (x=0.0,0.2,0.3) were measured. All of the data measured from these samples has been analysed following the procedure described in Chapter 3. Each data set was calibrated to a known reference (Cu and Mn metal foil) to be sure that the position of the edge obtained was the true value.
For the Cu K-edge, the value of E_0 for the x=0.0 and x=0.2 sample was set to $8981.55 \pm 0.4eV$, and for x=0.3 sample E_0 was set to $8981.64 \pm 0.4eV$. The values for E_0 were set based on the position of the first peak in the derivative of the XANES (see Figures 4.8 to 4.10). The same spline range in k was used for all samples, 0 to 14Å^{-1}, and the background parameter (Rbkg) was set to 1Å for all data sets. The data was also normalised as per the procedures discussed in Chapter 3, the pre-edge range was the same for each sample and was set to $-201.42eV$ to $-20.11eV$, with respect to E_0. The post-edge range was also the same for each sample and set to $74.81eV$ to $557.4eV$, with respect to E_0, and the normalisation order was set to 3. For the FT-EXAFS the same range in k was used in the transformation for each sample and temperature measured, 3 to 12Å^{-1}.
For the Mn K-edge, the value of E_0 for the x=0.0 sample was set to $6550.00 \pm 0.2eV$, for x=0.2 sample E_0 was set to $6550.065 \pm 0.2eV$, and for x=0.3 sample E_0 was set to $6550.27 \pm 0.2eV$. The values for E_0 were set based on the mid point of the rising edge observed in the XAS. The same spline range in k was used for all samples, 0 to 13Å^{-1}, and the background parameter (Rbkg) was set to 0.9Å for all data sets. The pre-edge range was the same for each sample and was set to $-113.15eV$ to $-19.69eV$. The post-edge range was also the same for each sample and set to $59.34eV$ to $434.38eV$, and the normalisation order was set to 3. For the FT-EXAFS the same range in k was used in the transformation for each sample and temperature measured, 3 to 11Å^{-1}.
The data for both edges have then been fit to a theoretical model [33] (obtained from the the diffraction data) using the software and procedures discussed in Chapter 3.

XANES

Figure 4.7 shows the comparison of the Cu K-edge XANES, for each sample at the two extreme temperatures measured. The features seen in the XANES for the x=0.0 and x=0.2 compounds are very similar, the features appear to be slightly more defined in the x=0.3 compound but the differences are not strong. As there is no energy shift, this suggests that the amount of Cu vacancies is not affecting the local electronic structure of the Cu ions. The position of the first peak does not change position with the amount of vacancy in the Cu sites, it is seen at $8983.23eV$ for all three samples at both temperatures. The reported oxidation state of Cu in this material is +1 [139], the

position of the first peak in the XANES supports this, as the peak is typically found at $\approx 8983 - 8984eV$ for Cu(I) compounds [140]. As the Cu is in an oxidation state of +1, the K-edge is probing mainly the $1s \rightarrow 4p$ transition.
The XANES data, of the Cu K-edge, presented in Figures 4.8 to 4.10 show no changes in the electronic structure or local symmetry with temperature, for any of the three samples. Hence, there is no signature of the reported structural transition which suggests that it may not produce any significant changes in the local electronic structure of the Cu ions. The first derivative of the XANES confirm there is no change in the oxidation state with temperature as the peak position is unchanged with temperature for each sample, the first derivative can be seen in Figures 4.8b, 4.9b and 4.10b.

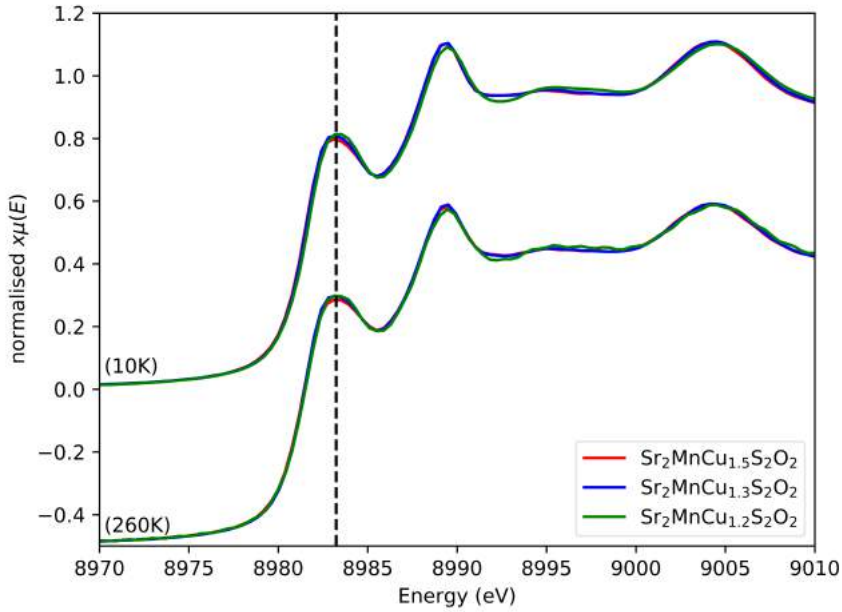

Figure 4.7: XANES of the Cu K-edge for each sample, measured at 10K and 260K. There is no visible energy shift between the samples.

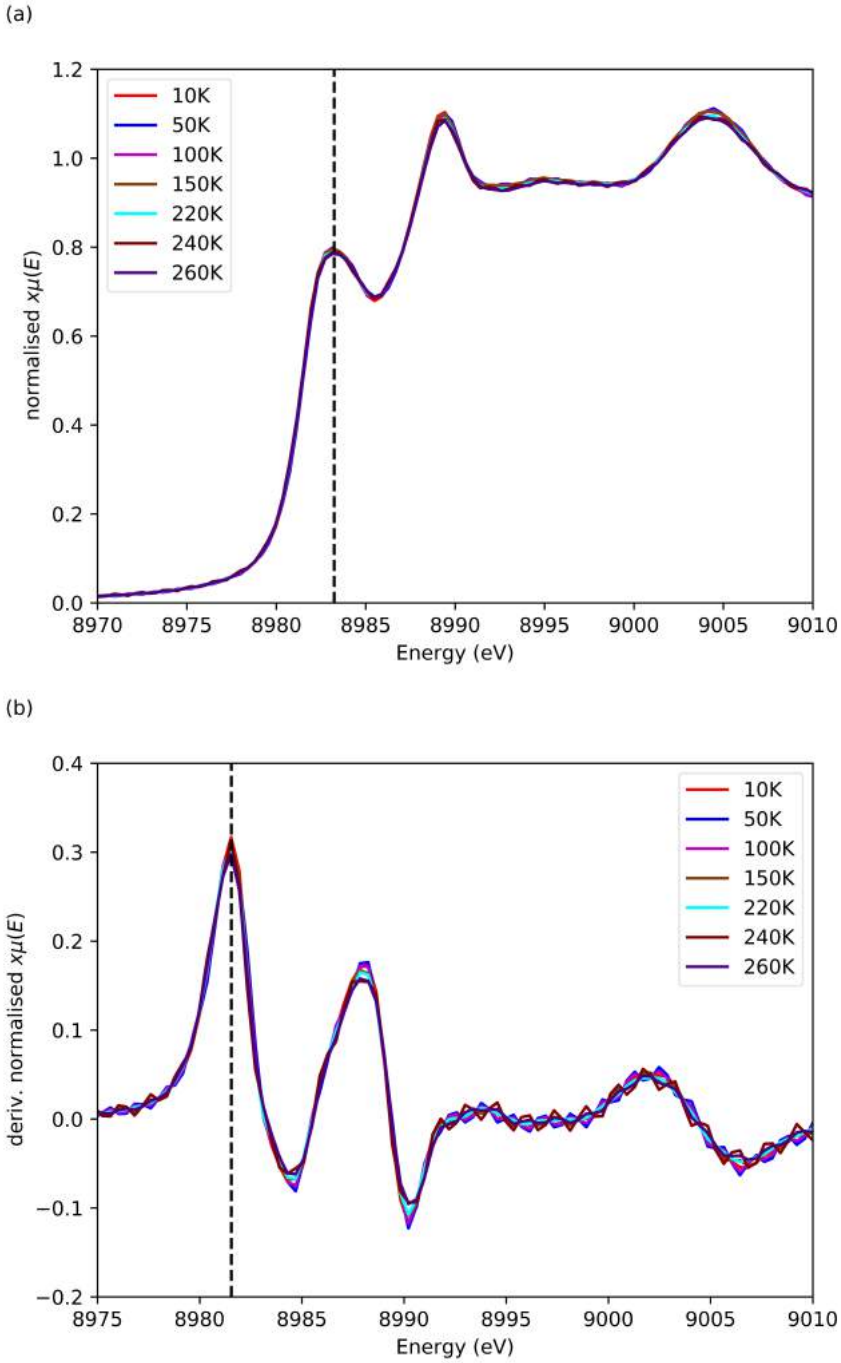

Figure 4.8: XANES, (a), and first derivative, (b), of the Cu K-edge of $Sr_2MnCu_{1.5}S_2O_2$, for different temperatures.

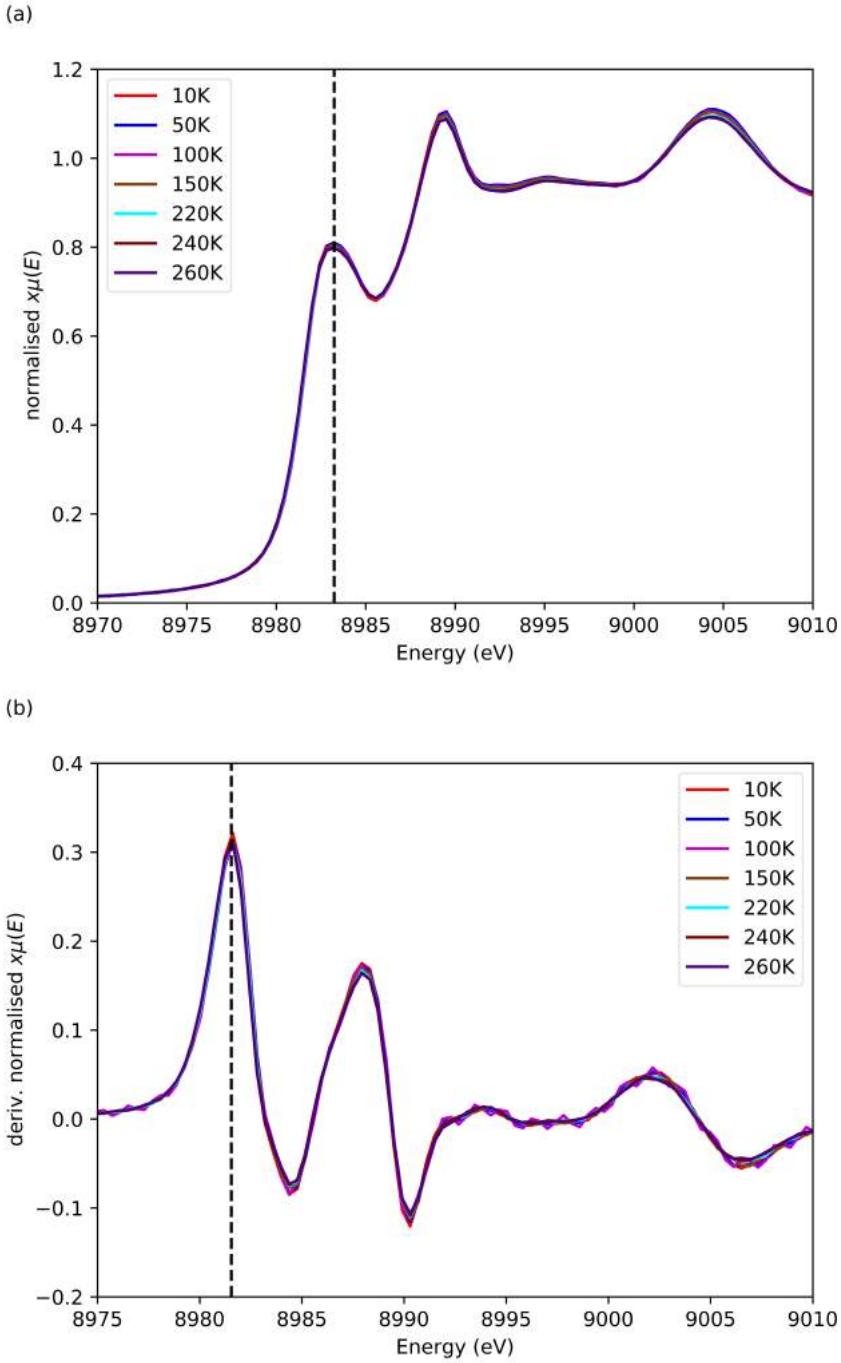

Figure 4.9: XANES, (a), and first derivative, (b), of the Cu K-edge of $Sr_2MnCu_{1.3}S_2O_2$, for different temperatures.

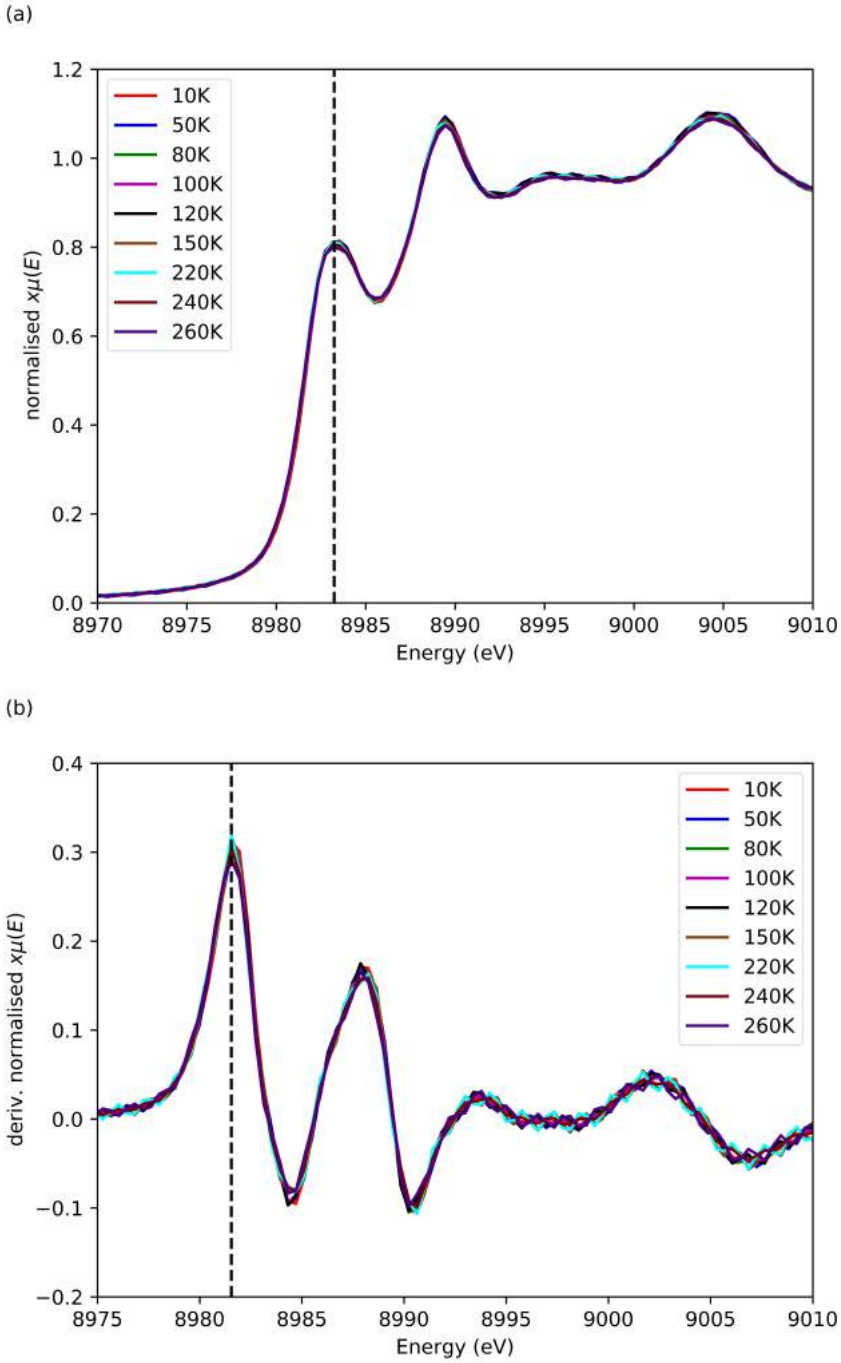

Figure 4.10: XANES, (a), and first derivative, (b), of the Cu K-edge of $Sr_2MnCu_{1.2}S_2O_2$, for different temperatures.

Figure 4.11 shows the XANES of the Mn K-edge, for each sample. The features seen in the XANES for all three samples are very similar at high temperature, 260K, however there are changes in the features seen below the transition temperature, at 10K. As we are measuring the Mn K-edge, the normal transition responsible for the absorption edge would be between s and p orbitals. However due to hybridisation between the O $2p$ orbitals and the Mn $3d$ orbitals, the absorption edge is indirectly probing the $1s$ to $3d$ transition [141]. The main absorption edge peak does not change position at 260K for the three samples, and is seen at $6556.65eV$. However the position of this peak at 10K does change for the different compositions, and is seen at $6556.47eV$ for the x=0.0 compound, $6556.61eV$ for the x=0.2 compound, and $6556.89eV$ for the x=0.3 compound.
The reported mean oxidation state of Mn in the material is +2.5, this may be a mix of +2 and +3, or +2, +3 and +4. The value found for E_0 for each sample ($\sim 6550eV$) is between the edge energies for Mn +3 and +4 [142]. This suggests that the Mn ions are more likely in a mixed oxidation state of +3 and +4. There is a visible pre-edge feature in this compound, which suggests that the symmetry allows for a quadrupole transition to occur. This could be due to disorder in the Mn sites reducing the symmetry, allowing for $1s$ to $3d$ transitions to occur.

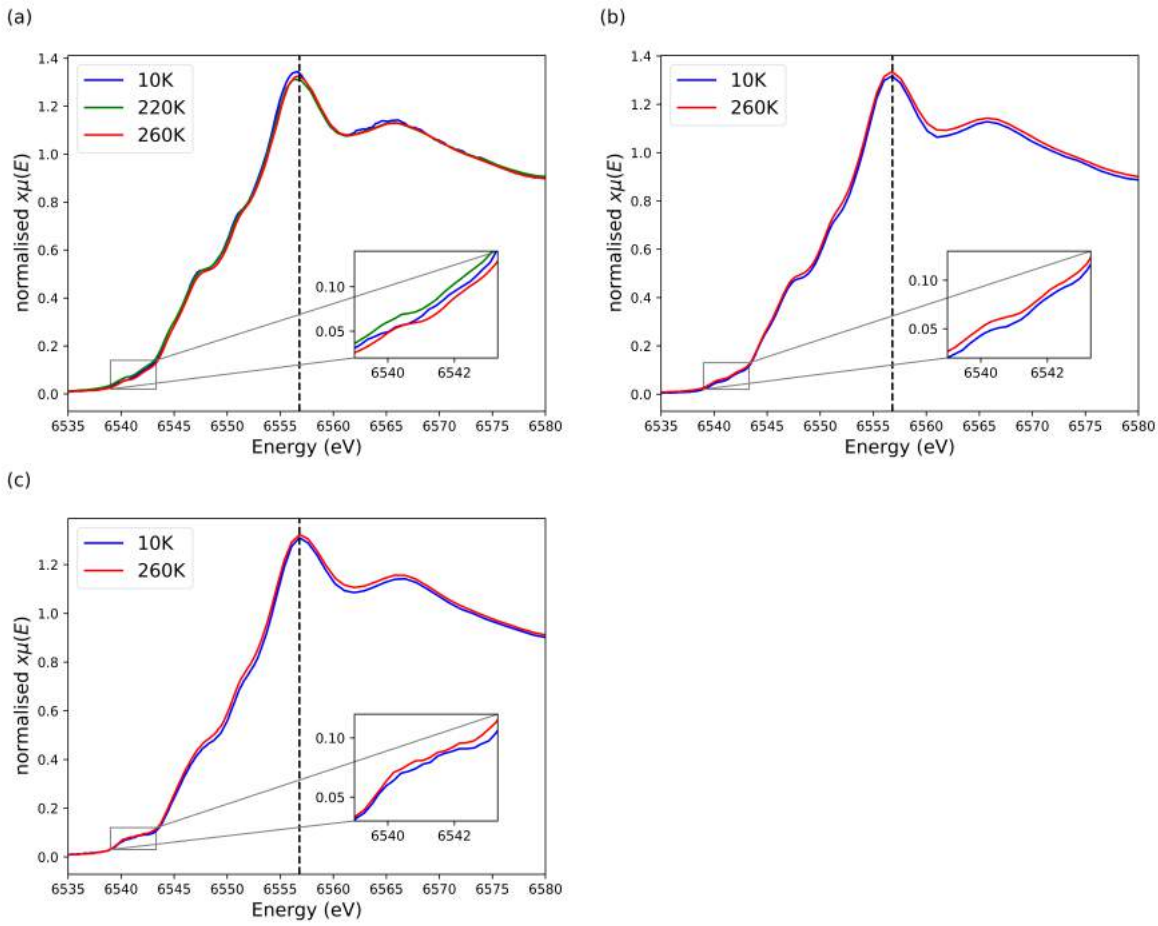

Figure 4.11: XANES of the Mn K-edge of all three samples. $Sr_2MnCu_{1.5}S_2O_2$ (a), $Sr_2MnCu_{1.3}S_2O_2$ (b), and $Sr_2MnCu_{1.2}S_2O_2$ (c).

EXAFS

Figure 4.12 shows the EXAFS and FT-EXAFS of the Cu K-edge of the x=0.0

compound. Plots of the data for the x=0.2, and x=0.3 compounds can be seen in Figures 4.13 and 4.14, respectively. The EXAFS and FT-EXAFS have been plotted with a k-weight of 2, and with a Fourier transform k-range of 3 to 12Å^{-1}. The FT-EXAFS presented have not been phase corrected, meaning the peak positions will not match the predicted positions from the model.
The path lengths with respect to an excited Cu ion can be seen in Table 4.1, obtained from the tetragonal model [33] and the orthorhombic model [34]. The orthorhombic model consists of two different Cu sites, which leads to more scattering paths contributing to a peak.

Table 4.1: Path lengths, with respect to Cu, obtained from both models of $Sr_2MnCu_{1.5}S_2O_2$, seen in Figure 4.2 [33, 34].

	Path distance (Å)		
Path	Tetragonal	Orthorhombic	
		Cu(1)	Cu(2)
1st Cu-S	2.433 (N=4)	2.418 (N=4)	2.406 (N=2), 2.440 (N=2)
1st Cu-Cu	2.838 (N=4)	2.891 (N=2)	2.837 (N=2), 2.891 (N=1)
Cu-Sr	3.269 (N=4)	3.269 (N=4)	3.218 (N=2), 3.302 (N=2)
2nd Cu-Cu	4.014 (N=4)	3.968 (N=4)	3.968 (N=2)
Cu-O	4.292 (N=2)	4.273 (N=2)	4.274 (N=2)
2nd Cu-S	4.694 (N=8)	4.685 (N=4)	4.646 (N=4)
Cu-Mn	4.738 (N=4)	4.712 (N=4)	4.723 (N=4)

There is a loss in the amplitude of the EXAFS signal with temperature. For the signal between 0 to $\sim$ 8Å^{-1} the positions of the peaks are roughly the same, for all the temperatures. The signal changes more with respect to temperature between 9 and 12Å^{-1}. The loss in amplitude is also seen in the FT-EXAFS, however the peak positions remain similar with temperature. This loss can be explained in terms of broadening from increased thermal fluctuations as the temperature increases, as the atom vibrations will increase at higher temperatures. The FT-EXAFS shows a clearer signature of changes due to temperature. For the data at the highest temperature only the first peak remains defined for all three samples. As there is not a large range of temperatures a transition temperature cannot be determined precisely.
The peaks are slightly more defined in the data for the x=0.0 sample than in the data for the x=0.2 sample. The EXAFS signal for the x=0.3 compound is very different, which is seen more clearly in the FT-EXAFS, see Figure 4.15. In the FT-EXAFS the second peak, found at $\sim$ 2.5Å for all samples, becomes broader and the amplitude is greatly reduced as the temperature increases. This peak has its strongest contribution from the first Cu-Cu scattering path (found at $\sim$ 2.85Å in the models), the reduction in this peak with increasing temperature suggests the Cu ions become more delocalised. The third peak is completely suppressed in the x=0.3 compound, for all temperatures. The suppression of this peak may be due to destructive interference of nearby scattering paths.

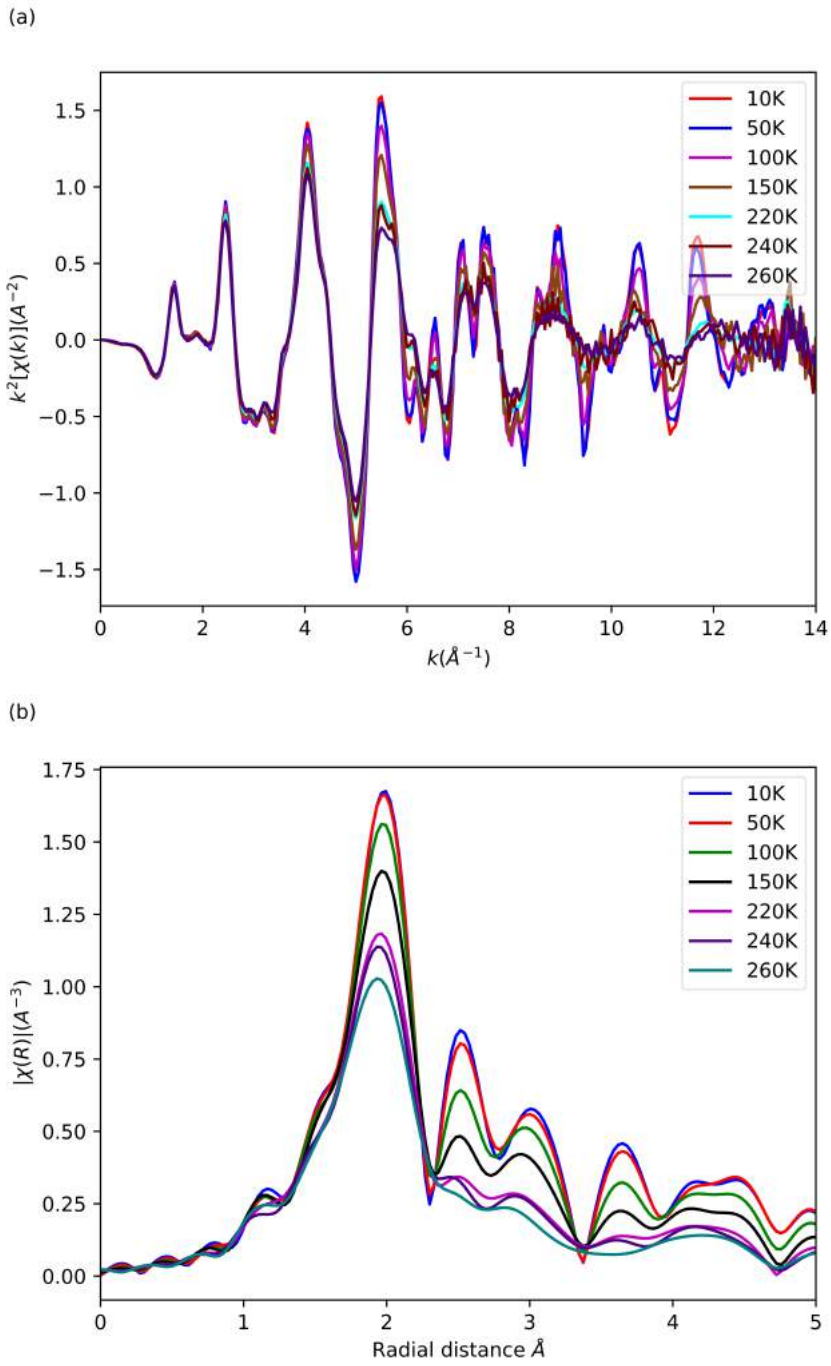

Figure 4.12: EXAFS, (a), and FT-EXAFS, (b), of the Cu K-edge of the $Sr_2MnCu_{1.5}S_2O_2$ sample, at different temperatures.

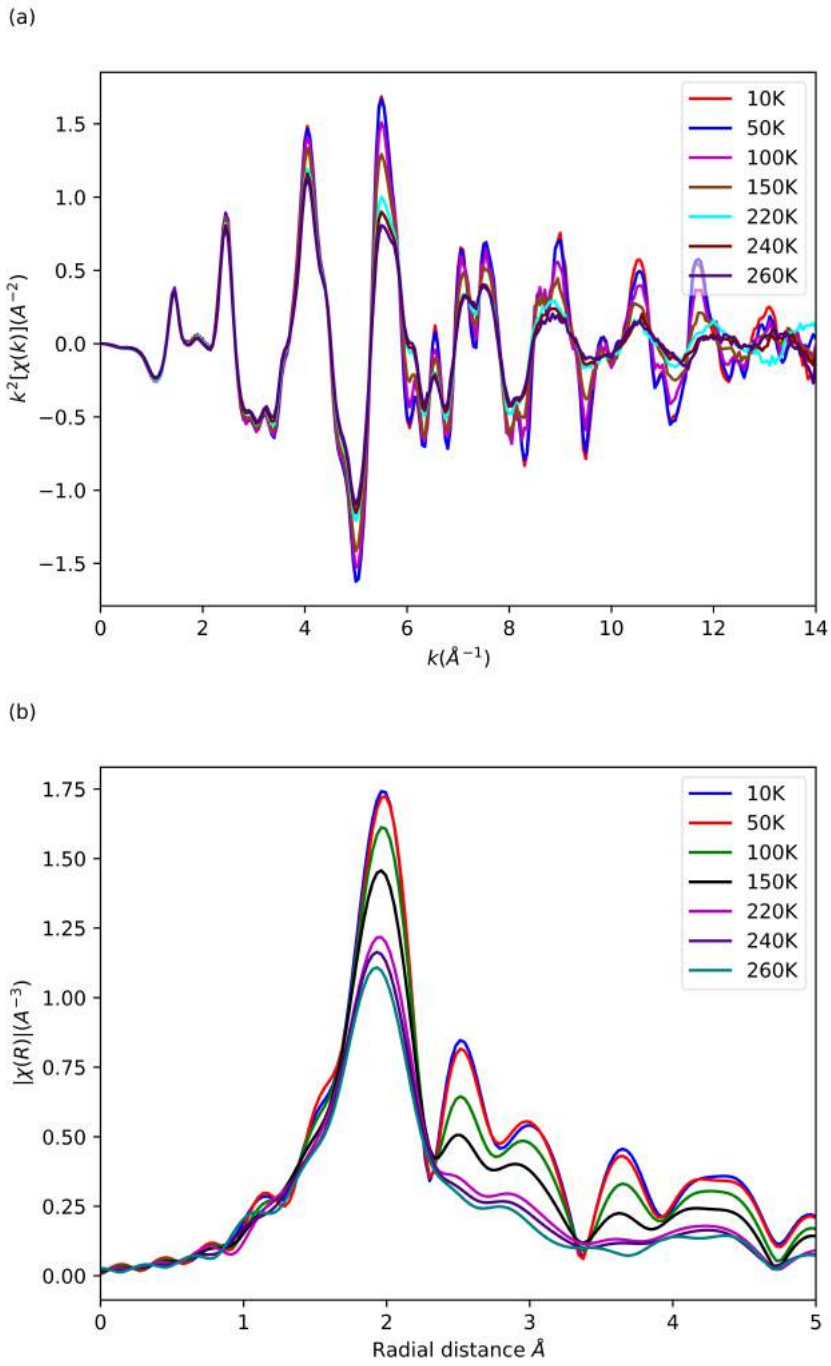

Figure 4.13: EXAFS, (a), and FT-EXAFS, (b), of the Cu K-edge of the $Sr_2MnCu_{1.3}S_2O_2$ sample, at different temperatures.

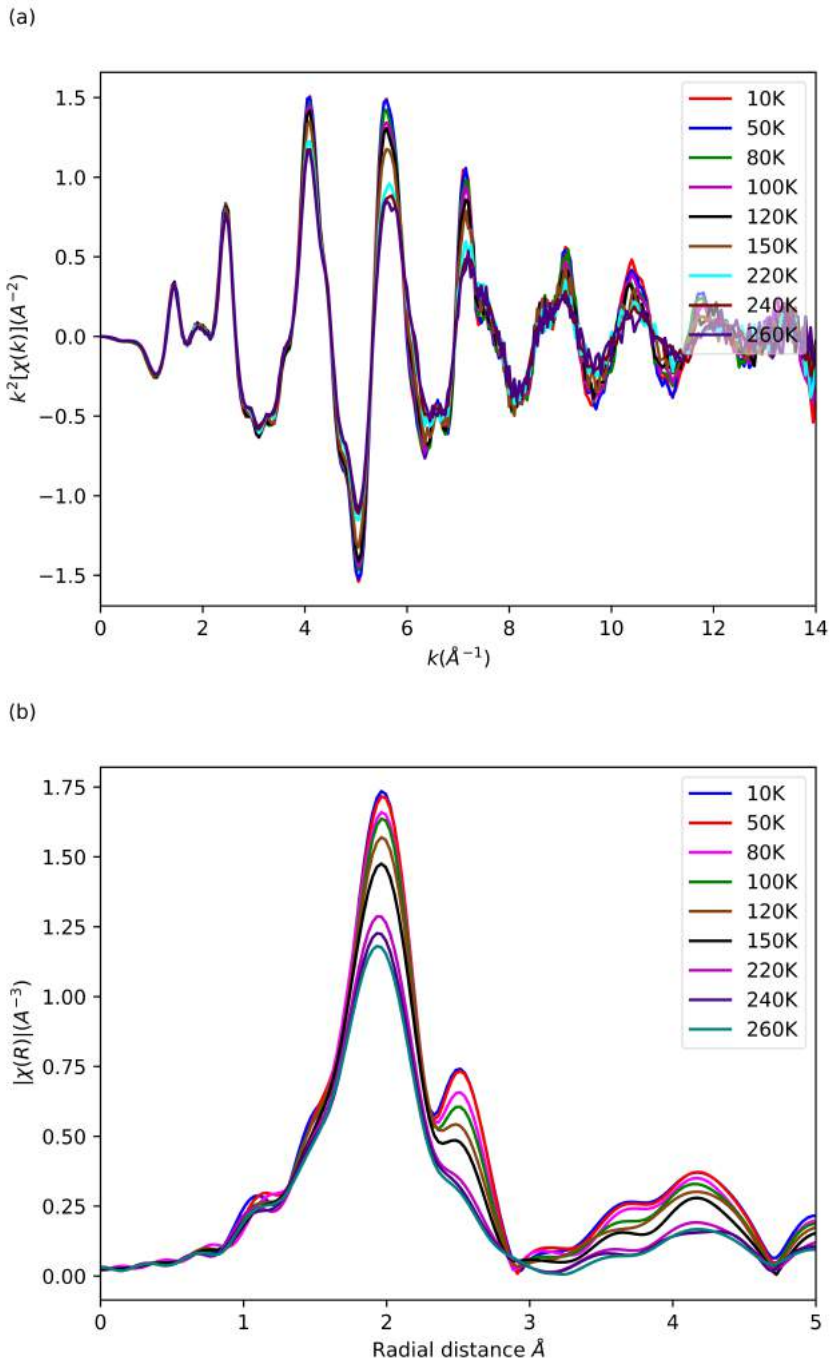

Figure 4.14: EXAFS, (a), and FT-EXAFS, (b), of the Cu K-edge of the $Sr_2MnCu_{1.2}S_2O_2$ sample, at different temperatures.

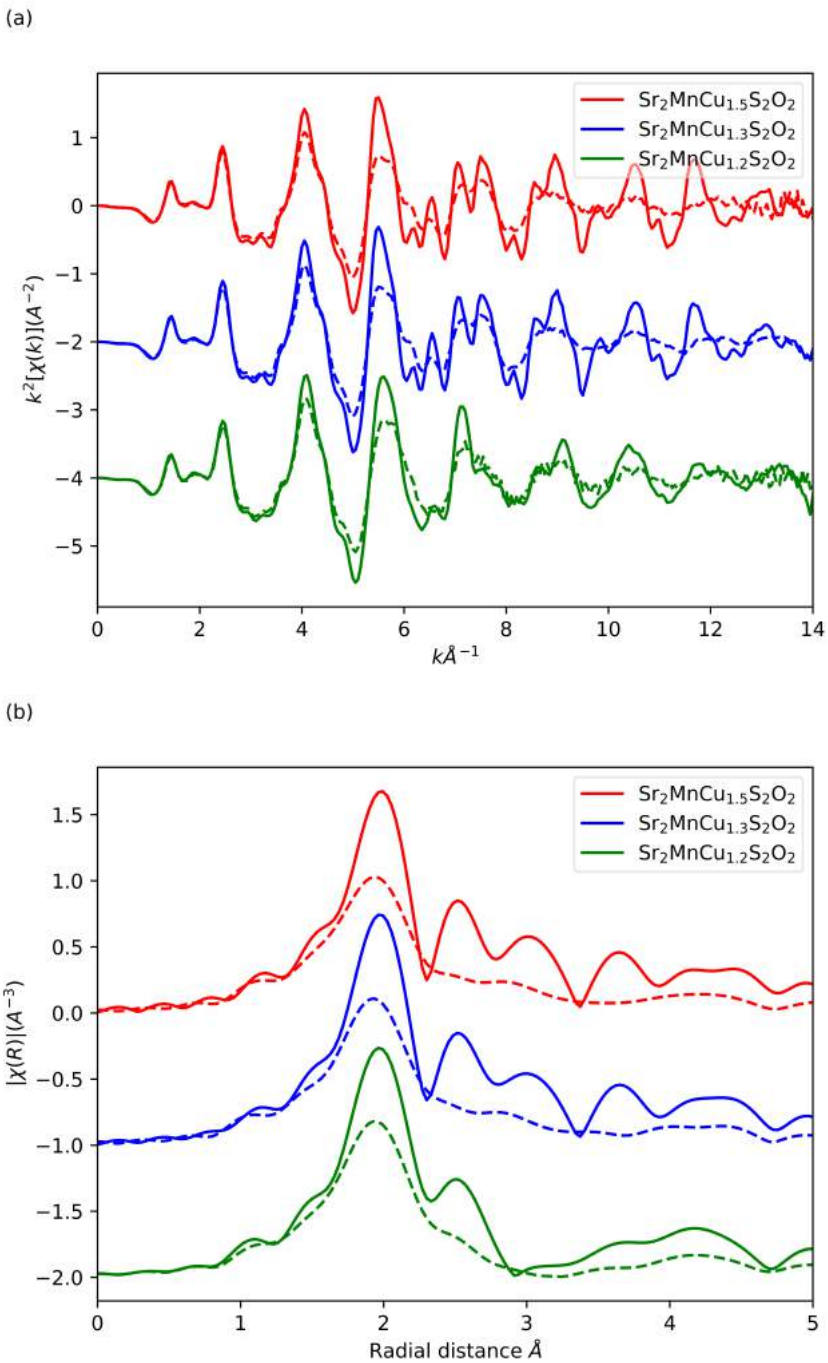

Figure 4.15: EXAFS, (a), and FT-EXAFS, (b), of the Cu K-edge of all three samples, at the highest and lowest temperature measured. Where the solid line corresponds to the measurement at 10K, and the dashed line corresponds to the measurement at 260K.

Figure 4.16 shows the EXAFS and FT-EXAFS of the Mn K-edge of all three samples. The EXAFS and FT-EXAFS have been plotted with a k-weight of 2, and a Fourier transform k-range of 3 to 11Å^{-1}. The FT-EXAFS presented have not been phase corrected, meaning the peak positions will not match the predicted positions from the model.
The path lengths with respect to an excited Mn ion can be seen in Table 4.2, obtained from the tetragonal model [33] and the orthorhombic model [34].

Table 4.2: Path lengths, with respect to Mn, obtained from both models of $Sr_2MnCu_{1.5}S_2O_2$, seen in Figure 4.2 [33, 34].

	Path distance (Å)	
Path	Tetragonal	Orthorhombic
1st Mn-O	2.007 (N=4)	1.998 (N=3), 2.022 (N=1)
Mn-S	2.915 (N=2)	2.902 (N=2)
Mn-Sr	3.314 (N=8)	3.292 (N=4), 3.326 (N=4)
Mn-Mn	4.014 (N=4)	3.971 (N=1), 4.021 (N=3)
2nd Mn-O	4.488 (N=8)	4.458 (N=3), 4.496 (N=5)
Mn-Cu	4.738 (N=8)	4.719 (N=6)

There is a loss in the amplitude of the EXAFS signal observed with respect to temperature. However the peaks are found in roughly the same position for the temperatures measured. The loss in amplitude is also seen in the FT-EXAFS. This loss can be explained in terms of broadening from increased thermal fluctuations, as the atom vibrations will increase at higher temperatures. The FT-EXAFS shows a clearer signature of changes due to temperature. The first peak, which has its strongest contribution from the Mn-O scattering path (found at $\sim$ 2Å in the models), changes depending on the sample. This peak becomes broader as the temperature increases, going from a peak with a clear shoulder to closer to a single peak. The change in this peak, with respect to temperture is roughly the same for the x=0 and x=0.2 samples, where the peak becomes broader for the x=0.3 sample. The relative weighting for the second and third peaks switches as the temperature increases, for all three samples. As there is not a large range of temperatures a transition temperature cannot be determined.

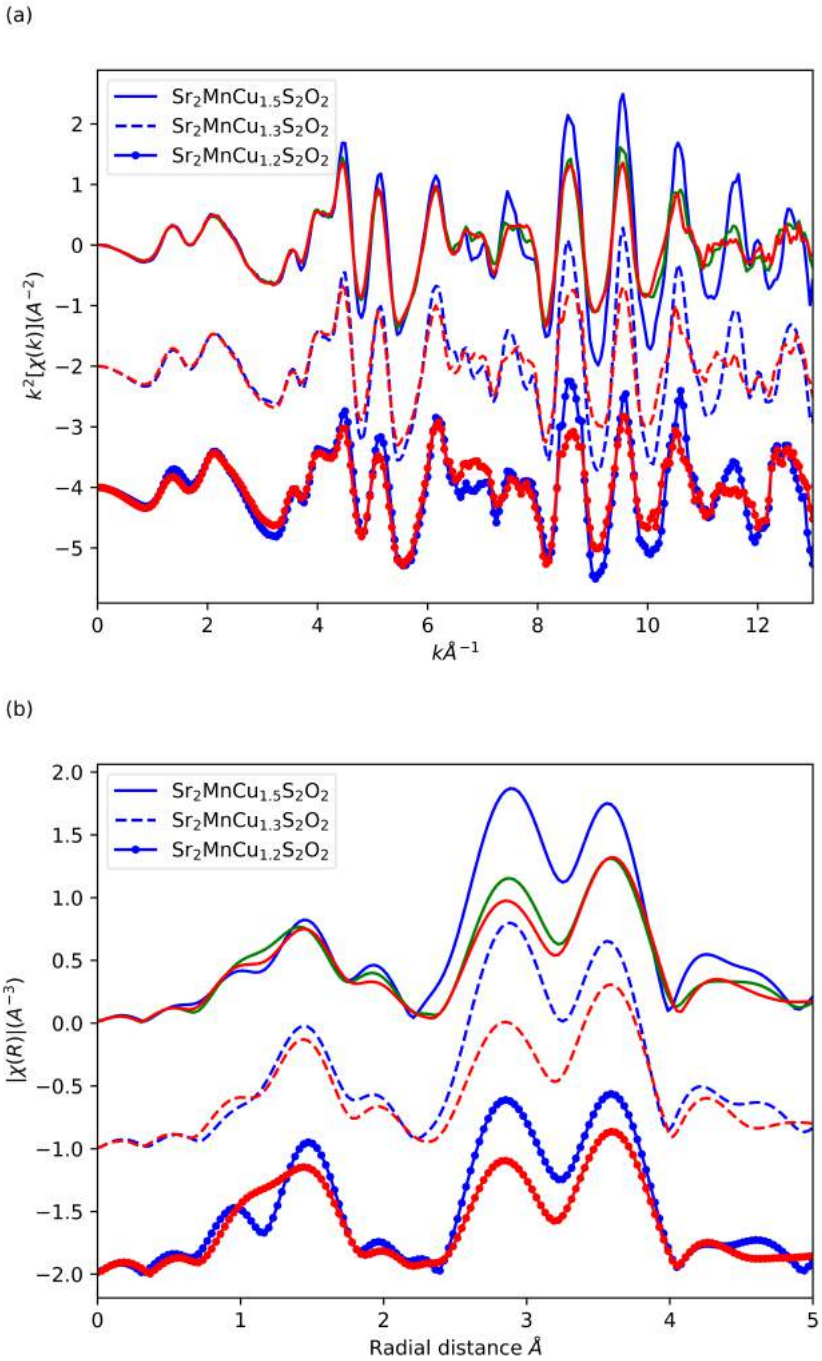

Figure 4.16: EXAFS, (a), and FT-EXAFS, (b), of the Mn K-edge of all three samples. Where the blue line corresponds to the measurement at 10K, the green line corresponds to the measurement at 220K, and the red line corresponds to the measurement at 260K.

Fit of EXAFS

To gain a better understanding of the local structural changes as a function of temperature and composition the EXAFS data, for both the Cu K-edge and Mn K-edge, were fitted. The data were fitted according to the method described in Chapter 3. Figures 4.12 to 4.14 show that there are strong features up to 4.8Å for the Cu K-edge of $Sr_2MnCu_{1.5-x}S_2O_2$ (x=0.0,0.2,0.3). Figure 4.16b shows that there are strong features up to ∼4Å for the Mn K-edge.

The fits for the Cu K-edge were produced by refining the tetragonal model against the measured data, where the path distances and DWs were allowed to change for each temperature, so that the changes in structure could be tracked. Fitting was carried out in R space, with k weightings of 1, 2, and 3, using 72 of 137 independent parameters for both the x=0.0 and x=0.2 samples, and 92 of 177 independent parameters for the x=0.3 sample, for all temperatures. The same paths were used in the fits for each sample, the single scattering paths were calculated from the tetragonal structure up to 4.69Å. The Cu-O path could not be fit to the data for any sample or any temperature, as the path produced unreasonable parameters. This suggests it is too delocalised to contribute to the EXAFS. The fits resulted in a R-factor of 0.014, 0.015, and 0.007, for the x=0.0, x=0.2, and x=0.3 samples, respectively. The reduced χ^2 produced from the fits were 342.76, 770.08, and 197.67 for the x=0.0, x=0.2, and x=0.3 samples, respectively. As the edge position does not vary with temperature ΔE_0 has been set to the same variable for all temperatures for each sample. The degeneracy (N) of each path has been set to the value of predicted by the tetragonal model (see Table 4.1). This parameter cannot be refined in ARTEMIS, so the amplitude reduction factor (S_0^2) takes into account changes in N. The value for S_0^2 reported for the fits is a global factor, so it accounts for all factors affecting the amplitude. This means it cannot directly be used to infer changes in N from the fits.

The refined parameters for the fits of the x=0.0, 0.2, and 0.3 samples can be found in Tables 4.3 to 4.5, respectively. All of the parameters are within their acceptable ranges, so the fits can be considered good. It is worth noting that the Debye-Waller factors (DW) are larger for the Cu-Cu scattering paths, than for paths further from the absorbing atom. For the x=0.0 sample the DW found for the first Cu-Cu scattering path ranges from 0.009 to 0.021Å^2, while the highest DW for any other path is 0.016Å^2 (for the second Cu-S scattering path at 4.694Å). For the x=0.2 compound the DW found for the first Cu-Cu scattering path ranges from 0.01 to 0.021Å^2, while the highest DW for any other path is 0.016Å^2 (for the second Cu-S scattering path). For the x=0.3 compound the DW found for the first Cu-Cu scattering path ranges from 0.011 to 0.02Å^2, while the highest DW for any other path is 0.023Å^2 (for the Cu-Sr scattering path at 3.269Å). This indicates delocalisation of the Cu-Cu scattering path, which suggests there is mobility in the Cu ions for the x=0.0 and x=0.2 compound. For the x=0.3 compound the DWs also suggest that the Cu ions are mobile. While the large DW for the Cu-Sr scattering path may be due to the peak this path corresponds to being suppressed, making it harder for the model to predict the location of the Cu-Sr path. The suppression of the third peak may be due to destructive interference affects between the nearest scattering paths. The second Cu-Cu scattering path (at 4.014Å) cannot be fit to the data for temperatures above 150K, for the x=0.0 and x=0.2 samples. For the x=0.3 compound the second Cu-Cu scattering paths cannot be fit to the data for temperatures above 120K. This suggests that the Cu ions may be more mobile in the x=0.3 compound when compared to the x=0.0 and x=0.2 compounds.

The structural model used for the fits does not take into account Cu vacancies and

is based on diffraction data of $Sr_2MnCu_{1.5}S_2O_2$ measured at 240K [33]. To track the effect temperature and Cu vacancies have on the local structure, each data set was fit to the same model. It is reported that there may be Cu/vacancies ordering below 240K [132]. The consequence of this ordering has been described by Rutt [134], where the unit cell structure will increase in size to a superstructure. This results in two Cu sites with different path lengths (see Table 4.1), this may cause the peaks to broaden. This could affect the DWs and errors in the fits, for measurements below the transition temperature, as the peaks may not be positioned where the tetragonal model expects. The peaks may also broaden as a consequence of the Cu vacancies. Another effect of the missing vacancies in the model is that the intensity of the scattering paths could be reduced as there are less Cu ions leading to a reduced absorption compared to the model. This would lead to smaller values for S_0^2 produced by the fit, as the amplitudes predicted by the model would need to be decreased to match the amplitudes of the experimental data. The model used in the fits is of the tetragonal phase of $Sr_2MnCu_{1.5}S_2O_2$, the x=0.2 and 0.3 samples produce a reasonable fit to this model suggesting that the Cu vacancies do not have a strong affect on the local structure of the samples measured for this experiment.

Table 4.3: Fit parameters for the Cu K-edge EXAFS of $Sr_2MnCu_{1.5}S_2O_2$, alongside the value obtained from the tetragonal structure. The degeneracy (N) of the paths were set to the values of the model. ΔE_0 found for these fits is $4.006 \pm 0.288eV$.

	Temperature(K):							
Parameter:	10	50	100	150	220	240	260	model (240K) [33]
S_0^2	0.73±0.04	0.75±0.08	0.74±0.06	0.7±0.1	0.72±0.03	0.7±0.1	0.71±0.06	-
1st Cu-S R (Å)	2.40±0.00	2.40±0.01	2.40±0.01	2.40±0.01	2.40±0.00	2.40±0.01	2.40±0.01	2.433
1st Cu-S σ^2 (Å^2)	0.004±0.001	0.004±0.001	0.005±0.001	0.006±0.002	0.007±0.001	0.008±0.003	0.009±0.001	-
1st Cu-Cu R (Å)	2.87±0.01	2.87±0.01	2.87±0.01	2.84±0.03	2.87±0.01	2.87±0.04	2.87±0.02	2.838
1st Cu-Cu σ^2 (Å^2)	0.009±0.001	0.010±0.002	0.012±0.002	0.015±0.004	0.019±0.002	0.019±0.007	0.021±0.004	-
Cu-Sr R (Å)	3.28±0.01	3.28±0.01	3.28±0.01	3.29±0.02	3.30±0.01	3.31±0.03	3.32±0.02	3.269
Cu-Sr σ^2 (Å^2)	0.007±0.001	0.007±0.002	0.008±0.002	0.010±0.003	0.013±0.001	0.012±0.005	0.015±0.003	-
2nd Cu-Cu R (Å)	3.97±0.01	3.98±0.03	4.0±0.4	4.0±0.1	-	-	-	4.014
2nd Cu-Cu σ^2 (Å^2)	0.009±0.002	0.010±0.004	0.013±0.005	0.02±0.02	-	-	-	-
2nd Cu-S R (Å)	4.72±0.01	4.72±0.03	4.72±0.02	4.71±0.04	4.71±0.01	4.71±0.05	4.70±0.02	4.694
2nd Cu-S σ^2 (Å^2)	0.007±0.002	0.007±0.004	0.009±0.003	0.012±0.006	0.014±0.002	0.014±0.009	0.016±0.004	-

Table 4.4: Fit parameters for the Cu K-edge EXAFS of $Sr_2MnCu_{1.3}S_2O_2$, alongside the value obtained from the tetragonal structure. The degeneracy (N) of the paths were set to the values of the model. ΔE_0 found for these fits is $3.78 \pm 0.31eV$.

	Temperature(K):							
Parameter:	10	50	100	150	220	240	260	model (240K) [33]
S_0^2	0.78±0.06	0.79±0.06	0.79±0.09	0.80±0.06	0.77±0.05	0.76±0.04	0.74±0.06	-
1st Cu-S R (Å)	2.40±0.01	2.40±0.00	2.40±0.01	2.40±0.01	2.40±0.01	2.40±0.00	2.39±0.01	2.433
1st Cu-S σ^2 (Å^2)	0.004±0.001	0.004±0.001	0.005±0.001	0.006±0.001	0.008±0.001	0.008±0.001	0.009±0.001	-
1st Cu-Cu R (Å)	2.86±0.01	2.86±0.01	2.86±0.02	2.84±0.02	2.86±0.02	2.86±0.01	2.86±0.02	2.838
1st Cu-Cu σ^2 (Å^2)	0.010±0.001	0.010±0.001	0.013±0.003	0.015±0.002	0.019±0.003	0.020±0.002	0.021±0.003	-
Cu-Sr R (Å)	3.27±0.01	3.27±0.01	3.27±0.02	3.28±0.01	3.29±0.01	3.29±0.01	3.30±0.02	3.269
Cu-Sr σ^2 (Å^2)	0.008±0.001	0.008±0.001	0.009±0.002	0.011±0.002	0.013±0.002	0.014±0.002	0.015±0.002	-
2nd Cu-Cu R (Å)	3.97±0.02	3.97±0.02	3.97±0.05	3.99±0.07	-	-	-	4.014
2nd Cu-Cu σ^2 (Å^2)	0.010±0.003	0.011±0.003	0.014±0.007	0.02±0.01	-	-	-	-
2nd Cu-S R (Å)	4.71±0.02	4.71±0.02	4.71±0.03	4.70±0.02	4.70±0.02	4.70±0.02	4.70±0.02	4.694
2nd Cu-S σ^2 (Å^2)	0.007±0.003	0.007±0.002	0.009±0.004	0.012±0.003	0.014±0.003	0.015±0.003	0.016±0.004	-

Table 4.5: Fit parameters for the Cu K-edge EXAFS of $Sr_2MnCu_{1.2}S_2O_2$, alongside the value obtained from the tetragonal structure. ΔE_0 found for these fits is $4.29 \pm 0.19eV$. The degeneracy (N) of the paths were set to the values of the model. More temperatures were measured for the x=0.3 compound than for the other samples.

	Temperature(K):									
Parameter:	10	50	80	100	120	150	220	240	260	model (240K) [33]
S_0^2	0.83±0.02	0.83±0.04	0.82±0.05	0.81±0.03	0.82±0.05	0.79±0.07	0.75±0.08	0.74±0.04	0.73±0.09	-
1st Cu-S R (Å)	2.40±0.00	2.40±0.00	2.40±0.00	2.40±0.00	2.40±0.00	2.40±0.01	2.39±0.01	2.39±0.00	2.39±0.01	2.433
1st Cu-S σ^2 (Å^2)	0.005±0.000	0.005±0.001	0.0052±0.0008	0.0052±0.0005	0.0059±0.0008	0.006±0.001	0.007±0.001	0.008±0.001	0.008±0.002	-
1st Cu-Cu R (Å)	2.83±0.00	2.83±0.01	2.83±0.01	2.83±0.01	2.83±0.01	2.84±0.02	2.82±0.02	2.82±0.01	2.82±0.03	2.838
1st Cu-Cu σ^2 (Å^2)	0.011±0.001	0.012±0.001	0.013±0.001	0.013±0.001	0.015±0.002	0.015±0.003	0.018±0.004	0.019±0.002	0.020±0.005	-
Cu-Sr R (Å)	3.36±0.02	3.36±0.03	3.35±0.04	3.36±0.02	3.36±0.03	3.34±0.04	3.35±0.05	3.34±0.03	3.35±0.06	3.269
Cu-Sr σ^2 (Å^2)	0.021±0.003	0.020±0.004	0.020±0.005	0.021±0.003	0.020±0.005	0.020±0.006	0.022±0.008	0.022±0.004	0.02±0.01	-
2nd Cu-Cu R (Å)	3.96±0.02	3.96±0.03	3.97±0.05	3.97±0.04	3.96±0.07	-	-	-	-	4.014
2nd Cu-Cu σ^2 (Å^2)	0.017±0.002	0.018±0.005	0.020±0.007	0.023±0.006	0.03±0.01	-	-	-	-	-
2nd Cu-S R (Å)	4.67±0.01	4.66±0.01	4.66±0.02	4.66±0.01	4.66±0.01	4.67±0.02	4.67±0.03	4.67±0.02	4.67±0.03	4.694
2nd Cu-S σ^2 (Å^2)	0.008±0.001	0.008±0.002	0.009±0.002	0.009±0.001	0.010±0.002	0.010±0.003	0.014±0.004	0.015±0.003	0.016±0.006	-

Figures 4.17 to 4.19 show the changes in the DWs, for the x=0.0, x=0.2, and x=0.3 samples, respectively. The DWs for each scattering path are included in the plot, with respect to temperature. The plots show that the DWs for the Cu-Cu paths are larger for the x=0.0 and x=0.2 samples. Although the DWs for Cu-Sr scattering path are higher than the Cu-Cu scattering paths in the fits of the x=0.3 sample, the DWs for the Cu-Cu paths are still very high. The large DWs for the Cu-Sr scattering path can be linked to the suppression of the peak this path corresponds to. The DWs for each path are larger for the x=0.3, than the x=0.0 and x=0.2 samples, this is consistent with the increased Cu vacancies causing a broadening of the peaks. The values of the DW factor obtained from the fit support the scenario in which the Cu ions are mobile. The second Cu-Cu path can be fit but with more difficulty than the other paths at higher temperatures which is suggestive of delocalisation. At high temperatures, 150K and above, the DWs for the first Cu-Cu scattering path are roughly the same for each sample, see Figure 4.20. For the lower temperatures the DWs for this scattering path are slightly larger for the x=0.3 compound. The DWs for the second Cu-Cu scattering path are much larger for the x=0.3 compound than the other samples, consistent with the idea that the increase in the Cu vacancies affects the delocalisation.

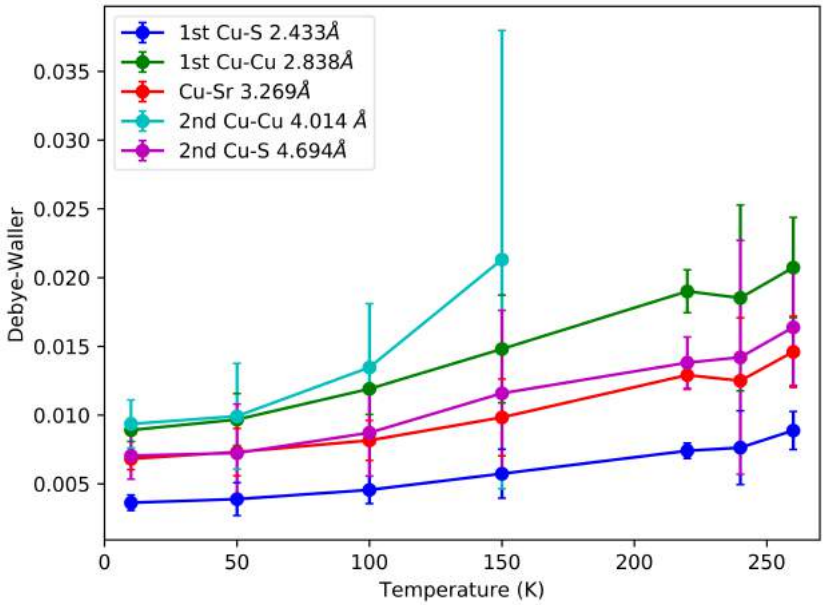

Figure 4.17: The Debye-Waller values for each path used in the fit of the tetragonal structure to the Cu K-edge measurement of $Sr_2MnCu_{1.5}S_2O_2$ sample.

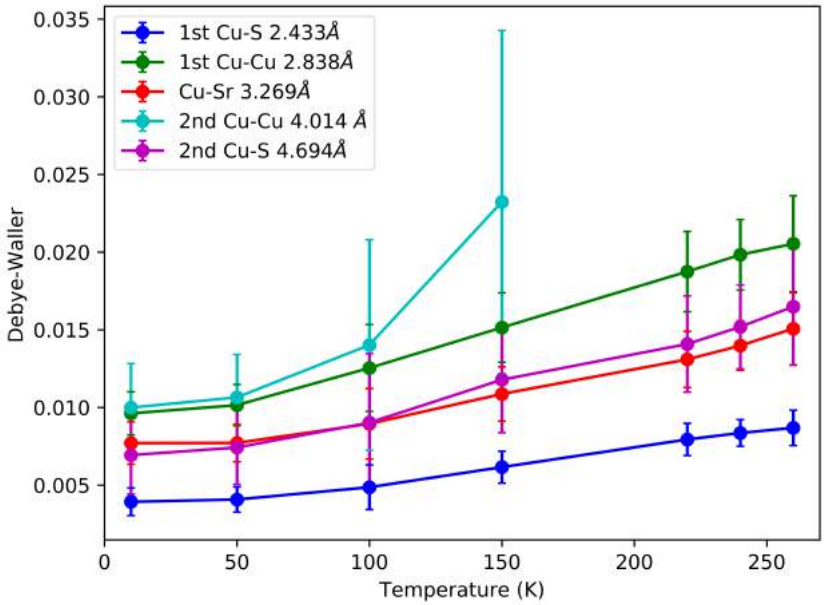

Figure 4.18: The Debye-Waller values for each path used in the fit of the tetragonal structure to the Cu K-edge measurement of the $Sr_2MnCu_{1.3}S_2O_2$ sample.

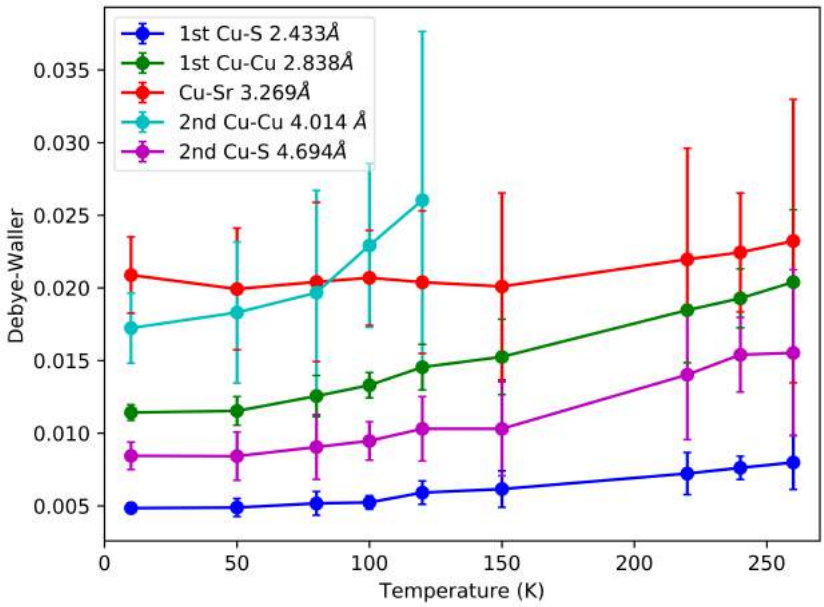

Figure 4.19: The Debye-Waller values for each path used in the fit of the tetragonal structure to the Cu K-edge measurement of the $Sr_2MnCu_{1.2}S_2O_2$ sample.

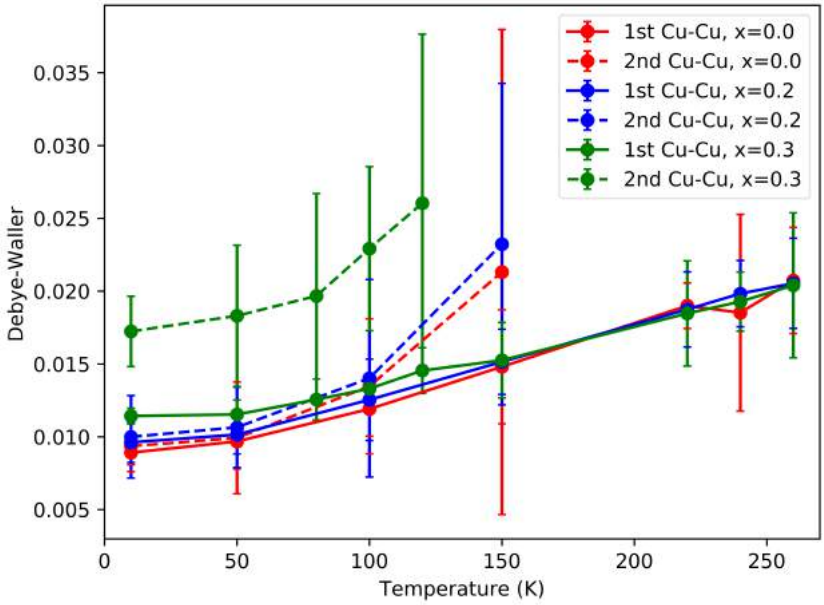

Figure 4.20: The Debye-Waller values for both Cu-Cu scattering paths used in the fit of the tetragonal structure to the Cu K-edge measurement of the $Sr_2MnCu_{1.5-x}S_2O_2$ samples.

Figures 4.21 to 4.23 shows the fit and the peaks corresponding to each path, at the two extreme temperatures measured, for the x=0.0, x=0.2, and x=0.3 samples, respectively. It can be seen in the fits at 260K that there is a discrepancy between the position of the third peak of the data and the Cu-Sr path. This could be due to missing multiple scattering events that contribute to this peak, that we were unable to include in the fit. When multiple scattering paths were introduced, the guess parameters produced from the fit were outside of their normal range, such as large ΔR's and negative DWs. From the fits to the 10K data, it can be seen that each single scattering path lines up well with each peak seen in the data. This may be due to the predicted orthorhombic distortion being small, where it is only expected to produce broadening in the EXAFS peaks. This can explain why the low temperature data produces sensible fits when using the tetragonal model.
The sum of all the relevant single scattering path contributions to the Cu K-edge EXAFS of the x=0, x=0.2 and x=0.3 samples, are shown in Figures 4.24 to 4.26 fitted against the EXAFS data, respectively. There is a discrepancy in the position of the third peak for all temperatures. This peak corresponds to the Cu-Sr scattering path and the shift in its position could be due to the orthorhombic distortion reported [132]. The orthorhombic model consists of two Cu local environments, where for one the Cu-Sr path is predicted to be 3.269Å, and for the other the Cu-Sr path is predicted to be 3.218Å or 3.302Å (3.269Å in the tetragonal model). Interference between the Cu-Cu paths and Cu-Sr paths could also explain the discrepancy between the experimental data and the fit for the third peak. The length of the first Cu-Cu path is found, in one environment at 2.837Å, and in the other environment at 2.891Å (2.838Å in the tetragonal model). This is only seen in the fits to the x=0.0 and x=0.2 samples as the Cu-Sr peak is suppressed in the x=0.3 sample. However, as the discrepancy of this peak affects the fit of every temperature, the orthorhombic distortion is unlikely to be responsible.
An attempt was made to fit the data to the orthorhombic structure, however there was an issue due to the fact that it called for 3 scattering paths to be fit for the first peak. This caused a problem in the fit produced by ARTEMIS, as this introduced too many variables, and reliable structural information could not be obtained from this method.

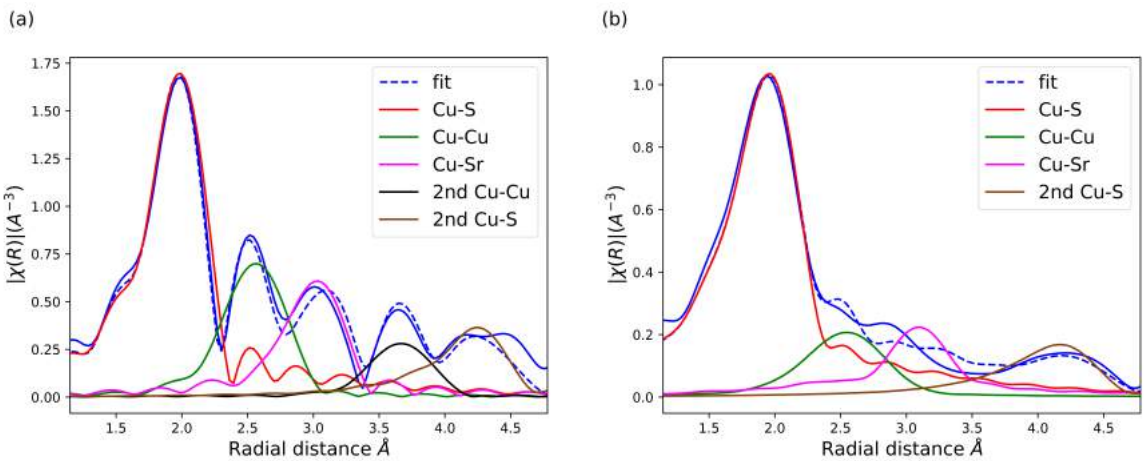

Figure 4.21: Fit of the Cu K-edge of the $Sr_2MnCu_{1.5}S_2O_2$ sample, and the individual paths, in R space, at 10K (a) and 260K (b), the data was fit to the tetragonal structural model.

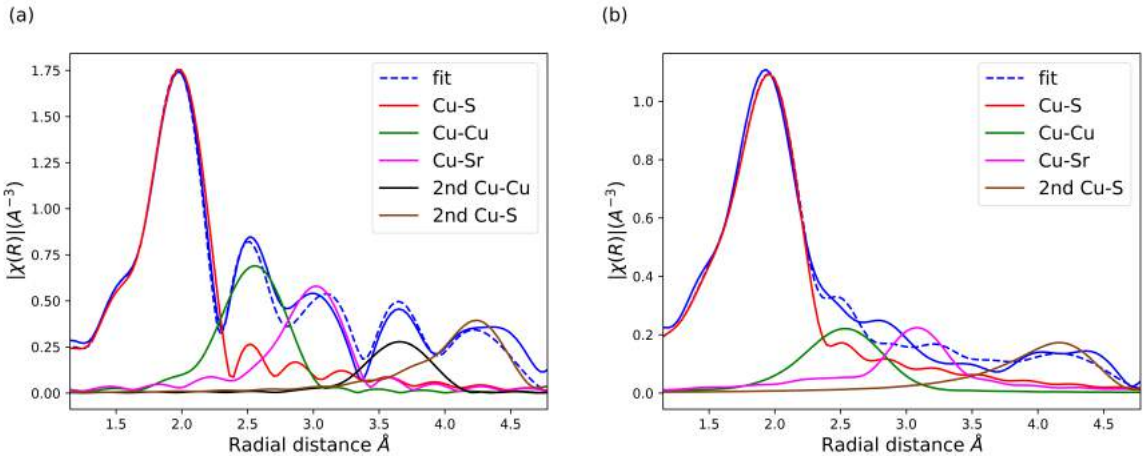

Figure 4.22: Fit of the Cu K-edge of the $Sr_2MnCu_{1.3}S_2O_2$ sample, and the individual paths, in R space, at 10K (a) and 260K (b), the data was fit to the tetragonal structural model.

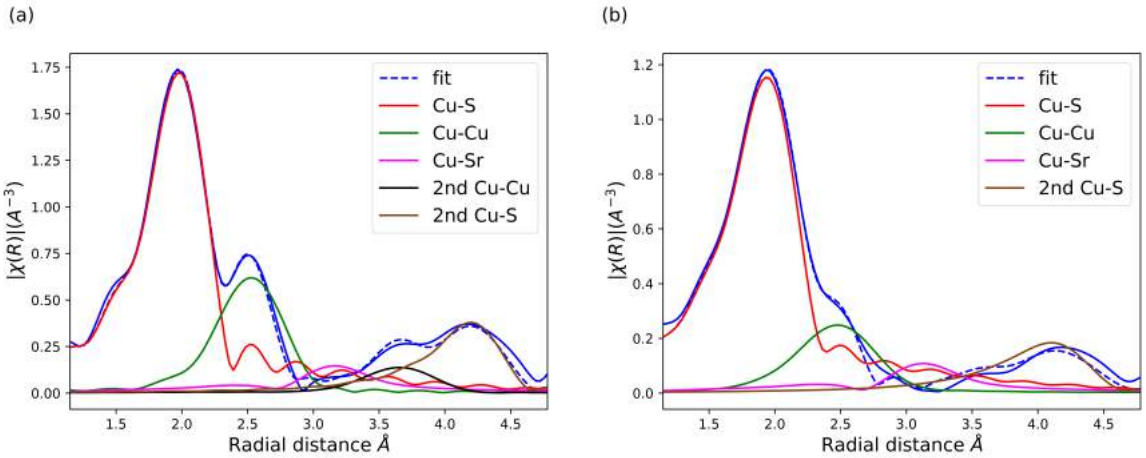

Figure 4.23: Fit of the Cu K-edge of the $Sr_2MnCu_{1.2}S_2O_2$ sample, and the individual paths, in R space, at 10K (a) and 260K (b), the data was fit to the tetragonal structural model.

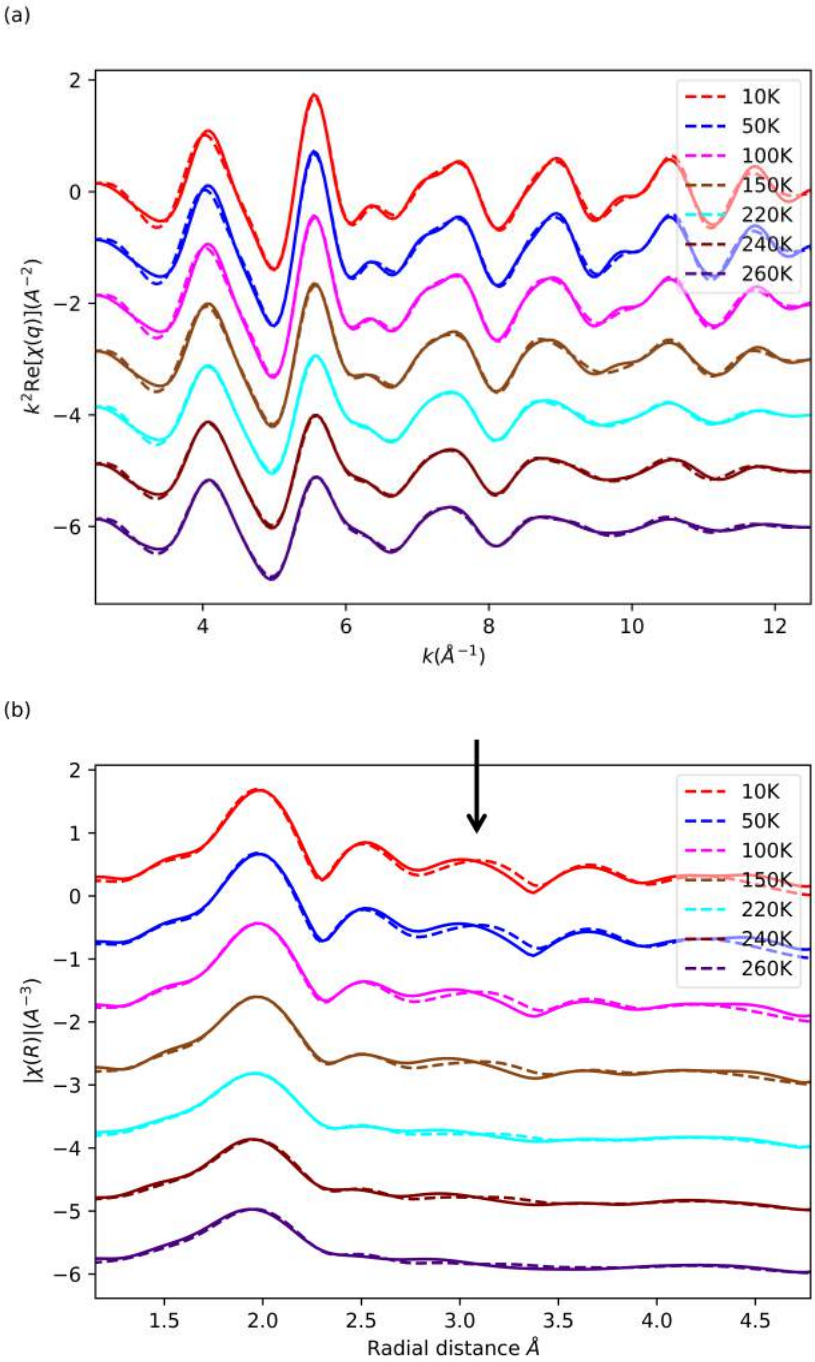

Figure 4.24: Fit of the Cu K-edge of the $Sr_2MnCu_{1.5}S_2O_2$ sample, in q space(a) and R space (b), the data was fit to the tetragonal structural model. The solid line corresponds to the experimental data and the dashed line corresponds to the fit.

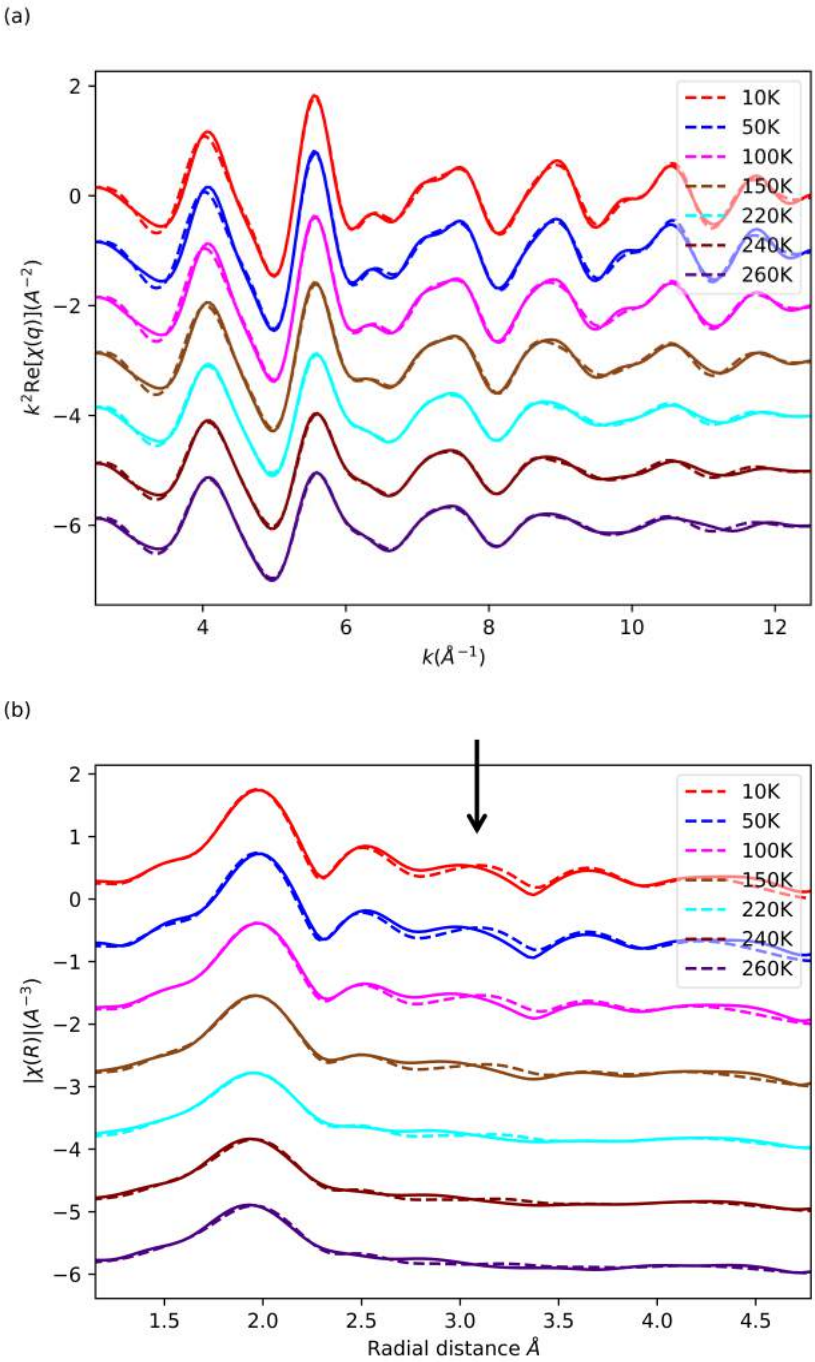

Figure 4.25: Fit of the Cu K-edge of the $Sr_2MnCu_{1.3}S_2O_2$ sample, in q space (a) and R space (b), the data was fit to the tetragonal structural model. The solid line corresponds to the experimental data and the dashed line corresponds to the fit.

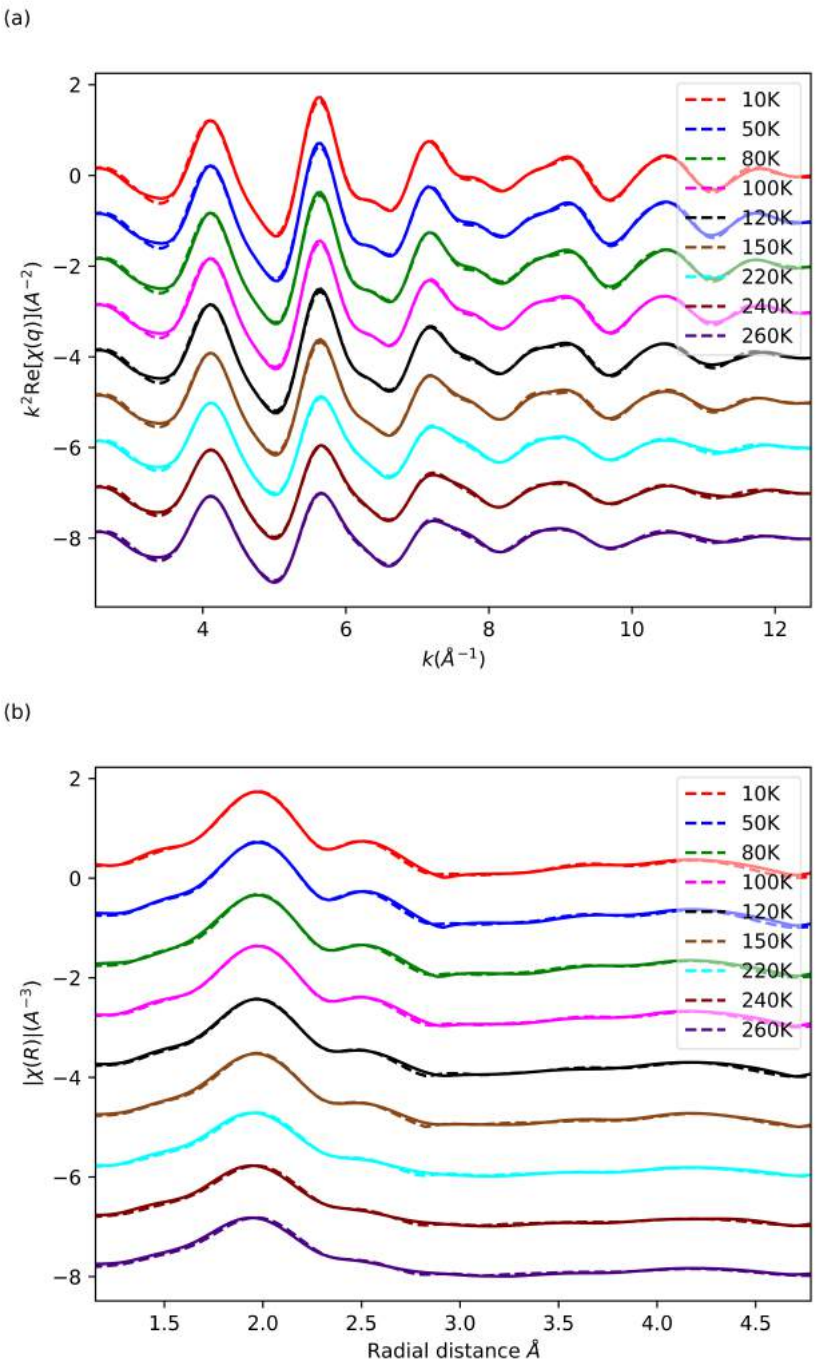

Figure 4.26: Fit of the Cu K-edge of the $Sr_2MnCu_{1.2}S_2O_2$ sample, in q space (a) and R space (b), the data was fit to the tetragonal structural model. The solid line corresponds to the experimental data and the dashed line corresponds to the fit.

The Mn K-edge data for all three samples, at each temperature, were fit to the tetragonal structural model. Fitting was carried out in R space, with k weightings of 1, 2, and 3, using 24 of 31 independent parameters for the x=0.0 sample, 16 of 21 independent parameters for the x=0.2 samples, and 16 of 20 independent parameters for the x=0.3 sample. The same paths were used in the fits for each sample, the single scattering paths calculated from the tetragonal structure up to 3.314Å. The fits resulted in a R-factor of 0.037, 0.027, and 0.034, for the x=0.0, x=0.2, and x=0.3 samples, respectively. The reduced χ^2 produced from the fits were 1021.89, 640.73, and 487.53 for the x=0.0, x=0.2, and x=0.3, respectively.
The refined parameters for the fits can be found in Table 4.6. The fits produce parameters outside of their acceptable ranges, this suggests that the structural model used is not modelling the local Mn structure accurately. The amplitude reduction factor, S_0^2, is much smaller than the normal acceptable range. The ΔE_0s found for each fit are much larger than those found in a good fit. Figures 4.27 to 4.29 show the fits of the Mn K-edge of the $Sr_2MnCu_{1.5-x}S_2O_2$, (x=0.0,0.2,0.3), data, respectively. The fits themselves do not appear to be bad, however the parameters found for the fits suggest that they are not good.
As the structural model produces good fits for the Cu K-edge it can not be concluded if the structural model is incorrect. However, given that the SEM measurements show the presence of Mn rich impurities, the bad match between the model and the Mn K-edge data is to be expected.

Table 4.6: Fit parameters for the Mn K-edge EXAFS of $Sr_2MnCu_{1.5-x}S_2O_2$ (x=0.0,0.2,0.3), alongside the value obtained from the tetragonal structural model.

	Sample:			
Parameters:	$Sr_2MnCu_{1.5}S_2O_2$	$Sr_2MnCu_{1.3}S_2O_2$	$Sr_2MnCu_{1.2}S_2O_2$	model(240K) [33]
Temperature(K)	10			
S_0^2	0.5±0.2	0.5±0.1	0.5±0.2	-
ΔE_0 (eV)	-9.1±3.2	-10.1±2.4	-10.5±3.7	-
Mn-O R (Å)	1.91±0.02	1.94±0.04	1.90±0.02	2.007
Mn-O σ^2 (Å^2)	0.005±0.005	0.003±0.003	0.002±0.004	-
Mn-S R (Å)	2.8±0.1	2.75±0.07	2.7±0.2	2.915
Mn-S σ^2 (Å^2)	0.01±0.02	0.01±0.01	0.02±0.03	-
Mn-Sr R (Å)	3.27±0.02	3.27±0.01	3.26±0.02	3.314
Mn-Sr σ^2 (Å^2)	0.000±0.002	0.001±0.001	0.002±0.002	-
Temperature(K)	220			
S_0^2	0.5±0.2	-	-	-
ΔE_0 (eV)	-11.0±4.2	-	-	-
Mn-O R (Å)	1.89±0.03	-	-	2.007
Mn-O σ^2 (Å^2)	0.005±0.006	-	-	-
Mn-S R (Å)	2.8±0.2	-	-	2.915
Mn-S σ^2 (Å^2)	0.02±0.03	-	-	-
Mn-Sr R (Å)	3.27±0.02	-	-	3.314
Mn-Sr σ^2 (Å^2)	0.003±0.003	-	-	-
Temperature(K)	260			
S_0^2	0.6±0.2	0.5±0.2	0.6±0.2	-
ΔE_0 (eV)	-11.9±3.3	-12.2±4.8	-12.2±3.8	-
Mn-O R (Å)	1.90±0.03	1.89±0.04	1.89±0.03	2.007
Mn-O σ^2 (Å^2)	0.006±0.005	0.004±0.006	0.005±0.004	-
Mn-S R (Å)	2.75±0.08	2.8±0.1	2.7±0.1	2.915
Mn-S σ^2 (Å^2)	0.02±0.02	0.01±0.02	0.03±0.03	-
Mn-Sr R (Å)	3.26±0.02	3.21±0.03	3.26±0.03	3.314
Mn-Sr σ^2 (Å^2)	0.006±0.003	0.005±0.003	0.007±0.003	-

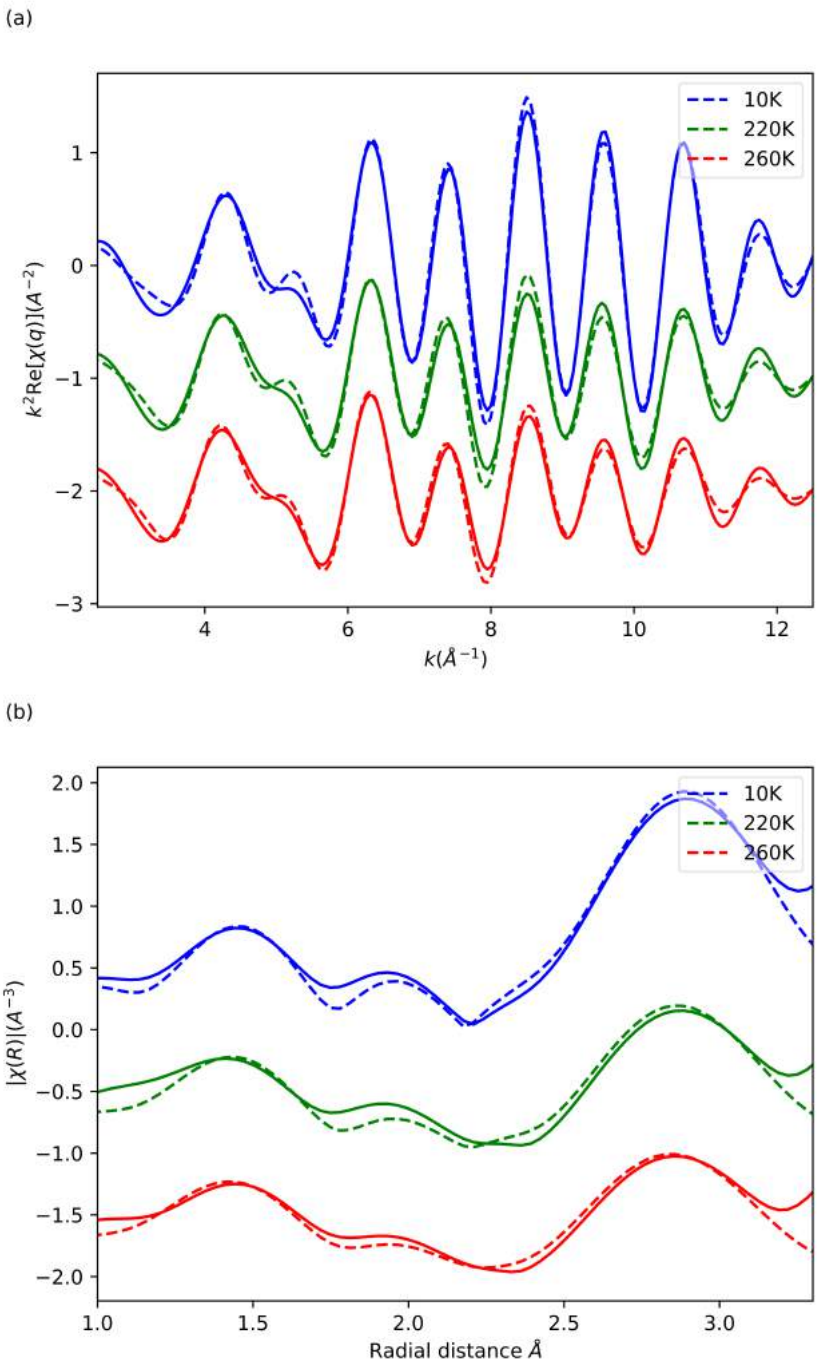

Figure 4.27: Fit of the Mn K-edge of the $Sr_2MnCu_{1.5}S_2O_2$ sample, in q space(a) and R space (b), the data was fit to the tetragonal structural model. The solid line corresponds to the experimental data and the dashed line corresponds to the fit.

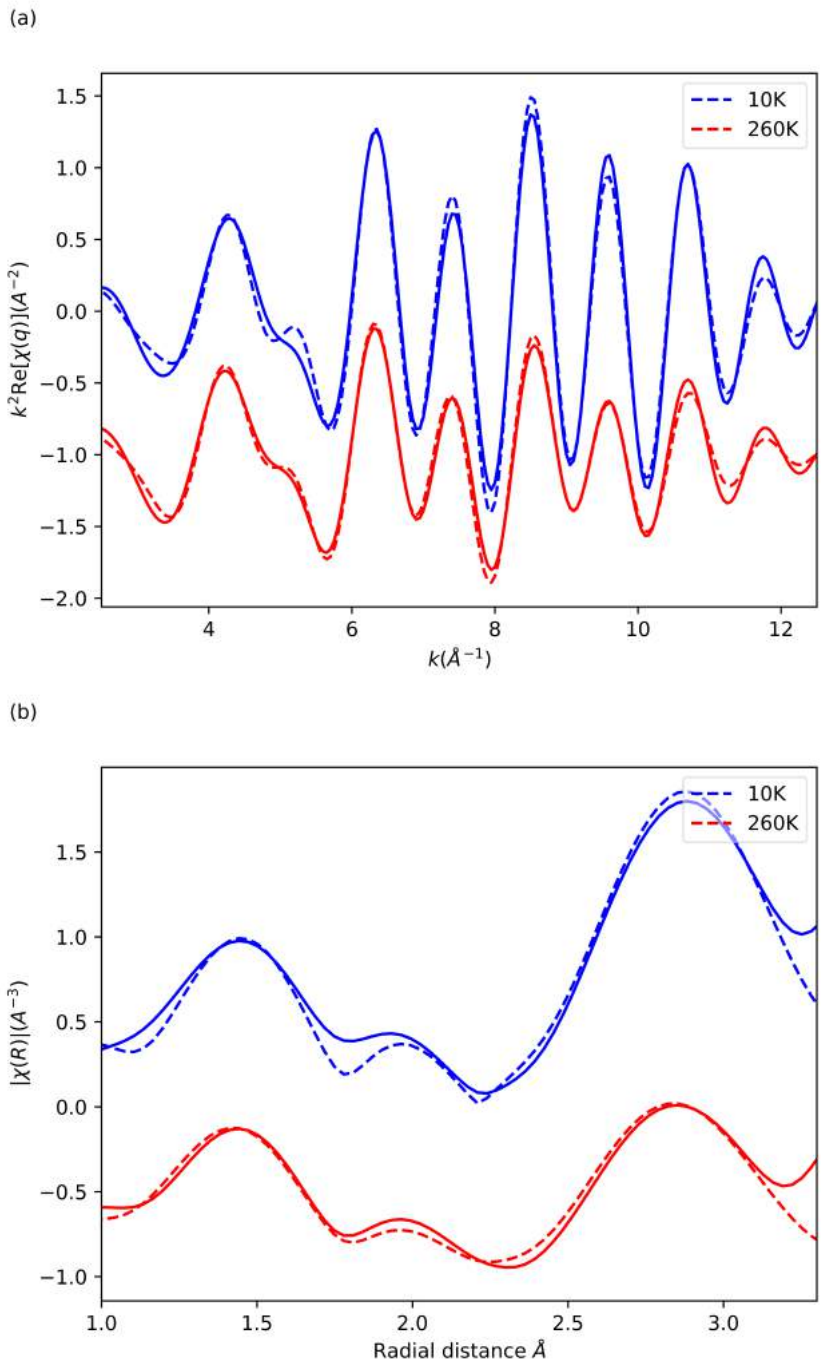

Figure 4.28: Fit of the Mn K-edge of the $Sr_2MnCu_{1.3}S_2O_2$ sample, in q space (a) and R space (b), the data was fit to the tetragonal structural model. The solid line corresponds to the experimental data and the dashed line corresponds to the fit.

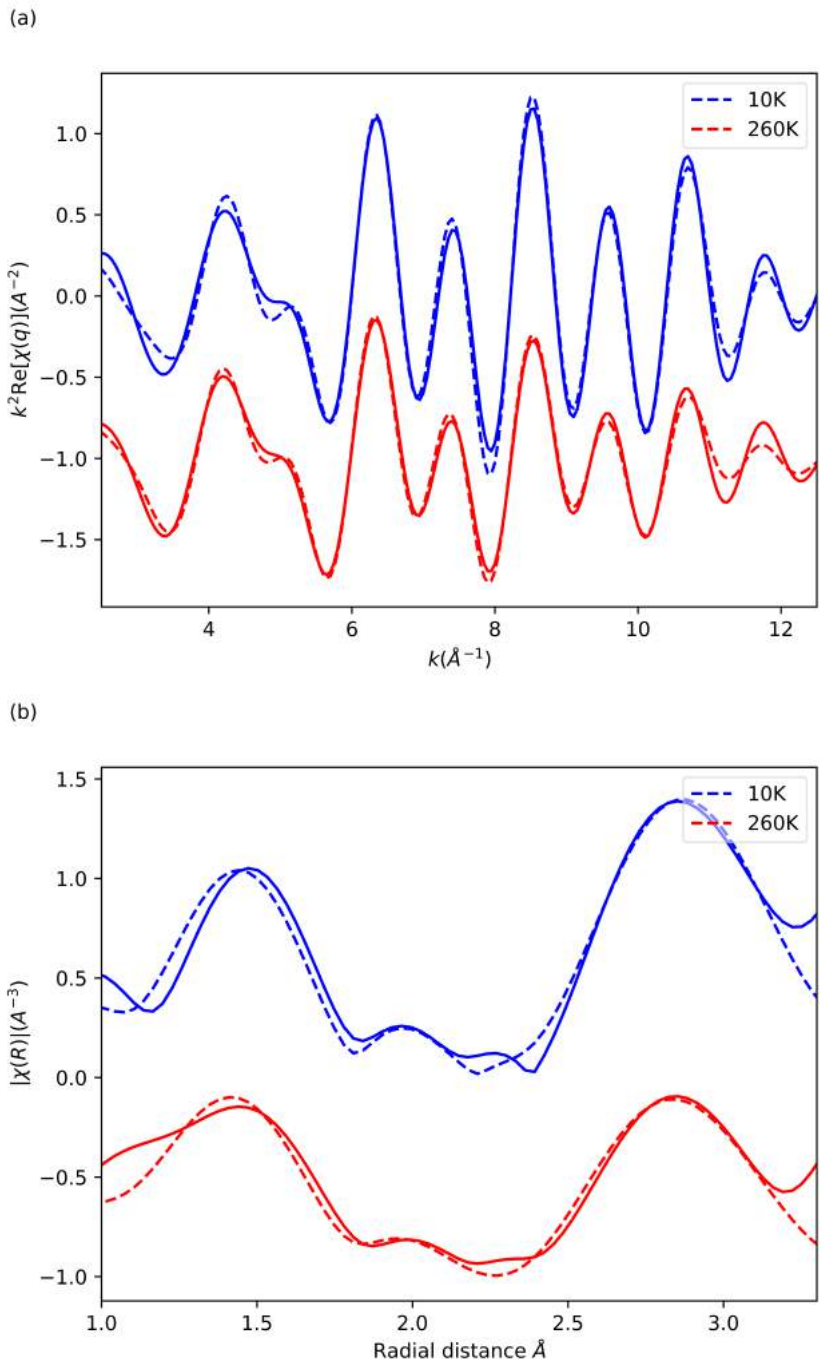

Figure 4.29: Fit of the Mn K-edge of the $Sr_2MnCu_{1.2}S_2O_2$ sample, in q space (a) and R space (b), the data was fit to the tetragonal structural model. The solid line corresponds to the experimental data and the dashed line corresponds to the fit.

4.4 $Sr_2MnCu_{1.5}S_2O_2$ single crystal P-XAS

4.4.1 Experimental set-up

The goal of this experiment was to study the mobility of the Cu ions along the different crystal directions. P-XAS was measured for the $Sr_2MnCu_{1.5}S_2O_2$ single crystal, at several angles with respect to the polarisation of the beam, and at two temperatures, above (300K) and below (112K) the reported transition temperature. The single crystals were grown by Dr. Dharmalingam Prabhakaran, in collaboration with Prof. Simon Clarke's group at Oxford University, via the flux method as described in [33]. For this experiment we measured P-XAS of the Cu and Mn K-edges of this sample, at the B18 beamline in Diamond Light Source, in Oxfordshire, UK.
The single crystals needed to be attached to the sample holders with something that would not have any absorption edges in the energy range that was being measured, kapton tape was used for this purpose (see Figure 4.30). Due to time constraints only one sample was measured during this experiment, this was sample (a) as seen in Figure 4.30. The single crystals grew with the c-axis perpendicular to the ab-plane (see Figure 4.2), where the c-axis is going into the page in Figure 4.30. The lower temperature was reached by using a cryojet. The cryojet available at B18, manufactured by Oxford Instruments, uses liquid nitrogen ($T_c = 63K$ [143]) and has a temperature range of 90K to 300K. The cryojet did cause some icing on the sample but not along the path of the beam (only at the back of the crystal) so it did not affect the P-XAS measurements. To test whether the temperature the sample matched the temperature the cryojet was set to, a hand-held thermocouple was used to measure the temperature of the cryojets nozzle and the surface of the sample, the temperatures were the same within ±1K. The beamline was set-up with the same configuration as it had been for the powder data experiment. The sample measured was small, $\sim 1818 \times 1591\mu m$, so the measurements were taken with a fully focused beam ($200\mu m$ x $200\mu m$). Each spectra was measured twice under the same conditions, with an energy step of $\sim 0.23eV$ at $\sim 0.07s$ per point. The monochromator was calibrated with a Cu foil, therefore no further calibrations were needed during the analysis. The measurements were taken in fluorescence mode using a Canberra 36 element Ge detector. The sample, for each temperature, was measured at a range of angles with respect to the beam and the c-axis, $\theta_b = 15^o$ to 75°, in steps of 15°, see Chapters 2 and 3 for more detail. The polarisation of the beam would be parallel to the c-axis when the sample was positioned at $\theta_b = 90^o$. A rotating table was used to position the sample in the different orientations. Both the Cu K-edge and Mn K-edge P-XAS were measured at all angles, for both temperatures. The range of angles that could be measured does not include $\theta_b = 90^o$ or 0° due to the geometry of the set up, where the sample was rotated about the z-axis with a rotating table. This restriction was introduced by the sample holder (see Figure 4.30). If the crystal was aligned so that the polarisation of the beam was parallel to the c-axis, $\theta_b = 90^o$, the beam would only see the side of the sample holder and not the crystal. When measuring perpendicular to the c-axis, $\theta_b = 0^o$, the detector would be perpendicular to the surface illuminated by the x-rays and hence a very low threshold of fluorescence photons would be measured.

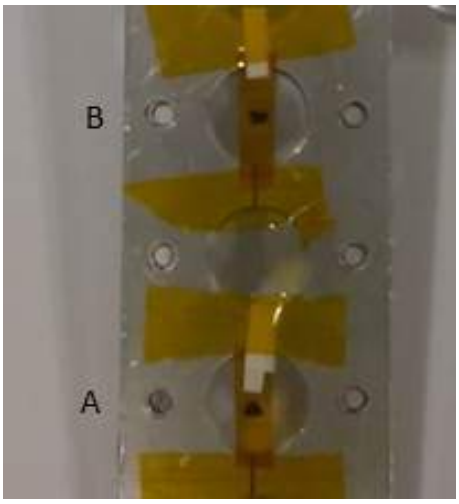

Figure 4.30: Sample holder used in the experiment at B18 to measure a single crystal of $Sr_2MnCu_{1.5}S_2O_2$.

4.4.2 Single crystal XAS results

While both the Cu and Mn K-edge were measured only the Cu K-edge data provided usable results, due to the Mn rich impurities in the sample, as seen in Section 4.2.
For the analysis it is more intuitive to have data along two perpendicular crystallographic axes, e.g. the *c*-axis and the *ab*-plane. This is because these are two independent components and are easy to connect to the structure. To produce data for these two angles we took advantage of the symmetry of the crystal, as it is tetragonal at room temperature, to build XAS using the experimental data from the angles we measured. As the orthorhombic distortion is subtle, the low temperature data can be assumed to have a tetragonal symmetry for this purpose, therefore the same method can be used to build XAS for the data at both temperatures. A code used to build XAS at any angle has been produced, and is discussed in Chapter 3. Figures 4.31 and 4.32 show that the XAS produced from the code match the experimental XAS, at an angle that was measured, for both the 300K and 112K data. From these plots it can be seen that for the 300K, and 112K data no significant structure is lost when building the XAS. Hence we can assume that the $\theta_b = 0^o$ and 90° data will also be a good representation of the real structure.

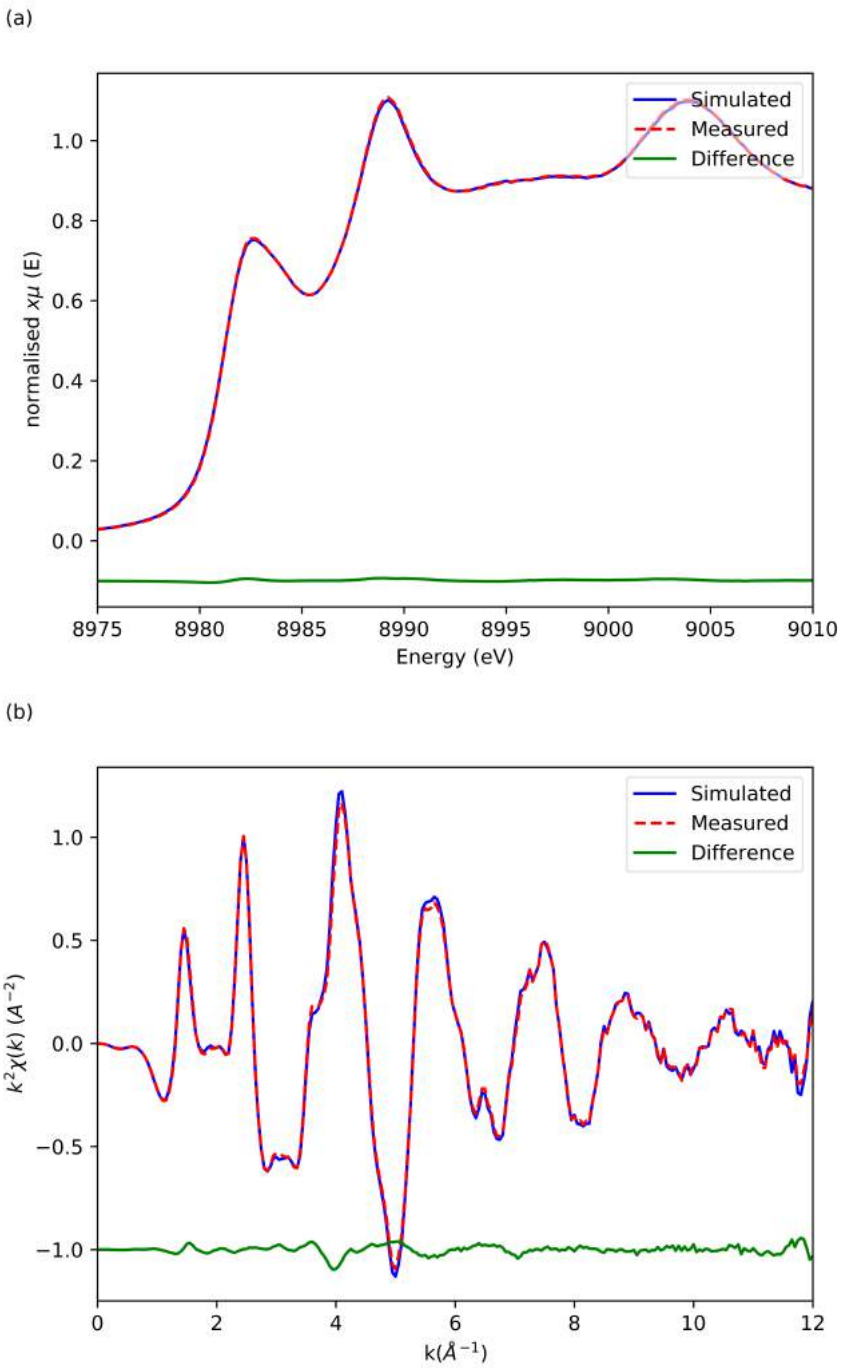

Figure 4.31: Simulated and measured XANES, (a), and EXAFS, (b), of the Cu K-edge of $Sr_2MnCu_{1.5}S_2O_2$. Measured at 300K and $\theta_b = 45^o$. The experimental data at 45° was not included in the building code.

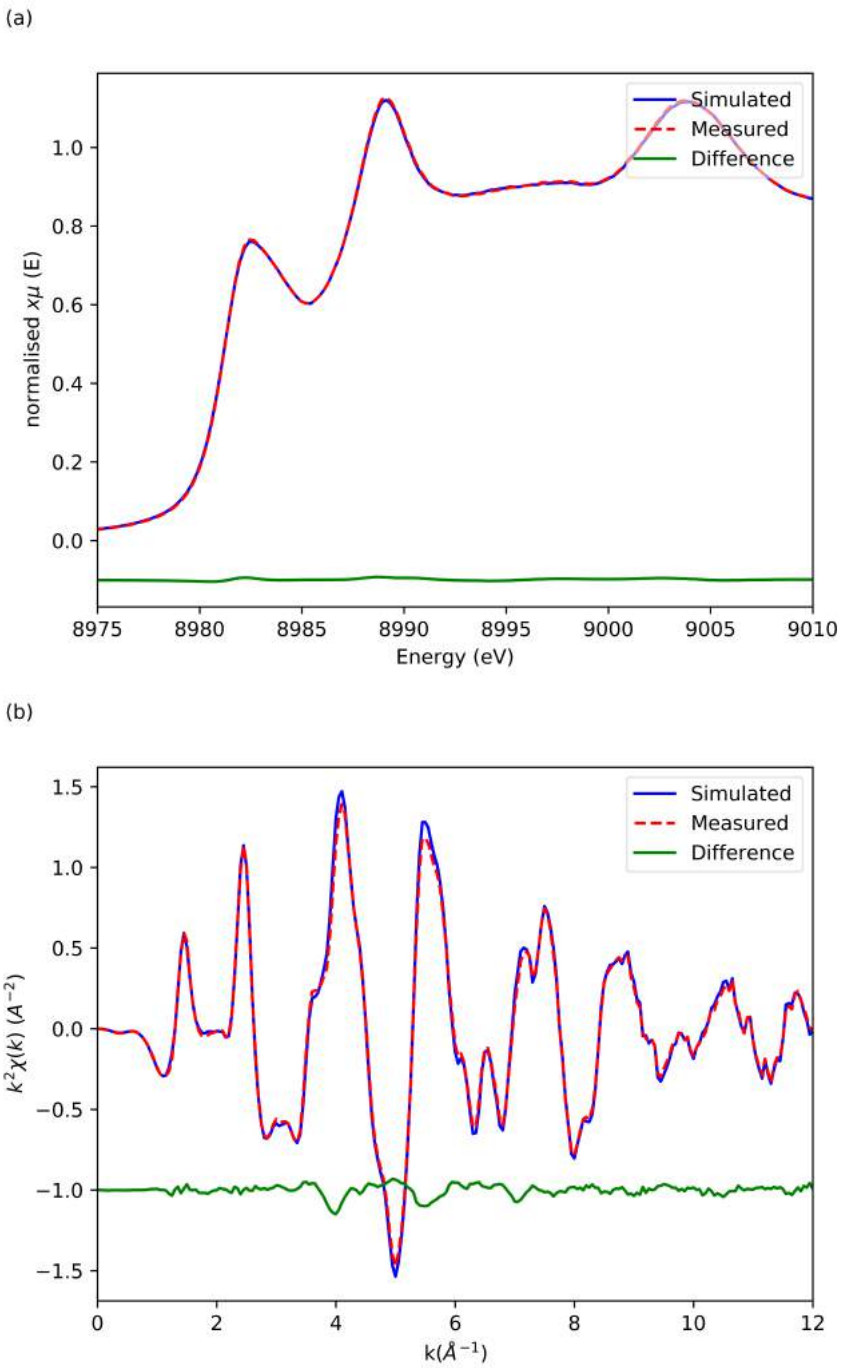

Figure 4.32: Simulated and measured XANES, (a), and EXAFS, (b), of the Cu K-edge of $Sr_2MnCu_{1.5}S_2O_2$. Measured at 112K and $\theta_b = 45^o$. The experimental data at 45° was not included in the building code.

An attempt to build XAS signal at other angles for the Mn K-edge data was made, see Figures 4.33 and 4.34. However there were large discrepancies between the built data and the measured data. This may be due to the Mn rich impurities affecting the measured data, causing it to not behave as if the structure has a tetragonal symmetry.

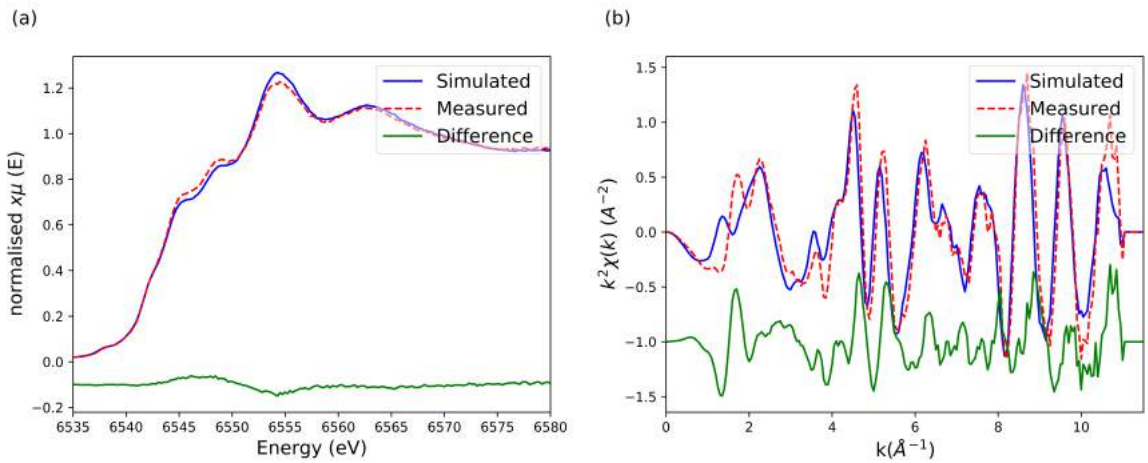

Figure 4.33: Simulated and measured XANES, (a), and EXAFS, (b), of the Mn K-edge of $Sr_2MnCu_{1.5}S_2O_2$. Measured at 300K and $\theta_b = 45^o$. The experimental data at 45° was not included in the building code.

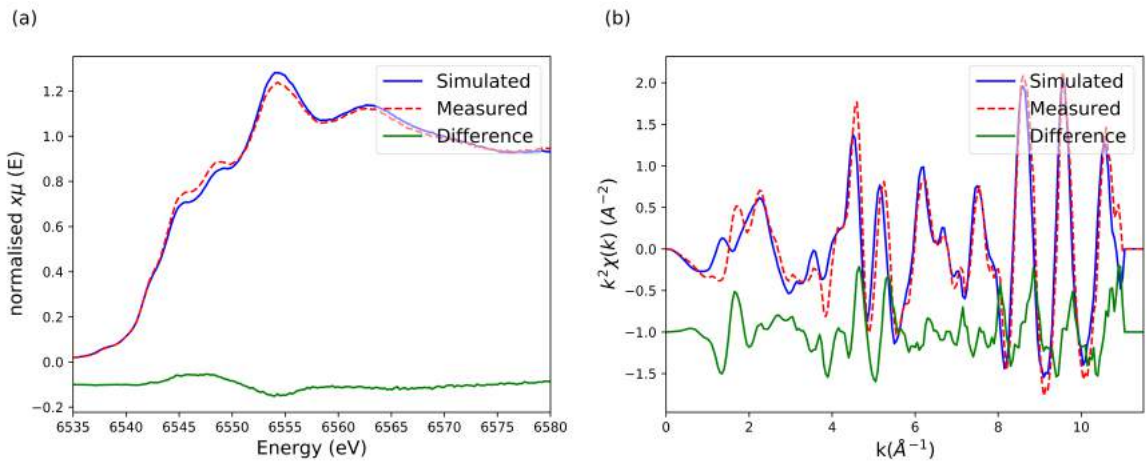

Figure 4.34: Simulated and measured XANES, (a), and EXAFS, (b), of the Mn K-edge of $Sr_2MnCu_{1.5}S_2O_2$. Measured at 112K and $\theta_b = 45^o$. The experimental data at 45° was not included in the building code.

All of the data presented has been through an initial data processing *i.e.* normalising the XANES, background removal to obtain the EXAFS, etc, as discussed in Chapter 3. For the Cu K-edge, the E_0 changed with respect to the angle between the beam and the c-axis (θ_b), the values it was set for each angle and temperature can be seen in Table 4.7. The values for E_0 were set based on the position of the first peak in the derivative of the XANES. The same spline range in k was used for both temperatures and all angles, 0 to 12Å^{-1}, and the background parameter (Rbkg) was set to 1Å for each data set. The pre-edge range, for both temperatures and all angles, was set to $-151.62eV$ to $-30eV$, with respect to E_0. The post-edge range used was different for both temperatures, but it was the same for all angles, and when extracting the XANES or the EXAFS. For the 300K, when extracting the XANES it was set to $18.17eV$ to

489.26eV, while for the EXAFS it was set to 150eV to 746.62eV, with respect to E_0. For the 112K data, when extracting the XANES it was set to 15.16eV to 423.72eV, while for the EXAFS it was set to 141.33eV to 747.2eV, with respect to E_0. The normalisation order was set to 3, for all data sets. For the FT-EXAFS the same range in k was used in the transformation for each temperature and angle, 2.6 to 10.8Å^{-1}.

Table 4.7: E_0's (eV) of the Cu K-edge, of $Sr_2MnCu_{1.5}S_2O_2$, for all θ_b's and temperatures.

	Temperature (K):	
θ_b:	112	300
0°	8981.60±0.23	8981.60±0.23
15°	8981.55±0.23	8981.50±0.23
30°	8981.37±0.23	8981.32±0.23
45°	8981.19±0.23	8981.26±0.23
60°	8981.10±0.23	8981.15±0.23
75°	8981.06±0.23	8981.05±0.23
90°	8981.04±0.23	8981.00±0.23

For the Mn K-edge, the E_0 changed with respect to the angle between the beam and the c-axis (θ_b), the values it was set for each angle and temperature can be seen in Table 4.8. The values for E_0 were set based on the mid point of the rising edge observed in the XAS. The same spline range in k was used for both temperatures and all angles, 0 to 11Å^{-1}, and the background parameter (Rbkg) was set to 0.9Å for each data set. The pre-edge range, for both temperatures and all angles, was set to $-191.94eV$ to $-30eV$, with respect to E_0. The post-edge range used was different for both temperatures, but it was the same for all angles. For the 300K data it was set to 170.98eV to 617.1eV, and for the 112K data it was set to 182.48eV to 603.76eV, with respect to E_0. The normalisation order was set to 3, for all data sets. For the FT-EXAFS the same range in k was used in the transformation for each temperature and angle, 3 to 10Å^{-1}.

Table 4.8: E_0's (eV) of the Mn K-edge, of $Sr_2MnCu_{1.5}S_2O_2$, for all θ_b's and temperatures measured.

	Temperature (K):	
θ_b:	112	300
15°	6550.49±0.23	6549.50±0.23
30°	6549.52±0.23	6547.85±0.23
45°	6544.00±0.23	6544.00±0.23
60°	6542.71±0.23	6542.69±0.23
75°	6541.42±0.23	6541.66±0.23

The data presented below has also been corrected to account for self-absorption, as the measurements were taken using fluorescence detection on a single crystal, hence with a particle size hundreds of times larger than the absorption length. The procedure for the self-absorption correction is discussed in Chapter 3.

XANES

The XANES of the Cu K-edge, seen in Figure 4.35, show a change in the local electronic structure of the Cu ions with angle. As XANES is sensitive to the anisotropy

of the local structure [67], measurements along different directions in the crystal should look different. As the Cu is in an oxidation state of +1, the K-edge is probing mainly the $1s \rightarrow 4p$ transition. There is no visible pre-edge feature in the XANES, this suggests that the symmetry of the Cu ions does not allow for quadrupole transitions to occur in a K-edge measurement.There is a slight change in the XANES with temperature (see Figure 4.36), with the peaks being broader for the 300K data, than the 112K data, this could be explained by the increased thermal fluctuations. The change observed is similar for both extreme angles, suggesting that the temperature affects the local electronic structure the same for different orientations.
For both the 300K and 112K data, the position and intensity of the edge changes with angle, with it being found at lower energies and higher intensity at $\theta_b = 90^o$. As the edge is sensitive to local structure [67], this suggests that the unoccupied $4p$ states along the c-axis have a lower energy, allowing the $1s \rightarrow 4p_z$ transition to occur more freely. This follows what would be expected by the structure of the material as there are more surrounding atoms along the ab-plane than the c-axis, see Figure 4.2.

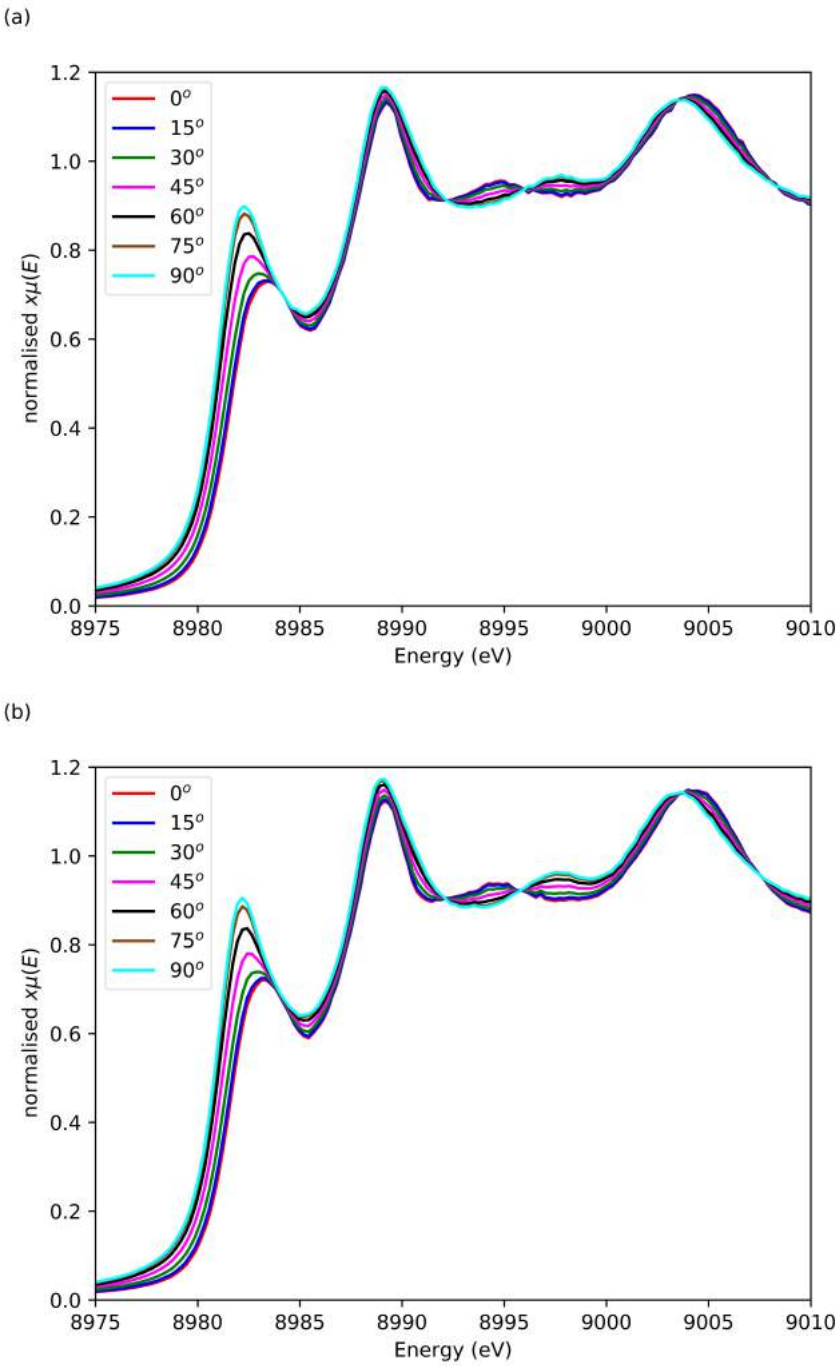

Figure 4.35: XANES of the Cu K-edge $Sr_2MnCu_{1.5}S_2O_2$, for 300K (a) and 112K (b). A range of angles are included, 0° to 90° in steps of 15°.

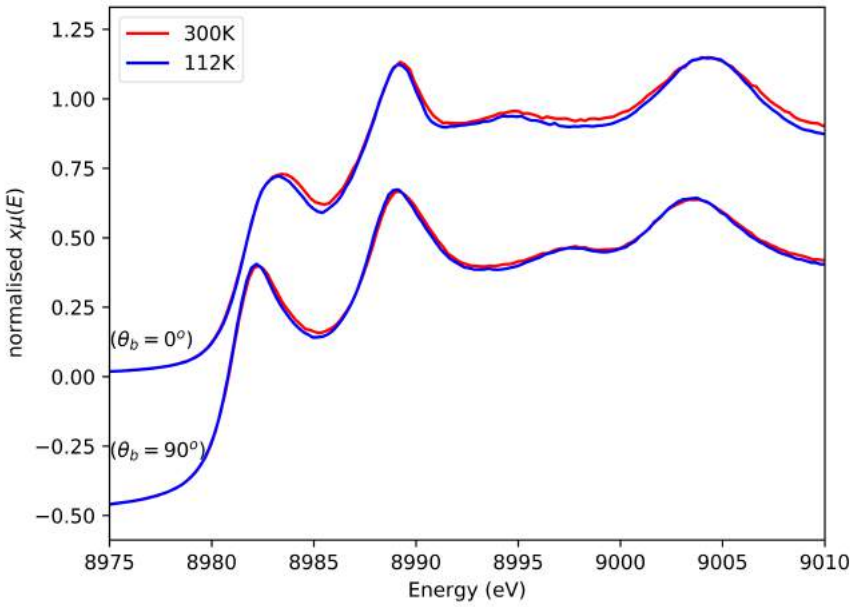

Figure 4.36: Comparison of the XANES of the Cu K-edge $Sr_2MnCu_{1.5}S_2O_2$, for the two extreme angles at both temperatures.

The XANES of the Mn K-edge, seen in Figure 4.35, also show a change in the local electronic structure of the Mn ions with angle. This, along with the values found for the absorption edge (see Table 4.8), shows there is substantial anisotropy in the local electronic structure of the Mn ions. There is a visible pre-edge feature in the XANES, this suggests that the symmetry is allowing quadrupole transitions to occur. The reported mean oxidation state of the Mn in this material is +2.5 [33]. As we are measuring the Mn K-edge, the normal transition responsible for the absorption edge would be between s and p orbitals. However due to hybridisation between the O $2p$ orbitals and the Mn $3d$ orbitals, the absorption edge is indirectly probing the $1s$ to $3d$ transition [144].
As the Mn ions nearest neighbours are along the ab-plane the change in the electronic structure is strongly affected by the angle the absorption is measured at. It can be seen in the XANES that there is a clear change in the electronic structure as the angle measured at changes. This is seen in the position of the first peak after the rising edge, where it is found at a lower energy when the polarisation is closer to the c-axis. This is consistent with there being more neighbouring atoms along the ab-plane, as the unoccupied states along the c-axis should have be at a lower energy. There is no prominent change in the XANES with temperature (see Figure 4.38).

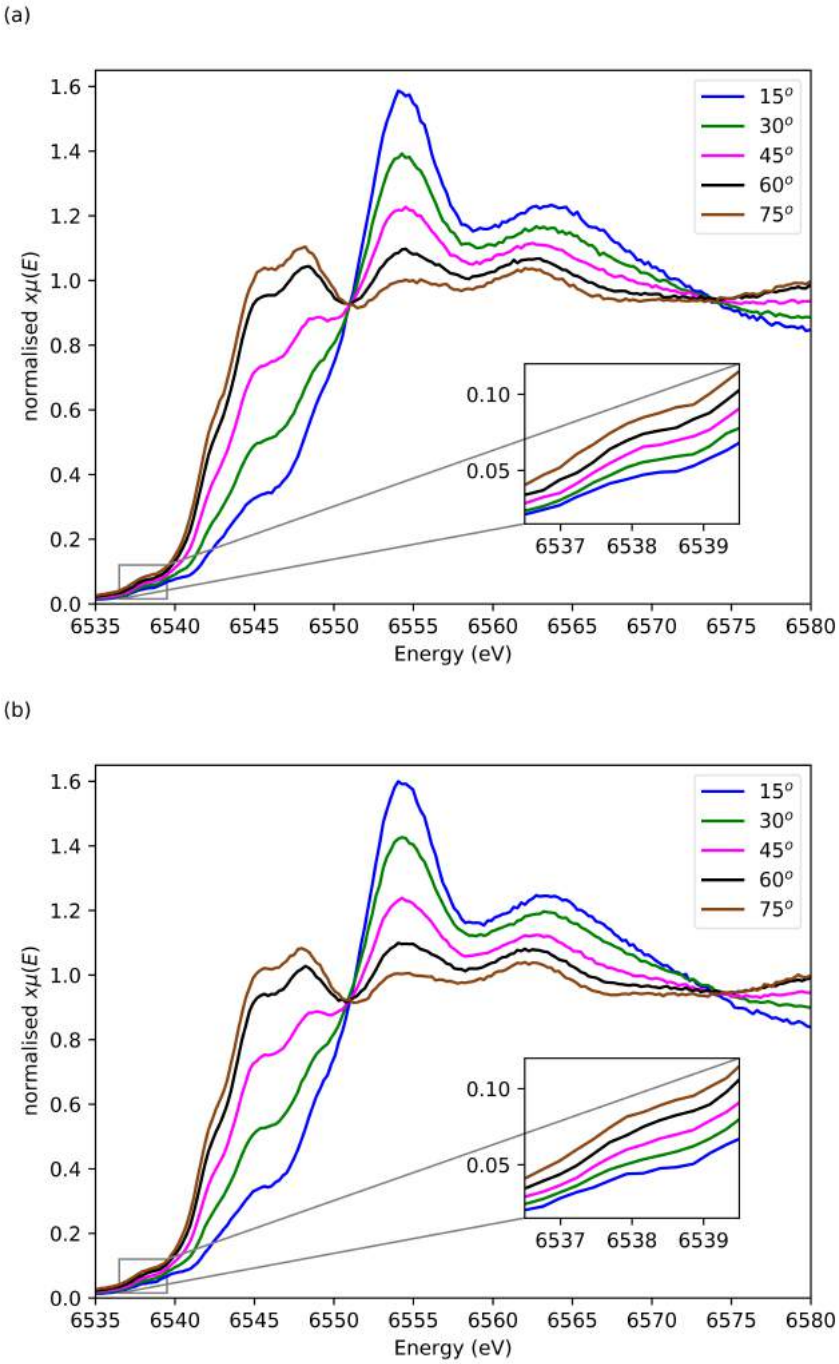

Figure 4.37: XANES of the Mn K-edge $Sr_2MnCu_{1.5}S_2O_2$, for 300K (a) and 112K (b). A range of angles are included, 15° to 75° in steps of 15°.

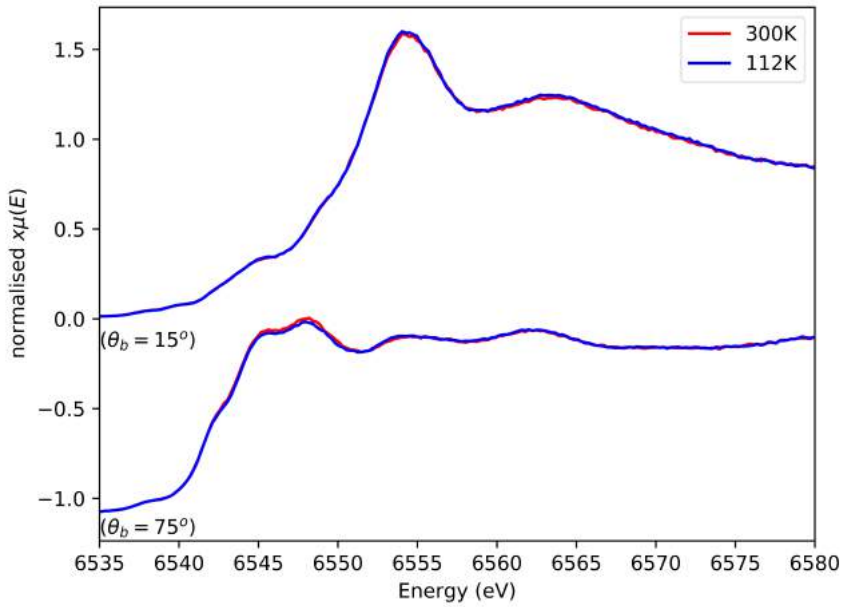

Figure 4.38: Comparison of the XANES of the Mn K-edge $Sr_2MnCu_{1.5}S_2O_2$, for the two extreme angles at both temperatures.

EXAFS

Figures 4.39 and 4.40 show the EXAFS and FT-EXAFS of the Cu K-edge of all angles, at 300K and 112K, respectively. The EXAFS and FT-EXAFS have been plotted with a k-weight of 2, and with a Fourier transform k-range of 2.6 to 10.8Å^{-1}. The FT-EXAFS presented have not been phase corrected, meaning the peak positions will not match the predicted positions from the model.
The path lengths and their angles, with respect to the c- and a-axis, can be seen in Table 4.9, for the tetragonal model (based on diffraction measurements at 240K [33]).

Table 4.9: Structural information, of the Cu single scattering paths, obtained from the tetragonal model, seen in Figure 4.2(b) [33].

Path	Path distance (Å)	θ_i (^{o})	ϕ_i (^{o})	Weighting of path
Cu-S	2.433	55.56	0	1
“ ”	“ ”	“ ”	90	1
“ ”	“ ”	124.44	0	1
“ ”	“ ”	“ ”	90	1
Cu-Cu	2.838	90	45	2
“ ”	“ ”	“ ”	-45	2
Cu-Sr	3.269	37.87	0	1
“ ”	“ ”	“ ”	90	1
“ ”	“ ”	142.13	0	1
“ ”	“ ”	“ ”	90	1
2nd Cu-Cu	4.014	90	0	2
“ ”	“ ”	“ ”	90	2
Cu-O	4.292	0	90	1
“ ”	“ ”	180	90	1
2nd Cu-S	4.694	72.95	26.57	1
“ ”	“ ”	“ ”	63.43	1
“ ”	“ ”	“ ”	-26.57	1
“ ”	“ ”	“ ”	-63.43	1
“ ”	“ ”	107.05	26.57	1
“ ”	“ ”	“ ”	63.43	1
“ ”	“ ”	“ ”	-26.57	1
“ ”	“ ”	“ ”	-63.43	1
Cu-Mn	4.738	25.06	0	1
“ ”	“ ”	“ ”	90	1
“ ”	“ ”	154.94	0	1
“ ”	“ ”	“ ”	90	1

The changes in the EXAFS between the two temperatures could be explained by increased thermal fluctuations, as the features seen at 300K are more defined in the 112K data. However when comparing the EXAFS of the two extreme angles (see Figure 4.41), there is a larger change in the signal with respect to temperature along the *ab*-plane. This suggests that the reported structural change affects the structure along the *ab*-plane more than along the *c*-axis.
From the EXAFS signal (see Figures 4.39 and 4.40) there is a clear change in the atomic structure with respect to the angle between the polarisation and the *c*-axis. There is a distinct change in the intensity in the middle range of the signal, $\sim$ 3 to 7Å^{-1}, however the position of the peaks are found in roughly the same place.
In the FT-EXAFS (see Figures 4.39b and 4.40b), the second peak ($\sim$ 2.5Å) most likely corresponds to the Cu-Cu single scattering path, predicted to be at 2.838Å from the tetragonal model. This peak is greatly reduced as the angle (θ_b) increases, this is in line with the Cu-Cu scattering path laying along the *ab*-plane. The suppression of the peak corresponding to the Cu-Cu scattering path is consistent with the theoretical structure and hence confirms that the P-XAS measurements allow us to resolve structure as a function of direction.
There is also a change with angle in the fourth peak ($\sim$ 4.2Å) seen in Figures 4.39b

and 4.40b. This peak most likely corresponds to the Cu-O, second Cu-S, and Cu-Mn single scattering paths, found at 4.292Å, 4.694Å, and 4.738Å in the tetragonal structure, respectively. There are also multiple scattering paths with path lengths that suggest they would contribute to this peak. This peak also changes with respect to temperature. In the 300K measurement there is one peak visible, while in the 112K measurement there is a splitting of the peak. In both temperatures the peak is suppressed as θ_b increases, and in both the second part of the peak is completely suppressed while the first part of the peak remains, but with less intensity. The distinct split in the peak at low temperature suggests that there is a clear distinction between the second Cu-S and Cu-Mn peak. The single peak seen at 300K may be due to the increased mobility of the Cu ions distorting the peaks from these two paths and appearing as one peak. As the Cu-O path is found along the c-axis, and the second Cu-S path and the Cu-Mn path are found between the ab-plane and the c-axis, this explains why at larger θ_b the peak is not completely suppressed. The suppression of the second part of the fourth peak at large θ_b's may be due to a destructive interference between these paths as the polarisation gets closer to the c-axis.

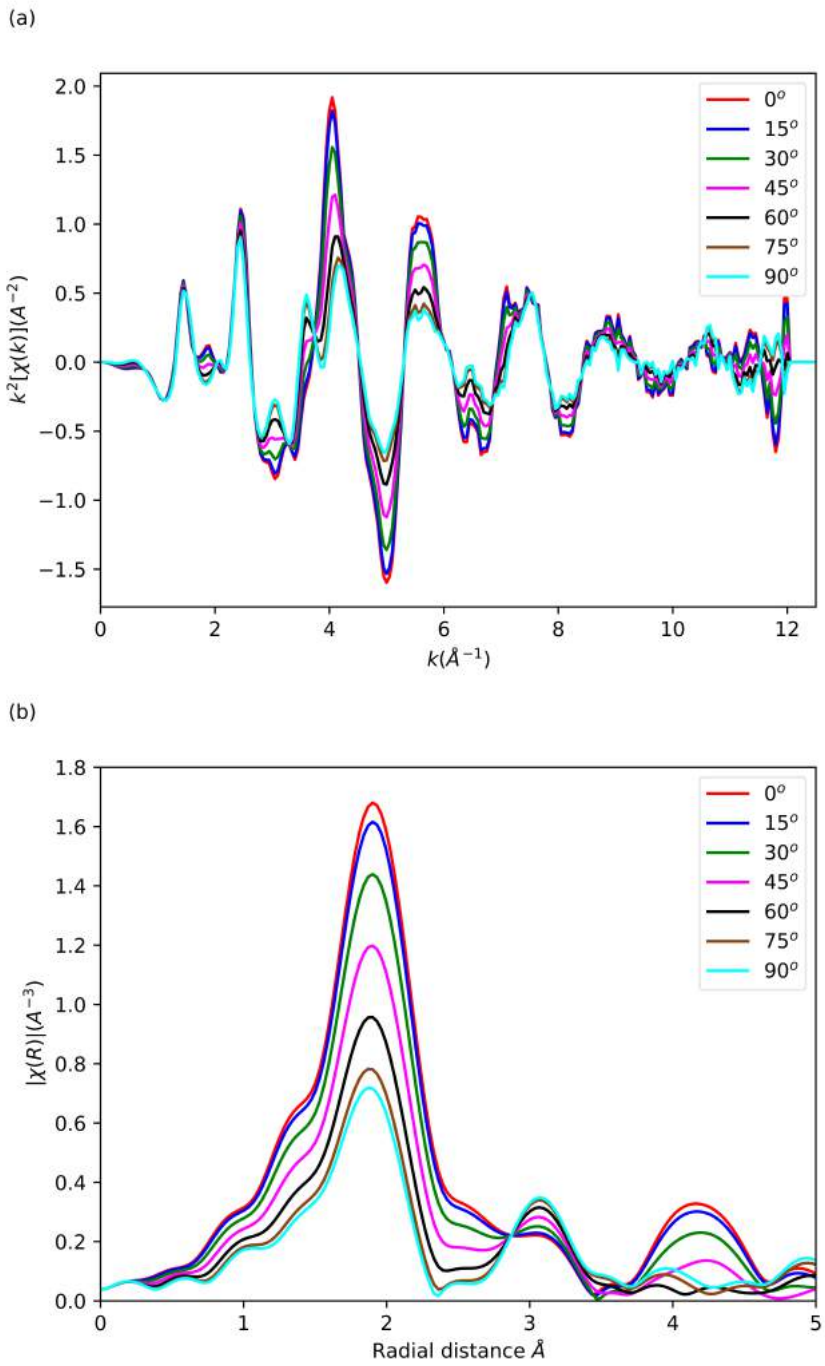

Figure 4.39: EXAFS, (a), and FT-EXAFS, (b), of the Cu K-edge $Sr_2MnCu_{1.5}S_2O_2$, at 300K. A range of angles are included, 0° to 90° in steps of 15°.

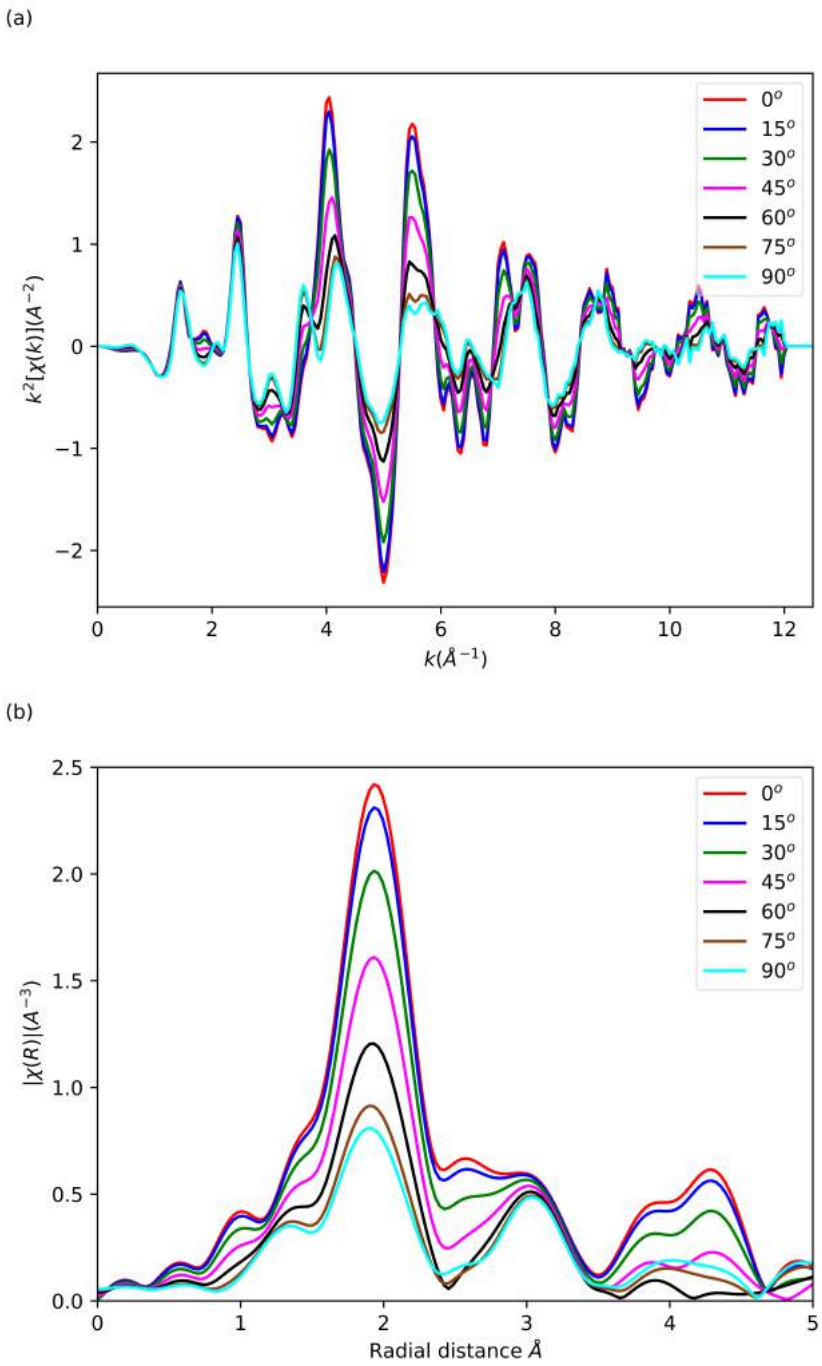

Figure 4.40: EXAFS, (a), and FT-EXAFS, (b), of the Cu K-edge $Sr_2MnCu_{1.5}S_2O_2$, at 112K. A range of angles are included, 0° to 90° in steps of 15°.

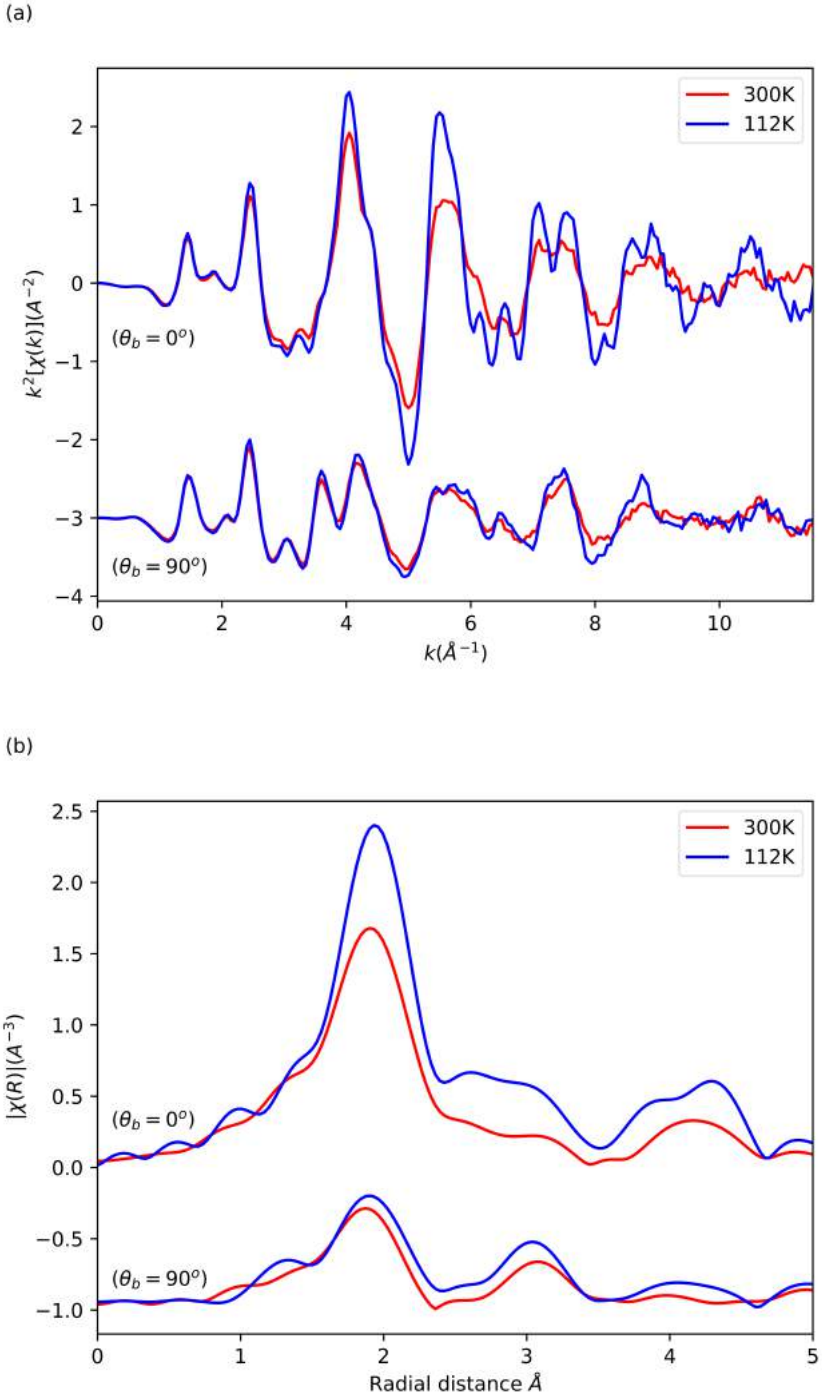

Figure 4.41: Comparison of the EXAFS (a) and FT-EXAFS (b) of the Cu K-edge $Sr_2MnCu_{1.5}S_2O_2$, for the two extreme angles at both temperatures.

Figures 4.42 and 4.43 show the EXAFS and FT-EXAFS of the Mn K-edge absorption, at 300K and 112K, respectively. The EXAFS and FT-EXAFS have been plotted with a k-weight of 2, and with a Fourier transform k-range of 3 to 10Å^{-1}. The FT-EXAFS presented have not been phase corrected, meaning the peak positions will not match the predicted positions from the model.
The path lengths and their angles, with respect to the c- and a-axis, can be seen in Table 4.10, for the tetragonal model (based on diffraction measurements at 240K [33]).

Table 4.10: Structural information, of the Mn single scattering paths, obtained from the tetragonal model, seen in Figure 4.2(b) [33].

Path	Path distance (Å)	θ_i (^{o})	ϕ_i (^{o})	Weighting of path
1st Mn-O	2.007	90	0	2
“ ”	“ ”	“ ”	90	2
Mn-S	2.915	0	90	1
“ ”	“ ”	180	90	1
Mn-Sr	3.314	58.92	45	2
“ ”	“ ”	“ ”	-45	2
“ ”	“ ”	121.08	45	2
“ ”	“ ”	“ ”	-45	2
Mn-Mn	4.014	90	0	2
“ ”	“ ”	“ ”	90	2
2nd Mn-O	4.488	90	26.57	2
“ ”	“ ”	“ ”	63.43	2
“ ”	“ ”	“ ”	-26.57	2
“ ”	“ ”	“ ”	-63.43	2

The changes in the EXAFS signal between the two temperatures can be explained by the increased thermal fluctuations (see Figure 4.44), as the features seen at 300K are more defined in the 112K data.
From the EXAFS signal (see Figures 4.42 and 4.43) there is a clear change in the atomic structure with respect to the angle between the polarisation and the c-axis. There is a distinct change in the structure of the signal for the whole k-range, however the position of the peaks further in k (> 7Å^{-1}) are found in roughly the same place and only their intensities differ. Comparing the two extreme angles (see Figure 4.44), the change in the signal with respect to temperature is roughly the same. This suggests that the reported structural change does not affect a specific direction for the local environment of the Mn ions.
In the FT-EXAFS (see Figures 4.42b and 4.43b), the first peak ($\sim$ 1.3Å), which most likely corresponds to the Mn-O scattering path (found at 2.007Å in the model). The peak is almost completely suppressed for larger θ_b's, those closer to the c-axis. From the expected structure (see Figure 4.2) this suppression makes sense as the Mn-O scattering paths lie exclusively along the ab-plane, and therefore should have no contribution to the signal measured perpendicular to the path. The second peak ($\sim$ 2.8Å), for both temperatures, is also greatly effected by the change in sample orientation. The strongest contributions to this peak are the Mn-S and Mn-Sr single scattering paths. The peak splits as the polarisation is closer to the c-axis, meaning the two paths are more distinguishable at larger angles. The Mn-S path is found along the c-axis so this can explain why it is suppressed for the measurements close to the ab-plane. The Mn-

Sr path is found between the *c*-axis and *ab*-plane, which can explain why this peak is found for all the angles measured.
Due to the Mn rich impurities seen in the SEM measurements (see Figure 4.5) it is unclear how much of the EXAFS structure measured is from $Sr_2MnCu_{1.5}S_2O_2$ or from the impurities. This means gaining a clear idea of the structural changes from the Mn K-edge is not possible. Several attempts were made to fit this data but the contributions from the impurities were large enough to make a reliable fit impossible.

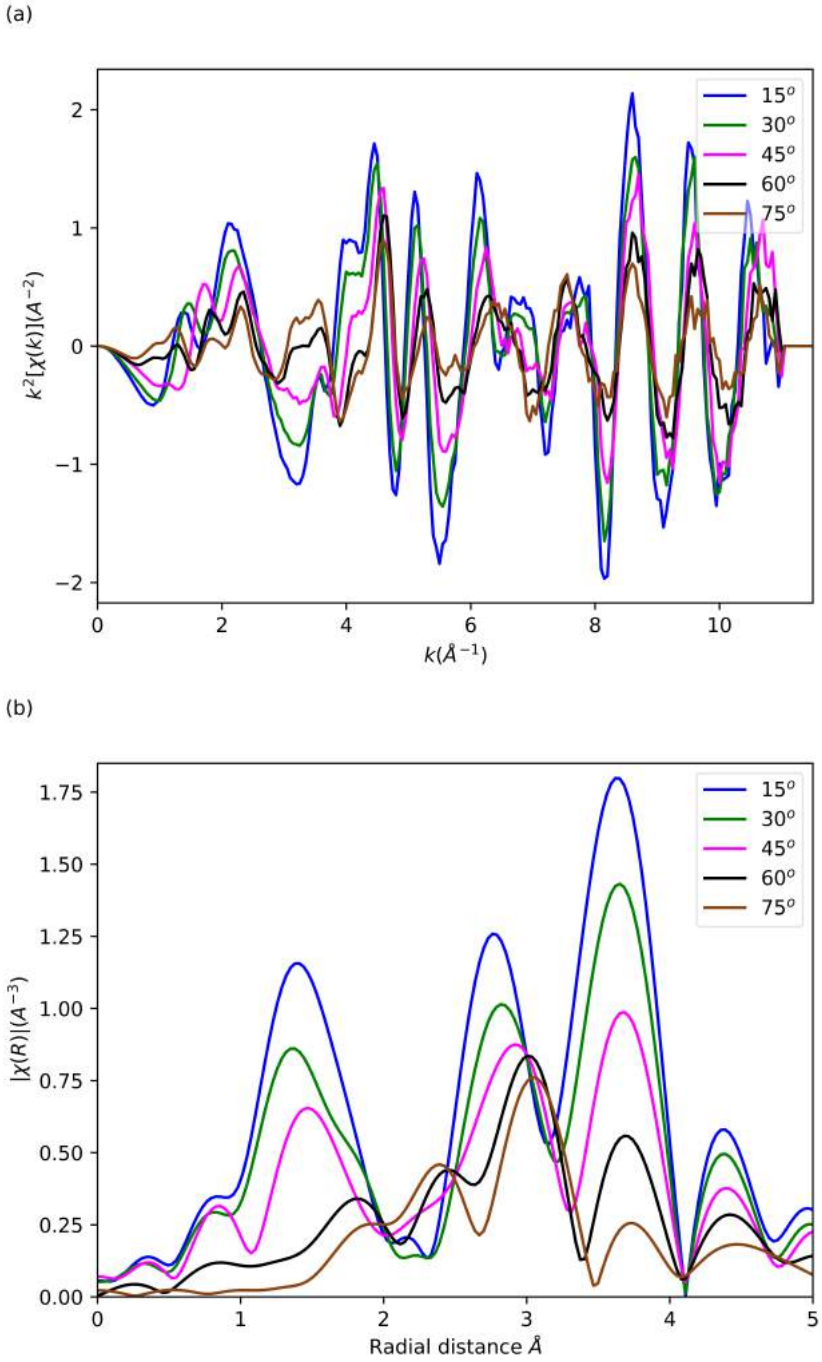

Figure 4.42: EXAFS, (a), and FT-EXAFS, (b), of the Mn K-edge $Sr_2MnCu_{1.5}S_2O_2$, at 300K. A range of angles are included, 15° to 75° in steps of 15°.

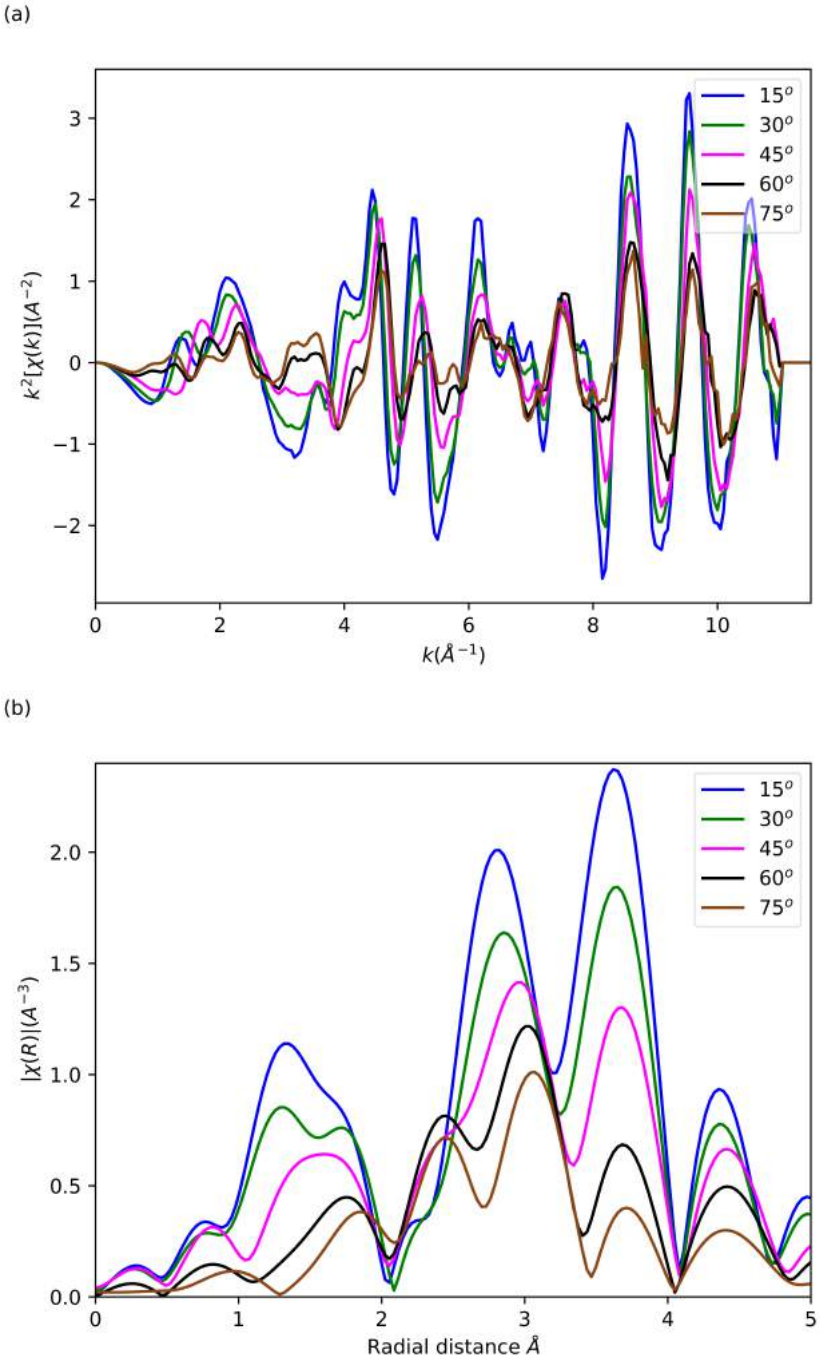

Figure 4.43: EXAFS, (a), and FT-EXAFS, (b), of the Mn K-edge $Sr_2MnCu_{1.5}S_2O_2$, at 112K. A range of angles were measured, 15° to 75° in steps of 15°.

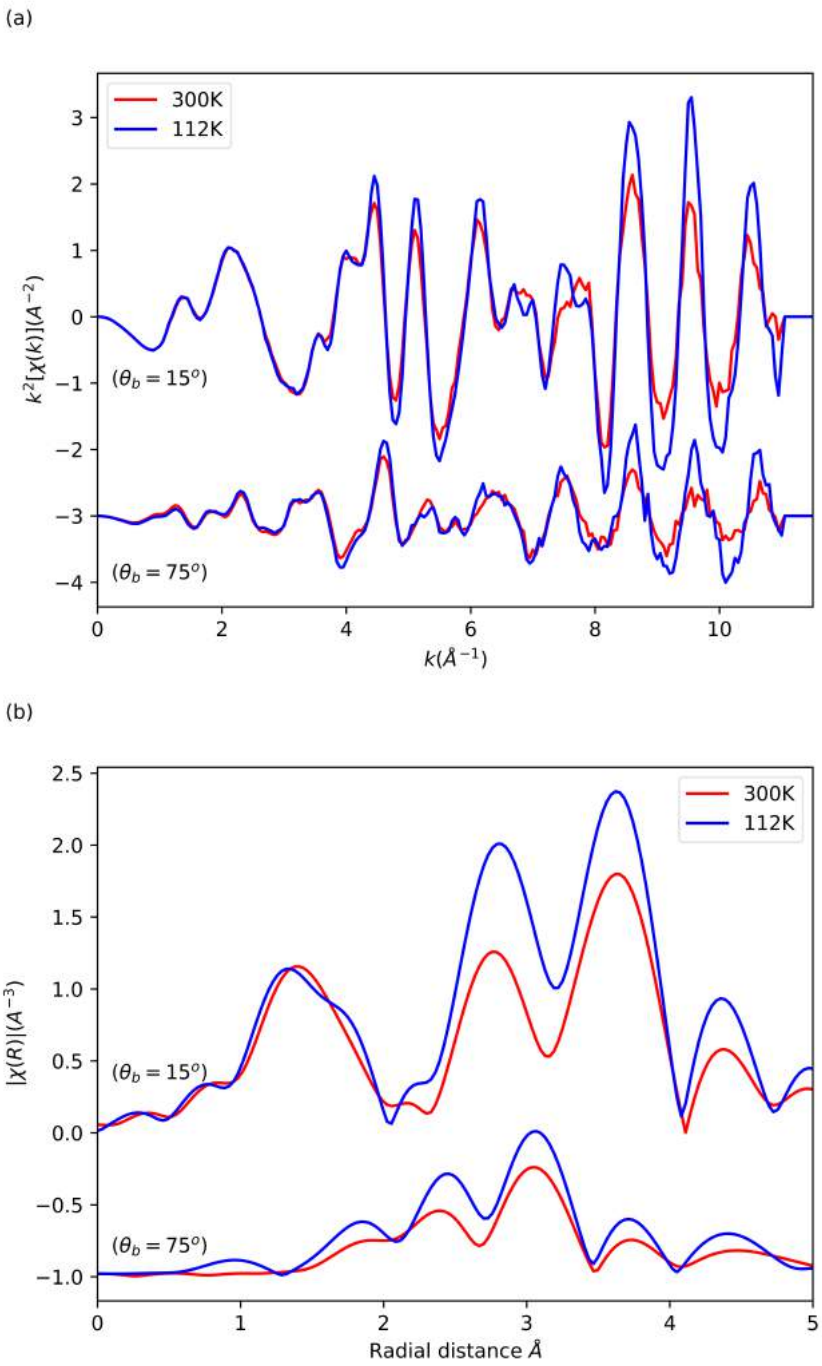

Figure 4.44: Comparison of the EXAFS (a) and FT-EXAFS (b) of the Mn K-edge $Sr_2MnCu_{1.5}S_2O_2$, for the two extreme angles at both temperatures.

Fit of EXAFS

To gain a better understanding of the changes in the local structure, at the different angles measured, the data needs to be fit to a theoretical model. Figures 4.39b and 4.40b show that there are strong features up to 4.8Å.
As the fit was obtained by modelling an averaged theoretical EXAFS signal, produced from the tetragonal structure [33], a weighting factor needs to be introduced to make the averaged theoretical EXAFS equivalent to the EXAFS along one direction. The weighting factor is discussed in full in Chapter 3. From Figure 4.45 it can be seen that there is more than one distinct scattering path of the same length within the unit cell. This is due to the angles the path is making with respect to the *c*- and *a*-axis, and needs to be taken into account when fitting the data. The path lengths are degenerate, however the θ_i and ϕ_i values change. This is accounted for in the weighting factor used in the fits. The degeneracy (N) of each single scattering path has been set to 1, and the multiple scattering paths have been set to the value predicted by the model. This parameter cannot be refined in ARTEMIS, so the amplitude reduction factor (S_0^2) takes into account changes in N. The value for S_0^2 reported for the fits is a global factor, so it accounts for all factors affecting the amplitude. This means it cannot directly be used to infer changes in N from the fits.
The refined parameters for the fits to the Cu K-edge EXAFS data, shown in Figures 4.46 and 4.47, can be found in Table 4.11. All of the parameters are within their acceptable ranges, so the fits are considered good. The double scattering paths used in the fits were obtained by producing a theoretical model with the polarisation built in, using ARTEMIS. Fitting was carried out in R space, with k weightings of 1, 2, and 3, using 33 of 115 independent parameters for the 300K data, and 32 of 115 independent parameters for the 112K data. The same single scattering paths were used, and three multiple scattering paths were used in the fits for both temperatures, they were calculated from the model up to 4.74Å. The fits resulted in a R-factor of 0.012, and 0.022, for the 300K and 112K data, respectively. For both temperatures, the DW factors for the Cu-Cu paths are the largest, aside from the Cu-Mn path which is the farthest fitted path from the central atom. This suggests that there is delocalisation in the Cu ions, which was seen in the powder data as well. The Cu-Cu paths do not contribute to the fit along the *c*-axis, this is consistent with the theoretical model as they should have no contribution to the signal measured perpendicular to the paths.
The single scattering paths used when fitting the Cu K-edge EXAFS data can be seen in Figure 4.45. It can be seen that certain paths lie along a specific crystallographic axis. This means that some single scattering paths will not add anything to the fit at certain angles. In a dipolar transition a path found completely in the *ab*-plane will not contribute to the fit along the *c*-axis, as the path lies perpendicular to the polarisation of the x-ray. Therefore certain paths will have a zero weighting in the fit along specific directions in the crystal.
The angles θ_i and ϕ_i (in the weighting factor) for the single scattering paths have been calculated from the model used to fit the data (see Table 4.9)[2]. As all angles measured are fit simultaneously, this additional data opens up more guess parameters for the fit. To account for the distinct paths each single scattering path is separated and the amplitude is multiplied by a weighting that corresponds to their frequency in the unit cell (see Table 4.9).

[2]The calculation and treatment of the angles in the weighting factor is discussed in Chapter 3.

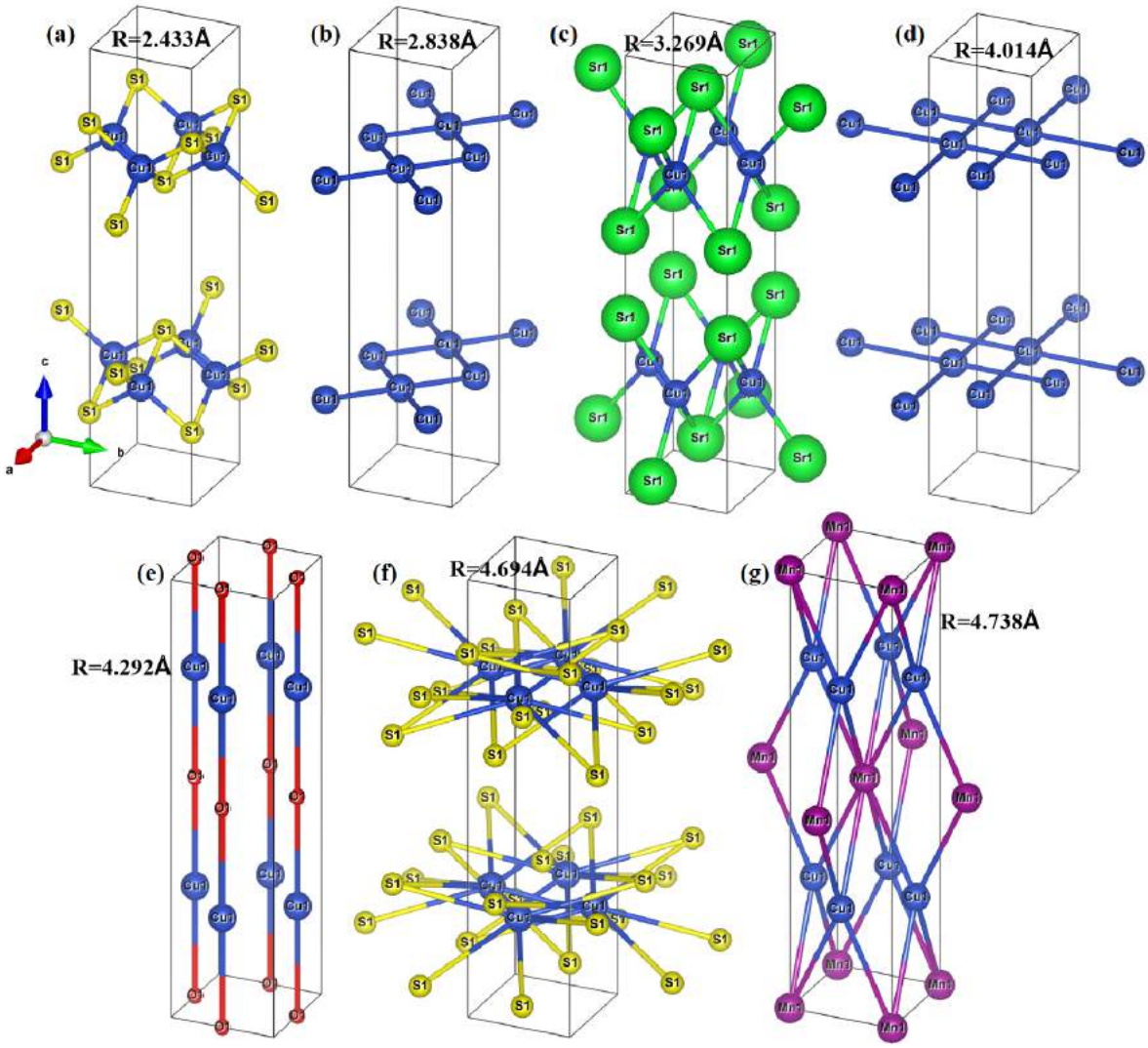

Figure 4.45: The single scattering paths used in the fit of the Cu K-edge $Sr_2MnCu_{1.5}S_2O_2$ data. With (a) 1st Cu-S, (b) 1st Cu-Cu, (c) Cu-Sr, (d) 2nd Cu-Cu, (e) Cu-O, (f) 2nd Cu-S, and (g) Cu-Mn.

Table 4.11: Fit parameters for the Cu K-edge EXAFS of the 300K and 112K single crystal data, alongside the value obtained from the tetragonal structure. The degeneracy (N) of each path was set to 1. The azimuthal angle of the polarisation with respect to the a-axis, ϕ, was set to -130°.

	Temperature (K):		
Parameter:	112	300	Model (240K) [33]
Reduced χ^2	289.51	108.30	-
S_0^2 at 0°	1.33±0.06	1.14±0.05	-
S_0^2 at 15°	1.28±0.06	1.10±0.05	-
S_0^2 at 30°	1.15±0.05	1.01±0.04	-
S_0^2 at 45°	0.94±0.04	0.86±0.03	-
S_0^2 at 60°	0.72±0.03	0.69±0.02	-
S_0^2 at 75°	0.56±0.03	0.57±0.02	-
S_0^2 at 90°	0.51±0.04	0.53±0.03	-
ΔE_0 (eV) at 0°	2.8±0.4	1.4±0.4	-
ΔE_0 (eV) at 15°	2.8±0.4	1.5±0.4	-
ΔE_0 (eV) at 30°	2.8±0.4	1.5±0.3	-
ΔE_0 (eV) at 45°	2.8±0.4	1.5±0.3	-
ΔE_0 (eV) at 60°	2.9±0.4	1.5±0.3	-
ΔE_0 (eV) at 75°	2.8±0.5	1.5±0.3	-
ΔE_0 (eV) at 90°	2.8±0.6	1.5±0.4	-
1st Cu-S R (Å)	2.39±0.00	2.37±0.00	2.433
1st Cu-S σ^2 (Å^2)	0.0067±0.0005	0.0096±0.0004	-
1st Cu-Cu R (Å)	2.85±0.01	2.82±0.01	2.838
1st Cu-Cu σ^2 (Å^2)	0.019±0.001	0.024±0.001	-
Cu-Sr R (Å)	3.28±0.01	3.28±0.01	3.269
Cu-Sr σ^2 (Å^2)	0.0113±0.0007	0.0163±0.0007	-
Cu-S-Cu R (Å), double	4.03±0.03	4.08±0.03	3.853
Cu-S-Cu σ^2 (Å^2), double	-0.003±0.003	0.006±0.005	-
2nd Cu-Cu R (Å)	4.02±0.03	-	4.014
2nd Cu-Cu σ^2 (Å^2)	0.016±0.004	-	-
Cu-O R (Å)	4.09±0.02	4.03±0.02	4.292
Cu-O σ^2 (Å^2)	0.011±0.005	0.013±0.003	-
Cu-S-S R (Å), double	4.53±0.02	4.51±0.02	4.410
Cu-S-S σ^2 (Å^2), double	-0.001±0.002	0.005±0.003	-
Cu-S-S R (Å), obtuse triangle	4.44±0.06	4.66±0.02	4.440
Cu-S-S σ^2 (Å^2), obtuse triangle	0.002±0.008	0.002±0.003	-
2nd Cu-S R (Å)	4.69±0.01	4.66±0.01	4.694
2nd Cu-S σ^2 (Å^2)	0.009±0.001	0.016±0.002	-
Cu-Mn R (Å)	4.78±0.03	4.74±0.03	4.738
Cu-Mn σ^2 (Å^2)	0.023±0.004	0.032±0.005	-

A good fit was produced by using the model obtained from the tetragonal structure and refining this model against the Cu K-edge EXAFS, the path distances and DWs were allowed to change for each temperature and are fit simultaneously for each angle. The sum of all the relevant single scattering, and double scattering path contributions to the Cu K-edge EXAFS of $Sr_2MnCu_{1.5}S_2O_2$ are shown in Figures 4.46 and 4.47 fitted against the 300K and 112K EXAFS data, respectively.
Figures 4.48 and 4.49 show the fits for the two extreme angles. It can be seen that the model produces a better fit for the data along the *c*-axis. While the fit along the *ab*-plane is missing components to properly fit the second and third peak. This is true for both the 300K and 112K data, but is more stark in the 112K. This suggests that some of the paths may be different than the model predicts. This may also be due to missing multiple scattering contributions that did not produce reasonable parameters when fit to the data.

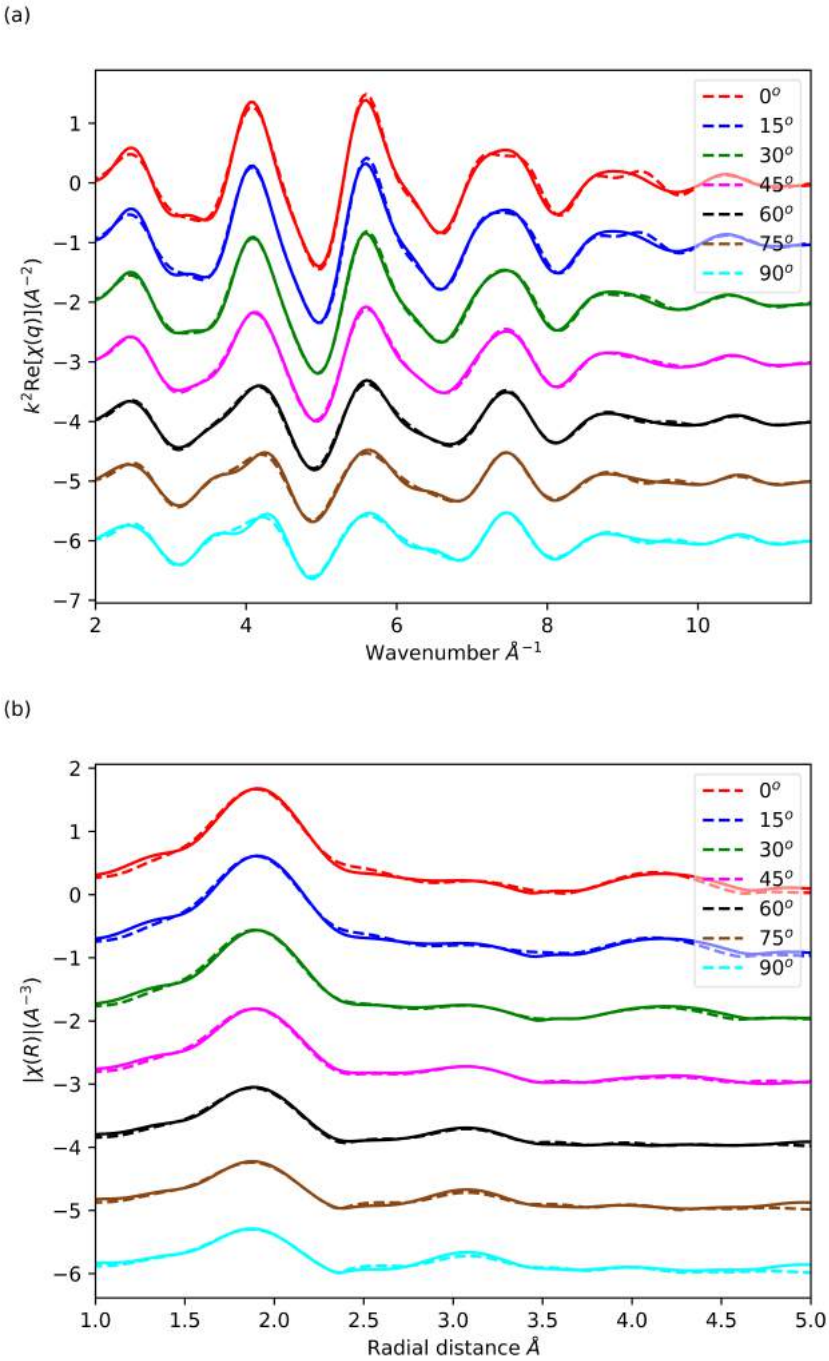

Figure 4.46: Fit of the Cu K-edge at 300K, in q space(a) and R space (b). The data was fitted to a tetragonal structure. The fits for all angles are presented in this plot. The solid line corresponds to the experimental data and the dashed line corresponds to the fit.

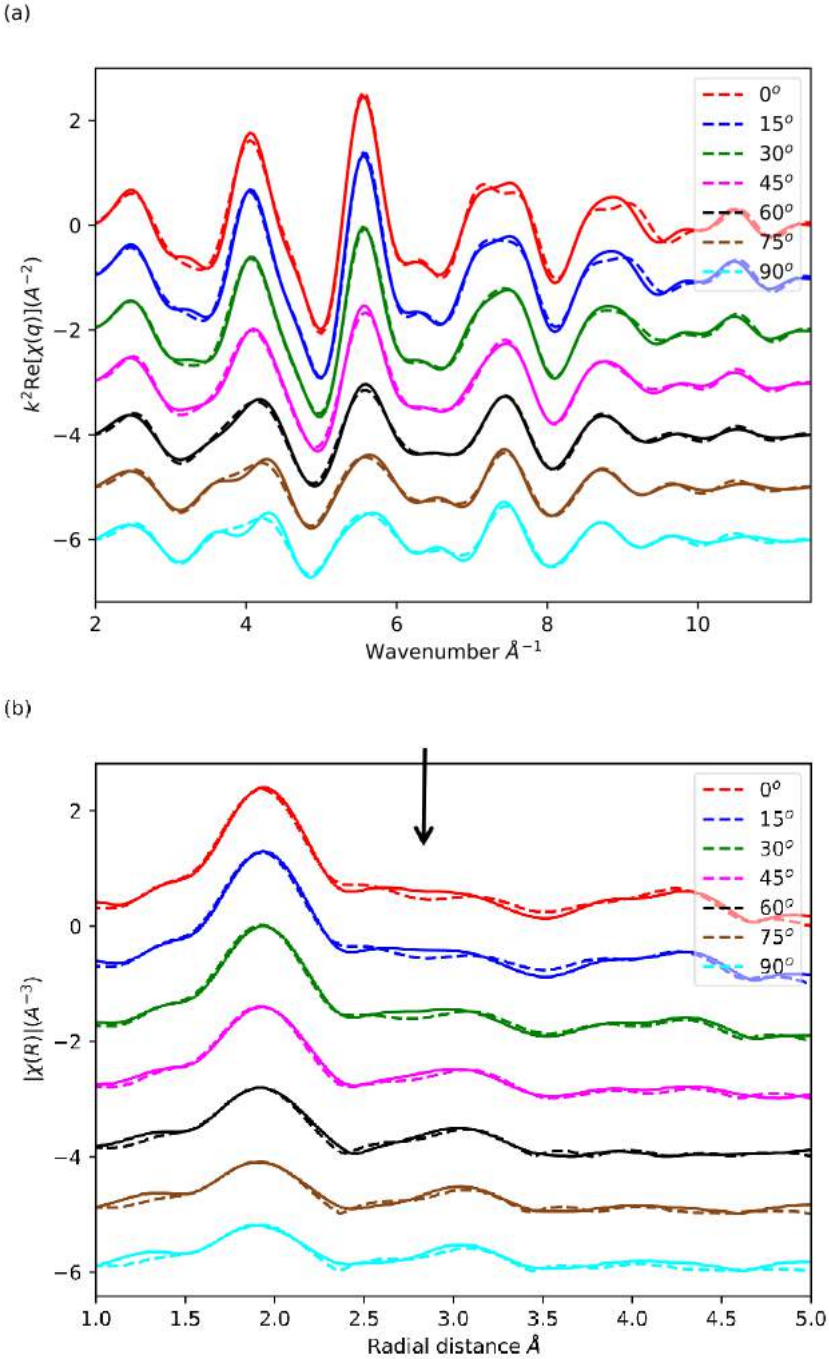

Figure 4.47: Fit of the Cu K-edge at 112K, in q space (a) and R space (b). The data was fitted to a tetragonal structure. The fits for all angles are presented in this plot. The solid line corresponds to the experimental data and the dashed line corresponds to the fit.

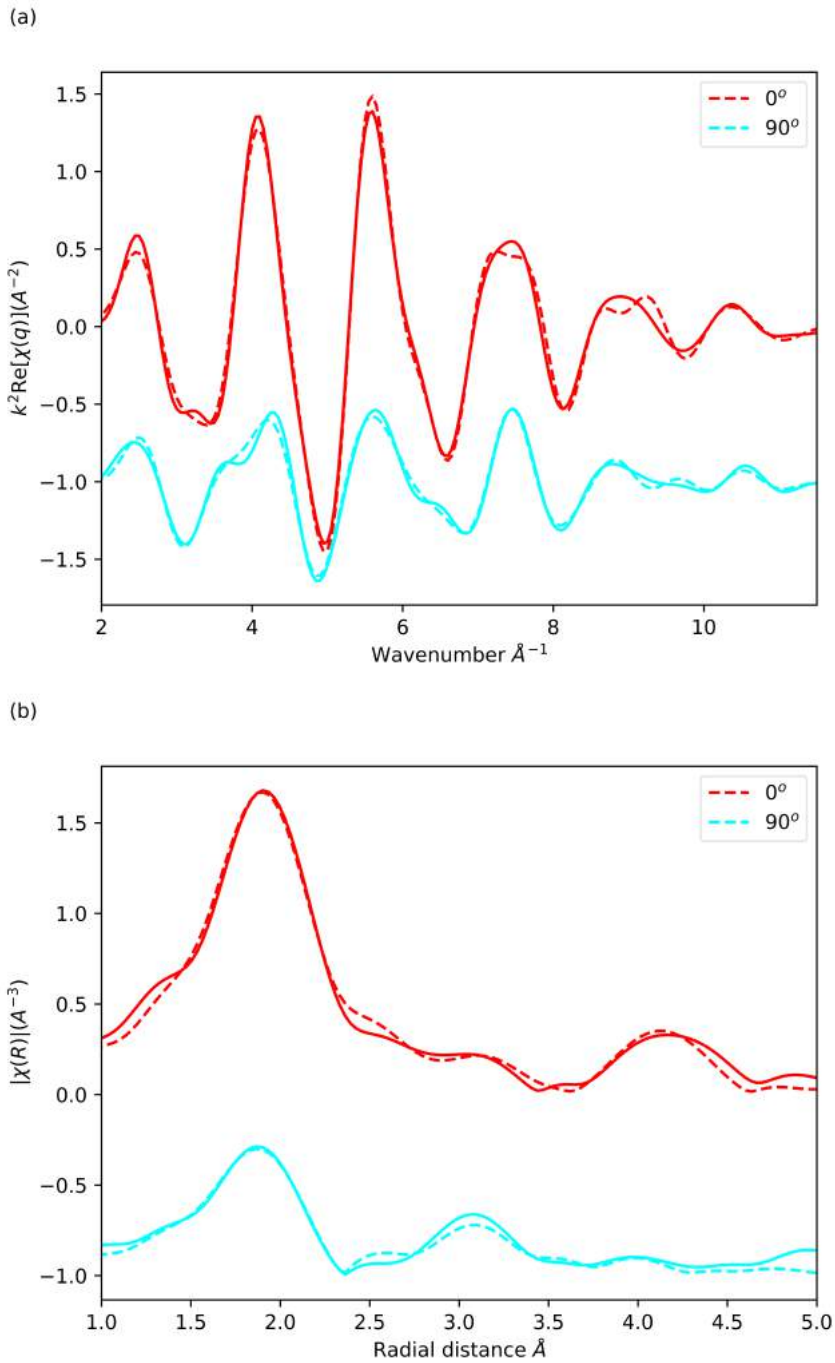

Figure 4.48: Fit of the Cu K-edge at 300K, in q space (a) and R space (b). The data was fitted to a tetragonal structure. The two extreme angles are presented in this plot. The solid line corresponds to the experimental data and the dashed line corresponds to the fit.

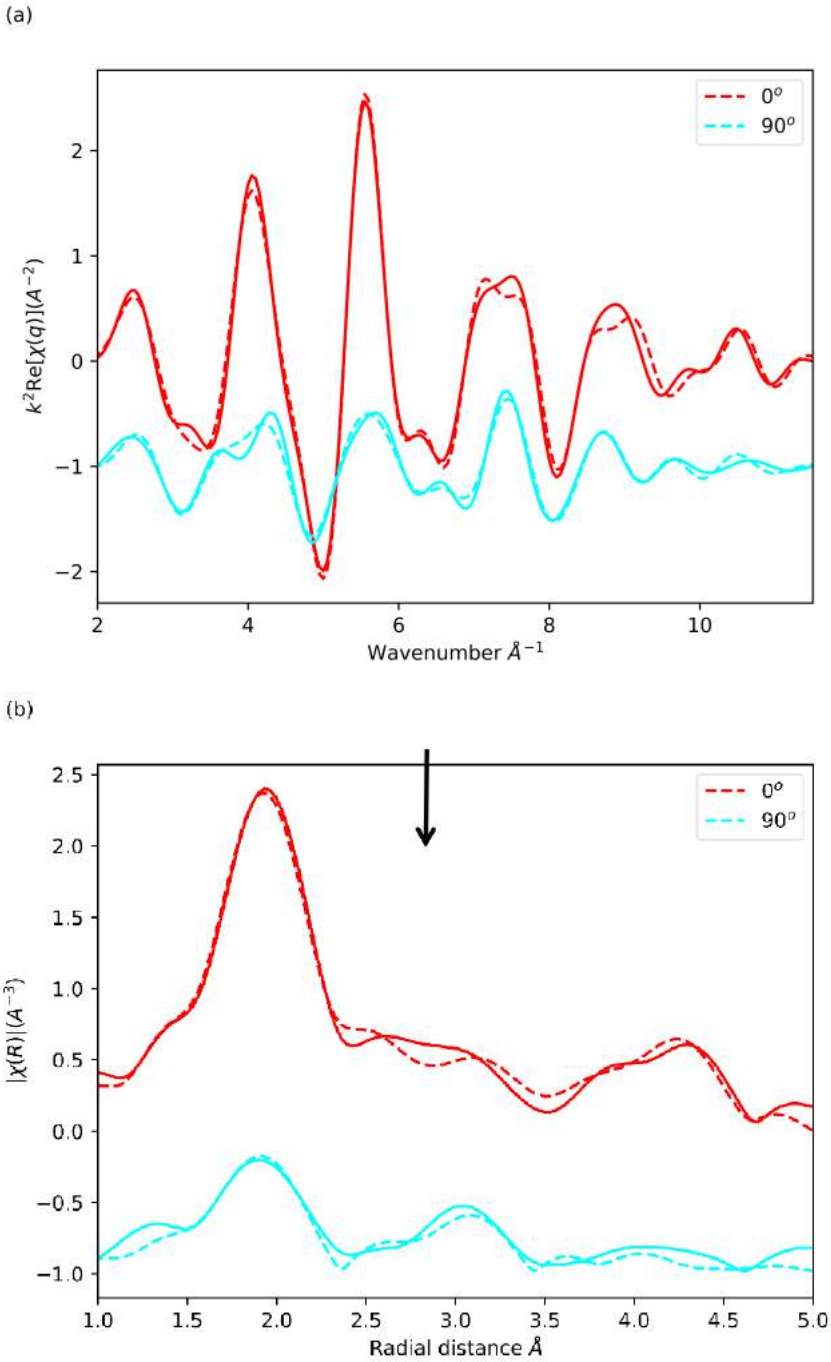

Figure 4.49: Fit of the Cu K-edge at 112K, in q space (a) and R space (b). The data was fitted to the tetragonal structure. The two extreme angles are presented in this plot. The solid line corresponds to the experimental data and the dashed line corresponds to the fit.

As mentioned earlier, attempts have been made to fit the Mn K-edge EXAFS data. However the fit does not match the data well, and produces values for the guess parameters which are outside the normal ranges.

4.5 Discussion

From the SEM measurements we can determine that the crystal used in the P-XAS experiment included Mn rich impurities. These impurities could explain why there are discrepancies in the measured Mn K-edge data and the expected local structure, and not in the Cu K-edge data. The XAS measured for the Mn K-edge will also include absorption due to the impurities in the sample. As the impurities did not appear to include any Cu ions, the Cu K-edge data could provide information on the structure of interest. For the Mn K-edge, for both the powder XAS and single crystal P-XAS, a fit has been attempted but unsurprisingly the data has not been possible to model. To understand the Mn K-edge measurements the nature of the impurities needs to be understood to produce a model that could be fit to the data. The SEM measurements were not thorough enough to accurately determine the amount, and stoichiometry, of the impurities, so a model which includes them was not possible to produce.
The Cu K-edge XANES measured using both techniques are in agreement with each other, both showing that the oxidation state of the Cu ions is +1, therefore the transition responsible for the XANES is $1s$ to $4p$. There is no visible pre-edge feature seen in the data, for either of the methods, suggesting that the symmetry does not allow quadrupole transitions to occur for the Cu ions. In the powder data there is only a slight change in the XANES with respect to Cu vacancies (see Figure 4.7), this suggests that the amount of Cu vacancies does not strongly affect the local electronic structure of the Cu ions. From the single crystal XANES (see Table 4.7 and Figure 4.35) there is not a large amount of anisotropy in the local electronic structure of the Cu ions.
For the Cu K-edge powder EXAFS (see Figure 4.50) there is a clear change in the local atomic structure with respect to the amount of Cu vacancies. While the local structure is similar for the x=0.0 and x=0.2 samples, there is a large change for the x=0.3 sample past the first two peaks. The third peak is almost completely suppressed in both the high temperature and low temperature data sets, this peak has the strongest contributions from the Cu-Sr scattering path (3.269Å). In the low temperature data set the fourth peak is also suppressed for the x=0.3 sample, this peak has the strongest contributions from the second Cu-Cu scattering path (4.014Å). The third and fourth peak suppression, in the x=0.3 sample, may be due to destructive interference between the scattering paths. The fourth peak is suppressed for all samples in the high temperature data. This is consistent with the Cu ions being mobile at room temperature, as the Cu sites will be more disordered if the Cu ions are mobile.
In the Cu K-edge single crystal EXAFS data (see Figure 4.41b) there is a change in the intensities of the peaks with angle. The second peak ($\sim$ 2.5Å) becomes suppressed when comparing the data along the ab-plane to the c-axis, the path that contributes to this peak is the first Cu-Cu scattering path. As this path lies completely in the ab-plane its suppression in the c-axis data is expected, as paths perpendicular to the polarisation should not be observed. There also appears to be a larger change with temperature for the data along the ab-plane, this suggests that the transition occurring with temperature has a stronger affect along the ab-plane of the Cu local structure.

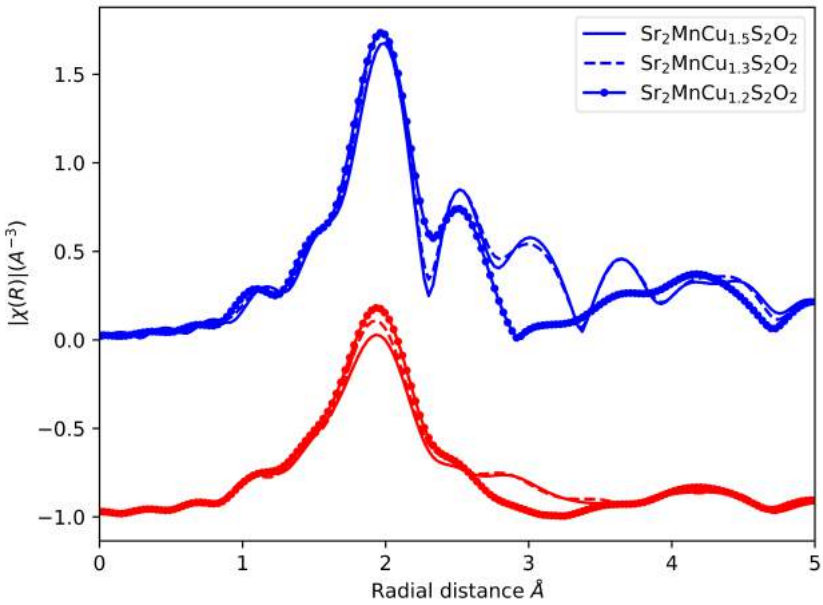

Figure 4.50: Comparison of the R space of the Cu K-edge, $Sr_2MnCu_{1.5-\delta}S_2O_2$, for the different samples with respect to the extreme temperatures measured. Where the blue line corresponds to the measurement at 10K, and the red line corresponds to the measurement at 260K.

From the fits to the powder Cu K-edge data it can be seen that there is a discrepancy in the fit of the third peak for both the x=0.0 and x=0.2 samples (see Figures 4.24 and 4.25). This may be due to multiple scattering paths not being included in the fit, however these paths did not produce sensible values when added into the fit, such as large values for the ΔR (> 1Å) or negative DW's outside of errors. This discrepancy is not seen in the fits of the x=0.3 sample, this may be because the third peak is mostly suppressed. The DW's of the paths fit to each sample show that the Cu ions have a lot of disorder (see Figures 4.17 to 4.19). For both the x=0.0 and x=0.2 samples the DW's of the Cu-Cu scattering paths are the largest, larger than those for paths further from the central ion. This suggests that the Cu ions are mobile and this mobility increases with temperature. For the x=0.3 sample the DWs are large for the Cu-Cu scattering paths as well as for the Cu-Sr scattering path. This may be due to the peak being suppressed, this suppression is potentially due to interference affects between the paths around this peak.

For the single crystal measurements, the most reliable parameters produced from the fits are ΔE_0 and ΔR. As the measurements were taken in fluorescence mode, the amplitude parameters produced from the fits may not be reliable. This is due to having to correct the data for self-absorption and the angle of incidence between the beam and the sample changing. However the amplitude parameters can be compared for the fits of the same angle at different temperatures, as the self-absorption correction will be consistent for the same θ_b.

From the fits to the single crystal data it can be seen that the model is in agreement with the structure the data presents for the 300K measurements. The fit is good for all angles (see Figure 4.46) and from the guessed parameters (see Table 4.11) it suggests that the structure is slightly compressed in comparison to the model. The Cu ions appear to still be mobile, as the DW's for the first Cu-Cu single scattering path were

found to be 0.024 ± 0.001Å^2 at 300K, and 0.019 ± 0.001Å^2 at 112K. It was not possible to fit the second Cu-Cu single scattering path to the 300K data, suggesting that the Cu ions are more delocalised at room temperature. The fit to the low temperature, 112K, data (see Figure 4.47) shows discrepancies to the fit of the second and third peak. This discrepancy is more noticeable in the data for the shallower angles (small θ_b's), this suggests that the model is having more issues predicting the *ab*-plane of the local structure. The second and third peaks correspond to the first Cu-Cu and Cu-Sr single scattering paths, respectively. The reported transition appears to affect the *ab*-plane more than the *c*-axis, this can be seen in both the raw data and the fit data, as there is a larger change with temperature for the shallower angles.
Comparing the fits of the Cu K-edge, of the powder data XAS to the single crystal P-XAS, it can be seen that when averaging over the sample valuable information is lost. The fit along the *ab*-plane shows this clearly as the fit cannot accurately model the second and third peak for both the 300K and the 112K data, whereas the fit to the powder data can model the second peak well. This suggests that while averaging over the structure some definition is lost, and while measuring along different directions a greater knowledge of the structure can be gained.
The path distances produced by the fits to the single crystal data suggest that the unit cell is larger at 112K than at 300K, the proposed transition is from tetragonal (>240K) to orthorhombic symmetry (<240K). The Cu-S scattering path gets longer as the temperature decreases, this path is found between the *ab*-plane and *c*-axis. The path length goes from 2.37 ± 0.00Å, at 300K, to 2.39 ± 0.00Å, at 112K (2.433Å in the model).The length of the Cu-Cu scattering paths, for both temperatures, suggests an enlargement of the unit cell along the *ab*-plane as the temperature is decreased, as this path lies exclusively in this plane. The first Cu-Cu path goes from 2.82 ± 0.01Å, at 300K, to 2.85 ± 0.01Å, at 112K (2.838Å in the model). The second Cu-Cu path is found at 4.02 ± 0.03Å, at 112K (4.014Åin the model), and is too delocalised to fit to the 300K data. The Cu-Sr scattering path is found to be roughly the same, within error, for both temperatures. The fit struggled to model the peak this path corresponds to accurately, most likely due to missing multiple scattering paths. Therefore it is difficult to predict what is happening to the unit cell based off this scattering path.
Comparing the x, y, and z components of the first three single scattering paths, Figure 4.51, it can be seen that they increase as the temperature is decreased. They are also smaller than the tetragonal model [33] predicts. The first two scattering paths in the fit suggest a increase in the size of the unit cell as the temperature is decreased.

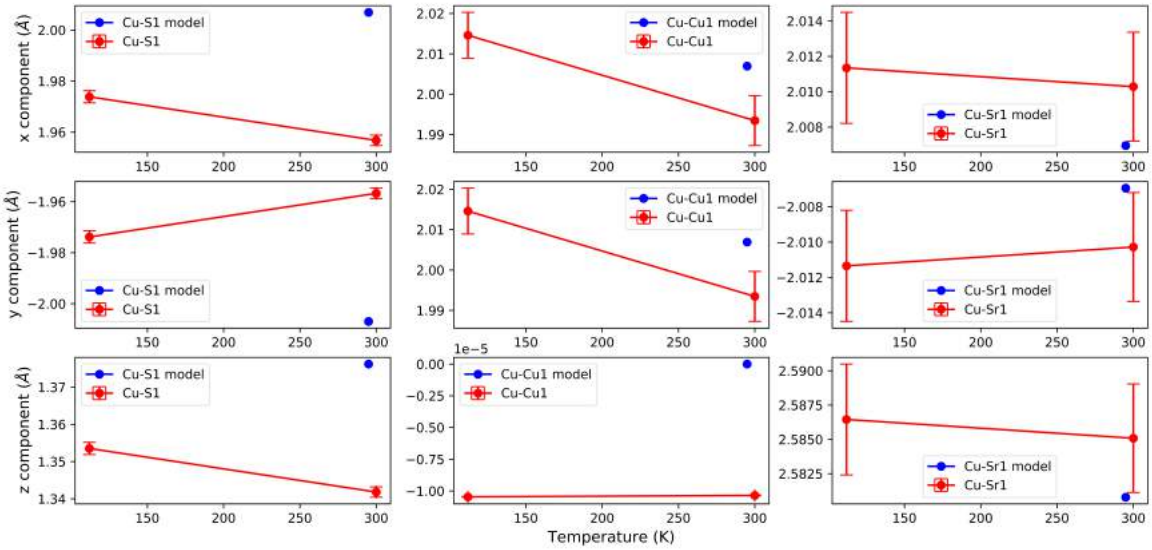

Figure 4.51: The change in the x, y, and z components of the scattering paths that contribute to the first three peaks. The components from the model are also included.

4.6 Conclusion

The powder data of the samples provides evidence that the Cu ions are mobile within this structure, where the DW factors are much larger for the Cu-Cu scattering paths than for other atoms at similar distances, as expected. There is no change in the XANES of the Cu K-edge with temperature, which suggests that there are no changes in the electronic structure over this temperature range. It is unclear if there is a transition from a tetragonal to an orthorhombic structure, as the data could not be fit to the orthorhombic model. When attempting to fit the low temperature data (<240K) to the orthorhombic model, the fit produced values outside of their normal range. The predicted orthorhombic distortion is small so this may explain why all temperatures could be fit using the tetragonal model. The fits do suggest that there may be a structural transition, this is clearer in scattering paths further away from the central ion. The peak that corresponds to the Cu-Sr single scattering path displays a discrepancy between the model and the experimental data. However this is most likely due to missing multiple scattering paths as the discrepancy is observed both above and below the transition temperature. As the orthorhombic model cannot be fit to the experimental data it cannot be concluded if the potential transition is the one predicted by the diffraction data. A reliable transition temperature cannot be obtained from these fits, as we do not have enough temperature points around 240K.
The P-XAS experiment has shown that the technique can be used to measure structural information with respect to direction along a sample. The P-XAS data shows that the XAS along different directions is distinguishable, and fitting this data can give an insight into the physics that is occurring in an anisotropic material. From the raw data it can be seen that the Cu-Cu path has a stronger contribution along the ab-plane, and it is suppressed along the c-axis. From the fits it is again clear that the Cu ions are mobile as the DW factors for these paths are large. Also there is no evidence of the Cu ions moving along the c-axis as the path cannot be fit to the EXAFS in this direction. This suggests that the Cu ions are mobile within the ab-plane, which can be assumed

from the structure derived from diffraction data [33].
The Mn K-edge data could not be fit to the same structure as the Cu K-edge for either the powder or single crystal. This may be due to the presence of impurities involving Mn atoms (rather than Cu). This suggests that the impurities seen in the single crystal sample could also be occurring in the powder samples. The maps of the sample surface, measured with the SEM, show that the material is not homogeneous and the impurities appear to be Mn compounds. To confirm this, SEM measurements of the powder sample could be taken to determine if Mn rich impurities are present. Further SEM measurements need to be taken to determine the amount, and the stoichiometry, of the impurities present in the samples. The Cu K-edge of both the powder and single crystal measurements produced sensible fits to the tetragonal model. Therefore it is unclear if the structural model is not valid for the samples, or if the Mn rich impurities make up a large fraction of the Mn sites measured.
It was of interest to determine if there was ordering of the Cu sites and the Cu vacancies at low temperatures, below 240K. The consequence of the Cu/vacancy ordering is reported to be the formation of a superstructure [132], with an expansion of the unit cell by $2\sqrt{2a} \times \sqrt{2a} \times c$. There is evidence of an expansion of the local atomic structure at low temperature compared to room temperature, based on the fits to the data. However, the low temperature model [34], which is based on the $2\sqrt{2a} \times \sqrt{2a} \times c$ unit cell expansion, could not be fit to the low temperature data, as it output unreasonable parameters. The ΔR values from the fits suggest that the path lengths increase as the temperature decreases, while the model suggests an average decrease in path length, with multiple single scattering paths corresponding to single peaks. However as all temperatures fit reasonably well to the tetragonal model it is unclear if the predicted orthorhombic distortion occurs. Therefore the predicted Cu/vacancy ordering could not be confirmed from this data.

Chapter 5

Investigating structural changes due to a CDW in $M_2Mo_6Se_6$ (M=Rb, Tl) using single crystal P-XAS.

5.1 Introduction

Charge-density waves (CDWs) occur in linear chain compounds or layered crystals, where the electrons form a fluid-like nature. The electrons within a CDW will form a standing wave pattern, and they have the ability to carry charge through a material. The standing wave can carry a current due to the combined affects of impurities in the material and electrostatic interactions (from net electric charges in any of the CDW kinks) [29]. They occur in materials where the electronic band structure is highly anisotropic [31]. The CDW ground state occurs due to the electron-phonon interaction within the material, and was first discovered by Peierls [145]. Moving CDWs were discovered roughly two decades later by Fogle and Perlstein [146], which can cause non-linear electric conduction. A CDW is often paired with a periodic distortion in the atomic structure of the material, which has been discussed in [31, 32, 3] among others, this allows for a CDW to be observed experimentally. The presence of a CDW can lead to interesting physical properties occurring in materials, such as metal-insulator transitions [147, 81]. The onset of high temperature superconductivity in certain materials has also been theorised to be due to competing superconducting and CDW states [148, 27, 26, 149, 150].

Quasi-one-dimensional materials are interesting for several reasons, one is to test theories of low dimensional physics. Other reasons for interest in quasi-one-dimensional materials include their use in nanoscale electronics [151], optoelectronics [152, 153, 154], sensing devices [155, 156], etc. Due to their unique geometry, with a high aspect ratio, they exhibit novel physical properties such as complex magnetoresistance [157] or nonlinear conductivity [158].

The materials studied in this research belong to the family $M_2Mo_6X_6$, where M = Tl, In, or an alkali metal, and X = S, Se, or Te. They were first discovered by Potel *et al.* [39] and Honle *et al.* [159], in the 80s. They form a highly uniaxial hexagonal crystal structure, $P6_3/m$, with chains of $(Mo_3Se_3)_\infty$ along the *c*-axis, and guest ions between the chains (Figure 5.1). Due to their structure, these materials can be thought of as quasi-one-dimensional, and can be used to test predictions of low-dimensional physics. These materials have been studied relatively little, however they have very interesting properties as, depending on the guest ion, they can have either superconducting or insulating instabilities [81]. The specific materials studied for this thesis are $Tl_2Mo_6Se_6$

and $Rb_2Mo_6Se_6$, where the Tl analogue becomes superconducting [160] and the Rb analogue goes through a Mott insulator transition [40]. The resistivity with respect to temperature for these materials is shown in Figure 5.2. Where the resistance minimum for the Rb analogue is thought to be the metal-insulating transition temperature. $Tl_2Mo_6Se_6$ displays anomalies in its transport properties, where there is a zero-crossing of the Hall coefficient at ∼80K, and an upturn of thermopower.
A CDW has been suspected to be the cause of the insulating ground state in the Rb analogue. While the study conducted by Petrović *et al.* [81], suggests that the unusual behaviour of the Hall effect in $Tl_2Mo_6Se_6$ could be explained by the presence of a CDW. The unusual behaviour manifests itself in a zero-crossing of the Hall coefficient, as observed by Brusetti *et al.* [161]. This research has shown that the material undergoes a progressive change in regime, from a metal, at 300K, to a semimetal, just above the superconducting transition temperature (∼6.5K), which could be explained by the presence of a CDW. However no direct observations of a lattice distortion, due to a CDW, in either material have been achieved.

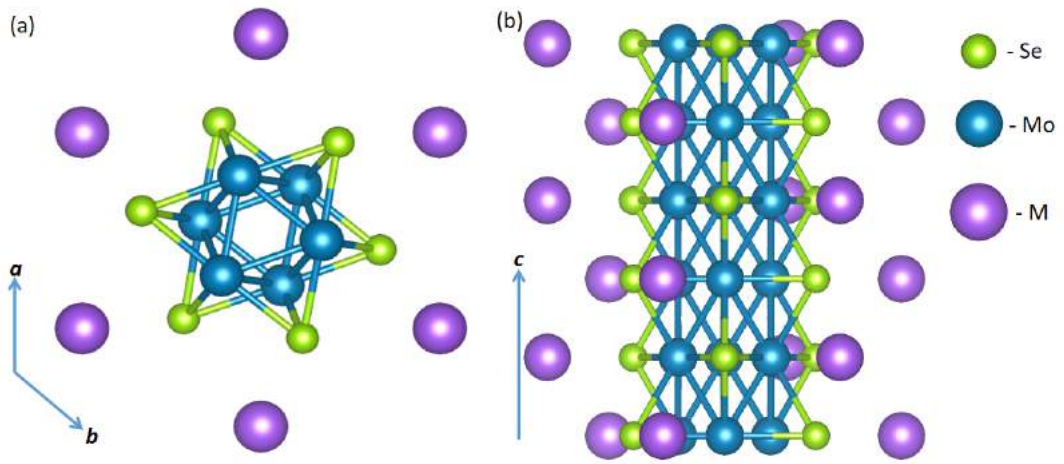

Figure 5.1: Top down view, (a), and side view, (b), of the $M_2Mo_6Se_6$ structure, where M = Rb, Tl [41, 42].

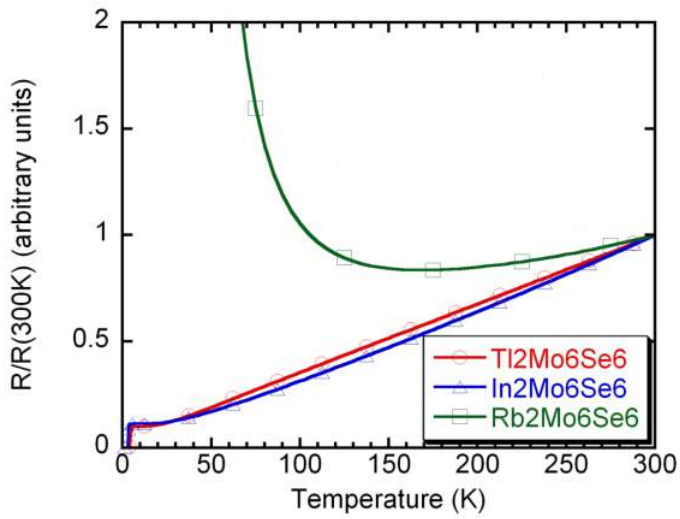

Figure 5.2: Resistivity of $M_2Mo_6Se_6$ normalised to 300K, for $Tl_2Mo_6Se_6$, $In_2Mo_6Se_6$, and $Rb_2Mo_6Se_6$. Adapted from [81].

These materials are specifically interesting to measure with P-XAS as CDWs are highly directional, therefore their effect on the material should also be directional. As there has been no observation of the proposed CDW in diffraction measurements, it is possible that the effect is either fluctuating or short-range. It has been suggested that the metal-insulator transition observed in $Rb_2Mo_6Se_6$ is due to a fluctuating Peierls gap that is uncorrelated from one Mo chain to the next [40], which could explain why a CDW has not been observed in the diffraction measurements. P-XAS is appropriate to investigate CDWs in these materials, as the technique can measure the structure along specific directions at a local level, meaning the distortion will not be averaged out.

5.2 SEM images

SEM images were taken of both the $Rb_2Mo_6Se_6$ and $Tl_2Mo_6Se_6$ samples used in the P-XAS experiment. The procedure for the SEM measurements and the detection methods are discussed in Chapter 2. Measurements were made using both secondary and backscattering electron detection. The goal of these measurements was to determine if the sample was homogeneous in composition. This could be shown by mapping the surface of the sample, and by measuring spectra at different parts of the surface.
The surface mapping can be seen in Figures 5.3 and 5.4, for the Rb and Tl samples respectively, for both secondary and backscattering electron detection. The SEM images of both samples clearly shows that the crystals are homogeneous, as the surfaces are consistently grey. The SEM images of the Rb sample show that the crystal is much thinner than that of the Tl sample. The Rb sample is also much more filamentary than the Tl sample, while some of the filaments are not fully aligned there is still a dominant orientation which is enough for P-XAS measurements.

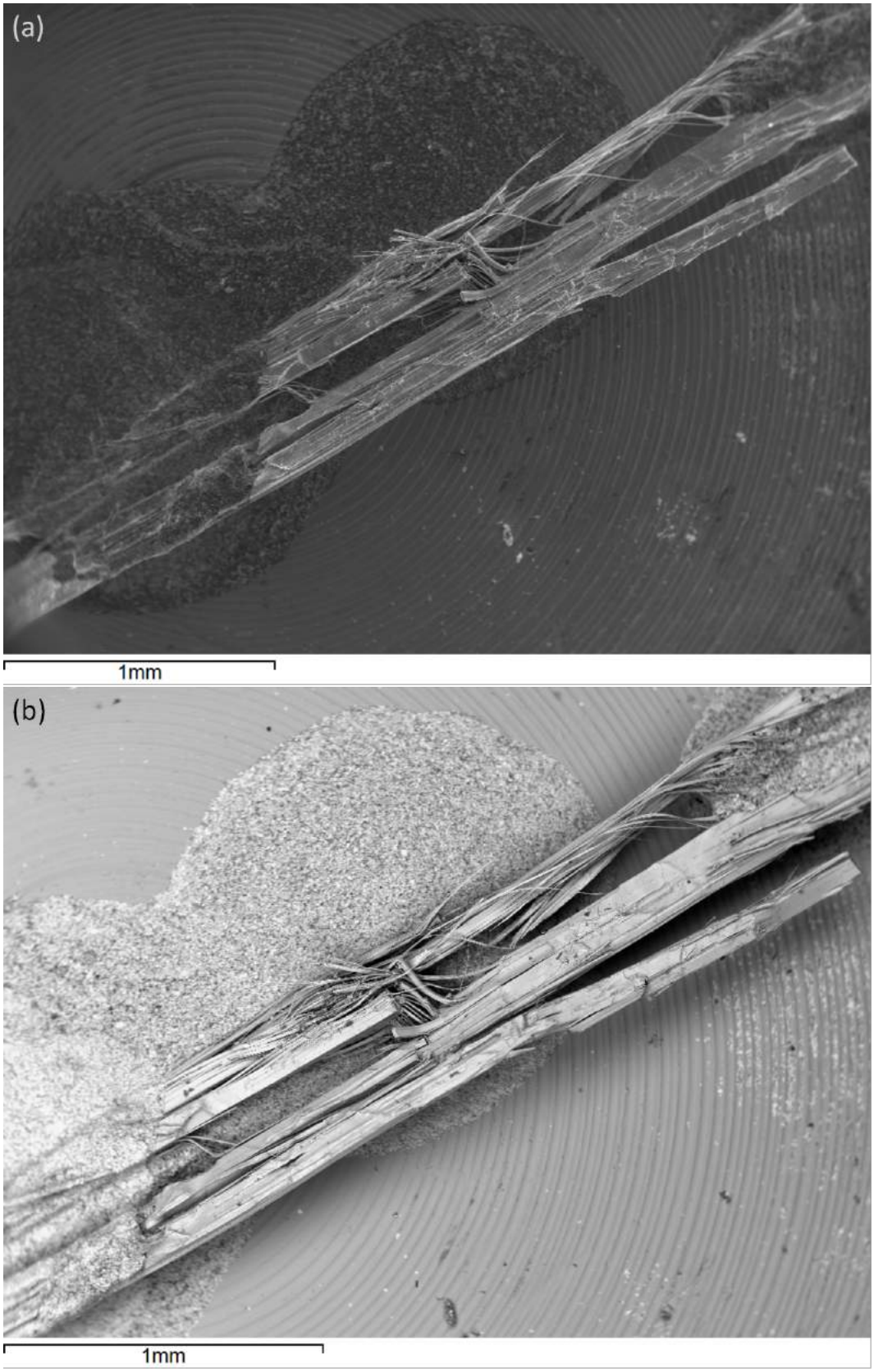

Figure 5.3: SEM image of the single crystal $Rb_2Mo_6Se_6$, measured with secondary electron (a) and backscattering electron (b) detection.

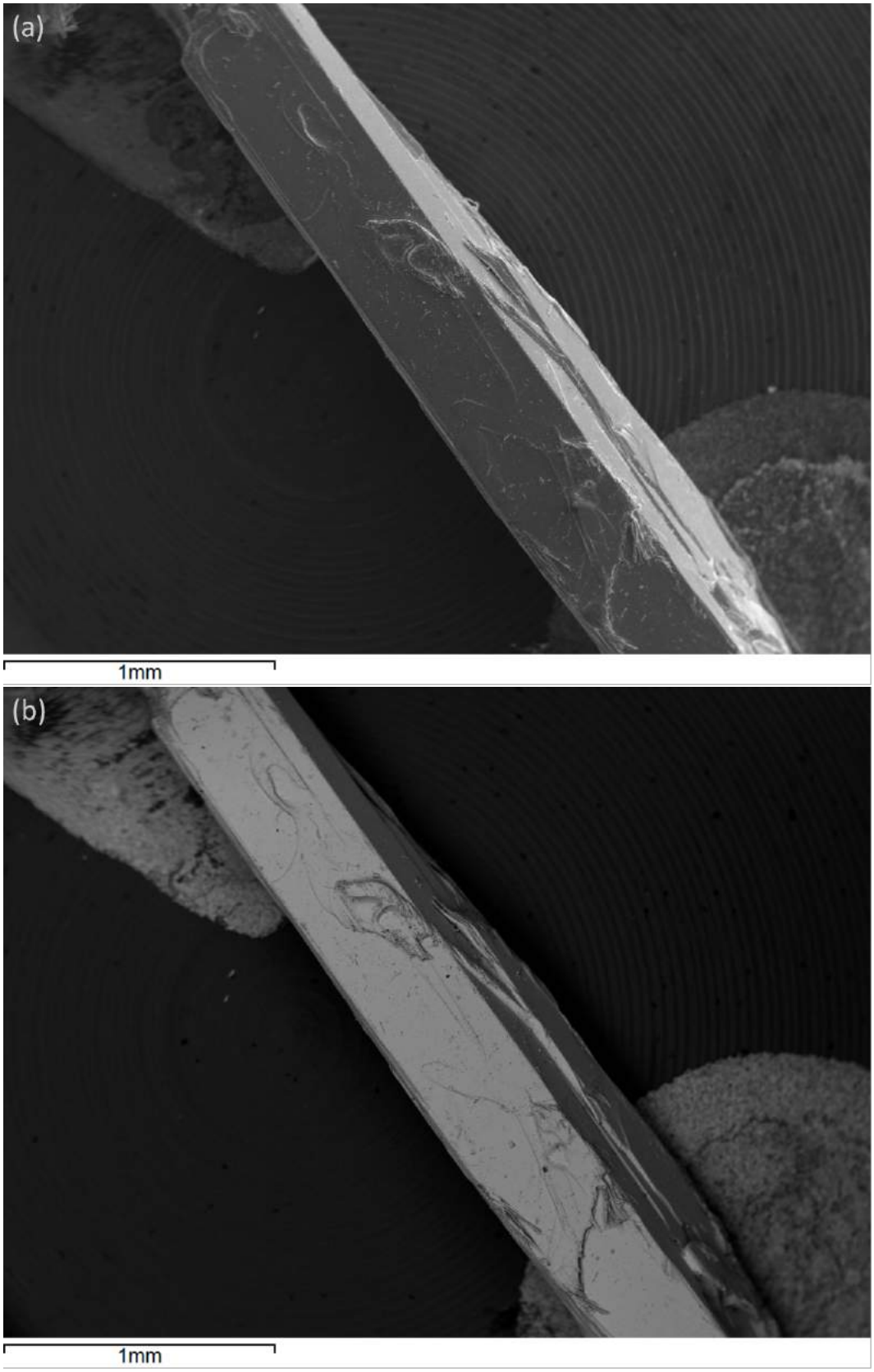

Figure 5.4: SEM image of the single crystal $Tl_2Mo_6Se_6$, measured with secondary electron (a) and backscattering electron (b) detection.

It is possible to use the characteristic x-ray spectra obtained from the SEM measurements to determine the stoichiometry of the sample. However, this was a secondary application of the SEM measurements taken for this thesis, and other experimental techniques would need to be used to obtain an accurate stoichiometry (as discussed in Chapter 2).
Spectra of the characteristic x-rays produced from the interaction between the sample and the electron beam at different points of the surface were measured to determine the composition of the features on the surface map (see Figures 5.5 and 5.6). The spectra show that the expected composition is seen in both samples, and that the composition is consistent in different areas of the sample.

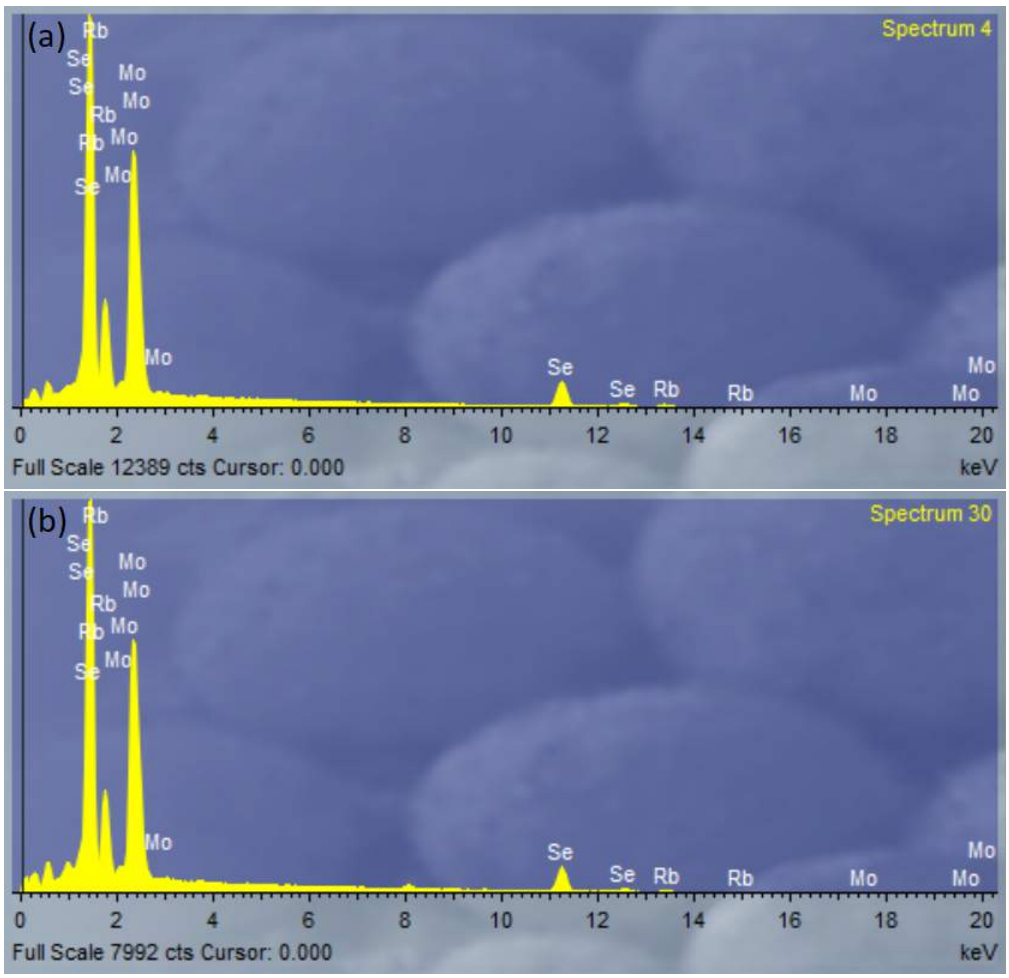

Figure 5.5: Spectra of $Rb_2Mo_6Se_6$, at a point to the right on the middle branch of the sample, (a), and at a point to the left on the bottom branch of the sample, (b). The crystal is homogeneous, and the elements in the spectra are consistent with the elements expected to be seen in this material.

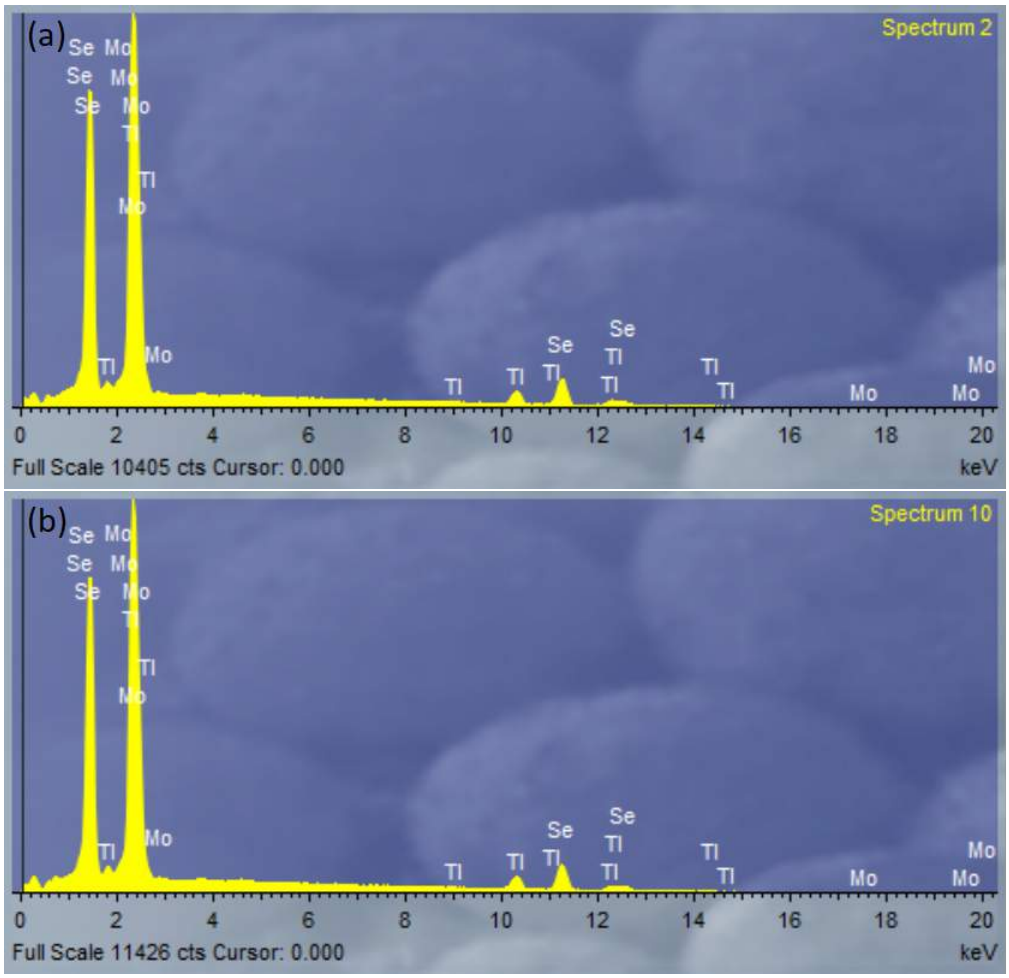

Figure 5.6: Spectra of $Tl_2Mo_6Se_6$, at a point in the middle of the sample, (a), and at a point in the upper part of the sample, (b). The crystal is homogeneous, and the elements in the spectra are consistent with the elements expected to be seen in this material.

To make an estimate of the stoichiometry, we have used the many spectra collected in different regions of the samples and averaged the weight percentages measured for each element in the sample. From these measurements, the most likely stoichiometry of the Rb sample is $Rb_2Mo_6Se_6$, as reported by Tarascon *et al.* [40]. The most likely stoichiometry of the Tl sample is $Tl_{1.5}Mo_6Se_6$, as there appear to be vacancies on the Tl sites. This will affect the fits of the data, as the model used has fully occupied Tl sites.

5.3 $M_2Mo_6Se_6$ (M=Rb, Tl) single crystal P-XAS

5.3.1 Experimental set up

The goal of this experiment was to determine if the proposed link between the unusual electronic properties observed in $M_2Mo_6Se_6$ could be due to the formation of CDWs in this family of materials. For this experiment we measured the P-XAS of the Se K-edge of the $M_2Se_6Mo_6$ (M = Rb, Tl) single crystals, at a range of angles and temperatures, at the XMaS beamline in the European Synchrotron Radiation Facility (ESRF), in Grenoble, France. Single crystals of the Rb and Tl analogues were grown by Dr Andrew Boothroyd's group at Oxford University, in the same procedure as reported in

[39].
The samples were glued to a puck with silver paint, an Al puck was used for the Tl sample and a Cu puck was used for the Rb sample, Figures 5.7 and 5.8. As the Se K-edge was being measured, the x-ray energies used ($> 12600eV$) were high enough that there are no absorption edges for Al, or Cu [162]. The K-edge energy for Ag ($\sim 25keV$) is much higher than the K-edge of Se.
To measure the samples the beamline was set up with the Si 111 double-crystal monochromator, and the Rh branch of the toroidal mirror was used. The single crystals grew with the c-axis along the length of the crystal. The samples were small, $\sim 3143 \times 657 \times 342\mu m$ for the Tl analogue and $\sim 3714 \times 571 \times 285\mu m$ for the Rb analogue, so the measurements were taken with a fully focused beam ($800\mu m$ x $500\mu m$). Each spectra was measured twice under the same conditions, with an energy step of $\sim 6eV$ before the absorption edge, $\sim 0.4eV$ in the XANES region, $\sim 2eV$ in the EXAFS region, and $\sim 5eV$ for the tail end of the EXAFS region, all at $5s$ per point. The measurements were taken in fluorescence mode using a Vortex Si drift detector.
The samples were rotated with respect to the c-axis to measure along different directions in the local structure, to do this one of the circles of the beamline's diffractometer was used. Due to the degrees of freedom of the diffractometer, and the direction of the c-axis in the samples, the incident angle between the beam and the sample (θ_b) remained static at 45°. This angle was chosen as it resulted in the best balance of a large fluorescence yield and a small self-absorption. The sample was oriented so that the c-axis was perpendicular to the polarisation direction of the x-ray beam when the diffractometer was set to $\theta_p = 0^o$, and parallel when it was set to $\theta_p = 90^o$. The samples, for each temperature, were measured at a range of angles with respect to the polarisation, $\theta_p = 0^o, 10^o, 30^o, 50^o, 70^o, 90^o$, see Chapters 2 and 3 for more detail.
P-XAS was measured at a range of temperatures; 150K, 100K, 75K, 8K (only the Tl analogue), and 4K. This range of temperatures was selected as the proposed transitions in both materials were to occur below 100K. In the $Rb_2Mo_6Se_6$ a metal to insulator transition occurs at ∼100K to 150K, sample dependent, while the $Tl_2Mo_6Se_6$ becomes superconducting at ∼6.2K. To reach these temperatures a liquid He cryostat with a Joule Thomson stage was used, available at the XMaS beamline and developed by the cryogenics laboratory at the Institut Laue Langevin, Grenoble.

Figure 5.7: $Tl_2Mo_6Se_6$ sample, glued onto the Al puck with Ag paint. The puck is attached to the sample holder used at the beamline.

Figure 5.8: $Rb_2Mo_6Se_6$ sample, glued onto the Cu puck with Ag paint. The puck is attached to the sample holder used when taking SEM measurements.

The Tl LIII-edge is at the same binding energy as the Se K-edge, at $12658eV$, meaning both the Tl and Se sites were excited for the $Tl_2Mo_6Se_6$ measurements. However the emission lines are at different energies so the window on the fluorescence detector was set up to ensure that only the emission from the Se K-edge would be measured (energy range $10734.95eV$ to $11483.9eV$ for the $K\alpha_1$ emission line for Se at $11222.4eV$). The closest Tl emission lines are the $L\alpha_1$, at $10268.5eV$, or the $L\beta_1$, at $12213.3eV$, both of which are far enough away from the window range to be certain that only the Se fluorescence was detected for this experiment. The Tl LIII line will also have a lower intensity of the Se K line, therefore it would not saturate the detector. We also made sure that the total counts did not saturate the detector.

5.3.2 $Rb_2Mo_6Se_6$ results

All of the data measured from this experiment has been through an initial data processing as described in Chapter 3.
The XAS for each temperature and angle were calibrated in energy assuming the Se was in a -2 oxidation state, as reported in [40], resulting in an energy shift of $-2eV$. The value for E_0 changed with respect to the angle between the polarisation and the c-axis (θ_p), the values it was set for each angle and temperature can be seen in Table 5.1. The values for E_0 were set based on the position of the first peak in the derivative of the XANES (see Figures 5.9b and 5.10b). The same spline range in k was used for all temperatures and angles, 0 to 14Å^{-1}. The background parameter (Rbkg) was set to 1.5Å for all data sets. When normalising the data the pre-edge range was the same for each temperature and angle, and was set to -150 to $-36.7eV$, with respect to E_0. The post-edge range was also the same for each temperature and angle, and was set to 94.2 to $616.4eV$, with respect to E_0. The normalisation order was set to 3, for all data sets. For the FT-EXAFS the same range in k was used in the transformation for each temperature and angle, 3 to 13Å^{-1}.

Table 5.1: E_0's (eV) of the Se K-edge, of $Rb_2Mo_6Se_6$, for all θ_p's and temperatures measured.

	Temperature (K):			
θ_p:	4	75	100	150
0°	12657.2±0.4	12656.8±0.4	12657.0±0.4	-
10°	12657.2±0.4	12657.3±0.4	12657.2±0.4	12656.9±0.4
30°	12657.2±0.4	12657.3±0.4	12657.0±0.4	12657.2±0.4
50°	12657.2±0.4	12657.4±0.4	12657.3±0.4	12657.3±0.4
70°	12657.5±0.4	12657.5±0.4	12657.5±0.4	12657.6±0.4
90°	12657.8±0.4	12657.8±0.4	12657.8±0.4	12657.8±0.4

XANES

The reported oxidation state of the Se ions in this material is -2 [40]. After the energy calibration, the position of the first peak in the XANES is in line with the Se ions being in this oxidation state [163].
From the XANES (Figures 5.9 and 5.10) it can be seen that there is a small change in the position of the absorption edge, as a function of the angle between the polarisation

and the crystal. There is also a difference in the intensities of the first peak, where the intensity of the absorption is greatest for the 90° data. As the Se is in an oxidation state of -2, the K-edge is probing mainly the $1s \rightarrow 5p$ transition. The XANES suggest that the unoccupied states along the c-axis are found at a lower energy than those along the ab-plane, allowing the $1s \rightarrow 5p_z$ transition to occur more freely. There are small changes in the XANES with respect to temperature for the data measured close to the ab-plane, $\theta_p = 10^o$ (see Figure 5.11). Where the intensity of the first peak varies slightly with temperature. However there are no changes in the XANES with respect to temperature for the data measured along the c-axis, $\theta_p = 90^o$. This suggests that the possible distortion caused by the predicted CDW mainly affects the local electronic structure of the Se ions along the ab-plane.
The XANES for the other temperatures can be seen in Appendix B.

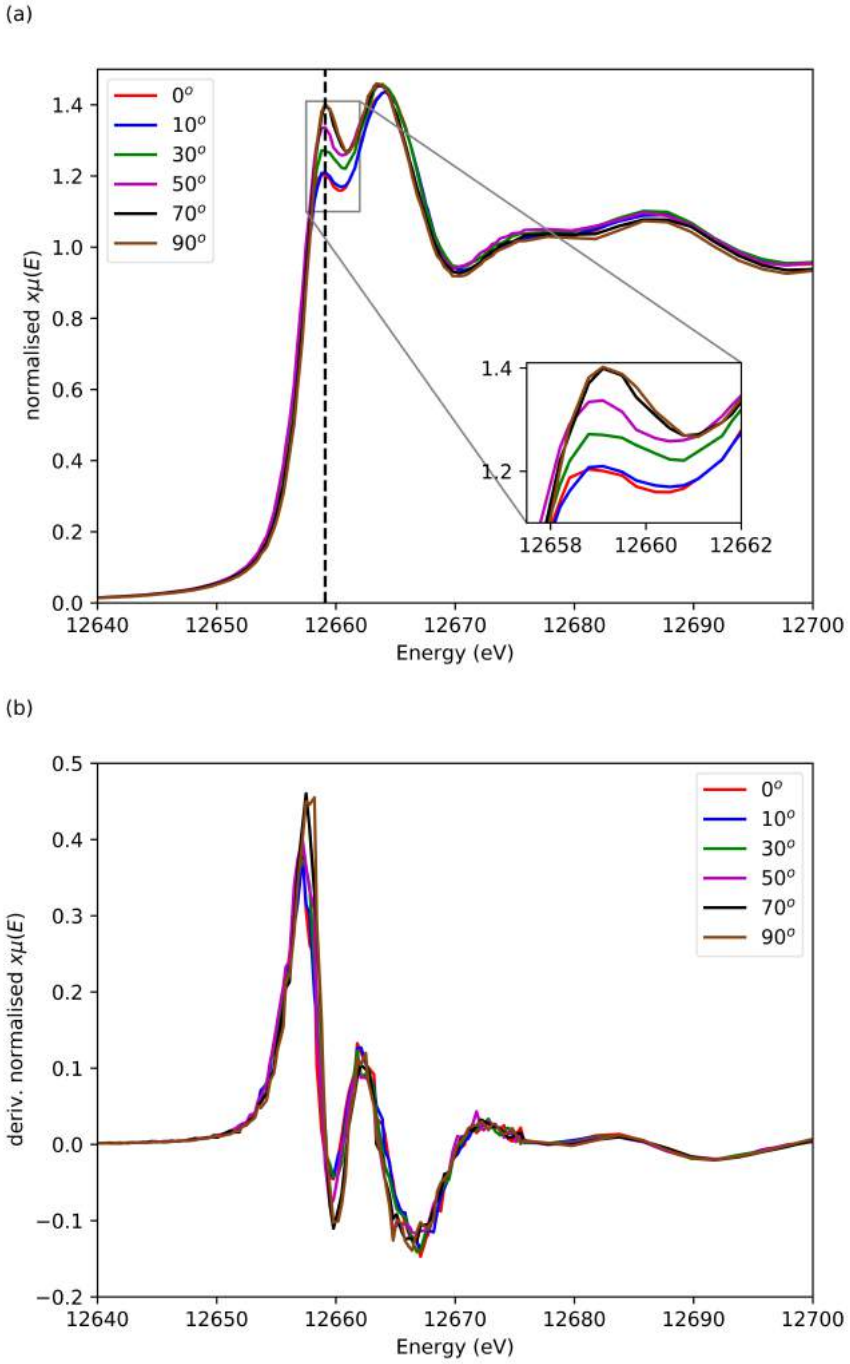

Figure 5.9: XANES, (a), and first derivative, (b), of the Se K-edge of $Rb_2Mo_6Se_6$, at 4K and different angles, with respect to the c-axis.

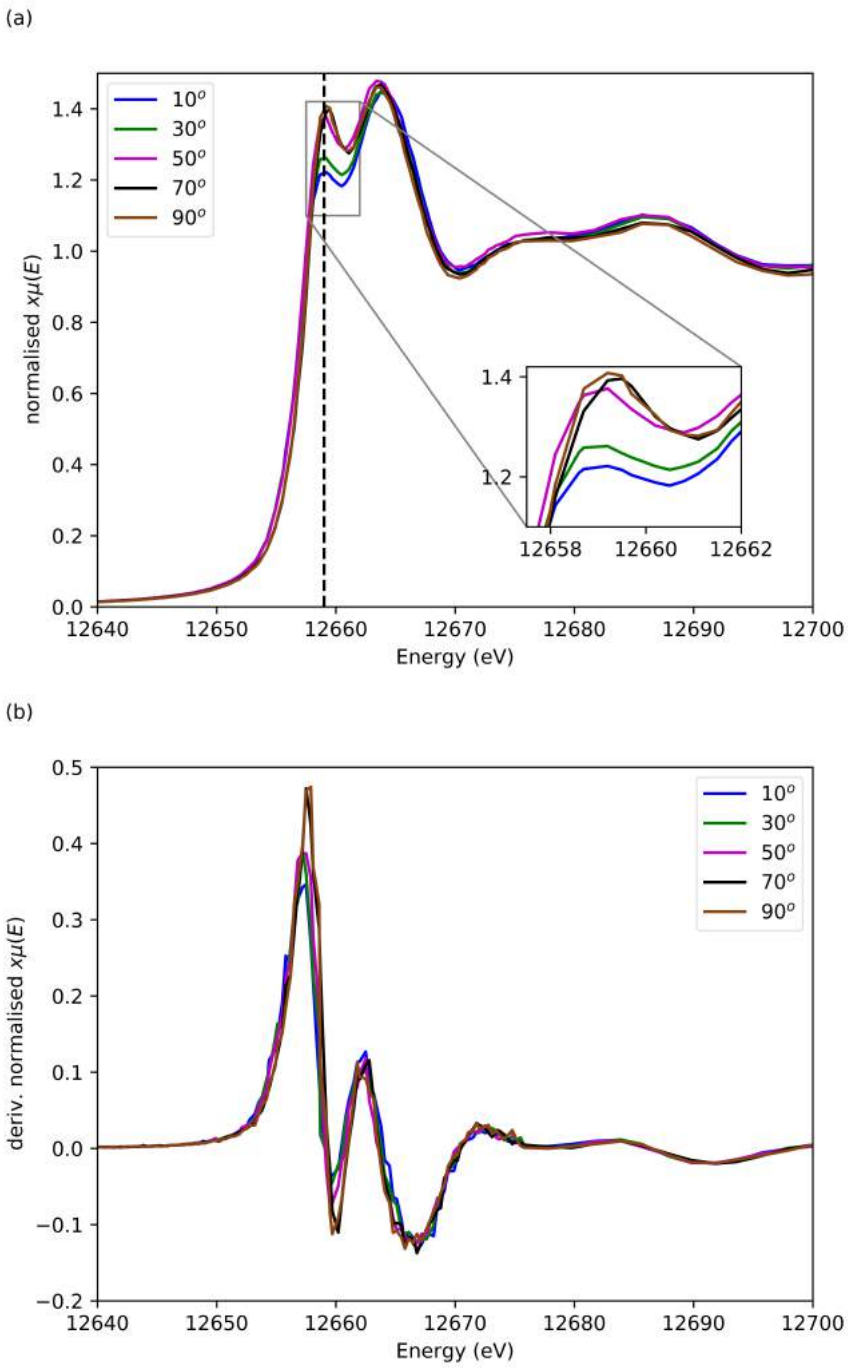

Figure 5.10: XANES, (a), and first derivative, (b), of the Se K-edge of $Rb_2Mo_6Se_6$, at 150K and different angles, with respect to the *c*-axis.

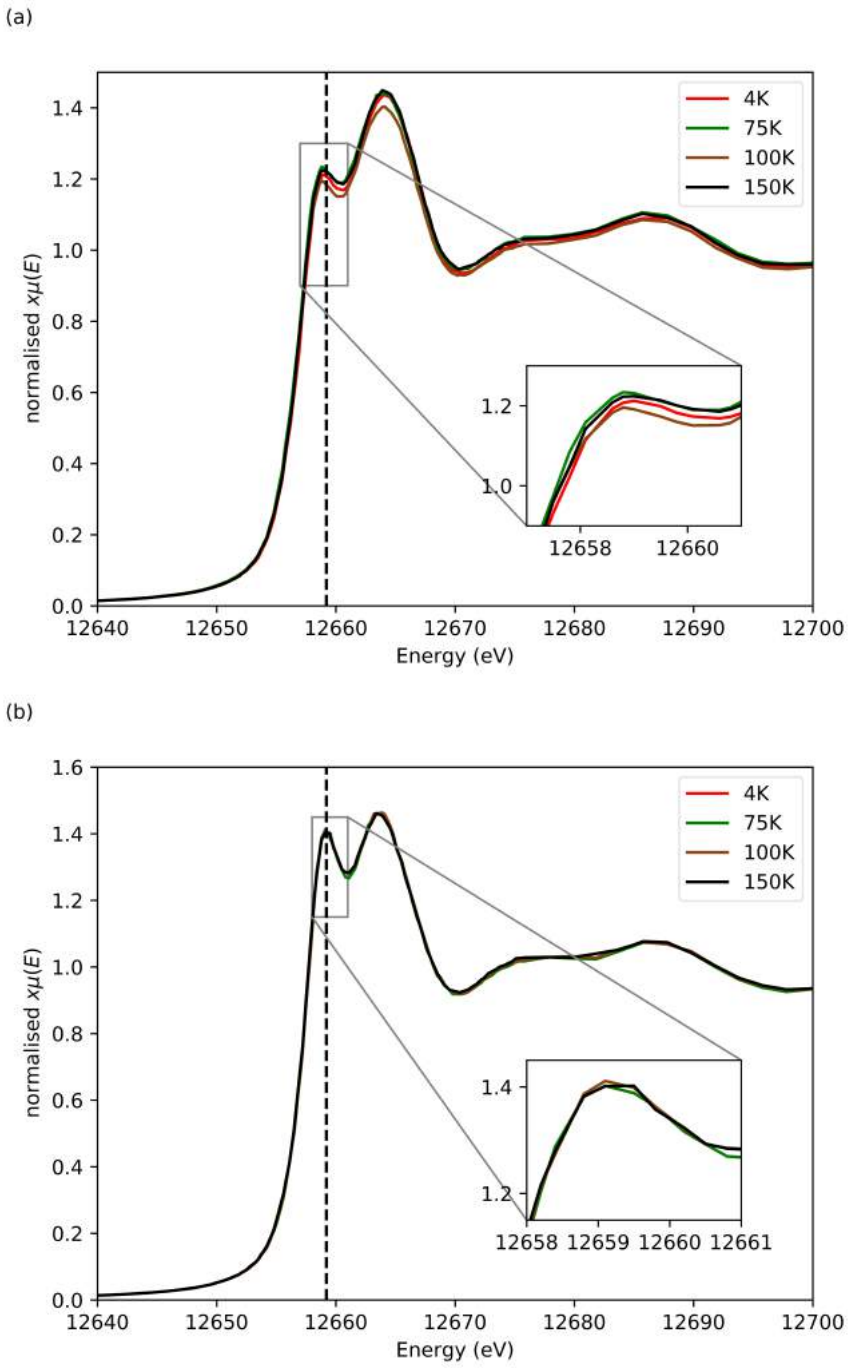

Figure 5.11: XANES of the Se K-edge of $Rb_2Mo_6Se_6$, at 10° (a) and 90° (b), at different temperatures.

EXAFS

Figures 5.12 and 5.13 show the EXAFS and FT-EXAFS data of the Se K-edge, at 4K and 150K, respectively. EXAFS for the other temperatures can be seen in Appendix B. The EXAFS and FT-EXAFS have been plotted with a k-weight of 2, and with a Fourier transform k-range of 3 to 13Å^{-1}. The FT-EXAFS presented have not been phase corrected, meaning the peak positions will not match the predicted positions from the model.
The path lengths and their angles, with respect to the c- and a-axis, can be seen in Table 5.2, obtained from the model [42].

Table 5.2: Structural information, of the single scattering paths, obtained from the room temperature model of $Rb_2Mo_6Se_6$, seen in Figure 5.1 [42].

Path	Path distance (Å)	θ_i (^{o})	ϕ_i (^{o})	Weighting of path
1st Se-Mo	2.620	90	38.14	1/3
“ ”	“ ”	“ ”	39.10	1/3
“ ”	“ ”	“ ”	-20.90	1/3
“ ”	“ ”	“ ”	-21.86	1/3
“ ”	“ ”	“ ”	-80.90	1/3
“ ”	“ ”	“ ”	-81.86	1/3
2nd Se-Mo	2.697	33.56	8.79	1/3
“ ”	“ ”	146.44	“ ”	1/3
“ ”	“ ”	33.56	68.79	1/3
“ ”	“ ”	146.44	“ ”	1/3
“ ”	“ ”	33.56	-51.21	1/3
“ ”	“ ”	146.44	“ ”	1/3
1st Se-Rb	3.514	90	57.50	1/3
“ ”	“ ”	“ ”	-2.50	1/3
“ ”	“ ”	“ ”	-62.50	1/3
1st Se-Se	3.769	53.39	8.62	2/4
“ ”	“ ”	126.61	“ ”	2/4
“ ”	“ ”	53.39	68.62	1/4
“ ”	“ ”	126.61	“ ”	1/4
“ ”	“ ”	53.39	-51.38	1/4
“ ”	“ ”	126.61	“ ”	1/4
2nd Se-Se	4.05	56.3	-15.61	2/5
“ ”	“ ”	123.7	“ ”	2/5
“ ”	“ ”	56.3	-75.61	2/5
“ ”	“ ”	123.7	“ ”	2/5
“ ”	“ ”	56.3	44.39	1/5
“ ”	“ ”	123.7	“ ”	1/5

The position of the peaks in the EXAFS signal, at the highest and lowest temperature measured (see Figures 5.12 and 5.13), change with respect to the angle between the polarisation and the c-axis. There is a distinct change in the structure of the EXAFS signal at $k\sim$ 7 to 8Å^{-1}, this is seen in both temperatures. There is also a clear change in the structure of the FT-EXAFS, where the peaks past $\sim$ 4Å change with respect to the angle measured. The change is similar for both temperatures, where there are two peaks visible for the signal closer to the ab-plane (low θ_p). Whereas, for

the measurements closer to the c-axis (high θ_p), there is only one visible peak. This could be due to interference between scattering paths causing the two peaks to lose distinction at higher θ_p's.
Comparing the signal of the two extreme angles measured (see Figures 5.14 and 5.15) there are visible changes for the measurement close to the ab-plane ($\theta_p = 0^o$) and along the c-axis ($\theta_p = 90^o$). For the signal close to the ab-plane there is a change in the intensities of the peaks found around $k\sim$ 9 to 11Å^{-1}. However the overall structure of the signal remains similar for all temperatures. For the signal along the c-axis there is a clear change in the intensities for $k>$ 7Å^{-1}. There is also a change in the structure of the signal around $k\sim$ 7 to 11Å^{-1}. This suggests that there is a possible structural transition that is affecting the local structure along the c-axis.
The FT-EXAFS measured close to the ab-plane (see Figure 5.15) shows the expected broadening of the peaks due to thermal fluctuations as the temperature is increased. This is the case for the first three peaks. While along the c-axis there are changes in the signal which cannot be fully explained with just increased thermal fluctuations (see Figure 5.14). These changes suggest the presence of a structural distortion with respect to temperature. There is a visible change in the second peak, where at 4K it is two peaks and as the temperature is increased the second peak is completely suppressed. The position of this peak ($\sim$ 3Å) suggests it most likely corresponds to a Se-Rb scattering path. The change in this peak suggests that there may be two Se-Rb components at low temperature, which cannot be distinguished as the temperature increases. This distortion is clearer in the third peak seen in the FT-EXAFS, as the peak becomes sharper as the temperature increases, which suggests a structural transition is occurring. As the third peak is found at $\sim$ 3.7Å, it most likely corresponds to the first Se-Se scattering path, it may also be affected by the tail of the second Se-Se scattering path. It appears as if a shoulder of the peak is being suppressed as the temperature is increased, this suggests that there is a change in both the first and second Se-Se scattering paths. For both the extreme angles measured, the fourth and fifth peaks show hints of a structural distortion as the peaks become more distinct as the temperature increases. These peaks have many single scattering and multiple scattering path contributions, therefore it would be difficult to pinpoint the cause of the distortion in these peaks.

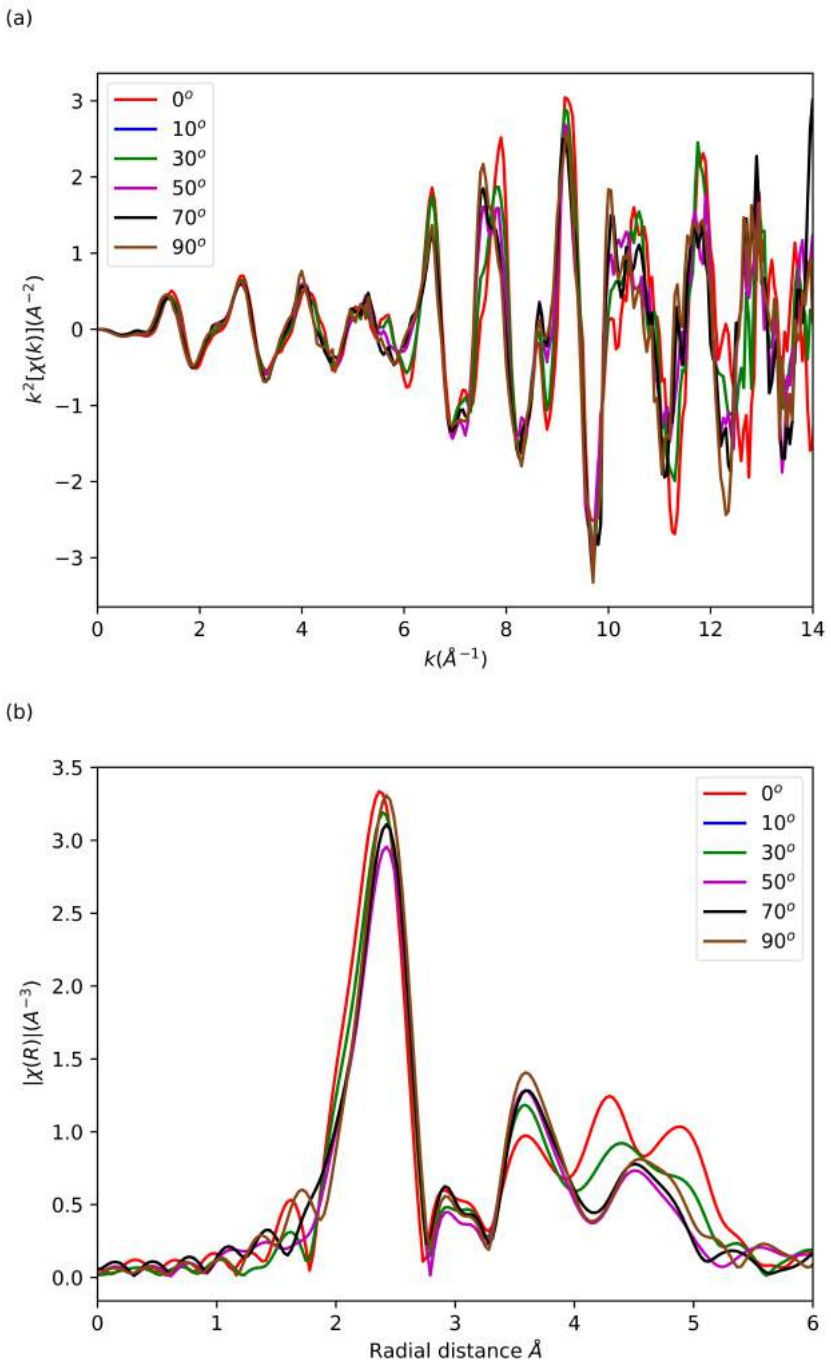

Figure 5.12: EXAFS, (a), and FT-EXAFS, (b), of the Se K-edge, at 4K, of $Rb_2Mo_6Se_6$, at different angles.

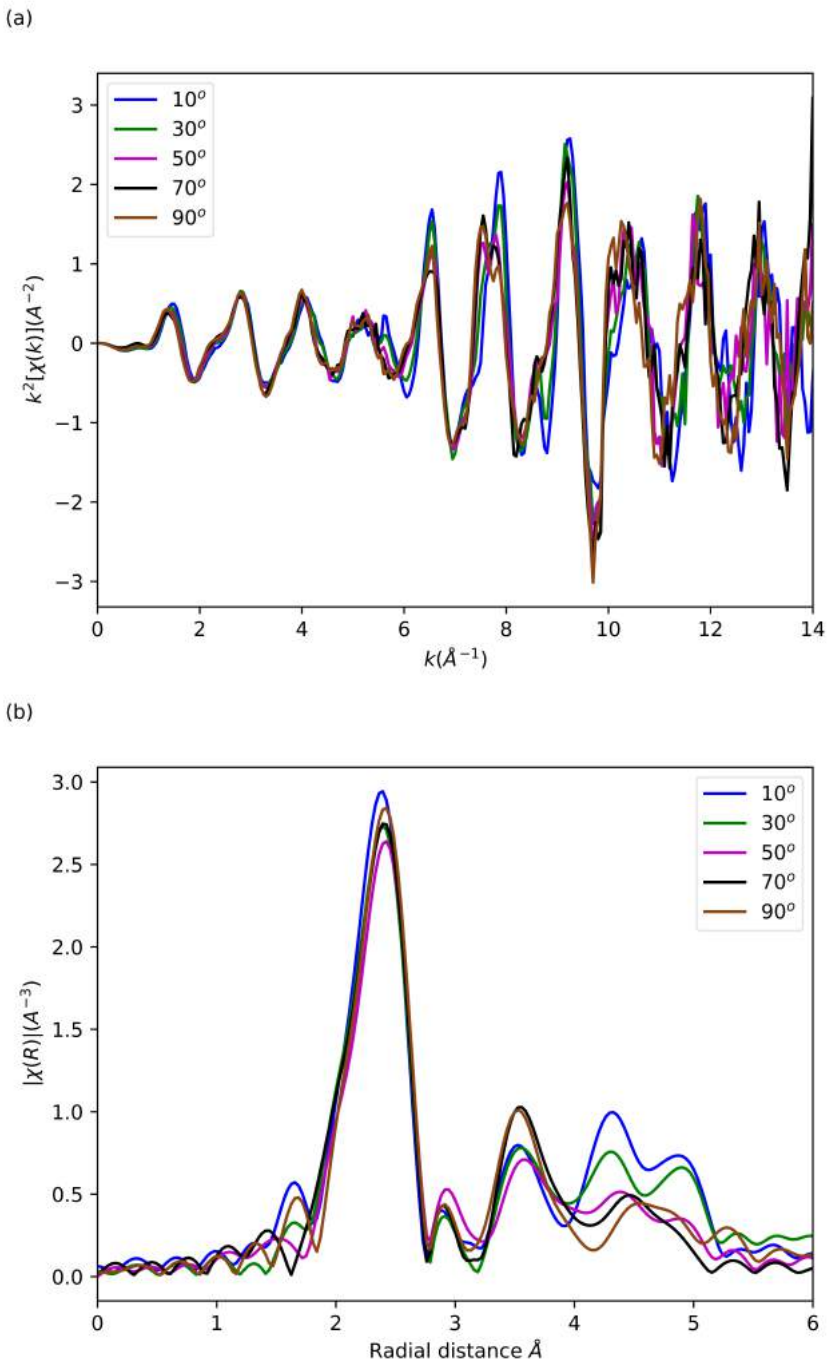

Figure 5.13: EXAFS, (a), and FT-EXAFS, (b), of the Se K-edge, at 150K, of $Rb_2Mo_6Se_6$, at different angles.

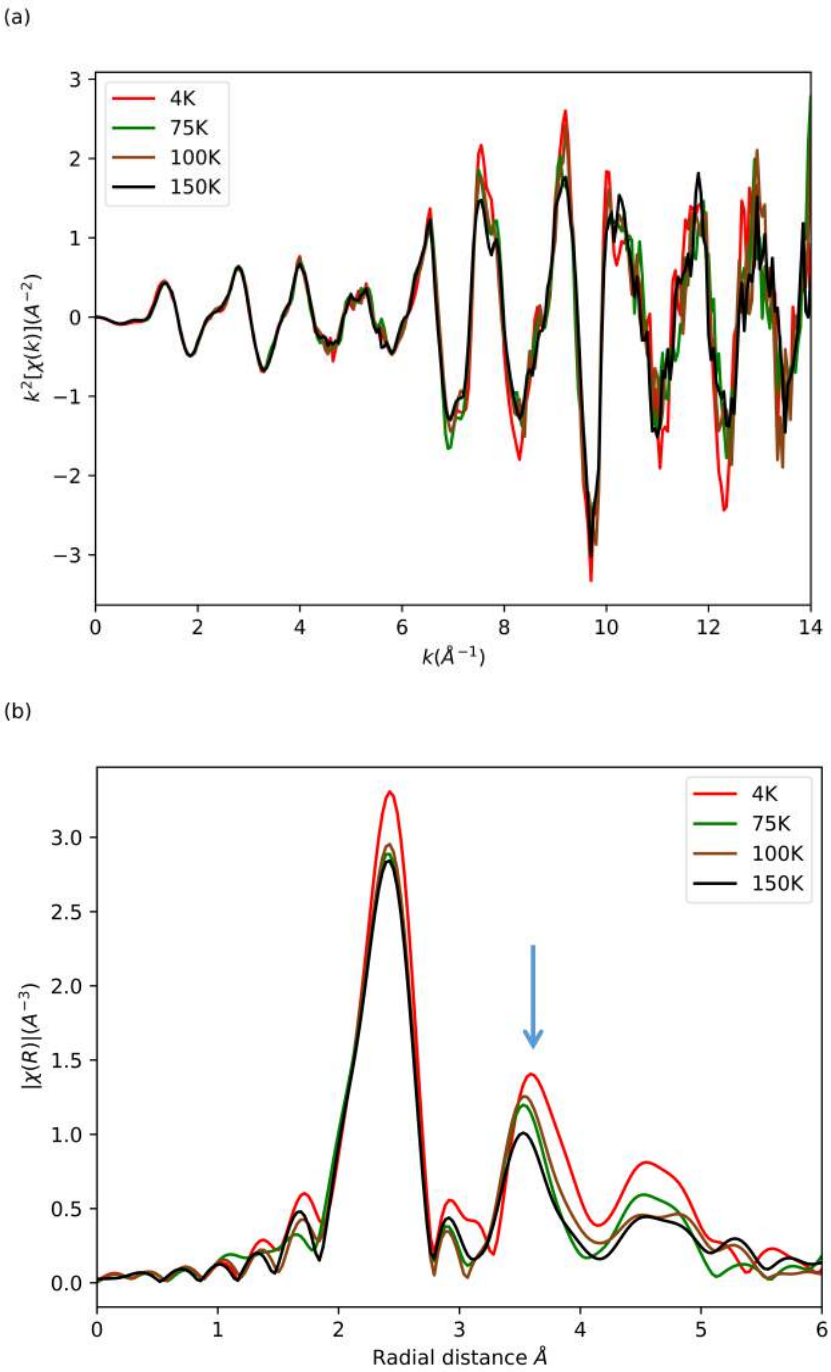

Figure 5.14: EXAFS, (a), and FT-EXAFS, (b), of the Se K-edge, at 90°, of $Rb_2Mo_6Se_6$, at different temperatures.

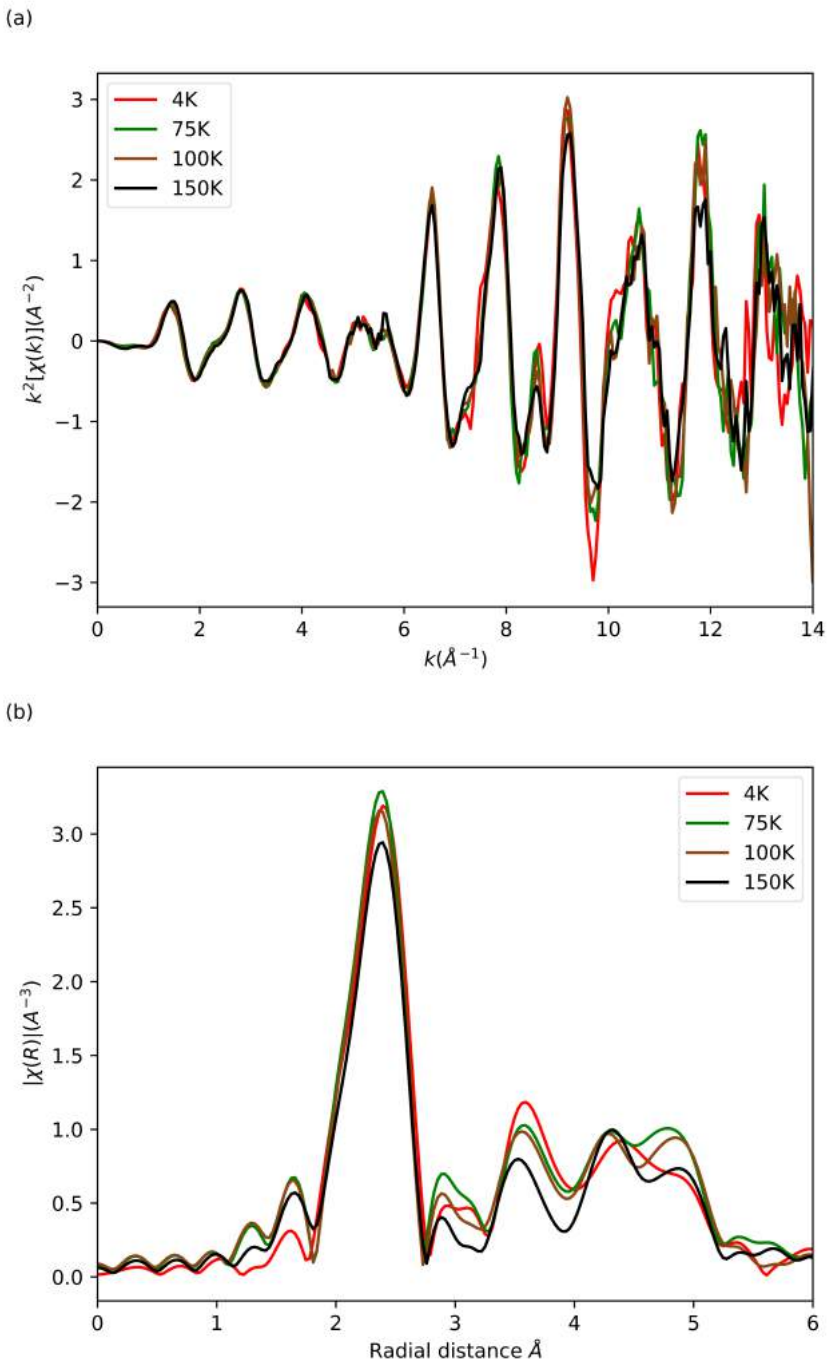

Figure 5.15: EXAFS, (a), and FT-EXAFS, (b), of the Se K-edge, at 10°, of $Rb_2Mo_6Se_6$, at different temperatures.

Fit of EXAFS

The model used in the fits was produced from a refinement to diffraction data which was measured at 40K [42]. As the fit is obtained by modelling an averaged theoretical EXAFS signal (a default FEFF output), obtained from this model, a weighting factor needs to be introduced to make the averaged theoretical EXAFS equivalent to the EXAFS along one direction. The weighting factor is discussed in full in Chapter 3. From Figure 5.16 it can be seen that there is more than one distinct scattering path of the same length within the unit cell. This is due to the angles the path is making with respect to the c- and a-axis, and needs to be taken into account when fitting the data. The path lengths are degenerate, however the θ_i and ϕ_i values change. This is accounted for in the weighting factor used in the fits. The degeneracy (N) of each single scattering path has been set to 1. This parameter cannot be refined in ARTEMIS, so the amplitude reduction factor (S_0^2) takes into account changes in N. The value for S_0^2 reported for the fits is a global factor, so it accounts for all factors affecting the amplitude. This means it cannot directly be used to infer changes in N from the fits.
The refined parameters for the fits to the Se K-edge EXAFS data, shown in Figures 5.17 to 5.20, can be found in Table 5.3. The fits to the other temperatures can be seen in Appendix B. All parameters are within their acceptable ranges, therefore the fits are considered good. Fitting was carried out in R space, with k weightings of 1, 2, and 3, using 28 of 69 independent parameters for the 4K data, and 20 of 71 independent parameters for the 150K data. The number of independent parameters is similar for the other temperatures. The angles θ_i and ϕ_i (in the weighting factor) for the single scattering paths have been set to those calculated from the model (see Table 5.2)[1]. As all angles measured are fit simultaneously, this additional data opens up more guess parameters for the fit. To account for the distinct paths each single scattering path is separated and the amplitude is multiplied by a weighting that corresponds to their frequency in the unit cell (see Table 5.2). The same single scattering paths were used in the fits for each temperature, they were calculated from the model up to ~ 4.2Å.
The fits resulted in a R-factor of 0.021, and 0.024, for the 4K data, and 150K data, respectively. The R-factor for the fits to the other temperatures is between these values. The first Se-Mo and Se-Rb paths do not contribute to the fit along the c-axis, this is consistent with the theoretical model as they should have no contribution to the signal measured perpendicular to the paths. Also the second Se-Rb scattering path cannot be fit to the structure as it produces unreasonable parameters, such as $\Delta R \sim 0.3$Å, and $\sigma^2 \sim -0.004$Å^2. This suggests it is too delocalised to contribute to the EXAFS.

[1]The calculation and treatment of the angles in the weighting factor is discussed in Chapter 3.

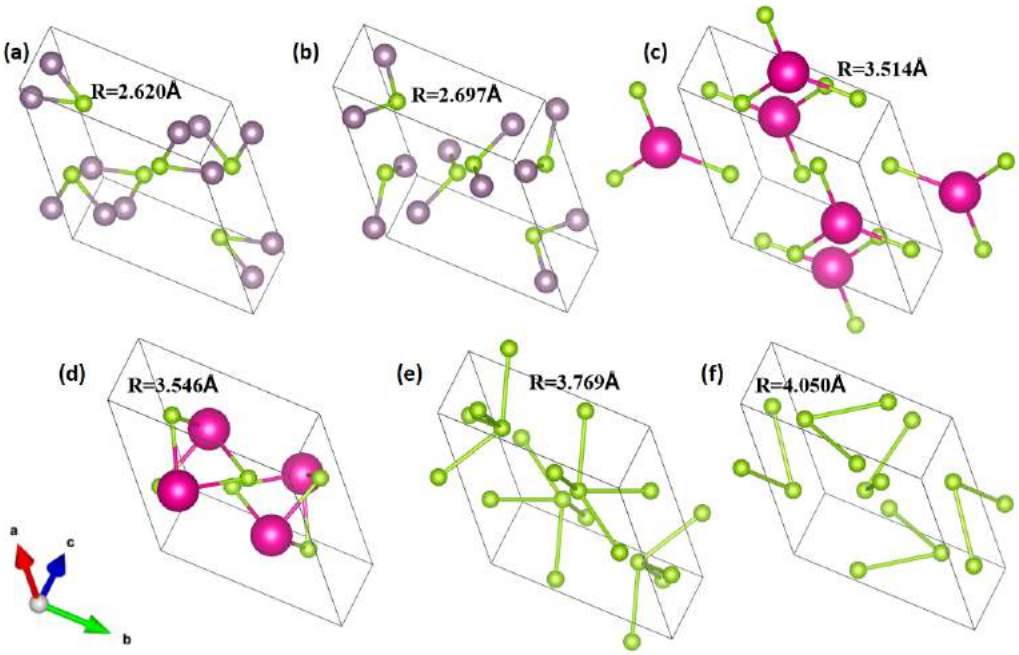

Figure 5.16: The single scattering paths used in the fit of the Se K-edge $Rb_2Mo_6Se_6$ data. Where the Se atoms are green, Mo atoms are purple, and the Rb atoms are pink. With (a) 1st Se-Mo, (b) 2nd Se-Mo, (c) 1st Se-Rb, (d) 2nd Se-Rb, (e) 1st Se-Se, and (f) 2nd Se-Se.

Table 5.3: Fit parameters for the Se K-edge EXAFS of the $Rb_2Mo_6Se_6$ single crystal, alongside the value obtained from the room temperature model [42]. The degeneracy (N) of each path was set to 1. The azimuthal angle of the polarisation with respect to the a-axis, ϕ, was set to 60°.

	Temperature (K):				
Parameter:	4	75	100	150	Model (40K) [42]
Reduced χ^2	69.67	53.14	39.30	40.50	-
S_0^2 at 0°	0.90±0.08	0.88±0.06	0.85±0.06	-	-
S_0^2 at 10°	0.89±0.07	0.92±0.06	0.86±0.06	0.91±0.07	-
S_0^2 at 30°	0.93±0.07	0.90±0.05	0.87±0.05	0.89±0.06	-
S_0^2 at 50°	0.89±0.08	0.89±0.06	0.80±0.06	0.86±0.07	-
S_0^2 at 70°	0.9±0.1	0.94±0.08	0.90±0.07	0.87±0.07	-
S_0^2 at 90°	1.0±0.1	0.82±0.08	0.83±0.07	0.87±0.07	-
ΔE_0 (eV) at 0°	4.2±0.8	5.3±0.6	4.3±0.6	-	-
ΔE_0 (eV) at 10°	2.5±0.8	4.1±0.6	4.7±0.6	4.4±0.7	-
ΔE_0 (eV) at 30°	4.2±0.8	3.8±0.5	3.7±0.5	3.5±0.6	-
ΔE_0 (eV) at 50°	3.6±0.9	3.3±0.6	3.3±0.7	2.7±0.7	-
ΔE_0 (eV) at 70°	4±1	3.1±0.8	4.1±0.7	3.6±0.7	-
ΔE_0 (eV) at 90°	3±1	3.4±0.8	4.0±0.8	3.1±0.7	-
1st Se-Mo R (Å)	2.61±0.00	2.62±0.00	2.62±0.00	2.61±0.00	2.62
1st Se-Mo σ^2 (Å^2)	0.0006±0.0005	0.0010±0.0004	0.0007±0.0004	0.0016±0.0005	-
2nd Se-Mo (up) R (Å)	2.68±0.01	2.66±0.00	2.66±0.00	2.66±0.00	2.697
2nd Se-Mo (up) σ^2 (Å^2)	0.0002±0.0009	0.0016±0.0004	0.0015±0.0004	0.0021±0.0004	-
2nd Se-Mo (down) R (Å)	2.62±0.02	“ ”	“ ”	“ ”	2.697
2nd Se-Mo (down) σ^2 (Å^2)	0.002±0.002	“ ”	“ ”	“ ”	-
1st Se-Rb R (Å)	3.46±0.02	3.47±0.01	3.48±0.02	3.49±0.04	3.514
1st Se-Rb σ^2 (Å^2)	0.004±0.003	0.002±0.001	0.004±0.002	0.008±0.005	-
1st Se-Se (up) R (Å)	3.70±0.03	3.70±0.01	3.713±0.009	3.70±0.01	3.769
1st Se-Se (up) σ^2 (Å^2)	0.007±0.004	0.005±0.001	0.0048±0.0009	0.006±0.001	-
1st Se-Se (down) R (Å)	3.66±0.07	“ ”	“ ”	“ ”	3.769
1st Se-Se (down) σ^2 (Å^2)	0.009±0.009	“ ”	“ ”	“ ”	-
2nd Se-Se (up) R (Å)	4.01±0.02	4.07±0.01	4.07±0.01	4.07±0.01	4.05
2nd Se-Se (up) σ^2 (Å^2)	-0.007±0.002	-0.0015±0.0006	-0.0009±0.0006	0.0000±0.0007	-
2nd Se-Se (down) R (Å)	4.12±0.02	“ ”	“ ”	“ ”	4.05
2nd Se-Se (down) σ^2 (Å^2)	-0.007±0.002	“ ”	“ ”	“ ”	-

A good fit was produced by using the model and refining this against the Se K-edge EXAFS, the path distances and DWs were allowed to change for each temperature and are fit simultaneously for each angle. The sum of all the relevant single scattering contributions to the Se K-edge EXAFS of $Rb_2Mo_6Se_6$, at 4K and 150K, are shown in Figures 5.17 and 5.18 fitted against the EXAFS data, respectively. The FT-EXAFS data was only fit up to ~ 4.2Å, as evidence of a distortion can already be observed in this range, in the broadening of the third peak (~ 3.6Å) at 4K (see Figure 5.14).
Figures 5.19 and 5.20 show the fits for the two extreme angles, that were measured at all temperatures, both angles can be modelled reasonably well. The best fit of the data at 4K, occurred when the 2nd Se-Mo scattering path was separated by its θ_i values, to its 'up' ($\theta_i = 146.44^o$) and 'down' ($\theta_i = 33.56^o$) components. Also when the paths that contributed to the third peak were separated into their 'up' and 'down' components. For the 1st Se-Se path it is $\theta_i = 126.61^o$ ('up') and $\theta_i = 53.39^o$ ('down'), and for the 2nd Se-Se path it is $\theta_i = 123.7^o$ ('up') and $\theta_i = 56.3^o$ ('down'). The separation did not produce reasonable parameters for the other temperatures, such as negative DW's outside of error, for paths close to the central atom, and large ΔR values. Suggesting that a distortion in the structure occurs below 75K (this is also hinted at in the experimental data, see Figures 5.14 and 5.15). The fit suggests that a buckling may be occurring where one Se-Mo layer will be shifted down slightly in the structure, and adjacent $(Mo_3Se_3)_\infty$ chains move up and down with respect to each other.
Alternative approaches to model this distortion were attempted, one method was to allow the θ_i values to be free to vary as a guess parameter. This was attempted with different combinations of paths with a variable θ_i however the differences between the model and values guessed by the fit were very large, so it was unclear if the fit was falling into a false minima. Another method attempted was to introduce a 'twist' parameter (ϕ_t) which would affect the values for ϕ_i for the scattering paths. This did not produce viable fits, as the parameters did not improve, and the fit was not visibly different. A 'buckling' parameter (θ_{buc}) was also introduced which would affect the values for θ_i for the scattering paths, but this produced the same result as the 'twist' parameter.

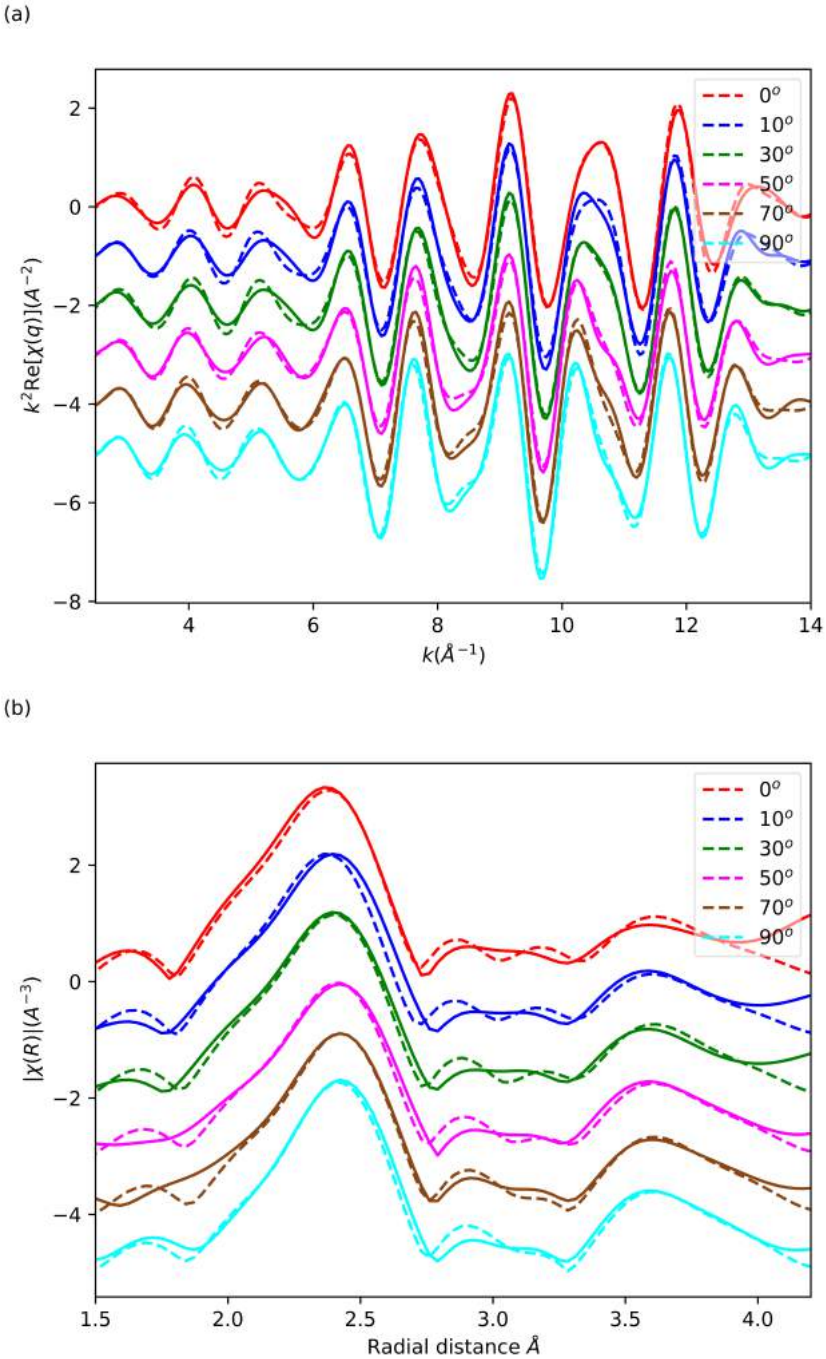

Figure 5.17: Fit of the Se K-edge at 4K, in q space (a) and R space (b). All angles measured and fitted are presented in this plot. The solid line corresponds to the experimental data and the dashed line corresponds to the fit.

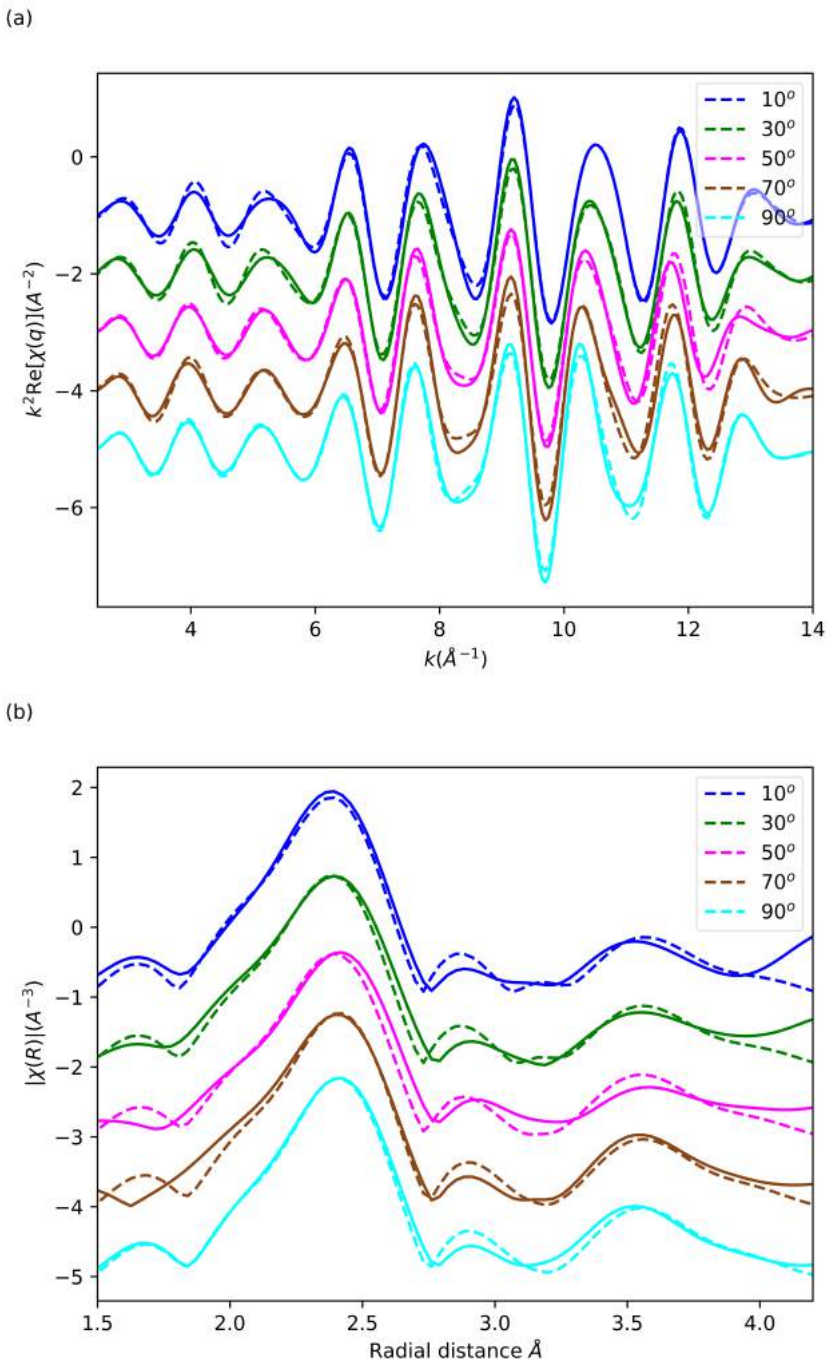

Figure 5.18: Fit of the Se K-edge at 150K, in q space (a) and R space (b). All angles measured and fitted are presented in this plot. The solid line corresponds to the experimental data and the dashed line corresponds to the fit.

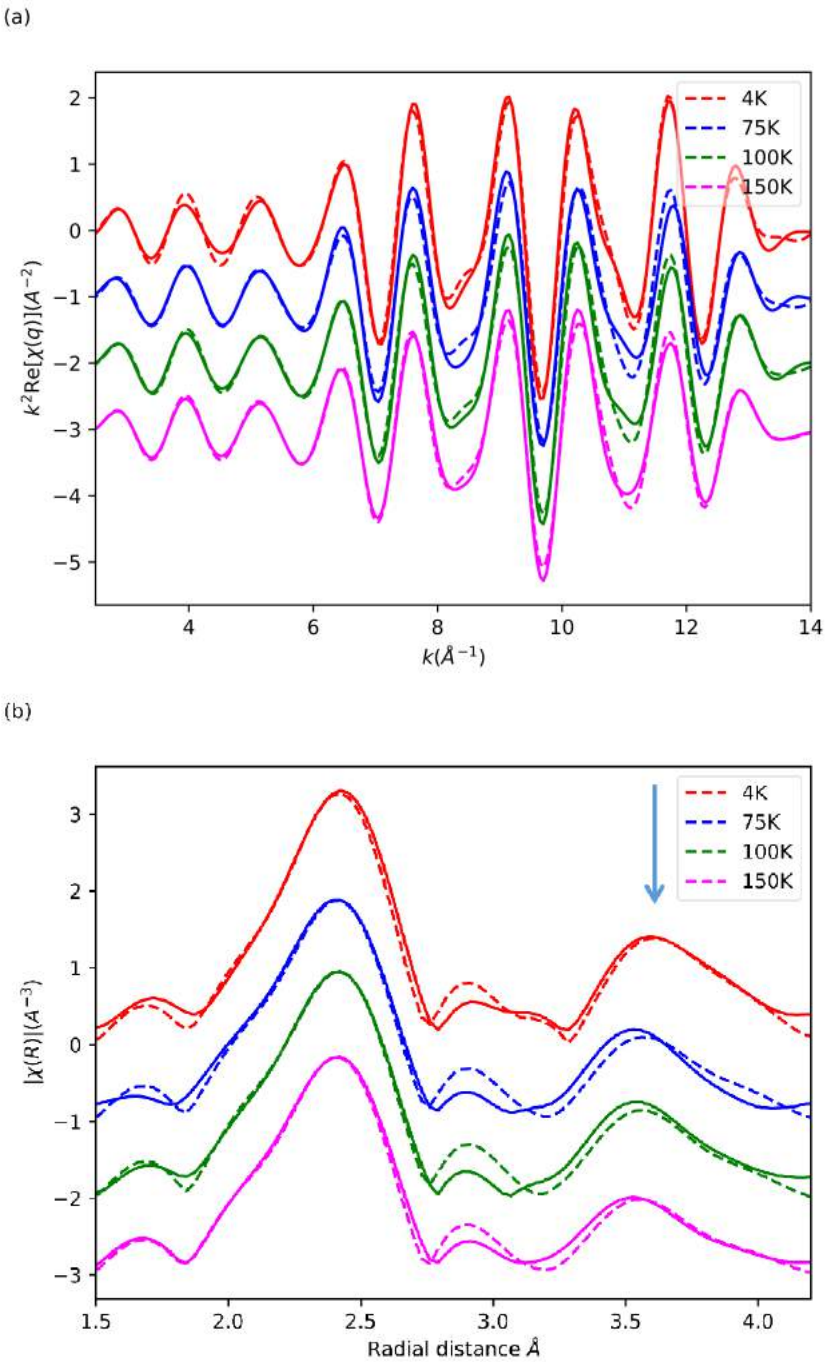

Figure 5.19: Fit of the Se K-edge at $\theta_p = 90^o$, in q space (a) and R space (b). All temperatures measured and fitted are presented in this plot. The solid line corresponds to the experimental data and the dashed line corresponds to the fit.

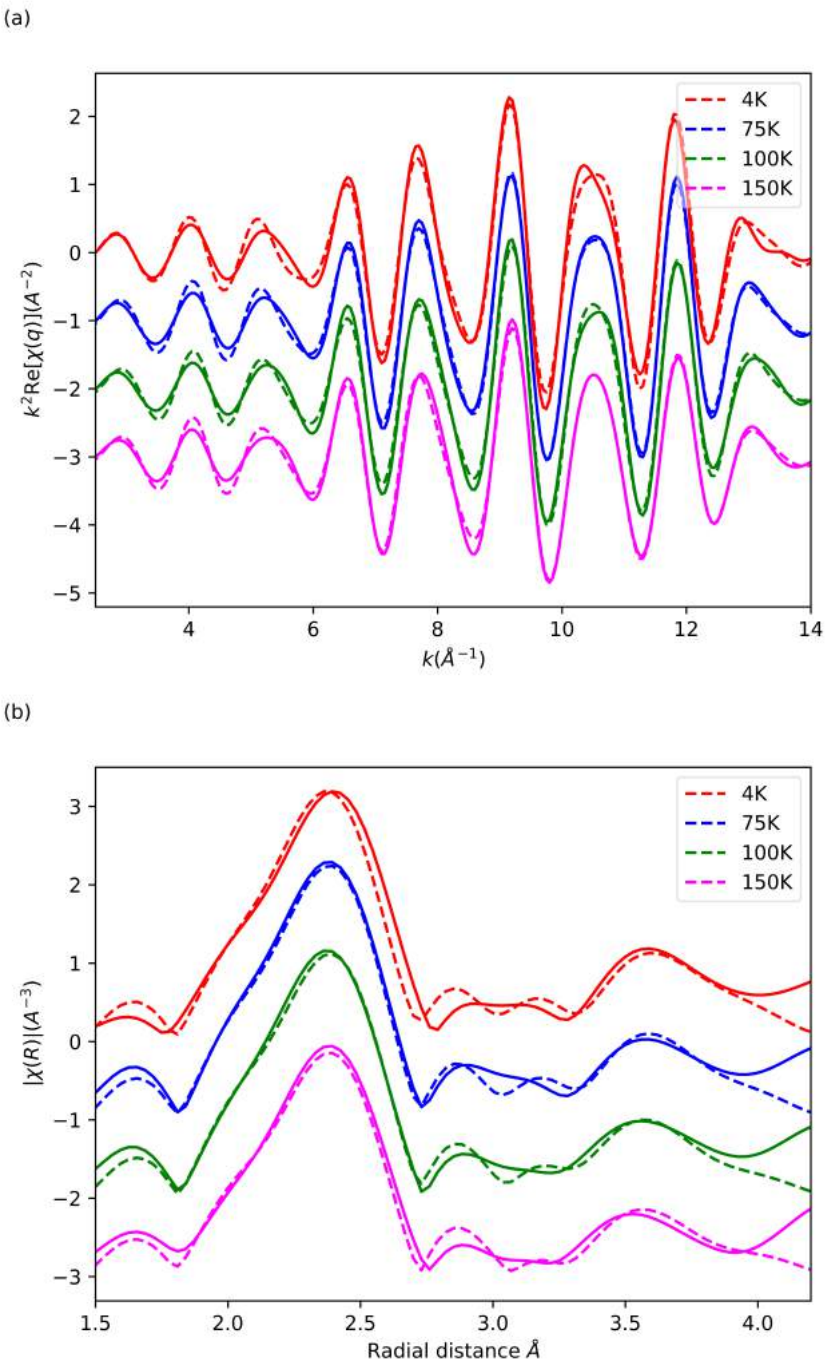

Figure 5.20: Fit of the Se K-edge at $\theta_p = 10^o$, in q space (a) and R space (b). All temperatures measured and fitted are presented in this plot. The solid line corresponds to the experimental data and the dashed line corresponds to the fit.

5.3.3 $Tl_2Mo_6Se_6$ results

For the Tl sample, the data were processed the same way as for the Rb sample, and the same energy calibration was performed. The values for E_0 (see Table 5.4) were set based on the position of the first peak in the derivative of the XANES (see Figures 5.21b and 5.22b). The same spline range in k was used for all temperatures and angles, 0 to 15Å^{-1}. The background parameter (Rbkg) was set to 1.4Å for all data sets. When normalising the data the pre-edge range was the same for each temperature and angle, and was set to -150 to $-35.3eV$, with respect to E_0. The post-edge range was also the same for each temperature and angle, and was set to 94.6 to $709.6eV$, with respect to E_0. The normalisation order was set to 3, for all data sets. For the FT-EXAFS the same range in k was used in the transformation for each temperature and angle, 3 to 13Å^{-1}.

Table 5.4: E_0's (eV) of the Se K-edge, of $Tl_2Mo_6Se_6$, for all θ_p's and temperatures measured.

	Temperature (K):				
θ_p:	4	8	75	100	150
0°	12657.4±0.4	12657.6±0.4	12657.4±0.4	12657.5±0.4	12657.4±0.4
10°	12657.6±0.4	12657.5±0.4	12657.3±0.4	12657.5±0.4	12657.4±0.4
30°	12657.8±0.4	12657.6±0.4	12657.6±0.4	12657.6±0.4	12657.6±0.4
50°	12657.9±0.4	12657.9±0.4	12657.9±0.4	12658.0±0.4	12658.0±0.4
70°	12658.1±0.4	12658.0±0.4	12658.2±0.4	12658.1±0.4	12657.9±0.4
90°	12657.9±0.4	12658.1±0.4	12658.2±0.4	12658.1±0.4	12658.0±0.4

XANES

The reported oxidation state of the Se ions in this material is -2 [40]. After the energy calibration, the position of the first peak in the XANES is in line with the Se ions being in this oxidation state [163].
From the XANES (Figures 5.21 and 5.22) it can be seen that there is a small change in the position of the absorption edge, as a function of the angle between the polarisation and the crystal. There is a difference in the intensities of the first peak, where the intensity of the absorption is greatest for the 90° data. As the Se is in an oxidation state of -2, the K-edge is probing mainly the $1s \rightarrow 5p$ transition. The XANES results suggest that the unoccupied states along the c-axis are found at a lower energy than than those along the ab-plane, allowing the $1s \rightarrow 5p_z$ transition to occur more freely. There are some small changes in the XANES with respect to temperature for the two extreme angles measured (see Figure 5.23). However these changes do not greatly affect the position of the absorption edge (see Table 5.4).
The XANES for the other temperatures can be seen in Appendix B.

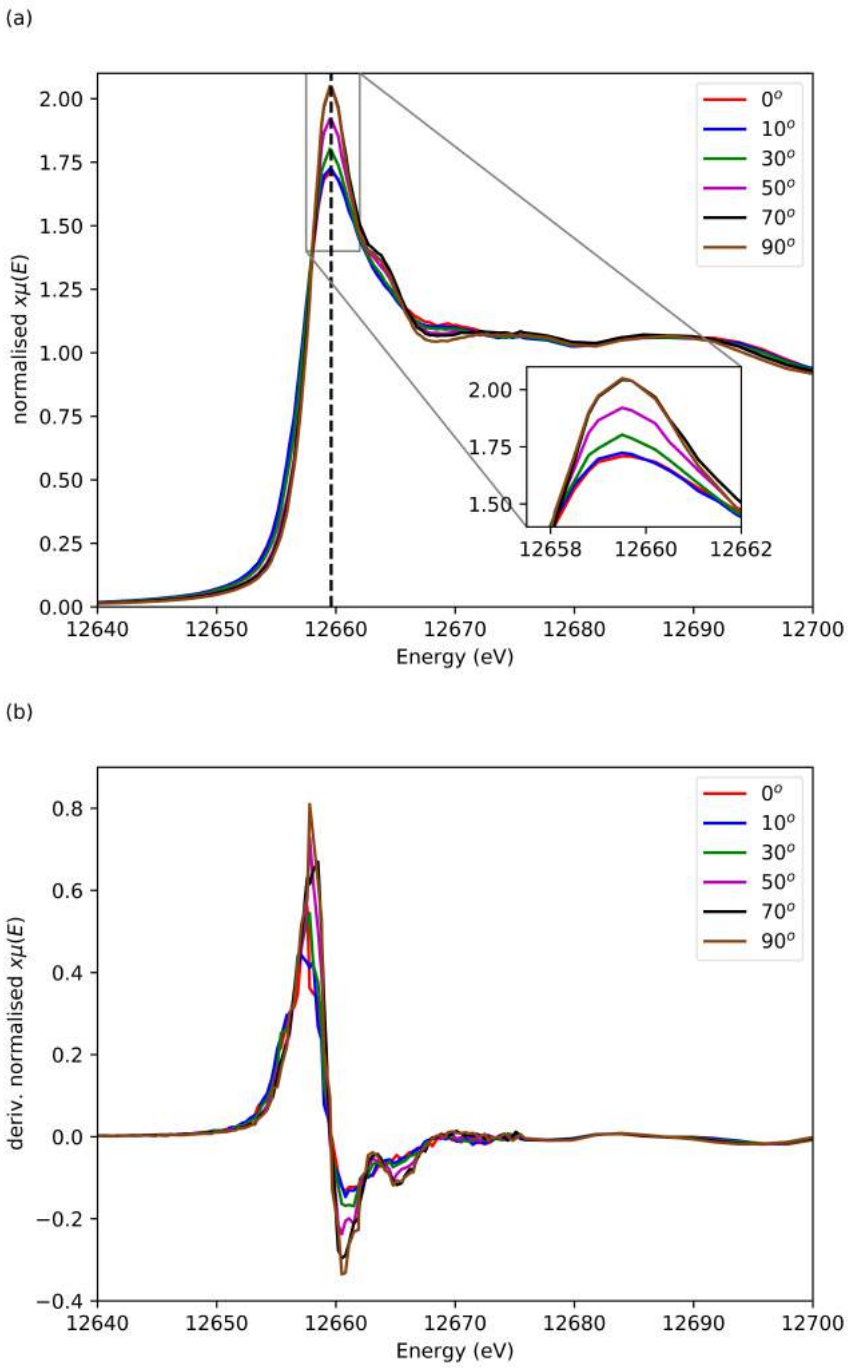

Figure 5.21: XANES, (a), and first derivative, (b), of the Se K-edge of $Tl_2Mo_6Se_6$, at 4K and different angles, with respect to the c-axis.

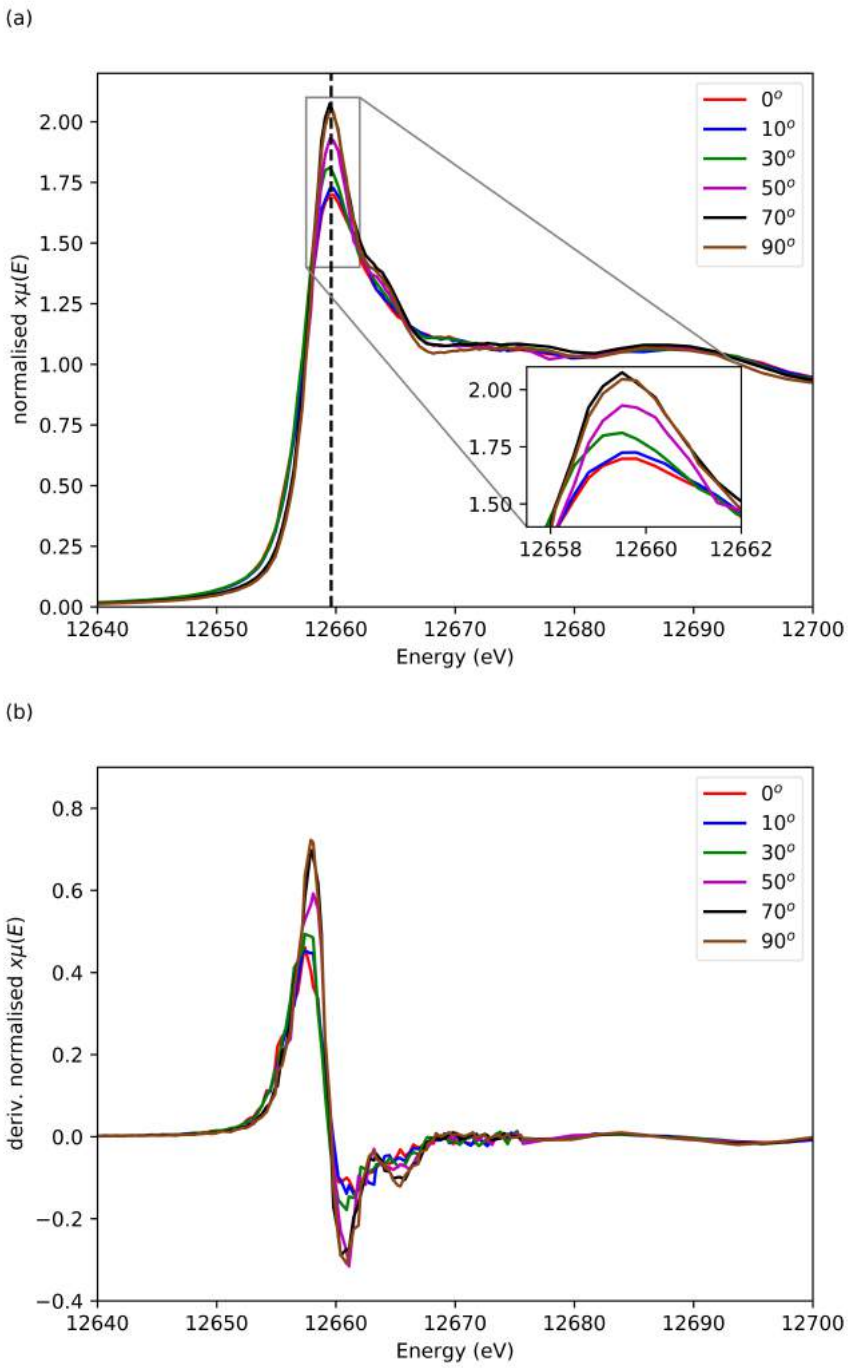

Figure 5.22: XANES, (a), and first derivative, (b), of the Se K-edge of $Tl_2Mo_6Se_6$, at 150K and different angles, with respect to the *c*-axis.

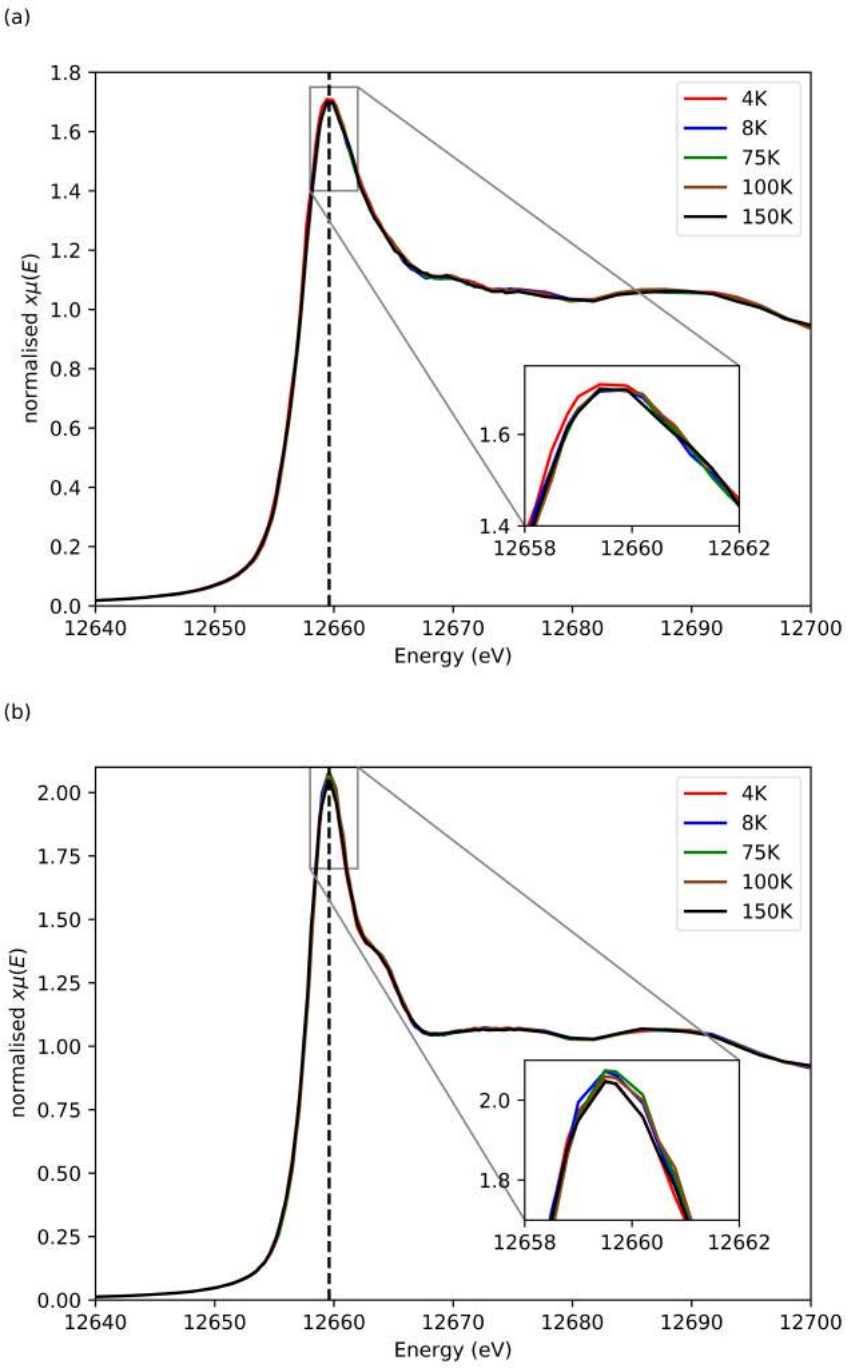

Figure 5.23: XANES of the Se K-edge of $Tl_2Mo_6Se_6$, at 0° (a) and 90° (b), at different temperatures.

EXAFS

Figures 5.24 and 5.25 show the EXAFS and FT-EXAFS of the Se K-edge absorption, at 4K and 150K, respectively. The EXAFS for the other temperatures can be seen in Appendix B. The EXAFS and FT-EXAFS have been plotted with a k-weight of 2, and with a Fourier transform k-range of 3 to 13Å^{-1}. The FT-EXAFS presented have not been phase corrected, meaning the peak positions will not match the predicted positions from the model.
The path lengths and their angles, with respect to the c- and a-axis, can be seen in Table 5.5, obtained from the model [41].

Table 5.5: Structural information, of the single scattering paths, obtained from the room temperature model of $Tl_2Mo_6Se_6$, seen in Figure 5.1 [41].

Path	Path distance (Å)	θ_i (^{o})	ϕ_i (^{o})	Weighting of path
1st Se-Mo	2.616	90	19.62	1/3
“ ”	“ ”	“ ”	20.81	1/3
“ ”	“ ”	“ ”	79.62	1/3
“ ”	“ ”	“ ”	80.81	1/3
“ ”	“ ”	“ ”	-39.19	1/3
“ ”	“ ”	“ ”	-40.38	1/3
2nd Se-Mo	2.695	33.39	50.02	1/3
“ ”	“ ”	146.61	“ ”	1/3
“ ”	“ ”	33.39	-9.98	1/3
“ ”	“ ”	146.61	“ ”	1/3
“ ”	“ ”	33.39	-69.98	1/3
“ ”	“ ”	146.61	“ ”	1/3
1st Se-Tl	3.401	48.58	5.84	1/3
“ ”	“ ”	131.42	“ ”	1/3
“ ”	“ ”	48.58	65.84	1/3
“ ”	“ ”	131.42	“ ”	1/3
“ ”	“ ”	48.58	-54.16	1/3
“ ”	“ ”	131.42	“ ”	1/3
1st Se-Se	3.766	53.32	50.22	2/4
“ ”	“ ”	126.68	“ ”	2/4
“ ”	“ ”	53.32	-9.78	1/4
“ ”	“ ”	126.68	“ ”	1/4
“ ”	“ ”	53.32	-69.78	1/4
“ ”	“ ”	126.68	“ ”	1/4
2nd Se-Se	3.878	54.54	18.97	2/5
“ ”	“ ”	125.46	“ ”	2/5
“ ”	“ ”	54.54	-41.03	2/5
“ ”	“ ”	125.46	“ ”	2/5
“ ”	“ ”	54.54	78.97	1/5
“ ”	“ ”	125.46	“ ”	1/5

The position of the peaks in the EXAFS signal, at the highest and lowest temperature measured (see Figures 5.24 and 5.25), do not change with respect to the angle between the polarisation and the c-axis. However there are changes in the intensities of the peaks further in k (> 7Å^{-1}), this is the same for both temperatures measured.

There is a change in the structure of the FT-EXAFS, where the fourth peak loses intensity for the larger angles measured. The change is similar for both temperatures, where the peak has it lowest intensity at $\theta_p = 50^o$. This could be due to interference between scattering paths when measuring at $\theta_p = 50^o$.
Comparing the signal of the two extreme angles measured (see Figures 5.26 and 5.27) there are more visible changes for the measurement along the *ab*-plane ($\theta_p = 0^o$). There is a clear change in the intensities of the peaks in the signal (7 to 9Å^{-1}) for the $\theta_p = 0^o$ data (see Figure 5.26) as the temperature is increased. Whereas the signal along the *c*-axis ($\theta_p = 90^o$) data shows a gradual decrease of the peaks intensity as the temperature is increased, which is similar for the whole k range. Along the *c*-axis the changes observed as a function of temperature can be attributed to the increased thermal fluctuations (see Figure 5.27).
The FT-EXAFS show the expected broadening of the peaks as the temperature is increased. However along the *ab*-plane there appears to be changes in the signal which cannot be fully explained with just increased thermal fluctuations. This is clear in the second peak seen in the Fourier transformed data (see Figure 5.26), as the peak becomes sharper as the temperature increases, which suggests a structural transition is occurring. As the second peak is found at $\sim$ 3Å, it most likely corresponds to the Se-Tl scattering path. The shift in peak positions suggests that the Se-Mo chains are closer to the guest ion Tl at the higher temperatures.

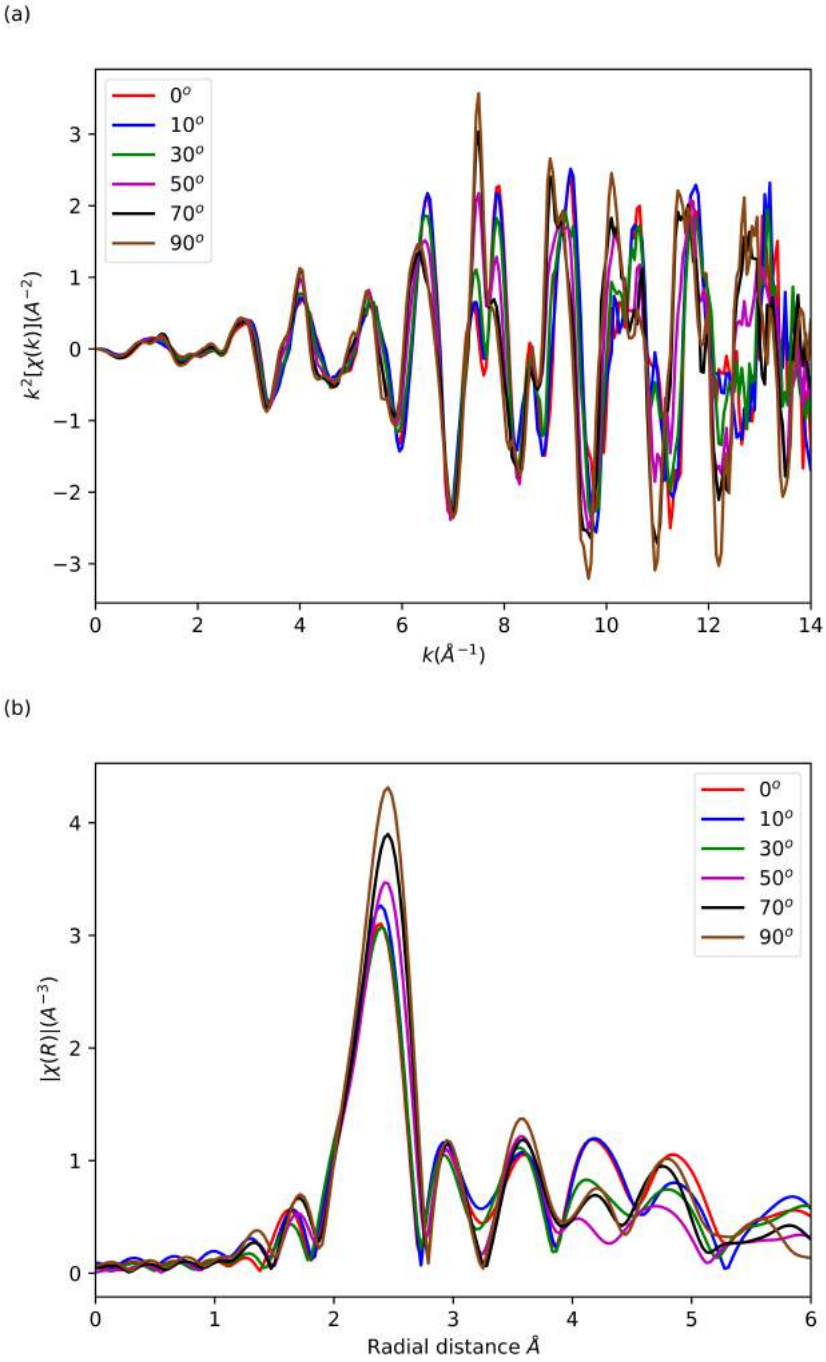

Figure 5.24: EXAFS, (a), and FT-EXAFS, (b), of the Se K-edge, at 4K, of $Tl_2Mo_6Se_6$, at different angles.

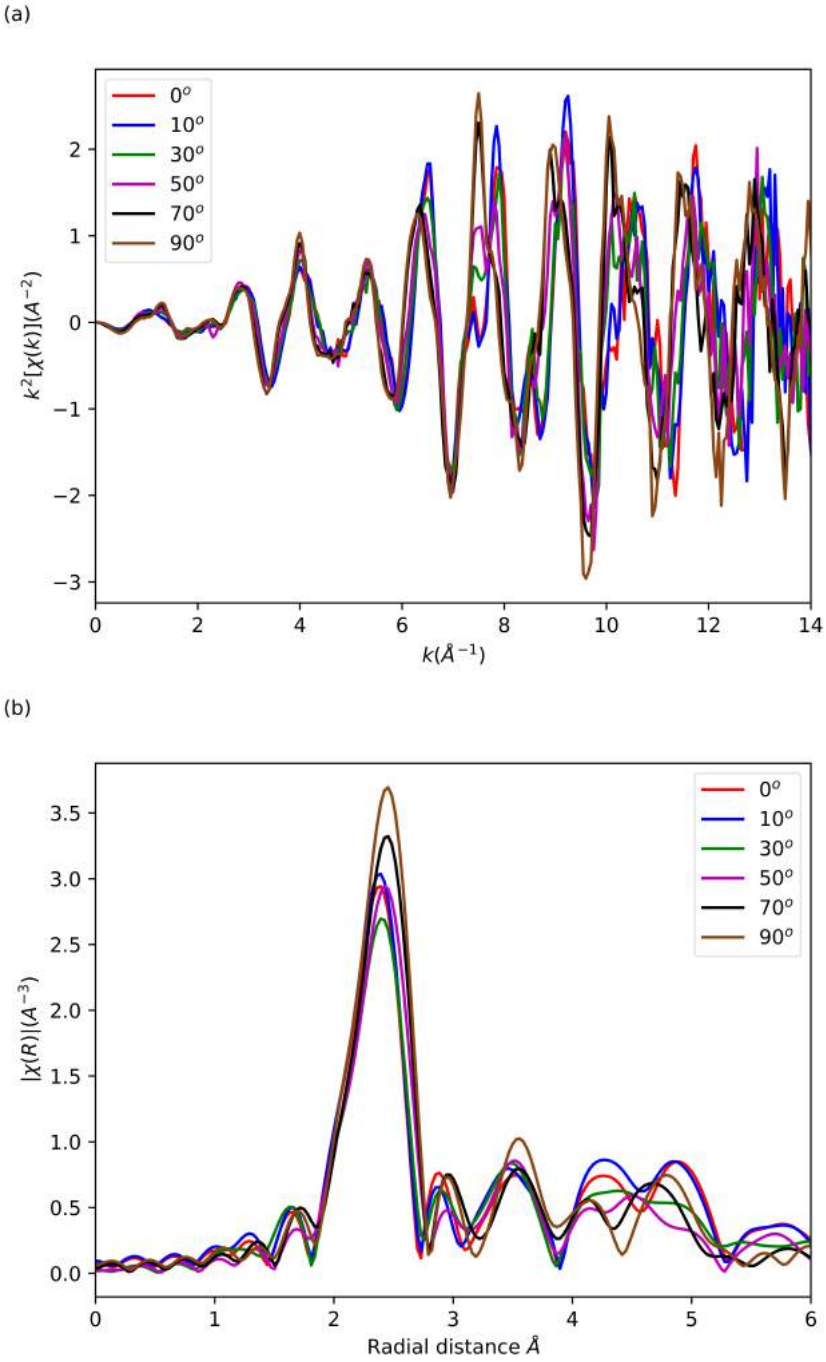

Figure 5.25: EXAFS, (a), and FT-EXAFS, (b), of the Se K-edge, at 150K, of $Tl_2Mo_6Se_6$, at different angles.

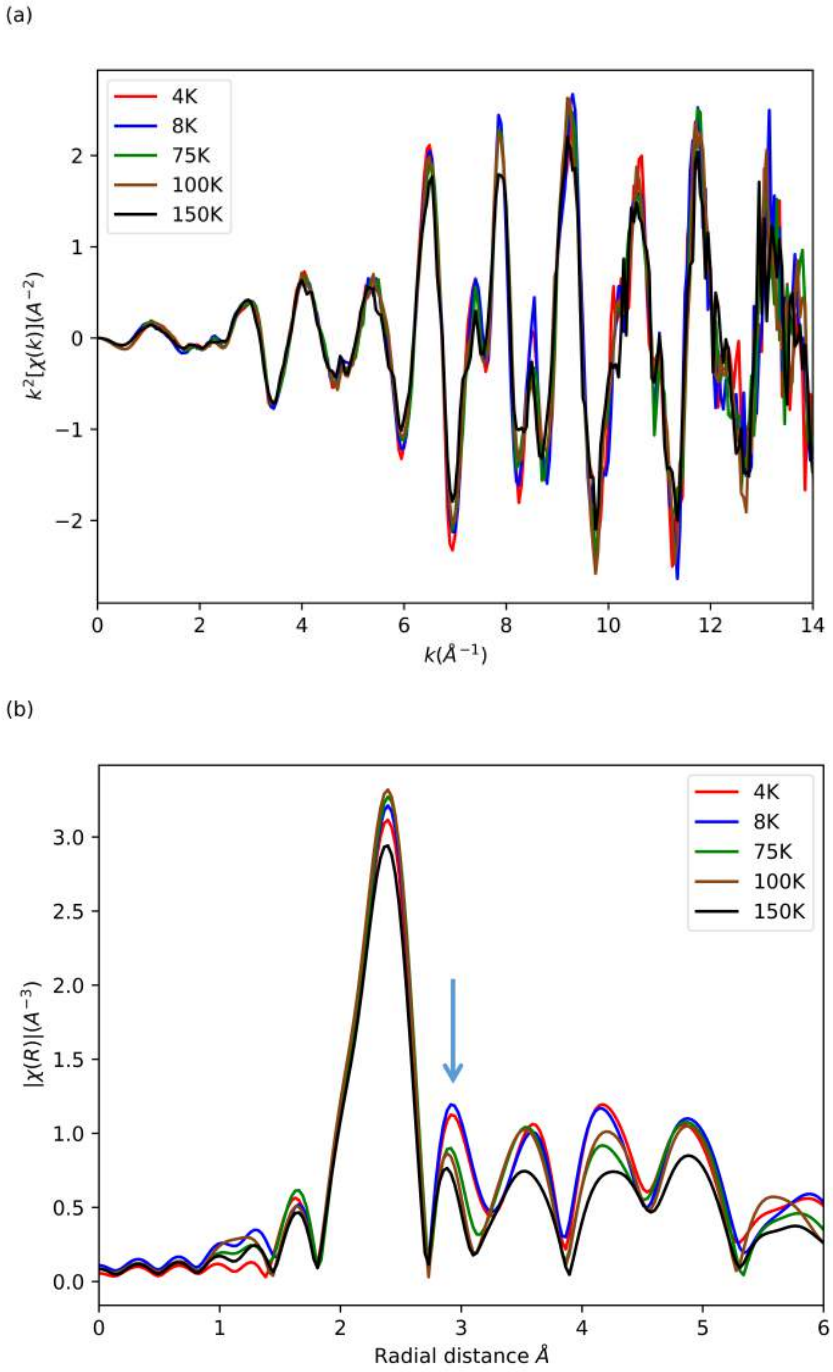

Figure 5.26: EXAFS, (a), and FT-EXAFS, (b), of the Se K-edge, at 0°, of $Tl_2Mo_6Se_6$, at different temperatures.

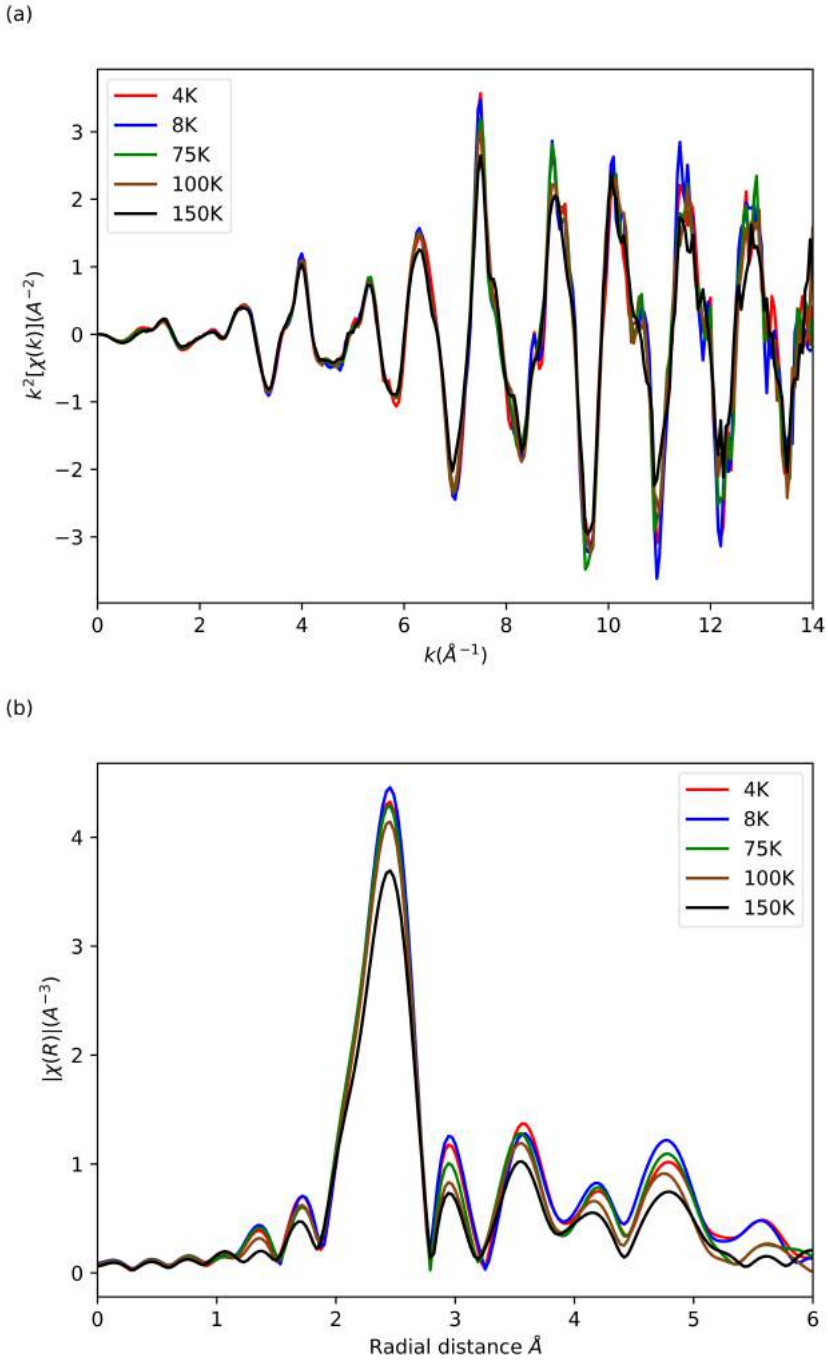

Figure 5.27: EXAFS, (a), and FT-EXAFS, (b), of the Se K-edge, at 90°, of $Tl_2Mo_6Se_6$, at different temperatures.

Fit of EXAFS

The model used in the fits was produced from a refinement to diffraction data which was measured at room temperature [41]. As the fit is obtained by modelling an averaged theoretical EXAFS signal (a default FEFF output), obtained from this model, a weighting factor needs to be introduced to make the averaged theoretical EXAFS equivalent to the EXAFS along one direction. The weighting factor is discussed in full in Chapter 3. From Figure 5.28 it can be seen that there is more than one distinct scattering path of the same length within the unit cell. This is due to the angles the path is making with respect to the c- and a-axis, and needs to be taken into account when fitting the data. The path lengths are degenerate, however the θ_i and ϕ_i values change. This is accounted for in the weighting factor used in the fits. The degeneracy (N) of each single scattering path has been set to 1. This parameter cannot be refined in ARTEMIS, so the amplitude reduction factor (S_0^2) takes into account changes in N. The value for S_0^2 reported for the fits is a global factor, so it accounts for all factors affecting the amplitude. This means it cannot directly be used to infer changes in N from the fits.

The refined parameters for the fits to the Se K-edge EXAFS data, shown in Figures 5.29 to 5.32, can be found in Table 5.6, the fits to the other temperatures can be seen in Appendix B. All parameters are within their acceptable ranges, therefore the fits are considered good. Fitting was carried out in R space, with k weightings of 1, 2, and 3, using 22 of 76 independent parameters for both the 4K, and 150K data, the number of independent parameters is similar for the other temperatures. The fits resulted in a R-factor of 0.008, and 0.005, for the 4K data, and 150K data, respectively. The R-factor for the fit to the other temperatures is between these values, with it decreasing for the higher temperatures. The angles θ_i and ϕ_i (in the weighting factor) for the single scattering paths have been set to those calculated from the model (see Table 5.5). As all angles measured are fit simultaneously, this additional data opens up more guess parameters for the fit. To account for the distinct paths each single scattering path is separated and the amplitude is multiplied by a weighting that corresponds to their frequency in the unit cell (see Table 5.5). The same single scattering paths were used in the fits for each temperature, they were calculated from the model up to ~ 3.9Å.

The first Se-Mo does not contribute to the fit along the c-axis, this is consistent with the theoretical model as it should have no contribution to the signal measured perpendicular to the path. The second Se-Tl scattering path cannot be fit to the structure as it produces unreasonable parameters, such as $\Delta R \sim 0.5$. This suggests that it is too delocalised to contribute to the EXAFS.

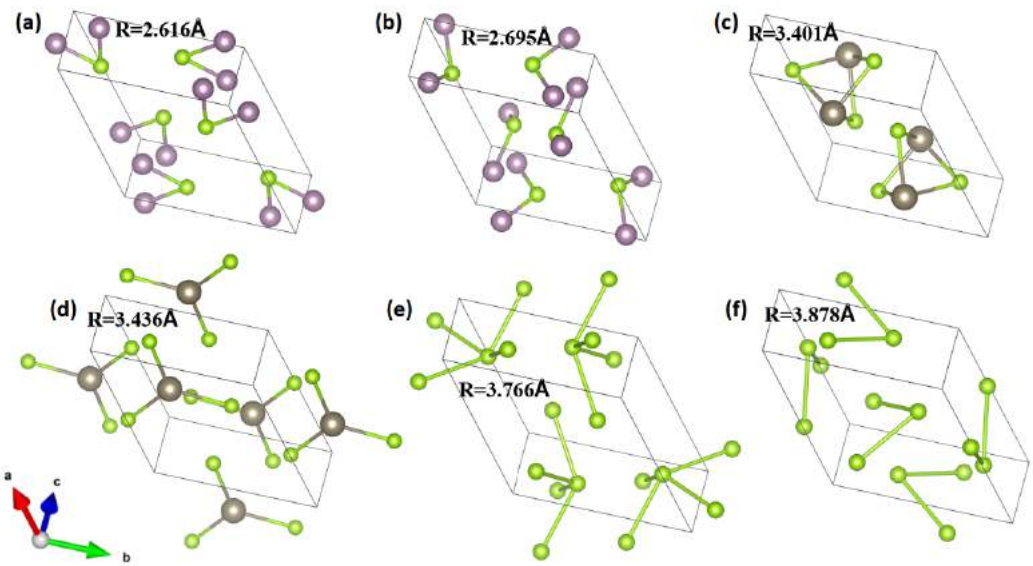

Figure 5.28: The single scattering paths used in the fit of the Se K-edge $Tl_2Mo_6Se_6$ data. Where the Se atoms are green, Mo atoms are purple, and Tl atoms are grey. With (a) 1st Se-Mo, (b) 2nd Se-Mo, (c) 1st Se-Tl, (d) 2nd Se-Tl, (e) 1st Se-Se, and (f) 2nd Se-Se.

Table 5.6: Fit parameters for the Se K-edge EXAFS of the $Tl_2Mo_6Se_6$ single crystal, alongside the value obtained from the room temperature model [41]. The degeneracy (N) of each path was set to 1. The azimuthal angle of the polarisation with respect to the a-axis, ϕ, was set to 30°.

	Temperature (K):					
Parameter:	4	8	75	100	150	Model (300K) [41]
Reduced χ^2	31.25	36.2	21.91	16.69	9.29	-
S_0^2 at 0°	1.06±0.06	1.00±0.06	1.03±0.04	1.09±0.04	1.03±0.04	-
S_0^2 at 10°	1.11±0.05	1.04±0.05	1.06±0.05	1.08±0.04	1.09±0.04	-
S_0^2 at 30°	1.13±0.05	1.07±0.06	1.09±0.04	1.07±0.05	1.09±0.05	-
S_0^2 at 50°	1.24±0.06	1.17±0.05	1.19±0.05	1.26±0.05	1.25±0.05	-
S_0^2 at 70°	1.25±0.06	1.20±0.06	1.27±0.05	1.32±0.06	1.31±0.05	-
S_0^2 at 90°	1.31±0.07	1.28±0.07	1.34±0.06	1.40±0.06	1.38±0.05	-
ΔE_0 (eV) at 0°	4.2±0.5	4.7±0.6	4.7±0.4	4.4±0.3	4.1±0.4	-
ΔE_0 (eV) at 10°	4.2±0.4	4.3±0.4	4.7±0.4	4.5±0.3	4.4±0.3	-
ΔE_0 (eV) at 30°	3.8±0.4	3.9±0.5	4.1±0.3	3.7±0.4	3.6±0.4	-
ΔE_0 (eV) at 50°	3.1±0.4	3.5±0.5	3.4±0.3	3.3±0.3	3.7±0.3	-
ΔE_0 (eV) at 70°	2.9±0.4	2.7±0.4	3.4±0.3	3.3±0.3	3.2±0.3	-
ΔE_0 (eV) at 90°	2.7±0.4	2.7±0.4	3.0±0.4	2.9±0.3	3.2±0.3	-
1st Se-Mo R (Å)	2.61±0.00	2.61±0.00	2.61±0.00	2.61±0.00	2.61±0.00	2.616
1st Se-Mo σ^2 ($Å^2$)	0.0015±0.0002	0.0010±0.0002	0.0011±0.0002	0.0013±0.0002	0.0017±0.0002	-
2nd Se-Mo R (Å)	2.68±0.00	2.68±0.00	2.68±0.00	2.68±0.00	2.69±0.00	2.695
2nd Se-Mo σ^2 ($Å^2$)	0.0021±0.0002	0.0018±0.0003	0.0021±0.0002	0.0025±0.0002	0.0030±0.0002	-
1st Se-Tl R (Å)	3.31±0.01	3.33±0.01	3.30±0.01	3.29±0.01	3.27±0.01	3.401
1st Se-Tl σ^2 ($Å^2$)	0.002±0.001	0.003±0.001	0.006±0.002	0.005±0.002	0.007±0.001	-
1st Se-Se R (Å)	3.68±0.01	3.69±0.01	3.69±0.00	3.78±0.00	3.69±0.00	3.766
1st Se-Se σ^2 ($Å^2$)	-0.0006±0.0007	-0.0004±0.0007	0.0010±0.0008	0.0006±0.0005	0.0025±0.0008	-
2nd Se-Se R (Å)	3.82±0.00	3.82±0.00	3.82±0.00	3.64±0.01	3.82±0.00	3.878
2nd Se-Se σ^2 ($Å^2$)	-0.0038±0.0005	-0.0037±0.0005	-0.0025±0.0005	-0.0018±0.0008	-0.0009±0.0006	-

A good fit was produced by using the model and refining this against the Se K-edge EXAFS, the path distances and DWs were allowed to change for each temperature and are fit simultaneously for each angle. The sum of all the relevant single scattering contributions to the Se K-edge EXAFS of $Tl_2Mo_6Se_6$, at 4K and 150K, are shown in Figures 5.29 and 5.30 fitted against the EXAFS data, respectively. The FT-EXAFS data was only fit up to $\sim$ 3.9Å as evidence of a distortion can already be observed in this range, in the broadening of the second peak ($\sim$ 3.0Å) at 4K (see Figure 5.26). Figures 5.31 and 5.32 show the fits for the two extreme angles, that were measured at all temperatures. It can be seen that the fit along the *c*-axis is closer to the experimental EXAFS, the fit along the *ab*-plane is missing components to properly fit the second peak at lower temperatures. A similar approach to model the distortion, as used for the Rb analogue, of separating the 'up' and 'down' paths was attempted for this data. However this did not produce a reasonable fit, this was to be expected as the potential distortion presents itself differently in the raw data. A 'twist', a change in the ϕ_i value, was included in different paths to model the predicted distortion [164]. This did not produce viable fits, as the parameters did not improve and the fit was not visually different. From the parameters produced from the fits (see Table 5.6) it can be seen that the amplitude reduction factor (S_0^2) is large for all angles and temperatures, this could be due to there being no vacancies in the Tl sites in the model. The SEM measurements suggest that there are Tl vacancies in this material. This may also be why a distortion could not be modelled, as the strongest hint of a distortion is viewed in the second peak which has its largest contribution from the first Se-Tl path. There are also hints of a structural transition occurring at $\sim$100K, as the ΔR values for the first Se-Se path increases at this temperature, and decreases for the second Se-Se path. While for the lower temperatures, these paths are found at roughly the same position they are found for the fit at 150K.

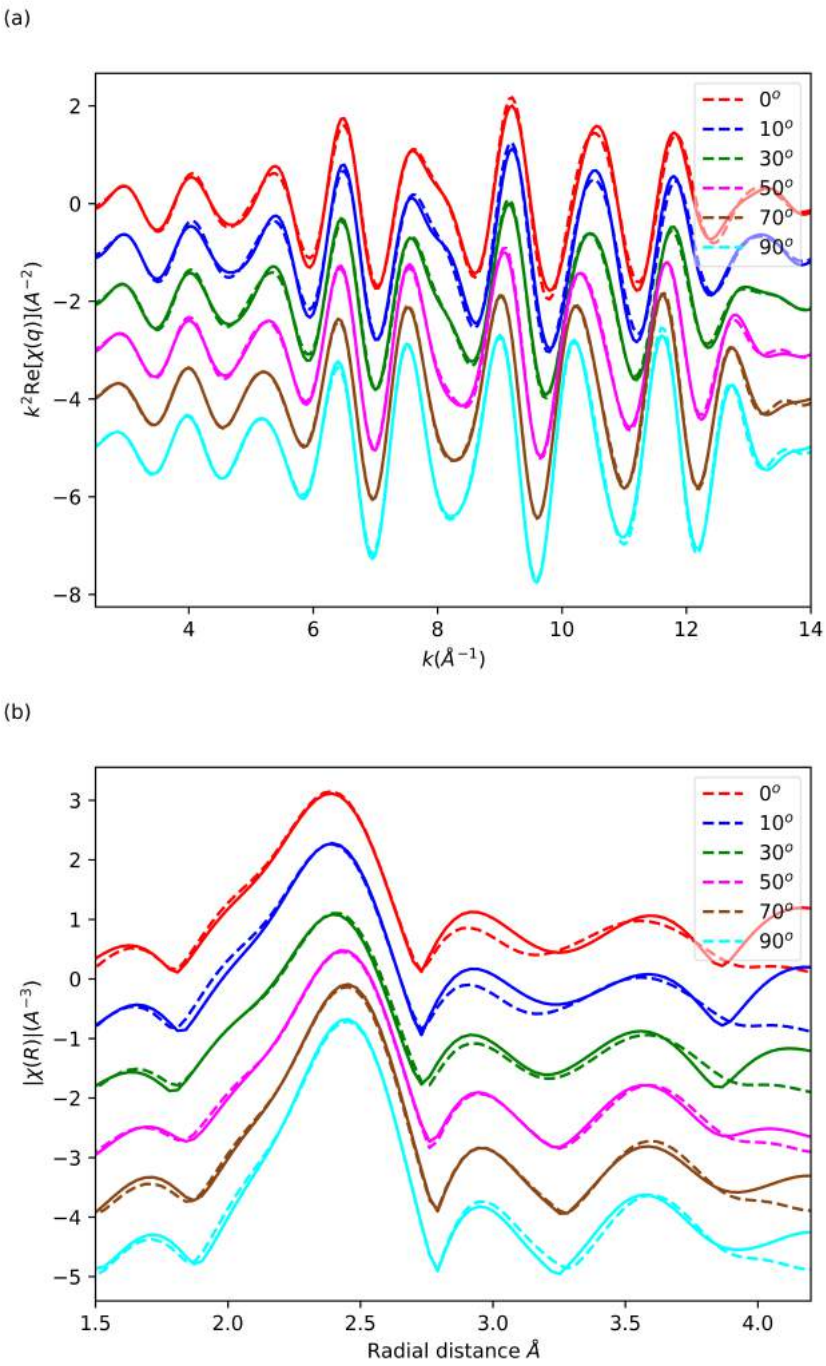

Figure 5.29: Fit of the Se K-edge at 4K, in q space (a) and R space (b). All angles measured and fitted are presented in this plot. The solid line corresponds to the experimental data and the dashed line corresponds to the fit.

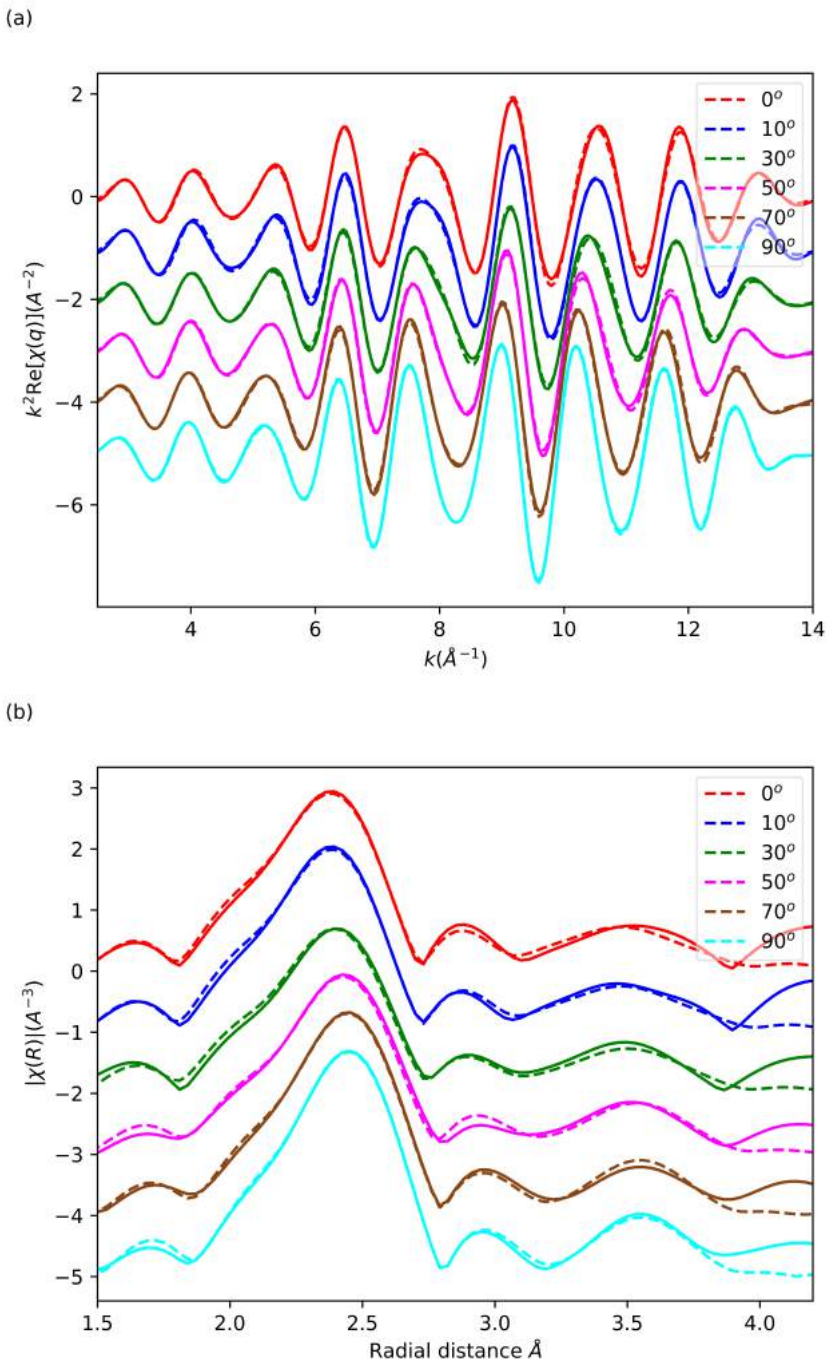

Figure 5.30: Fit of the Se K-edge at 150K, in q space (a) and R space (b). All angles measured and fitted are presented in this plot. The solid line corresponds to the experimental data and the dashed line corresponds to the fit.

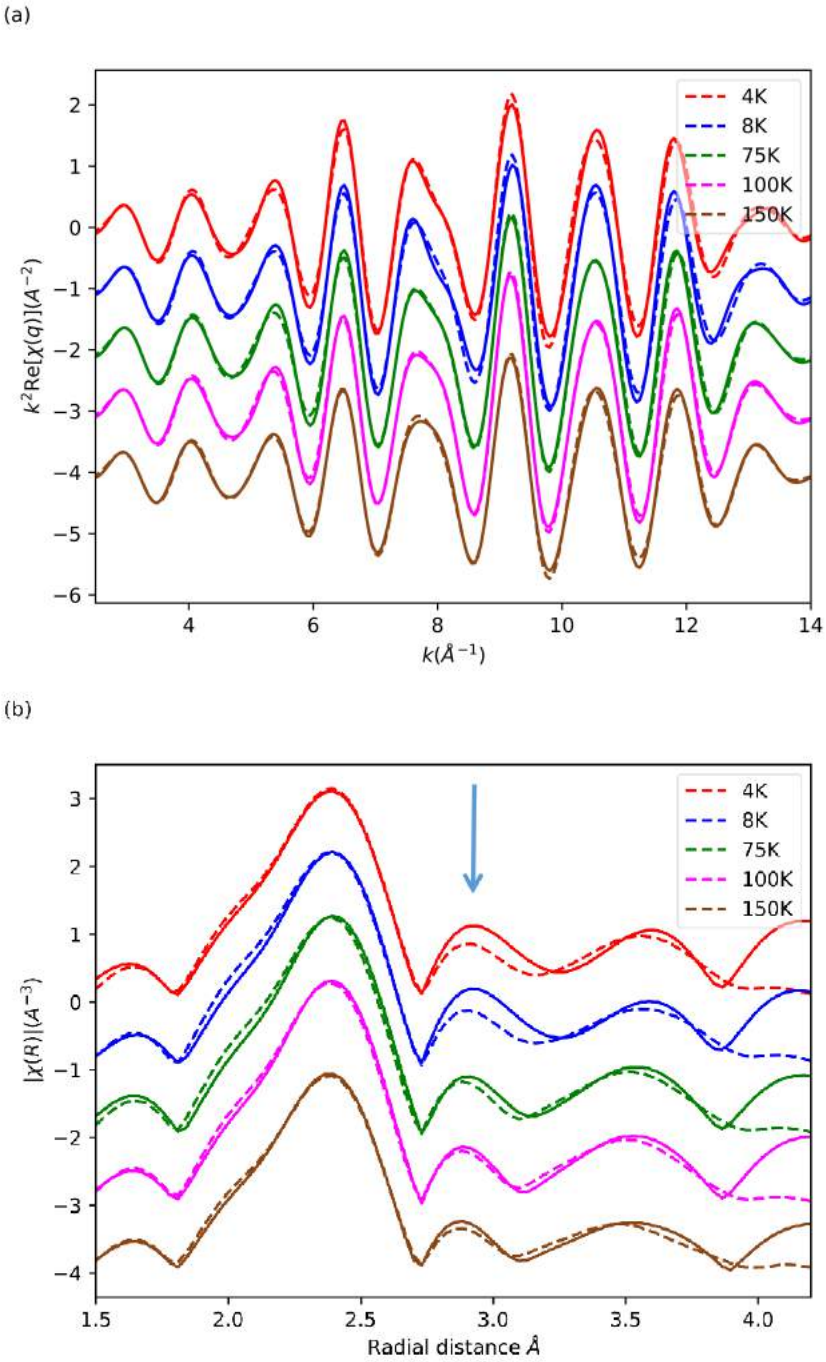

Figure 5.31: Fit of the Se K-edge at $\theta_p = 0^o$, in q space (a) and R space (b). All temperatures measured and fitted are presented in this plot. The solid line corresponds to the experimental data and the dashed line corresponds to the fit.

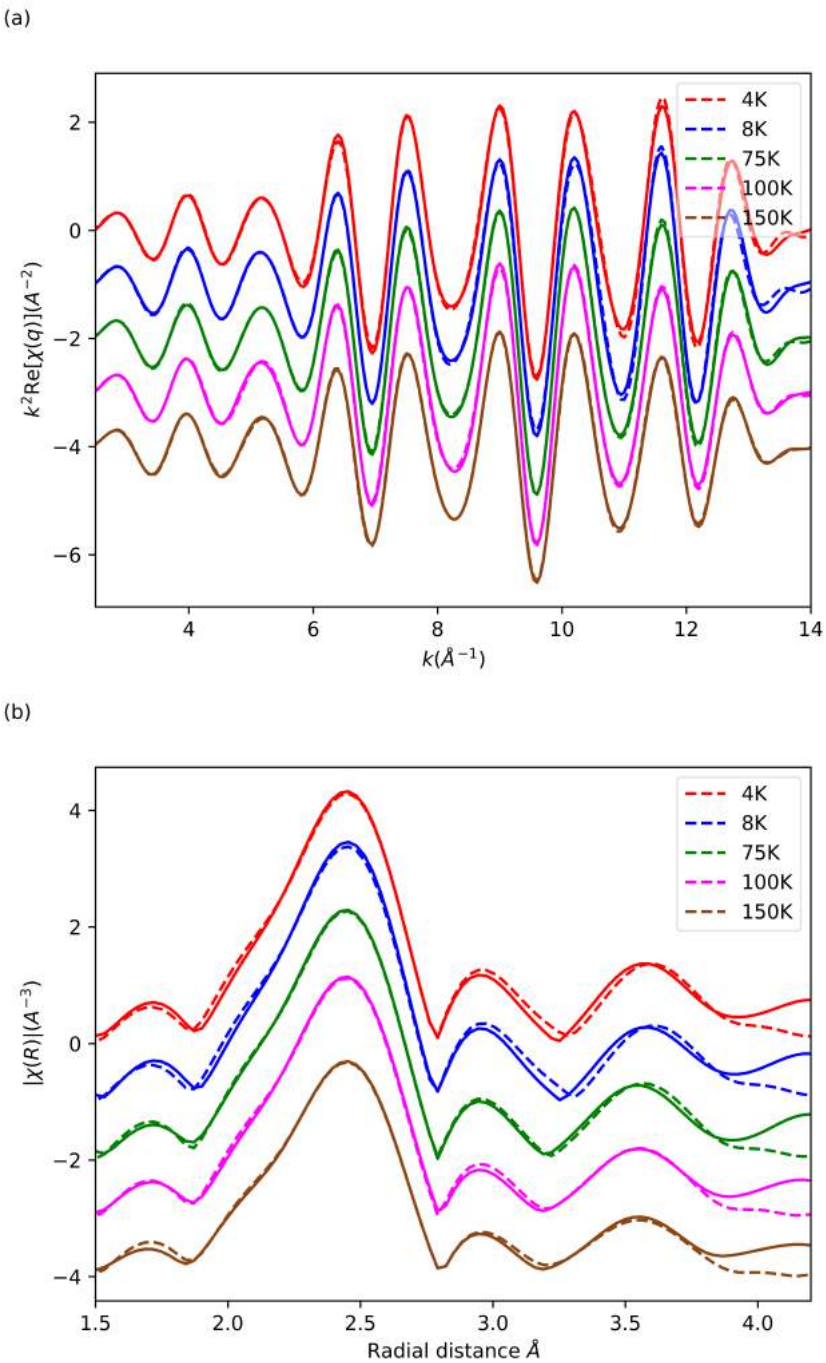

Figure 5.32: Fit of the Se K-edge at $\theta_p = 90^o$, in q space (a) and R space (b). All temperatures measured and fitted are presented in this plot. The solid line corresponds to the experimental data and the dashed line corresponds to the fit.

5.4 Discussion

From the SEM measurements of both materials a rough estimate of the stoichiometry has been made. The data suggests that the Rb sample has the same stoichiometry as reported in [81, 165], which is $Rb_2Mo_6Se_6$. While the data for the Tl sample suggests that the Tl sites are not fully occupied, and the most likely stoichiometry for this material is $Tl_{1.5}Mo_6Se_6$. Vacancies in the Tl sites for this material have been discussed by Huang *et al.* [166], which is consistent with our observations. Comparing the path lengths of the 1st scattering path (Se-Mo), can give insight into the oxidation state of the Se ions. The model for both materials predicts the path to be ~ 2.62Å, and the fits to both samples produce a similar value of ~ 2.61Å, for all temperatures. This suggests that the oxidation state of the Se ions does not change, and is not affected by the Tl vacancies. The vacancies in the Tl sites will affect the DW for the Se-Tl paths in the fit, as the model used in the fits has full occupancy of the Tl sites. This was observed in the fits, as the DW's were larger than those for paths further from the central atom. This could be dealt with by constructing more than one environment for the Se-Tl paths, where one is fully occupied and the other has a 25% vacancy. This is difficult to implement for P-XAS measurements as each path is separated based on the angle, therefore prior knowledge about where the vacancy should occur is needed. A strategy to include the vacancies in the fit needs to be developed. As the fits to the data using the fully occupied model are good, it is difficult to determine the affect the vacancies have on the local structure.

The XANES for the Tl analogue shows only one peak, while for the Rb analogue the first peak is split, this suggests that the local electronic structure of the Se ions may be affected by the metal ion in the structure. While the structures differ from each other, the position of the absorption edge is roughly the same for both, suggesting a -2 oxidation state for the Se ion [163]. The change in intensity with respect to angle for both samples was the same suggesting that for the Se ions in these materials the unoccupied states available along the c-axis have a lower energy than those along the ab-plane [67]. This is consistent with increased electronic conductivity along the chains [167, 160].

From the FT-EXAFS, seen in Figures 5.12, 5.13, 5.24 and 5.25, a change in the data with respect to the angle between the polarisation and the c-axis is observed, this is expected for an anisotropic structure. The structure also appears to change with temperature, for the Rb analogue a change which cannot be fully explained with increased thermal fluctuations is seen for the data measured along the c-axis (see Figure 5.14). While for the Tl analogue a change of similar nature is seen in the data measured along the ab-plane (see Figure 5.26). The changes seen in the samples are affecting different directions depending on the guest ion. This could help explain the different physical properties found in each sample. A structural transition could explain the changes seen in the FT-EXAFS data, to understand the most likely nature of these changes the data was fit to a model.

As the measurements were taken in fluorescence mode, the amplitude parameters produced from the fits may not be reliable. This is due to potential issues in the self-absorption correction. As the set up for this experiment allowed for the angle of incidence, between the beam and the sample, to remain static, the self-absorption correction is consistent for all temperatures and angles measured. The amplitude parameters can be compared for the fits, but they must be treated with caution. The most reliable values produced from the fits are ΔE_0 and ΔR.

The $Rb_2Mo_6Se_6$ sample fits well to the model provided (see Table 5.3) if there is a

slight compression of the structure. The first Se-Mo path (along the *ab*-plane), which forms the inner triangle, remains the same for all temperatures, at 2.61 ± 0.00Å (2.62Å in the model [42]). The other path along the *ab*-plane, Se-Rb, suggests the triangle becomes more compressed as the temperature decreases. Where it goes from 3.49 ± 0.04Å at 150K, to 3.46 ± 0.02Å at 4K (3.514Å in the model). The paths that are not found along the plane show the same trend of the structure becoming more compressed as the temperature decreases. However to model the distortion certain paths were separated into their 'up' (large θ_i) and 'down' (small θ_i) components. They were the 2nd Se-Mo, the 1st Se-Se, and the 2nd Se-Se single scattering paths. This leads to a buckling where the Se-Mo planes buckle with respect to each other, where one plane will shift down at a corner while the plane below will shift up at the opposite corner, see Figure 5.33. The second Se-Mo path is found at 2.658 ± 0.003Å for 150K, and at 4K its 'up' component is 2.68 ± 0.01Å and its 'down' component is 2.62 ± 0.02Å (2.697Å in the model). The first Se-Se path does not vary as much with temperature, and is found at 3.7 ± 0.01Å at 150K, and at 4K its 'up' component is 3.70 ± 0.03Å and its 'down' component is 3.66 ± 0.07Å (3.769Å in the model). The change in the second Se-Se path suggests that the adjacent $(Mo_3Se_3)_\infty$ chains are moving up and down with respect to each other at low temperature, where it is found at 4.066 ± 0.008Å for 150K, and at 4K its 'up' component is 4.01 ± 0.02Å and its 'down' component is 4.12 ± 0.02Å (4.05Å in the model). There is a negative DW for the furthest path fit, this could be due to the fit trying to compensate for missing paths in the third peak ($\sim$ 3.3 to 4.1Å). There are some multiple scattering paths which may contribute to this peak, which have not been included as the parameters produced for these paths were outside their normal range. Other models for this distortion were attempted, such as a chiral 'twist' in the Se-Mo planes. To try and model this a 'twist' parameter was introduced which would affect the ϕ_i values for each scattering path. However this did not lead to a visible improvement in the fit and the parameters were also not improved using this method. An angular 'buckling' parameter was also implemented to the fit, that would affect the θ_i values for each scattering path. This also did not lead to an improvement in the fit. The fit was most improved when a buckling in the path lengths was modelled, leading to the conclusion that this is the most likely form of the distortion observed in the structure.

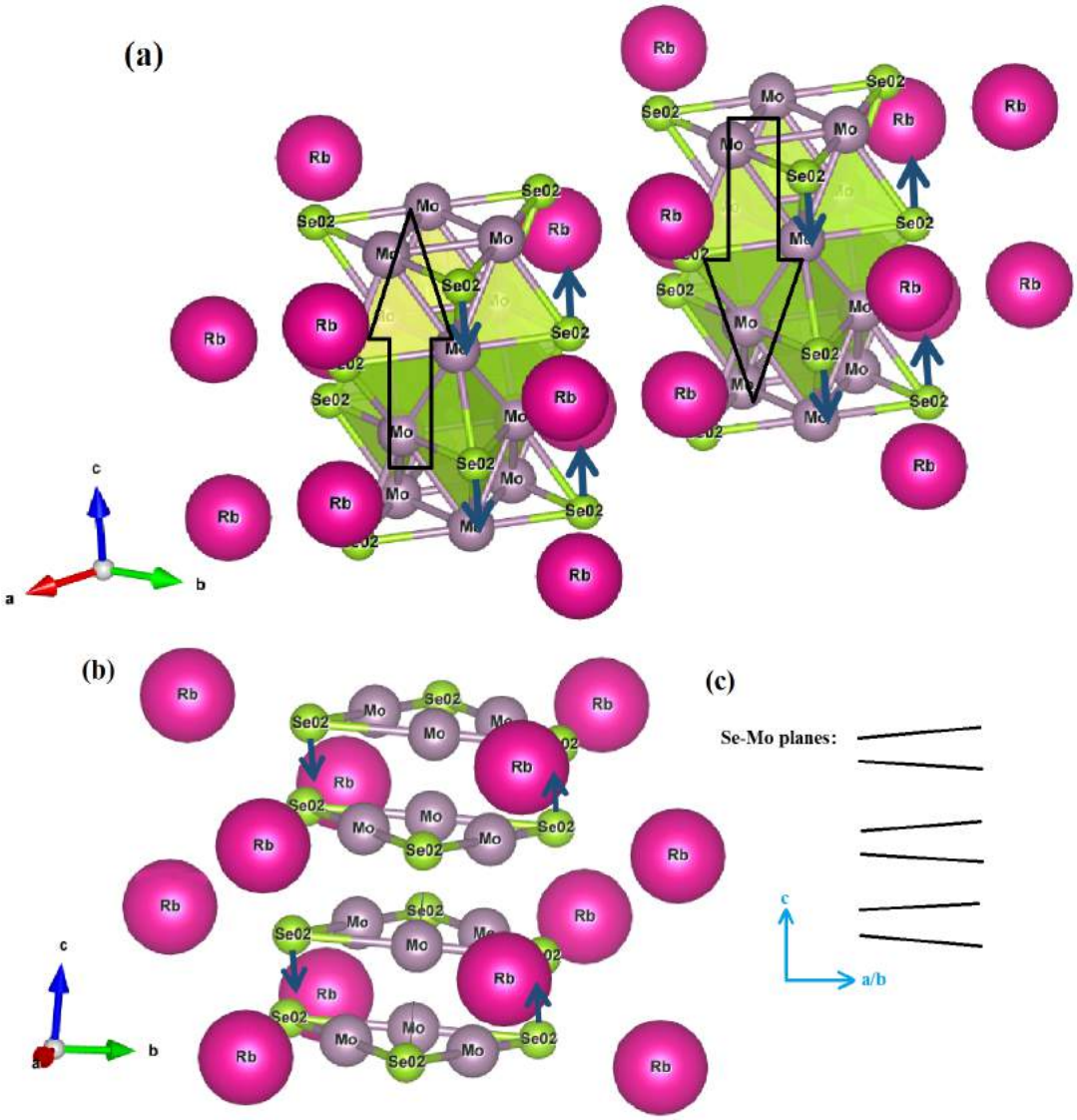

Figure 5.33: Two simple diagrams of the most likely distortion observed in the fit of $Rb_2Mo_6Se_6$ at 4K. The distortion with respect to two unit cells (a), the distortion on one unit cell (b), and a side view of the distortion (c).

An acceptable fit can be produced for the $Tl_2Mo_6Se_6$ (see Table 5.6). The fit suggests that there is no change in the size of the inner triangles (Se-Mo). This can be seen in the parameters as the path length for the first Se-Mo (along the *ab*-plane), which forms the Se-Mo triangles, is found at 2.61 ± 0.00Å for all temperatures (2.616Å in the model [41]). The paths that are not along the *ab*-plane hint at a slight compression along the *c*-axis, when compared to the model. Where the second Se-Mo path length is found at 2.69 ± 0.00Å at 150K, and 2.68 ± 0.00Å at 4K (2.695Å in the model), and the first Se-Se path length is found at 3.69 ± 0.00Å at 150K, and 3.68 ± 0.01Å at 4K (3.766Å in the model). The second Se-Se path length remains the same size for all temperatures which suggests that the chains do not move with respect to each other, but are closer than the model suggests.The path length is found at 3.82 ± 0.00Å at 150K, and 3.82 ± 0.00Å at 4K (3.878Å in the model). However there is a noticeable change in the path lengths for the Se-Se paths at 100K, with the 1st Se-Se path at 3.64 ± 0.01Å and the 2nd Se-Se path at 3.78 ± 0.00Å. This suggests that there may be a structural transition occurring between 75K and 150K. The Se-Tl path has an opposite trend to the other paths, where the path length increases with temperature. It goes from a path length of 3.27 ± 0.01Å at 150K to 3.31 ± 0.01Å at 4K (3.401Å in the model). This suggests that the neighbouring chains are becoming more in line with each other. There are negative DWs for the paths further out, this could be due to the fit trying to compensate for missing paths in the third peak ($\sim$ 3.2 to 4.0Å). There are some multiple scattering paths which may contribute to this peak, which have not been included. When attempting to include multiple scattering paths the parameters produced by the fit for these paths were outside their normal ranges. A comparison of the fit just above and below the superconducting transition shows that the atomic structure does not appear to change due to this transition. Where the parameters produced from the fit are roughly the same within error.

A similar model for the distortion used in the fit of the Rb analogue cannot be used in the fit of the Tl analogue data. The distortion in the Tl analogue cannot be determined from the fits to data. Attempts have been made to model the distortion using the same method used for the Rb analogue, the separation of 'up' and 'down' components. However no combination of independent 'up' and 'down' components produced a sensible fit with realistic parameters, suggesting the distortion is different and more complicated to model for the Tl analogue.

The full fits, seen in Figures 5.17, 5.18, 5.29 and 5.30, show that the difference between the model and the measured structure is dependent on the guest ion. For the Tl analogue the difference between the model and measured structure is greatest along the *ab*-plane, while for the Rb analogue the greatest difference is seen along the *c*-axis. Suggesting that the type of distortion observed in the materials may be one of the driving factors behind their different physical properties, where the Tl analogue is superconducting and the Rb analogue is insulating [81]. The most likely distortion in the $Rb_2Mo_6Se_6$ is a buckling of the structure along the *c*-axis. A predicted buckling, along the *c*-axis, in the structure caused by a Peierls distortion has been discussed by Liu *et al.* [147]. Whereas the most likely distortion caused in the $Tl_2Mo_6Se_6$ cannot be confirmed. While there are defined peaks up until $\sim$ 5Å for the FT-EXAFS of both samples, they were both only fit up until $\sim$ 4Å. The data was only fit this far as the parameters produced by the fits were outside of their normal range when trying to model the peaks further than 4Å. Evidence of the proposed distortion can be observed when only fitting the first three peaks for both samples, which are composed of only single scattering paths.

5.5 Conclusion

From the fits to both samples it can be concluded that the local structures observed in the P-XAS are much more distinct than the previous diffraction measurements have suggested. This is clear in the Se-guest ion path that can be fit to either material, in the Rb analogue the Se-Rb path that is out of the *ab*-plane is too delocalised to be sensibly included in the fit. Whereas for the Tl analogue, it is the Se-Tl along the *ab*-plane is too delocalised to be included in the fit. While the distortion cannot be modelled for the Tl analogue, it can be determined that it is distinct from the distortion occurring in the Rb analogue. This is the case, as the distortion observed in the data affects the *ab*-plane rather than the *c*-axis (as in the Rb analogue). It can be further concluded this was the case as the distortion cannot be modelled the same way for both samples. There is also no great change between the fit at 4K and 8K, suggesting the superconducting state does not affect the distortion caused by the proposed CDW.
We see evidence of a distortion that is most likely linked to a CDW in both materials. The structural distortion observed is different depending on what guest ion is present in the material. This suggests that different distortions will result in different physical properties of the material. As discussed in [81], a uniaxial stress induced along the *c*-axis, of $Tl_2Mo_6Se_6$, suppresses the superconducting transition and drives the material to a metal-insulator transition. A metal-insulator transition is observed in $Rb_2Mo_6Se_6$ and our data shows that the distortion in this material is strongest along the *c*-axis. While the distortion observed in our data for the $Tl_2Mo_6Se_6$ sample, is seen along the *ab*-plane. This can help explain why the materials exhibit such different physical properties.
The distortion observed in the Rb analogue can explain why the material becomes insulating. The buckling of the Se-Mo triangles within the chain will create a periodic charge difference which will break the flow of the electrons, thus leading to a insulating phase.
A recent study by Zhao *et al.* [168] discusses a similar quasi-one-dimensional material, $Rb_2Mo_3As_3$, where there is a superconducting transition at $\sim 10K$. Further work to establish if these materials have behaviours in common could be beneficial to understanding the nature of superconductivity in $M_2Mo_6Se_6$. Whether the lack of a superconducting state in $Rb_2Mo_6Se_6$ is due to the nature of the CDW or the electronic nature of the material is unclear. This could be investigated by measuring P-XAS on single crystals of $Rb_2Mo_3As_3$ to determine if a CDW is present, or if it undergoes any structural changes similar to $Tl_2Mo_6Se_6$. If the changes are similar to those observed in the Tl analogue, then potentially a superconducting state in the Rb analogue could be formed by inducing the same structural changes.
This work could also be expanded to measure the affect of the Tl deficiency, observed in the material, has on the superconductivity. The distortion observed may also be affected by the amount of Tl deficiency in the sample.

Chapter 6

Investigating Jahn-Teller distortions in Ca_2RuO_4 using single crystal P-XAS.

6.1 Introduction

In certain materials, a distortion in the electronic configuration will lead to change in the atomic structure, where an octahedra containing bonds with d orbitals will either compress or elongate (see Figure 6.1). This affects systems where there is a degeneracy in the electronic ground state. To stabilise the octahedra, a distortion will occur, which leads to a break in the degeneracy (and as a consequence reduces the symmetry). This results in a structural change, known as a Jahn-Teller distortion, which was first discovered by Hermann Jahn and Edward Teller in 1937 [47]. The Jahn-Teller theorem states that "stability and degeneracy are not possible simultaneously unless the molecule is a linear one". These distortions occur mostly in materials with octahedral structures [169, 170, 171, 172], but can also be observed in materials with tetrahedral structures [173, 174]. The change in structure can affect the physical properties of the material, resulting in the materials becoming superconducting [175, 176, 177], or insulating [178, 179].

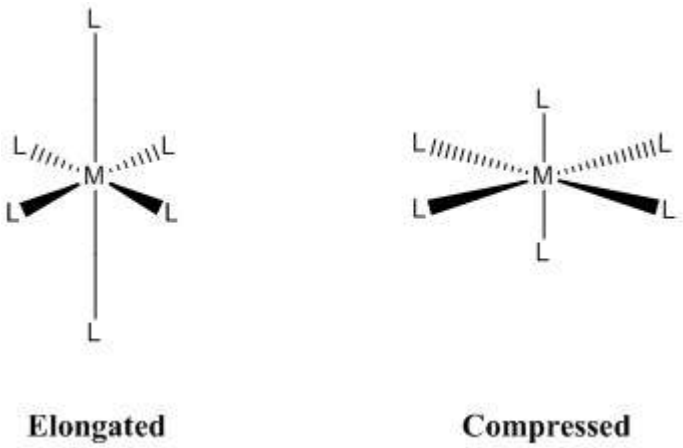

Figure 6.1: Simple schematic of the possible Jahn-Teller distortions for a metal ligand octahedra [180].

There are two types of Jahn-Teller distortions that can occur in an octahedral compound, compression and elongation. The type of distortion that occurs is controlled by the interaction between the metal and ligand orbitals. In a compression Jahn-Teller distortion the octahedra, built of metal and ligand atoms, compresses (the axial bonds, those along the c-axis, become shorter than the equatorial ones, those along the ab-plane). While in an elongation Jahn-Teller distortion the axial bonds become longer than the equatorial ones.

In this chapter, the nature of the Jahn-Teller distortion and the Mott insulator transition in Ca_2RuO_4 will be discussed. This material undergoes a metal-insulator transition at ∼360K (paramagnetic metal >360K, paramagnetic insulator <360K [44]). While in the Mott insulator phase it becomes antiferromagnetic at ∼ 110K. It has been difficult to determine the driving force behind the Mott-insulator transition, and the role the orbital degrees of freedom play [43, 44, 45]. Two scenarios have been proposed, i) the transition is orbital selective and only affects the xy band, or ii) the Mott-insulator transition is not orbital selective and is assisted only by the crystal field splitting. In the first case, i), the proposed scenario is that only the xy band becomes metallic therefore it is less occupied. In the second case, ii), the proposed scenario is similar to what occurs in $3d^1$ perovskites [181].

This material forms a structure with symmetry group $Pbca$, see Figure 6.2. As the temperature is increased the unit cell decreases in size slightly along the a-, and b-axis, while a lengthening along the c-axis is observed. There is a slight change in the Ru-O octahedra for the two unit cells. As the temperature is increased the octahedra elongate along the c-axis and compress along the ab-plane. The relative angle the octahedra make with the c-axis also changes with temperature, where the angle becomes shallower as the temperature is increased [44].

In perovskite-type transition metal oxides the energy splitting of the electron orbitals increases with the energy level of the metal. Therefore transition metals with $4d$, or $5d$ electrons, are more likely to lead to a low spin state [182]. A low spin state is one in which the t_{2g} component of the d-orbitals are at a much lower energy than the e_g component, due to a larger crystal filed splitting, and therefore will be filled first [183]. The reported electron state of the $4d$ electrons in this material is $4d^4$ (t_{2g}^4, e_g^0) [43, 44], consistent with the material being in a low spin state. The nature of a Jahn-Teller distortion is affected by the spin state of the d electrons, and certain electron configurations do not exhibit Jahn-Teller distortions. If the d electrons are in a high spin state then the d^3, d^5, d^8, and d^{10} will not allow a distortion. If the electrons are in a low spin state then the d^3, d^6, d^8, and d^{10} will not allow a distortion. This is due to the electron configurations being stable, with no possible degenerate states to allow the distortion to occur. When an ion has d^4 electrons it will display a strong Jahn-Teller distortion if the electrons are in a high spin state (unevenly occupied e_g orbitals). When the electrons are in a low spin state the ion will display a weak Jahn-Teller distortion (unevenly occupied t_{2g} orbitals).

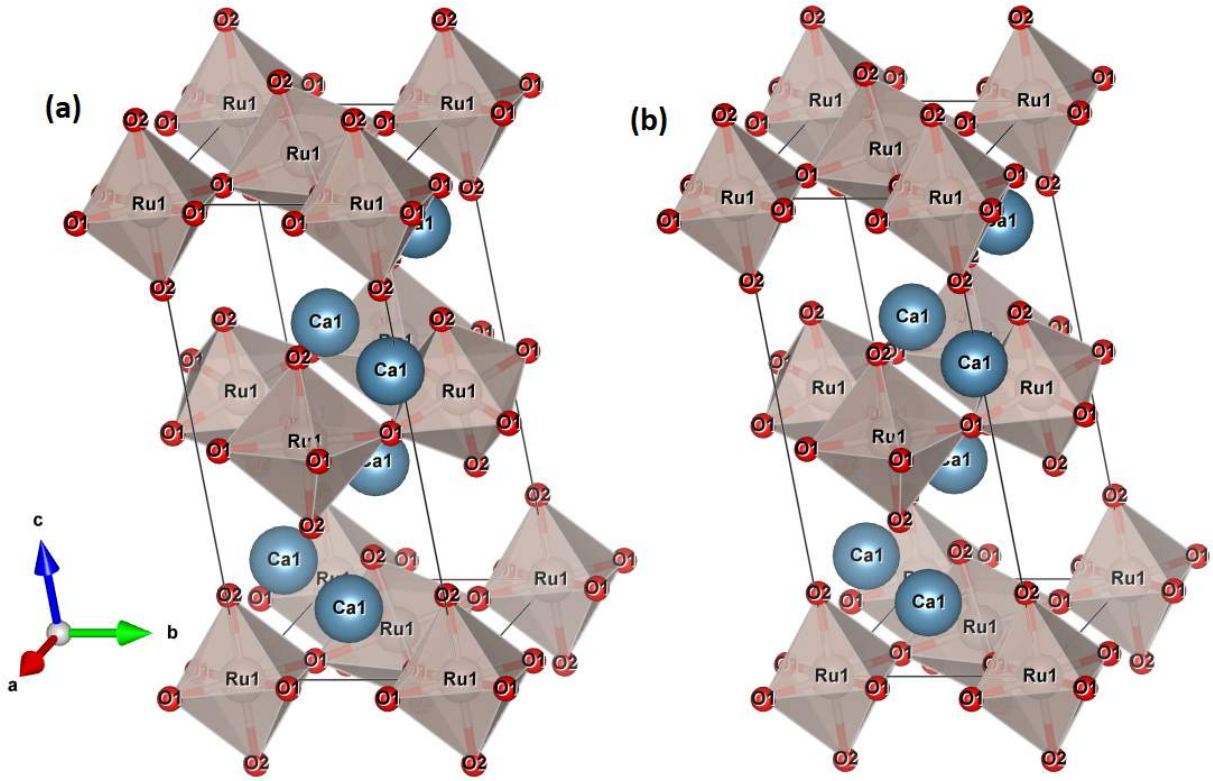

Figure 6.2: Structure of Ca_2RuO_4, at room temperature [46] (a), and at 400K [184] (b).

6.2 SEM images

SEM images were taken of the Ca_2RuO_4 sample used in the P-XAS experiment. The procedure for the SEM measurements and the detection methods are discussed in Chapter 2. Measurements were made using both secondary and backscattering electron detection. The goal of these measurements was to determine if the sample was homogeneous in composition. This could be shown by mapping the surface of the sample and by measuring spectra at different parts of the surface.
The surface mapping can be seen in Figure 6.3, for both secondary and backscattering electron detection. The SEM images of the sample clearly shows that the crystals are homogeneous, as the surfaces are consistently grey. The SEM images show that the crystal has a slight crack in it which could affect the P-XAS measurements. If the beam was unfocused (large beam size) or not stable we would observe increased noise in the measurements, if the beam moved across the crack. However, as the beam size used for the P-XAS experiment was small enough in comparison to the sample size, the crack seen in Ca_2RuO_4 did not appear to affect the results, as the beam was positioned more towards the centre of the sample. This also suggests that the beam was stable during the experiment, as the measurements show no evidence of the beam moving across the crack.

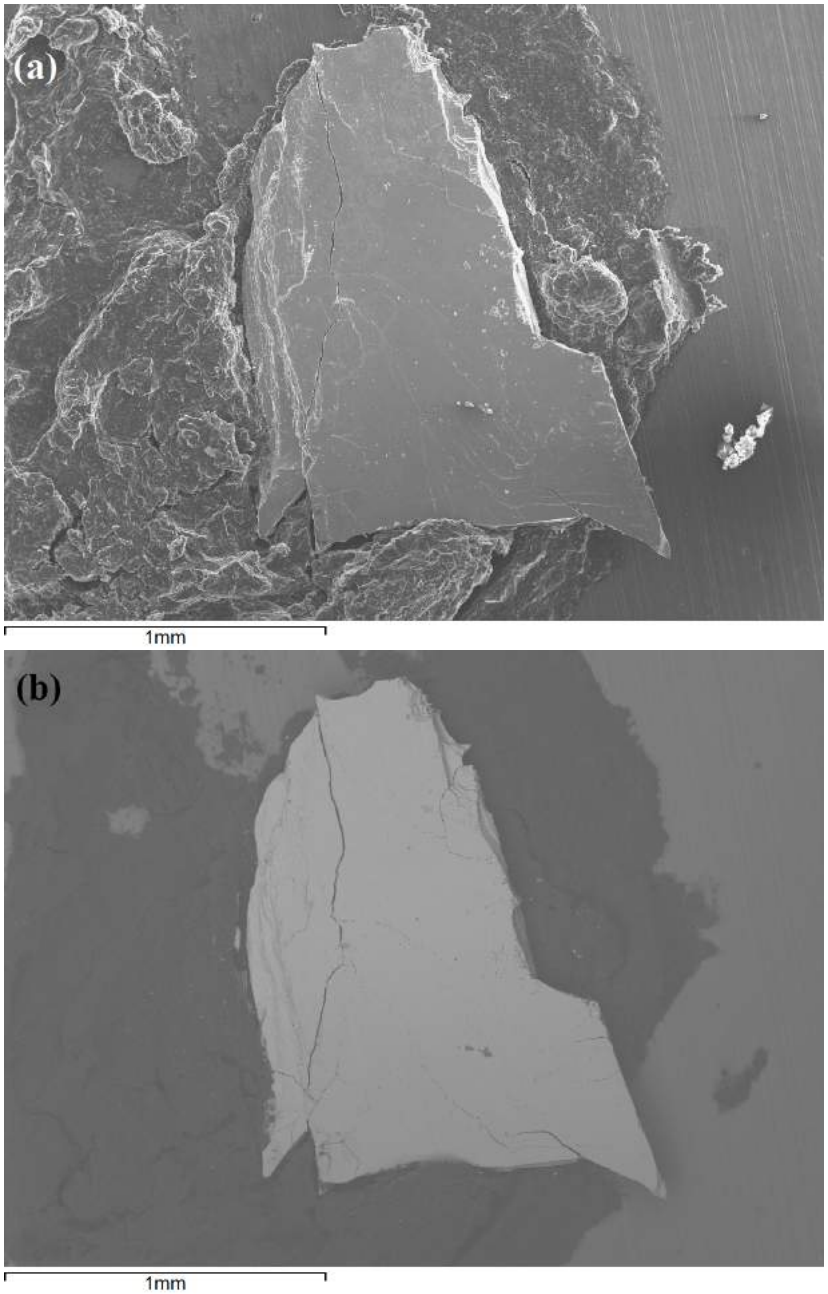

Figure 6.3: SEM image of the single crystal Ca_2RuO_4, measured with secondary electron (a) and backscattering electron (b) detection.

It is possible to use the characteristic x-ray spectra obtained from the SEM measurements to determine the stoichiometry of the sample. However, this was a secondary application of the SEM measurements taken for this thesis, and other experimental techniques would need to be used to obtain an accurate stoichiometry (as discussed in Chapter 2).
Spectra of the characteristic x-rays produced from the interaction between the sample and the electron beam at different points of the surface were measured to determine the composition of the features on the surface map, Figure 6.4. The spectra show that the expected composition is seen in the sample, and that the composition is consistent in different areas of the sample.

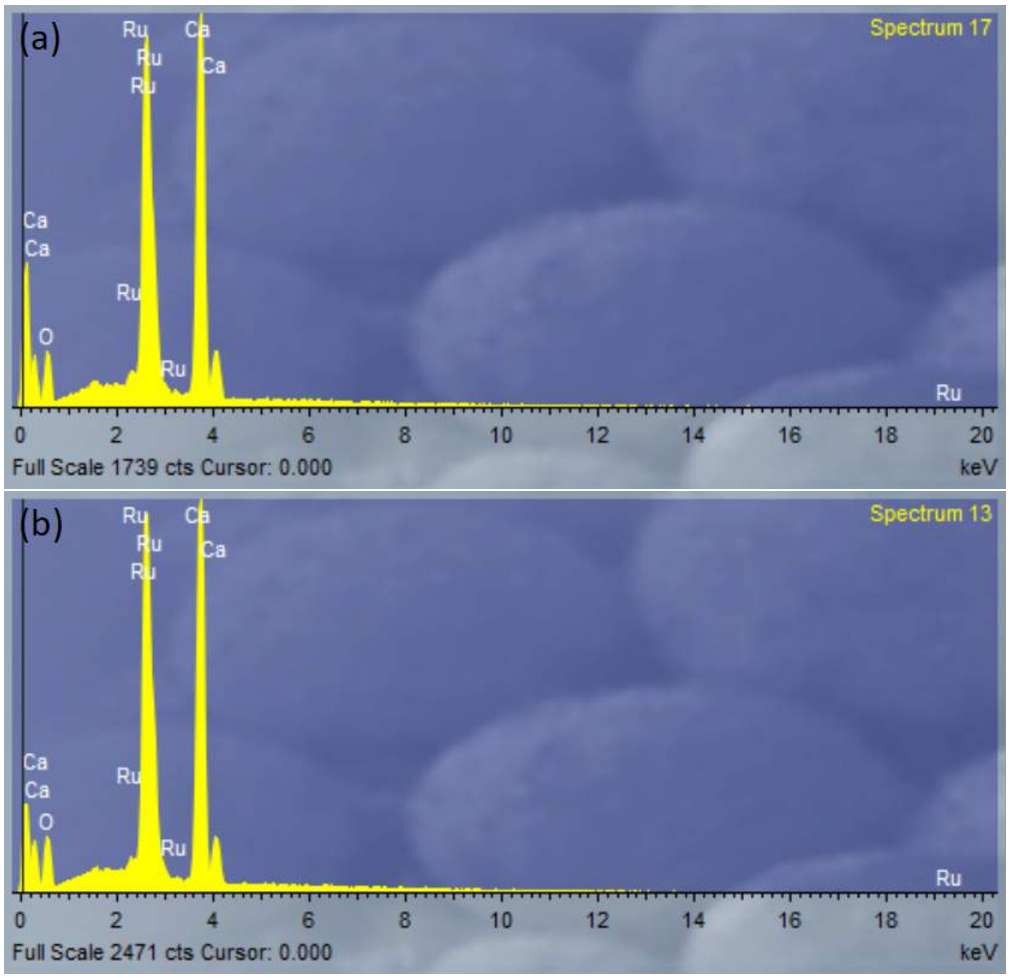

Figure 6.4: Spectra of Ca_2RuO_4, at a point in the bottom right of the sample, (a), and at point in the top right of the sample, (b). The crystal is homogeneous, and the elements in the spectra are consistent with the elements expected to be seen in this material.

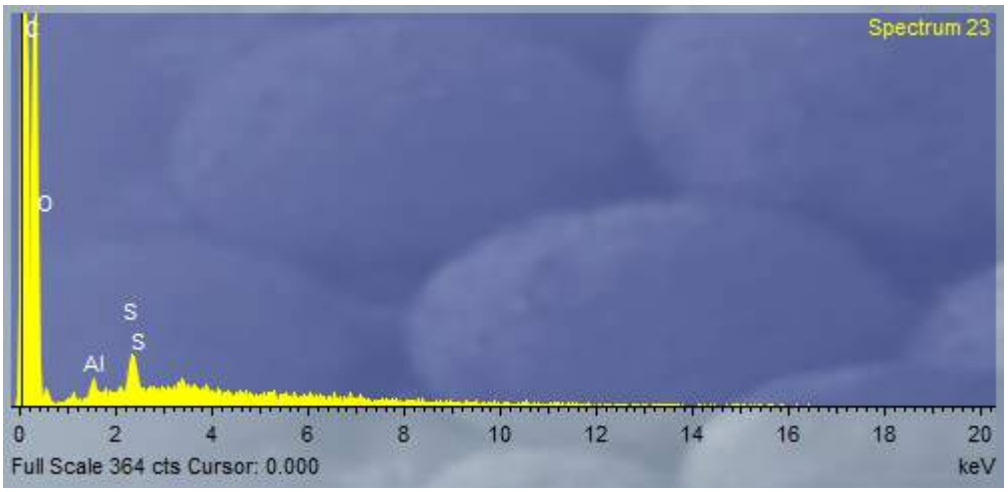

Figure 6.5: Spectra of the carbon paint used to glue the sample to the sample holder.

To make an estimate of the stoichiometry, we have used the many spectra collected in different regions of the samples and averaged the weight percentages measured for each element in the sample. As the sample contains oxygen, and due to it being such a light element, it is hard to accurately calculate how much is present. There was a unknown amount of O in the carbon paint which maybe be measured as a background, Figure 6.5. The value of O is not consistent in each spectra measured of the carbon paint therefore it is not possible to estimate how much O was measured from the sample or the background. From these measurements, the most likely stoichiometry is Ca_2RuO_4, as reported by [46].

6.3 Ca_2RuO_4 single crystal P-XAS

6.3.1 Experimental set-up

This aim of this experiment was to determine the nature of the Jahn-Teller distortions occurring in Ca_2RuO_4, and to investigate which scenario is most likely behind the Mott-insulator transition. P-XAS of the Ru K-edge was measured for the Ca_2RuO_4 single crystal, at several angles with respect to the polarisation of the beam, and at two temperatures either side of the Mott-insulator transition (300K and 400K). These measurements were carried out at the B18 beamline in Diamond Light Source, in Oxfordshire, UK. The samples were provided by Dr Robin Perry's group at University College London, and ISIS at the Rutherford Appleton Laboratory. Single crystals of this material were grown using the floating zone technique in a four mirror optical furnace, as described in [185].
The samples were glued to an Al sample holder with carbon paint (see Figure 6.6) this was chosen as the components of the paint and sample holder do not have absorption edges in the same energy range as Ru [162]. As the Ru K-edge was being measured, the x-ray energies used ($> 22000eV$) were high enough that there are no absorption edges for Al, or C [162].
To measure the samples the beamline was set up with the Si 311 double-crystal monochromator. The Pt branch was used, and no harmonic rejection mirrors were needed. An energy calibration was performed using a Ru foil sample. The single crystals grew with the c-axis perpendicular to the ab-plane, where the c-axis is going into the page in Figure 6.6. Due to time constraints only the crystal in the middle

was measured. The samples were small, $\sim 909 \times 1500 \times 112\mu m$ for Ca_2RuO_4, so the measurements were taken with a fully focused beam ($200\mu m$ x $200\mu m$). Each spectra was measured four times under the same conditions, with an energy step of $\sim 1eV$ at $\sim 0.44s$ per point. This energy step was chosen as there were vibrations due to the sample environment equipment, and this step and time combination allowed for the oscillations to be averaged out. A large energy step like this can be used when dealing with EXAFS, as the core width of Ru K-edge is $5.33 \pm 0.21eV$ [186]. The XANES measured during this experiment will only be analysed qualitatively, therefore we do not need as high a resolution as for quantitative analysis. The measurements were taken in fluorescence mode using a Canberra 36 element Ge detector. The sample, for each temperature, was measured at a range of angles with respect to the beam, $\theta_b = 15^o$ to 75°, in steps of 15°, see Chapters 2 and 3 for more detail. The polarisation of the beam would be parallel to the c-axis when the sample was positioned at $\theta_b = 90^o$. A rotating table was used to position the sample in the different orientations. The sample was heated up using cartridge heaters provided at the beamline.
The range of angles that could be measured does not include $\theta_b = 90^o$ or 0° due to the geometry of the set up, where the sample was rotated about the z-axis with a rotating table. This restriction was introduced by the sample holder (see Figure 6.6). If the crystal was aligned so that the polarisation of the beam was parallel to the c-axis, $\theta_b = 90^o$, the beam would only see the side of the sample holder and not the crystal. When measuring perpendicular to the c-axis, $\theta_b = 0^o$, the detector would be perpendicular to the surface illuminated by the x-rays and hence a very low threshold of fluorescence photons would be measured.

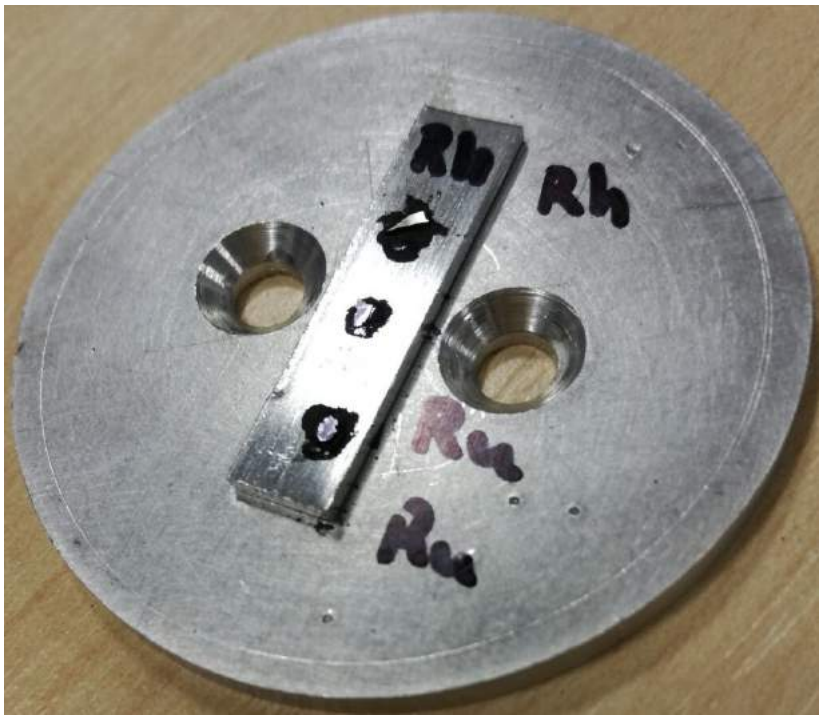

Figure 6.6: Sr_2RhO_4 sample, top, Ca_2RuO_4, middle and bottom, glued onto an Al sample holder with C paint. Only the measurements of the middle sample are reported in this thesis.

6.3.2 Ca_2RuO_4 results

All of the data measured from this experiment has been through an initial data processing as described in Chapter 3.
An energy calibration was produced by measuring a reference sample of Ru foil before the experiment. The value for E_0 changed with respect to the angle between the beam and the c-axis (θ_b) and temperature (see Table 6.1 for values). The values for E_0 were set based on the position of the first peak in the derivative of the XANES (see Figures 6.9b and 6.10b). The same spline range in k was used for all temperatures and angles, 0 to 10.4Å^{-1}. The background parameter (Rbkg) was set to 0.9Å for all data sets. The pre-edge range was the same for each temperature and angle, and was set to -208.2 to $-72.1eV$, with respect to E_0. The post-edge range was also the same for each temperature and angle, and was set to 57.6 to $414.0eV$, with respect to E_0. The normalisation order was set to 2, for all data sets. For the FT-EXAFS the same range in k was used in the transformation for each temperature and angle, 3 to 9Å^{-1}

Table 6.1: E_0's (eV) of the Ru K-edge for all θ_b's and both temperatures measured.

	Temperature (K):		
θ_b:	300	400	ΔE(HT-RT)
15°	22128.2±1	22128.8±1	0.6
30°	22128.0±1	22128.5±1	0.5
45°	22127.0±1	22127.5±1	0.5
60°	22126.8±1	22127.0±1	0.2
75°	22125.9±1	22126.0±1	0.1

It was not possible to correct for the self-absorption in the XANES region for this material, this is due to a numerical instability in the calculation: the denominator becomes very small and this leads to a divergence in the data. Therefore the XANES could only be analysed qualitatively for this material. The self-absorption correction could not be reliably accounted for in the EXAFS region as well, therefore the fits and subsequent analysis are performed on uncorrected data. This affects the amplitudes produced by the fits and the DWs, as the theoretical EXAFS signal will be calculated with the expected intensity, which will be larger than the measured intensity. This means that the fit parameters accounting for the amplitude will not be reliable. Therefore only the ΔE_0 and ΔR parameters resulting from the fits are reliable and can be discussed.
In some cases it is beneficial to have data along the two perpendicular crystallographic axes, the c-axis and the ab-plane. An attempt was made to build the data to produce a signal along these two axes (see Figures 6.7 and 6.8). However, it can be seen that the difference between the measured and built data appears to carry structural information in the EXAFS region. This cannot be dismissed when analysing the data. The symmetry group reported for this material is orthorhombic, this explains why the built XAS are not in line with the experimental data, as the build is constructed under the assumption that the material is in a symmetry group with $N > 2$ rotational axis. While it is reported that the orthorhombic shift is only small [184], the discrepancy between the built XAS and measured XAS suggests that the shift is large enough that the material cannot be assumed to be tetragonal. In the case of this experiment there were enough angles measured to produce a fit to a single model, so building more angles was not necessary.

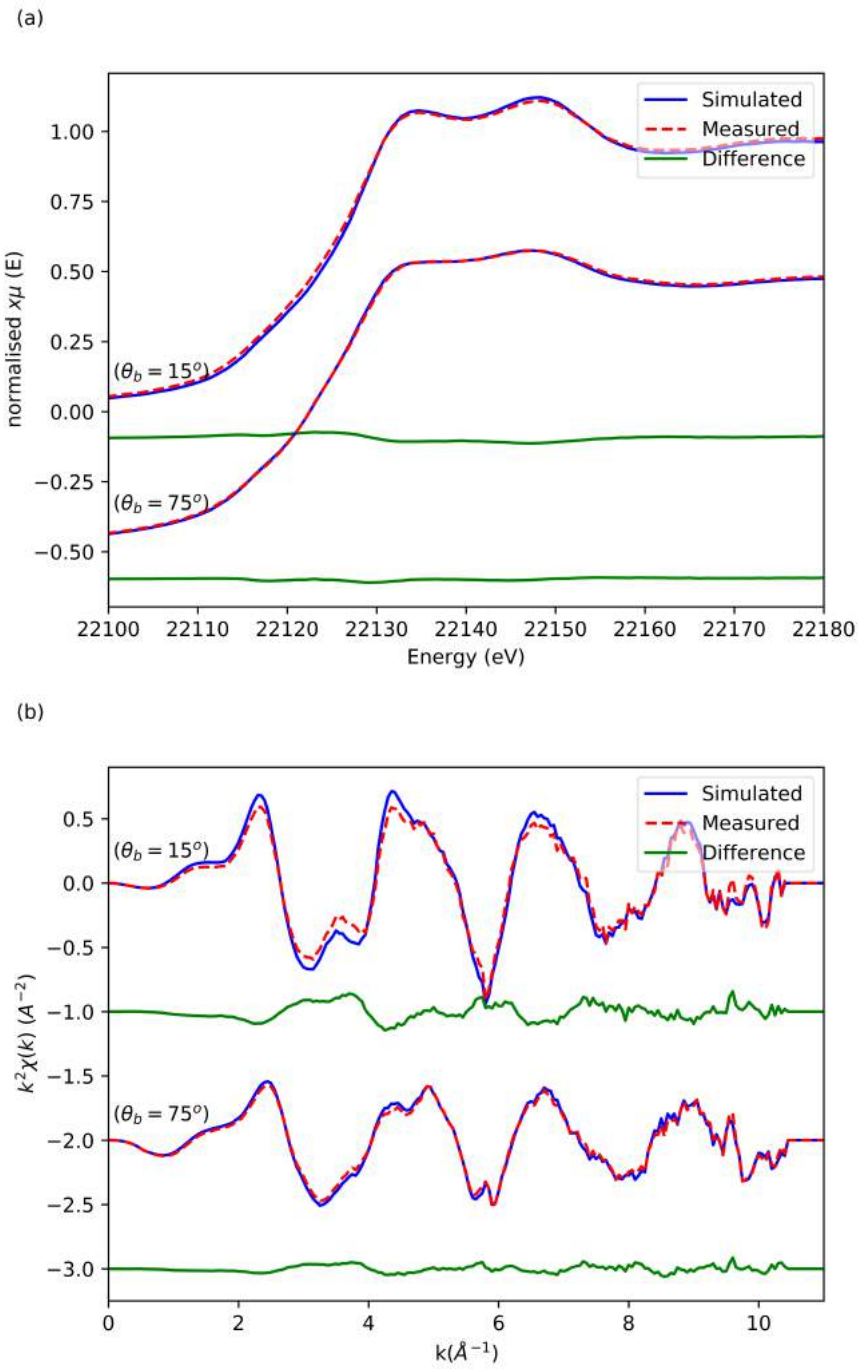

Figure 6.7: Simulated and measured XANES, (a), and EXAFS, (b), of the Ru K-edge of Ca_2RuO_4. Measured at 300K, and at 75° and 15° between c-axis and the beam.

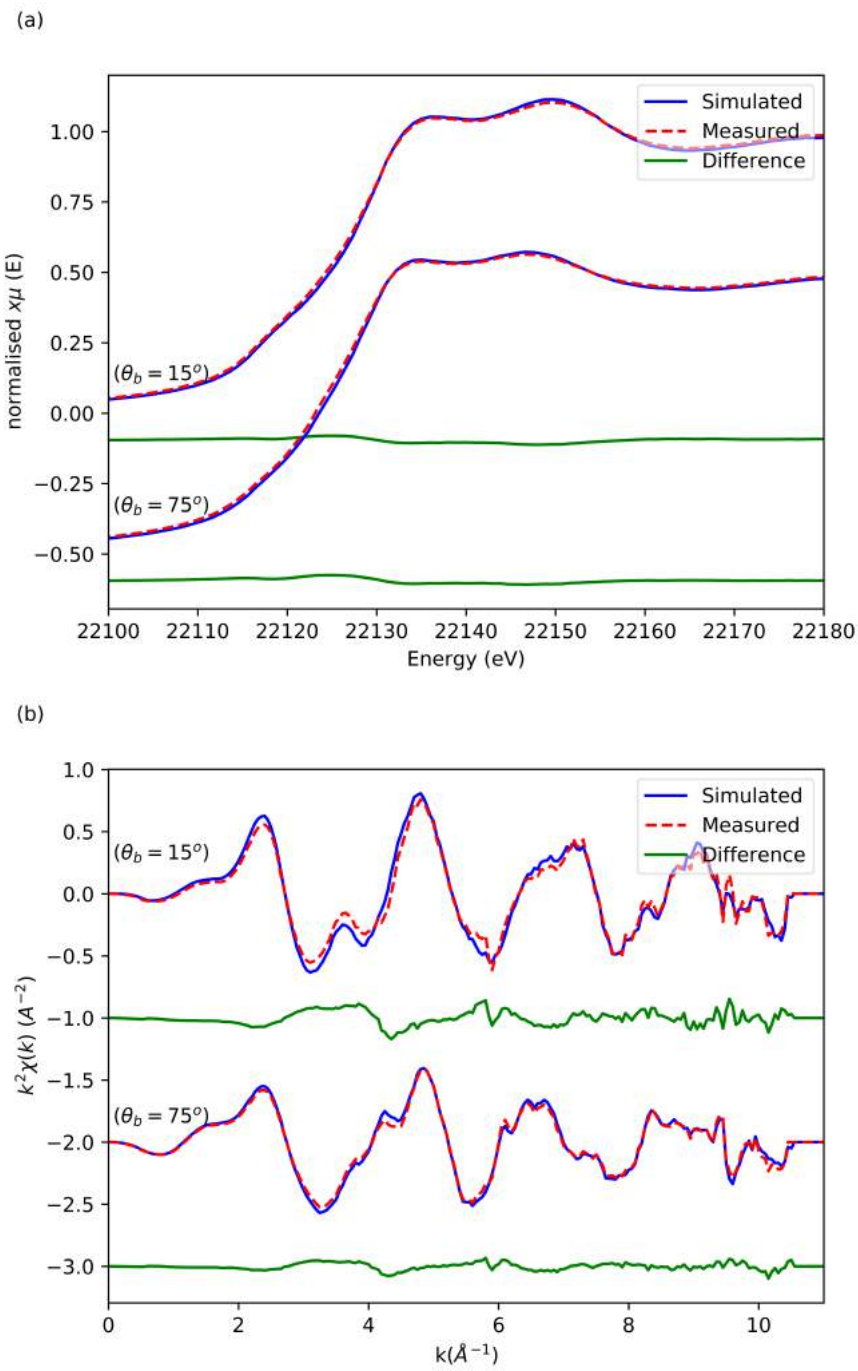

Figure 6.8: Simulated and measured XANES, (a), and EXAFS, (b), of the Ru K-edge of Ca_2RuO_4. Measured at 400K, and at 75° and 15° between c-axis and the beam.

XANES

From the position of the first peak in the XANES, seen in Figures 6.9 and 6.10, Ru is most likely in an oxidation state of +4 [187]. As we are measuring the Ru K-edge, the normal transition responsible for the absorption edge would be between s and p orbitals. However due to hybridisation between the O $2p$ orbitals and the Ru $4d$ orbitals, the absorption edge is indirectly probing the $1s$ to $4d$ transition [141]. In a Jahn-Teller distortion of an octahedral structure, it is the d orbitals that are affected [188]. Probing these orbitals, either directly or indirectly, can provide information on the nature of the e_g and t_{2g} states.

From the XANES (Figures 6.9 and 6.10) it can be seen that there is not a great change in the signal with respect to the angle, for the 300K data. However for the data measured at 400K the positions of the peaks shift with angle. As there was no self-absorption correction performed on the XANES, no conclusions can be drawn from the intensities of the peaks because they will not be reliable. There is a clear trend in the XANES with respect to the angle, for both temperatures, with respect to the position of the absorption edge. This can be seen in the E_0 values found for the XANES (see Table 6.1). The absorption edge is found at a higher energy for the data measured close to the *ab*-plane. This suggests that the unoccupied states close to the *c*-axis are found at a lower energy than those close to the *ab*-plane. Therefore there may be more $1s$ to $t_{2g}(xz)$ or $t_{2g}(yz)$ transitions available for the Ru ions, as the $t_{2g}(xy)$ orbitals will be fully occupied [43, 44].
Comparing the XANES at both temperatures for the two extreme angles measured (see Figure 6.11), there is a visible shift for the measurement close to the *ab*-plane. This may be due to a change in occupancy, but could also indicate a structural distortion. The most likely scenario is a structural distortion as the XANES close to the *c*-axis does not change with respect to temperature. The XANES suggest that as the temperature is decreased there is an increase in unoccupied states close to the *ab*-plane, as the absorption edge is found at a lower energy at 300K ($22128.2 \pm 1eV$) than at 400K ($22128.8 \pm 1eV$). If the shift observed was due to a change in the occupancy, a consequence of there being more unoccupied states along the *ab*-plane (at 300K) is that there should be less unoccupied states along the *c*-axis. This would lead to an opposite shift, to the one observed close to the *ab*-plane, occurring in the data close to the *c*-axis. However the XANES close to the *c*-axis do not change much with temperature, and the position of the absorption edge is found at roughly the same position for both temperatures ($22125.9 \pm 1eV$ at 300K and $22126.0 \pm 1eV$ at 400K).

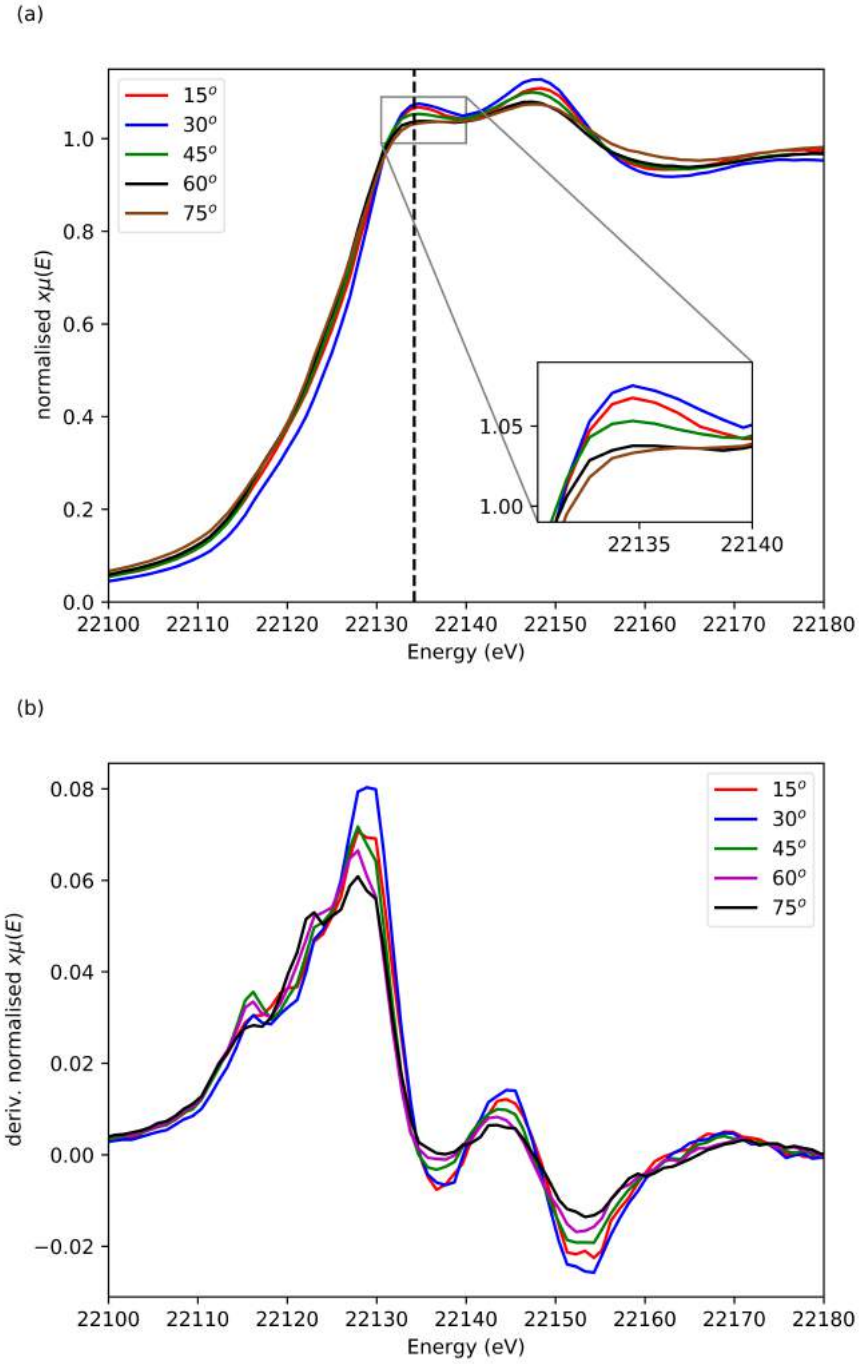

Figure 6.9: XANES of the Ru K-edge of Ca_2RuO_4, at 300K and different angles, with respect to the c-axis.

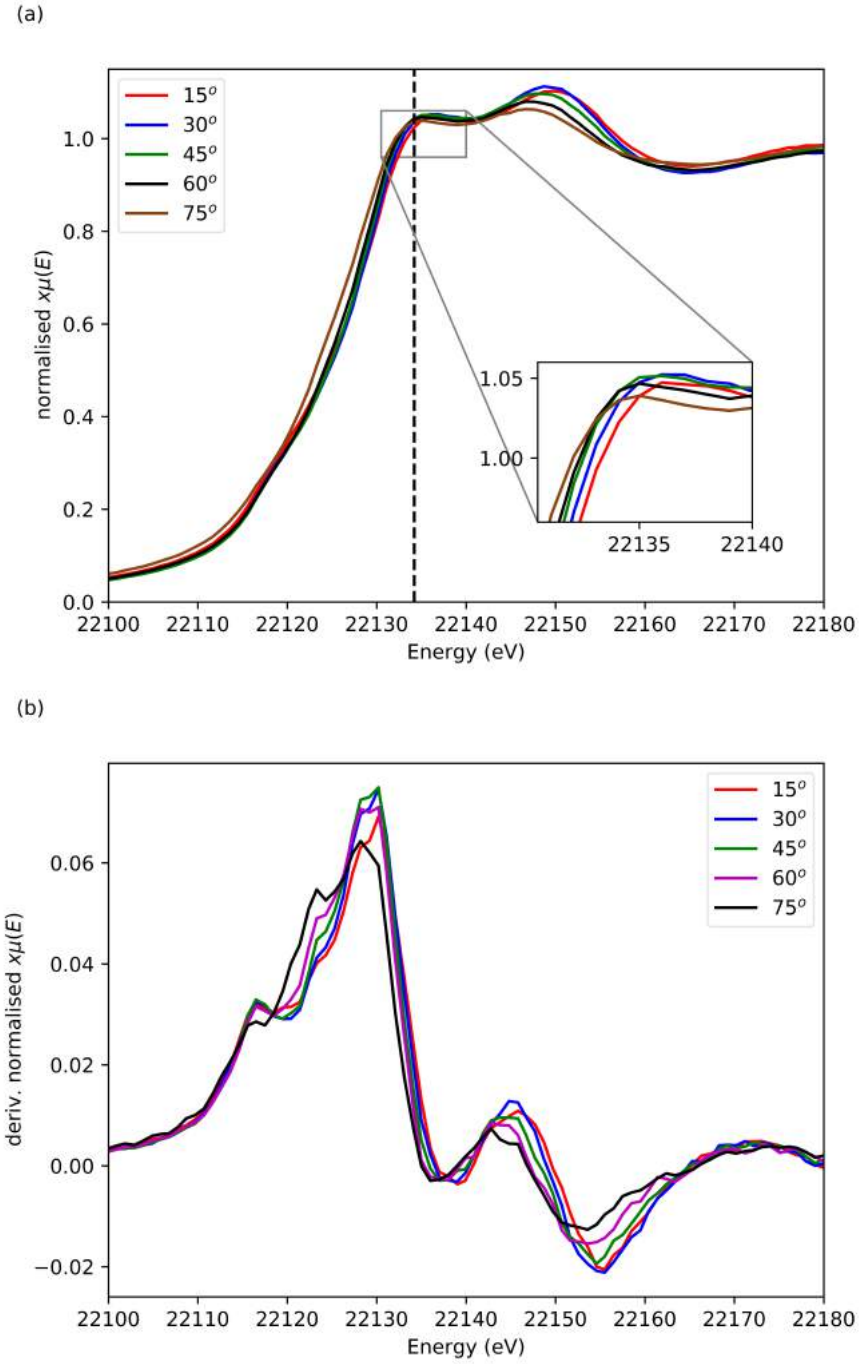

Figure 6.10: XANES, (a), and first derivative, (b), of the Ru K-edge of Ca_2RuO_4, at 400K and different angles, with respect to the c-axis.

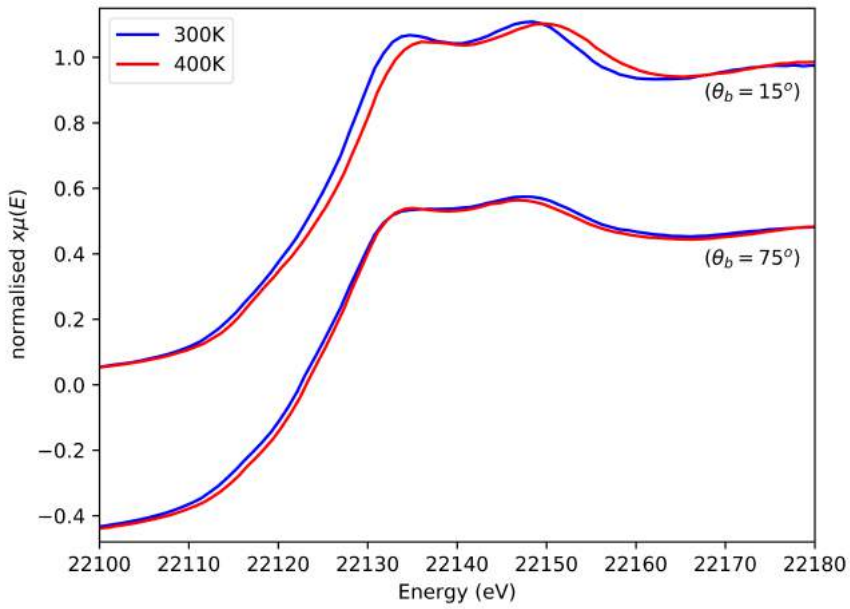

Figure 6.11: XANES of the Ru K-edge of Ca_2RuO_4 for the two extreme angles measured, comparing the temperatures 300K and 400K.

Additional XANES measurements were made as a function of two angles, between the beam and the c-axis (θ_b), and the ab-plane (ϕ_b)[1]. The values reported for ϕ_b below are with reference to the initial position of the crystal, with respect to the beam and the ab-plane. Where the full XAS measurements were taken at $\phi_b = 0^o$. The value for ϕ was not measured during the experiment, and is calculated as a fitting parameter when modelling the EXAFS.
From Figure 6.12 it can be seen that the position of the first peak in the XANES changes with respect to the angle between the polarisation and the ab-plane. There is also a change in the value of E_0, where the values are roughly the same for $\phi_b \geq 30^o$ (see Table 6.2). The change in the values for E_0, between the two extreme angles measured, is slightly larger for the $\phi_b \geq 30^o$ ($2.9eV$) than for the $\phi_b = 0^o$ ($2.3eV$). This indicates there is anisotropy in the ab-plane, as the XANES suggest that the electronic configuration changes with respect to the position of the beam within the ab-plane.

Table 6.2: E_0's (eV) of the Ru K-edge for all θ_b's and ϕ_b's measured.

	ϕ_b:			
θ_b:	0°	30°	60°	90°
15°	22128.2±1	22129.8±1	22129.8±1	22129.9±1
30°	22128.0±1	22129.5±1	22129.5±1	22129.5±1
45°	22127.0±1	22128.8±1	22128.8±1	22128.8±1
60°	22126.8±1	22128.0±1	22128.0±1	22128.0±1
75°	22125.9±1	22126.9±1	22126.9±1	22126.9±1

[1]These measurements were only taken in the XANES region at 300K, with an energy step of $\sim 1eV$ and count time of ~ 0.4s. Only one scan per angle was measured.

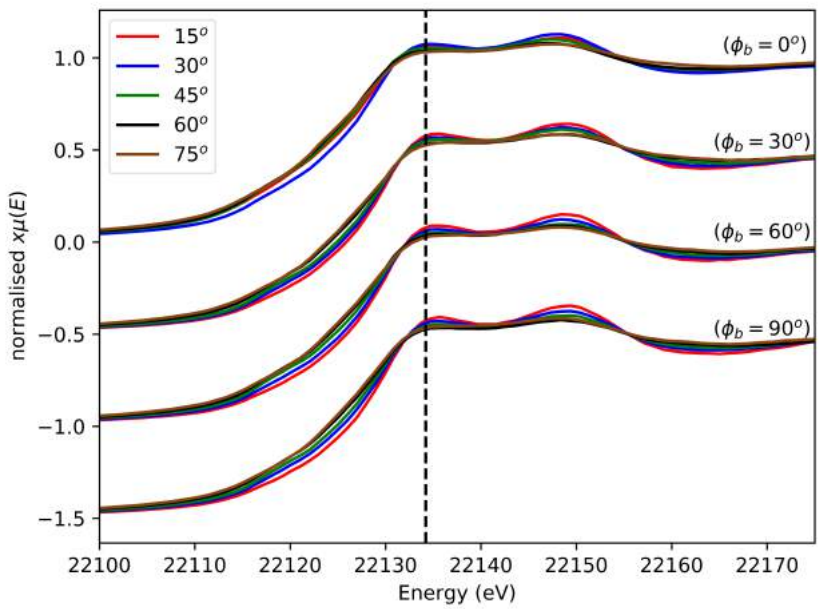

Figure 6.12: XANES of the Ru K-edge of Ca_2RuO_4, at 300K, and at different angles, with respect to the c-axis. Where the sample has been rotated in the ab-plane.

EXAFS

Figures 6.15 and 6.16 show the EXAFS and FT-EXAFS of the Ru K-edge absorption, at 300K, and 400K, respectively. The EXAFS and FT-EXAFS have been plotted with a k-weight of 2, and with a Fourier transform k-range of 3 to 9Å^{-1}. The FT-EXAFS presented have not been phase corrected, meaning the peak positions will not match the predicted positions from the model.
The path lengths and their angles, with respect to the c- and a-axis, can be seen in Table 5.5, obtained from the room temperature model [46].

Table 6.3: Structural information, of the single scattering paths, obtained from the room temperature model, seen in Figure 6.2(a) [46].

Path	Path distance (Å)	θ_i (^{o})	ϕ_i (^{o})	Weighting of path
1st Ru-O	1.98	81.87	-33.84	5/7
“ ”	“ ”	“ ”	33.84	2/7
“ ”	“ ”	98.13	-33.84	5/7
“ ”	“ ”	“ ”	33.84	2/7
2nd Ru-O	1.994	81.93	56.94	5/7
“ ”	“ ”	“ ”	-56.94	2/7
“ ”	“ ”	98.07	56.94	5/7
“ ”	“ ”	“ ”	-56.94	2/7
3rd Ru-O	1.995	9.31	15.19	5/7
“ ”	“ ”	“ ”	-15.19	2/7
“ ”	“ ”	170.67	15.19	5/7
“ ”	“ ”	“ ”	-15.19	2/7
1st Ru-Ca	3.054	54.51	88.93	5/7
“ ”	“ ”	“ ”	-88.93	2/7
“ ”	“ ”	125.49	88.93	5/7
“ ”	“ ”	“ ”	-88.93	2/7
2nd Ru-Ca	3.206	56.43	-5.59	5/7
“ ”	“ ”	“ ”	5.59	2/7
“ ”	“ ”	123.57	-5.59	5/7
“ ”	“ ”	“ ”	5.59	2/7
3rd Ru-Ca	3.283	57.32	5.41	5/7
“ ”	“ ”	“ ”	-5.41	2/7
“ ”	“ ”	122.68	5.41	5/7
“ ”	“ ”	“ ”	-5.41	2/7
4th Ru-Ca	3.491	59.48	-89.11	5/7
“ ”	“ ”	“ ”	89.11	2/7
“ ”	“ ”	120.52	-89.11	5/7
“ ”	“ ”	“ ”	89.11	2/7
Ru-Ru	3.855	90	45.43	2
“ ”	“ ”	“ ”	-45.43	2
4th Ru-O	3.946	85.93	16.10	5/7
“ ”	“ ”	“ ”	-16.10	2/7
“ ”	“ ”	94.07	16.10	5/7
“ ”	“ ”	“ ”	-16.10	2/7
5th Ru-O	3.996	85.98	-74.32	5/7
“ ”	“ ”	“ ”	74.32	2/7
“ ”	“ ”	94.02	-74.32	5/7
“ ”	“ ”	“ ”	74.32	2/7
6th Ru-O	4.085	61.19	-48.04	5/7
“ ”	“ ”	“ ”	48.04	2/7
“ ”	“ ”	118.81	-48.04	5/7
“ ”	“ ”	“ ”	48.04	2/7
7th Ru-O	4.197	62.03	49.79	5/7
“ ”	“ ”	“ ”	-49.79	2/7
“ ”	“ ”	117.97	49.79	5/7
“ ”	“ ”	“ ”	-49.79	2/7
5th Ru-Ca	4.216	3.60	79.87	5/7
“ ”	“ ”	“ ”	-79.87	2/7
“ ”	“ ”	176.40	79.87	5/7
“ ”	“ ”	“ ”	-79.87	2/7

As the data could not be reliably corrected for self-absorption, the amplitudes of the k-space data and the intensity of the peaks in the real space data cannot be discussed thoroughly. The positions of the peaks, in the FT-EXAFS, however can be discussed in more detail.
There are visible changes in the EXAFS signal, with respect to angle, for both temperatures (Figures 6.15 and 6.16). The structure of the signal changes in the 3 to 6Å^{-1} range in the 300K data. Whereas in the 400K data the structure of the signal changes further out, in the 6 to 8Å^{-1} range. Comparing the two extreme angles measured (Figure 6.17), there is a larger change in the EXAFS signal in the $\theta_b = 15^o$ data, with respect to temperature. Whereas the signal measured at $\theta_b = 75^o$ does not change much with temperature. This suggests that the local structure of the Ru ions undergoes larger changes close to the ab-plane.
Comparing the position of the first peak of the FT-EXAFS for both temperatures (see Figures 6.15 and 6.16) it can be concluded that the Ru-O octahedra undergoes a structural change with respect to temperature. This peak has its strongest contributions from the first three Ru-O scattering paths, which make up the Ru-O octahedra. The changes in the Ru-O octahedra between the room temperature and 400K models can be seen in Figure 6.13. Where the z and x/y axes have been marked with respect to the centre of the absorbing atom, to make the changes clearer. The angle between the z-axis and the Ru-O1, and Ru-O2 paths become shallower in the high temperature (400K) model. The position of this peak remains the same at all angles for the 300K data, suggesting that the Ru-O paths are the same length in the octahedra. For the data measured at 400K, the position of the first peak changes with respect to the angle. This suggests that the Ru-O paths that lay nearer the ab-plane are shorter than the paths that lay near the c-axis.

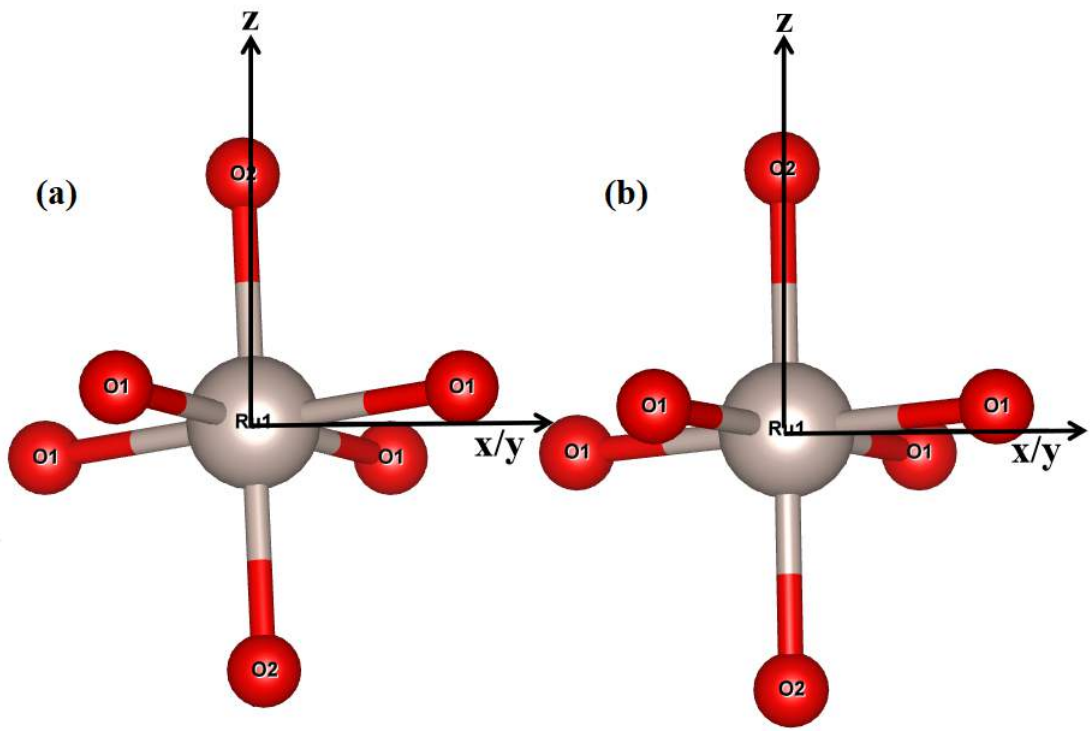

Figure 6.13: The single scattering paths that contribute to the first peak of the FT-EXAFS of Ca_2RuO_4, at room temperature [46] (a), and at 400K citefriedt01 (b).

From the FT-EXAFS at 300K (Figure 6.15b) it can be seen that there is a small change in the position of the second peak with respect to the angle. The peak also splits

at $\theta_b = 15^o$. This peak has it largest contributions from the first four Ru-Ca scattering paths, these paths form a tilted cuboid shape when viewed together (Figure 6.14). For the 400K data (Figure 6.16b) the position of this peak changes with angle, but remains as one peak. This suggests that there is a greater structural change in the Ru-Ca cuboid at 300K, as the peak displays a much larger variation with respect to the angle. Comparing the FT-EXAFS of the two extreme angles measured (see Figure 6.17b) it can be seen that the largest change with respect to temperature is seen in the second peak. This peak undergoes a much larger change with respect to the temperature when measured close to the *ab*-plane ($\theta_b = 15^o$). This suggests that the proposed structural transition greatly affects the Ru-Ca scattering paths.

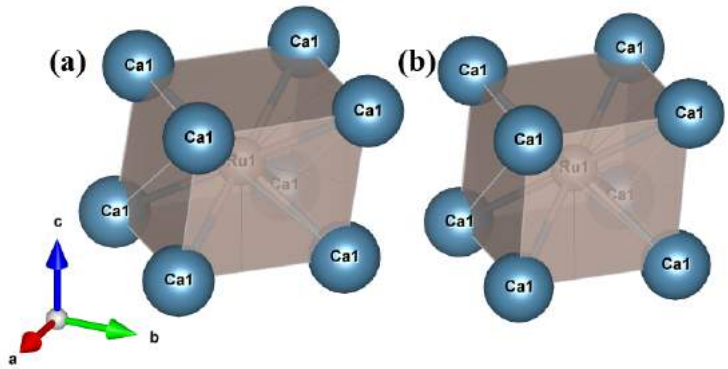

Figure 6.14: Tilted cuboid formed by the first four Ru-Ca single scattering paths, obtained from the models, (a) at room temperature [46] and (b) at 400K [184].

The peak at $\sim$ 3.855Å has its strongest contributions from the Ru-Ru scattering path. This peak is almost completely suppressed for the higher angles measured. This is due to the scattering path being found along the ab-plane, therefore it would be perpendicular to the polarisation and would not contribute to the EXAFS signal. The reduction of this peak is consistent for both temperatures, however at 400K the peak is not completely reduced, which suggests that the Ru-Ru path may not lay completely in the *ab*-plane in the paramagnetic structure. This could be a consequence of the predicted tilt in the Ru-O octahedra.

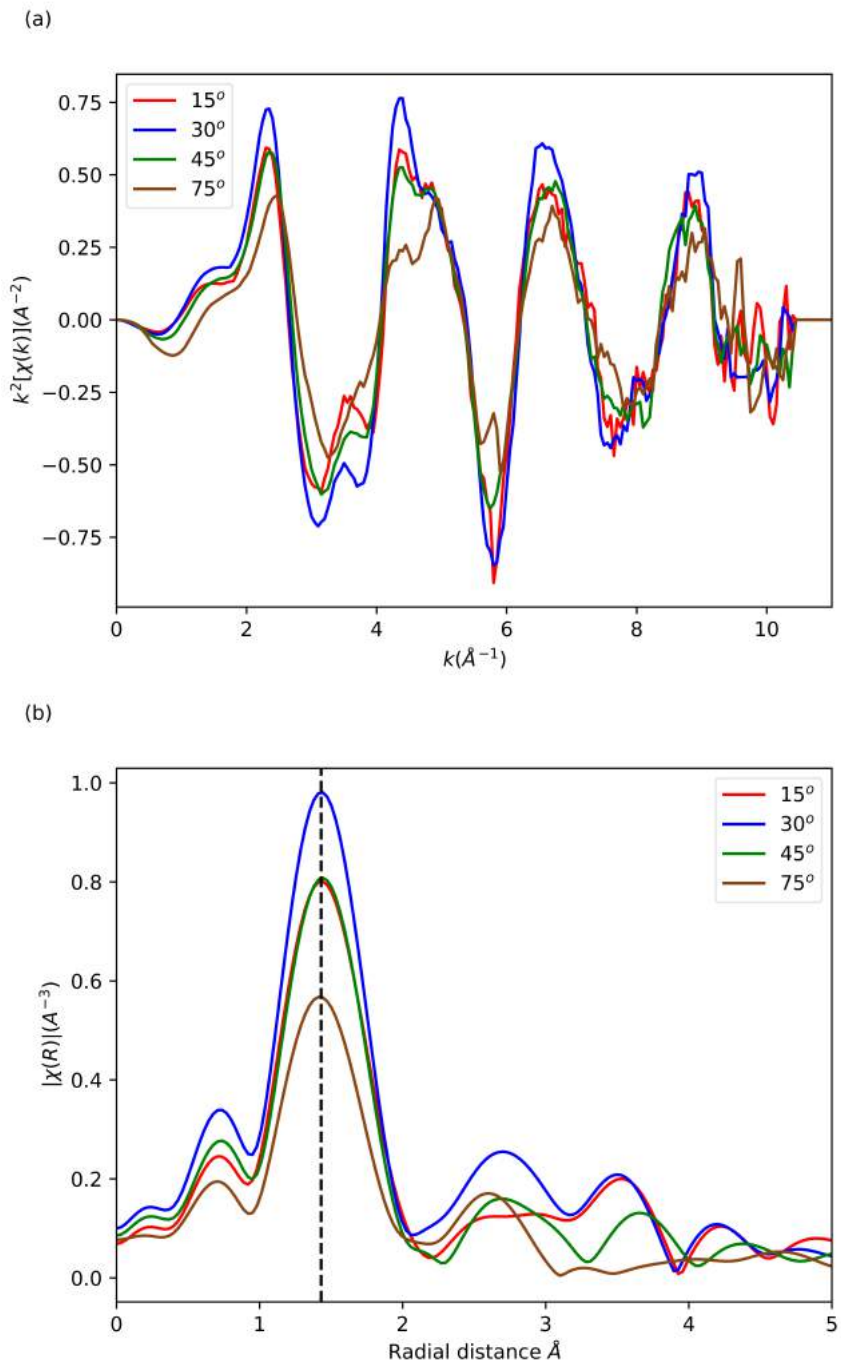

Figure 6.15: EXAFS, (a), and FT-EXAFS, (b), of the Ru K-edge of Ca_2RuO_4, at 300K and different angles, with respect to the c-axis.

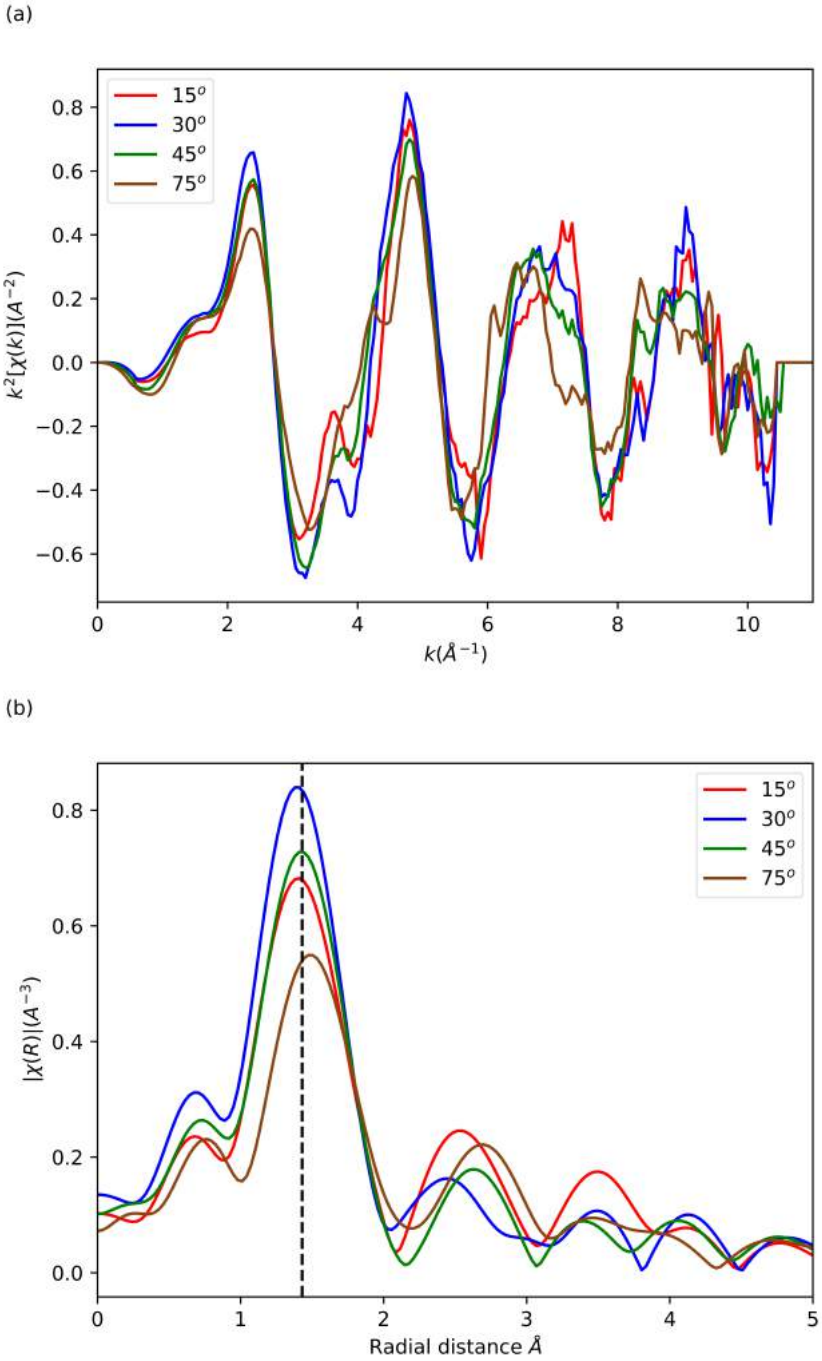

Figure 6.16: EXAFS, (a), and FT-EXAFS, (b), of the Ru K-edge of Ca_2RuO_4, at 400K and different angles, with respect to the c-axis.

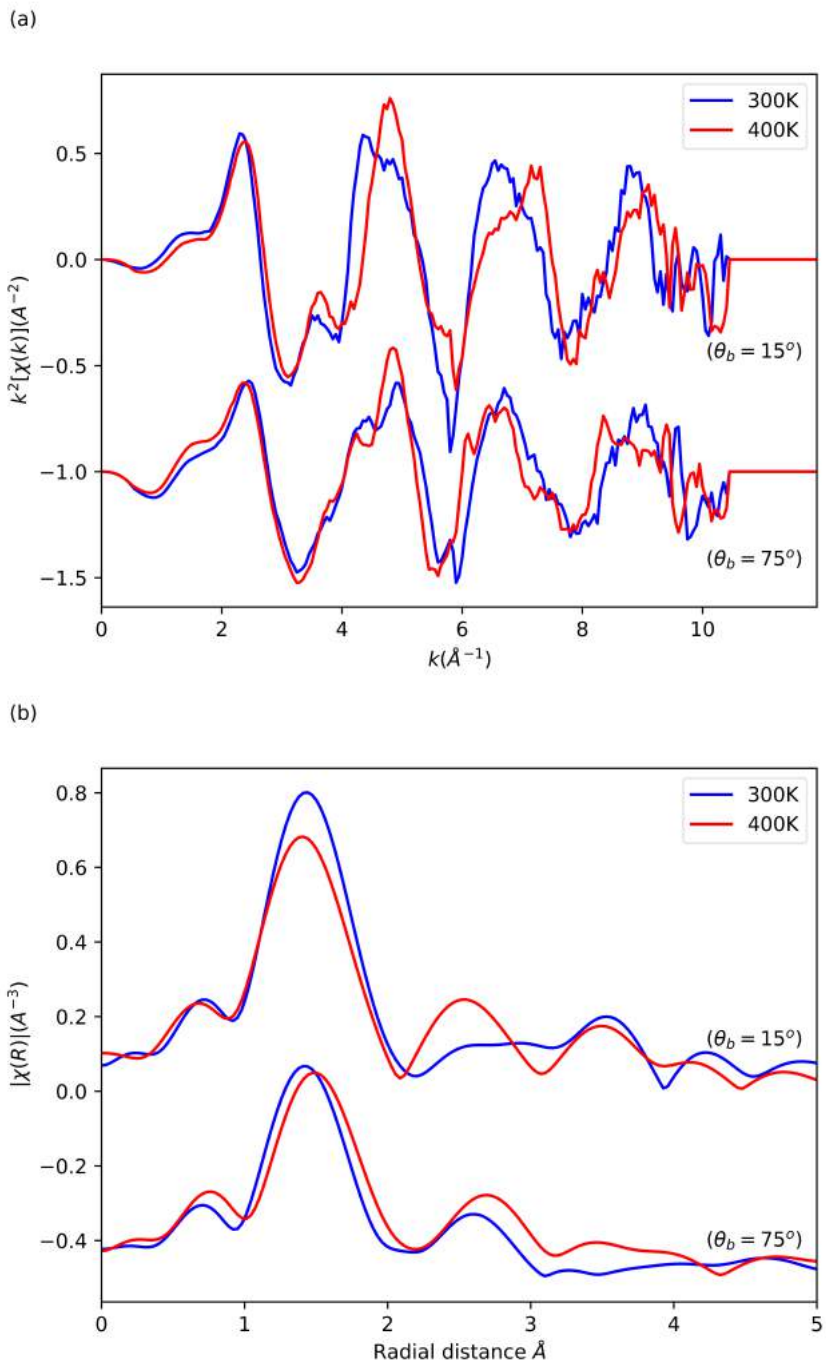

Figure 6.17: EXAFS, (a), and FT-EXAFS, (b), of the Ru K-edge of Ca_2RuO_4, comparing the temperatures 300K and 400K, at the two extreme angles.

Fit of EXAFS

The model used in the fits, for both temperatures, was produced from a refinement to diffraction data, which was measured at room temperature [46]. A model produced from diffraction at 400K [184] was used as a comparison to the fit of the 400K EXAFS data. As the fit is obtained by modelling an averaged theoretical EXAFS signal (a default FEFF output), obtained from this model, a weighting factor needs to be introduced to make the averaged theoretical EXAFS equivalent to the EXAFS along one direction. The weighting factor is discussed in full in Chapter 3. Figures 6.18 and 6.19 show that there is more than one distinct scattering path of the same length within the unit cell, in both models[2]. When separating the scattering paths by angles there are degeneracies of each path within the unit cell. In the case of the scattering paths with a central Ru ion there are two sets of degenerate paths, 10 of one and 4 of the other. This is due to the angle the path is making with respect to the a-axis, and needs to be taken into account when fitting the data. The path lengths are degenerate, however the θ_i's and ϕ_i's change. This is accounted for in the weighting factor used in the fits. The refined parameters for the fits to the Ru K-edge EXAFS data, shown in Figures 6.20 and 6.21, can be found in Table 6.4. The parameters for the paths closer to the central atom are within their acceptable ranges, therefore the fits can be accepted. Fitting was carried out in R space, with k weightings of 1, 2, and 3, using 17 of 51, and 17 of 52 independent parameters for the 300K data, and the 400K, respectively. The fits resulted in a R-factor of 0.120, and 0.107, for the 300K data, and 400K data, respectively. The amplitudes, S_0^2, for the fits were set to the same value (0.55) for all angles and temperatures. When S_0^2 was allowed to vary for eahc θ_b, the values produced by the fit were not sensible. This is due to the data not being corrected for self-absorption, and the fit trying to compensate between the model and the data. The angles θ_i and ϕ_i (in the weighting factor) for the single scattering paths have been set to those calculated from the model (see Table 6.3)[3]. As all angles measured are fit simultaneously, this additional data opens up more guess parameters for the fit. For a comparison as to how the structure changes with temperature, both data sets have been fit to the room temperature model. All single scattering paths have been included in the fit with a degeneracy (N) of 1. To account for the distinct paths each single scattering path is separated and the amplitude is multiplied by a weighting that corresponds to their frequency in the unit cell. The single scattering paths used were calculated from the model up to $\sim$ 4.2Å.

[2]The single scattering paths are visually very similar in both models, with a slight angle difference. Therefore an image of the single scattering paths for the 400K model has not been included.

[3]The calculation and treatment of the angles in the weighting factor is discussed in Chapter 3.

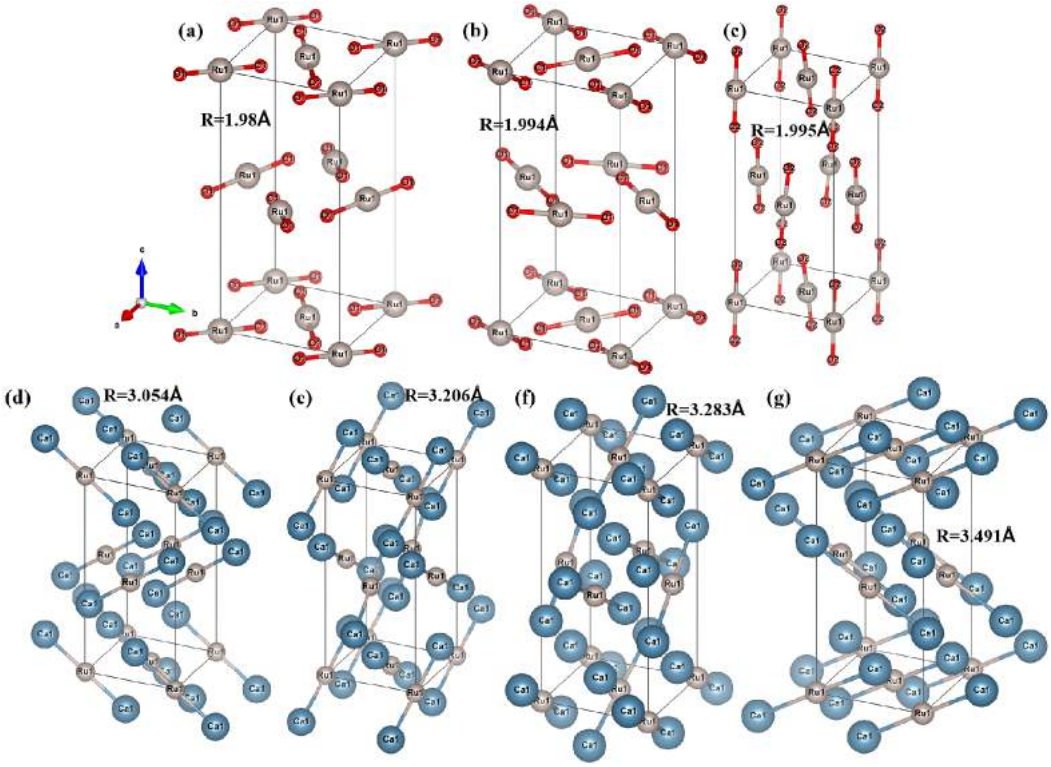

Figure 6.18: The single scattering paths, up to 3.491Å, used in the fit of the Ru K-edge Ca_2RuO_4 data. With (a) 1st Ru-O, (b) 2nd Ru-O, (c) 3rd Ru-O, (d) 1st Ru-Ca, (e) 2nd Ru-Ca, (f) 3rd Ru-Ca, and (g) 4th Ru-Ca.

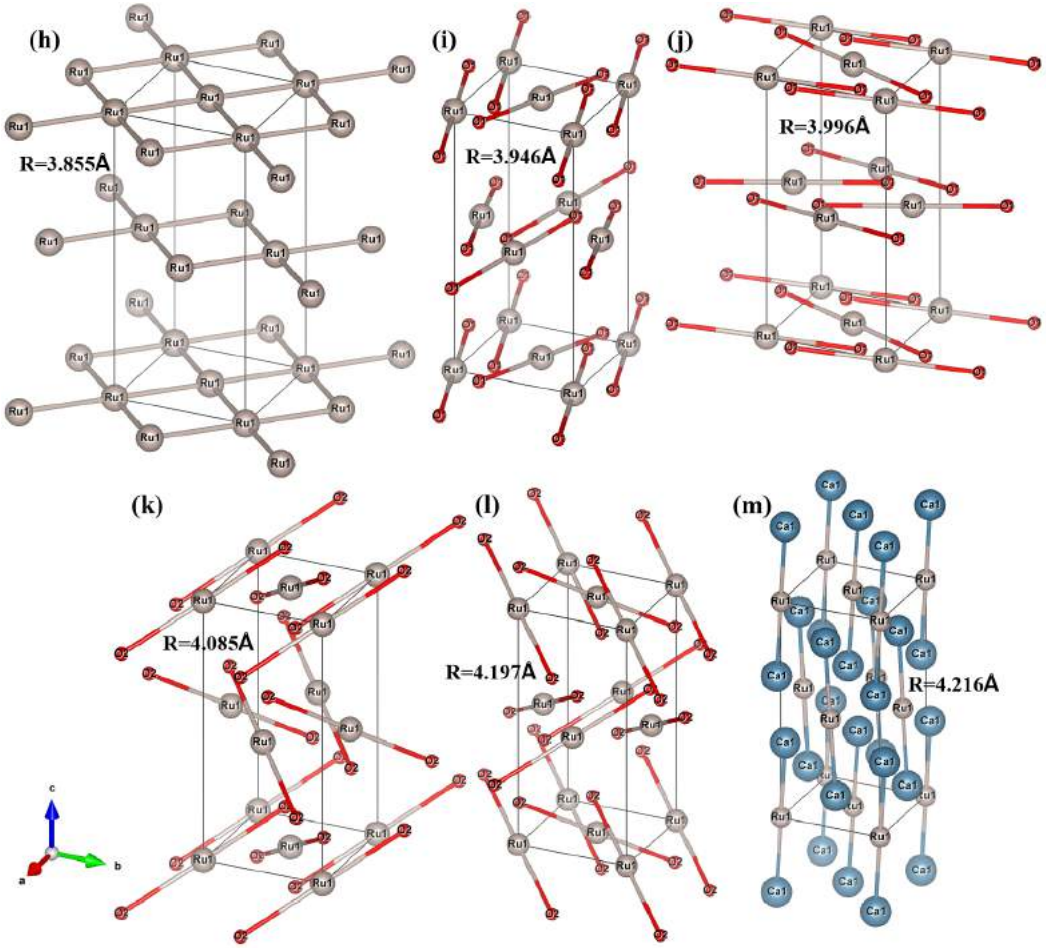

Figure 6.19: The single scattering paths, from 3.855Å to 4.216Å, used in the fit of the Ru K-edge Ca_2RuO_4 data. With (h) Ru-Ru, (i) 4th Ru-O, (j) 5th Ru-O, (k) 6th Ru-O, (l) 7th Ru-O, and (m) 5th Ru-Ca.

Table 6.4: Fit parameters for the Ru K-edge EXAFS of the 300K and 400K single crystal data. The amplitudes of the fit have been set to 0.55 for each angle and temperature. The energy shift of these fits was set to one value for each temperature. The degeneracy (N) of each path was set to 1. The azimuthal angle of the polarisation, ϕ, was set to 30°.

	Temperature (K):		
Parameter:	300	400	Model (300K) [46]
Reduced χ^2	1028.29	1023.23	-
ΔE_0 (eV)	-5±2	-4±2	-
1st Ru-O R (Å)	1.96±0.01	1.94±0.01	1.980
1st Ru-O σ^2 (Å^2)	0.0012±0.0009	0.006±0.001	-
2nd Ru-O R (Å)	1.98±0.01	1.95±0.01	1.994
2nd Ru-O σ^2 (Å^2)	0.0012±0.0009	0.006±0.001	-
3rd Ru-O R (Å)	1.96±0.02	2.01±0.02	1.995
3rd Ru-O σ^2 (Å^2)	0.018±0.003	0.013±0.002	-
1st Ru-Ca R (Å) (up/down)	3.00±0.03/3.06±0.08	3.07±0.03/3.13±0.08	3.054
1st Ru-Ca σ^2 (Å^2) (up/down)	0.013±0.005/0.01±0.01	0.006±0.003/0.01±0.01	-
2nd Ru-Ca R (Å) (up/down)	3.15±0.03/3.22±0.08	3.22±0.03/3.29±0.08	3.206
2nd Ru-Ca σ^2 (Å^2) (up/down)	0.013±0.005/0.01±0.01	0.006±0.003/0.01±0.01	-
3rd Ru-Ca R (Å) (up/down)	3.23±0.03/3.29±0.08	3.30±0.03/3.36±0.08	3.283
3rd Ru-Ca σ^2 (Å^2) (up/down)	0.013±0.005/0.01±0.01	0.006±0.003/0.01±0.01	-
4th Ru-Ca R (Å) (up/down)	3.44±0.03/3.50±0.08	3.51±0.03/3.57±0.08	3.491
4th Ru-Ca σ^2 (Å^2) (up/down)	0.013±0.005/0.01±0.01	0.006±0.003/0.01±0.01	-
Ru-Ru R (Å)	4.01±0.05	3.90±0.07	3.855
Ru-Ru σ^2 (Å^2)	0.001±0.007	0.010±0.008	-
4th Ru-O R (Å)	3.98±0.04	3.9±0.1	3.946
4th Ru-O σ^2 (Å^2)	-0.014±0.005	0.00±0.02	-
5th Ru-O R (Å)	4.03±0.04	3.9±0.1	3.996
5th Ru-O σ^2 (Å^2)	-0.014±0.005	0.00±0.02	-
6th Ru-O R (Å)	3.74±0.04	3.7±0.2	4.085
6th Ru-O σ^2 (Å^2)	-0.010±0.006	0.01±0.03	-
7th Ru-O R (Å)	3.86±0.04	3.9±0.2	4.197
7th Ru-O σ^2 (Å^2)	-0.010±0.006	0.01±0.03	-
5th Ru-Ca R (Å)	4.3±0.1	4.38±0.04	4.216
5th Ru-Ca σ^2 (Å^2)	0.02±0.02	0.009±0.005	-

An acceptable fit was produced by using the room temperature model and refining this against the Ru K-edge EXAFS, the path distances and DWs were allowed to change for each temperature and are fit simultaneously for each angle. The sum of all the relevant single scattering contributions to the Ru K-edge EXAFS of Ca_2RuO_4, at 300K and 400K, are shown in Figures 6.20 and 6.21 fitted against the EXAFS data, respectively. The FT-EXAFS was fit up to 4.2Å, as the peaks further out did not produce sensible parameters when modelled.
The best fit was produced when certain single scattering paths were grouped, this was the case for both temperatures. The first two Ru-O paths, that are found along the *ab*-plane, were paired [(a)-(b) in Figure 6.18]. The first four Ru-Ca paths, that form a tilted cuboid, were grouped [(d)-(e)-(g)-(f) in Figure 6.18, also see Figure 6.14]. They have also been separated by their 'up' (large θ_i) and 'down' (small θ_i) components, so that the Ru-Ca cuboid can only vary in length with respect to the *c*-axis. The fourth and fifth Ru-O paths are both found along the *ab*-plane, these paths have been paired in the fit [(i)-(j) in Figure 6.19]. The sixth and seventh Ru-O paths are found at a $\sim 55^o$ angle to the *ab*-plane, these paths have been paired in the fit [(k)-(l) in Figure 6.19].
The first peak corresponds to the Ru-O octahedra, this is where the Jahn-Teller distortion will occur. An angular change was needed for the Ru-O octahedra to improve the fit at 400K, a tilt in θ_i was set to 3.00^o, and a twist in ϕ_i was set to 1.13^o for the paths along the *ab*-plane, and 5.36^o for the paths along the *c*-axis. These angular changes were inferred from the change in the Ru-O octahedra between the room temperature model and the 400K model.
The overall structure of the data is modelled to a reasonable level for both temperatures. However there are discrepancies between the fit and the data, the intensities of the peaks could not be modelled accurately for the two extreme angles measured. The miss alignment of the intensities between the fit and the measured EXAFS most likely stems from the data not being corrected for self-absorption. There are also some peak positions that do not align well from the fit. There are also negative DWs for the fit at 300K, they affect the paths that are found further away from the central atom (> 3.946Å). These negative DWs can be justified as the model will be trying to compensate for the lack of self-absorption correction.

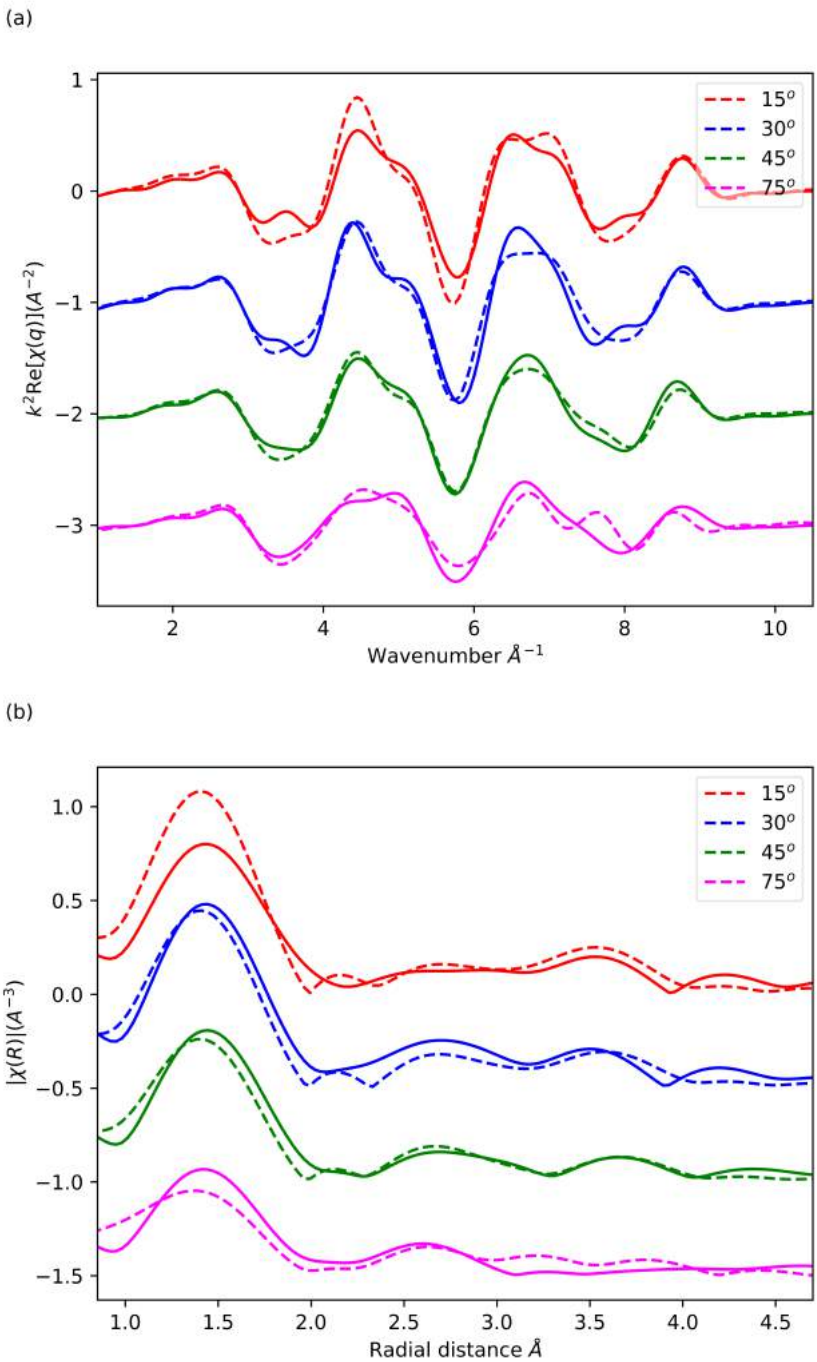

Figure 6.20: Fit of the Ru K-edge at 300K, in q space (a) and R space (b). The data was fitted to the room temperature orthorhombic structure [46]. All angles measured and fitted are presented in this plot. The solid line corresponds to the experimental data and the dashed line corresponds to the fit.

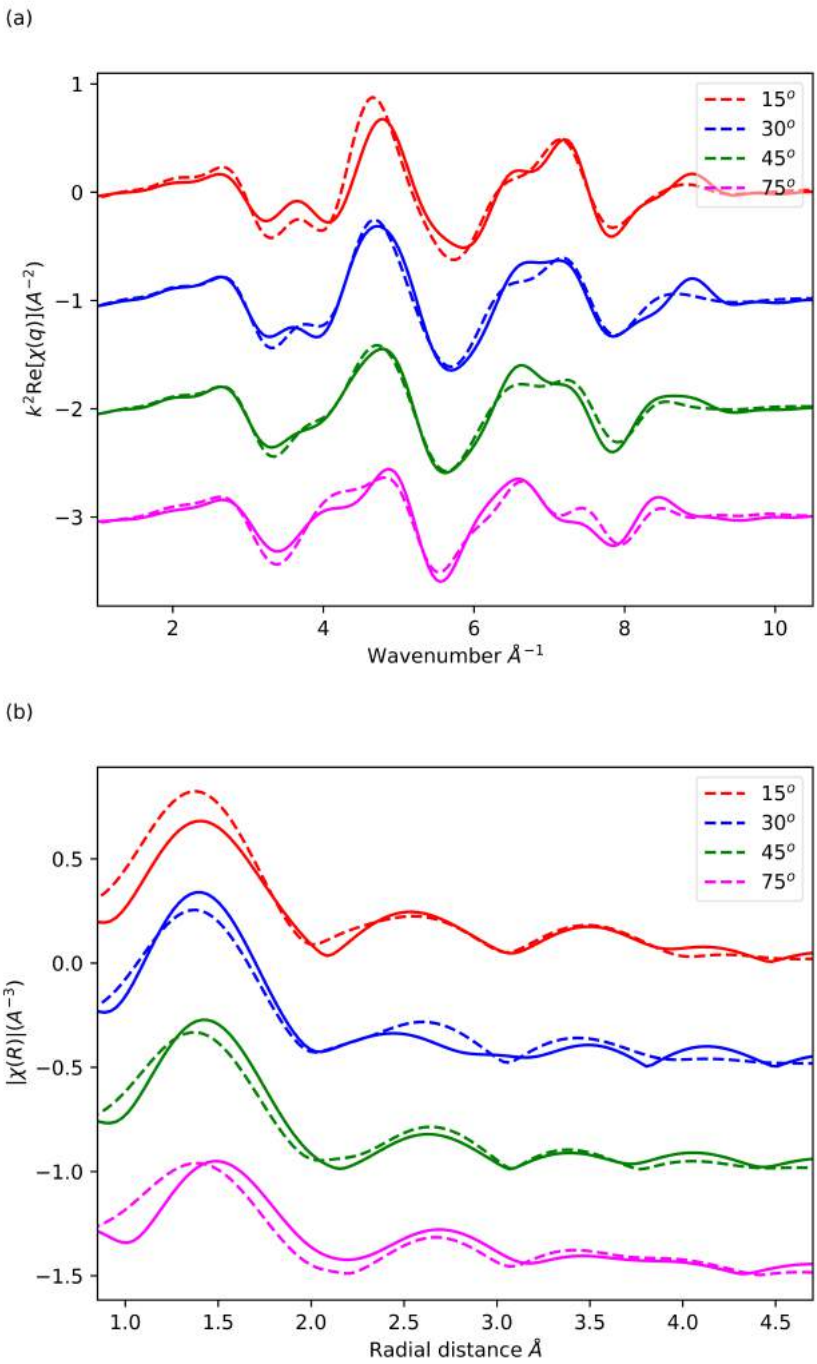

Figure 6.21: Fit of the Ru K-edge at 400K, in q space (a) and R space (b). The data was fitted the to the room temperature orthorhombic structure [46]. All angles measured and fitted are presented in this plot. The solid line corresponds to the experimental data and the dashed line corresponds to the fit.

6.4 Discussion

From the XANES measurements we observe that there is splitting of the white line (see Figures 6.9 to 6.11). There is no visible pre-edge feature in the XANES for either temperature measured (see Figures 6.9 and 6.10), this suggests that there are no quadrupole transitions allowed for this symmetry.
There is a greater change in the XANES, with respect to decreasing temperature, for the measurements closer to the *ab*-plane. The absorption edge shifts, requiring a lower energy for an absorption interaction to occur at 300K, compared to 400K. This is consistent with a compression Jahn-Teller distortion as the temperature is decreased. In a compression Jahn-Teller distortion the d orbitals split, where the orbitals with z components are at higher energies than the orbitals without z components, see Figure 6.22. This would mean it requires less energy for transition to occur for an orbital without a z component. As Ca_2RuO_4 is reported to have an electron configuration of $4d^4$ (t_{2g}^4,e_g^0), its nearest unoccupied state will be either $t_{2g}(xz)$ or $t_{2g}(yz)$, this may explain why there is no large change in the XANES with respect to angle, for the 300K data.
In a elongation Jahn-Teller distortion, the orbitals with z components are found at a lower energy than the orbitals without z components. This would mean, in the case of a low spin material, the $t_{2g}(xy)$ would be the nearest unoccupied state. This would be clearer in the data as this should result in a more distinct change in the XANES with respect to angle.

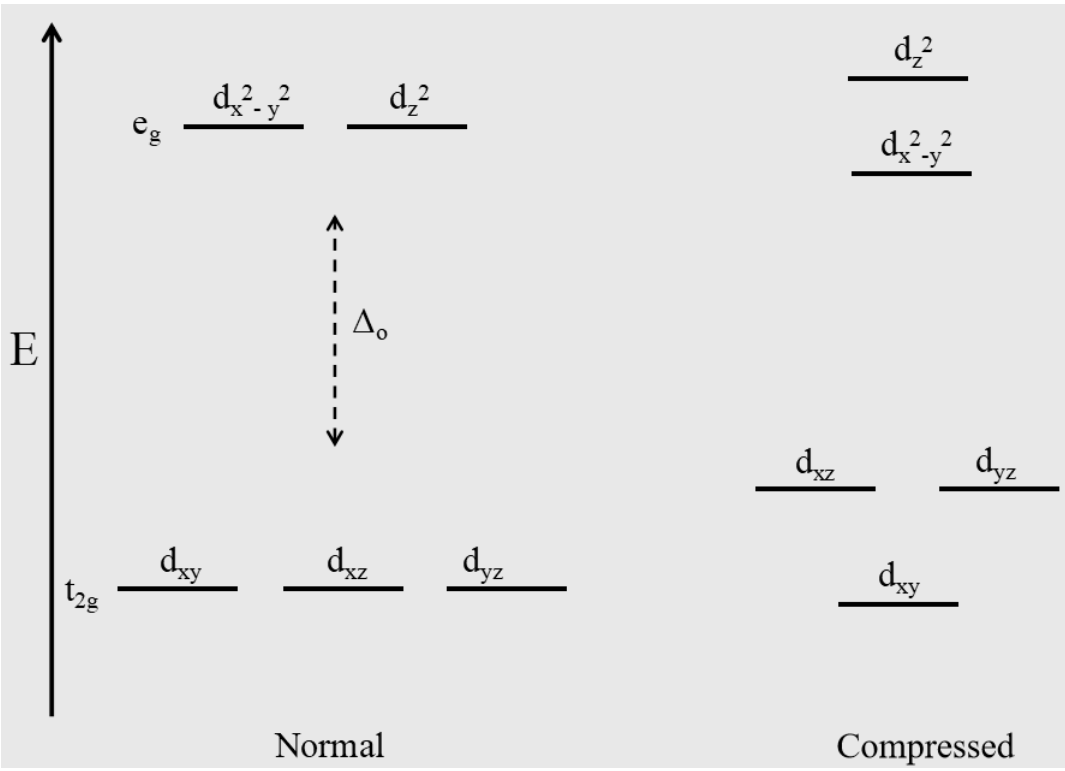

Figure 6.22: A simple diagram of the effect of a Jahn-Teller compression on d orbitals [47].

Comparing the XANES at each temperature (Figures 6.9 and 6.10), both peaks do not display a large change due to the angle they are measured at. This suggests that either the transition is not orbital selective, or that the orbitals cannot be distinguished in the K-edge measurements. As there is no clear distinction of the orbitals in the XANES this suggests that the energy splitting is smaller than the core-hole width.

While the positions of the peaks at 300K do not vary much with angle, the positions of the peaks in the XANES at 400K do vary with angle, suggesting that there is a larger change in the electronic structure in the metallic phase.
From the FT-EXAFS there is a hint of a compression along the *c*-axis in the O octahedra surrounding the Ru atom, as the Mott insulator transition is followed. Where the FT-EXAFS at 300K (insulating phase) suggests a compression compared to the FT-EXAFS at 400K (metallic phase), this can be seen in Figure 6.17. As the position of the first peak for the data measured at 15° shifts further from the central atom as the temperature decreases, and the opposite occurs for the data at 75°.
From the fits, there appears to be an overall compression of the structure compared to both models. Both temperatures were fit to the room temperature model, meaning this model can be seen as a reference. The fit for the 300K data follows the hypothesis that there is a compression of the Ru-O octahedra in the insulating phase, where the axial paths are shorter than the equatorial paths. The fit for the 400K data (the metallic phase) suggests the axial paths are longer than the equatorial paths, for the Ru-O octahedra. The first Ru-O scattering path, found close to the *ab*-plane, increases in length as the temperature decreases, from 1.94 ± 0.01Å (at 400K) to 1.96 ± 0.01Å (at 300K). The second Ru-O scattering path, found close to the *ab*-plane, increases in length as the temperature decreases, from 1.95 ± 0.01Å (at 400K) to 1.98 ± 0.01Å (at 300K). The third Ru-O path, found close to the *c*-axis, decreases as the temperature decreases, from 2.01 ± 0.02Å (at 400K) to 1.96 ± 0.02Å (at 300K). A tilt (of $\theta_t = 3.00^o$) and twist (of $\phi_t = 1.13^o$ for the first two Ru-O paths, and $\phi_t = 5.36^o$ for the third Ru-O path) was also introduced for the Ru-O octahedra at 400K. This was inferred from the difference between the octahedra in the room temperature model (the reference) and the 400K model. As this improved the fit, this suggests that the Ru-O octahedra undergo an angular change, as well as a compression, as the temperature decreases. This is consistent with the conclusions from diffraction measurements, where there is a compression of the Ru-O octahedra following the Mott-insulator transition [44].
The other paths follow a compression, where the paths that lie closer to the *c*-axis (axial paths) decrease in length as the temperature decreases. Whereas the paths that lie closer to the *ab*-plane (equatorial paths) increase in length as the temperature decreases. The Ru-Ca cuboid (found between the *c*-axis and *ab*-plane) decreases in size as the temperature is decreased (see Table 6.4), as each path length is larger at 400K. The difference between the 'up' and 'down' components of the grouped Ru-Ca paths is the same for both temperatures (~ 0.6Å), this suggests that there is no additional structural change in the Ru-Ca cuboid between the two phases. While the Ru-Ru scattering path (found along the *ab*-plane) increases in size as the temperature decreases, from 3.90 ± 0.07Å (at 400K) to 4.01 ± 0.05Å (at 300K). The structural changes discerned from the fits are consistent with the reported changes seen in the diffraction measurements [189, 44, 184].
Figure 6.23 shows the *xyz* components of the first three scattering paths included in the fit, these paths contribute to the first peak and form the Ru-O octahedra. The fits to both temperatures were carried out using the room temperature model, where Ru-O1 is found at 1.98Å, Ru-O2 is found at 1.994Å, and Ru-O3 is found at 1.995Å. The *xyz* components of these paths show that the fits to the data follow the changes in the model rather closely. The only discrepancy is in the change of the *y* component for the second Ru-O path, where the fit follows the opposite trend of the model. This could be due to the change in angle for this path in the 400K fit. The trends seen in these components follow the predicted structural change in [44]. Where for a decreasing temperature the paths along the *ab*-plane increase in length, and the paths along the

c-axis decrease in length.

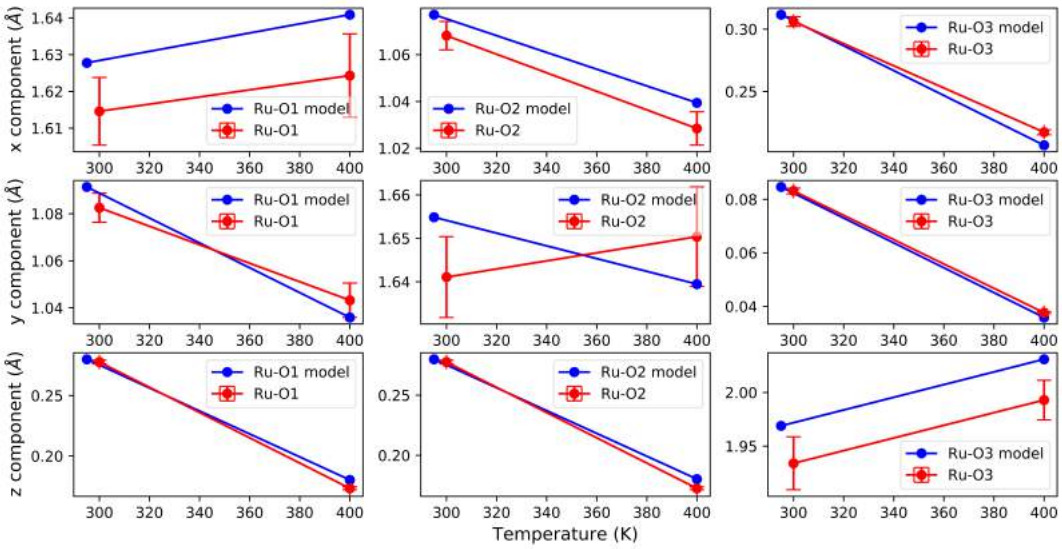

Figure 6.23: The change in the x, y, and z components of the scattering paths that contribute to the first peak. These paths make up the Ru-O octahedra in which the Jahn-Teller distortion will occur. The components from the room temperature and 400K models are also included.

6.5 Conclusion

In conclusion the structural transition occurring in the material, as the Mott-insulator transition is tracked, is a compressed Jahn-Teller distortion. This is consistent with the observations in both the XANES and the fits to the EXAFS. The FT-EXAFS also follows this conclusion based on the position of the first peak (which corresponds to the Ru-O octahedra). Where the peak is roughly in the same position for all angles at 300K, but there is a shift at 400K, where the peak gets closer nearer to the ab-axis and further nearer to the c-axis. This is consistent with the c-axis being longer at 400K than at 300K. From the fits of the EXAFS this is found to be consistent with all paths, where the paths along the ab-plane get longer, and the paths along the c-axis get shorter, as the temperature decreases.

As we are measuring K-edge, we are reliant on the hybridisation of the O $2p$ orbitals and the Ru $4d$ orbitals to indirectly probe the Ru d-orbitals. Therefore we do not have a high enough resolution to confirm which scenario is most likely the driving force of the Mott-insulator transition. There are changes in the value for E_0 for the XANES, this suggests that there may be a larger change in the occupation of the xy-band than the z-band, as the value, from 400K to 300K, changes by $0.6eV$ at 15° and $0.1eV$ at 75°.

However, due to issues with the self-absorption correction a quantitative analysis of the XANES was not possible. The self-absorption in the EXAFS region also displayed problems, therefore the fits were performed on uncorrected data. This means that the only reliable parameters from the fits were ΔE_0 and ΔR. To gain a clearer analysis from the Ru K-edge, the effects of the overcorrection in the self-absorption calculations should be investigated to determine where the breakdown in the numerics occurs and

if it can be resolved.
From the data measured and analysed it is not clear whether or not the Jahn-Teller compression is the main driving force of the Mott-insulator transition or not. There is no clear change in the orbital occupancy seen in the XANES measurements, with respect to the angle between the polarisation and the c-axis. Due to the large core-hole width in these measurements, a change in orbital occupancy would be smeared out. Therefore it cannot be concluded whether there is orbital ordering occurring or not.
To more definitively determine which scenario is the driving force of the Mott insulator transition, measurements of the Ru L-edges should be taken to directly probe the changes in the metal d-orbitals. This can be used to directly investigate the occupancy of the d-orbitals and the potential splitting of the t_{2g} and e_g components of them. A smaller core-hole width should be used, as this will produce data with better resolution.

Chapter 7

Conclusion.

This thesis reports on the development of using linear polarised x-rays when measuring single crystals (P-XAS), and the analysis techniques developed. The materials discussed in this thesis have anisotropic properties, which were investigated using P-XAS to gain more information than is available when using other techniques. In this chapter the results of each material are discussed, as well as the technique used and the analysis method.

The results discussed in Chapter 4 ($Sr_2MnCu_{1.5-x}S_2O_2$) have shown that the Cu ions are indeed mobile at room temperature, based on the large disorder in the Cu-Cu paths. This was consistent in both the powder data and single crystal data. Samples with different amounts of Cu vacancies, $Sr_2MnCu_{1.5-x}S_2O_2$ (x=0.0,0.2,0.3), were measured with powder XAS, to investigate the link between the unusual magnetic properties observed in the materials and the amount of Cu vacancies. In this material the long-range magnetic ordering of the Mn moments is destroyed for the x=0.2 sample, and restored with a different structure for the x=0.3 sample [138]. While the XANES of the Mn K-edge do suggest that the Cu vacancies affect their electronic structure, it cannot be concluded that this is the cause for the change in the XANES, due to evidence of Mn rich impurities in the sample. The goal of the P-XAS measurements on single crystals of the parent material, $Sr_2MnCu_{1.5}S_2O_2$, was to confirm the mobility of the Cu ions, and whether their movement is restricted to the *ab*-plane. The results confirmed that the Cu ions are mobile, with evidence that they remain mobile at low temperatures ($\sim$112K). This was concluded from the large DWs for the Cu-Cu scattering paths, produced by the fit to the data measured at 300K ($\sigma^2 = 0.024 \pm 0.001$) and 112K ($\sigma^2 = 0.019 \pm 0.001$). Evidence of the proposed Cu/vacancy ordering at low temperature [132] could not be confirmed with this data, as the ordered structure did not fit the 112K data. The fit of the room temperature model to the 112K data did suggest an enlargement of the unit cell, but not to the scale predicted by Cu/vacancy ordering.

The results discussed in Chapter 5 ($M_2Mo_6Se_6$ (M=Tl,Rb)) have shown evidence of a structural distortion that may indicate the presence of a CDW in both materials. This evidence can be seen in the changes observed in the EXAFS measurements with respect to temperature and angle. In the Tl analogue there is a change with respect to temperature in the second peak of the FT-EXAFS observed when the signal was measured along the *ab*-plane. The peak becomes sharper as the temperature is increased. If there was no structural transition the peak would broaden as the thermal fluctuations increase. It was not possible to confirm the nature of this structural transition with the data measured. Both a twist in the $(Mo_3Se_3)_\infty$ chains, or a buckling of the Se-Mo planes were fit to the EXAFS signal, neither improved on the fit using the room temperature model [41]. In the Rb analogue there is a change with respect to temperature

observed in the third peak of the FT-EXAFS, when measured along the c-axis. The peak becomes sharper, and loses a visible shoulder, as the temperature is increased. If there was no structural transition the peak would broaden as the thermal fluctuations increase. A model with a buckling in the structure (see Figure 7.1) was fit to the data at 4K. This improved the overall fit, when compared to the fit produced from the room temperature model [42], suggesting that this is the most likely form of the distortion observed in the structure.

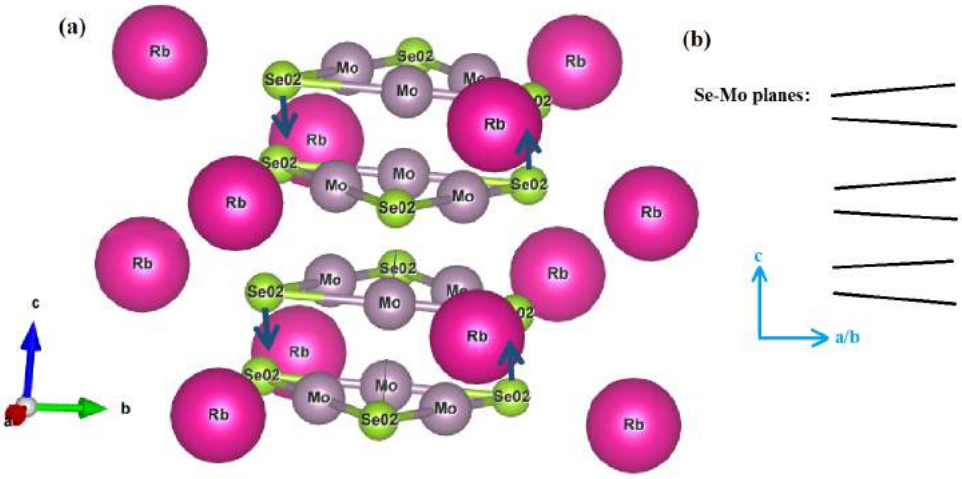

Figure 7.1: A simple diagram of the most likely distortion observed in the fit of $Rb_2Mo_6Se_6$ at 4K (a), side view of distortion (b).

The results discussed in Chapter 6 (Ca_2RuO_4) have shown evidence of a compressed Jahn-Teller distortion as the temperature is decreased, tracking the reported Mott-insulator transition [43, 44, 45]. The fits to the EXAFS data suggest a Jahn-Teller distortion where the Ru-O octahedra compresses (see Figure 7.2), *i.e.* the axial paths are shorter than the equatorial paths. The goal of this experiment was to confirm the scenario that drives the Mott-insulator transition, whether it is orbital selective and only affects the xy band, or it is assisted by crystal field splitting. As we were measuring the Ru K-edge, the d-orbitals were only probed indirectly, this made it difficult to determine if the transition was orbital selective or not. The large core-hole width for this experiment also made it difficult to form a conclusion, as the orbitals could not be distinguished.

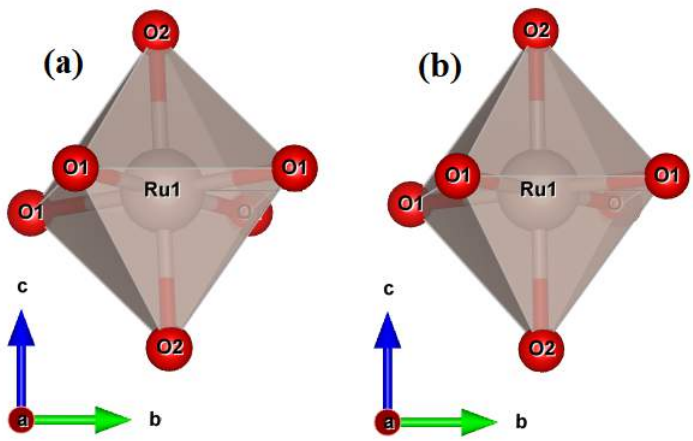

Figure 7.2: Comparison of the Ru-O octahedra in Ca_2RuO_4 at room temperature (a) [46], and 400K (b) [184].

From measurements of the three types of materials discussed in this thesis, it can be concluded that this technique is sensitive to changes along the different crystallographic orientations. In this case the differences were between the c-axis and the ab-plane, due to the structural nature of the materials studied, where there was strong anisotropy along the c-axis. The differences observed in the absorption with respect to the orientation of the sample proves that the measurements can be used to discriminate between different orientations when measuring local structure. This allows for analysis to be performed along a specific axis.

While the experimental side of P-XAS is no more complex than the set up for conventional XAS experiments, the analysis is a lot more involved. Due to the increased sensitivity of the technique, where the signal varies due to the direction measured, the degeneracies that arise as the paths are separated by angle need to be thought of more carefully before fitting data. When scattering paths are separated by angle, depending on the structure of the material, a unit cell can have more than one set of degenerate scattering paths from the excited atom. As the technique is sensitive to the angles between scattering paths, each environment must be accounted for. Once each angle has been calculated for the scattering paths included in the fit, the weightings of them must also be accounted for. In the case of the material discussed in Chapter 4 the scattering paths around the excited atom (e.g. Cu), within the unit cell, were degenerate for each Cu ion. This simplified the fit, as the unit cell could be thought of as having only one degenerate scattering path from the Cu ions. However for the materials discussed in Chapters 5 and 6, there were two sets of degenerate scattering paths from each excited atom within the unit cell, and therefore a weighting needed to be introduced into the fit.

When fitting the data measured using this technique, using the weighting factor discussed in Chapter 3, the different orientations can be fit simultaneously. The weighting factor is applied to the powder FEFF calculations to implement a polarisation dependence on the calculated signal. Fitting the orientations simultaneously allows for more guess parameters to be freed up, as only the angles between the paths (θ_i and ϕ_i) should differ. Therefore, certain parameters can be set as one variable for multiple data sets, such as the change in path length (ΔR). This is useful when there are many paths that contribute to a peak, where for conventional measurements less data would be read into the fit, and the fitting program can only cope with a smaller number of variables. In the case of the Ca_2RuO_4 measurements, discussed in Chapter 6, the first peak consists

of three distinct paths, according to the model used [46]. If the fit was performed on one data set (as for a powder), the parameters for the first three paths would need to be restricted as there would not be enough parameter space, when fitting the first peak, to allow for them to be separate. This would then restrict the information we could obtain from this fit, and in the case of this material the fit of the first peak is important as the Jahn-Teller distortion is occurring within this region.
As the materials investigated in this thesis were well ordered the degeneracy of the paths (N) was not explored in the fits, and set to the value of the model. The fits, presented in this thesis, allowed S_0^2 to remain a variable for each angle, and the global value was presented. This was the case, as the angular dependence of S_0^2 has not been fully understood, therefore an assumption for the value would be difficult to determine. In the fits S_0^2 accounts for other discrepancies in the amplitude, not just the affect the presence a core-hole has on the EXAFS signal. This makes it harder to predict a reliable value for S_0^2 in the fits. There is also dependence between S_0^2 and N, this can be used to investigate changes in N by refining the fit to a set value of S_0^2. As ARTEMIS does not allow for N to be a variable parameter in the fit, it can be difficult to refine a fit to directly determine the change in N. To determine N when fitting with ARTEMIS, a prediction for the change in degeneracy is useful, otherwise the fitting process would be very time consuming as the value of N for each path needs to be changed by hand. Understanding the angular dependence of S_0^2 can be used to predict the most likely values of N for each path, therefore the value of N for each path can be refined more succinctly.
It is possible to build a FEFF calculation with linear polarisation dependence, however the exact orientation of the crystal with respect to the beam is needed. The benefit of using the weighting factor is that it is not necessary to know the exact orientation of the sample. It is only necessary to know the orientation of the crystal with respect to the angle made between the beam and the axis of interest. This reduces the amount of preparation time for an experiment, as the exact orientation of each axis of the crystal with respect to the beam does not need to be known before data can be measured. By using the weighting factor, the angle that the polarisation is making within the ab-plane (ϕ) can be added into the fit as a guess parameter. For the EXAFS results presented in this thesis the samples orientation was not changed in the ab-plane, therefore ϕ will be the same value for each data set, meaning only one guess parameter is needed for this. The fit of the first peak can be used to find the most likely value of ϕ, as the first peak of an EXAFS signal should be comprised of single scattering events only. Therefore the exact orientation of all axes can be input into FEFF to build a polarised FEFF calculation when fitting multiple scattering paths.
A benefit to using P-XAS is that this technique is capable of separating paths of the same length and type by their angle, e.g. the Ru-O paths that contribute to the first peak in the Ru K-edge EXAFS (see Chapter 6). This separation allows for the exact nature of the Jahn-Teller distortion to be observed, *i.e.* whether it is an elongation or compression. While it is possible to observe this through x-ray diffraction measurements, if there is a break in the long-range order it would not be observed. In that case a local probe would be necessary to directly observe the transition.
From the results discussed in Chapter 4, we found that the purity of the sample is very important when analysing P-XAS data. As distortions in 3D space open up many variables to be considered, the analysis becomes more involved when a technique is capable of separating the local structure with respect to its orientation. If a sample is not phase pure then it is not possible to adapt a fit based off the known model. This lead to the procedure of imaging the samples with an SEM before any analysis is

carried out. As the samples were single crystals it is safe to assume that if the surface is homogeneous, then this carries through to the bulk. By using SEM measurements we were able to confirm that the $Sr_2MnCu_{1.5}S_2O_2$ single crystal sample contained Mn rich impurities. However, due to the selective nature of XAS it was possible to still perform analysis on the local structure of the Cu ions in $Sr_2MnCu_{1.5}S_2O_2$, due to the impurities being Mn rich, and not containing any Cu.
By adapting this technique to measure and analyse single crystals, the scope of materials that can be measured has increased. Previously P-XAS has been performed mostly on oriented powders [63, 64], while this is a viable use of this technique it limits the pool of potential materials, as they are required to be magnetic for orientation purposes. Using single crystals also allows for direct comparisons to be made with other techniques that use single crystals for their measurements (e.g. neutron diffraction, transport measurements, ARPES). Measuring a range of angles with this technique also improves the usefulness when analysing the data. In previous experiments, using linearly polarised x-rays to measure absorption in single crystals, a small range of angles has been measured (commonly $\theta = 90^o, 45^o, 0^o$), or FEFF calculations have been used for the fits [190]. These types of measurements have also been used on polycrystalline samples, and have shown that the separation of orientations is possible with this technique [97]. However when using the weighting factor discussed in this thesis, a larger range of angles can improve the fit as more guess parameters will be available.
Certain techniques that can measure a material along different orientations rely on long-range order of the properties (single crystal x-ray diffraction), or they are only a surface probe (ARPES). This can make it difficult to observe certain directional specific properties in a material if there is a break in the long-range order. This was the case for the material discussed in Chapter 5, where theoretical predictions, based on the differing properties for the different metal analogues, strongly suggested the presence of a CDW [81]. However no direct observations were possible with diffraction. This lead to the conclusion that the material formed short-range ordered modulations due to a CDW. To directly measure this a local probe was necessary, of which XAS was an ideal candidate. However if the material was measured using conventional XAS, due to a mixture of orientations, a direct observation of the periodic modulations due to a CDW would be very difficult to achieve. Using the technique discussed in this thesis, it is possible to separate the orientations along a material, and using single crystals negates the issue of having a mixture of orientations. An orientation specific periodic distortion, similar to one predicted by the theory, has been observed using our technique (see Chapter 5), proving that this technique is very useful in these situations.

Chapter 8

Future work.

At present this technique relies heavily on user input when dealing with the analysis of the results. The user needs to interpret the model themselves and calculate the angles (θ_i and ϕ_i) for the weighting factor by hand. One way in which this can be improved is to implement a code which can read in the coordinates of each atom in the unit cell and calculate all the possible angles for all possible scattering paths. This could be optimised further by having the option to inform the code which element is being excited, eliminating possible paths that do not include this element. A list of angles for each scattering path can then be produced by this code and the user can use this, along with knowledge of the model, to determine which angles are required for the weighting factor. This could save time when analysing the data.
The current weighting factor being used in this thesis only includes the contributions from single scattering events. The next stage in advancing this technique will be to update the weighting factor so that multiple scattering events can be included. Currently when accounting for multiple scattering in the fitting procedure, polarisation dependent FEFF calculation have been made using ARTEMIS. This works when the exact orientation of the crystal with respect to the polarisation of the beam is known. Whereas when using the weighting factor, only the orientation of the c-axis is needed as the angle that accounts for the orientation along the ab-plane, ϕ, can be added as a variable parameter in the fit. This frees up time at an experiment as only one axis needs to be orientated accurately before measurements are taken. The equipment needed at the beamline also simplifies as only one degree of rotational freedom is necessary, meaning a rotating table can be all that is needed rather than a diffractometer. The inclusion of multiple scattering events in the weighting factor is not simple, as only the first leg of the process will be polarisation dependent. This is the case, as the photoelectron released from the absorption event will be a spherical wave and therefore can interact with atoms along any given direction.
The effect that the separation of the directions has on the amplitude reduction factor (S_0^2) for the fits has not been understood completely for this thesis. From the fits discussed in Chapters 4 and 5, it can be seen that the amplitude factor does not follow the same trend for both of these materials. This could be due to the difference in the space group of the materials, as $Sr_2MnCu_{1.5}S_2O_2$ is either I4/mmm [33] or Ibam [34], and $M_2Mo_6Se_6$ is $P6_3/m$ [41, 42]. One of the differences between these space groups is the number of rotational axes, for Ibam N=2, I4/mmm N=4, and $P6_3/m$ N=6. The link between the amplitude and number of rotational axes is not clear, it is also not clear if this is the only property factoring into the difference between the trends of the amplitudes. Knowing the exact nature of how the directional dependence of the fit affects the amplitude is important, as sometimes it is necessary to set the ampli-

tude to a reasonable number to produce the best fit possible. The amplitude cannot be arbitrarily set to any number, and understanding the value to set it to will help when working with difficult to fit data to gain a starting point in understanding the structure of the material.
Another possible property that affects how the amplitude changes with orientation is the self-absorption correction. The self-absorption correction is dependent on the set up of the measurements, this differed between these two samples due to the equipment available at the beamlines and the direction of the c-axis in the sample. For the $Sr_2MnCu_{1.5}S_2O_2$ sample the c-axis was along the thickness of the plate-like crystal. A rotating table, with one rotational degree of freedom, was available at the beamline used for this experiment. This meant that for each angle between the polarisation and the c-axis (θ), the angle between the sample and the detector (θ_b) changed, leading to a larger correction when θ_b was larger. While for the $M_2Mo_6Se_6$ samples the c-axis was along the length of the needle-like crystals. A diffractometer, with three rotational degrees of freedom, was available at the beamline used for this experiment. This meant that the angle between the sample and the detector (θ_b) was static, as it was possible to rotate the c-axis with respect to the polarisation without changing the angle between the sample and the beam. Understanding the relationship between the orientation of the sample and the amplitude of the XAS signal is also important when trying to quantitatively analyse the XANES. As the effect due to the core-hole produced in the absorption process is important when modelling XANES.
As the path degeneracy (N) has a dependency on S_0^2, it is important to understand how to deal with S_0^2 for P-XAS experiments. When fitting with ARTEMIS, S_0^2 is calculated separately for each path, and a global parameter is reported. One way to understand the connection between S_0^2 and N for P-XAS would be to observe the value for S_0^2 for each path in the fit. This could provide insight on the degeneracy of the path along a specific direction. Another was to investigate the change in N would be fitting the data with a set value for S_0^2 and refining N. This would provide knowledge on how the path degeneracy is affected by the angular dependence of the measurements. For anisotropic materials the value of N should change depending on the angle measured, as not all paths of degenerate length will be along the path of the polarisation.
During the experiments performed for this thesis the polarisation of the beam was not checked. By using a focused beam from a bending magnet the percentage of linear polarisation of the beam should be high [191, 53]. However if the beam was not fully polarised this would affect the results, as the absorption cross section would have a different dependence on the orientation of the sample. This would affect the errors in the fits to the data, as the theoretical signal calculated will assume a fully linearly polarised beam. In future work with this technique it would be advantageous to check the polarisation of the beam at the start of each experiment.
The python code (see Appendix A.4) that was written to build XAS at different orientations is only optimised for space groups with N>2 rotational axes. This code has been used, in the context of this thesis, as a further quality control check to determine that the samples have their reported space group. By building XAS at orientations that have been measured, a comparison between the simulated and measured data can determine if the crystal does have the rotational symmetry it is expected to have. This code utilises the dipole approximation and has been derived for crystals with lower symmetry, this can be seen in Appendix A. The code can be adapted so that XAS can be built for crystals with N≤2, however for this thesis it was not necessary for the work.
If we were to carry on investigating $Sr_2MnCu_{1.5}S_2O_2$ using this technique, it would be

useful to measure P-XAS of samples with different amounts of Cu vacancies. Conventional XAS measurements on powdered samples of $Sr_2MnCu_{1.5-x}S_2O_2$ (x=0.0,0.2,0.3) have already been carried out and the analysis was reported in Chapter 4. However these samples also indicated the presence of Mn rich impurities. To carry on this line of research, pure powder and single crystal samples of the material are needed.
An avenue to further research into $M_2Mo_6Se_6$ would be to measure P-XAS and track the superconductivity or Mott-insulator transition with respect to applying uniaxial stress. Previous work has been carried out on $Tl_2Mo_6Se_6$, where a uniaxial stress along the *c*-axis was applied, this was found to suppress the superconducting state [81]. It is also possible to measure the Mo K-edge, this would help to determine what the distortion observed in the Se K-edge means for the structure.
A way in which to continue the work done on Ca_2RuO_4 would be to directly probe the Ru d-orbitals to determine the nature of the Mott-insulator transition. This can be done by measuring the Ru L-edges with P-XAS, to separate the orbitals and determine if the transition is orbital selective. This experiment has already been carried out by another student in my research group. However the analysis of these measurements is still ongoing. Another continuation of this work would be to investigate the full effect of the divergence seen in the self-absorption correction to the XAS data. The divergence is observed for the shallower angles of θ_b, and is clear in the XANES region. The EXAFS region also indicates an issue in the self absorption correction. Determining the problem in the correction in the EXAFS region would help determine if a full analysis of this data is possible.
The experiments performed in the research for this thesis focused on tracking structural transitions with respect to temperature. The sample environment necessary for a P-XAS is simple, as the only requirement is one degree of rotational freedom (this can be achieved with a rotating table). As the set up for P-XAS is relatively simple it is possible to track transitions with respect to different external factors, such as applied magnetic field, or pressure. These types of experiments can be performed at any beamline capable of measuring XAS with linearly polarised x-rays. This technique can also be used for different types of materials, other than the ones discussed in this thesis. Where the material of interest has anisotropy, either in its structure or its electronic properties.

Bibliography

[1] A. G. Lebed, *The physics of organic superconductors and conductors*, vol. 110. Springer, 2008.

[2] W. Wise, M. Boyer, K. Chatterjee, T. Kondo, T. Takeuchi, H. Ikuta, Y. Wang, and E. Hudson, "Charge-density-wave origin of cuprate checkerboard visualized by scanning tunnelling microscopy," *Nature Physics*, vol. 4, no. 9, p. 696, 2008.

[3] B. H. Savitzky, I. El Baggari, A. S. Admasu, J. Kim, S.-W. Cheong, R. Hovden, and L. F. Kourkoutis, "Bending and breaking of stripes in a charge ordered manganite," *Nature communications*, vol. 8, no. 1, p. 1883, 2017.

[4] P. Kuiper, G. Kruizinga, J. Ghijsen, G. A. Sawatzky, and H. Verweij, "Character of holes in $Li_xNi_{1-x}O$ and their magnetic behavior," *Physical review letters*, vol. 62, no. 2, p. 221, 1989.

[5] J. H. de Boer and E. J. Verwey, "Semi-conductors with partially and with completely filled 3d-lattice bands," *Proceedings of the Physical Society*, vol. 49, no. 4S, p. 59, 1937.

[6] N. Mott and R. Peierls, "Discussion of the paper by de Boer and Verwey," *Proceedings of the Physical Society*, vol. 49, no. 4S, p. 72, 1937.

[7] N. F. Mott, "The basis of the electron theory of metals, with special reference to the transition metals," *Proceedings of the Physical Society. Section A*, vol. 62, no. 7, p. 416, 1949.

[8] J. Freericks, V. Turkowski, and V. Zlatić, "Nonequilibrium dynamical mean-field theory," *Physical review letters*, vol. 97, no. 26, p. 266408, 2006.

[9] A. Fuhrmann, D. Heilmann, and H. Monien, "From Mott insulator to band insulator: A dynamical mean-field theory study," *Physical Review B*, vol. 73, no. 24, p. 245118, 2006.

[10] H. Park, K. Haule, and G. Kotliar, "Cluster dynamical mean field theory of the Mott transition," *Physical review letters*, vol. 101, no. 18, p. 186403, 2008.

[11] M. Eckstein, T. Oka, and P. Werner, "Dielectric breakdown of Mott insulators in dynamical mean-field theory," *Physical review letters*, vol. 105, no. 14, p. 146404, 2010.

[12] T. D. Stanescu, P. Phillips, and T.-P. Choy, "Theory of the Luttinger surface in doped Mott insulators," *Physical Review B*, vol. 75, no. 10, p. 104503, 2007.

[13] T. D. Stanescu and P. Phillips, "Pseudogap in doped Mott insulators is the near-neighbor analogue of the Mott gap," *Physical review letters*, vol. 91, no. 1, p. 017002, 2003.

[14] K. Segawa, M. Kofu, S. Lee, I. Tsukada, H. Hiraka, M. Fujita, S. Chang, K. Yamada, and Y. Ando, "Zero-doping state and electron-hole asymmetry in an ambipolar cuprate," *Nature Physics*, vol. 6, no. 8, p. 579, 2010.

[15] R. G. Leigh, P. Phillips, and T.-P. Choy, "Hidden charge 2e boson in doped Mott insulators," *Physical review letters*, vol. 99, no. 4, p. 046404, 2007.

[16] M. Meinders, H. Eskes, and G. Sawatzky, "Spectral-weight transfer: Breakdown of low-energy-scale sum rules in correlated systems," *Physical Review B*, vol. 48, no. 6, p. 3916, 1993.

[17] D. M. Newns, "Junction Mott transition field effect transistor (JMTFET) and switch for logic and memory applications," Sept. 19 2000. US Patent 6,121,642.

[18] Y. Zhou and S. Ramanathan, "Correlated electron materials and field effect transistors for logic: a review," *Critical Reviews in Solid State and Materials Sciences*, vol. 38, no. 4, pp. 286–317, 2013.

[19] J. Son, S. Rajan, S. Stemmer, and S. James Allen, "A heterojunction modulation-doped Mott transistor," *Journal of Applied Physics*, vol. 110, no. 8, p. 084503, 2011.

[20] P. Monceau, N. P. Ong, A. M. Portis, A. Meerschaut, and J. Rouxel, "Electric Field Breakdown of Charge-Density-WaveInduced Anomalies in $NbSe_3$," *Physical Review Letters*, vol. 37, no. 10, p. 602, 1976.

[21] P. Anderson, P. Lee, and M. Saitoh, "Remarks on giant conductivity in TTF-TCNQ," *Solid State Communications*, vol. 13, no. 5, pp. 595–598, 1973.

[22] M. Fowler, "Electrons in one dimension: the peierls transition '*http://galileo.phys.virginia.edu/classes/752.mf1i.spring03/PeierlsTrans.pdf*'," 2020.

[23] W. McMillan, "Landau theory of charge-density waves in transition-metal dichalcogenides," *Physical Review B*, vol. 12, no. 4, p. 1187, 1975.

[24] R. Hovden, A. W. Tsen, P. Liu, B. H. Savitzky, I. El Baggari, Y. Liu, W. Lu, Y. Sun, P. Kim, A. N. Pasupathy, *et al.*, "Atomic lattice disorder in charge-density-wave phases of exfoliated dichalcogenides ($1T - TaS_2$)," *Proceedings of the National Academy of Sciences*, vol. 113, no. 41, pp. 11420–11424, 2016.

[25] T. Wu, H. Mayaffre, S. Krämer, M. Horvatić, C. Berthier, W. Hardy, R. Liang, D. Bonn, and M.-H. Julien, "Magnetic-field-induced charge-stripe order in the high-temperature superconductor $YBa_2Cu_3O_y$," *Nature*, vol. 477, no. 7363, p. 191, 2011.

[26] J. Chang, E. Blackburn, A. Holmes, N. Christensen, J. Larsen, J. Mesot, R. Liang, D. Bonn, W. Hardy, A. Watenphul, *et al.*, "Direct observation of competition between superconductivity and charge density wave order in $YBa_2Cu_3O_{6.67}$," *Nature Physics*, vol. 8, no. 12, p. 871, 2012.

[27] G. Ghiringhelli, M. Le Tacon, M. Minola, S. Blanco-Canosa, C. Mazzoli, N. Brookes, G. De Luca, A. Frano, D. Hawthorn, F. He, *et al.*, "Long-range incommensurate charge fluctuations in $(Y, Nd)Ba_2Cu_3O_{6+x}$," *Science*, vol. 337, no. 6096, pp. 821–825, 2012.

[28] R. Fleming and C. Grimes, "Sliding-Mode Conductivity in $NbSe_3$: Observation of a Threshold Electric Field and Conduction Noise," *Physical Review Letters*, vol. 42, no. 21, p. 1423, 1979.

[29] P. Monceau, J. Richard, and M. Renard, "Interference Effects of the Charge-Density-Wave Motion in $NbSe_3$," *Physical Review Letters*, vol. 45, no. 1, p. 43, 1980.

[30] P. W. Anderson, "Basic notions of condensed matter physics," *Frontiers in physics*, vol. 55, p. 49, 1984.

[31] G. Grüner, "The dynamics of charge-density waves," *Reviews of modern physics*, vol. 60, no. 4, p. 1129, 1988.

[32] P. Monceau, "Electronic crystals: an experimental overview," *Advances in Physics*, vol. 61, no. 4, pp. 325–581, 2012.

[33] Z. A. Gál, O. J. Rutt, C. F. Smura, T. P. Overton, N. Barrier, S. J. Clarke, and J. Hadermann, "Structural chemistry and metamagnetism of an homologous series of layered manganese oxysulfides," *Journal of the American Chemical Society*, vol. 128, no. 26, pp. 8530–8540, 2006.

[34] S. J. Clarke, P. Adamson, S. J. Herkelrath, O. J. Rutt, D. R. Parker, M. J. Pitcher, and C. F. Smura, "Structures, physical properties, and chemistry of layered oxychalcogenides and oxypnictides," *Inorganic chemistry*, vol. 47, no. 19, pp. 8473–8486, 2008.

[35] S. Okada, M. Matoba, S. Fukumoto, S. Soyano, Y. Kamihara, T. Takeuchi, H. Yoshida, K. Ohoyama, and Y. Yamaguchi, "Magnetic properties of layered oxysulfide $Sr_2Cu_2(Co, Cu)O_2S_2$ with Cu-doped CoO_2 square planes," *Journal of applied physics*, vol. 91, no. 10, pp. 8861–8863, 2002.

[36] K. Ueda, K. Takafuji, and H. Hosono, "Preparation and crystal structure analysis of CeCuOS," *Journal of Solid State Chemistry*, vol. 170, no. 1, pp. 182–187, 2003.

[37] M. Yasukawa, K. Ueda, and H. Hosono, "Thermoelectric properties of layered oxyselenides $La_{1-x}Sr_xCuOSe$ (x= 0 to 0.2)," *Journal of applied physics*, vol. 95, no. 7, pp. 3594–3597, 2004.

[38] L. Zhao, D. Berardan, Y. Pei, C. Byl, L. Pinsard-Gaudart, and N. Dragoe, "$Bi_{1-x}Sr_xCuSeO$ oxyselenides as promising thermoelectric materials," *Applied Physics Letters*, vol. 97, no. 9, p. 092118, 2010.

[39] M. Potel, R. Chevrel, M. Sergent, J. Armici, M. Decroux, and Ø. Fischer, "New pseudo-one-dimensional metals: $M_2Mo_6Se_6$ $(M = Na, In, K, TI)$, $M_2Mo_6S_6$ $(M = K, Rb, Cs)$, $M_2Mo_6Te_6$ $(M = In, TI)$," *Journal of Solid State Chemistry*, vol. 35, no. 2, pp. 286–290, 1980.

[40] J. Tarascon, F. DiSalvo, and J. Waszczak, "Physical properties of several $M_2Mo_6X_6$ compounds $(M = \text{group IA metal}; X = Se, Te)$," *Solid state communications*, vol. 52, no. 3, pp. 227–231, 1984.

[41] M. Potel, R. Chevrel, and M. Sergent, "Structure du séléniure de molybdène et de thallium $Tl_2Mo_6Se_6$: clusters monodimensionnels $(Mo_{6/2})^1_\infty$," *Acta Crystallographica Section B*, vol. 36, no. 7, pp. 1545–1548, 1980.

[42] M. Hoesch. private communication, 2016.

[43] J. Jung, Z. Fang, J. He, Y. Kaneko, Y. Okimoto, and Y. Tokura, "Change of Electronic Structure in Ca_2RuO_4 Induced by Orbital Ordering," *Physical review letters*, vol. 91, no. 5, p. 056403, 2003.

[44] E. Gorelov, M. Karolak, T. Wehling, F. Lechermann, A. Lichtenstein, and E. Pavarini, "Nature of the Mott transition in Ca_2RuO_4," *Physical review letters*, vol. 104, no. 22, p. 226401, 2010.

[45] C. Fatuzzo, M. Dantz, S. Fatale, P. Olalde-Velasco, N. Shaik, B. Dalla Piazza, S. Toth, J. Pelliciari, R. Fittipaldi, A. Vecchione, *et al.*, "Spin-orbit-induced orbital excitations in Sr_2RuO_4 and Ca_2RuO_4: A resonant inelastic x-ray scattering study," *Physical Review B*, vol. 91, no. 15, p. 155104, 2015.

[46] M. Braden, G. André, S. Nakatsuji, and Y. Maeno, "Crystal and magnetic structure of Ca_2RuO_4: Magnetoelastic coupling and the metal-insulator transition," *Physical Review B*, vol. 58, no. 2, p. 847, 1998.

[47] H. A. Jahn and E. Teller, "Stability of polyatomic molecules in degenerate electronic states I - Orbital degeneracy," *Proc. R. Soc. Lond. A*, vol. 161, no. 905, pp. 220–235, 1937.

[48] V. I. Veksler, "A new method of accelerating relativistic particles," *Comptes Rendus de l'Académie des Sciences de l'URSS*, vol. 43, pp. 346–348, 1944.

[49] E. M. McMillan, "The synchrotron-a proposed high energy particle accelerator," *Physical Review*, vol. 68, no. 5-6, p. 143, 1945.

[50] L. R. V. Elder F R, Gurewitsch A M and P. H. C, "Radiation from Electrons in a Synchrotron," *Physical Review*, vol. 71, pp. 829–830, June 1947.

[51] H. C. Pollock, "The discovery of synchrotron radiation," *American Journal of Physics*, vol. 51, no. 3, pp. 278–280, 1983.

[52] J. Als-Nielsen and D. McMorrow, *Elements of modern X-ray physics*. John Wiley & Sons, 2011.

[53] A. Thompson, D. Attwood, E. Gullikson, M. Howells, J. Kortright, A. Robinson, *et al.*, "X-ray data booklet (2009)," *'http://xdb.lbl.gov'*, 2009.

[54] R. S. Von Bordwehr, "A history of X-ray absorption fine structure," in *Annales de Physique*, vol. 14, pp. 377–465, EDP Sciences, 1989.

[55] E. A. Stern, "Theory of the extended x-ray-absorption fine structure," *Physical Review B*, vol. 10, no. 8, p. 3027, 1974.

[56] P. Eisenberger and G. S. Brown, "The study of disordered systems by EXAFS: limitations," *Solid State Communications*, vol. 29, no. 6, pp. 481–484, 1979.

[57] G. Bunker, "Application of the ratio method of EXAFS analysis to disordered systems," *Nuclear Instruments and Methods in Physics Research*, vol. 207, no. 3, pp. 437–444, 1983.

[58] E. Stern, "EXAFS of disordered systems," in *Physical Properties of Amorphous Materials*, pp. 201–219, Springer, 1985.

[59] M. Newville, "IFEFFIT: interactive XAFS analysis and FEFF fitting," *Journal of synchrotron radiation*, vol. 8, no. 2, pp. 322–324, 2001.

[60] B. Ravel and M. Newville, "*ATHENA*, *ARTEMIS*, *HEPHAESTUS*: data analysis for X-ray absorption spectroscopy using *IFEFFIT*," *Journal of Synchrotron Radiation*, vol. 12, no. 4, pp. 537–541, 2005.

[61] S. Tomic, B. Searle, A. Wander, N. Harrison, A. Dent, J. Mosselmans, and J. Inglesfield, "The DL EXCURV Package," *Council for the Central Laboratory of the Research Councils*, 2005.

[62] A. Filipponi, *GNXAS extended suite of programs for advanced x-ray absorption data-analysis: methodology and practice*. Task, 2009.

[63] V. Polinger, D. Haskel, and E. A. Stern, "Dopant Induced Enhancement of the Jahn-Teller Effect in Perovskite Cuprates," in *Vibronic Interactions: Jahn-Teller Effect in Crystals and Molecules*, pp. 215–219, Springer, 2001.

[64] M. Giorgetti, M. Berrettoni, S. Passerini, and W. H. Smyrl, "Absorption of polarized X-rays by V2O5-based cathodes for lithium batteries: an application," *Electrochimica acta*, vol. 47, no. 19, pp. 3163–3169, 2002.

[65] J.-H. Choy, J.-B. Yoon, and H. Jung, "Polarization-dependent X-ray absorption spectroscopic study of $[Cu(cyclam)]^{2+}$-intercalated saponite," *The Journal of Physical Chemistry B*, vol. 106, no. 43, pp. 11120–11126, 2002.

[66] R. d. L. Kronig, "The theory of fine structure in the X-ray absorption specta. II," *Zeitschrift für Physik*, vol. 75, pp. 191–210, 1932.

[67] C. Brouder, "Angular dependence of X-ray absorption spectra," *Journal of Physics: Condensed Matter*, vol. 2, no. 3, p. 701, 1990.

[68] H.-K. Mao, A. Jephcoat, R. Hemley, L. Finger, C. Zha, R. Hazen, and D. Cox, "Synchrotron X-ray diffraction measurements of single-crystal hydrogen to 26.5 Gigapascals," *Science*, vol. 239, no. 4844, pp. 1131–1134, 1988.

[69] M. Christensen, N. Lock, J. Overgaard, and B. B. Iversen, "Crystal structures of thermoelectric n-and p-type $Ba_8Ga_{16}Ge_{30}$ studied by single crystal, multitemperature, neutron diffraction, conventional X-ray diffraction and resonant synchrotron X-ray diffraction," *Journal of the American Chemical Society*, vol. 128, no. 49, pp. 15657–15665, 2006.

[70] M. Merlini and M. Hanfland, "Single-crystal diffraction at megabar conditions by synchrotron radiation," *High Pressure Research*, vol. 33, no. 3, pp. 511–522, 2013.

[71] P. M. Piccoli, T. F. Koetzle, and A. J. Schultz, "Single crystal neutron diffraction for the inorganic chemist–a practical guide," *Comments on Inorganic Chemistry*, vol. 28, no. 1-2, pp. 3–38, 2007.

[72] R. J. Cava, F. Reidinger, and B. Wuensch, "Single-crystal neutron-diffraction study of AgI between 23° and 300°C," *Solid State Communications*, vol. 24, no. 6, pp. 411–416, 1977.

[73] A. Goldman, D. Argyriou, B. Ouladdiaf, T. Chatterji, A. Kreyssig, S. Nandi, N. Ni, S. BudKo, P. Canfield, and R. McQueeney, "Lattice and magnetic instabilities in $CaFe_2As_2$: A single-crystal neutron diffraction study," *Physical Review B*, vol. 78, no. 10, p. 100506, 2008.

[74] Y. Eltsev, S. Lee, K. Nakao, N. Chikumoto, S. Tajima, N. Koshizuka, and M. Murakami, "Anisotropic superconducting properties of MgB_2 single crystals probed by in-plane electrical transport measurements," *Physical Review B*, vol. 65, no. 14, p. 140501, 2002.

[75] F. Chou, J. Cho, P. A. Lee, E. Abel, K. Matan, and Y. S. Lee, "Thermodynamic and transport measurements of superconducting $Na_{0.3}CoO_2 \cdot 1.3H_2O$ single crystals prepared by electrochemical deintercalation," *Physical review letters*, vol. 92, no. 15, p. 157004, 2004.

[76] R. Amin, P. Balaya, and J. Maier, "Anisotropy of electronic and ionic transport in $LiFePO_4$ single crystals," *Electrochemical and Solid State Letters*, vol. 10, no. 1, p. A13, 2006.

[77] A. Damascelli, "Probing the electronic structure of complex systems by ARPES," *Physica Scripta*, vol. 2004, no. T109, p. 61, 2004.

[78] H.-B. Yang, S.-C. Wang, A. Sekharan, H. Matsui, S. Souma, T. Sato, T. Takahashi, T. Takeuchi, J. Campuzano, R. Jin, *et al.*, "ARPES on $Na_{0.6}CoO_2$: fermi surface and unusual band dispersion," *Physical review letters*, vol. 92, no. 24, p. 246403, 2004.

[79] D. Lu, M. Yi, S.-K. Mo, J. Analytis, J.-H. Chu, A. Erickson, D. J. Singh, Z. Hussain, T. Geballe, I. Fisher, *et al.*, "ARPES studies of the electronic structure of LaOFe (P, As)," *Physica C: Superconductivity*, vol. 469, no. 9-12, pp. 452–458, 2009.

[80] H. Ding, C. Reese, A. J. Mäkinen, Z. Bao, and Y. Gao, "Band structure measurement of organic single crystal with angle-resolved photoemission," *Applied Physics Letters*, vol. 96, no. 22, p. 222106, 2010.

[81] A. Petrović, R. Lortz, G. Santi, M. Decroux, H. Monnard, Ø. Fischer, L. Boeri, O. Andersen, J. Kortus, D. Salloum, *et al.*, "Phonon mode spectroscopy, electron-phonon coupling, and the metal-insulator transition in quasi-one-dimensional $M_2Mo_6Se_6$," *Physical Review B*, vol. 82, no. 23, p. 235128, 2010.

[82] G. Bunker, *Introduction to XAFS: a practical guide to X-ray absorption fine structure spectroscopy.* Cambridge University Press, 2010.

[83] R. Johnson, "Grating monochromators and optics for the VUV and soft x-ray region," *Handbook on synchrotron radiation*, vol. 1, pp. 173–260, 1983.

[84] Diamond Light Source, "'*https://www.diamond.ac.uk/instruments/spectroscopy/b18/specification.html*'," 2018.

[85] Australian Synchrotron, "*http://archive.synchrotron.org.au/synchrotron-science/how-is-synchrotron-light-created*," 2019.

[86] Diamond Light Source, "'*https://www.diamond.ac.uk/public/how-diamond-works.html*'," 2018.

[87] D. Swinehart, "The Beer-Lambert law," *Journal of chemical education*, vol. 39, no. 7, p. 333, 1962.

[88] S. M. Heald and E. A. Stern, "Anisotropic X-ray absorption in layered compounds," *Physical Review B*, vol. 16, no. 12, p. 5549, 1977.

[89] L. Corbari, M.-A. Cambon-Bonavita, G. J. Long, F. Grandjean, M. Zbinden, F. Gaill, and P. Compère, "Iron oxide deposits associated with the ectosymbiotic bacteria in the hydrothermal vent shrimp Rimicaris exoculata," *Biogeosciences Discussions*, vol. 5, no. 2, pp. 1825–1865, 2008.

[90] J. D. Young, "INCA: a computational platform for isotopically non-stationary metabolic flux analysis," *Bioinformatics*, vol. 30, no. 9, pp. 1333–1335, 2014.

[91] C. C. Chang, "Auger electron spectroscopy," *Surface Science*, vol. 25, no. 1, pp. 53–79, 1971.

[92] D. Briggs, *Handbook of X-ray and ultraviolet photoelectron spectroscopy.* Heyden London, 1977.

[93] R. Jenkins, *Quantitative X-ray spectrometry.* CRC Press, 1995.

[94] T. Ohta, K. Seki, T. Yokoyama, I. Morisada, and K. Edamatsu, "Polarized XANES studies of oriented polyethylene and fluorinated polyethylenes," *Physica Scripta*, vol. 41, no. 1, p. 150, 1990.

[95] L. J. Furnare, A. Vailionis, and D. G. Strawn, "Polarized XANES and EXAFS spectroscopic investigation into copper (II) complexes on vermiculite," *Geochimica et Cosmochimica Acta*, vol. 69, no. 22, pp. 5219–5231, 2005.

[96] G. Cibin, A. Mottana, A. Marcelli, and M. F. Brigatti, "Angular dependence of potassium K-edge XANES spectra of trioctahedral micas: Significance for the determination of the local structure and electronic behavior of the interlayer site," *American Mineralogist*, vol. 91, no. 7, pp. 1150–1162, 2006.

[97] N. Finck, M. Schlegel, and A. Bauer, "Structural iron in dioctahedral and trioctahedral smectites: a polarized XAS study," *Physics and Chemistry of Minerals*, vol. 42, no. 10, pp. 847–859, 2015.

[98] T. Yamamoto, "Assignment of pre-edge peaks in K-edge x-ray absorption spectra of 3d transition metal compounds: electric dipole or quadrupole?," *X-Ray Spectrometry*, vol. 37, no. 6, pp. 572–584, 2008.

[99] J. E. Hahn, R. A. Scott, K. O. Hodgson, S. Doniach, S. R. Desjardins, and E. I. Solomon, "Observation of an electric quadrupole transition in the X-ray absorption spectrum of a Cu (II) complex," *Chemical Physics Letters*, vol. 88, no. 6, pp. 595–598, 1982.

[100] R. A. Scott, J. E. Hahn, S. Doniach, H. C. Freeman, and K. O. Hodgson, "Polarized X-ray absorption spectra of oriented plastocyanin single crystals. Investigation of methionine-copper coordination," *Journal of the American Chemical Society*, vol. 104, no. 20, pp. 5364–5369, 1982.

[101] T. A. Smith, J. E. Penner-Hahn, M. A. Berding, S. Doniach, and K. O. Hodgson, "Polarized X-ray absorption edge spectroscopy of single-crystal copper (II) complexes," *Journal of the American Chemical Society*, vol. 107, no. 21, pp. 5945–5955, 1985.

[102] J. J. Sakurai, *Advanced quantum mechanics*. Pearson Education India, 1967.

[103] Python Software Foundation, "Python Language Reference, version 2.7. Available at *http://www.python.org*," 2018.

[104] P. Lee and J. Pendry, "Theory of the extended x-ray absorption fine structure," *Physical Review B*, vol. 11, no. 8, p. 2795, 1975.

[105] J. Rehr and R. Albers, "Scattering-matrix formulation of curved-wave multiple-scattering theory: Application to x-ray-absorption fine structure," *Physical Review B*, vol. 41, no. 12, p. 8139, 1990.

[106] J. Rehr, R. Albers, C. Natoli, and E. Stern, "New high-energy approximation for X-ray-absorption near-edge structure," *Physical Review B*, vol. 34, no. 6, p. 4350, 1986.

[107] J. M. De Leon, J. Rehr, S. Zabinsky, and R. Albers, "Ab initio curved-wave x-ray-absorption fine structure," *Physical Review B*, vol. 44, no. 9, p. 4146, 1991.

[108] J. J. Rehr and R. Albers, "Theoretical approaches to x-ray absorption fine structure," *Reviews of Modern Physics*, vol. 72, no. 3, p. 621, 2000.

[109] B.-K. Teo and P. Lee, "Ab initio calculations of amplitude and phase functions for extended X-ray absorption fine structure spectroscopy," *Journal of the American Chemical Society*, vol. 101, no. 11, pp. 2815–2832, 1979.

[110] J. Rehr, J. Mustre de Leon, S. Zabinsky, and R. Albers, "Theoretical X-ray absorption fine structure standards," *Journal of the American chemical society*, vol. 113, no. 14, pp. 5135–5140, 1991.

[111] E. Stern and S. Heald, "Basic principles and applications of EXAFS," *Handbook on synchrotron radiation*, vol. 1, pp. 955–1014, 1983.

[112] J. Rehr, E. Stern, R. Martin, and E. Davidson, "Extended x-ray-absorption fine-structure amplitudes — Wave-function relaxation and chemical effects," *Physical Review B*, vol. 17, no. 2, p. 560, 1978.

[113] D. Konigsberger and R. Prins, "X-ray absorption: principles, applications, techniques of EXAFS, SEXAFS and XANES," *Wiley/Interscience, New York*, vol. 159, p. 160, 1988.

[114] K. Momma and F. Izumi, "*VESTA*: a three-dimensional visualization system for electronic and structural analysis," *Journal of Applied Crystallography*, vol. 41, no. 3, pp. 653–658, 2008.

[115] J. Rehr, R. Albers, and S. Zabinsky, "High-order multiple-scattering calculations of X-ray-absorption fine structure," *Physical Review Letters*, vol. 69, no. 23, p. 3397, 1992.

[116] A. Ankudinov and J. Rehr, "Sum rules for polarization-dependent x-ray absorption," *Physical Review B*, vol. 51, no. 2, p. 1282, 1995.

[117] S. Zabinsky, J. Rehr, A. Ankudinov, R. Albers, and M. Eller, "Multiple-scattering Calculations of X-ray-absorption Spectra," *Physical Review B*, vol. 52, no. 4, p. 2995, 1995.

[118] A. Tenderholt, B. Hedman, and K. O. Hodgson, "PySpline: A Modern, Cross-platform program for the processing of raw averaged XAS edge and EXAFS data," in *AIP conference Proceedings*, vol. 882, pp. 105–107, AIP, 2007.

[119] S. Webb, "SIXpack: a graphical user interface for XAS analysis using IFEFFIT," *Physica scripta*, vol. 2005, no. T115, p. 1011, 2005.

[120] L. Tröger, D. Arvanitis, K. Baberschke, H. Michaelis, U. Grimm, and E. Zschech, "Full correction of the self-absorption in soft-fluorescence extended x-ray-absorption fine structure," *Phys. Rev. B*, vol. 46, pp. 3283–3289, 1992.

[121] P. Pfalzer, J. Urbach, M. Klemm, S. Horn, M. L. denBoer, A. I. Frenkel, and J. P. Kirkland, "Elimination of self-absorption in fluorescence hard-x-ray absorption spectra," *Phys. Rev. B*, vol. 60, pp. 9335–9339, 1999.

[122] B. Ravel, "*ATOMS*: crystallography for the X-ray absorption spectroscopist," *Journal of Synchrotron Radiation*, vol. 8, no. 2, pp. 314–316, 2001.

[123] C. Booth and F. Bridges, "Improved self-absorption correction for fluorescence measurements of extended X-ray absorption fine-structure," *Physica Scripta*, vol. 2005, no. T115, p. 202, 2005.

[124] J. H. Hubbell and S. M. Seltzer, "Tables of X-ray mass attenuation coefficients and mass energy-absorption coefficients 1 keV to 20 MeV for elements Z= 1 to 92 and 48 additional substances of dosimetric interest," tech. rep., National Inst. of Standards and Technology-PL, Gaithersburg, MD (United States). Ionizing Radiation Div., 2004.

[125] M. Newville, "EXAFS analysis using FEFF and FEFFIT," *Journal of synchrotron radiation*, vol. 8, no. 2, pp. 96–100, 2001.

[126] P. Bevington, "Data Reduction and Error Analysis for Physicists," 1969.

[127] D. W. Marquardt, "An algorithm for least-squares estimation of nonlinear parameters," *Journal of the society for Industrial and Applied Mathematics*, vol. 11, no. 2, pp. 431–441, 1963.

[128] M. Newville, B. Boyanov, and D. Sayers, "Estimation of measurement uncertainties in XAFS data," *Journal of synchrotron radiation*, vol. 6, no. 3, pp. 264–265, 1999.

[129] W. Zhu, P. Hor, A. Jacobson, G. Crisci, T. Albright, S.-H. Wang, and T. Vogt, "$A_2Cu_2CoO_2S_2(A = Sr, Ba)$, A Novel Example of a Square-Planar CoO_2 Layer," *Journal of the American Chemical Society*, vol. 119, no. 50, pp. 12398–12399, 1997.

[130] C. F. Smura, D. R. Parker, M. Zbiri, M. R. Johnson, Z. A. Gal, and S. J. Clarke, "High-spin cobalt (II) ions in square planar coordination: structures and magnetism of the oxysulfides $Sr_2CoO_2Cu_2S_2$ and $Ba_2CoO_2Cu_2S_2$ and their solid solution," *Journal of the American Chemical Society*, vol. 133, no. 8, pp. 2691–2705, 2011.

[131] F. Ryan, E. Pugh, and R. Smoluchowski, "Superparamagnetism, Nonrandomness, and Irradiation Effects in Cu − Ni Alloys," *Physical Review*, vol. 116, no. 5, p. 1106, 1959.

[132] P. Adamson, J. Hadermann, C. F. Smura, O. J. Rutt, G. Hyett, D. G. Free, and S. J. Clarke, "Competing Magnetic Structures and the Evolution of Copper Ion/Vacancy Ordering with Composition in the Manganite Oxide Chalcogenides $Sr_2MnO_2Cu_{1.5}(S_{1-x}Se_x)_2$," *Chemistry of Materials*, vol. 24, no. 14, pp. 2802–2816, 2012.

[133] B. J. Sternlieb, J. P. Hill, U. C. Wildgruber, G. M. Luke, B. Nachumi, Y. Moritomo, and Y. Tokura, "Charge and Magnetic Order in $La_{0.5}Sr_{1.5}MnO_4$," *Phys. Rev. Lett.*, vol. 76, pp. 2169–2172, 1996.

[134] O. J. Rutt. PhD thesis, University of Oxford, 2008.

[135] O. J. Rutt, G. R. Williams, and S. J. Clarke, "Reversible lithium insertion and copper extrusion in layered oxysulfides," *Chemical communications*, no. 27, pp. 2869–2871, 2006.

[136] S. Indris, J. Cabana, O. J. Rutt, S. J. Clarke, and C. P. Grey, "Layered Oxysulfides $Sr_2MnO_2Cu_{2m-0.5}S_{m+1}$ (m= 1, 2, and 3) as Insertion Hosts for Li Ion Batteries," *Journal of the American Chemical Society*, vol. 128, no. 41, pp. 13354–13355, 2006.

[137] J. N. Blandy, J. C. Boskovic, and S. J. Clarke, "Synthesis and magnetic structure of the layered manganese oxide selenide $Sr_2MnO_2Ag_{1.5}Se_2$," *Journal of Solid State Chemistry*, vol. 245, pp. 61–66, 2017.

[138] P. Adamson, *Synthesis and characterisation of layered oxychalcogenides.* PhD thesis, Oxford University, 2010.

[139] W. Zhu and P. Hor, "Unusual layered transition-metal oxysulfides: $Sr_2Cu_2MO_2S_2(M = Mn, Zn)$," *Journal of Solid State Chemistry*, vol. 130, no. 2, pp. 319–321, 1997.

[140] L. S. Kau, D. J. Spira-Solomon, J. E. Penner-Hahn, K. O. Hodgson, and E. I. Solomon, "X-ray absorption edge determination of the oxidation state and coordination number of copper. Application to the type 3 site in Rhus vernicifera laccase and its reaction with oxygen," *Journal of the American Chemical Society*, vol. 109, no. 21, pp. 6433–6442, 1987.

[141] J. Shay, B. Tell, H. Kasper, and L. Schiavone, "$p-d$ Hybridization of the Valence Bands of I-III-VI 2 Compounds," *Physical Review B*, vol. 5, no. 12, p. 5003, 1972.

[142] P. Ghigna, G. Flor, and G. Spinolo, "An Mn K-Edge XAS Investigation on the Crystal Chemistry of $Cd_{1-\delta}Mn_2O_y$," *Journal of Solid State Chemistry*, vol. 149, no. 2, pp. 252–255, 2000.

[143] W. Umrath, "Cooling bath for rapid freezing in electron microscopy," *Journal of Microscopy*, vol. 101, no. 1, pp. 103–105, 1974.

[144] J. Clayden, N. Greeves, S. Warren, and P. Wothers, "Organic chemistry," 2001.

[145] R. E. Peierls and R. S. Peierls, *Quantum theory of solids.* Oxford University Press, 1955.

[146] W. Fogle and J. H. Perlstein, "Semiconductor-to-Metal Transition in the Blue Potassium Molybdenum Bronze, $K_{0.30}MoO_3$; Example of a Possible Excitonic Insulator," *Physical Review B*, vol. 6, no. 4, p. 1402, 1972.

[147] Q. Liu and A. Zunger, "Predicted realization of cubic dirac fermion in quasi-one-dimensional transition-metal monochalcogenides," *Physical Review X*, vol. 7, no. 2, p. 021019, 2017.

[148] R. Daou, J. Chang, D. LeBoeuf, O. Cyr-Choiniere, F. Laliberté, N. Doiron-Leyraud, B. Ramshaw, R. Liang, D. Bonn, W. Hardy, *et al.*, "Broken rotational symmetry in the pseudogap phase of a high-Tc superconductor," *Nature*, vol. 463, no. 7280, p. 519, 2010.

[149] E. Blackburn, J. Chang, M. Hücker, A. Holmes, N. B. Christensen, R. Liang, D. Bonn, W. Hardy, U. Rütt, O. Gutowski, *et al.*, "X-ray diffraction observations of a charge-density-wave order in superconducting ortho-II $YBa_2Cu_3O_{6.54}$ single crystals in zero magnetic field," *Physical review letters*, vol. 110, no. 13, p. 137004, 2013.

[150] R. Comin, A. Frano, M. M. Yee, Y. Yoshida, H. Eisaki, E. Schierle, E. Weschke, R. Sutarto, F. He, A. Soumyanarayanan, Y. He, M. Le Tacon, I. S. Elfimov, J. E. Hoffman, G. A. Sawatzky, B. Keimer, and A. Damascelli, "Charge Order Driven by Fermi-Arc Instability in $Bi_2Sr_{2-x}La_xCuO_{6+\delta}$," *Science*, vol. 343, no. 6169, pp. 390–392, 2014.

[151] J. G. Lu, P. Chang, and Z. Fan, "Quasi-one-dimensional metal oxide materials — Synthesis, properties and applications," *Materials Science and Engineering: R: Reports*, vol. 52, no. 1-3, pp. 49–91, 2006.

[152] W. C. Hopman, P. Pottier, D. Yudistira, J. Van Lith, P. V. Lambeck, R. M. De La Rue, A. Driessen, H. J. Hoekstra, and R. M. De Ridder, "Quasi-one-dimensional photonic crystal as a compact building-block for refractometric optical sensors," *IEEE journal of selected topics in quantum electronics*, vol. 11, no. 1, pp. 11–16, 2005.

[153] T. Ogasawara, M. Ashida, N. Motoyama, H. Eisaki, S. Uchida, Y. Tokura, H. Ghosh, A. Shukla, S. Mazumdar, and M. Kuwata-Gonokami, "Ultrafast optical nonlinearity in the quasi-one-dimensional Mott insulator Sr_2CuO_3," *Physical review letters*, vol. 85, no. 10, p. 2204, 2000.

[154] T. Zhai, X. Fang, M. Liao, X. Xu, H. Zeng, B. Yoshio, and D. Golberg, "A comprehensive review of one-dimensional metal-oxide nanostructure photodetectors," *Sensors*, vol. 9, no. 8, pp. 6504–6529, 2009.

[155] E. Comini, C. Baratto, G. Faglia, M. Ferroni, A. Vomiero, and G. Sberveglieri, "Quasi-one dimensional metal oxide semiconductors: Preparation, characterization and application as chemical sensors," *Progress in Materials Science*, vol. 54, no. 1, pp. 1–67, 2009.

[156] A. Kolmakov and M. Moskovits, "Chemical sensing and catalysis by one-dimensional metal-oxide nanostructures," *Annu. Rev. Mater. Res.*, vol. 34, pp. 151–180, 2004.

[157] C. Umbach, S. Washburn, R. Laibowitz, and R. A. Webb, "Magnetoresistance of small, quasi-one-dimensional, normal-metal rings and lines," *Physical Review B*, vol. 30, no. 7, p. 4048, 1984.

[158] J. Dumas, C. Schlenker, J. Marcus, and R. Buder, "Nonlinear Conductivity and Noise in the Quasi One-Dimensional Blue Bronze $K_{0.30}MoO_3$," *Physical Review Letters*, vol. 50, no. 10, p. 757, 1983.

[159] W. Hönle, H. Von Schnering, A. Lipka, and K. Yvon, "New compounds with infinite chains of face-condensed octahedral Mo6 clusters: $InMo_3Se_3$, $InMo_3Te_3$, $TlMo_3Se_3$ and $TlMo_3Te_3$," *Journal of the Less Common Metals*, vol. 71, no. 1, pp. 135–145, 1980.

[160] R. Lepetit, P. Monceau, M. Potel, P. Gougeon, and M. Sergent, "Superconductivity of the linear chain compound $Tl_2Mo_6Se_6$," *Journal of low temperature physics*, vol. 56, no. 3-4, pp. 219–235, 1984.

[161] R. Brusetti, A. Briggs, O. Laborde, M. Potel, and P. Gougeon, "Superconducting and dielectric instabilities in $Tl_2Mo_6Se_6$: Unusual transport properties and unsaturating critical field," *Physical Review B*, vol. 49, no. 13, p. 8931, 1994.

[162] J. Bearden and A. Burr, "Reevaluation of X-ray atomic energy levels," *Reviews of Modern Physics*, vol. 39, no. 1, p. 125, 1967.

[163] A. L. Ryser, D. G. Strawn, M. A. Marcus, J. L. Johnson-Maynard, M. E. Gunter, and G. Möller, "Micro-spectroscopic investigation of selenium-bearing minerals from the Western US Phosphate Resource Area," *Geochemical Transactions*, vol. 6, no. 1, p. 1, 2005.

[164] M. Hoesch. private communication.

[165] L. Gannon, L. Boeri, C. A. Howard, P. Gougeon, P. Gall, M. Potel, D. Salloum, A. P. Petrović, and M. Hoesch, "Lattice dynamics of the cluster chain compounds $M_2Mo_6Se_6$ $(M = K, Rb, Cs, In, and Tl)$," *Phys. Rev. B*, vol. 98, p. 014104, 2018.

[166] S.-M. Huang, C.-H. Hsu, S.-Y. Xu, C.-C. Lee, S.-Y. Shiau, H. Lin, and A. Bansil, "Topological superconductor in quasi-one-dimensional $Tl_{2-x}Mo_6Se_6$," *Physical Review B*, vol. 97, no. 1, p. 014510, 2018.

[167] J. Armici, M. Decroux, Ø. Fischer, M. Potel, R. Chevrel, and M. Sergent, "A new pseudo-one-dimensional superconductor: $Tl_2Mo_6Se_6$," *Solid State Communications*, vol. 33, no. 6, pp. 607–611, 1980.

[168] K. Zhao, Q.-G. Mu, T. Liu, B.-J. Pan, B.-B. Ruan, L. Shan, G.-F. Chen, and Z.-A. Ren, "Superconductivity in novel quasi-one-dimensional ternary molybdenum pnictides $Rb_2Mo_3As_3$ and $Cs_2Mo_3As_3$," *arXiv preprint arXiv:1805.11577*, 2018.

[169] M. C. O'Brien, "The dynamic JahnTeller effect in octahedrally co-ordinated d^9 ions," *Proceedings of the Royal Society of London. Series A. Mathematical and Physical Sciences*, vol. 281, no. 1386, pp. 323–339, 1964.

[170] M. Veidis, G. Schreiber, T. Gough, and G. J. Palenik, "Jahn-Teller distortions in octahedral copper (II) complexes," *Journal of the American Chemical Society*, vol. 91, no. 7, pp. 1859–1860, 1969.

[171] J. Alonso, M. Martinez-Lope, M. Casais, and M. Fernandez-Diaz, "Evolution of the Jahn- Teller distortion of MnO_6 octahedra in $RMnO_3$ perovskites (R= Pr, Nd, Dy, Tb, Ho, Er, Y): a neutron diffraction study," *Inorganic chemistry*, vol. 39, no. 5, pp. 917–923, 2000.

[172] M. W. Lufaso and P. M. Woodward, "Jahn-Teller distortions, cation ordering and octahedral tilting in perovskites," *Acta Crystallographica Section B: Structural Science*, vol. 60, no. 1, pp. 10–20, 2004.

[173] J. B. Goodenough, "Jahn-Teller distortions induced by tetrahedral-site Fe2+ ions," *Journal of Physics and Chemistry of Solids*, vol. 25, no. 2, pp. 151–160, 1964.

[174] D. Reinen, M. Atanasov, G. Nikolov, and F. Steffens, "Local and cooperative Jahn-Teller distortions of nickel (2+) and copper (2+) in tetrahedral coordination," *Inorganic Chemistry*, vol. 27, no. 10, pp. 1678–1686, 1988.

[175] O. Gunnarsson, H. Handschuh, P. S. Bechthold, B. Kessler, G. Ganteför, and W. Eberhardt, "Photoemission Spectra of C_60^-: Electron-Phonon Coupling, Jahn-Teller Effect, and Superconductivity in the Fullerides," *Physical review letters*, vol. 74, no. 10, p. 1875, 1995.

[176] J. Han, O. Gunnarsson, and V. H. Crespi, "Strong superconductivity with local Jahn-Teller phonons in C_60 solids," *Physical Review Letters*, vol. 90, no. 16, p. 167006, 2003.

[177] H. Keller, A. Bussmann-Holder, and K. A. Müller, "Jahn–Teller physics and high-Tc superconductivity," *Materials Today*, vol. 11, no. 9, pp. 38–46, 2008.

[178] M. Fabrizio and E. Tosatti, "Nonmagnetic molecular Jahn-Teller Mott insulators," *Physical Review B*, vol. 55, no. 20, p. 13465, 1997.

[179] I. Loa, P. Adler, A. Grzechnik, K. Syassen, U. Schwarz, M. Hanfland, G. K. Rozenberg, P. Gorodetsky, and M. Pasternak, "Pressure-induced quenching of the Jahn-Teller distortion and insulator-to-metal transition in $LaMnO_3$," *Physical review letters*, vol. 87, no. 12, p. 125501, 2001.

[180] Chemistry LibreTexts, "Jahn-Teller Distortions '*https://chem.libretexts.org/*'," 2019.

[181] E. Pavarini, S. Biermann, A. Poteryaev, A. Lichtenstein, A. Georges, and O. Andersen, "Mott transition and suppression of orbital fluctuations in orthorhombic $3d^1$ perovskites," *Physical review letters*, vol. 92, no. 17, p. 176403, 2004.

[182] M. Itoh, M. Shikano, and T. Shimura, "High-and low-spin transition of Ru^{4+} in the perovskite-related layered system $Sr_{n+1}Ru_nO_{3n+1}$ (n= 1, 2, and ∞) with the change in n," *Physical Review B*, vol. 51, no. 22, p. 16432, 1995.

[183] G. Miessler, P. Fischer, and D. Tarr, "Inorganic chemistry fifth edition," 2014.

[184] O. Friedt, M. Braden, G. André, P. Adelmann, S. Nakatsuji, and Y. Maeno, "Structural and magnetic aspects of the metal-insulator transition in $Ca_{2-x}Sr_xRuO_4$," *Physical Review B*, vol. 63, no. 17, p. 174432, 2001.

[185] S. Riccò, M. Kim, A. Tamai, S. M. Walker, F. Y. Bruno, I. Cucchi, E. Cappelli, C. Besnard, T. K. Kim, P. Dudin, *et al.*, "In situ strain tuning of the metal-insulator-transition of Ca_2RuO_4 in angle-resolved photoemission experiments," *Nature communications*, vol. 9, no. 1, p. 4535, 2018.

[186] M. O. Krause and J. Oliver, "Natural widths of atomic K and L levels, K α X-ray lines and several KLL Auger lines," *Journal of Physical and Chemical Reference Data*, vol. 8, no. 2, pp. 329–338, 1979.

[187] L. Vigara, M. Z. Ertem, N. Planas, F. Bozoglian, N. Leidel, H. Dau, M. Haumann, L. Gagliardi, C. J. Cramer, and A. Llobet, "Experimental and quantum chemical characterization of the water oxidation cycle catalysed by $[RuII(damp)(bpy)(H_2O)]^{2+}$," *Chemical Science*, vol. 3, no. 8, pp. 2576–2586, 2012.

[188] M. Sturge, "The Jahn-Teller effect in solids," in *Solid state physics*, vol. 20, pp. 91–211, Elsevier, 1968.

[189] C. Alexander, G. Cao, V. Dobrosavljevic, S. McCall, J. Crow, E. Lochner, and R. Guertin, "Destruction of the Mott insulating ground state of Ca_2RuO_4 by a structural transition," *Physical Review B*, vol. 60, no. 12, p. R8422, 1999.

[190] B. Joseph, A. Ricci, N. Poccia, V. G. Ivanov, A. A. Ivanov, A. P. Menushenkov, N. L. Saini, and A. Bianconi, "Temperature-dependent as K-edge EXAFS studies of $LaFe_{1-x}Co_xAsO$ (x= 0.0 and 0.11) single crystals," *Journal of Superconductivity and Novel Magnetism*, vol. 29, no. 12, pp. 3041–3047, 2016.

[191] D. Laundy, "Calculation of the polarisation of synchrotron radiation," *Nuclear Instruments and Methods in Physics Research Section A: Accelerators, Spectrometers, Detectors and Associated Equipment*, vol. 290, no. 1, pp. 248–253, 1990.

Appendix A

Theoretical methods calculations and codes used.

A.1 General XAS theory.

The absorption coefficient, $\mu(E)$, for x-ray experiments can be derived from Beer-Lambert's law[87]:

$$I(E) = I_0(E)e^{\mu(E)x} \tag{A.1}$$

where $I(E)$ is the intensity of the transmitted beam, $I_0(E)$ is the intensity of the incoming beam, and x is the thickness of the sample.
The absorption of all of the atoms in the sample can be written as:

$$\mu(E) = \sum_i n_i \sigma_i(E) \tag{A.2}$$

where n_i is the number of atoms of type i per unit volume, and $\sigma_i(E)$ is the contribution to the cross section of each i atom.
The probability of an incoming x-ray releasing a core electron per unit time, in which the system goes from an initial bound state, $|i >= |i, n_{\vec{k},\alpha} >$, to a final unbound state, $|f >= |f, n_{\vec{k},\alpha} >$ is given by Fermi's Golden rule[102].

$$\Omega_{i\to f}(\omega) = \frac{2\pi}{\hbar}| < f|H_I|i > |^2 \delta(E_f - E_i - \hbar\omega)\rho(E_f) \tag{A.3}$$

Here H_I is the interaction Hamiltonian between the x-ray beam and the core electron, $\rho(E_f)$ is the density of unoccupied states at the final energy E_f, $\hbar\omega$ is the energy of the incoming photon which satisfies $E_f - E_i = \hbar\omega$, and $n_{\vec{k},\alpha}$ is the number of photons with wavenumber $\vec{k}$ and polarisation α.
The cross section is the transition rate normalised to the flux of the incoming x-rays:

$$\sigma(\omega) = \frac{\Omega(\omega)}{nc} \tag{A.4}$$

where n is the number of photons per unit volume of the x-ray beam, and c is the velocity of light.

quantised radiation field (which the electron momentum is modified by):

$$\vec{A}(\vec{r}, t) = \frac{1}{\sqrt{V}} \sum_{\vec{k}} \sum_{\alpha} c\sqrt{2\pi\hbar/\omega}[a_{\vec{k},\alpha}(t) \cdot \vec{\epsilon} e^{i\vec{k}\vec{r}} + a^{\dagger}_{\vec{k},\alpha}(t) \cdot \vec{\epsilon} e^{-i\vec{k}\vec{r}}] \tag{A.5}$$

where V is the volume of the incoming beam, ω is the frequency of the photons, $a_{\vec{k}\alpha}(t)$ and $a^{\dagger}_{\vec{k}\alpha}(t)$ are annihilation and creation operators which destroy/create photons with wavenumber $\vec{k}$ and polarisation α, and $\vec{\epsilon}$ is the polarisation of the photon.
The single particle Hamiltonian describing the deep core electron and its interaction with the x-ray field is given by:

$$H = H_o + H_I = \frac{1}{2m}\left(\vec{p} - \frac{e\vec{A}}{c}\right)^2 + V(\vec{r}) \tag{A.6}$$

where $V(\vec{r})$ is the electrostatic potential binding the electron to the atom.
The perturbation introduced by the field, H_I, is then given by:

$$H_I = \left[\frac{-e}{2mc}(\vec{p}\cdot\vec{A}(\vec{r},t) + \vec{A}(\vec{r},t)\cdot\vec{p}) + \frac{e^2}{2mc^2}\vec{A}(\vec{r},t)\cdot\vec{A}(\vec{r},t)\right] \tag{A.7}$$

Using the commutation relation $[\vec{A},\vec{p}] = i\hbar\nabla\vec{A}$ the Hamiltonian can be simplified:

$$\text{as } \vec{A}\cdot\vec{p} - \vec{p}\cdot\vec{A} = [\vec{A},\vec{p}]$$
$$\therefore -\vec{p}\cdot\vec{A} = i\hbar\nabla\vec{A} - \vec{A}\cdot\vec{p}$$
$$\vec{p}\cdot\vec{A} = -i\hbar\nabla\vec{A} + \vec{A}\cdot\vec{p}$$

because of the transversality condition (Coloumb gauge) REF $\nabla\cdot\vec{A} = 0$

$$\therefore \vec{p}\cdot\vec{A} = \vec{A}\cdot\vec{p}$$
$$H_I = \left[\frac{-e}{2mc}(\cdot\vec{A}(\vec{r},t)\vec{p} + \vec{A}(\vec{r},t)\cdot\vec{p}) + \frac{e^2}{2mc^2}\vec{A}(\vec{r},t)\cdot\vec{A}(\vec{r},t)\right]$$
$$H_I = \left[\frac{-e}{mc}\cdot\vec{A}(\vec{r},t)\vec{p} + \frac{e^2}{2mc^2}\vec{A}(\vec{r},t)\cdot\vec{A}(\vec{r},t)\right] \tag{A.8}$$

To simplify this further $\vec{A}(\vec{r},t)\cdot\vec{A}(\vec{r},t)$ needs to be calculated.

$$\vec{A}(\vec{r},t)\cdot\vec{A}(\vec{r},t) = \frac{1}{V}\sum_{\vec{k}}\sum_{\alpha}\frac{c^2 2\pi\hbar}{\omega}\vec{\epsilon}^2[a_{\vec{k},\alpha}(t)e^{i\vec{k}\vec{r}} + a^{\dagger}_{\vec{k},\alpha}(t)e^{-i\vec{k}\vec{r}}]^2$$
$$\frac{2\pi\hbar c^2\vec{\epsilon}^2}{V\omega}\sum_{\vec{k}}\sum_{\alpha}(a_{\vec{k},\alpha}(t)a_{\vec{k},\alpha}(t)e^{2i\vec{k}\vec{r}} + 2a_{\vec{k},\alpha}(t)a^{\dagger}_{\vec{k},\alpha}(t)e^{i\vec{k}\vec{r}}e^{-i\vec{k}\vec{r}}$$
$$+a^{\dagger}_{\vec{k},\alpha}(t)a^{\dagger}_{\vec{k},\alpha}(t)e^{-2i\vec{k}\vec{r}})$$

As you can not have $a^{\dagger}\times a^{\dagger}$ or $a\times a$ this equation goes to:

$$\vec{A}(\vec{r},t)\cdot\vec{A}(\vec{r},t) = \frac{2\pi\hbar c^2\vec{\epsilon}^2}{V\omega}\sum_{\vec{k}}\sum_{\alpha}2a_{\vec{k},\alpha}(t)a^{\dagger}_{\vec{k},\alpha}(t) \tag{A.9}$$

This will change the particle number by 0 or 2 it does not contribute to the absorption, as in an absorption interaction the particle number will only change by one. Therefore the Hamiltonian becomes:

$$H_I = \frac{-e}{mc}\vec{A}(\vec{r},t)\cdot\vec{p} \tag{A.10}$$

Where the only operator in $\vec{A}(\vec{r},t)$ adding a non zero term to the absorption is the annihilation operator, as during this process a photon will be absorbed, i.e. annihilated. Taking this into account the Hamiltonian becomes:

$$H_I = \frac{-e}{mc}\sqrt{\frac{2\pi\hbar c^2}{V\omega}}[a_{\vec{k},\alpha}(t)\vec{\epsilon}e^{i\vec{k}\vec{r}}]\cdot\vec{p} \tag{A.11}$$

The commutation relations can be used to get:

$$< f|\vec{p} \cdot \vec{\epsilon}|i >= \frac{im}{\hbar}(\hbar\omega) < f|\vec{r} \cdot \vec{\epsilon}|i > \tag{A.12}$$

Combining Equations (A.3), (A.4) and (A.12) we can obtain the final expression of the cross section in terms of the polarisation $\vec{r} \cdot \vec{\epsilon}$.

$$< f|H_I|i >= \frac{-e}{m}\sqrt{\frac{2\pi\hbar n_{\vec{k},\alpha}}{\omega V}} < f|e^{i\vec{k}\cdot\vec{r}}\vec{p} \cdot \vec{\epsilon}|i > e^{-i\omega t}$$

as $\vec{r}$ is very small, $e^{i\vec{k}\cdot\vec{r}} \approx 1$

$$< f|H_I|i >= \frac{-e}{m}\sqrt{\frac{2\pi\hbar n_{\vec{k},\alpha}}{\omega V}}e^{-i\omega t} < f|\vec{p} \cdot \vec{\epsilon}|i >$$

using eq. (A.12) we can write this in terms of $\vec{r} \cdot \vec{\epsilon}$

$$< f|H_I|i >= \frac{-eim\hbar\omega}{m\hbar}\sqrt{\frac{2\pi\hbar n_{\vec{k},\alpha}}{\omega V}}e^{-i\omega t} < f|\vec{r} \cdot \vec{\epsilon}|i >$$

$$< f|H_I|i >= -ei\omega\sqrt{\frac{2\pi\hbar n_{\vec{k},\alpha}}{\omega V}}e^{-i\omega t} < f|\vec{r} \cdot \vec{\epsilon}|i >$$

therefore when squaring the matrix element we get:

$$| < f|H_I|i > |^2 = \left(-ei\omega\sqrt{\frac{2\pi\hbar n_{\vec{k},\alpha}}{\omega V}}e^{-i\omega t}\right)$$

$$\times \left(ei\omega\sqrt{\frac{2\pi\hbar n_{\vec{k},\alpha}}{\omega V}}e^{i\omega t}\right) | < f|\vec{r} \cdot \vec{\epsilon}|i > |^2$$

$$| < f|H_I|i > |^2 = e^2\omega^2\frac{2\pi\hbar n_{\vec{k},\alpha}}{\omega V}| < f|\vec{r} \cdot \vec{\epsilon}|i > |^2$$

$$| < f|H_I|i > |^2 = \frac{2\pi\hbar n_{\vec{k},\alpha}e^2\omega}{V}| < f|\vec{r} \cdot \vec{\epsilon}|i > |^2$$

putting this into eq. (A.3) we get:

$$\Omega(\omega) = \frac{2\pi}{\hbar}\frac{2\pi\hbar n_{\vec{k},\alpha}e^2\omega}{V}| < f|\vec{r} \cdot \vec{\epsilon}|i > |^2\delta(E_f - E_i - \hbar\omega)\rho(E_f)$$

$$\Omega(\omega) = \frac{4\pi^2 n_{\vec{k},\alpha}e^2\omega}{V}| < f|\vec{r} \cdot \vec{\epsilon}|i > |^2\delta(E_f - E_i - \hbar\omega)\rho(E_f)$$

putting this into eq. (A.4) we get an equation for the cross section in terms of the polarisation

$$\sigma(\omega) = \frac{4\pi^2 n_{\vec{k},\alpha}e^2\omega}{ncV}| < f|\vec{r} \cdot \vec{\epsilon}|i > |^2\delta(E_f - E_i - \hbar\omega)\rho(E_f)$$

as the fine structure constant is $\alpha_{fs} = e^2/\hbar c$:

$$\sigma(\omega) = \frac{4\pi^2 n_{\vec{k},\alpha}\alpha_{fs}\omega\hbar}{nV}| < f|\vec{r} \cdot \vec{\epsilon}|i > |^2\delta(E_f - E_i - \hbar\omega)\rho(E_f) \tag{A.13}$$

As we are dealing with synchrotron radiation we can assume that all of the photons in the beam have wavenumber $\vec{k}$ and polarisation α, in fact the percentage of polarisation of the beam is roughly 95%. This means that Equation (A.13) can be simplified further as $nV \approx n_{\vec{k},\alpha}$.

$$\sigma(\omega) = 4\pi^2\alpha_{fs}\omega\hbar| < f|\vec{r} \cdot \vec{\epsilon}|i > |^2\delta(E_f - E_i - \hbar\omega)\rho(E_f) \tag{A.14}$$

A.2 Dipole approximation calculations.

A dipole approximation can be formed from the absorption probability:

$$\mu \propto \hat{\epsilon} \cdot M \cdot \hat{\epsilon} \tag{A.15}$$

where the second rank tensor M has components:

$$M_{jk} \propto \sum_j < \psi_i | r_j | \psi_f >< \psi_f | r_k | \psi_i > \tag{A.16}$$

and $\hat{\epsilon}$ is the x-ray polarisation vector expressed in spherical coordinates θ, and ϕ:

$$\hat{\epsilon} = (\sin\theta\cos\phi, \sin\theta\sin\phi, \cos\theta) \tag{A.17}$$

By doing the calculation $\hat{\epsilon} \cdot M \cdot \hat{\epsilon}$ a general equation for the absorption can be found:

$$= (\sin\theta\cos\phi, \sin\theta\sin\phi, \cos\theta) \cdot \begin{pmatrix} M_{aa} & M_{ab} & M_{ac} \\ M_{ba} & M_{bb} & M_{bc} \\ M_{ca} & M_{cb} & M_{cc} \end{pmatrix} \cdot \begin{pmatrix} \sin\theta\cos\phi \\ \sin\theta\sin\phi \\ \cos\theta \end{pmatrix}$$

$$= \begin{pmatrix} (\sin\theta\cos\phi M_{aa} + \sin\theta\sin\phi M_{ba} + \cos\theta M_{ca}) \\ (\sin\theta\cos\phi M_{ab} + \sin\theta\sin\phi M_{bb} + \cos\theta M_{cb}) \\ (\sin\theta\cos\phi M_a c + \sin\theta\sin\phi M_{bc} + \cos\theta M_{cc}) \end{pmatrix} \cdot (\sin\theta\cos\phi, \sin\theta\sin\phi, \cos\theta)$$

$= (\sin\theta\cos\phi M_{aa} + \sin\theta\sin\phi M_{ba} + \cos\theta M_{ca})\sin\theta\cos\phi + (\sin\theta\cos\phi M_{ab} + \sin\theta\sin\phi M_{bb} + \cos\theta M_{cb})\sin\theta\sin\phi + (\sin\theta\cos\phi M_a c + \sin\theta\sin\phi M_{bc} + \cos\theta M_{cc})\cos\theta$
$= \sin^2\theta\cos^2\phi M_{aa} + \sin^2\theta\sin^2\phi M_{bb} + \cos^2\theta M_{cc} + \sin^2\theta\sin\phi\cos\phi M_{ba} + \sin^2\theta\cos\phi\sin\phi M_{ab} + \sin\theta\cos\theta\cos\phi M_{ca} + \sin\theta\cos\theta\cos\phi M_{ac} + \sin\theta\cos\theta\sin\phi M_{cb} + \sin\theta\cos\theta\sin\phi M_{bc}$

We can say that $M_{jk} = M_{kj}$, because the double sum is symmetric, therefore the above equation can be simplified further to:

$$\mu \propto \sin^2\theta\cos^2\phi M_{aa} + \sin^2\theta\sin^2\phi M_{bb} + \cos^2\theta M_{cc}$$
$$+2(\sin^2\theta\sin\phi\cos\phi M_{ba} + \sin\theta\cos\theta\cos\phi M_{ca} + \sin\theta\cos\theta\sin\phi M_{cb}) \tag{A.18}$$

To take into account the symmetry of the crystal this equation can be simplified significantly. In our case we are working with layered non-cubic crystals, this means that we will need to consider the rotation about the z-axis. The matrix for a rotation by and angle α about the z-axis is:

$$R(\alpha) = \begin{pmatrix} \cos(\alpha) & -\sin(\alpha) & 0 \\ \sin(\alpha) & \cos(\alpha) & 0 \\ 0 & 0 & 1 \end{pmatrix}$$

where $\alpha = \frac{2\pi}{N}$. A second rank tensor is rotated by applying the rotation matrix and its inverse:

$$M = R \cdot M \cdot R^{-1} \tag{A.19}$$

$$\Downarrow$$

$$\begin{pmatrix} \cos(\alpha) & -\sin(\alpha) & 0 \\ \sin(\alpha) & \cos(\alpha) & 0 \\ 0 & 0 & 1 \end{pmatrix} \cdot \begin{pmatrix} M_{aa} & M_{ab} & M_{ac} \\ M_{ba} & M_{bb} & M_{bc} \\ M_{ca} & M_{cb} & M_{cc} \end{pmatrix} \cdot \begin{pmatrix} \cos(\alpha) & \sin(\alpha) & 0 \\ -\sin(\alpha) & \cos(\alpha) & 0 \\ 0 & 0 & 1 \end{pmatrix}$$

$$\Downarrow$$

$$\begin{pmatrix} (\cos\alpha M_{aa} - \sin\alpha M_{ba}) & (\cos\alpha M_{ab} - \sin\alpha M_{bb}) & (\cos\alpha M_{ac} - \sin\alpha M_{bc}) \\ (\sin\alpha M_{aa} + \cos\alpha M_{ba}) & (\sin\alpha M_{ab} + \cos\alpha M_{bb}) & (\sin\alpha M_{ac} + \cos\alpha M_{bc}) \\ M_{ca} & M_{cb} & M_{cc} \end{pmatrix} \cdot$$
$$\begin{pmatrix} \cos(\alpha) & \sin(\alpha) & 0 \\ -\sin(\alpha) & \cos(\alpha) & 0 \\ 0 & 0 & 1 \end{pmatrix}$$

This leads to 9 equations for each element of the tensor.

$$\begin{aligned}
M_{aa} &= (\cos\alpha M_{aa} - \sin\alpha M_{ba})\cos\alpha - (\cos\alpha M_{ab} - \sin\alpha M_{bb})\sin\alpha \\
M_{ab} &= (\cos\alpha M_{aa} - \sin\alpha M_{ba})\sin\alpha + (\cos\alpha M_{ab} - \sin\alpha M_{bb})\cos\alpha \\
M_{ac} &= (\cos\alpha M_{ac} - \sin\alpha M_{bc}) \\
M_{ba} &= (\sin\alpha M_{aa} + \cos\alpha M_{ba})\cos\alpha - (\sin\alpha M_{ab} + \cos\alpha M_{bb})\sin\alpha \\
M_{bb} &= (\sin\alpha M_{aa} + \cos\alpha M_{ba})\sin\alpha + (\sin\alpha M_{ab} + \cos\alpha M_{bb})\cos\alpha \\
M_{bc} &= (\sin\alpha M_{ac} + \cos\alpha M_{bc}) \\
M_{ca} &= (\cos\alpha M_{ca} - \sin\alpha M_{cb}) \\
M_{cb} &= (\sin\alpha M_{ca} + \cos\alpha M_{cb}) \\
M_{cc} &= M_{cc}
\end{aligned}$$

These equations can be simplified by multiplying out the brackets:

$$M_{aa} = \cos^2\alpha M_{aa} + \sin^2\alpha M_{bb} - \cos\alpha\sin\alpha(M_{ba} + M_{ab}) \tag{A.20}$$
$$M_{ab} = \cos^2\alpha M_{ab} - \sin^2\alpha M_{ba} + \cos\alpha\sin\alpha(M_{aa} - M_{bb}) \tag{A.21}$$
$$M_{ac} = \cos\alpha M_{ac} - \sin\alpha M_{bc} \tag{A.22}$$
$$M_{ba} = \cos^2\alpha M_{ba} - \sin^2\alpha M_{ab} + \cos\alpha\sin\alpha(M_{aa} - M_{bb}) \tag{A.23}$$
$$M_{bb} = \sin^2\alpha M_{aa} + \cos^2\alpha M_{bb} + \cos\alpha\sin\alpha(M_{ba} + M_{ab}) \tag{A.24}$$
$$M_{bc} = \sin\alpha M_{ac} + \cos\alpha M_{bc} \tag{A.25}$$
$$M_{ca} = \cos\alpha M_{ca} - \sin\alpha M_{cb} \tag{A.26}$$
$$M_{cb} = \sin\alpha M_{ca} + \cos\alpha M_{cb} \tag{A.27}$$
$$M_{cc} = M_{cc} \tag{A.28}$$

A crystal with hexagonal symmetry has a 6 fold rotation axis, $N = 6$. To find the equation of the absorption in terms of the angular dependence the rotated tensor

needs to be calculated with $\alpha = \frac{2\pi}{6}$, ($\cos\alpha = 1/2$, and $\sin\alpha = \sqrt{3}/2$). This leads to:

$$
\begin{aligned}
M_{aa} &= \left(\frac{1}{2}\right)^2 \cdot M_{aa} + \left(\frac{\sqrt{3}}{2}\right)^2 \cdot M_{bb} - \frac{1}{2} \cdot \frac{\sqrt{3}}{2} \cdot (M_{ba} + M_{ab}) \\
M_{ab} &= \left(\frac{1}{2}\right)^2 \cdot M_{ab} - \left(\frac{\sqrt{3}}{2}\right)^2 \cdot M_{ba} + \frac{1}{2} \cdot \frac{\sqrt{3}}{2} \cdot (M_{aa} - M_{bb}) \\
M_{ac} &= \frac{1}{2} \cdot M_{ac} - \frac{\sqrt{3}}{2} \cdot M_{bc} \\
M_{ba} &= \left(\frac{1}{2}\right)^2 \cdot M_{ba} - \left(\frac{\sqrt{3}}{2}\right)^2 \cdot M_{ab} + \frac{1}{2} \cdot \frac{\sqrt{3}}{2} \cdot (M_{aa} - M_{bb}) \\
M_{bb} &= \left(\frac{\sqrt{3}}{2}\right)^2 \cdot M_{aa} + \left(\frac{1}{2}\right)^2 \cdot M_{bb} + \frac{\sqrt{3}}{2} \cdot \frac{1}{2} \cdot (M_{ba} + M_{ab}) \\
M_{bc} &= \frac{\sqrt{3}}{2} \cdot M_{ac} + \frac{1}{2} \cdot M_{bc} \\
M_{ca} &= \frac{1}{2} \cdot M_{ca} - \frac{\sqrt{3}}{2} \cdot M_{cb} \\
M_{cb} &= \frac{\sqrt{3}}{2} \cdot M_{ca} + \frac{1}{2} \cdot M_{cb} \\
M_{cc} &= M_{cc}
\end{aligned}
$$

This leads to:

$$
\begin{aligned}
M_{aa} &= \frac{1}{4} \cdot M_{aa} + \frac{3}{4} \cdot M_{bb} - \frac{\sqrt{3}}{4} \cdot (M_{ba} + M_{ab}) \\
M_{ab} &= \frac{1}{4} \cdot M_{ab} - \frac{3}{4} \cdot M_{ba} + \frac{\sqrt{3}}{4} \cdot (M_{aa} - M_{bb}) \\
M_{ac} &= \frac{1}{2} \cdot M_{ac} - \frac{\sqrt{3}}{2} \cdot M_{bc} \\
M_{ba} &= \frac{1}{4} \cdot M_{ba} - \frac{3}{4} \cdot M_{ab} + \frac{\sqrt{3}}{4} \cdot (M_{aa} - M_{bb}) \\
M_{bb} &= \frac{3}{4} \cdot M_{aa} + \frac{1}{4} \cdot M_{bb} + \frac{\sqrt{3}}{4} \cdot (M_{ba} + M_{ab}) \\
M_{bc} &= \frac{\sqrt{3}}{2} \cdot M_{ac} + \frac{1}{2} \cdot M_{bc} \\
M_{ca} &= \frac{1}{2} \cdot M_{ca} - \frac{\sqrt{3}}{2} \cdot M_{cb} \\
M_{cb} &= \frac{\sqrt{3}}{2} \cdot M_{ca} + \frac{1}{2} \cdot M_{cb} \\
M_{cc} &= M_{cc}
\end{aligned}
$$

By rearranging the first and fifth equation we find:

$$
\begin{aligned}
\text{First equation: } \frac{\sqrt{3}}{4}(M_{ba} + M_{ab}) &= -\frac{3}{4}M_{aa} + \frac{3}{4}M_{bb} \\
\text{Fifth equation: } \frac{\sqrt{3}}{4}(M_{ba} + M_{ab}) &= \frac{3}{4}M_{bb} - \frac{3}{4}M_{aa}
\end{aligned}
$$

Therefore we can say $M_{aa} = M_{bb}$. Using this we can find M_{ab} in terms of M_{ba}.

$$\begin{aligned} M_{ab} = \frac{1}{4} \cdot M_{ab} - \frac{3}{4} \cdot M_{ba} + \frac{\sqrt{3}}{4} \cdot (M_{aa} - M_{aa}) \\ M_{ab} - \frac{1}{4} \cdot M_{ab} = -\frac{3}{4} \cdot M_{ba} \\ \frac{3}{4} \cdot M_{ab} = -\frac{3}{4} \cdot M_{ba} \end{aligned}$$

Therefore $M_{ab} = -M_{ba}$, the reverse is also true.
Now focusing on the terms that include c, we can rearrange each equation to find the relation between these parameters:

$$\begin{aligned} \frac{1}{2} \cdot M_{ac} = -\frac{\sqrt{3}}{2} \cdot M_{bc} \\ \frac{1}{2} \cdot M_{bc} = \frac{\sqrt{3}}{2} \cdot M_{ac} \\ \frac{1}{2} \cdot M_{ca} = -\frac{\sqrt{3}}{2} \cdot M_{cb} \\ \frac{1}{2} \cdot M_{cb} = \frac{\sqrt{3}}{2} \cdot M_{ca} \end{aligned}$$

They can be further simplified to:

$$\begin{aligned} M_{ac} = -\sqrt{3} \cdot M_{bc} \\ M_{bc} = \sqrt{3} \cdot M_{ac} \\ M_{ca} = -\sqrt{3} \cdot M_{cb} \\ M_{cb} = \sqrt{3} \cdot M_{ca} \end{aligned}$$

By using this simplified form, we can find:

$$\begin{aligned} M_{ac} = \frac{1}{2} \cdot M_{ac} - \frac{\sqrt{3}}{2} \cdot M_{bc} \\ \text{as } M_{bc} = \sqrt{3} M_{ac} \\ M_{ac} = \frac{1}{2} \cdot M_{ac} - \frac{\sqrt{3}}{2} \cdot \sqrt{3} M_{ac} \\ M_{ac} = \frac{1}{2} \cdot M_{ac} - \frac{3}{2} M_{ac} \\ M_{ac} = -M_{ac} \end{aligned}$$

For M_{bc} we find:

$$\begin{aligned} M_{bc} = \frac{\sqrt{3}}{2} \cdot M_{ac} + \frac{1}{2} \cdot M_{bc} \\ \text{as } M_{ac} = -\sqrt{3} M_{bc} \\ M_{bc} = \frac{\sqrt{3}}{2} \cdot (-\sqrt{3} M_{bc}) + \frac{1}{2} \cdot M_{bc} \\ M_{bc} = -\frac{3}{2} M_{bc} + \frac{1}{2} M_{bc} \\ M_{bc} = -M_{bc} \end{aligned}$$

The same process finds $M_{ca} = -M_{ca}$, and $M_{cb} = -M_{cb}$.

This leads to nine new equations for the rotated tensor:

$$M_{aa} = M_{bb} \tag{A.29}$$
$$M_{ab} = -M_{ba} \tag{A.30}$$
$$M_{ac} = -M_{ac} \tag{A.31}$$
$$M_{ba} = -M_{ab} \tag{A.32}$$
$$M_{bb} = M_{aa} \tag{A.33}$$
$$M_{bc} = -M_{bc} \tag{A.34}$$
$$M_{ca} = -M_{ca} \tag{A.35}$$
$$M_{cb} = -M_{cb} \tag{A.36}$$
$$M_{cc} = M_{cc} \tag{A.37}$$

Therefore the rotated tensor for hexagonal symmetries can be written as:

$$M_{hex} = \begin{pmatrix} M_{aa} & M_{ab} & -M_{ac} \\ -M_{ab} & M_{aa} & -M_{bc} \\ -M_{ca} & -M_{cb} & M_{cc} \end{pmatrix} \tag{A.38}$$

Using this tensor in the calculation of $\mu \propto \hat{\epsilon} \cdot M \cdot \hat{\epsilon}$, an equation for the dipole absorption for crystals with hexagonal symmetry can be formed:
$= \sin^2\theta\cos^2\phi M_{aa} + \sin^2\theta\sin^2\phi M_{aa} + \cos^2\theta M_{cc} - \sin^2\theta\sin\phi\cos\phi M_{ab} +$
$\sin^2\theta\cos\phi\sin\phi M_{ab} - \sin\theta\cos\theta\cos\phi M_{ca} - \sin\theta\cos\theta\cos\phi M_{ac} - \sin\theta\cos\theta\sin\phi M_{cb} -$
$\sin\theta\cos\theta\sin\phi M_{bc}$
$= \sin^2\theta M_{aa}(\cos^2\phi + \sin^2\phi) + \cos^2\theta M_{cc} - \sin\theta\cos\theta\cos\phi M_{ca} - \sin\theta\cos\theta\cos\phi M_{ac} -$
$\sin\theta\cos\theta\sin\phi M_{cb} - \sin\theta\cos\theta\sin\phi M_{bc}$
as $(\cos^2\phi + \sin^2\phi)$, $-M_{ca} = M_{ca}$, and $-M_{cb} = M_{cb}$:
$= \sin^2\theta M_{aa} + \cos^2\theta M_{cc} + \sin\theta\cos\theta\cos\phi M_{ca} + \sin\theta\cos\theta\cos\phi M_{ac} +$
$\sin\theta\cos\theta\sin\phi M_{cb} - \sin\theta\cos\theta\sin\phi M_{bc}$

$$= \sin^2\theta M_{aa} + \cos^2\theta M_{cc} + \sin\theta\cos\theta(\cos\phi M_{ca} - \cos\phi M_{ac} + \sin\phi M_{cb} - \sin\phi M_{bc})$$

as $M_{jk} = M_{kj}$, because the double sum is symmetric:

$$= \sin^2\theta M_{aa} + \cos^2\theta M_{cc} + \sin\theta\cos\theta(\cos\phi M_{ca} - \cos\phi M_{ca} + \sin\phi M_{cb} - \sin\phi M_{cb})$$

This means that the dipole absorption for a crystal with hexagonal symmetry can be written as:

$$\mu \propto \sin^2\theta M_{aa} + \cos^2\theta M_{cc} \tag{A.39}$$

A crystal with tetragonal symmetry has a 4 fold rotation axis, $N = 4$. To find the equation of the absorption in terms of the angular dependence the rotated tensor needs to be calculated with $\alpha = \frac{2\pi}{4}$, ($\cos\alpha = 0$, and $\sin\alpha = 1$). This leads to:

$$\begin{aligned}
M_{aa} &= 0 \cdot M_{aa} + 1^2 \cdot M_{bb} - 1 \cdot 0 \cdot (M_{ba} + M_{ab}) \\
M_{ab} &= 0 \cdot M_{ab} - 1^2 \cdot M_{ba} + 0 \cdot (M_{aa} - M_{bb}) \\
M_{ac} &= 0 \cdot M_{ac} - 1 \cdot M_{bc} \\
M_{ba} &= 0 \cdot M_{ba} - 1^2 \cdot M_{ab} + 0 \cdot (M_{aa} - M_{bb}) \\
M_{bb} &= 1^2 \cdot M_{aa} + 0 \cdot M_{bb} + 1 \cdot 0 \cdot (M_{ba} + M_{ab}) \\
M_{bc} &= 1 \cdot M_{ac} + 0 \cdot M_{bc} \\
M_{ca} &= 0 \cdot M_{ca} - 1 \cdot M_{cb} \\
M_{cb} &= 1 \cdot M_{ca} + 0 \cdot M_{cb} \\
M_{cc} &= M_{cc}
\end{aligned}$$

This leads to nine new equations for the rotated tensor:

$$M_{aa} = M_{bb} \tag{A.40}$$
$$M_{ab} = -M_{ba} \tag{A.41}$$
$$M_{ac} = -M_{bc} \tag{A.42}$$
$$M_{ba} = -M_{ab} \tag{A.43}$$
$$M_{bb} = M_{aa} \tag{A.44}$$
$$M_{bc} = M_{ac} \tag{A.45}$$
$$M_{ca} = -M_{cb} \tag{A.46}$$
$$M_{cb} = M_{ca} \tag{A.47}$$
$$M_{cc} = M_{cc} \tag{A.48}$$

Therefore the rotated tensor for tetragonal symmetries can be written as:

$$M_{tetr} = \begin{pmatrix} M_{aa} & M_{ab} & -M_{bc} \\ -M_{ab} & M_{aa} & M_{ac} \\ -M_{cb} & M_{ca} & M_{cc} \end{pmatrix} \tag{A.49}$$

Using this tensor in the calculation of $\mu \propto \hat{\epsilon} \cdot M \cdot \hat{\epsilon}$, an equation for the dipole absorption for crystals with tetragonal symmetry can be formed:
$= \sin^2\theta\cos^2\phi M_{aa} + \sin^2\theta\sin^2\phi M_{aa} + \cos^2\theta M_{cc} - \sin^2\theta\sin\phi\cos\phi M_{ab} +$
$\sin^2\theta\cos\phi\sin\phi M_{ab} - \sin\theta\cos\theta\cos\phi M_{cb} - \sin\theta\cos\theta\cos\phi M_{bc} + \sin\theta\cos\theta\sin\phi M_{ca} +$
$\sin\theta\cos\theta\sin\phi M_{ac}$
$= \sin^2\theta M_{aa}(\cos^2\phi + \sin^2\phi) + \cos^2\theta M_{cc} - \sin\theta\cos\theta\cos\phi M_{cb} - \sin\theta\cos\theta\cos\phi M_{bc} +$
$\sin\theta\cos\theta\sin\phi M_{ca} + \sin\theta\cos\theta\sin\phi M_{ac}$
as $(\cos^2\phi + \sin^2\phi) = 1$, $M_{ca} = -M_{cb}$, and $M_{ac} = -M_{bc}$:
$= \sin^2\theta M_{aa} + \cos^2\theta M_{cc} - \sin\theta\cos\theta\cos\phi M_{cb} - \sin\theta\cos\theta\cos\phi M_{bc} -$
$\sin\theta\cos\theta\sin\phi M_{cb} - \sin\theta\cos\theta\sin\phi M_{bc}$
$= \sin^2\theta M_{aa} + \cos^2\theta M_{cc} + \sin\theta\cos\theta(-\cos\phi M_{cb} - \cos\phi M_{bc} - \sin\phi M_{cb} - \sin\phi M_{bc})$
as $-M_{bc} = -M_{ac}$ and $-M_{ac} = M_{bc}$ it can be concluded that $-M_{bc} = M_{bc}$:

$$= \sin^2\theta M_{aa} + \cos^2\theta M_{cc} + \sin\theta\cos\theta(-\cos\phi M_{cb} + \cos\phi M_{bc} - \sin\phi M_{cb} + \sin\phi M_{bc})$$

as $M_{jk} = M_{kj}$, because the double sum is symmetric:

$$= \sin^2\theta M_{aa} + \cos^2\theta M_{cc} + \sin\theta\cos\theta(-\cos\phi M_{cb} + \cos\phi M_{cb} - \sin\phi M_{cb} + \sin\phi M_{cb})$$

This means that the dipole absorption for a crystal with tetragonal symmetry can be written as:

$$\mu \propto \sin^2\theta M_{aa} + \cos^2\theta M_{cc} \tag{A.50}$$

A crystal with orthorhombic symmetry has a 2 fold rotation axis, $N = 2$. To find the equation of the absorption in terms of the angular dependence the rotated tensor

needs to be calculated with $\alpha = \frac{2\pi}{2}$, ($\cos\alpha = -1$, and $\sin\alpha = 0$). This leads to:

$$\begin{aligned}
M_{aa} &= (-1)^2 \cdot M_{aa} + 0 \cdot M_{bb} - 0 \cdot -1 \cdot (M_{ba} + M_{ab}) \\
M_{ab} &= (-1)^2 \cdot M_{ab} - 0 \cdot M_{ba} + 0 \cdot (M_{aa} - M_{bb}) \\
M_{ac} &= -1 \cdot M_{ac} - 0 \cdot M_{bc} \\
M_{ba} &= (-1)^2 \cdot M_{ba} - 0 \cdot M_{ab} + 0 \cdot (M_{aa} - M_{bb}) \\
M_{bb} &= 0 \cdot M_{aa} + (-1) \cdot M_{bb} + 0 \cdot -1 \cdot (M_{ba} + M_{ab}) \\
M_{bc} &= 0 \cdot M_{ac} - 1 \cdot M_{bc} \\
M_{ca} &= -1 \cdot M_{ca} - 0 \cdot M_{cb} \\
M_{cb} &= 0 \cdot M_{ca} - 1 \cdot M_{cb} \\
M_{cc} &= M_{cc}
\end{aligned}$$

This leads to nine new equations for the rotated tensor:

$$M_{aa} = M_{aa} \tag{A.51}$$
$$M_{ab} = M_{ab} \tag{A.52}$$
$$M_{ac} = -M_{ac} \tag{A.53}$$
$$M_{ba} = M_{ba} \tag{A.54}$$
$$M_{bb} = M_{bb} \tag{A.55}$$
$$M_{bc} = -M_{bc} \tag{A.56}$$
$$M_{ca} = -M_{ca} \tag{A.57}$$
$$M_{cb} = -M_{cb} \tag{A.58}$$
$$M_{cc} = M_{cc} \tag{A.59}$$

Therefore the rotated tensor for orthorhombic symmetries can be written as:

$$M_{orth} = \begin{pmatrix} M_{aa} & M_{ab} & -M_{ac} \\ M_{ba} & M_{bb} & -M_{bc} \\ -M_{ca} & -M_{cb} & M_{cc} \end{pmatrix} \tag{A.60}$$

Using this tensor in the calculation of $\mu \propto \hat{\epsilon} \cdot M \cdot \hat{\epsilon}$, an equation for the dipole absorption for crystals with orthorhombic symmetry can be formed:
$= \sin^2\theta\cos^2\phi M_{aa} + \sin^2\theta\sin^2\phi M_{bb} + \cos^2\theta M_{cc} + \sin^2\theta\sin\phi\cos\phi M_{ba} +$
$\sin^2\theta\cos\phi\sin\phi M_{ab} - \sin\theta\cos\theta\cos\phi M_{ca} - \sin\theta\cos\theta\cos\phi M_{ac} - \sin\theta\cos\theta\sin\phi M_{cb} -$
$\sin\theta\cos\theta\sin\phi M_{bc}$
$= \sin^2\theta\cos^2\phi M_{aa} + \sin^2\theta\sin^2\phi M_{bb} + \cos^2\theta M_{cc} + \sin^2\theta\sin\phi\cos\phi(M_{ba} + M_{ab}) -$
$\sin\theta\cos\theta\cos\phi(M_{ca} + M_{ac}) - \sin\theta\cos\theta\sin\phi(M_{cb} + M_{bc})$
as $M_{ca} = -M_{ca}$ and $M_{cb} = -M_{cb}$:
$= \sin^2\theta\cos^2\phi M_{aa} + \sin^2\theta\sin^2\phi M_{bb} + \cos^2\theta M_{cc} + \sin^2\theta\sin\phi\cos\phi(M_{ba} + M_{ab}) -$
$\sin\theta\cos\theta\cos\phi(-M_{ca} + M_{ac}) - \sin\theta\cos\theta\sin\phi(-M_{cb} + M_{bc})$
as $M_{jk} = M_{kj}$, because the double sum is symmetric:
$= \sin^2\theta\cos^2\phi M_{aa} + \sin^2\theta\sin^2\phi M_{bb} + \cos^2\theta M_{cc} + \sin^2\theta\sin\phi\cos\phi(M_{ab} + M_{ab}) -$
$\sin\theta\cos\theta\cos\phi(-M_{ca} + M_{ca}) - \sin\theta\cos\theta\sin\phi(-M_{cb} + M_{cb})$
This means that the dipole absorption for a crystal with orthorhombic symmetry can be written as:

$$\mu \propto \sin^2\theta\cos^2\phi M_{aa} + \sin^2\theta\sin^2\phi M_{bb} + \cos^2\theta M_{cc} + 2\sin^2\theta\sin\phi\cos\phi M_{ab} \tag{A.61}$$

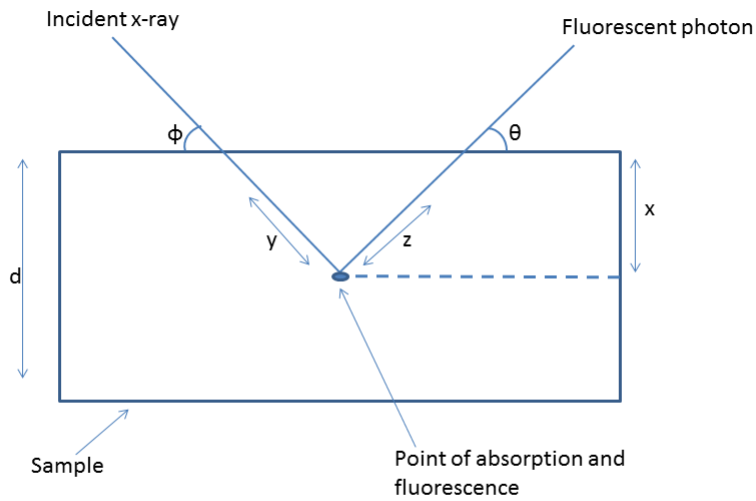

Figure A.1: Geometry used in calculating self-absorption correction in EXAFS.

A.3 Self-absorption correction.

Figure A.1 shows the geometry used in the following calculation.
In a fluorescence experiment the intensity of the fluorescence photons is calculated by:

$$I_f = I_o e^{-\mu(E)y} \cdot e^{-\mu(E_f)z} \epsilon_a(E) \mu_a(E) \tag{A.62}$$

where I_o is the intensity of the incoming beam, $\mu_a(E)$ is the absorption due to the given core excitation of the absorbing atom, $\mu(E)$ is the total absorption due to all of the elements in the sample, $\mu(E_f)$ is the absorption due to all of the elements in the sample at the fluorescence energy of the excited atom, and $\epsilon_a(E)$ is the fluorescence efficiency per unit solid angle.
Assuming that all the measured fluorescence is coming from the desired process (e.g. Se K-edge) then any other counts can be subtracted off.
Equation A.62 is only true for a specific y and z value so to make it more general it

can be integrated:

$$I_f = \int I_o e^{-\mu(E)y} \cdot e^{-\mu(E_f)z} \epsilon_a(E)\mu_a(E)dy$$

$$I_f = I_o\epsilon_a(E)\mu_a(E) \int e^{-\mu(E)y} \cdot e^{-\mu(E_f)z} dy$$

$$I_f = I_o\epsilon_a(E)\mu_a(E) \int e^{-(\mu(E)y+\mu(E_f)z)} dy$$

As $y \sin\phi = x$ and $z \sin\theta = x$, there can be some substitutions:

$$I_f = I_o\epsilon_a(E)\mu_a(E) \int e^{-(\frac{\mu(E)x}{\sin\phi}+\frac{\mu(E_f)x}{\sin\theta})} dy$$

$$y = \frac{x}{\sin\phi} \therefore \frac{dy}{dx} = \frac{1}{\sin\phi}$$

let $\mu_T = \mu(E)$, $\mu_f = \mu(E_f)$, $\mu_a = \mu_a(E)$, and $\epsilon_a = \epsilon(E)$

$$I_f = I_o\epsilon_a\mu_a \int e^{-(\frac{\mu_T x}{\sin\phi}+\frac{\mu_f x}{\sin\theta})} \frac{dx}{\sin\phi}$$

$$I_f = \frac{I_o\epsilon_a\mu_a}{\sin\phi} \int e^{-(\frac{\mu_T x}{\sin\phi}+\frac{\mu_f x}{\sin\theta})} dx$$

$$I_f = \frac{I_o\epsilon_a\mu_a}{\sin\phi} \int_0^d e^{-x(\frac{\mu_T}{\sin\phi}+\frac{\mu_f}{\sin\theta})} dx$$

$$I_f = \frac{I_o\epsilon_a\mu_a}{\sin\phi} \frac{1}{\frac{\mu_T}{\sin\phi}+\frac{\mu_f}{\sin\theta}} \left[-e^{-x(\frac{\mu_T}{\sin\phi}+\frac{\mu_f}{\sin\theta})}\right]_0^d$$

$$I_f = \frac{I_o\epsilon_a\mu_a}{\sin\phi} \frac{\sin\phi\sin\theta}{\mu_T\sin\theta+\mu_f\sin\phi} \left(1 - e^{-d(\frac{\mu_T}{\sin\phi}+\frac{\mu_f}{\sin\theta})}\right)$$

$$I_f = \frac{I_o\epsilon_a\mu_a\sin\theta}{\mu_T\sin\theta+\mu_f\sin\phi} \left(1 - e^{-d(\frac{\mu_T}{\sin\phi}+\frac{\mu_f}{\sin\theta})}\right)$$

$$I_f = I_o\epsilon_a\mu_a \frac{\sin\theta}{\mu_T\sin\theta+\mu_f\sin\phi} \left(1 - e^{-d(\frac{\mu_T}{\sin\phi}+\frac{\mu_f}{\sin\theta})}\right)$$

let $g = \frac{\sin\phi}{\sin\theta}$:

$$I_f = I_o\epsilon_a\mu_a \frac{1}{\mu_T+g\mu_f} \left(1 - e^{-d(\frac{\mu_T}{\sin\phi}+\frac{\mu_f}{\sin\theta})}\right)$$

$$I_f = \frac{I_o\epsilon_a\mu_a}{\mu_T+g\mu_f} \left(1 - e^{-d(\frac{\mu_T}{\sin\phi}+\frac{\mu_f}{\sin\theta})}\right) \tag{A.63}$$

This equation describes the fluorescence in the direction of θ. To be complete this equation needs to be integrated over the solid angle of the detector. In the case where $\theta + \phi = 90^o$ the maximum error in g is ~7% even for $\Delta\theta \approx 5^o$ at $\theta = 10^o$ so the solid angle can be neglected and this equation can be used for the fluorescence intensity. When correcting the self-absorption in a XAS experiment, when looking at the XANES region, the desired signal is $\mu_a(E)/\mu_a(E_o^+)$ where E_o^+ is an energy above the absorption edge (usually the edge-step energy used in the normalisation). What is actually measured in an XAS experiment is equation A.63. Around the XANES region certain approximation can be made to simplify this equation and obtain an equation for the desired signal. In most XAS experiments $0^o \geq \theta + \phi \leq 90^o$, it is also assumed that the sample is infinitely thick so $\mu_T \gg d^{-1}$, therefore:

$$\left[\frac{\mu_T}{\sin\phi} + \frac{\mu_f}{\sin\theta}\right] \gg d^{-1} \tag{A.64}$$

This means we can neglect the exponential term as it will go to $e^{-\infty}$. This leaves the equation as:

$$\frac{I_f}{I_o} = \epsilon_a \frac{\mu_a}{\mu_T + g\mu_f} \tag{A.65}$$

The total absorption, μ_T above the edge includes contributions from both the element of interest and the other atoms in the sample, so it can be rewritten as:

$$\mu_T = \mu_a + \mu_b \tag{A.66}$$

where μ_b is the absorption due to the other atoms in the sample.
Adding an edge step normalisation to $\frac{I_f}{I_o}$ we obtain the normalised data, this normalisation can be done using ATHENA.

$$N = \frac{\frac{I_f}{I_o}(E)}{\frac{I_f}{I_o}(E_o^+)} = \left[\frac{\epsilon_a(E)\mu_a(E)}{\epsilon_a(E_o^+)\mu_a(E_o^+)}\right]\left[\frac{\mu_f g + \mu_b(E_o^+) + \mu_a(E_o^+)}{\mu_f g + \mu_b(E) + \mu_a(e)}\right] \tag{A.67}$$

Dividing the numerator and denominator by $\mu_a(E_o^+)$ an expression for the desired (self-absorption corrected) signal can be produced.

$$N = \frac{(\epsilon_a(E)\mu_a(E))/\mu_a(E_o^+)}{(\epsilon_a(E_o^+)\mu_a(E_o^+))/\mu_a(E_o^+)}\left[\frac{(\mu_f/\mu_a(E_o^+))g + \mu_b(E_o^+)/\mu_a(E_o^+) + \mu_a(E_o^+)/\mu_a(E_o^+)}{(\mu_f/\mu_a(E_o^+))g + \mu_b(E)/\mu_a(E_o^+) + \mu_a(E)/\mu_a(E_o^+)}\right]$$

To simplify let $\beta = \frac{\mu_f}{\mu_a(E_o^+)}$, $\gamma = \frac{\mu_b(E)}{\mu_a(E_o^+)}$, and $\gamma' = \frac{\mu_b(E_o^+)}{\mu_a(E_o^+)}$

$$N = \frac{(\epsilon_a(E)\mu_a(E))}{(\epsilon_a(E_o^+)\mu_a(E_o^+))}\left[\frac{\beta g + \gamma' + 1}{\beta g + \gamma + \mu_a(E)/\mu_a(E_o^+)}\right]$$

The fluorescence efficiency is roughly equal at E and E_o^+ therefore $\frac{\epsilon_a(E)}{\epsilon_a(E_o^+)} \approx 1$

$$N = \frac{\mu_a(E)}{\mu_a(E_o^+)}\left[\frac{\beta g + \gamma' + 1}{\beta g + \gamma + \mu_a(E)/\mu_a(E_o^+)}\right]$$

As the desired signal in the XANES region is $\mu_a(E)/\mu_a(E_o^+)$, this equation needs to be rearranged to find the expression for this.

$$N(\beta g + \gamma + \frac{\mu_a(E)}{\mu_a(E_o^+)}) = \frac{\mu_a(E)}{\mu_a(E_o^+)}(\beta g + \gamma' + 1)$$

$$N\beta g + N\gamma + N\frac{\mu_a(E)}{\mu_a(E_o^+)} = \frac{\mu_a(E)}{\mu_a(E_o^+)}\beta g + \frac{\mu_a(E)}{\mu_a(E_o^+)}\gamma' + \frac{\mu_a(E)}{\mu_a(E_o^+)}$$

$$\frac{\mu_a(E)}{\mu_a(E_o^+)}\beta g + \frac{\mu_a(E)}{\mu_a(E_o^+)}\gamma' + \frac{\mu_a(E)}{\mu_a(E_o^+)} - N\frac{\mu_a(E)}{\mu_a(E_o^+)} = N\beta g + N\gamma$$

$$\frac{\mu_a(E)}{\mu_a(E_o^+)}(\beta g + \gamma' + 1 - N) = N\beta g + N\gamma$$

$$\frac{\mu_a(E)}{\mu_a(E_o^+)} = \frac{N\beta g + N\gamma}{\beta g + \gamma' + 1 - N}$$

in this small energy range, so we can estimate $\mu_b(E) \approx \mu_b(E_o^+) \therefore$

$$\frac{\mu_a(E)}{\mu_a(E_o^+)} = \frac{N(\beta g + \gamma)}{\beta g + \gamma + 1 - N} \tag{A.68}$$

In EXAFS experiments we want to measure:

$$\chi = \frac{\mu_a - \bar{\mu}_a}{\bar{\mu}_a} \tag{A.69}$$

where $\bar{\mu}_a$ is the absorption due to the given core excitation of the absorbing atom, with no EXAFS oscillations. This can be approximated by the absorption at an energy above the absorption edge, the typical energy to use is the edge-step in the normalisation.
What we actually measure in a fluorescence EXAFS experiment is:

$$\chi_{exp} = \frac{I_f - \bar{I}_f}{\bar{I}_f} \tag{A.70}$$

where $\bar{I}_f$ is the spline function fit to the data to simulate the "embedded atom" background fluorescence (roughly I_f without EXAFS oscillations).
Therefore the experimentally measured EXAFS is:

$$\chi_{exp} = \frac{I_f}{\bar{I}_f} - \frac{\bar{I}_f}{\bar{I}_f}$$
$$\chi_{exp} = \frac{I_F}{\bar{I}_f} - 1$$
$$\chi_{exp} + 1 = \frac{I_f}{\bar{I}_f}$$

Using equation 3.43 we can derive an equation for the experimental EXAFS:

$$\chi_{exp} + 1 = \frac{\frac{I_o \epsilon_a \mu_a}{\mu_T + g\mu_f}\left(1 - e^{-d(\frac{\mu_T}{\sin\phi} + \frac{\mu_f}{\sin\theta})}\right)}{\frac{I_o \epsilon_a \bar{\mu}_a}{\bar{\mu}_T + g\mu_f}\left(1 - e^{-d(\frac{\bar{\mu}_T}{\sin\phi} + \frac{\mu_f}{\sin\theta})}\right)}$$
$$\chi_{exp} + 1 = \frac{\frac{\mu_a}{\mu_T + g\mu_f}}{\frac{\bar{\mu}_a}{\bar{\mu}_T + g\mu_f}} \frac{\left(1 - e^{-d(\frac{\mu_t}{\sin\phi} + \frac{\mu_f}{\sin\theta})}\right)}{\left(1 - e^{-d(\frac{\bar{\mu}_t}{\sin\phi} + \frac{\mu_f}{\sin\theta})}\right)}$$
$$\chi_{exp} + 1 = \frac{\mu_a(\bar{\mu}_T + g\mu_f)}{\bar{\mu}_a(\mu_T + g\mu_f)} \frac{\left(1 - e^{-d(\frac{\mu_t}{\sin\phi} + \frac{\mu_f}{\sin\theta})}\right)}{\left(1 - e^{-d(\frac{\bar{\mu}_t}{\sin\phi} + \frac{\mu_f}{\sin\theta})}\right)}$$

This can be simplified with a few substitutions, let $\alpha = \bar{\mu}_T + g\mu_f$ and $\mu_T = \bar{\mu}_T + \chi\bar{\mu}_a$:

$$\chi_{exp} + 1 = \frac{\mu_a \alpha}{\bar{\mu}_a(\alpha + \chi\bar{\mu}_a)} \frac{\left(1 - e^{-d(\frac{\mu_t}{\sin\phi} + \frac{\mu_f}{\sin\theta})}\right)}{\left(1 - e^{-d(\frac{\bar{\mu}_t}{\sin\phi} + \frac{\mu_f}{\sin\theta})}\right)}$$

Divide both sides by $1 + \chi$:

$$\frac{\chi_{exp} + 1}{1 + \chi} = \frac{\mu_a \alpha}{\bar{\mu}_a(\alpha + \chi\bar{\mu}_a)} \frac{1}{1 + \chi} \frac{\left(1 - e^{-d(\frac{\mu_t}{\sin\phi} + \frac{\mu_f}{\sin\theta})}\right)}{\left(1 - e^{-d(\frac{\bar{\mu}_t}{\sin\phi} + \frac{\mu_f}{\sin\theta})}\right)}$$

The following substitution can be made $\mu_a = \bar{\mu}_a(1 + \chi)$:

$$\frac{\chi_{exp} + 1}{1 + \chi} = \frac{\mu_a \alpha}{\mu_a(\alpha + \chi\bar{\mu}_a)} \frac{\left(1 - e^{-d(\frac{\mu_t}{\sin\phi} + \frac{\mu_f}{\sin\theta})}\right)}{\left(1 - e^{-d(\frac{\bar{\mu}_t}{\sin\phi} + \frac{\mu_f}{\sin\theta})}\right)}$$

$$\frac{\chi_{exp} + 1}{1 + \chi} = \frac{\alpha}{(\alpha + \chi\bar{\mu}_a)} \frac{\left(1 - e^{-d(\frac{\mu_t}{\sin\phi} + \frac{\mu_f}{\sin\theta})}\right)}{\left(1 - e^{-d(\frac{\bar{\mu}_t}{\sin\phi} + \frac{\mu_f}{\sin\theta})}\right)}$$

As $g = \dfrac{\sin\phi}{\sin\theta}$:

$$\frac{\chi_{exp} + 1}{1 + \chi} = \frac{\alpha}{(\alpha + \chi\bar{\mu}_a)} \frac{\left(1 - e^{-d(\frac{\mu_t}{\sin\phi} + \frac{g\mu_f}{\sin\phi})}\right)}{\left(1 - e^{-d(\frac{\bar{\mu}_t}{\sin\phi} + \frac{g\mu_f}{\sin\phi})}\right)}$$

$$\frac{\chi_{exp} + 1}{1 + \chi} = \frac{\alpha}{(\alpha + \chi\bar{\mu}_a)} \frac{\left(1 - e^{-\frac{d}{\sin\phi}(\mu_t + g\mu_f)}\right)}{\left(1 - e^{-\frac{d}{\sin\phi}(\bar{\mu}_t + g\mu_f)}\right)}$$

$$\frac{\chi_{exp} + 1}{1 + \chi} = \frac{\alpha}{(\alpha + \chi\bar{\mu}_a)} \frac{\left(1 - e^{-\frac{d}{\sin\phi}(\alpha + \chi\bar{\mu}_a)}\right)}{\left(1 - e^{-\frac{d}{\sin\phi}(\alpha)}\right)}$$

$$\chi_{exp} = \frac{\alpha(1 + \chi)}{(\alpha + \chi\bar{\mu}_a)} \frac{\left(1 - e^{-\frac{d}{\sin\phi}(\alpha + \chi\bar{\mu}_a)}\right)}{\left(1 - e^{-\frac{d}{\sin\phi}(\alpha)}\right)} - 1 \tag{A.71}$$

The relationship between χ and χ_{exp} is exact. This equation gives us χ_{exp} in terms of χ but in order to calculate the EXAFS without self-absorption we need to have χ in terms of χ_{exp}. In order to invert equation A.71 we can make a simple approximation. Assuming that $\frac{\chi\bar{\mu}_a d}{\sin\phi} \ll 1$, we can then do a Taylor expansion of the exponential in the numerator:

$$1 - e^{\frac{-d}{\sin\phi}(\alpha + \chi\bar{\mu}_a)} = 1 - e^{\frac{-d\alpha}{\sin\phi}} e^{\frac{-d}{\sin\phi}(\chi\bar{\mu}_a)}$$

Taylor expand $e^{\frac{-d}{\sin\phi}(\chi\bar{\mu}_a)}$:

$$1 - \frac{\chi\bar{\mu}_a d}{\sin\phi} + ...$$

$$\therefore 1 - e^{\frac{-d}{\sin\phi}(\alpha + \chi\bar{\mu}_a)} = (1 - e^{\frac{-d\alpha}{\sin\phi}})(1 - \frac{\chi\bar{\mu}_a d}{\sin\phi})$$

This approximation gets worse with large χ and $\bar{\mu}_a$. It also has a maximum for both ϕ and d, because of the $e^{\frac{-d\alpha}{\sin\phi}}$ term. Various combinations of the above parameters can contribute to produce errors above 1%, so the approximation should be monitored when making the corrections outlined below.

With the above approximation, and making the following substitutions:

$$\beta = \frac{\bar{\mu}_a d\alpha}{\sin\phi} e^{\frac{-d\alpha}{\sin\phi}}, \text{ and } \gamma = 1 - e^{\frac{-d\alpha}{\sin\phi}}$$

We can derive an equation with χ in terms of χ_{exp}:

$$\begin{aligned}
\chi_{exp} &= \frac{\alpha(1+\chi)}{(\alpha+\chi\bar{\mu}_a)} \frac{\left(1 - e^{\frac{-d\alpha}{\sin\phi}}\right)\left(1 - \frac{\chi\bar{\mu}_a d}{\sin\phi}\right)}{\left(1 - e^{-\frac{d}{\sin\phi}(\alpha)}\right)} - 1 \\
\chi_{exp} &= \frac{\alpha(1+\chi)}{(\alpha+\chi\bar{\mu}_a)} \frac{1 - e^{-\frac{d\alpha}{\sin\phi}} - \frac{\chi\bar{\mu}_a d}{\sin\phi} + \frac{\chi\bar{\mu}_a d}{\sin\phi} e^{-\frac{d\alpha}{\sin\phi}}}{\gamma} - 1 \\
\chi_{exp} &= \frac{\alpha(1+\chi)}{(\alpha+\chi\bar{\mu}_a)} \frac{\gamma - \frac{\chi\bar{\mu}_a d}{\sin\phi} + \frac{\chi\beta}{\alpha}}{\gamma} - 1 \\
&\text{As } \frac{\chi\bar{\mu}_a d}{\sin\phi} \ll 1 \text{ it can be neglected:} \\
\chi_{exp} &= \frac{\alpha(1+\chi)}{(\alpha+\chi\bar{\mu}_a)} \frac{\gamma + \frac{\chi\beta}{\alpha}}{\gamma} - 1 \\
\chi_{exp} + 1 &= \frac{\alpha(1+\chi)}{(\alpha+\chi\bar{\mu}_a)} \frac{\gamma + \frac{\chi\beta}{\alpha}}{\gamma} \qquad \text{(A.72)} \\
\chi_{exp} + 1 &= \frac{(\alpha\chi+\alpha)(\gamma + \frac{\chi\beta}{\alpha})}{\gamma(\alpha+\chi\bar{\mu}_a)} \\
(\chi_{exp}+1)(\gamma\alpha + \gamma\chi\bar{\mu}_a) &= (\alpha\chi+\alpha)(\gamma + \frac{\chi\beta}{\alpha}) \\
\gamma\alpha\chi_{exp} + \gamma\chi\bar{\mu}_a\chi_{exp} + \gamma\alpha + \gamma\chi\bar{\mu}_a &= \alpha\chi\gamma + \chi^2\beta + \alpha\gamma + \chi\beta \\
0 &= \alpha\chi\gamma + \chi^2\beta + \alpha\gamma + \chi\beta - \gamma\alpha\chi_{exp} - \gamma\chi\bar{\mu}_a\chi_{exp} - \gamma\alpha - \gamma\chi\bar{\mu}_a \\
0 &= \chi^2\beta + \chi(\alpha\gamma + \beta - \gamma\bar{\mu}_a - \gamma\bar{\mu}_a\chi_{exp}) - \gamma\alpha\chi_{exp} + \gamma\alpha - \gamma\alpha \\
0 &= \chi^2\beta + \chi(\alpha\gamma + \beta - \gamma\bar{\mu}_a - \gamma\bar{\mu}_a\chi_{exp}) - \gamma\alpha\chi_{exp} \qquad \text{(A.73)}
\end{aligned}$$

This is now a quadratic equation and using the quadratic formula a solution for χ can be derived from equation A.73.

$$\chi = \frac{-[\gamma(\alpha - \bar{\mu}_a(\chi_{exp}+1)) + \beta] \pm \sqrt{[\gamma(\alpha - \bar{\mu}_a(\chi_{exp}+1)) + \beta]^2 + 4\beta\gamma\alpha\chi_{exp}}}{2\beta} \qquad \text{(A.74)}$$

Taking the thin and tick limits you find that the sign of the square root is positive. In the thin limit this equation reduces to $\chi = \chi_{exp}$ as expected.
For the thick limit take equation A.72, at this point in the derivation we can introduce the limit where $d \to \infty$, this means that β will go to zero and γ will go to 1, reducing the equation to:

$$\chi_{exp} + 1 = \frac{\alpha\chi + \alpha}{\alpha + \chi\bar{\mu}_a} \frac{1+0}{1}$$

Therefore in the thick limit, χ can be calculated by equation A.75:

$$
\begin{aligned}
(\chi_{exp}+1)(\alpha+\chi\bar{\mu}_a) &= \alpha\chi+\alpha \\
\alpha+\chi\bar{\mu}_a+\alpha\chi_{exp}+\chi\bar{\mu}_a\chi_{exp} &= \alpha\chi+\alpha \\
0 = \alpha\chi-\chi\bar{\mu}_a-\chi\bar{\mu}_a\chi_{exp}-\alpha\chi_{exp}+\alpha-\alpha \\
0 &= \chi(\alpha-\bar{\mu}_a-\bar{\mu}_a\chi_{exp})-\alpha\chi_{exp} \\
\alpha\chi_{exp} &= \chi(\alpha-\bar{\mu}_a-\bar{\mu}_a\chi_{exp}) \\
\chi &= \frac{\alpha\chi_{exp}}{\alpha-\bar{\mu}_a-\bar{\mu}_a\chi_{exp}} \\
\chi &= \frac{\chi_{exp}}{1-\frac{\bar{\mu}_a}{\alpha}-\frac{\bar{\mu}_a\chi_{exp}}{\alpha}}
\end{aligned}
\tag{A.75}
$$

A.4 Building XAS code.

```
#code for working our the XAS for different angles
#written by Sinead Rowe
import numpy as np
import matplotlib.pylab as plt
import pylab as py

#reads in the data from the txt file
def getData(filename):
        data = np.loadtxt(filename)
        """
        Shows how the data is read into the code
        k_array = data[:,0]
        energy_array = data[:,1]
        75_array = data[:,2]
        45_array = data[:,3]
        30_array = data[:,4]
        15_array = data[:,5]

        return (energy_array, 0_array, 15_array, 30_array, 45_array
        60_array, 75_array)
        """
        return data

#function for saving data to a file
def writeData(filename,data):
        np.savetxt(filename, data)

#function for the best fit, it will do a polyfit but if the degree
#is 1 then it will just be a line of best fit. It also returns the
#values of the gradient of the line and its y intercept
def bestFit(x, y):

        p = np.polyfit(x, y, 1)

        grad = p[0]
```

```
        yintercept = p[1]

        return grad, yintercept


#function for naming the files
def createFilename(angle, ion):
        if ion==1:
                fileout = "Ru_400K_X_Theta%0.0f.txt" % angle
        elif ion==2:
                fileout = "Ru_400K_E_Theta%0.0f.txt" % angle
        else:
                print "ERROR: unrecognised ion. Must be 1 or 2"

        return fileout

ion = 1
#this indicates which type of data is being loaded, EXAFS or XANES
#so the data is saved it is saved with the correct filename
filename = 'CaRuO_EXAFS_RT.chik2'
#this is file that will be loaded into the code
data = getData(filename)
#this calls the function which tells the code how to load the file
theta = np.deg2rad(np.array([15.0,30.0,45.0,75.0]))
#theta = np.deg2rad(np.arange(10.0,90.0,5.0))
#this gives a range of values for theta
x1 = np.sin(theta)**2.0
#this will give the values for the x axis for the fit, for sin^2
x2 = np.cos(theta)**2.0
#this will give the values for the x axis for the fit, for cos^2
ydata = np.transpose(data[:,[2,3,4,5]])
#this will input the values for the y axis, it needs to be
#transposed as both axes are verticle matrices, so the matrix
#calculations will work. It will input the values of each row of
#the data file
angle = np.deg2rad(75)
angle2 = np.deg2rad(15)
ang = np.rad2deg(angle)
ang2 = np.rad2deg(angle)
#this gives the angle for the equation when working out the
#absorption for any angle
grads1, yints1 = bestFit(x1,ydata)
#this will call of the function for the best fit and let it know
#what values of x and y are being input and for it to give us the
#gradient and the y intercept for each fit
per = grads1 + yints1
#this will caluclate the perpendicular absorption from these fits
grads2, yints2 = bestFit(x2,ydata)
#this will call of the function for the best fit and let it know
#what values of x and y are being input and for it to give us the
```

```
#gradient and the y intercept for each fit
par = grads2 + yints2
#this will caluclate the parallel absorption from these fits
para = (yints1 + par)/2
#this will work out the average value of the parallel absorption
#from both the sin^2 and cos^2 fits
perp = (yints2 + per)/2
#this will work out the average value of the perpendicular
#absorption from both the sin^2 and cos^2 fits
mu = para*np.cos(angle)**2.0 + perp*np.sin(angle)**2.0
mu2 = para*np.cos(angle2)**2.0 + perp*np.sin(angle2)**2.0
#this will work out, using the linear combination of the para and
#perp absorptions, the absorption for any angle
"""
Plotting part of the code
"""
fig = plt.figure()
plt.plot(data[:,0], mu2, 'b', label='Theoretical')
plt.plot(data[:,0], data[:,2], 'r--', label='Experimental')
plt.plot(data[:,0],(data[:,2]-mu2)-3, 'g', label='Difference')
plt.plot(data[:,0], mu-5, 'b')
plt.plot(data[:,0], data[:,5]-5, 'r--')
plt.plot(data[:,0],(data[:,5]-mu)-6, 'g')
fig.text(0.13,0.60, "($\\theta=15^o$)")
fig.text(0.125,0.25, "($\\theta=75^o$)")
py.xlim([0, 11])
#py.xlim([22100,22180])
#py.ylim([-0.2,1.2])
leg = plt.legend(loc='upper right') #This labels the plot
leg.get_frame().set_alpha(0.5)
fig.text(0.025,0.95, "(b)")
#plt.xlabel('Energy (eV)')
#plt.ylabel('normalised $x\mu$ (E)')
plt.xlabel('k($\AA^{-1}$)')
plt.ylabel('$k^2\chi(k)$ $(A^{-2})$')
plt.savefig("Ru_RT_E.png", format='png', dpi=1000)
fileout = createFilename((np.rad2deg(angle)), ion)
#this will create the filename for the data depending on the angle
#and inputed data
dataout = np.transpose(np.vstack((data[:,0], mu, yints1)))
#this will choose the data that is being saved, it needs to be
#transposed to put it into a form that can be read by athena
writeData(fileout, dataout)
#this will write the data
```

A.5 Self-absorption correction code.

```
"""
Code for self-absorption corrections in XAS,
Written by Sinead Rowe
```

```
"""
"""
In this code there are certain variables that need to be input by
the user.
-The user must provide their our XAS data.
-The user also needs to provide the equation of the line for the
mass attenuation coefficients. NOTE: these coefficients are
specific to atoms in the samples of my own work and they are also
specific to a certain energy range. If the edge of interest is
changed (i.e. Ru K-edge to Ru L-edge) the equations for mass
attenuation must also be changed.
-The user must specify which sample they are using, this can be done
by updating the variable 'ion' this will make sure that the code is
using the correct mass attenuation values for the correction.
-The user must specify which type of data they are uploading, e.g.
XANES. This can be done by updating the variable 'E', this will make
sure that the correct self-absorption equation is used for the
correction.
-The user has to input the angles in the experiment (i.e. incoming
angle from beam to sample, and outgoing angle from sample to
detector).
-The user must input the mass attenuation coefficients for the atoms
in the sample at the fluorescence energy of the excited atom.
-The user must input the density and thickness of the sample (this
code will calculate the self-absorption correction, for EXAFS, in
the thick limit as well. So comparison between the corrections can
be made and the user can decide which correction they would like to
use).
-The user will need to input the temperature the data was measured
at (this, along with the incoming angle, will create a unique
filename for each correction).
"""
import numpy as np
import matplotlib.pylab as plt
import pylab as py

def getDataX(filenameX):
dataX = np.loadtxt(filenameX)
"""
Loads in the experimental EXAFS data.
The array is:
(when loading in EXAFS):
k_array = dataX[:,0]
chi = dataX[:,1]
chik = dataX[:,2]
chik2 = dataX[:,3]
chik3 = dataX[:,4]
win = dataX[:,5]
energy = dataX[:,6]
(when loading in XANES):
```

```
energy_array = dataX[:,0]
norm = dataX[:,1]
nbkg = dataX[:,2]
flat = dataX[:,3]
fbkg = dataX[:,4]
nder = dataX[:,5]
nsec = dataX[:,6]
"""
return dataX

def writeData(filename,data):
"""
This function will save the data to a file so it can be used however
it needs to be
"""
np.savetxt(filename, data)

def createFilename(ion, temp, angle, E):
"""
Creates a filename based on variables in the experimental EXAFS
Inputs:
ion - the sample that the data is loading in
temp - the temperature the experimental EXAFS was measured at
angle- the angle the experimental EXAFS was measured at
E - this indicates whether EXAFS or XANES data is being loaded in
Output:
fileout - the filename for the output of the code
"""
if ion == 1:
if E == 1:
fileout = "Ca2RuO4_EXAFS_Temp%0.0f_Theta%0.0f.txt" % (temp, angle)
elif E == 2:
fileout = "Ca2RuO4_XANES_Temp%0.0f_Theta%0.0f.txt" % (temp, angle)

elif ion == 2:
if E == 1:
fileout = "Rb2Mo6Se6_EXAFS_Temp%0.0f_Theta%0.0f.txt" % (temp, angle)
elif E == 2:
fileout = "Rb2Mo6Se6_XANES_Temp%0.0f_Theta%0.0f.txt" % (temp, angle)

elif ion == 3:
if E == 1:
fileout = "Tl2Mo6Se6_EXAFS_Temp%0.0f_Theta%0.0f.txt" % (temp, angle)
elif E == 2:
fileout = "Tl2Mo6Se6_XANES_Temp%0.0f_Theta%0.0f.txt" % (temp, angle)
elif ion == 4:
if E == 1:
fileout = "Sr2RhO4_EXAFS_Temp%0.0f_Theta%0.0f.txt" % (temp, angle)
elif E == 2:
fileout = "Sr2RhO4_XANES_Temp%0.0f_Theta%0.0f.txt" % (temp, angle)
```

```
elif ion == 5:
if E == 1:
fileout = "Sr2MnCu2S2O2_Cuedge_EXAFS_Temp%0.0f_Theta%0.0f.txt"
% (temp, angle)
elif E == 2:
fileout = "Sr2MnCu2S2O2_Cuedge_XANES_Temp%0.0f_Theta%0.0f.txt"
% (temp, angle)
elif ion == 6:
if E == 1:
fileout = "Sr2MnCu2S2O2_Mnedge_EXAFS_Temp%0.0f_Theta%0.0f.txt"
% (temp, angle)
elif E == 2:
fileout = "Sr2MnCu2S2O2_Mnedge_XANES_Temp%0.0f_Theta%0.0f.txt"
% (temp, angle)

return fileout

def mupCa(dataX, E):
"""
Creates the mass attenuation coefficients for the energy range of
the experimental XAS. It uses the equation of the line created by
the two points in the mass attenuation table that the energy range
is between.
The user must find this equation themselves.
Input:
dataX[:,0 or 6] - the energy array of the experimental XAS
E - indicates whether EXAFS or XANES data is being loaded in
Output:
mupCa - mass attenuation array for the Ca element in the sample
"""
if E == 1:
mupCa = -0.000902*dataX[:,6]+31.14
elif E == 2:
mupCa = -0.000902*dataX[:,0]+31.14
return mupCa

def mupO(dataX, E):
"""
Does the same as the function above, has the same input.
Output:
mupO - mass attenuation array for the O element in the sample
"""
if E == 1:
mupO = -0.00004872*dataX[:,6]+1.8395
elif E == 2:
mupO = -0.00004872*dataX[:,0]+1.8395
return mupO

def mupSr(dataX, E):
if E == 1:
```

```
mupSr = -0.004229*dataX[:,6]+148.44
elif E == 2:
mupSr = -0.004229*dataX[:,0]+148.44
return mupSr

def mupRb(dataX, E):
"""
Does the same as the function above, has the same input.
Output:
mupRb - mass attenuation array for the Rb element in the sample
"""
if E == 1:
mupRb = -0.007714*dataX[:,6]+134.8
elif E == 2:
mupRb = -0.007714*dataX[:,0]+134.8
return mupRb

def mupMo(dataX, E):
"""
Does the same as the function above, has the same input.
Output:
mupMo - mass attenuation array for the Mo element in the sample
"""
if E == 1:
mupMo = -0.011444*dataX[:,6]+200.2
elif E == 2:
mupMo = -0.011444*dataX[:,0]+200.2
return mupMo

def mupTl(dataX, E):
"""
Does the same as the function above, has the same input.
Output:
mupTl - mass attenuation array for the Tl element in the sample
"""
mupTl = np.zeros(np.size(dataX,0))
if E == 1:
for i, energy in enumerate(dataX[:,6]):
if dataX[i,6] < 12657.5:
mupTl[i] = -0.02123424271*dataX[i,6]+338.3424271
else:
mupTl[i] = -0.02715153891*dataX[i,6]+512.9706038
elif E == 2:
for i, energy in enumerate(dataX[:,0]):
if dataX[i,0] < 12657.5:
mupTl[i] = -0.02123424271*dataX[i,0]+338.3424271
else:
mupTl[i] = -0.02715153891*dataX[i,0]+512.9706038
return mupTl
```

```
def mupCu(dataX, E):
"""
Does the same as the function above, has the same input.
Output:
mupCu - mass attenuation array for the Cu element in the sample
"""
if E == 1:
mupCu = -0.031525*dataX[:,6]+304.75
elif E == 2:
mupCu = -0.031525*dataX[:,0]+304.75

return mupCu

def mupMn(dataX, E):
"""
Does the same as the function above, has the same input.
Output:
mupMn - mass attenuation array for the Mn element in the sample
"""
if E == 1:
mupMn = -0.061*dataX[:,6]+761.4
elif E == 2:
mupMn = -0.061*dataX[:,0]+761.4

return mupMn

def mupOo(dataX, E, ion):
"""
Does the same as the function above, has the same input, apart from
ion.
Input:
ion - this will use the correct mass attenuation equation depending
on the absorption edge
Output:
mupOo - mass attenuation array for the O element in the sample
"""
if ion < 5:
mupOo = 0
elif ion == 5:
if E == 1:
mupOo = -0.002839*dataX[:,6]+34.342
elif E == 2:
mupOo = -0.002839*dataX[:,0]+34.342
elif ion == 6:
if E == 1:
mupOo = -0.008035*dataX[:,6]+75.91
elif E == 2:
mupOo = -0.008035*dataX[:,0]+75.91
return mupOo
```

```
def mupSro(dataX, E, ion):
"""
Does the same as the function above, has the same input.
Output:
mupSro - mass attenuation array for the Sr element in the sample
"""
if ion < 5:
mupSro = 0
elif ion == 5:
if E == 1:
mupSro = -0.02613*dataX[:,6]+324.04
elif E == 2:
mupSro = -0.02613*dataX[:,0]+324.04
elif ion == 6:
if E == 1:
mupSro = -0.0673*dataX[:,6]+653.4
elif E == 2:
mupSro = -0.0673*dataX[:,0]+653.4
return mupSro

def mupS(dataX, E, ion):
"""
Does the same as the function above, has the same input.
Output:
mupS - mass attenuation array for the S element in the sample
"""
if ion < 5:
mupS = 0
elif ion == 5:
if E == 1 and ion == 5:
mupS = -0.022265*dataX[:,6]+272.77
elif E == 2 and ion == 5:
mupS = -0.022265*dataX[:,0]+272.77
elif ion == 6:
if E == 1:
mupS = -0.058475*dataX[:,6]+562.45
elif E == 2:
mupS = -0.058475*dataX[:,0]+562.45
return mupS

def mubcalc(ion, mpCa, mpO, mpRb, mpMo, mpTl, mpSr, mpCu, mpMn, mpOo
, mpSro, mpS, p):
"""
Calculates the mean absorption due to all of the elements in the
sample, except the element of interest.
Inputs:
mp_i - array which has the mass attenuation coefficients
g_i - which are the mass fractions of the elements
p - the density of the sample
Outputs:
```

```
mubcalc - array of absorptions with respect to energy due to all of
the elements in the sample other than the element of interest
"""
if ion == 1:
#This is the mass fraction of Ca in the sample
g2 = 0.326871162

#This is the mass fraction of O in the sample
g3 =     0.260971691

mutCa = g2*mpCa
mutO = g3*mpO

mubcalc = p*(mutCa + mutO)

elif ion == 2:
#This is the mass fraction of Rb in the sample
g2 = 0.140062

#This is the mass fraction of Mo in the sample
g3 = 0.471707

mutRb = g2*mpRb
mutMo = g3*mpMo

mubcalc = p*(mutRb + mutMo)
elif ion == 3:
#This is the mass fraction of Tl in the sample
g2 = 0.280304

#This is the mass fraction of Mo in the sample
g3 = 0.394777

mutTl = g2*mpTl
mutMo = g3*mpMo

mubcalc = p*(mutTl + mutMo)

elif ion == 4:
#This is the mass fraction of Sr in the sample
g2 = 0.512185

#This is the mass fraction of O in the sample
g3 = 0.187045

mutSr = g2*mpSr
mutO = g3*mpO

mubcalc = p*(mutSr + mutO)
elif ion == 5:
```

```
#This is the mass fraction of Mn in the sample
g2 = 0.121172

#This is the mass fraction of Sr in the sample
g3 = 0.386512

#This is the mass fraction of S in the sample
g4 = 0.141424

#this is the mass fraction of O in the sample
g5 = 0.070575

mutMn = g2*mpMn
mutSr = g3*mpSro
mutS = g4*mpS
mutO = g5*mpOo

mubcalc = p*(mutMn+mutSr+mutS+mutO)
elif ion == 6:
#This is the mass fraction of Cu in the sample
g1 = 0.280316

#This is the mass fraction of Sr in the sample
g3 = 0.386512

#This is the mass fraction of S in the sample
g4 = 0.141424

#this is the mass fraction of O in the sample
g5 = 0.070575

mutCu = g1*mpCu
mutSr = g3*mpSro
mutS = g4*mpS
mutO = g5*mpOo

mubcalc = p*(mutCu+mutSr+mutS+mutO)

return mubcalc

def muacalc(ion, mutRu, mutSe, mutRh, mutCu, mutMn, p):
if ion == 1:
#This is the mass fraction of Ru in the sample
g1 = 0.412157147

muacalc = p*g1*mutRu

elif ion == 2:
#This is the mass fraction of Se in the sample
g1 = 0.388231
```

```
muacalc = p*g1*mutSe

elif ion == 3:
#This is the mass fraction of Se in the sample
g1 = 0.324919

muacalc = p*g1*mutSe

elif ion == 4:
#This is the mass fraction of Rh in the sample
g1 = 0.300770

muacalc = p*g1*mutRh
elif ion == 5:
#This is the mass fraction of Cu in the sample
g1 = 0.280316

muacalc = p*g1*mutCu
elif ion == 6:
#This is the mass fraction of Mn in the sample
g1 = 0.121172

muacalc = p*g1*mutMn

return muacalc

def mufcalc(ion, mufRb, mufSe, mufMo, mufTl, mufRu, mufCa, mufO,
mufRh, mufSr, mufCu, mufMn, mufS, p):
if ion == 1:
#This is the mass fraction of Ru in the sample
g1 = 0.412157147

#This is the mass fraction of Ca in the sample
g2 = 0.326871162

#This is the mass fraction of O in the sample
g3 =    0.260971691

mufcalc = p*((g1*mufRu) + (g2*mufCa) +(g3*mufO))

elif ion == 2:
#This is the mass fraction of Se in the sample
g1 = 0.388231

#This is the mass fraction of Rb in the sample
g2 = 0.140062

#This is the mass fraction of Mo in the sample
g3 = 0.471707
```

```
mufcalc = p*((g1*mufSe) + (g2*mufRb) +(g3*mufMo))

elif ion == 3:
#This is the mass fraction of Se in the sample
g1 = 0.324919

#This is the mass fraction of Tl in the sample
g2 = 0.280304

#This is the mass fraction of Mo in the sample
g3 = 0.394777

mufcalc = p*((g1*mufSe) + (g2*mufTl) +(g3*mufMo))

elif ion == 4:
#This is the mass fraction of Rh in the sample
g1 = 0.300770

#This is the mass fraction of Sr in the sample
g2 = 0.512185

#This is the mass fraction of O in the sample
g3 = 0.187045

mufcalc = p*((g1*mufRh)+(g2*mufSr)+(g3*mufO))
elif ion == 5:
#This is the mass fraction of Cu in the sample
g1 = 0.280316

#This is the mass fraction of Mn in the sample
g2 = 0.121172

#This is the mass fraction of Sr in the sample
g3 = 0.386512

#This is the mass fraction of S in the sample
g4 = 0.141424

#this is the mass fraction of O in the sample
g5 = 0.070575

mufcalc = p*((g1*mufCu)+(g2*mufMn)+(g3*mufSr)+(g4*mufS)+(g5*mufO))
elif ion == 6:
#This is the mass fraction of Cu in the sample
g1 = 0.280316

#This is the mass fraction of Mn in the sample
g2 = 0.121172
```

```
#This is the mass fraction of Sr in the sample
g3 = 0.386512

#This is the mass fraction of S in the sample
g4 = 0.141424

#this is the mass fraction of O in the sample
g5 = 0.070575

mufcalc = p*((g1*mufCu)+(g2*mufMn)+(g3*mufSr)+(g4*mufS)+(g5*mufO))

return mufcalc

"""
These are the variables that will have to be input by the user:
"""

#This will select the correct absorptions depending on the sample
#the data uploaded is for, ion=1 is for Ca2RuO4, ion=2 is for
#Rb2Mo6Se6, ion=3 is for Tl2Mo6Se6, ion=4 is for Sr2RhO4, ion=5 is
#for Cu K-edge of Sr2Cu2MnS2O2, and ion=6 is for Mn K-edge of
#Sr2Cu2MnS2O2
ion = 3

#This will indicate whether you are uploading XANES or EXAFS data,
#the code will then use the correct corrections for the data range
#given.
E = 1 #E=1 is EXAFS, E=2 is XANES

#phi is the angle between the sample and the incident x-ray beam
phi = np.deg2rad(45)

#theta is the angle between the sample and the detector (the angle
#between the measured fluorescent x-ray and the detector)
theta = np.deg2rad(45)


#The temperature this EXAFS was measured at, for the filename
temp = 150

if ion == 1:
#This is the variable used for the filename for Ca2RuO4
angle = np.rad2deg(phi)
elif ion == 2:
#This is the variable used for the filename for Rb2Mo6Se6
angle = 90
elif ion == 3:
#This is the variable used for the filename for Tl2Mo6Se6
angle = 0
elif ion == 4:
```

```
#This is the variable used for the filename for Sr2RhO4
angle = np.rad2deg(phi)
elif ion == 5:
#This is the variable used for the filename for Sr2MnCu2S2O2 Cu edge
angle = np.rad2deg(phi)
elif ion == 6:
#This is the variable used for the filename for Sr2MnCu2S2O2 Mn edge
angle = np.rad2deg(phi)

if E == 1:
#Name of the file with the EXAFS data in it
filenameX = 'Tl0EXAFS150K.chik'
elif E == 2:
filenameX = 'Tl90XANES150K.txt'

#This calls the data for the measured EXAFS
dataX = getDataX(filenameX)

#This is the density of the sample
p = 5

#d is the sample thickness
if ion == 1:
d = 0.0112 #for Ca2RuO4
elif ion == 2:
d = 0.0285 #for Rb2Mo6Se6
elif ion == 3:
d = 0.0342 #for Tl2Mo6Se6
elif ion == 4:
d = 0.0350 #for Sr2RhO4

#These are the values for the mass attenuation coefficients at the
#fluorescence energy
mufRb = 48.39

mufMo = 72.27

mufSe = 34.35

mufTl = 100.043

mufRu = 17.543

mufCa = 15.472

if ion == 1:
mufO = 1.0056
elif ion == 4:
mufO = 0.8546
elif ion == 5:
```

```
mufO = 11.4944
elif ion == 6:
mufO = 29.7453
else:
mufO = 0

if ion == 4:
mufSr = 62.946
elif ion == 5:
mufSr = 113.7515
elif ion == 6:
mufSr = 265.4153
else:
mufSr = 0

mufRh = 15.772

if ion == 5:
mufCu = 51.854
elif ion == 6:
mufCu = 124.123
else:
mufCu = 0

if ion == 5:
mufMn = 270.485
elif ion == 6:
mufMn = 78.330
else:
mufMn = 0

if ion == 5:
mufS = 93.5862
elif ion == 6:
mufS = 225.4814
else:
mufS = 0

#These are the values for the mass attenuation coefficients for the
#absorption due to the excited atom, at an energy over the
#absorption edge
mutSe = 158.84

mutRu = 69.759

mutRh = 64.0894

mutCu = 278.1804

mutMn = 450.3530
```

```
"""
These are the variables that the code will deal with, they will use
the above variables but they do not need to be input manually by
the user.

Need to make a table full of zeros so that the arrays do not
overwrite for each energy
"""

mpCa = np.zeros(np.size(dataX,0))

mpCa = mupCa(dataX, E)

mpO = np.zeros(np.size(dataX,0))

mpO = mupO(dataX, E)

mpSr = np.zeros(np.size(dataX,0))

mpSr = mupSr(dataX, E)

mpRb = np.zeros(np.size(dataX,0))

mpRb = mupRb(dataX, E)

mpMo = np.zeros(np.size(dataX,0))

mpMo = mupMo(dataX, E)

mpTl = np.zeros(np.size(dataX,0))

mpTl = mupTl(dataX, E)

mpCu = np.zeros(np.size(dataX,0))

mpCu = mupCu(dataX, E)

mpMn = np.zeros(np.size(dataX,0))

mpMn = mupMn(dataX, E)

mpS = np.zeros(np.size(dataX,0))

mpS = mupS(dataX, E, ion)

mpSro = np.zeros(np.size(dataX,0))

mpSro = mupSro(dataX, E, ion)
```

```
mpOo = np.zeros(np.size(dataX,0))

mpOo = mupOo(dataX, E, ion)

muf = mufcalc(ion, mufRb, mufSe, mufMo, mufTl, mufRu, mufCa, mufO,
mufRh, mufSr, mufCu, mufMn, mufS, p)

mub = np.zeros(np.size(dataX,0))

mub = mubcalc(ion, mpCa, mpO, mpRb, mpMo, mpTl, mpSr, mpCu, mpMn,
mpOo, mpSro, mpS, p)

mua = muacalc(ion, mutRu, mutSe, mutRh, mutCu, mutMn, p)

#Xexp is the measured EXAFS from the experiment
Xexp = dataX[:,1]

g = (np.sin(phi))/(np.sin(theta))

beta = muf/mua

gamma = mub/mua

N = Xexp

mut = mub + mua

alp = mut + g*muf

bet = ((mua*d*alp)/(np.sin(phi)))*np.exp(-(alp*d)/(np.sin(phi)))

gam = 1 - np.exp(-(alp*d)/(np.sin(phi)))

a = bet

b = gam*(alp - mua*(Xexp +1)) + beta

c = -gam*alp*Xexp

"""
Xt is the desired XANES that will take into account any self-
absorption during the experiment, EX and EXt are the desired
EXAFS.

This is our end product and it is the EXAFS or XANES with the self-
absorption corrections.
"""

#This is the self-absorption corrected XANES in the thick limit
Xt=(N*((beta*g)+gamma))/(1 + (beta*g) + gamma - N)
```

```
#This is the self-absorption corrected EXAFS data
EX = (-b + np.sqrt((b**2) - 4*a*c))/(2*a)

#This is the self-absorption corrected EXAFS data in the thick limit
EXt=(N)/(1-(mua/alp)-((mua*N)/alp))

#This is the corrected EXAFS with a weighting factor of k
k = dataX[:,0]*EXt

#This is the corrected EXAFS with a weighting factor of k^2
k2 = ((dataX[:,0])**2)*EXt

#This is the corrected EXAFS with a weighting factor of k^3
k3 = ((dataX[:,0])**3)*EXt

#This will use the filename function to create a filename for the
#data
fileout = createFilename(ion, temp, angle, E)

if E == 1:
"""
This will plot the self corrected EXAFS superimposed with the
experimental EXAFS data
"""
fig = plt.figure()
plt.plot(dataX[:,0], EXt, label='SAcorr thick', color="g")
#plt.plot(dataX[:,0], EX, label='SAcorr', color="r")
plt.plot(dataX[:,0], dataX[:,1], label='experimental', color="b")
plt.legend(loc='best') #This labels the plot
if ion == 1:
fig.suptitle('self-absorption correction of $Ca_2RuO_4$ at %0.0fK
and %0.0f$^o$' % (temp, angle))
elif ion == 2:
fig.suptitle('self-absorption correction of $Rb_2Se_6Mo_6$ at %0.0fK
and %0.0f$^o$' % (temp, angle))
elif ion == 3:
fig.suptitle('self-absorption correction of $Tl_2Se_6Mo_6$ at %0.0fK
and %0.0f$^o$' % (temp, angle))
elif ion == 4:
fig.suptitle('self-absorption correction of $Sr_2RhO_4$ at %0.0fK
and %0.0f$^o$' % (temp, angle))
elif ion == 5:
fig.suptitle('self-absorption correction of $Sr_2MnCu_2S_2O_2$, Cu
K-edge at %0.0fK and %0.0f$^o$' % (temp, angle))
elif ion == 6:
fig.suptitle('self-absorption correction of $Sr_2MnCu_2S_2O_2$, Mn
K-edge at %0.0fK and %0.0f$^o$' % (temp, angle))
plt.xlabel('Wavenumber ($\AA^{-1}$)')
plt.ylabel('$\chi(k)$ ($A^{-2}$)')
```

```
#if ion == 1:
#    plt.savefig("CaRuOSAEXAFS%0.0fK%0.0fdeg.svg" % (temp, angle))
#elif ion == 2:
#    plt.savefig("RbMoSeSAEXAFS%0.0fK%0.0fdeg.svg" % (temp, angle))
#elif ion == 3:
#    plt.savefig("TlMoSeSAEXAFS%0.0fK%0.0fdeg.svg" % (temp, angle))
#elif ion == 4:
#    plt.savefig("SrRhOSAEXAFS%0.0fK%0.0fdeg.svg" % (temp, angle))
#elif ion == 5:
#    plt.savefig("SrMnCuSOCuedgeSAEXAFS%0.0fK%0.0fdeg.svg"
% (temp, angle))
#elif ion == 6:
#   plt.savefig("SrMnCuSOMnedgeSAEXAFS%0.0fK%0.0fdeg.svg"
% (temp, angle))
elif E == 2:
"""
This will plot the self corrected EXAFS superimposed with the
experimental XANES data
"""
fig = plt.figure()
plt.plot(dataX[:,0], Xt, label='SAcorr thick', color="r")
plt.plot(dataX[:,0], dataX[:,1], label='experimental', color="b")
plt.legend(loc='best') #This labels the plot
if ion == 1:
fig.suptitle('self-absorption correction of $Ca_2RuO_4$ at %0.0fK
and %0.0f$^o$' % (temp, angle))
elif ion == 2:
fig.suptitle('self-absorption correction of $Rb_2Se_6Mo_6$ at %0.0fK
and %0.0f$^o$' % (temp, angle))
elif ion == 3:
fig.suptitle('self-absorption correction of $Tl_2Se_6Mo_6$ at %0.0fK
and %0.0f$^o$' % (temp, angle))
elif ion == 4:
fig.suptitle('self-absorption correction of $Sr_2RhO_4$ at %0.0fK
and %0.0f$^o$' % (temp, angle))
elif ion == 5:
fig.suptitle('self-absorption correction of $Sr_2MnCu_2S_2O_2$, Cu
K-edge at %0.0fK and %0.0f$^o$' % (temp, angle))
elif ion == 6:
fig.suptitle('self-absorption correction of $Sr_2MnCu_2S_2O_2$, Mn
K-edge at %0.0fK and %0.0f$^o$' % (temp, angle))
plt.xlabel('Energy (eV)')
plt.ylabel('normalised $x\mu$ (E)')
py.ylim([0, 2.1])
py.xlim([12629.2, 12739.2])
"""
if ion == 1:
plt.savefig("CaRuOSAXANES%0.0fK%0.0fdeg.svg" % (temp, angle))
elif ion == 2:
plt.savefig("RbMoSeSAXANES%0.0fK%0.0fdeg.svg" % (temp, angle))
```

```
elif ion == 3:
plt.savefig("TlMoSeSAXANES%0.0fK%0.0fdeg.svg" % (temp, angle))
elif ion == 4:
plt.savefig("SrRhOSAXANES%0.0fK%0.0fdeg.svg" % (temp, angle))
elif ion == 5:
plt.savefig("SrMnCuSOCuedgeSAXANES%0.0fK%0.0fdeg.svg"
% (temp, angle))
elif ion == 6:
plt.savefig("SrMnCuSOMnedgeSAXANES%0.0fK%0.0fdeg.svg"
% (temp, angle))
"""
#This will produce the table of k-space, the SA corrected EXAFS and
#the energy each value is associated to.
if E == 1:
dataout = np.transpose(np.vstack((dataX[:,0], EXt, k, k2, k3,
dataX[:,5], dataX[:,6])))
elif E == 2:
dataout = np.transpose(np.vstack((dataX[:,0], Xt)))


#This will write the data to a file that will use the function to
#save it.
writeData(fileout, dataout)
```

Appendix B

$M_2Mo_6Se_6$ plots.

B.1 $Rb_2Mo_6Se_6$

B.1.1 XANES

The following plots display the XANES for the intermediate temperatures measured for the $Rb_2Mo_6Se_6$ sample. They show a similar trend with respect to the angle between the *c*-axis and the polarisation, where there is a higher intensity of the first peak for the measurement at 90°. The peak intensities show more grouping for the 75K data, while there is a more smooth transition for the 100K data.

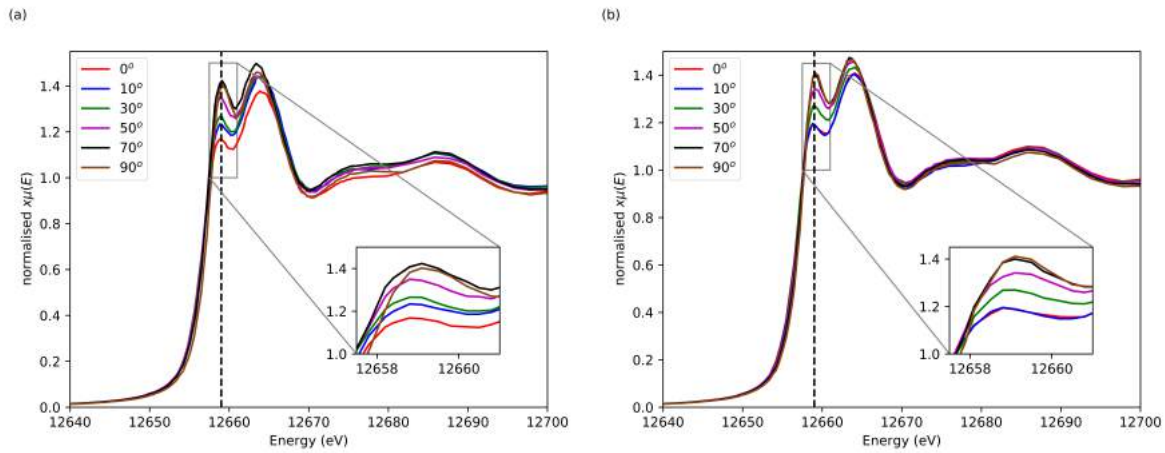

Figure B.1: XANES of the Se K-edge of $Rb_2Mo_6Se_6$, at 75K (a) and 100K (b), at different angles.

B.1.2 EXAFS

The following plots display the EXAFS and FT-EXAFS for the intermediate temperatures measured for the $Rb_2Mo_6Se_6$ sample. Both show a similar trend with respect to the angle between the *c*-axis and the polarisation. However the second peak in the FT-EXAFS at 75K show a similar intensity for all angles, while for the 100K data shows a decrease in intensity as the angle becomes shallower.

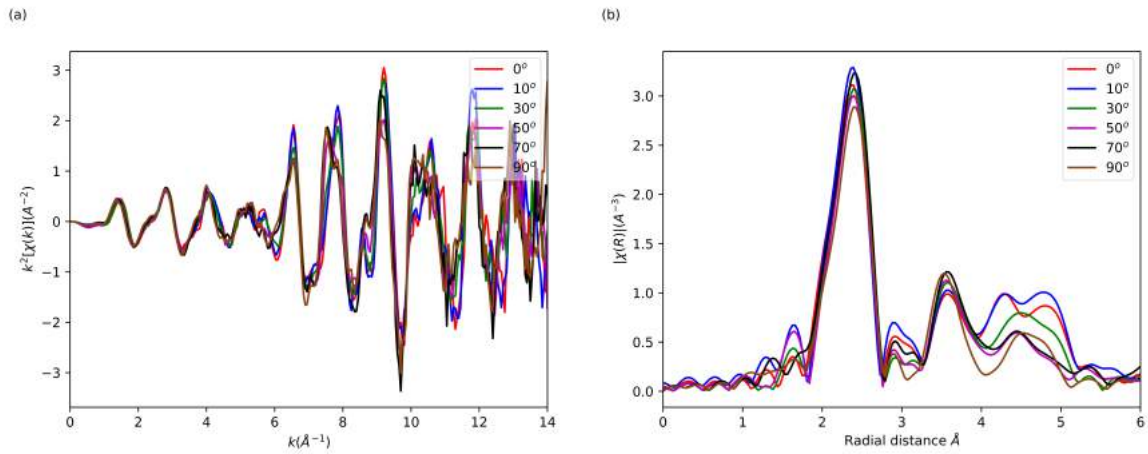

Figure B.2: EXAFS, (a), and Fourier transformed EXAFS, (b), of the Se K-edge, at 75K, of $Rb_2Mo_6Se_6$, at different angles.

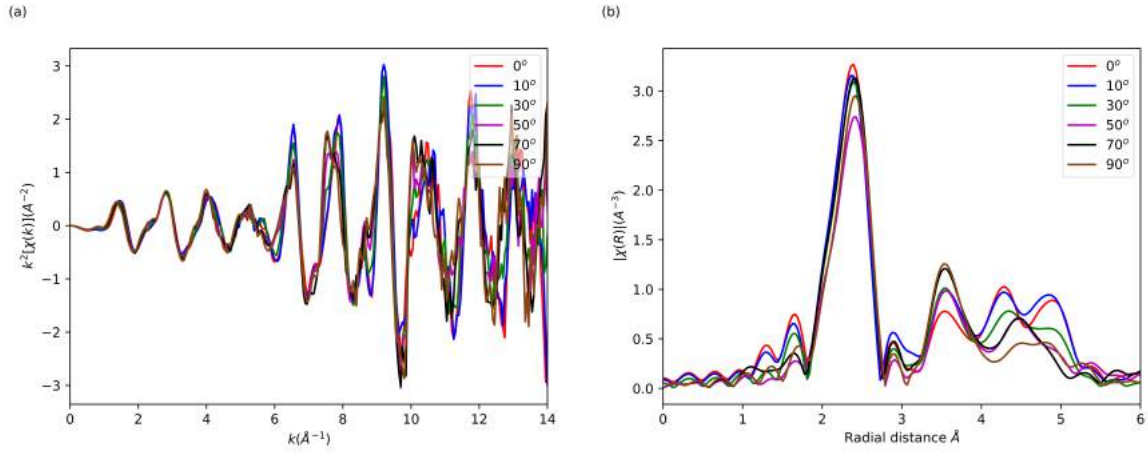

Figure B.3: EXAFS, (a), and Fourier transformed EXAFS, (b), of the Se K-edge, at 100K, of $Rb_2Mo_6Se_6$, at different angles.

B.1.3 Fits of EXAFS

The following plots display fits to the EXAFS and FT-EXAFS for the intermediate temperatures measured for the $Rb_2Mo_6Se_6$ sample. The fit is good for both temperatures, and displays the same small discrepancy at $7 - 9\text{Å}^{-1}$ in the k space, and the shoulder of the second peak in the FT-EXAFS.

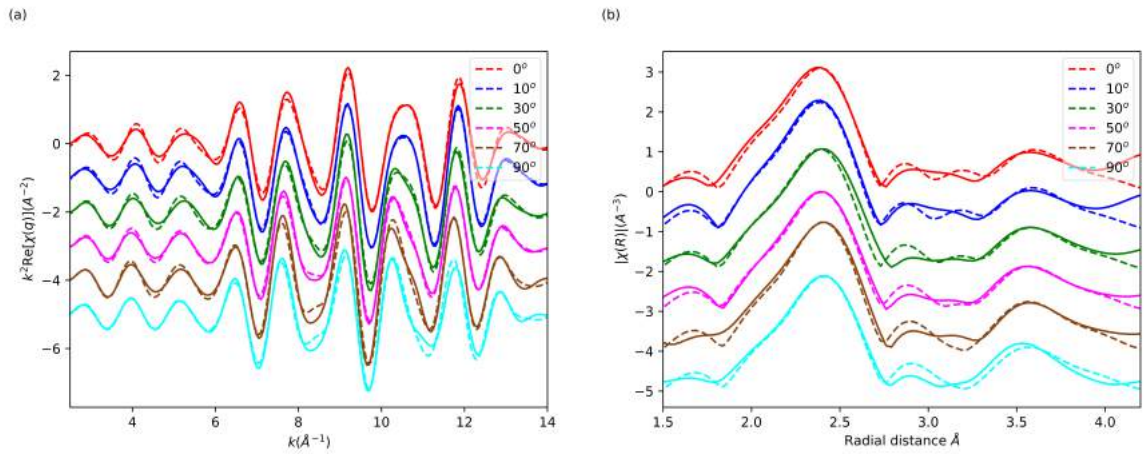

Figure B.4: Fit of the Se K-edge at 75K, in q space(a) and R space (b). All angles measured and fitted are presented in this plot. The solid line corresponds to the experimental data and the dashed line corresponds to the fit.

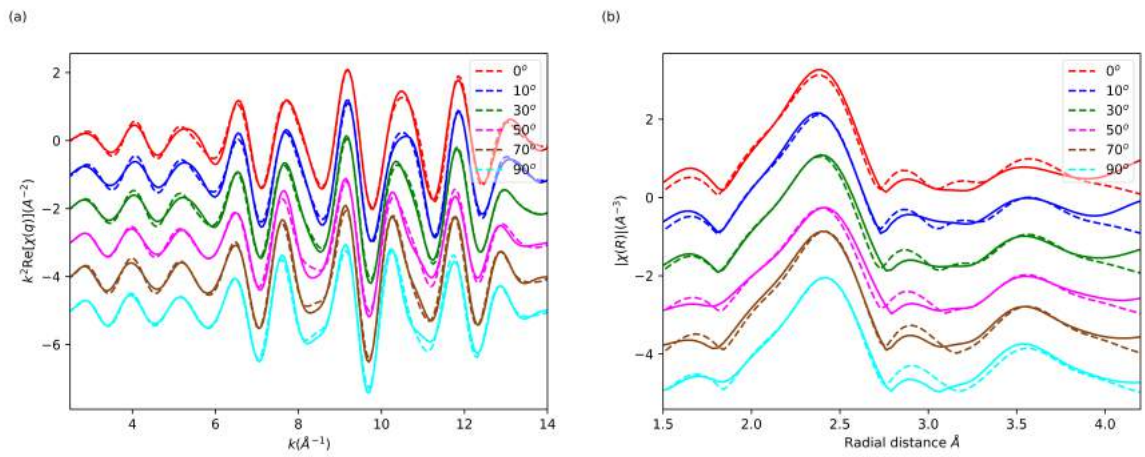

Figure B.5: Fit of the Se K-edge at 100K, in q space(a) and R space (b). All angles measured and fitted are presented in this plot. The solid line corresponds to the experimental data and the dashed line corresponds to the fit.

B.2 $Tl_2Mo_6Se_6$

B.2.1 XANES

The following plots display the XANES for the intermediate temperatures measured for the $Tl_2Mo_6Se_6$ sample. They show a similar trend with respect to the angle between the *c*-axis and the polarisation, where there is a higher intensity of the first peak for the measurement at 90°. The peak intensities show more grouping for the 8K data, while there is a more smooth transition for both the 75K and 100K data.

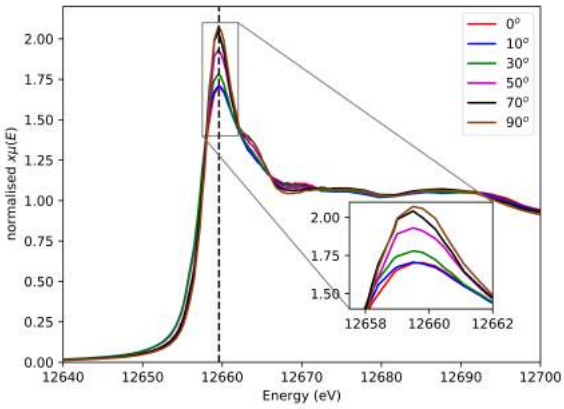

Figure B.6: XANES of the Se K-edge of $Tl_2Mo_6Se_6$, at 8K, at different angles.

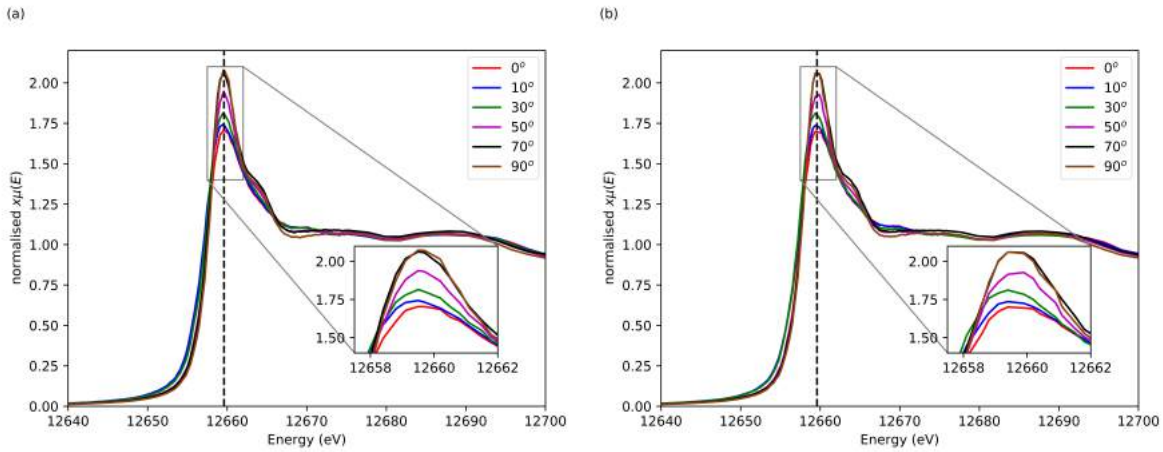

Figure B.7: XANES of the Se K-edge of $Tl_2Mo_6Se_6$, at 75K (a) and 100K (b), at different angles.

B.2.2 EXAFS

The following plots display the EXAFS and FT-EXAFS for the intermediate temperatures measured for the $Tl_2Mo_6Se_6$ sample. Both show a similar trend with respect to the angle between the *c*-axis and the polarisation. However the fourth peak in the FT-EXAFS at 75K show a similar intensity for all angles, while both the 8K and 100K data shows a decrease in intensity as the angle becomes larger.

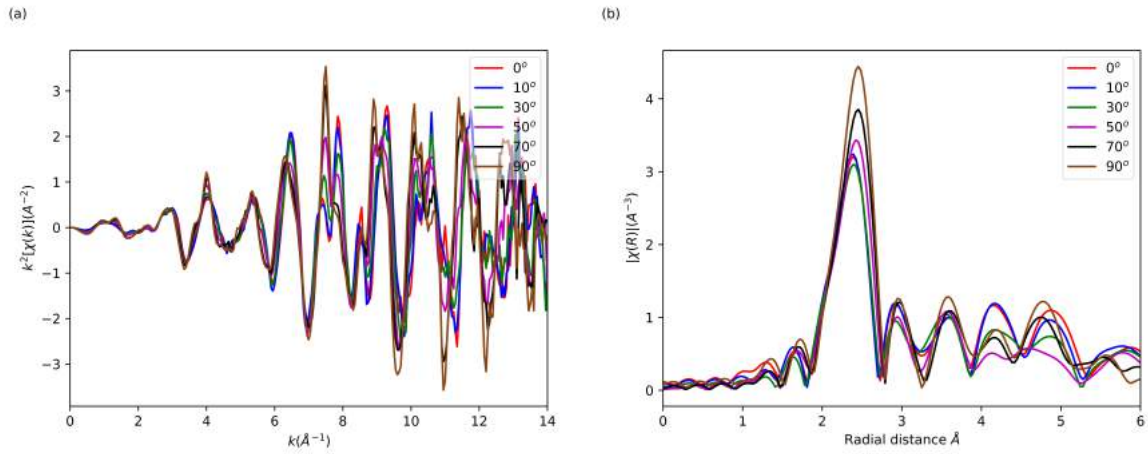

Figure B.8: EXAFS, (a), and Fourier transformed EXAFS, (b), of the Se K-edge, at 8K, of $Tl_2Mo_6Se_6$, at different angles.

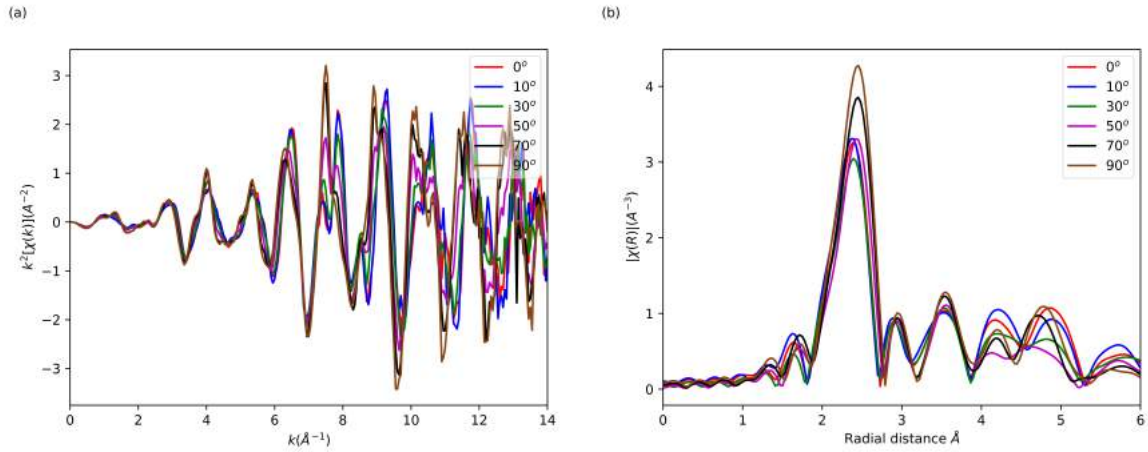

Figure B.9: EXAFS, (a), and Fourier transformed EXAFS, (b), of the Se K-edge, at 75K, of $Tl_2Mo_6Se_6$, at different angles.

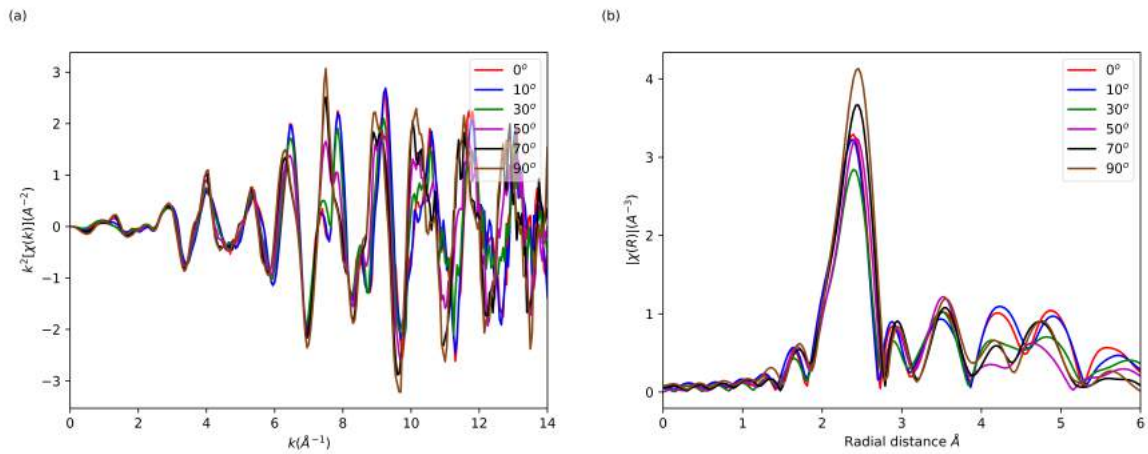

Figure B.10: EXAFS, (a), and Fourier transformed EXAFS, (b), of the Se K-edge, at 100K, of $Tl_2Mo_6Se_6$, at different angles.

B.2.3 Fits of EXAFS

The following plots display fits to the EXAFS and FT-EXAFS for the intermediate temperatures measured for the $Tl_2Mo_6Se_6$ sample. The fit is good for all temperatures, however there is a small discrepancy at $7 - 9\text{Å}^{-1}$ in the k space, and the second peak in the FT-EXAFS for the 8K data, at the shallower angles.

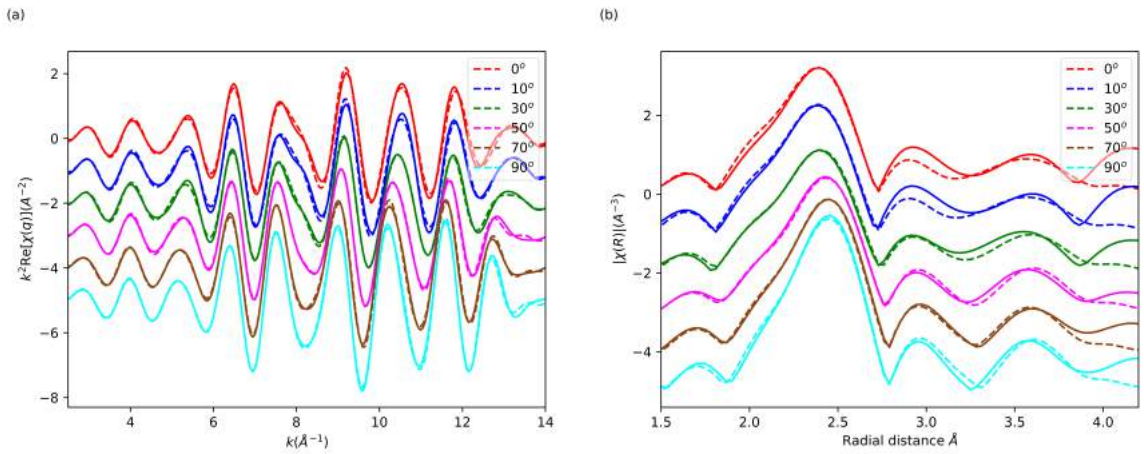

Figure B.11: Fit of the Se K-edge at 8K, in q space(a) and R space (b). All angles measured and fitted are presented in this plot. The solid line corresponds to the experimental data and the dashed line corresponds to the fit.

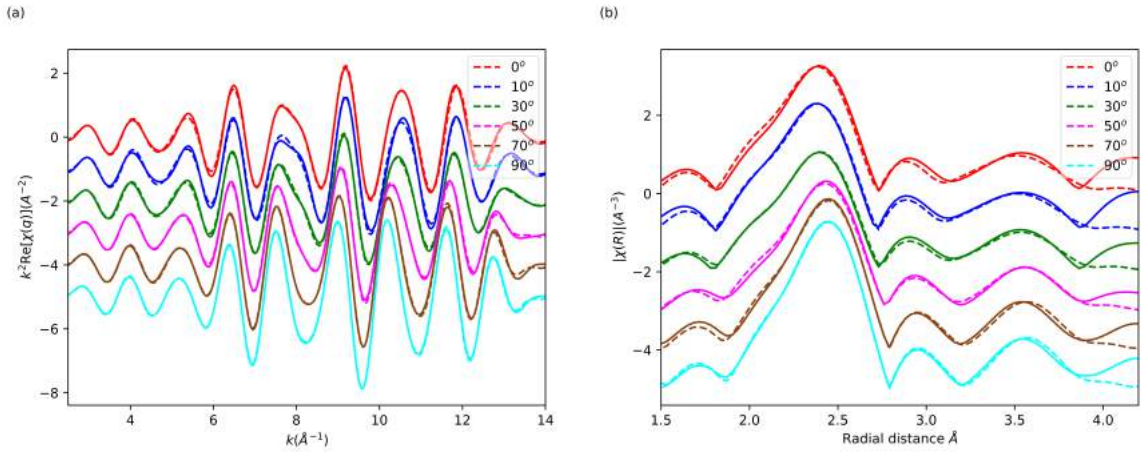

Figure B.12: Fit of the Se K-edge at 75K, in q space(a) and R space (b). All angles measured and fitted are presented in this plot. The solid line corresponds to the experimental data and the dashed line corresponds to the fit.

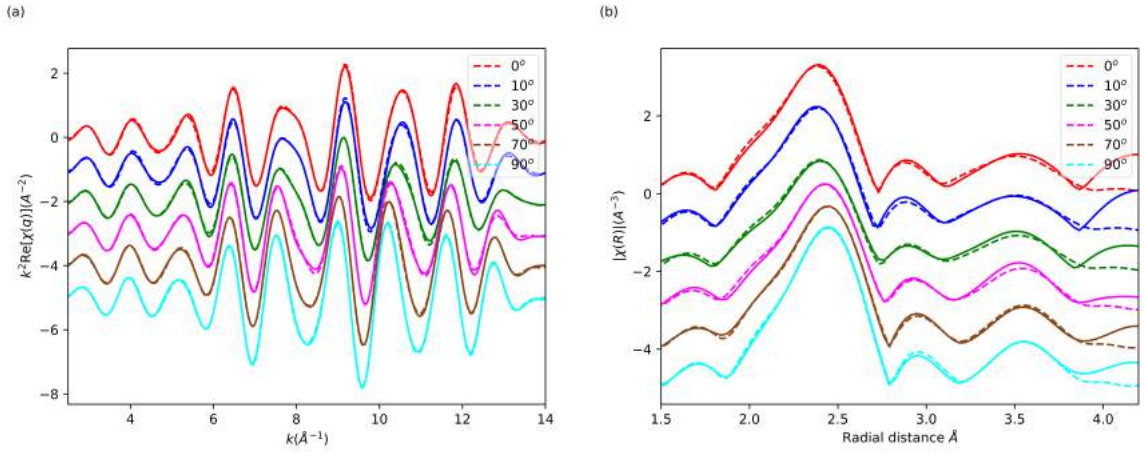

Figure B.13: Fit of the Se K-edge at 100K, in q space(a) and R space (b). All angles measured and fitted are presented in this plot. The solid line corresponds to the experimental data and the dashed line corresponds to the fit.